



Universidade de Aveiro

2021

Gidewon Goitom  
Tekeste

**Ensaios Híbridos em Tempo Real com Mesa Sísmica -  
Desenvolvimento e Aplicação à Interação Solo-Estrutura**

**Real-Time Hybrid Simulation including a Shaking Table -  
Development and Application to Soil-Structure Interaction**





Universidade de Aveiro

2021

Gidewon Goitom  
Tekeste

**Ensaios Híbridos em Tempo Real com Mesa Sísmica -  
Desenvolvimento e Aplicação à Interação Solo-Estrutura**

Tese apresentada à Universidade de Aveiro para cumprimento dos requisitos necessários à obtenção do grau de Doutor em Engenharia Civil, realizada sob a orientação científica do Doutor António Santos Carvalho Cabral Araújo Correia, Investigador Auxiliar do Laboratório Nacional de Engenharia Civil (LNEC) e coorientação científica do Doutor Aníbal Guimarães da Costa, Professor Catedrático do Departamento de Engenharia Civil da Universidade de Aveiro.





Universidade de Aveiro

2021

Gidewon Goitom  
Tekeste

**Real-Time Hybrid Simulation including a Shaking Table -  
Development and Application to Soil-Structure Interaction**

Thesis submitted to the University of Aveiro to fulfill the requirements for the degree of Doctor of Philosophy in Civil Engineering, under the scientific supervision of Doctor António Santos Carvalho Cabral Araújo Correia, Assistant Researcher at the National Laboratory for Civil Engineering (LNEC) and co-supervision of Doctor Aníbal Guimarães da Costa, Full Professor at the Department of Civil Engineering of the University of Aveiro.



I dedicate this work to my parents, for their unconditional support and love, and to my beloved wife, Yohanna, for giving me a lovely son, Eyoel. This work is also a tribute to my father who had no chance to see its end.



**the jury**

**president**

**Prof. Carlos Fernandes da Silva**  
Full professor at the University of Aveiro

**Prof. Oreste Salvatore Bursi**  
Full professor at the University of Trento

**Prof. Stathis Bousias**  
Full professor at the University of Patras

**Doctor Paulo Barreto Cachim**  
Associate professor at the University of Aveiro

**Doctor Hugo Filipe Pinheiro Rodrigues**  
Associate professor at the University of Aveiro

**Doctor António Santos Carvalho Cabral Araújo Correia**  
Assistant researcher at the National Laboratory for Civil Engineering (LNEC)



## **agradecimentos**

Esta tese marca o fim de um capítulo importante da minha vida, durante o qual me desafiei intelectual e profissionalmente. Mas, graças a Deus que continua a tornar o impossível possível, aprendi a abraçar os desafios e a exceder-me. No entanto, sem a ajuda e orientação do meu orientador, Dr. António Correia, os resultados alcançados nesta investigação não teriam sido possíveis. Assim, deixo-lhe os meus profundos agradecimentos pelo seu apoio incondicional e encorajamento ao longo do meu caminho de doutoramento. Estendo a minha profunda gratidão ao Dr. Alfredo Campos Costa e Dr. Paulo Candeias, do Laboratório Nacional de Engenharia Civil (LNEC), pelos seus apoios, disponibilidade para ajudar e por todas as discussões produtivas e troca de ideias que partilhámos. Aprendi com eles lições valiosas durante os últimos cinco anos. Devo também sinceros agradecimentos ao Prof. Aníbal Costa pelo seu apoio como coorientador e pelo disponibilidade de acesso ao equipamento do laboratório da Universidade de Aveiro.

Também estendo a minha palavra de agradecimento a todos os colegas e amigos do Núcleo de Engenharia Sísmica e Dinâmica de Estruturas (NESDE) do Departamento de Estruturas do LNEC. Deixo agradecimentos especiais à minha colega, Sanam Moghimi, por ser uma amiga solidária e motivadora tanto dentro e fora da academia. Agradeço também a outros colegas do LNEC, Vasco Bernardo, Dr. João André, Dr. Romain Sousa, Dr. Alexandra Carvalho e Dr. Filipe Ribeiro, pelos sentimentos de amizade e inclusão. Agradecimentos especiais ao Artur e ao Aurélia, técnicos de laboratório do NESDE, por me ajudarem sempre a encontrar a ferramenta certa para construir os setups de ensaio necessários para a parte experimental do trabalho aqui apresentado. Agradeço também ao Diretor do Departamento de Estruturas do LNEC, Dr. José Catarino, pelo seu apoio durante o meu percurso, e à Fátima Martins, secretária do NESDE, pela sua pronta disponibilidade para ajudar. Muitos agradecimentos também ao José Rocha, da BridgePoint, pelo apoio no desenvolvimento de um controlador digital para a mesa sísmica uniaxial do LNEC.

Agradeço calorosamente ao Dr. Giuseppe Abbiati, Professor Auxiliar da Universidade de Aarhus, pela sua colaboração e por me ter disponibilizado os dados dos seus ensaios híbridos, a partir dos quais validei os estudos de sensibilidade global realizados na tese. Gostaria de enviar uma palavra de agradecimento ao Dr. Hassan Fatemi, antigo aluno de doutoramento na Universidade de Sherbrooke, pela partilha dos seus códigos computacionais necessários para a execução de ensaios híbridos num ambiente LabVIEW. Gostaria também de agradecer sinceramente ao Conselho de Diretores do Programa Doutoral InfraRisk, pela organização de workshops para reforçar a colaboração entre os estudantes, professores e outros investigadores. Assim, gostaria de aproveitar esta oportunidade para agradecer a todos aqueles com quem me cruzei ao longo dos últimos cinco anos. Agradecimentos especiais ao Prof. Carlos Sousa Oliveira e à Prof. Rita Bento, pelas suas incansáveis orientação e encorajamento. Estou grato à Fundação para a Ciência e a Tecnologia (FCT), pelo financiamento da minha investigação de doutoramento através das bolsas PD/BI/113722/2015 e PD/BD/128305/2017.

Finalmente, gostaria de expressar a minha profunda gratidão à minha esposa, Yohanna, pelo seu apoio durante as minhas dificuldades e por me dar um filho adorável, Eyoel. Agradeço também aos meus pais, pelo seu amor incondicional, e aos meus irmãos e irmãs, por confiarem em mim.



## acknowledgments

This thesis marks the end of an important chapter of my life, during which I challenged myself intellectually and professionally. But, thanks to God the Divine who continues to make the impossible possible, I learned to embrace challenges and excel. Nevertheless, without the help and guidance of my supervisor, Dr. António Correia, the results achieved in this research would not have been possible. Thus, my heartfelt thanks to him, for his unconditional support and encouragement throughout my Ph.D. journey. I also extend my deepest gratitude to Dr. Alfredo Campos Costa and Dr. Paulo Candeias, from the National Laboratory for Civil Engineering (LNEC), for their support, willingness to help, all the productive discussions and exchange of ideas we shared. I learned valuable lessons from them over the past five years. I also owe thanks to Prof. Aníbal Costa for his support as co-supervisor and for providing access to the laboratory equipment of the University of Aveiro.

I extend my word of thanks to all colleagues and friends of the Earthquake Engineering and Structural Dynamics Unit (NESDE) of the Department of Structures of LNEC. Special thanks to my colleague, Sanam Moghimi, for being a supportive and motivational friend inside and outside of academia. I also thank other colleagues of LNEC, Vasco Bernardo, Dr. João André, Dr. Romain Sousa, Dr. Alexandra Carvalho, and Dr. Filipe Ribeiro, for showing me friendship and inclusiveness. Special thanks to Artur and Aurélio, lab technicians of NESDE, for always helping me to find the right tool to build setups necessary for the experimental part of the work presented herein. I also thank the Head of the Department of Structures of LNEC, Dr. José Catarino, for his support during my endeavors, and to Fátima Martins, secretary of NESDE, for her readiness to help. Many thanks also to José Rocha, from BridgePoint, for assisting me while developing a digital controller for LNEC's uniaxial shaking table.

I would like to extend my warmest thanks to Dr. Giuseppe Abbiati, Assistant Professor at the Aarhus University, for his collaboration and for making his hybrid test data available to me, from which I validated the global sensitivity studies performed in this thesis. I would like to send my word of thanks to Dr. Hassan Fatemi, former Ph.D. student at the Université de Sherbrooke, for sharing the codes necessary for executing hybrid simulation tests in a LabVIEW environment. I also want to sincerely thank the Board of Directors of the InfraRisk Doctoral Program, for arranging workshops to enhance the collaboration among the students, professors, and other researchers. Hence, I would like to take this chance to thank all with whom I crossed paths over the past five years. Special thanks to Prof. Carlos Sousa Oliveira and Prof. Rita Bento, for their relentless guidance and encouragement. I am indebted to the Fundação para a Ciência e a Tecnologia (FCT), for funding my Ph.D. research through the fellowships PD/BI/113722/2015 and PD/BD/128305/2017.

Finally, I would like to express my deepest gratitude to my wife, Yohanna, for her support during my hardships and for giving me a lovely child, Eyoel. I also thank my parents, for their unconditional love, and my brothers and sisters, for trusting in me.



## **palavras-chave**

Mesa sísmica; Ensaios híbridos; Análise de fiabilidade e sensibilidade; Interação solo-estrutura; Curvas de fragilidade; Atualização Bayesiana

## **resumo**

A humanidade testemunhou inúmeros eventos catastróficos devido a sismos, que destruíram cidades e importantes infraestruturas. Assim, um melhor entendimento do comportamento dinâmico das estruturas é muito importante para mitigar este problema. Ensaios em mesa sísmica são uma ferramenta excelente e fiável para simular experimentalmente a resposta dinâmica de estruturas. No entanto, ensaios à escala real de grandes estruturas são impraticáveis, senão impossíveis, em mesas sísmicas devido às limitações de tamanho, capacidade do atuador, custo do espécime a ensaiar e limitações e custos de outros equipamentos de laboratório. Atualmente, a utilização de programas e algoritmos muito sofisticados tem aumentado no campo da engenharia civil. Consequentemente, o uso de métodos numéricos para análise de estruturas submetidas a ações sísmicas, é a técnica com melhor custo-benefício, apesar das suas deficiências. No entanto, as abordagens numéricas, incluindo o método dos elementos finitos, podem falhar na simulação de modos complexos de rotura de estruturas, que podem ser locais ou globais. Por outro lado, os ensaios híbridos (ensaios de subestruturação) combinam as duas abordagens modelando fisicamente a parte mais complexa de uma estrutura, enquanto a parte restante é representada numericamente.

Nas últimas duas décadas, foi realizada uma quantidade substancial de investigação em ensaios híbridos e a técnica foi utilizada em diversas aplicações, tais como no desempenho sísmico de sistemas estruturais, dispositivos de dissipação de energia, isolamento sísmico e características termomecânicas de sistemas estruturais. No entanto, o potencial desta técnica de ensaios não foi esgotado. Por exemplo, a realização de ensaios com interação solo-estrutura (SSI) em ensaios híbridos não se encontra bem estudada até à data. Atualmente, o principal desafio na condução de ensaios SSI através de ensaios híbridos é a falta de algoritmos de controle robustos, necessários para satisfazer as condições de fronteira.

O objetivo desta tese é duplo. Primeiro, construir um enquadramento de software para ensaios híbridos no LNEC, o primeiro do seu género em Portugal. Em segundo lugar, utilizar resultados de ensaios em mesa sísmica na atualização de curvas de fragilidade de estruturas de betão armado. O primeiro objetivo engloba o desenvolvimento do enquadramento de software para a realização de ensaios híbridos com SSI em mesas sísmicas, bem como a realização de estudos globais de sensibilidade e fiabilidade. Um software flexível e modular para ensaios híbridos, denominado "*LNEC-HS*", que utiliza uma arquitetura de três ciclos, foi desenvolvido em LabVIEW. A concepção da máquina de estado deste software permite a inicialização, preparação, coordenação da simulação e tarefas de controlo de forma fácil e prática. Este software foi validado através da realização de ensaios híbridos de estruturas porticadas em aço. O software também permite a realização de ensaios híbridos com SSI em que uma mesa sísmica e um atuador adicional aplicam as condições de fronteira de uma subestrutura física. Assim, foram implementadas estratégias de controlo avançadas para o rastreio da aceleração em mesa sísmica e de controlo em força equivalente dos atuadores. Neste trabalho, foi realizado testes para ensaios híbridos que inclui os efeitos de SSI para apoiar a concepção de ensaios e para obter previamente a sensibilidade dos resultados a atingir.

Num outro desenvolvimento, foi adoptada a abordagem de ensaios híbridos simulados para testar a viabilidade dos ensaios híbridos para estudos de fiabilidade e sensibilidade global através do Multiplicative Dimensional Reduction Method (M-DRM). O método proposto foi estudado numericamente e validado utilizando ensaios híbridos realizados numa viga simplesmente apoiada. Os efeitos da instabilidade em ensaios híbridos foram também cuidadosamente avaliados e explorados num ambiente simulado. Consistentemente com um dos objectivos acima referidos, este trabalho também contribui para o desenvolvimento da atualização Bayesiana das curvas de fragilidade de pórticos em betão armado através de ensaios em mesa sísmica. Os métodos ATC-58 e Markov Chain Monte Carlo (MCMC) para a atualização Bayesiana foram examinados utilizando um ensaio em mesa sísmica realizado numa estrutura em betão armado.



**keywords**

Shaking table; Hybrid simulations; Reliability & sensitivity analysis; Soil-structure interaction; Fragility curves; Bayesian updating

**abstract**

Humankind has witnessed numerous catastrophic events due to earthquakes, which destroyed cities and important infrastructures. Thus, a better understanding of the dynamic behavior of structures is crucial for mitigating this problem. Shaking table tests are an excellent and reliable tool for experimentally simulating the dynamic response of structures. Nevertheless, full-scale tests of large structures are impractical, if not impossible, in shaking tables due to limitations in size, actuator capacity, cost of a test specimen, and other laboratory equipment. At present, the use of very sophisticated programs and algorithms has increased in the civil engineering field. Consequently, the use of numerical methods for analyzing structures subjected to seismic actions is the most cost-effective technique despite its shortcomings. However, numerical approaches, including finite element methods, may fail to capture complex modes of failure in structures, which can be local or global. On the other hand, hybrid simulation (substructuring test) blends the two approaches by analyzing the more complex part of a structure physically while the remaining part is represented in a numerical model.

In the last two decades, a substantial amount of research was conducted on hybrid simulations and the technique was used for several applications such as seismic performance of structural systems, energy dissipation devices, seismic isolation, and thermo-mechanical characteristics of structural systems. Nevertheless, the potential of this technique has not been exhausted. For example, conducting soil-structure interaction (SSI) tests in hybrid simulation is not fully exploited up to date. Currently, the main challenge of conducting SSI tests using hybrid simulations is the lack of robust control algorithms that are necessary to satisfy boundary conditions.

The objective of this thesis is twofold. First, to build a software framework for hybrid simulations at LNEC, the first of its kind in Portugal. Second, to use shaking table test results for updating fragility curves of RC structures. The first objective encompasses the development of the software framework towards conducting SSI hybrid tests in shaking tables as well as performing global sensitivity and reliability studies. Thus, a flexible and modular software framework for hybrid simulation, termed “*LNEC-HS*”, was developed in LabVIEW that adopts a three-loop architecture. The state-machine design of this software makes the initialization, preparation, simulation-coordination, and control tasks easy and manageable. This software was validated by performing hybrid tests of moment-resisting steel frames. The software can also perform SSI hybrid tests whereby a shaking table and an additional actuator apply the boundary conditions of a physical substructure. Thus, advanced control strategies for acceleration tracking of shaking tables and equivalent force control of actuators were implemented. Simulated hybrid tests that account for SSI effects were conducted in this work to assist in designing experiments and to obtain the sensitivity of test results beforehand.

In another development, the simulated hybrid test approach was adopted to make hybrid simulation tests viable for reliability and global sensitivity studies through a Multiplicative Dimensional Reduction Method (M-DRM). The proposed method was studied numerically and validated using hybrid tests conducted on a simply supported beam. The effects of instability in hybrid simulations were also carefully assessed and explored in a simulated environment. Consistently with one of the above objectives, this work also shed light on the Bayesian updating of RC frames' fragility curves through shaking table tests. The ATC-58 and Markov Chain Monte Carlo (MCMC) methods for Bayesian updating were examined using a shaking table test conducted on a RC structure.



*Research is to see what everybody else has seen, and to think what nobody else has thought.*

Albert Szent-Györgyi



## Table of contents

---

List of Figures .....	vii
List of Tables.....	xvii
List of Acronyms .....	xix
List of Symbols .....	xxii
1 Introduction .....	1
1.1 Motivation and research objectives.....	1
1.2 Shaking table testing of structures .....	5
1.3 History of hybrid simulation and its applications .....	6
1.4 Overview of dissertation .....	11
2 Literature Review on Hybrid Simulation .....	13
2.1 Introduction to hybrid simulation.....	13
2.2 Slow, fast, and hard real-time hybrid simulation .....	15
2.3 Approaches for conducting hybrid simulation.....	18
2.3.1 Displacement-based hybrid simulation.....	18
2.3.2 Force-based hybrid simulation.....	19
2.4 Framework for hybrid simulation .....	20
2.5 Time-stepping algorithms .....	23
2.5.1 Explicit integration scheme .....	24
2.5.1.1 Explicit Newmark method.....	25
2.5.1.2 CR integration algorithm .....	26
2.5.1.3 KR- $\alpha$ integration algorithm .....	28
2.5.2 Implicit integration scheme .....	29
2.5.2.1 Newmark hybrid simulation (NMHS) .....	30
2.5.3 Operator-splitting method.....	32
2.5.4 Accuracy and stability analysis of integration algorithms.....	34
2.5.4.1 Stability analysis.....	34
2.5.4.2 Accuracy analysis .....	36

2.6	Experimental errors .....	37
2.6.1	Error measurement and tracking indicators.....	41
2.7	Delay compensation algorithms .....	44
2.7.1	Feedforward compensation.....	46
2.7.2	Adaptive inverse compensation.....	49
2.7.3	Adaptive time series compensation.....	51
2.8	Control algorithms for hybrid simulation .....	55
2.8.1	Proportional-Integral-Derivative controller.....	56
2.8.2	Shaking table acceleration tracking.....	58
2.8.2.1	Optimal acceleration tracking via a feedforward-feedback controller.....	61
2.8.3	Force control of actuators .....	65
2.8.3.1	Equivalent force control through added compliance.....	67
2.8.4	Prediction-correction methods for actuator control.....	71
2.8.4.1	Conventional algorithm .....	72
2.8.4.2	Algorithm based on last predicted displacement .....	74
2.8.4.3	Algorithm based on trial velocity .....	75
2.8.5	Simultaneous control of an actuator and shaking table.....	77
2.9	Summary.....	78
3	Simulated Hybrid Testing of Structures-Applications .....	81
3.1	Introduction .....	81
3.2	Virtual Hybrid Simulation .....	84
3.2.1	VHS through OpenSees-OpenFresco framework.....	84
3.3	System identification of a uniaxial shaking table at LNEC.....	86
3.3.1	Modeling shaking table dynamics .....	87
3.3.2	Experimental identification of shaking table forces .....	88
3.3.2.1	Elastic force .....	89
3.3.2.2	Inertial force .....	91
3.3.2.3	Dissipative force .....	92
3.3.3	Identification of shaking table parameters .....	93
3.4	Choice of time-stepping algorithms for hybrid testing .....	96
3.4.1	Application to a steel frame structure .....	96

3.4.2	Results and discussions .....	98
3.5	Stability analysis of linear and nonlinear SDOF systems in hybrid tests....	103
3.5.1	Routh stability criterion for linear time-invariant systems.....	104
3.5.2	Application to linear SDOF systems.....	105
3.5.2.1	Results and discussions.....	106
3.5.3	Application to nonlinear SDOF systems.....	110
3.5.3.1	Results and discussions.....	111
3.6	Reliability and global sensitivity studies in hybrid simulation.....	113
3.6.1	Multiplicative Dimensional Reduction Method .....	113
3.6.2	Global sensitivity indices.....	113
3.6.3	Reproduction of full probabilistic distribution.....	116
3.6.4	Application to a steel frame structure.....	118
3.6.4.1	Choice of the Gauss-quadrature order.....	120
3.6.4.2	Results and discussions.....	124
3.6.5	Experimental validation of M-DRM in hybrid tests.....	136
3.6.5.1	Introduction.....	136
3.6.5.2	Case study structure.....	136
3.6.5.3	Global sensitivity analysis through Polynomial Chaos Expansion.....	138
3.6.5.4	Test setup.....	139
3.6.5.5	Global sensitivity analysis using M-DRM method .....	139
3.6.5.6	Results of M-DRM method and comparison with PCE-based GSA .....	140
3.7	Summary.....	143
4	Development and Validation of a Software Framework for Hybrid Simulation .....	147
4.1	Development of a software framework for hybrid simulation.....	147
4.1.1	OpenSees software framework .....	149
4.1.2	Middleware software.....	150
4.1.3	Simulation coordinator VI.....	151
4.1.4	FPGA VI.....	157
4.1.5	TCP/IP interface .....	160
4.1.6	Command generation and tracking .....	163
4.1.7	Delay compensation .....	165

4.1.8	Tracking indicator for hybrid testing .....	169
4.1.9	Data acquisition and transducers.....	170
4.2	Validation of LNEC-HS software through hybrid tests .....	171
4.2.1	Case study.....	171
4.2.2	Test setup .....	172
4.2.3	Rehearsal experiment for hybrid simulation .....	177
4.2.4	Hybrid test experiment.....	178
4.3	Advanced control strategies for substructuring in shaking table tests .....	180
4.3.1	Introduction.....	180
4.3.2	Robustness test of a feedforward-feedback controller.....	182
4.3.3	Equivalent force control through added compliance .....	188
4.3.3.1	Equivalent force control using the Smith Predictor compensator.....	189
4.3.3.2	Adaptive method for equivalent force control.....	197
4.4	Implementation of a middleware-free framework .....	198
4.4.1	Numerical simulation program .....	198
4.4.2	Implementation of advanced control algorithms.....	199
4.4.2.1	Feedforward-feedback controller.....	199
4.4.2.2	Displacement control of a shaking table with offline adaptation .....	201
4.4.2.3	Equivalent force control through added compliance.....	201
4.5	Summary.....	202
5	Soil-Structure Interaction Testing in Hybrid Simulation.....	205
5.1	Introduction .....	205
5.2	Numerical modelling of soil-structure interaction .....	208
5.2.1	Beam on Nonlinear Winkler Foundation.....	212
5.2.1.1	Mechanistic springs of the BNWF model.....	213
5.2.1.2	Performance evaluation of BNWF using experimental tests .....	215
5.2.2	Macro-element approach for soil-structure interaction analysis .....	218
5.3	Experimental methods for soil-structure interaction.....	222
5.3.1	Centrifuge and 1g shaking table tests.....	223
5.3.2	Hybrid testing.....	227
5.4	Hybrid simulation in shaking table tests — application to SSI .....	230

5.4.1	Hybrid simulation tests in a shaking table .....	230
5.4.2	Soil container in 1g shaking table tests .....	231
5.4.3	Pre-test identification and test setup .....	232
5.4.4	Rehearsal for soil-structure interaction test in hybrid simulation .....	233
5.4.4.1	Case study .....	234
5.4.4.2	Modeling .....	235
5.4.4.3	Results and discussions .....	241
5.4.5	Hybrid testing of soil-structure interaction using LNEC-HS .....	247
5.4.5.1	Modelling .....	247
5.4.5.2	Problem analysis .....	249
5.5	Summary .....	252
6	Bayesian Updating of RC Fragilities using Shaking Table Tests .....	255
6.1	Introduction .....	255
6.2	Fragility modeling .....	257
6.3	Bayesian framework for updating fragility curves .....	257
6.3.1	Introduction .....	257
6.3.2	Bayesian methods for updating fragilities of RC structures .....	258
6.3.2.1	Unscented transformation (UT) approach for Bayesian updating .....	258
6.3.2.2	Markov Chain Monte Carlo (MCMC) approach for Bayesian updating .....	260
6.4	Updating RC fragilities through sequential shaking table tests .....	264
6.4.1	Damage based equivalent input intensity .....	264
6.4.1.1	Parametric analysis .....	266
6.4.1.2	Results and discussion .....	270
6.4.2	Optimization of Bayesian updating using shaking table tests .....	276
6.4.2.1	The effect of experimental data before exceedance of a DS .....	276
6.4.2.2	The optimum size of experiments given all DSs are exceeded .....	277
6.5	Application case study .....	278
6.5.1	Two-story RC frame .....	278
6.5.2	Numerical modeling and generation of fragility curves .....	279
6.5.3	Experimental test .....	282
6.5.4	Bayesian updating of analytical fragilities .....	284

6.5.4.1	HAZUS damage states.....	285
6.5.4.2	Strain-based damage states.....	287
6.6	Summary.....	289
7	Conclusions and Future Works .....	291
7.1	Conclusions.....	291
7.2	Future works.....	296
	References.....	299
	Appendix-1 .....	319
	Appendix-2.....	320
	Appendix-3 .....	321
	Appendix-4 .....	329
	Appendix-5 .....	343
	Appendix-6 .....	344
	Appendix-7 .....	346

## List of Figures

---

Figure 1-1: Comparing observed (center) and hybrid test outputs (left and right) from the MISST project (after Spencer et al., 2006) .....	2
Figure 1-2: SSI in RTHS test: Benchmark test (left) and substructuring test (right) (after Dietz et al., 2015) .....	4
Figure 1-3: (a) Full-scale six-story reinforced concrete structure tested at E-Defense (after Kim et al., 2012); (b) In-plane and out-of-plane test of RC portal frame with masonry infill at LNEC (after Correia et al., 2015) .....	5
Figure 1-4: Pseudo-dynamic test of a two-degree of freedom structure (after Dermitzakis & Mahin, 1985) .....	7
Figure 1-5: Substructuring test of RC bridge subjected to vertical and horizontal earthquakes (after Kim et al., 2011) .....	9
Figure 2-1: Schematic diagram of a hybrid simulation (after Schellenberg et al., 2009) .....	13
Figure 2-2: Classification of hybrid simulation.....	15
Figure 2-3: Ramp-and-hold method (after Pegon, 2008).....	16
Figure 2-4: Continuous PSD scheme (after Pegon, 2008) .....	16
Figure 2-5: Displacement-based approach for hybrid simulation.....	19
Figure 2-6: Force-based approach for hybrid simulation.....	20
Figure 2-7: Two configurations of the NEES three-tier software architecture for hybrid simulation (after Schellenberg et al., 2009) .....	21
Figure 2-8: UI-SimCor architecture.....	22
Figure 2-9: Approximation of nonlinear resisting forces in Operator-splitting integration .....	33
Figure 2-10: Period elongation (PE): (a) Explicit NM and NMHS(INM2) algorithms (Schellenberg et al., 2009) and (b) KR- $\alpha$ and CR algorithms (Kolay & Ricles, 2014) .....	36
Figure 2-11: Numerical Damping: (a) Explicit NM and NMHS(INM2) algorithms (Schellenberg et al., 2009) and (b) KR- $\alpha$ and CR algorithms (Kolay & Ricles, 2014) .....	37
Figure 2-12: Block diagram of a hybrid simulation test .....	38
Figure 2-13: Critical time-delay of an actuator for a stable hybrid simulation test of a linear-elastic SDOF structure considering rate-dependent experimental substructure .....	40
Figure 2-14: Two-stage servo-valve: neutral position (left) and displaced position (right).....	41
Figure 2-15: Phase-lag of measured displacement (left) and sub-space synchronization plot (right) .....	42
Figure 2-16: Definition for tracking indicator (TI) .....	43
Figure 2-17: Third-order polynomial extrapolation .....	45
Figure 2-18: Block diagram of a feedforward controller.....	47
Figure 2-19: Feedforward control of MR damper using improper inverses constructed from BDM and CDM methods (after Phillips et al., 2014) .....	48
Figure 2-20: Actuator response under time-delay (after Chen & Ricles, 2010) .....	49
Figure 2-21: Input-output relationship for an actuator (after Chae et al., 2013) .....	52
Figure 2-22: Simulink block diagram for ATS compensator (adopted from Chae et al., 2013)....	54
Figure 2-23:PID controller .....	56

Figure 2-24: Block diagram of acceleration trajectory tracking control (after Nakata, 2010).....	60
Figure 2-25: Block diagram of a feedforward-feedback controller (after Phillips & Spencer, 2012) .....	60
Figure 2-26: Model-based feedforward-feedback controller for acceleration tracking of a shaking table (after Phillips et al., 2014) .....	61
Figure 2-27: Optimal observer (Kalman filter).....	63
Figure 2-28: OpenFresco UML class diagram for computing tangent stiffness of an experimental element (after Kim, 2011).....	67
Figure 2-29: Dynamic force control using added compliance technique: physical model (top) and block diagram(bottom) (after Sivaselvan et al., 2008).....	68
Figure 2-30: Smith Predictor compensation(after Sivaselvan et al., 2008) .....	69
Figure 2-31: Block diagram of D-ATS (after Chae et al., 2018).....	70
Figure 2-32: Block diagram of F-ATS (after Chae et al., 2018).....	70
Figure 2-33: Sequence of execution in the predictor-corrector approach for synchronizing numerical integration and command generation (modified from Schellenberg et al., 2009).....	71
Figure 2-34: Velocity at switching interval of an extrapolation-interpolation algorithm (after Nakashima & Masaoka, 1999).....	73
Figure 2-35: Algorithm based on last predicted displacement(modified from Schellenberg et al., 2009) .....	74
Figure 2-36: Flow diagram for hybrid testing using a shaking table and an auxiliary actuator when added compliance force control, based on Smith Predictor compensation, is adopted to control the auxiliary actuator (after Shao et al., 2012).....	77
Figure 3-1: ExpSignalFilter object of the OpenFresco software .....	85
Figure 3-2: Uniaxial shaking table at LNEC .....	86
Figure 3-3: Schematic diagram of a shaking table system .....	87
Figure 3-4: Estimation of elastic force using a triangular input displacement.....	90
Figure 3-5: Elastic force estimates from T6 (right) and T5 (left) experiments .....	90
Figure 3-6: Mass estimation using sinusoidal input displacement .....	91
Figure 3-7: Effective horizontal mass estimates of LNEC's uniaxial shaking table .....	92
Figure 3-8: Choice of samples for estimating dissipative force: T6 test .....	93
Figure 3-9: Curve fitting of LNEC's uniaxial shaking table dissipative force .....	93
Figure 3-10: Curve fitting of the LNEC's uniaxial shaking table transfer function.....	94
Figure 3-11: Curve fitting of time-delay (left) and validation of the estimated model of LNEC's uniaxial shaking table (right) .....	95
Figure 3-12: Control-structure interaction of LNEC's uniaxial shaking table .....	95
Figure 3-13: Steel portal frame case study.....	96
Figure 3-14 Energy plot of the steel portal frame, using the $\alpha$ -OS integration, without experimental errors, subjected to Kobe earthquake scaled to 1.642 g PGA (left) and El Centro earthquake scaled to 0.478 g PGA (middle); and norm L2 of $P_{eff}$ (right) .....	98
Figure 3-15: Lateral displacement and EEI of the steel portal frame subjected to the El Centro earthquake scaled to 0.478 g PGA (top row) and Kobe earthquake scaled to 1.642 g PGA (bottom row) .....	99

Figure 3-16: Lateral displacement and EEI of the steel portal frame subjected to the El Centro (top row) and Kobe (bottom row) earthquakes.....	100
Figure 3-17: EEI of the steel portal frame using $\alpha$ -OS and NMHS methods: subjected to the El Centro (left column) and Kobe (right column) earthquakes .....	101
Figure 3-18: Lateral displacement and EEI of the steel portal frame, for various $\Delta t$ of analysis, subjected to the El Centro (top row) and Kobe (bottom row) earthquakes.....	101
Figure 3-19: (a) Lateral displacement of the steel portal frame; (b) $\Delta EEI$ ; (c) NRMSE of displacement and restoring force.....	102
Figure 3-20: EEI of the steel portal frame, considering undershoot and overshoot experimental errors, subjected to El Centro (right) and Kobe (left) earthquakes.....	103
Figure 3-21: Schematic diagram of a substructuring test in a shaking table.....	105
Figure 3-22: Hypothetical test setup of a SDOF structure in hybrid simulation .....	106
Figure 3-23: Stability contours of stiffness versus damping at constant $M_{exp}/M_{SDOF}$ .....	106
Figure 3-24: Stability contours of stiffness versus damping at $M_{exp}/M_{SDOF} = 20\%$ .....	107
Figure 3-25: Validation of the Routh's stability test for stiffness versus damping contour at $M_{exp}/M_{SDOF} = 20\%$ .....	108
Figure 3-26: Stability contours of mass versus damping at constant $K_{exp}/K_{SDOF}$ .....	108
Figure 3-27: Stability contours plot of mass versus damping at $K_{exp}/K_{SDOF} = 20\%$ .....	109
Figure 3-28: Validation of Routh's stability test for mass versus damping at $K_{exp}/K_{SDOF} = 20\%$ .109	109
Figure 3-29: Stability contour of mass versus damping for all $C_{exp}/C_{SDOF}$ but 100% .....	110
Figure 3-30: Idealization of the Bouc-Wen model.....	110
Figure 3-31: Simulink model for a simulated hybrid test of an inelastic SDOF structure using the Bouc-Wen hysteresis to model the experimental substructure .....	111
Figure 3-32: Comparing the stability of hybrid simulations of elastic and inelastic structures: displacement plot (left) and hysteresis plot (right) .....	112
Figure 3-33: The effect of the degree of inelasticity of an experimental element in the stability of a hybrid test.....	112
Figure 3-34: Steel frame structure and its column properties .....	119
Figure 3-35: (a) First-order and total sensitivity indices versus the number of integration points for the PGA1-CV1 scenario; (b) first-order sensitivity indices of the maximum drift response by changing the CV of input variables and the PGA of the input motion.....	121
Figure 3-36: Relative error quantities versus the number of integration points for the PGA1-CV3 scenario.....	121
Figure 3-37: Relative error quantities versus the number of integration points for the PGA3-CV3 scenario.....	122
Figure 3-38: Comparison of PDFs estimated by the M-DRM and MCS methods for the PGA1-CV3 scenario.....	123
Figure 3-39: First-order sensitivity indices of the maximum drift response considering the El Centro earthquake input.....	124
Figure 3-40: First-order sensitivity indices of the maximum drift response considering the Kobe earthquake input.....	125

Figure 3-41: First-order sensitivity of the maximum shear force of the experimental column considering the El Centro earthquake input.....	125
Figure 3-42: First-order sensitivity indices of the maximum roof acceleration considering the El Centro earthquake input .....	126
Figure 3-43: PDFs of the maximum drift estimated by the MCS, assumed-lognormal, and M-DRM methods for the PGA3-CV3 scenario considering the El Centro earthquake input.....	127
Figure 3-44: POE and CDF of the maximum drift for the PGA3-CV3 scenario considering the El Centro earthquake input .....	128
Figure 3-45: PDFs of the maximum shear force of the experimental column estimated by the MCS, assumed-lognormal and M-DRM (left); and POE of the total shear demand (right) for the PGA3-CV3 scenario considering the El Centro earthquake input .....	129
Figure 3-46: POE and CDF of the maximum shear force of the experimental column for the PGA3-CV3 scenario considering the El Centro earthquake input .....	129
Figure 3-47: PDFs of the maximum drift, at $\xi=5\%$ , $CV_\xi=20\%$ and $CV_k=5\%$ , considering the Northridge earthquake, scaled to 0.471 g PGA, estimated by the MCS, assumed-lognormal and M-DRM methods (left); and the hysteresis of the experimental column at the median values of the RVs (right).....	130
Figure 3-48: PDFs of the maximum shear force of the experimental column, at $\xi=5\%$ and $CV_\xi=20\%$ , $CV_k=5\%$ , considering the Northridge earthquake input, scaled to 0.471 g PGA, estimated by the MCS, assumed-lognormal and M-DRM methods (left); and POE and CDF estimates (right) ....	131
Figure 3-49: POE and CDF of the maximum lateral displacement at $\xi=5\%$ , $CV_\xi=20\%$ and $CV_k=5\%$ considering the Northridge earthquake input scaled to 0.471 g PGA .....	132
Figure 3-50: Global sensitivity indices of the steel frame at $CV_k=5\%$ , $CV_\xi=10\%$ and $CV_{f_y}=10\%$ considering the El Centro earthquake input.....	133
Figure 3-51: PDFs of the maximum drift (right) and maximum shear force (left ) estimated by the MCS, assumed-lognormal; and M-DRM methods considering the unscaled El Centro earthquake input motion .....	134
Figure 3-52: POE and CDF estimates of the total shear demand considering the unscaled El Centro earthquake input motion.....	135
Figure 3-53: Substructuring the prototype structure into physical (PS) and numerical (NS) parts (after Abbiati et al., 2020).....	137
Figure 3-54: Spectral acceleration of the velocity-pulse function .....	138
Figure 3-55: Test rig and software architecture for hybrid testing (after Abbiati et al., 2020) .....	139
Figure 3-56: Comparison between measured and M-DRM estimates of $u_{1,max}$ and $r_{1,max}$ responses .....	140
Figure 3-57: Convergence of the mean and variance estimates of $u_{1,max}$ with increasing number of hybrid tests .....	141
Figure 3-58: Convergence of mean and variance estimates of $r_{1,max}$ with increasing number of hybrid tests .....	141
Figure 3-59: <i>SI</i> and <i>TSI</i> estimates of $u_{1,max}$ .....	142
Figure 3-60: <i>SI</i> and <i>TSI</i> estimates of $r_{1,max}$ .....	142

Figure 3-61: Comparing PDFs fitted to the univariate and bivariate M-DRM estimates against the PDF fitted to the measured responses .....	143
Figure 4-1: Three-loop architecture framework for hybrid simulation.....	147
Figure 4-2: Graphical user interface (GUI) of LNEC-HS software framework .....	151
Figure 4-3: Schematic diagram of the middleware-based scheme of LNEC-HS software.....	153
Figure 4-4: Schematic diagram of the middleware-free scheme of LNEC-HS software .....	156
Figure 4-5: PID control loop at the FPGA VI.....	158
Figure 4-6: Tuning the ST1D's PID controller .....	158
Figure 4-7: Characterization signal of the ST1D .....	159
Figure 4-8: Frequency response function of the ST1D (after replacing the ST1D's analog controller by the NI PXI-7841R digital controller).....	159
Figure 4-9: <i>LNTCP</i> dataflow .....	160
Figure 4-10: Implementation of the replier loop of the <i>LNTCP</i> for interfacing with the OpenFresco framework .....	162
Figure 4-11: Schematic representation of dataflow in LNEC-HS software.....	163
Figure 4-12: Implementation of the prediction loop of the simulation coordinator VI .....	164
Figure 4-13: Implementation of the correction loop in the simulation coordinator VI.....	165
Figure 4-14: Implementation of the Adaptive Time Series (ATS) compensator in the simulation coordinator VI.....	166
Figure 4-15: Magnitude of $G_{ATS}$ without gain error.....	169
Figure 4-16: Magnitude of $G_{ATS}$ in the presence of gain error for a time-step of 4 ms.....	169
Figure 4-17: Transducers and data acquisition hardware for hybrid simulation.....	170
Figure 4-18: Calibration of transducers .....	171
Figure 4-19: Implementation of data acquisition loop in the simulation coordinator VI .....	171
Figure 4-20: Case study structure for validating LNEC-HS software.....	172
Figure 4-21: Schematic of setup for hybrid simulation .....	173
Figure 4-22: Identification of gaps in the test setup (left); and displacement of the experimental column versus displacement of ST1D (right) .....	173
Figure 4-23: Modal identification of the experimental substructure using impulsive excitation (hammer test).....	174
Figure 4-24: Column identification using Canonical Variate Analysis (left); and modeling the semi-rigid base connection of the experimental setup (right).....	175
Figure 4-25: Quad-linear stress-strain curve for hot-rolled steel (Yun & Gardner, 2017).....	176
Figure 4-26: Command versus measured displacement of the ST1D subjected to the WGN input (left) and a closer view on the time-delay, $\delta_{err}$ ; and the gain error, $G_{err}$ (right) .....	177
Figure 4-27: Comparing roof displacements between open-loop hybrid test and purely numerical analysis of the case study structure (left); and identification of control errors in the open-loop hybrid test (right) .....	178
Figure 4-28: Comparing roof displacement between the actual hybrid test and the purely numerical analysis of the case study structure (left); and hysteresis loop (right).....	179

Figure 4-29: Comparing the Fourier amplitude of the roof displacement between the actual hybrid testing and the purely numerical analysis (left); and error in restoring force obtained by comparing the numerical and measured forces (right) .....	179
Figure 4-30: Transfer function of the uniaxial shaking table at the University of Illinois when rigidly attached to a two-story shear building (from Phillips et al., 2014) .....	182
Figure 4-31: Performance of the LQG controller when $R_{LQR}=10^{14}$ and $R_{Kal}=0.1$ .....	185
Figure 4-32: The performance of LQG controller when $Q_{Kal}$ is a unit matrix .....	185
Figure 4-33: Acceleration tracking of a feedforward-feedback controller applied to a nonlinear structure in a substructuring test using a shaking table .....	186
Figure 4-34: Target versus measured acceleration during a shaking table test of a two-story shear building using a feedforward-feedback controller: Intact structure (top) and damaged structure (bottom) .....	187
Figure 4-35: Performance of acceleration tracking of the LQG controller as a function of the number of feedback corrections: $\Delta t_{sim}=10$ ms (top) and $\Delta t_{sim}=100$ ms (bottom) .....	187
Figure 4-36: Equivalent force control of a SDOF structure using added compliance .....	189
Figure 4-37: Schematic diagram of the equivalent force control of a SDOF structure through the Smith Predictor compensator .....	190
Figure 4-38: Performance of equivalent force control using Smith Predictor compensation (left) and its robustness to model deviations (right) .....	191
Figure 4-39: Performance of the equivalent force control, using the Smith Predictor compensation, to erroneous modeling of the experimental substructure .....	192
Figure 4-40: Performance of the equivalent force control, using the Smith Predictor compensation, to erroneous modeling of the load transfer system .....	193
Figure 4-41: Performance of the equivalent force control, using the Smith Predictor compensation, as a function of the flexibility of the compliance spring .....	193
Figure 4-42: Substructuring test with the lower part of a shear building as the physical part .....	194
Figure 4-43: Simulink block diagram for a simulated hybrid test of a two-story shear building including the equivalent force control based on the Smith Predictor controller .....	195
Figure 4-44: Ground motion suite and scaling .....	196
Figure 4-45: Top displacement of the shear building subjected to Kobe (1995) earthquake .....	196
Figure 4-46: NRMSE of structural responses in substructuring tests involving the equivalent force control of actuator, with and without the Smith Predictor compensation .....	197
Figure 4-47: Newmark-based numerical program for linear-elastic MDOF shear building structures .....	199
Figure 4-48: Implementation of acceleration tracking using a feedforward-feedback controller .....	200
Figure 4-49: Implementation of a feedback control using Linear Quadratic Gaussian controller .....	200
Figure 4-50: Implementation of equivalent force control using the Adaptive Time-Series (ATS) compensator .....	202
Figure 5-1: Soil-structure interaction of a SDOF structure (after Correia, 2011) .....	206
Figure 5-2: Period elongation and damping ratios of a SDOF structure taking $v=0.4$ and $m=0.15$ (after Veletsos & Nair, 1975) .....	207

Figure 5-3: Effect of soil-structure interaction in the base shear of a structure (adopted from NIST, 2012) .....	208
Figure 5-4: Direct approach for analyzing soil-structure interaction effects (adopted from NIST, 2012) .....	209
Figure 5-5: Substructure approach for analyzing soil-structure interaction effects (adopted from NIST, 2012) .....	210
Figure 5-6: Coefficients for dynamic stiffness and damping for arbitrarily shaped shallow foundations on homogenous half-space (after Gazetas, 1991) .....	211
Figure 5-7: Spring-dashpot-mass model for a rocking footing (after Correia, 2011).....	212
Figure 5-8: Implementation of the Beam on Nonlinear Winkler Foundation (BNWF) model in the OpenSees software (after Raychowdhury & Hutchinson, 2009).....	213
Figure 5-9: Conceptual diagram for mechanistic springs of the BNWF model (after Boulanger et al., 1999) .....	214
Figure 5-10: Cyclic response of the <i>QzSimple2</i> , <i>PxSimple1</i> , and <i>TxSimple1</i> materials (after Raychowdhury & Hutchinson, 2009).....	215
Figure 5-11: Dynamic testing of a shear wall resting on a strip footing, reference to SSG04-06 experiment (Gajan et al., 2003a): (a) prototype; (b) numerical modeling using the BNWF approach; (c) experimental versus numerically obtained responses; (d) moment-rotation plot (top) and settlement-rotation plot (bottom) (after Raychowdhury & Hutchinson, 2009) .....	217
Figure 5-12: Dynamic testing of a bridge column supported on a square foundation, reference to JAU01-E08 experiment (Ugalde et al., 2007): (a) Test setup and instrumentation; (b) numerical modeling using the BNWF approach; (c) experimental versus numerically obtained responses; (d) moment-rotation plot (top) and settlement-rotation plot (bottom) (after Raychowdhury & Hutchinson, 2009) .....	218
Figure 5-13: Macro-element approach for modeling soil-structure interaction (after Chatzigogos et al., 2009) .....	219
Figure 5-14: (a) Rheological model for macro-element method; (b) $Q_N$ - $Q_V$ plane; (c) $Q_N$ - $Q_M$ plane (after Chatzigogos et al., 2009).....	220
Figure 5-15: Bounding surface for the hypoplastic model in the macro-element modeling (after Chatzigogos et al., 2009) .....	221
Figure 5-16: CAMUS IV test setup and moment-rotation response (from CEA, 2000) .....	223
Figure 5-17: Centrifuge test of a mixed steel-concrete structure, at UC Davis, subjected to a dynamic base input scaled to 0.65 g PGA (after Chang et al., 2007) .....	224
Figure 5-18: Centrifuge test of a shear wall structure, at UC Davis, under static cyclic and dynamic loadings (shows the results of SSG02 experiment) (after Gajan et al., 2005) .....	225
Figure 5-19: Restrained rocking and balanced design approaches for a steel frame in centrifuge tests at UC Davis (after Liu et al., 2013).....	225
Figure 5-20: TRISEE test: Test rig (left) and results of phase III of the test (right) (after Faccioli et al., 1998) .....	226
Figure 5-21: 1g shaking table tests of a pier model, at the PWRI laboratory: Test rig (left) and pressure distribution under Kobe (1995) earthquake input, scaled to 0.568 g PGA (right) (after Shirato et al., 2008) .....	226

Figure 5-22: Multi-Site Soil-Structure-Foundation Interaction Test (MISSIT) (adopted from Saouma & Sivaselvan, 2008).....	228
Figure 5-23: Hybrid simulation involving a physical model for soil-structure interaction (after Stefanaki et al., 2015) .....	229
Figure 5-24: Idealization of a test rig for soil-structure interaction test in hybrid simulation .....	230
Figure 5-25: Idealization of a soil-container assembly as a SDOF in a shaking table test .....	232
Figure 5-26: Transfer functions from the displacement command to the measured displacement and acceleration of the ST1D that is attached to a laminar box filled with dry sandy soil (SP-49 type) .....	233
Figure 5-27: Details of the Collector-Distributor 36 under-crossing, Los Angeles, USA .....	234
Figure 5-28: Damage of pier-1 (leftmost pier) of the Collector-Distributor 36 during the Northridge (1994) earthquake (after Spencer et al., 2006).....	235
Figure 5-29: Substructuring scheme.....	236
Figure 5-30: Hypothetical test rig for laboratory testing of SSI in hybrid simulation.....	236
Figure 5-31: Experimental two-node link element ( <i>EETwoNodeLink</i> ) of the OpenFresco framework (after Schellenberg et al., 2009) .....	238
Figure 5-32: Data exchange in finite-element coupling approach of the OpenFresco framework (after Schellenberg et al., 2019) .....	239
Figure 5-33: Spectral accelerations of the Northridge (1994) earthquake recorded at two different stations.....	240
Figure 5-34: Capacity curves of the Collector-Distributor 36 under-crossing considering different boundary conditions and classes of the foundation soil .....	241
Figure 5-35: Capacity curves from monolithic and substructured modeling approaches.....	242
Figure 5-36: The response of the bridge that is founded on the SP-49 sand; and subjected to the Northridge (1994) earthquake, recorded at the Santa Monica City Hall station, scaled to 0.55 g PGA: (a) Pier-1 responses; (b) F- $\delta$ plot; (c) M- $\theta$ plot of the bridge footings.....	243
Figure 5-37: Rotation-settlement plot of the bridge's foundation.....	244
Figure 5-38: Input ground motion for evaluating the complete response of the bridge.....	244
Figure 5-39: The response of the bridge that is founded on the SP-49 sand; and subjected to the Northridge (1994) earthquake, recorded at the Santa Monica City Hall station, scaled to 0.55 g PGA, followed by the unscaled Northridge earthquake, recorded at the New Hall Fire Station, 0.58 g PGA: (a) Pier-1 responses; (b) F- $\delta$ plot; (c) M- $\theta$ plot of the bridge footings .....	245
Figure 5-40: Rotation-settlement plot of the bridge's foundation.....	245
Figure 5-41: The response of the bridge that is founded on class C type of clayey soil; and subjected to Northridge (1994) earthquake, recorded at the Santa Monica City Hall station, scaled to 0.55 g PGA, followed by the unscaled Northridge earthquake recorded at the New Hall Fire Station, 0.58 g PGA: F- $\delta$ plot (left) and M- $\theta$ plot of the bridge footings (right).....	246
Figure 5-42: Vertical displacement of the bridge foundation.....	246
Figure 5-43: Rotation-settlement plot of the bridge foundation .....	247
Figure 5-44: Test setup for a soil-structure interaction test in hybrid simulation .....	248
Figure 5-45: Idealization of test setup.....	250
Figure 5-46: Transfer function from target acceleration to foundation input motion .....	250

Figure 5-47: Power spectral density of acceleration responses .....	251
Figure 5-48: (a) Lateral displacement of the two-story shear building subjected to Kobe earthquake, scale to $Sa(T_1)=0.05$ g; (b) hysteresis plot.....	251
Figure 6-1: (a) Burn-in; (b) autocorrelation function before and after thinning.....	264
Figure 6-2: (a) 5-stage input acceleration for a sequential analysis (bottom) and non-sequential analysis (top); (b) Hysteretic response of a cantilever column ( $f_1=3$ Hz; 3 <sup>rd</sup> stage) .....	267
Figure 6-3: Structures considered for damage-based equivalent intensity measure .....	268
Figure 6-4: Capacity curves: (a) Cantilever RC column and (b) Portal RC frame .....	269
Figure 6-5: Spectral acceleration of unscaled earthquakes.....	270
Figure 6-6: DI versus maximum drift plot of the RC cantilever column: (a) <i>Non-sequential</i> analysis and (b) <i>Sequential</i> analysis .....	271
Figure 6-7: DI versus maximum drift plot of the RC portal frame: (a) <i>Non-sequential</i> analysis and (b) <i>Sequential</i> analysis .....	271
Figure 6-8: DI versus $Sa(T_1)$ of the RC cantilever column: (a) $f=1$ Hz, (b) $f=2$ Hz and (c) $f=3$ Hz .....	272
Figure 6-9: DI versus $Sa(T_1)$ of RC portal frame: (a) $f=2$ Hz, (b) $f=3$ Hz and (c) $f=5$ Hz .....	272
Figure 6-10: Logarithmic fitting: a) cantilever RC column and (b) RC portal frame.....	273
Figure 6-11: Damage index ratio: (a) cantilever RC column and (b) RC portal frame .....	274
Figure 6-12: Validation of $Sa(T_1)_{eq}$ for the RC column: (a) $f=1$ Hz, (b) $f=2$ Hz and (c) $f=3$ Hz .....	274
Figure 6-13: Validation of $Sa(T_1)_{eq}$ for Portal frame: (a) $f=2$ Hz, (b) $f=3$ Hz and (c) $f=5$ Hz .....	275
Figure 6-14: Validation of DI ratio: cantilever RC column (left) and RC portal frame (right) .....	275
Figure 6-15: Effect of experiments before exceedance of a particular DS: (a) Data for Bayesian update, (b) Posterior value of median and (c) Posterior value of $\beta$ .....	276
Figure 6-16: Optimum size of experiments for updating fragility curves: (a) Data for Bayesian update, (b) Posterior value of median and (c) Posterior value of $\beta$ .....	277
Figure 6-17: 2D RC frame tested under the Teixeira Duarte Award .....	279
Figure 6-18: Numerical modeling in Seismostruct.....	280
Figure 6-19: First-story IDA capacity curves.....	280
Figure 6-20: First-story IDA capacity curves for PGA, PGV, ASA <sub>20</sub> , and ASA <sub>40</sub> .....	281
Figure 6-21: Median value of $ISD_{max}$ for observable damages .....	282
Figure 6-22: Test setup: (a) Mounting RC frame and (b) Mounting the guidance structure .....	282
Figure 6-23: Tensile tests of steel reinforcement .....	283
Figure 6-24: (a) Input spectra; (b) Performance of shaking table controller at stage-5 .....	283
Figure 6-25: Evolution of frequencies during the stages of the shaking table test .....	284
Figure 6-26: MCMC results: (a) Auto-correlation function (ACF) and (b) Prior vs. posterior distributions .....	286
Figure 6-27: Bayesian updating of case study fragilities for HAZUS damage states .....	287
Figure 6-28: (a) Damage of the J6 beam-column joint; (b) damage of the J5 beam-column joint; (c) flexural damage at the base of the middle column (J2); (d) crushing of concrete core at the J1 joint; (e) damage of the J4 beam-column joint (see Figure 6-18 to locate joints).....	288
Figure 6-29: Bayesian updating of strain-based damage states.....	289

Figure A-1: Axonometric view of a test rig for hybrid simulation of a simply supported beam (with permission from Abbiati et al. (2020)) .....	319
Figure A-2: Hybrid test outputs at the mean values of the random variables .....	319
Figure A-3: Photo taken during the hybrid simulation test of the one-story steel two-bay steel frame (one of its outer columns being the experimental substructure) .....	321
Figure A-4: (a) Hierarchy of ShallowFoundationGen in the uniaxial materials class of the OpenSees software framework; (b) Schematic diagram for conducting a rehearsal hybrid test of the bridge case study (refer to Figure 5-27) using the finite-element coupling approach and the BNWF model for soil-structure interaction .....	329
Figure A-5: (a) $Sa(\xi=5\%)$ of ground motion suite adopted for IDA of the SPARCS frame; (b) spectral acceleration of the ground motion input to the shaking table test and its comparison to earthquake records adopted during the IDAs of the SPARCS frame.....	345
Figure A-6: Bayesian update of SPARCS frame considering HRC damage states.....	347

## List of Tables

---

Table 2-1: Resources supported by OpenFresco and UI-SimCor.....	23
Table 2-2: Properties of error tracking methods for real-time hybrid simulation.....	44
Table 2-3: Properties of delay compensation algorithms for hybrid simulation .....	46
Table 2-4: Ziegler-Nicholas rule for tuning PID controllers.....	58
Table 3-1: Input signals for characterization of LNEC's uniaxial shaking table .....	89
Table 3-2: Estimated parameters of LNEC's uniaxial shaking table.....	95
Table 3-3: Hurwitz matrix.....	104
Table 3-4: Coefficient of variation (CV) of random variables .....	120
Table 3-5: Ground motion input for the implementation of the M-DRM in hybrid tests .....	120
Table 3-6: Sensitivity indices of the maximum lateral displacement to the stiffness RV .....	123
Table 3-7: Sensitivity indices of different responses to the stiffness RV.....	123
Table 3-8: Application of MaxEnt to the maximum drift response for the PGA3-CV3 scenario considering the El Centro earthquake input.....	126
Table 3-9: MaxEnt estimates of the maximum drift for the PGA3-CV3 scenario considering the El Centro earthquake input .....	127
Table 3-10: Relative error of the maximum lateral displacement estimate of the M-DRM for the PGA3-CV3 scenario considering the El Centro earthquake input.....	128
Table 3-11: Relative errors of the M-DRM estimates of the maximum shear force of the experimental column, for the PGA3-CV3, considering the El Centro earthquake input.....	130
Table 3-12: MaxEnt estimates at $\xi=5\%$ , $CV_\xi=20\%$ , and $CV_k=5\%$ considering the Northridge (1994) earthquake input scaled to 0.471 g PGA.....	130
Table 3-13: Relative error of the M-DRM estimates at $\xi=5\%$ , $CV_\xi=20\%$ and $CV_k=5\%$ considering the Northridge earthquake input scaled to 0.471 g PGA.....	131
Table 3-14: MaxEnt estimates at $\xi=5\%$ , $CV_\xi=20\%$ and $CV_k=5\%$ considering the Northridge earthquake input scaled to 0.471 g PGA .....	132
Table 3-15: Relative error of the M-DRM estimates at $\xi=5\%$ , $CV_\xi=20\%$ and $CV_k=5\%$ considering the Northridge earthquake input scaled to 0.471 g PGA.....	132
Table 3-16: Relative error of the M-DRM estimates considering the unscaled El Centro earthquake input .....	134
Table 3-17: MaxEnt estimates considering the unscaled El Centro earthquake .....	134
Table 3-18: Relative error of the M-DRM estimates considering the unscaled El Centro earthquake input motion .....	135
Table 3-19: Random variables of the hybrid model.....	138
Table 4-1: <i>Initialization</i> state .....	151
Table 4-2: <i>Start-up</i> state.....	152
Table 4-3: <i>Centering</i> state.....	152
Table 4-4: <i>Pre-run</i> state.....	153
Table 4-5: <i>PreCor</i> state .....	154
Table 4-6: <i>Error</i> state .....	155
Table 4-7: <i>Pre-directHS</i> state .....	155

Table 4-8: <i>DirectHS</i> state .....	157
Table 4-9: Modal identification results and model updating of the experimental substructure ....	175
Table 5-1: Closed-form expressions for stiffness and radiation damping of arbitrarily shaped shallow foundations on homogenous half-space (after Gazetas, 1991) .....	211
Table 5-2: Foundation soil considered for the bridge case study .....	237
Table 5-3: Vibration modes of the case study bridge .....	242
Table 6-1: Coordinates of sigma points in Unscented Transformation .....	259
Table 6-2: Metropolis-Hastings algorithm .....	263
Table 6-3: Modelling properties and capacity of cantilever RC columns .....	269
Table 6-4: Modelling properties and capacity of RC portal frames.....	270
Table 6-5: Exceedance parameter, $\varepsilon$ , for the HAZUS damage states .....	285
Table 6-6: Posterior point estimates of HAZUS damage states: MCMC vs ATC-58 .....	286
Table 6-7: Exceedance parameter, $\varepsilon$ , for the observable damage states .....	288
Table 6-8: Posterior point estimates of observable damage states: MCMC vs ATC-58 .....	289
Table A-1: Ground motion suite for the $Sa(T1)_{eq}$ parametric study.....	343
Table A-2: Suite of ground motions for the IDAs of the SPARCS frame.....	344
Table A-3: Exceedance parameter, $\varepsilon$ , for the HRC damage states .....	346
Table A-4: Posterior point estimates of HRC damage states: MCMC vs ATC-58.....	346

## List of Acronyms

---

AIC	Adaptive Inverse Compensation
ASA	Average Spectral Acceleration
ATS	Adaptive Time Series
ATTC	Acceleration Trajectory Tracking Control
BD	Back Difference
BFGS	Broyden-Fletcher-Goldfarb-Shanno
BLWN	Band Limited White Noise
BNWF	Beam on Nonlinear Winkler Foundation
CDF	Cumulative Density Function
CPT	Cone Penetration Tests
CSI	Control-Structure Interaction
CSM	Continuous Strength Method
CV	Coefficient of Variation
CVA	Canonical Variate Analysis
DAQ	Data Acquisition
DFC	Discrete Feedforward Compensation
DFF	Discrete Feedforward
DHSA	Deterministic Seismic Hazard Analysis
DI	Damage Index
DMA	Direct Access Memory
DOF	Degree of Freedom
EBE	Energy Balance Error
EDP	Engineering Demand Parameter
EE	Energy Error
EFDD	Enhanced Frequency Domain Decomposition
EFT	Effective Force Testing
ELSA	European Laboratory for Structural Assessment
EMA	Experimental Modal Analysis
ESB	Equivalent Shear Beam
FB	Feedback
FCT	Fundação para a Ciência e a Tecnologia
FE	Finite Element
FEA	Finite Element Analysis
FEI	Frequency Error Indicator
FERA	Finite Element Reliability Analysis
FF	Feedforward
FFT	Fast Fourier Transform
FORM	First Order Reliability Method
FPGA	Field Programmable Gate Array
FRF	Frequency Response Function

GSA	Global Sensitivity Analysis
HHT	Hilber-Hughes-Taylor
HHTHS	Hilber-Hughes-Taylor Hybrid Simulation
HRC	Homogenized Reinforced Concrete
HS	Hybrid Simulation
HSEM	Hybrid Simulation Error Monitor
HSM	Hydraulic Service Manifold
IC	Inverse Compensation
IDA	Incremental Dynamic Analysis
IG- $\alpha$	Implicit Generalized Alpha
IM	Intensity Measure
INM	Implicit Newmark
IP	Internet Protocol
LAR	Least Angle Regression
LNEC	Laboratório Nacional de Engenharia Civil
LQE	Linear Quadratic Estimator
LQG	Linear Quadratic Gaussian
LQR	Linear Quadratic Regulator
LS	Least Square
LSE	Least Square Error
LTI	Linear Time-Invariant
LVDT	Linear Variable Differential Transducer
MaxEnt	Maximum Entropy
MBIC	Model-Based Inverse Compensation
MCMC	Markov Chain Monte Carlo
MCS	Minimal Control Synthesis
MCS	Monto Carlo Simulation
MDOF	Multi-Degree of Freedom
M-DRM	Multiplicative Dimensional Reduction Method
MISST	Multi-Site Soil-Structure-Foundation Interaction Test
MOST	Multi-Site Online Simulation Test
MR	Magneto-Rheological
MRAC	Model Reference Adaptive Control
MRF	Moment-Resisting Frame
MTE	Maximum Tracking Error
ND	Numerical Dispersion
NEES	Network for Earthquake Engineering Simulation
NEHRP	National Earthquake Hazards Reduction Program
NESDE	Núcleo de Engenharia Sísmica e Dinâmica de Estruturas
NI	National Instruments
NMHS	Newmark Hybrid Simulation
NMRSE	Normalized RMS Error

OMA	Operational Modal Analysis
OOA	Object-Oriented Analysis
OpenFresco	Open-Source Framework for Experimental Setup and Control
OpenSees	Open System for Earthquake Engineering Simulation
OS	Operator Splitting
PAEI	Phase and Amplitude Error Indices
PBEE	Performance-Based Earthquake Engineering
PCE	Polynomial Chaos Expansion
PDF	Probability Density Function
PE	Period Error
PE	Polynomial Extrapolation
PGA	Peak Ground Acceleration
PGV	Peak Ground Velocity
PHSA	Probabilistic Seismic Hazard Analysis
PID	Proportional-Integral-Derivative
POE	Probability of Exceedance
PsD	Pseudo-Dynamic
RC	Reinforced Concrete
RMS	Root Mean Square
RTHS	Real-Time Hybrid Simulation
SDOF	Single Degree of Freedom
SFEA	Stochastic Finite Element Analysis
SFSI	Soil-Structure-Foundation Interaction
SORM	Second-Order Reliability Method
SSI	Soil-Structure Interaction
SSP	Sub-space Synchronization Plot
TCP	Transmission Control Protocol
TCV	Tri-Variable Control
TFI	Transfer Function Iteration
TI	Tracking Indicator
UBC	Uniform Building Code
UI-SIMCOR	University of Illinois Simulation Coordinator
UT	Unscented Transformation
UT	Unscented Transformation
VFFF	Velocity Feedback & Feedforward
VI	Virtual Instruments
WGN	White Gaussian Noise
2D	Two-Dimensional
3D	Three-Dimensional

## List of Symbols

---

$\lambda$	Time scale factor of hybrid simulation
$\Delta t$	Integration time-step
$\delta T$	Controller clock-speed
$P_r^N$	Numerical restoring force
$P_r^E$	Experimental restoring force
M	Mass matrix
K	Stiffness matrix
C	Damping matrix
$\xi$	Damping coefficient
$\rho_\infty$	Spectral radius at infinity
$K_{eff}^{(k)}$	Effective stiffness matrix at the $k$ th time-step
$K_t$	Tangent stiffness matrix
$\tilde{U}_i$	Trial displacement at the $i$ th time-step
$\tau_{crt}$	Critical time-delay of an actuator
$TI_i^j$	Tracking indicator at the $j$ th sub-step of the $i$ th time-step
$G_{FF}$	Transfer function of a feedforward controller
$k_p$	Proportional gain
$k_I$	Integral gain
$k_D$	Derivative gain
$u_{FF}$	Feedforward displacement
$u_{FB}$	Feedback displacement
$K_{LQR}$	Optimal gain of LQR controller
$L_{Kal}$	Optimal gain of Kalman filter
$d_p$	Predictor displacement
$d_c$	Corrector displacement
$\tau_{ST}$	Time-delay of a shaking table
$\tau_a$	Time-delay of an actuator
$G_{x_p u_c}$	Input-output transfer function of a shaking table
$H_{sp}$	Transfer function relating SDOF displacement to shaking table displacement
$F_I$	Inertial force
$F_E$	Elastic force
$F_D$	Damping force
$F_A$	Actuator force
$EEI_k$	Energy error indicator at $k$ th time-step
$\left  P_{eff_i} \right _2$	Norm-2 of the effective residual force
$S_i$	First-order Sobol index

$TS_i$	Total Sobol index
$M_r^{\alpha_i}$	Fractional moment
$rel_{err}^i$	Relative error of $i$ th moment
$G_{ATS}$	Discrete transfer function of ATS compensator
$K_s$	Stiffness of compliance spring in added compliance force control
$\tilde{T}/T$	Period elongation due to SSI
$DS_i$	Damage State $i$
$\mu$	Median Intensity of a fragility curve
$\beta$	Dispersion of a fragility curve
$\theta'$	Prior value of a parameter
$\theta''$	Posterior value of a parameter
$\varepsilon_j$	Exceedance indicator at the $j$ th test
$L$	Likelihood function
$w'_i$	Weight of a joint PDF at $i$ th coordinate
$s_i$	Coordinate $i$ of a joint PDF
$q$	Proposal PDF for MCMC
$S_a(T_1)$	Spectral acceleration at the fundamental frequency
$S_a(T_1)_{eq}$	Equivalent spectral acceleration at the fundamental frequency
$f_1$	Fundamental frequency of a structure
AR	Acceptance Ratio
ISDmax	Maximum inter-story drift
$T_p$	Pulse period of an earthquake



# 1 Introduction

## 1.1 Motivation and research objectives

To mitigate severe damage of structures due to natural hazards, mainly earthquakes, a better understanding of their response to such actions has paramount importance. A shaking table test allows us to comprehend the dynamic response of structures subjected to earthquakes. Nevertheless, full-scale shaking table tests are often impractical, if not impossible, due to the limited size of shaking tables and the cost of equipment required in conducting these tests.

On the other hand, numerical methods are the most affordable techniques for analyzing structures subjected to seismic actions. However, numerical approaches, including the finite element method, might fail to capture complex mechanisms of damage, local and/or global, in structures. Besides, geometric and/or material non-linearities of structures may not be fully represented by numerical methods.

Hence, an alternative method that blends the numerical and experimental approaches is compelling. The prime goal of this method is to establish a practical, easy to implement, and economic solution to accurately determine the response of structures under seismic load (or dynamic loads in general). An alternative approach to bridge the drawbacks of the two simulation methodologies was proposed by Hakuno et al. (1969). Further developments in this technique were carried out by many others (Mahin & Williams, 1980; Takanashi & Nakashima, 1987; Igarashi et al., 2000). In the early stage of development, the technique went by the name *pseudo-dynamic (PsD) testing* in the USA. Nowadays, the names ‘*substructuring test*’, ‘*hybrid simulation*’, and ‘*online-testing*’ are interchangeably used. It will be addressed as ‘*hybrid simulation*’ in the current document, nonetheless, the term substructuring is also used whenever appropriate. In this technique, the dynamic testing of a structure is conducted by experimentally testing a critical component (or a substructure) while numerically modeling the rest of the structure. Restoring forces measured in a laboratory are returned to the numerical program at each time-step of the analysis.

In hybrid simulation, the loading history of actuators is not known *a priori* as with the case of shaking table testing. Instead, it is determined during the course of an experiment. Intuitively, the speed of execution of a hybrid simulation test is therefore dependent on the rate of data communication between the two substructures. The advancement in the speed of execution of an actuator command and speed of communication between the physical and analytical parts gave birth to real-time hybrid simulation (RTHS). Besides, geographically distributed hybrid simulation has also been developed and implemented in the past. The research developed here makes its focus on local hybrid simulations and no references will be made to geographically distributed hybrid simulations.

In the past two decades, a considerable amount of research has been conducted in hybrid testing to make it a reliable method for dynamic testing of structures. Among its widespread applications, it

enabled researchers to experimentally simulate the effectiveness of energy dissipation devices in structures, subjected to earthquakes, without the need for experimental testing of the complete structures (Carrion et al., 2009). It also allowed full-scale testing of critical components that make part of bigger structures such as piers in bridges. Hence, scale effects, which are inevitable during experimental testing of reduced-scale models of large structures, can be minimized. Figure 1-1 shows the observed damage of a bridge structure and the damage of identical piers that were tested on a geographically distributed hybrid simulation. The bridge, which is located in the Santa Monica (I10) Freeway in California, was heavily damaged during January 17, 1994, Northridge earthquake. The tested piers were  $\frac{1}{2}$  scale model of the prototype structure. The hybrid testing remarkably reproduced the observed damage of the prototype structure. During the experiment, a numerical model of the SSI of the bridge was included. Due to its strong potential, the application of hybrid simulation was not limited to structural/earthquake engineering, but it was extended to other fields of study such as thermo-mechanical testing, industrial piping systems, and multi-hazard testing (Memari et al., 2020; Chen et al., 2008 and Strelelas et al., 2020). It also motivated small-sized laboratories to actively engage in research using their limited equipment, including participation in geographically distributed hybrid testing projects.



Figure 1-1: Comparing observed (center) and hybrid test outputs (left and right) from the MISST project (after Spencer et al., 2006)

Nevertheless, hybrid simulation was never without challenges. Its difficulties are the result of splitting a system into substructures, then forcing it to behave like the original structure by satisfying boundary conditions at the interface. Besides, many platforms need to be monitored at the same time, namely the numerical model, simulation coordinator, and actuator/shaking table controller. State-of-the-art hardware and efficient control algorithms are also pivotal for a successful hybrid simulation test.

Thus, the implementation of an efficient and modular hybrid testing framework appears timely and important for any structural laboratory. Having this in mind, a robust framework software for hybrid simulation tests was developed and validated in the scope of the current thesis at the Earthquake Engineering and Structural Dynamics Unit (NESDE) of the National Laboratory for Civil Engineering (LNEC), Lisbon, Portugal. In addition to the challenges in hybrid testing discussed above, the stability of hybrid simulation tests is problematic. Although studied in the past, a thorough understanding of stability limits and actuator (or shaking table) error compensation is essential while conducting a hybrid test. An uncompensated dynamics of an actuator may lead to premature damage of a test specimen and test equipment. Hence, a simplified method for stability analysis of hybrid simulation tests was carried out in the current development, following a parametric system identification of the uniaxial shaking table at LNEC. The execution of simulated hybrid tests has been convened through simulated studies in some of the existing software frameworks such as the Open-Source Framework for Experimental Setup and Control (OpenFresco)(Schellenberg et al., 2019).

In the domain of seismic risk analysis, the contribution of experimental methods has been very limited, given its significant costs. Similarly, the application of experimental testing for reliability and global sensitivity studies is rare for the same reason. However, reliability and global sensitivity studies can be essential for designing experimental tests and for the development of design guidelines. To bridge this knowledge gap, the application of hybrid simulation tests in global sensitivity studies can be handy. This objective was implemented in the thesis using surrogate modeling techniques, which enable the evaluation of reliability statistics and sensitivity indices from a few hybrid tests.

Still, in the domain of seismic risk analysis, numerical methods are generally adopted for deriving fragility curves that account for all the uncertainties in geometry, material response, and the seismic load of structures. Experimental methods for deriving fragility curves are impractical due to the need for a large number of model evaluations. At the same time, simulation of structural response using numerical models may not be fully trusted, especially in the near-collapse region. In the past, Bayesian updating of numerical fragilities using experimental testing has proven to be valuable (Porter et al., 2006; Koutsourelakis, 2010). Besides, the application of hybrid testing for updating numerical fragilities has been explored recently (Li et al., 2013). The current research develops on the improvement of updating algorithms, in the framework of Bayesian updating, applied to shaking table tests.

To the knowledge of the author, only a few attempts have been made, up to date, for simulating the response of structures that exhibit significant soil-structure interaction effects in substructuring tests using shaking tables. Experimental testing of soil and structure in centrifuge tests has been widely used to study shallow and deep foundations subjected to earthquake shaking; nevertheless, due to scale limits and problems in controlling the dynamics of the superstructure, system-level tests are challenging. 1g-shaking table tests using geotechnical laminar boxes were thus practiced in many laboratories to model soil-structure interaction (SSI) effects. Such tests are also restricted to simple tower-like superstructures due to laboratory space and other limitations. Thus, it is interesting for the engineering community to refine and apply the hybrid simulation to further

improve the knowledge needed to comprehend the complex nature of the interaction between soil and structure during seismic events.

In hybrid testing, SSI effects can be experimentally tested at scales close to full scale, whilst most of the superstructure is modeled in a computer. Few research studies (e.g., Sivaselvan 2015) have been conducted in this area because of its complexity. Nevertheless, there exists a good number of studies that model the SSI effect numerically, using full 3D finite element models of soil strata or simplified lumped-parameter types, while superstructure elements are treated as physical substructures (Spencer et al., 2006; Wang et al., 2011; Dietz et al., 2015). Nonetheless, structural responses may not be fully reliable since the solution to SSI effects is derived from numerical methods.

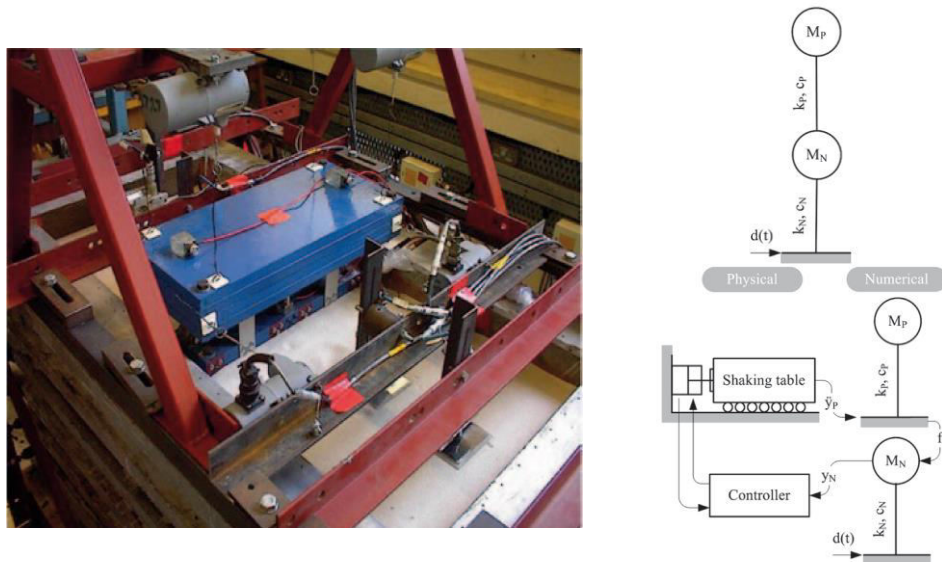


Figure 1-2: SSI in RTHS test: Benchmark test (left) and substructuring test (right) (after Dietz et al., 2015)

In performing SSI hybrid tests in 1g shaking tables, proper application of boundary conditions between the numerical superstructure and the physically modeled soil-foundation-structure substructure must be ensured in addition to building a framework coordinator to drive the hybrid model. Advanced control strategies for shaking table acceleration tracking as well as force control of actuators thus need to be devised. Both feedforward-feedback control, for acceleration tracking of a shaking table, and the equivalent force control of actuators, using added compliance principles, were implemented in the current framework, following numerical studies of the control schemes. These developments clear the path to the execution of the SSI hybrid tests in 1g shaking tables. Contrary to traditional shaking table tests, by simply changing the numerical model in a computer, several superstructure models can be tested in this scheme, thus enabling parametric tests that are necessary for the improvement of design code provisions relative to SSI effects.

## 1.2 Shaking table testing of structures

Shaking table testing was developed around the 1940s (Sabnis et al., 1983) to simulate the complex and nonlinear seismic response of structures. By the end of the 20<sup>th</sup> century, the application of shaking table tests spread to many areas of civil engineering for instance in energy dissipation systems, dams, high-rise buildings, composite structures, etc. A shaking table test is conducted by applying an earthquake motion to a test structure that is mounted on a platform, called platen, driven by a single or by a group of actuators. It is highly reliable in reproducing the response of structures subjected to earthquakes. To ensure the fidelity of the base acceleration produced by the shaker, complex control mechanisms, and state-of-the-art equipment are required. Due to their limited size, test specimens are commonly reduced-scale models of the prototype structures. The scaling is conducted based on the Cauchy or Froude similitude relationships, for example. The model is thus built by altering the scales of length, density, time, acceleration, etc., to produce a response that is representative of the prototype structure. According to report No. 8 of the CASCADE European project, several testing facilities were developed around Europe to fulfill the research needs for understanding the complex behavior of structures subjected to earthquakes (Bairrao & Severn, 2007).

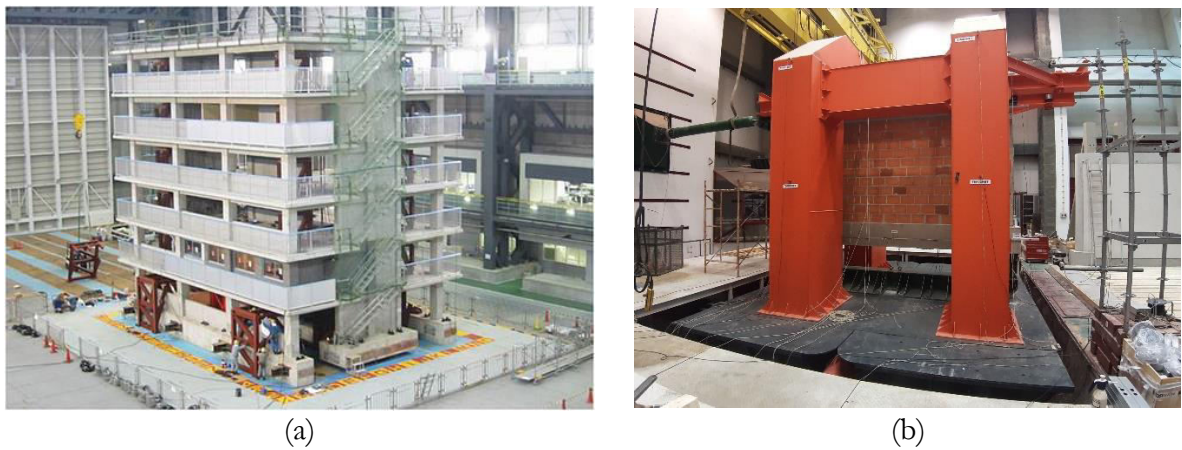


Figure 1-3: (a) Full-scale six-story reinforced concrete structure tested at E-Defense (after Kim et al., 2012); (b) In-plane and out-of-plane test of RC portal frame with masonry infill at LNEC (after Correia et al., 2015)

In 1995, after the earthquake in the North Kobe area of Miki city, Japan, the E-Defense shaking table facility was built. It is the largest shaking table platform with 19.8 m x 14.9 m plan dimensions. It can support specimens weighing up to 11120 kN with a maximum load of 9 m/s<sup>2</sup> and 15 m/s<sup>2</sup> accelerations in the horizontal and vertical directions, respectively. The shaking table facility at LNEC, Portugal, is capable of applying translation motions in the three axes. It has a 40-ton payload capacity and 5.6 m x 6.4 m of plan dimensions. The shaking table facility can reach velocities as large as 70 cm/s and displacements up to 200 cm.

A shaking table which is driven by servo-controlled hydraulic actuators is designed to be rigid enough to simulate an earthquake motion. Shaking tables can be unidirectional, driven in one

direction only, or multi-directional, where more than one of the six degrees of freedom of a shaking table are controlled. Uniaxial shaking tables are typically constructed using a rail and guide system that can cancel any undesirable motion (Bursi & Wagg, 2008). Bidirectional controlled shaking tables can have two (or more) horizontal actuators, positioned to avoid the yawing motion, or vertical and horizontal actuators positioned to avoid the roll and pitch motions. Triaxial shaking tables, such as the one at LNEC, can reproduce realistic 3D earthquake input motions. Shaking tables with six degrees of freedom are versatile and capable of simulating deformation modes that cannot be realized in centrifuge testing, nonetheless, complex algorithms need to be employed to control all six DOFs and their interaction. In the latter, eight actuators are commonly used, where four of them are vertically positioned at corners while the remaining four are positioned horizontally in the form of a cruciform.

As pointed out above, if a prototype structure is too large to be physically erected in a shaking table platform or under financial restrictions for building a model at a 1:1 scale, the test specimen is prepared by downscaling the prototype structure. Scales adopted may range from full scale (1:1) to 1:50, typical in testing long bridges. Full compliance with the similitude laws is often impossible thus making a test specimen to be an approximate representation of the prototype structure. To effectively reproduce the characteristics of the prototype structure and promote simplicity in the construction of models, the same material type is commonly used and the scaling ratio for the stress of the model to that of the prototype is kept as one. It is therefore customary to add dummy masses when adopting the Froude (acceleration) law of similitude to avoid the specific density of materials used in the model from being scaled. However, stiffness contribution from the additional masses must be avoided. Contrarily, using the Cauchy law the specific density is not scaled down and no dummy masses are needed. But the acceleration input to the shaking table is scaled according to the similitude rule.

A shaking table test gives valuable insight into the nonlinear characteristics of structures under earthquakes. They are commonly employed for the development of design guidelines for buildings, bridges, etc. They also serve as a validation tool for new materials, energy dissipation devices, and new design methodologies. Several shaking table tests have also been conducted aiming at calibrating numerical models. Knowing the *value of the information* provided by a shaking table test, one can easily agree on its maximized utilization. In the context of seismic risk analysis, the direct application of shaking table testing is impractical since risk analysis involves response estimation considering uncertainties in geometry, material response, and earthquake variability. With the advent of computational methods, however, experiences and observations gained during shaking table tests can be used for improving responses evaluated from numerical methods. Therefore, the output obtained from shaking table tests can be used to improve the seismic risk assessment of structures by updating fragility curves, derived by numerical methods, through Bayesian methods.

### 1.3 History of hybrid simulation and its applications

Hybrid simulation was born in the early 1970s, and it has been subjected to numerous improvements in terms of its fidelity, robustness, and spectrum of applications throughout the

years. Early after its conception, the propagation of errors in hybrid simulation, both random and systematic, were studied (Schellenberg et al., 2009). Around that time, in the USA, the technique was referred to as pseudo-dynamic testing.

The performance of the integration scheme used for a hybrid simulation test can dictate the accuracy of response simulation. Extensive studies have been conducted in this niche since the conception of hybrid simulation. Shing & Mahin (1987) investigated the Newmark integration families while developing stable explicit algorithms suitable for PsD testing (Schellenberg et al., 2009). A mixed implicit-explicit algorithm was also developed by Dermitzakis & Mahin, (1985) to account for large nonlinearities in structural response. They conducted several PsD tests of multi-degree of freedom structures, such as the one depicted in Figure 1-4, to verify the reliability of substructuring techniques. The developments were not just confined in the USA and Japan by the end of the 20<sup>th</sup> century, since the technique also took a step forward in Europe.

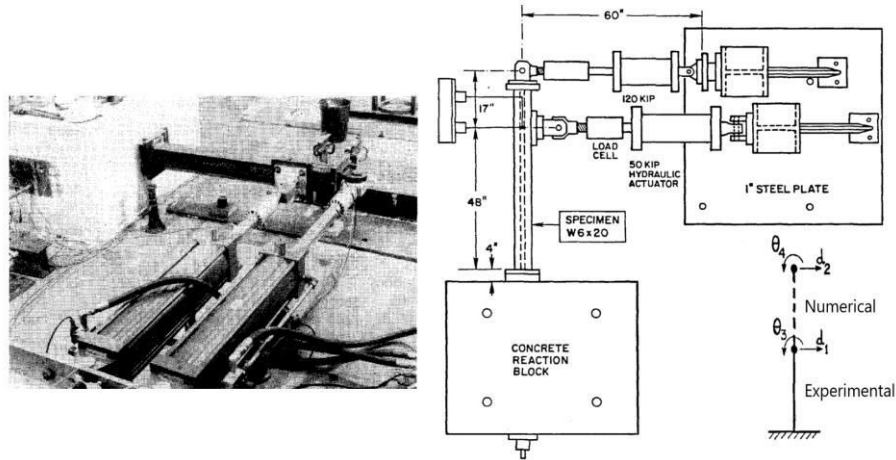


Figure 1-4: Pseudo-dynamic test of a two-degree of freedom structure (after Dermitzakis & Mahin, 1985)

On the other hand, actuator control using the traditional shaking table control was found insufficient and researchers explored advanced solutions. In the late 1980s, Thewalt & Mahin (1987) developed a mixed force and displacement actuator control which led to the birth of effective force testing.

Further, enormous research was carried out in the areas of integration algorithms aiming for improved error propagation and stability characteristics to meet the requirements for testing the ever-increasing complexity of structural systems. These research studies led to the development of unconditionally stable explicit algorithms, explicit Operator Splitting (OS) algorithms, implicit methods, and mixed algorithms.

The first implementation of hybrid simulation for real-time testing was achieved by utilizing improved hardware, such as dynamic actuators and a digital servo-mechanism, as well as a staggered integration approach to improve the computational efficiency (Nakashima et al., 1992). In the

following years, the development of nonlinear finite element software, e.g. DRAIN 2D, gave rise to the FEM approach in hybrid simulations (Schneider & Roeder, 1994). The estimation of the tangent stiffness of an experimental element using the BFGS (Broyden-Fletcher-Goldfarb-Shanno) algorithm was implemented by Thewalt & Roman (1994). Combescure & Pegon (1997) also studied the accuracy of the OS algorithm that was developed by Nakashima et al. (1993). Soon after that, the activities and developments of Magonette & Negro (1998) at the European Laboratory for Structural Assessment (ELSA) was published (Saouma & Sivaselvan, 2008).

To improve real-time hybrid simulation tests, Horiuchi et al. (1999) developed actuator compensation methods using a prediction methodology through extrapolating polynomials, which was implemented by Nakashima & Masaoka (1999). At the same time, a real-time hybrid simulation test was performed using a control system approach (Darby et al., 2001). On the other hand, works at ELSA were focused on the development of continuous pseudo-dynamic testing to prove the effectiveness of continuous PsD tests in limiting the force relaxation phenomena caused by the hold phase in the ramp-and-hold method (Magonette, 2001).

In 2003, the hybrid simulation test was further extended through the development of a three-loop architecture framework for a continuous geographically distributed hybrid simulation test (Hanley et al., 2003). The event-driven approach significantly improved the force relaxation issues exhibited in the ramp-and-hold method. A year later, Reinhorn et al. (2004) proposed force control approaches of actuators applicable to both the effective force method and real-time dynamic hybrid testing. In their approach, they attempted to modify the mechanically stiff nature of actuators (good in position control) to suit the low impedance (compliant system) requirements of force control. Thus, they implemented their scheme using a spring element as a compliant system while the inner loop was controlled in displacement. Takahashi & Fenves (2006) developed an object-oriented software framework made up of interlaced software classes that allowed modular and standardized means for the computational driver to talk to laboratory hardware. The framework was also designed to handle both local and distributed tests. Two years later, Schellenberg et al. (2008) modified the Open-Source Framework for Experimental Setup and Control (OpenFresco), enabling collapse simulation through hybrid simulation.

Force control and mixed control strategies as well as switching between force and displacement control during a simulation (Elkhoraibi & Mosalam, 2007; Wu et al., 2007) emerged in 2007 to overcome the challenges imposed in testing stiff specimens using the conventional displacement control. In the same year, Mercan & Ricles (2007) investigated the stability of real-time and pseudo-dynamic testing by numerically modeling experimental errors using pure time-delay and amplitude error. They explored the influence of experimental errors in the accuracy of a hybrid test.

Soil-structure interaction (SSI) or Soil-Structure-Foundation Interaction (SFSI) was not experimentally tested in a hybrid simulation until that time, even though its potential for SSI studies was discussed before. However, 1g-shaking table tests were widely practiced for experimentally studying SSI effects (Shirato et al., 2008; Maugeri et al., 2000; Paolucci et al., 2008). In the ‘unified

*view for hybrid simulation'*, Sivaselvan (2006) proposed a scheme for SSI testing where the excitation of the soil and foundation system is provided by an earthquake simulator (shaking table) while the interface conditions are imposed by an actuator. Shortly after, the George E. Brown, Jr., Network for Earthquake Engineering Simulation (NEES) facility executed a geographically distributed test termed as *Multi-Site Soil-Structure-Foundation Interaction Test (MISST)* (Spencer et al., 2006). The Multi-Site Online Simulation Test (MOST) platform was used to conduct the hybrid test of a bridge structure where the SFSI effect was modeled numerically while two piers of the bridge were tested experimentally at remote sites (Saouma & Sivaselvan, 2008). The experimental campaign in MISST was performed using the University of Illinois Simulation Coordinator (UI-SIMCOR), a hybrid simulation coordinator framework software developed by Kwon et al. (2007).

Researchers were fascinated by the diverse applicability of hybrid testing. As a result, various experimental tests were conducted, e.g. application to magnetorheological dampers (Carrion et al., 2009; Lin 2009; Kim et al., 2012; Phillips & Spencer, 2012; Friedman et al., 2014), base isolation system (Lanese, 2012) and so on forth. In parallel, the capability of OpenFresco to interface with MATLAB as a computational driver was demonstrated and the implementation of LabVIEW as an experimental controller was accomplished. Moreover, OpenFresco was extended to support mixed and switch controls by modifying the *ExperimentalSignalFilter* abstract class of OpenFresco (Kim, 2009). Kim et al. (2011) used those control approaches in studying the effects of vertical ground motion on the loading and behavior of bridge piers.

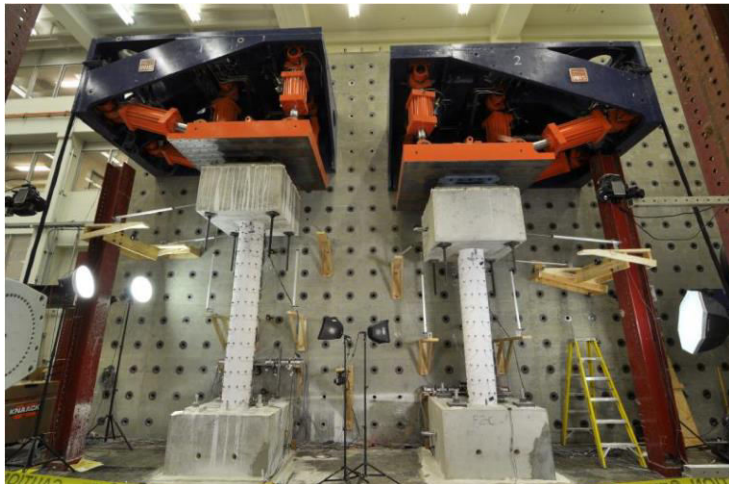


Figure 1-5: Substructuring test of RC bridge subjected to vertical and horizontal earthquakes  
(after Kim et al., 2011)

HybridFEM, a software for nonlinear analysis of 2D inelastic frame structures, was modified to support hybrid testing, although the program is not open-source software. An online optimization method in hybrid simulations with multiple identical substructures of a bridge structure was also implemented (Yang et al., 2012). One experimental pier is used for online updating of the remaining piers by optimizing a set of parameters from the experimental data. Due to the stringent time

requirements of real-time hybrid testing, control strategies based on  $H_\infty$  loop shaping and Model Reference Adaptive Control (MRAC) were proposed by Gao et al. (2013). Other researchers explored on how to measure the performance of hybrid simulation tests through error tracking methods that are applicable to real-time error monitoring (Ahmadizadeh & Mosqueda, 2009). In this direction, Tracking Indicators (TI), and Phase and Amplitude Error Indices (PAEI) were developed (Hessabi & Mercan, 2015). This algorithm was developed to decouple the phase and amplitude errors in hybrid testing. However, the PAEI algorithm needs to solve large eigenvalue problems at each time step of analysis, thus limiting its application to post-processing. To enable online tracking during a hybrid test, the authors implemented a computationally lighter frequency-based error indicator.

Actuator control and delay compensation studies were also under tremendous development. Carrion & Spencer (2007) applied a model-based compensation in continuation of the extrapolation scheme explained by Horiuchi et al. (1999). This niche was investigated thoroughly by many researchers considering model-based and adaptive techniques (Phillips, et al., 2014 – feedforward-feedback compensator; Zhao et al., 2006 – PLC compensator; Chen & Ricles, 2010 – Inverse and Adaptive Inverse compensation; etc.). In 2013, a novel adaptive technique was proposed that combines the Taylor series and least-square (LS) optimization (Chae et al., 2013). The method could be computationally demanding; nonetheless, reducing the size of the gradient matrix used in solving the least-square problem makes it affordable for implementing it online.

Time-stepping integration algorithms that are suitable for real-time hybrid testing continued its development and many of those methods were integrated into the OpenFresco framework. Newmark implicit algorithm with fixed iterations, Newmark implicit algorithm with increment reduction factor, Implicit Generalized Alpha (IG- $\alpha$ ) method with constant iterations, Operator-Splitting (OS) algorithm with tangent and mixed experimental stiffnesses, etc., were applied and explored by Schellenberg et al. (2009). Extensive reports on the subject of predictor-corrector integration algorithms can be found in Schellenberg et al. (2009). Many researchers were also in quest of developing explicit and unconditionally stable algorithms suitable for real-time hybrid testing. Kolay & Ricles (2014) modified the two-parameter IG- $\alpha$  method into an explicit single parameter integration method called KR- $\alpha$ . They optimized the period dispersion properties of the algorithm to reduce the distortion of contributing modes of a structure.

Although physical modeling of SFSI in hybrid tests has proven to be challenging, some innovative schemes have been published recently. First of its kind, Stefanaki et al. (2015) conducted a hybrid test of a structure resting on a deep pile-group foundation. The superstructure was modeled in numerical software while the foundation and soil deposit were physically modeled in a laboratory. The piles were inserted into saturated sand contained in a laminar box. The entire assembly was driven by a one-dimensional shaking table at the base while a second small shaking table, which mimics the superstructure, applies the interface conditions. They demonstrated that the hybrid simulation of SFSI is viable. They have also highlighted that SFSI can significantly influence

structural responses and the demand on structures.

## 1.4 Overview of dissertation

In the introductory chapter, the role of shaking table tests in dynamic testing of structures and the history of hybrid simulation are briefly discussed after presenting the motivation and research objectives of the thesis.

Chapter two contains a detailed study of the ingredients of hybrid simulation. Starting from its basic principles, different approaches for its implementation and the existing software frameworks are reviewed. This survey played an important role in selecting the framework implemented in the LNEC hybrid simulation facility. The development of time-stepping algorithms for hybrid testing is explored focusing on the requirements for hybrid testing. After presenting the explicit, implicit, and operator-splitting methods, the implementation and properties of three representative methods, one from each category, are investigated. Particular attention is given to time-stepping algorithms that are preferred for real-time hybrid testing. The stability and accuracy characteristics of these methods are also analyzed and compared. Additionally, the chapter discusses sources for experimental errors in hybrid simulation, tracking methods, and their compensation using offline and adaptive techniques. In the end, the approaches for controlling servo-hydraulic actuators are explained. Conventional position control and advanced control approaches such as acceleration tracking and force control are discussed in depth. Displacement-based and velocity-based prediction-correction algorithms that are necessary for continuous movement of actuators during a hybrid test are also explored, in support of their implementation as a control scheme in LabVIEW.

In chapter three, several applications that were studied through a simulated hybrid test approach are presented. To assist in modeling the laboratory conditions during the simulated hybrid testing, a detailed shaking table identification work conducted on the uniaxial shaking table of LNEC is presented. After a short introduction to a simulated hybrid test and its implementation in the OpenFresco framework, three domains of application are proposed and elucidated with examples. In the first application, the potential of a simulated hybrid test in selecting time-stepping integration algorithms is examined. Stability analysis of hybrid tests and substructuring approaches, applied to elastic and inelastic SDOF structures, is tackled in the second application. This study sheds light on the stability margins during substructuring, but the results are unique to the characteristics of the shaking table considered. The third application presented can be performed only under real hybrid testing; nonetheless, the proof-of-concept of the proposed approach was conducted in simulated tests, consisting on the examination of the effects of a gradually increasing complexity in the response uncertainty of a steel frame structure. The derivation of global sensitivity indices and the reproduction of full probability density functions under the multiplicative dimensional reduction method (M-DRM) formulation are reviewed. Finally, the proposed approach is validated using hybrid tests of a simply supported beam. Comparisons of global sensitivity analysis between the M-DRM and polynomial chaos expansion (PCE) techniques concludes this chapter.

Chapter four of the thesis is all about the development of a LabVIEW-based software framework for hybrid simulation, capable of communicating laboratory equipment and numerical simulation software such as OpenSees. Herein, the development and implementation of a modular and extensible state-machine architecture is investigated. In detail, the development of two frameworks, one based on OpenFresco middleware and another as middleware free, are included. In-depth discussions about the development and implementation of a simulation coordinator and its intricacies in communication with the OpenFresco through TCP/IP network makes a large part of the chapter. Greater attention was paid to the time-delay compensation, predictor-corrector methods for command generation, error tracking, etc., of the simulation coordinator. Besides, the programming control algorithms in the Field Programmable Gate Array (FPGA) board are elucidated starting from simple PID algorithms to complex feedforward-feedback control approaches. After explaining the hybrid test setup used for validating the framework, test results and challenges are discussed. Two advanced control strategies for substructuring tests on shaking tables, which are indispensable for SSI studies, are examined. Simulated studies are also presented to study the characteristics of the control strategies and to tune their parameters. Their implementation and integration into the framework are discussed at the end.

Soil-structure interaction testing in substructuring tests is the main objective of chapter five. After introducing the SSI problem in structures, some of the common numerical techniques in modeling SSI effects are reviewed. The Beam on Nonlinear Winkler Foundation (BNWF) and macro-element approaches are explained in depth. Later, a discussion on the 1g shaking table and centrifuge methods for experimental test served as a background to jump into SSI studies in substructuring tests. The history and up to date developments in SSI studies in hybrid testing are explored and the knowledge gap in this area of study is highlighted. Towards the end, the initial contribution of the current research to the implementation of SSI substructuring tests in shaking tables, in the form of a simulated case-studies, is expounded. The first case study loudlys the advantages of rehearsal hybrid testing in SSI substructuring tests whereas the second case study attest the adequacy of the middleware-free scheme of *LNEC-HS* in conducting SSI hybrid tests of shear buildings with dominant soft-story mechanism.

Chapter six starts by stating the objective of maximizing the usefulness of a shaking table output in seismic risk assessment by updating fragility curves that are derived from numerical methods. Bayesian updating methods are reviewed in detail subsequently. In this review, the Unscented Transformation (UT) approach for approximating a joint distribution and the Markov Chain Monte Carlo (MCMC) simulation method of sampling from the posterior distribution are studied in chronological order. The application of the proposed approaches to a shaking table test conducted on a reinforced concrete plane frame, tested at the premises of LNEC, is elaborately discussed. The implementation of these Bayesian methods in MATLAB software is also briefed. The chapter ends with recommendations for Bayesian updating of RC fragilities after examining its applicability for several damage-state categories.

The summary and conclusions of the thesis are presented in chapter seven. A handful of future developments are also proposed and discussed which develop on ideas and methods established in this research work.

## 2 Literature Review on Hybrid Simulation

### 2.1 Introduction to hybrid simulation

Hybrid simulation (HS) testing divides a reference structure into analytical and physical parts by modeling the analytical part in a finite element software, or computational program, and experimentally testing the physical part in a laboratory. The two parts interact with each other at interface points throughout the execution of the test. Part of a structure that has complex behavior, or a component whose computational model is well not established, is typically chosen as the physical model. Figure 2-1 shows the schematic diagram of a HS test which is based on displacement; hence, termed as a displacement-based method.

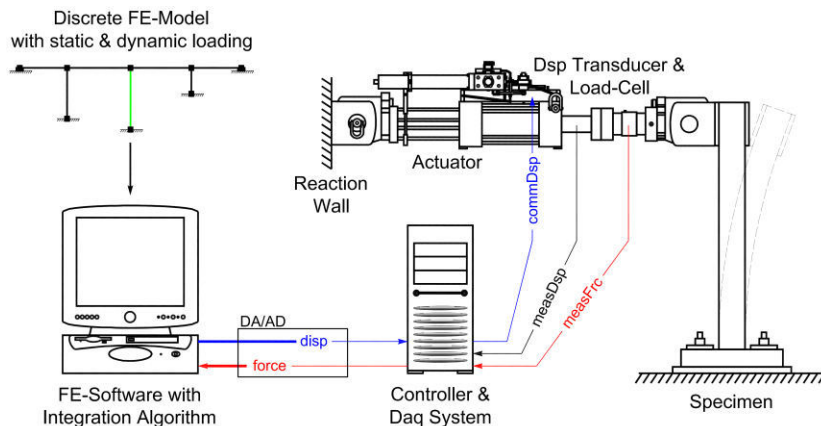


Figure 2-1: Schematic diagram of a hybrid simulation (after Schellenberg et al., 2009)

The HS technique was proven to be an effective technique for seismic testing of structures in the 1970s and 1980s in Japan and the United States. The Japanese activities on online-testing until the mid-1980s were summarized by Takanashi & Nakashima (1987). They discuss the reliability issues in hybrid simulation making it worthwhile to mention the advantages of HS.

- ✓ Since the equation of motion is solved analytically, different loads, other than an earthquake, can be considered such as wind, blast, moving traffic, traffic impact, etc.
- ✓ Unlike a shaking table test, where scaled structures are typically tested, a full-scale test of substructures can be more easily implemented in hybrid simulation, which avoids the consequences of scaling. Moreover, smaller capacity actuators may be employed because the physical models are mostly structural elements or small portions of a structure.
- ✓ It is economically advantageous since laboratory tests can be carried out with just small improvements of the quasi-static testing equipment, especially for slow hybrid testing.
- ✓ Depending on the similitude requirements of a scaled model, a hybrid test can be executed

at a desired rate relative to the actual time scale.

- ✓ Geographically distributed hybrid simulation allows equipment in different laboratories to be shared and utilized efficiently.
- ✓ Desired effects like geometric nonlinearity and 3D-effects can be modeled analytically.
- ✓ Less concern in imposing appropriate boundary conditions, unlike shaking tables tests.
- ✓ Hybrid simulation can be conducted in shaking table tests, also accounting for soil-structure interaction, tuned mass dampers, etc. Here, real-time control of the simulator platform may be required.

Nonetheless, hybrid simulation is not easy to implement since the boundary condition at the interface needs to be satisfied properly. It may also require complex control mechanisms that are challenging for real-time testing conditions. A shortlist of the challenges in contemporary hybrid simulation includes:

- The absence of environment-independent software for the implementation of HS, which is robust, transparent, and extensible for various specificities. The development of such a framework is very important both for the advancement of the technique and as a basis for interaction among researchers and labs.
- Highly vulnerable to errors from the numerical modeling, nonlinearities of a load transfer system, and measurement devices. These errors may lead to unstable experiments. Error reduction using improved time-stepping algorithms, advanced actuator control algorithms and improved data acquisition systems have been explored up to date.
- Challenges in carrying out displacement control of stiff experimental substructures such as a squat wall. Mixed control or switching control, between displacement and force controls, are alternative solutions that are not fully exploited up to date.
- Difficulties in the convergence of explicit time-stepping algorithms during experimental testing that possess strong geometrical and/or material nonlinearity. On the other hand, implicit algorithms are not suitable for fast and real-time hybrid tests.
- Real-time monitoring of the accuracy of simulation for fast and real-time hybrid simulation may be prohibitive under the conventional methods.
- High-performance computing environments may be required when complex structures are considered for hybrid simulation. The complexity of the test structure is measured by the number of DOFs and the nonlinearity of the problem. Under such conditions, near real-time simulations can be challenging.
- The need to reduce inertial forces developed during a fast or real-time hybrid simulation and making a proper account for them may be difficult.
- Interaction of experimental substructures, the coupling of actuators during multi-axis hybrid testing, and coupling between a shaking table and an actuator can be complex.
- Challenges in conducting geographically distributed hybrid simulation due to network latency.

## 2.2 Slow, fast, and hard real-time hybrid simulation

The speed at which the HS can be performed determines its capacity to model the rate-dependent behavior of a physically modeled structure or component thereof. For example, when an energy dissipation device is tested physically, the speed of the test should be enough to capture the rate-dependent behavior of the device. For obvious reasons, better actuator control is achieved under slow speeds as compared to fast or real-time execution of a test. Based on the speed and continuity of test execution, HS can be classified as shown in Figure 2-2.

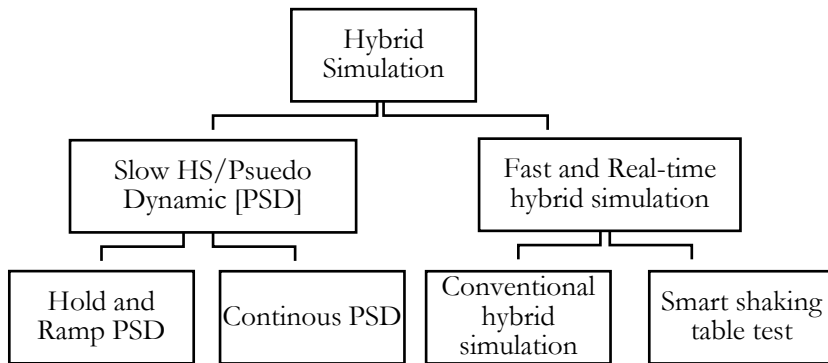


Figure 2-2: Classification of hybrid simulation

Pseudo-dynamic (PsD) testing is a technique in which the dynamic response of a structure is determined by numerically simulating the analytical substructure and laboratory testing of the experimental substructure, while allowing them to dialogue through command displacements and measured restoring forces. This technique has been implemented at the European Laboratory for Structural Assessment (ELSA) using two parallel processes dialoguing with each other: one responsible for the experimental structure and another for the analytical structure (Bursi & Wagg, 2008). In this technique, the inertial and damping forces are fully modeled analytically, and the experimental substructure does not contribute to damping and inertial forces owing to the slow speed of the test. Generally, it has a time scale,  $\lambda$ , greater than 100. The command displacement is applied in a ramp-and-hold manner as shown in Figure 2-3. Here, the actual time needed for the execution of a test is extended due to the hold period and exhibits a velocity discontinuity. Force relaxation during the hold period and actuator stick-slip difficulties are the main drawbacks of this technique. Besides, due to its slow execution, rate-dependent devices cannot be represented physically. In PsD testing, the equation of motion can be expressed as:

$$\begin{aligned} M\ddot{U}_{i+1} + C\dot{U}_{i+1} + P_r^N(U_{i+1}, \dot{U}_{i+1}) + P_r^E(U_{i+1}) &= P_{i+1} - P_{0,i+1} \\ P_r^E(U_{i+1}) &= P_{r,i+1}^E \end{aligned} \quad (2.1)$$

where  $M$  and  $C$  are the mass and damping matrices, respectively;  $P_r^N$  and  $P_r^E$  are the numerical and experimental restoring forces, respectively;  $P_{i+1}$  and  $P_{0,i+1}$  are the external applied nodal loads and element assembled nodal loads, respectively; and  $P_{r,i+1}^E$  are the restoring forces of the experimental

substructure that are measured by load cells.

$$\Delta T = \frac{\Delta T_{h1} + \Delta T_{h2} + \Delta T_{h3} + \Delta T_{ramp}}{\text{hold period}} \quad (2.2)$$

$$\lambda = \frac{\Delta T}{\Delta t}$$

where  $\Delta T_{h1}$ ,  $\Delta T_{h2}$  and  $\Delta T_{h3}$  are explained in Figure 2-3;  $\Delta t$  is the integration time-step;  $\Delta T$  is the experimental time-step (typically larger than 1 s in PsD testing); and  $\lambda$  is the time-scale factor. In subsequent discussions,  $T$  is the total time for the experimental process and  $t$  is the total time of the analytical process.

On the other hand, a continuous PsD test abolishes the hold period, thus allowing for a continuous motion of the actuators, and hence, a reduced time of test execution. The time spent by the analytical process in solving the equilibrium equation is generally large compared to the clock-speed of a controller (which corresponds to a sampling interval of 2 ms or less).

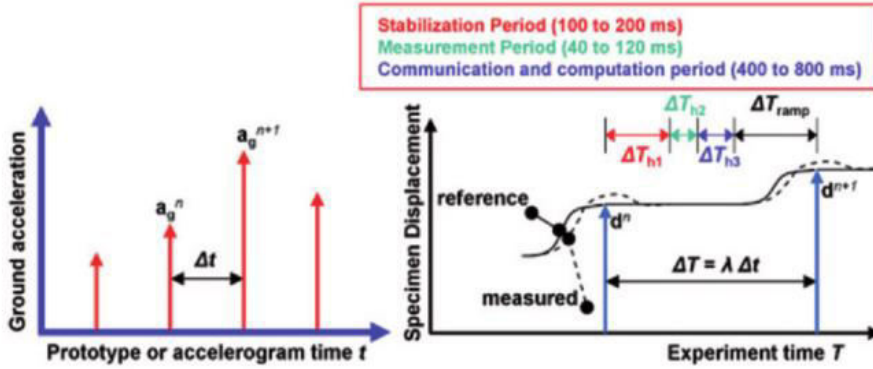


Figure 2-3: Ramp-and-hold method (after Pagon, 2008)

Hence, the experimental process is executed in multiple steps for a single step of the analytical process, having a smooth and continuous trajectory of commands. Large and highly nonlinear structures are typical examples of a much slower analytical process.

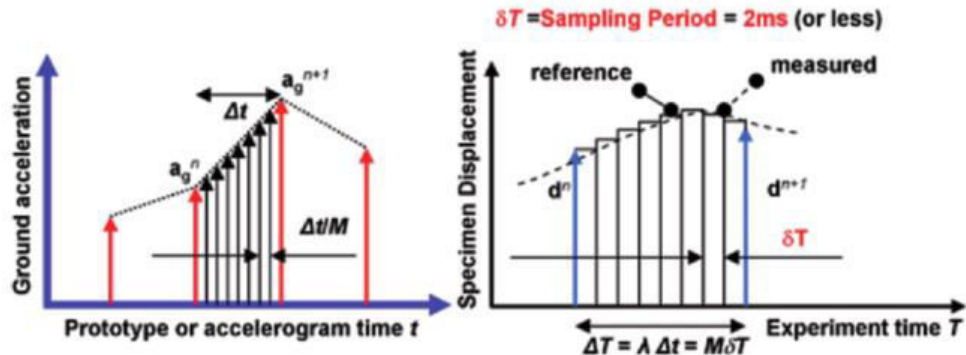


Figure 2-4: Continuous PSD scheme (after Pagon, 2008)

In the continuous PsD test, the execution time of each integration step is  $\delta T$  (digital controller sampling rate), e.g., 2 ms in the ELSA project, and it reduces the force relaxation problem yielding a cleaner restoring force signal. The execution time in continuous PsD test is thus given by:

$$\Delta T = \Delta T_{h2} + \Delta T_{h3} = \lambda \Delta t$$

$$\lambda = \frac{\delta T}{\Delta t / M} \quad (2.3)$$

The method is executed at the sampling rate of the controller,  $\delta T$ , making  $M$  sub-steps ( $\delta T = \Delta t / M$ ) in each time-step  $\Delta t$ , as shown in Figure 2-4. For example, if  $\Delta t = 4$  ms, the controller is operating at a rate of 1 kHz ( $\delta T = 1$  ms) and considering  $M = 200$ , then  $\lambda = 1/4 \times 200 = 50$ , which can be interpreted as if 1 s duration of an accelerogram needs 50 s in the actual experimental test.  $\lambda$  can be decreased until the control error exceeds a defined threshold which depends on the complexity of the test. The value for  $\lambda$  can vary from 1, for an experimental substructure with negligible inertial forces, to values of 250-500, for complex and large experimental components.

The continuous PsD test is sensitive to actuator time-delay leading to negative damping when considering high frequencies of lightly damped structures. The energy loss  $\Delta E$  which can be used for estimating this damping error can be computed from the measured forces and displacements:

$$\Delta E = \int r^T du_m - \int r^T du_c \quad (2.4)$$

where  $r^T$  is the measured restoring force;  $u_m$  and  $u_c$  represent the measured and command displacements, respectively. In general, energy errors less than 5% are acceptable. To verify this criterion, a test should start by applying a low-intensity input at varying  $M$  values. Once the energy criterion is fulfilled, the actual hybrid test can be carried out. In the case of a damaged structure, the damping ratio is expected to increase. At the same time, the reduced stiffness of the structure causes a smaller damping error since the negative damping is proportional to the stiffness of the structure.

In HS, the speed of the test is important when rate-dependent devices like dampers and friction pendulum isolators exist in the experimental or physical substructure. Rapid hybrid simulation tests have a small time-scale factor, typically in the range of 10-50, and, because of its higher speed, the restoring force measured may include significant inertial and viscous forces. Real-time tests are rapid hybrid simulation tests where the time-scale factor is reduced to unity, i.e., the duration of a hybrid test is the real one (the same as that of the input accelerogram). Hence, it is evident that the measured restoring forces can include inertial and viscous forces. Considering fast hybrid testing, the equilibrium equation can be written as:

$$M\ddot{U}_{i+1} + C\dot{U}_{i+1} + P_r^N(U_{i+1}, \dot{U}_{i+1}) + P_r^E(U_{i+1}) = P_{i+1} - P_{0,i+1} \quad (2.5)$$

$$P_r^E(U_{i+1}) = P_{r,i+1}^E - M^E\ddot{U}_{i+1}^E - C^E\dot{U}_{i+1}^E$$

where  $\dot{U}_{i+1}^E$  and  $\ddot{U}_{i+1}^E$  are the measured velocity and acceleration of the experimental substructure, respectively. The measured force,  $P_r^E$ , may include inertial and damping forces, hence it is modified,

at actuator's degrees of freedom, to account for it. Similarly, the equilibrium equation of a Real-Time Hybrid Simulation (RTHS) may be preferred to be written as:

$$\begin{aligned} M\ddot{U}_{i+1} + C^N\dot{U}_{i+1} + P_r^N(U_{i+1}, \dot{U}_{i+1}) + P_r^E(U_{i+1}, \dot{U}_{i+1}, \ddot{U}_{i+1}) &= P_{i+1} - P_{0,i+1} \\ P_r^E(U_{i+1}, \dot{U}_{i+1}, \ddot{U}_{i+1}) &= P_{r,i+1}^E - M^E\ddot{U}_{i+1}^E \end{aligned} \quad (2.6)$$

where the terms with the superscript N are assembled from the numerical substructure whereas the terms with the superscript E are assembled from the experimental substructure. In the above equation,  $P_r^E$  include damping and inertial forces of the experimental substructure. Hence, the measured restoring force  $P_{r,i+1}^E$  needs to be corrected for the inertial action. The above formulation is for illustrative purposes otherwise the restoring forces are assembled entirely from measured forces.

In hybrid simulation tests that are executed using shaking tables absolute response quantities are utilized. The mass of the physical substructure can generate an important inertial component and the shaking table is commanded using absolute displacements or accelerations defined by the analytical model. The equilibrium equation of this category of hybrid testing can be illustrated by:

$$\begin{aligned} M^N\ddot{U}_{i+1} + C^N\dot{U}_{i+1} + P_r^N(U_{i+1}, \dot{U}_{i+1}) + P_r^E(U_{t,i+1}, \dot{U}_{t,i+1}, \ddot{U}_{t,i+1}) &= P_{i+1} - P_{0,i+1} \\ P_r^E(U_{t,i+1}, \dot{U}_{t,i+1}, \ddot{U}_{t,i+1}) &= P_{r,i+1}^E + M^E\ddot{U}_{t,i+1} \end{aligned} \quad (2.7)$$

In equation (2.7),  $P_{r,i+1}^E$  of the experimental structure, which is mounted on a shaking table, and the external loads correspond to the numerical DOFs only. A portion of the current research falls on this domain where a soil-structure interaction of a given structure is studied by testing the soil on a shaking table platform while a hydraulic actuator imposes command displacements, computed from a numerical model of the superstructure, at the interface of the subassemblies.

## 2.3 Approaches for conducting hybrid simulation

Interface parameters at the boundary of substructures play an important role in hybrid simulation because they serve as a means of interaction. The condition that must be satisfied at the interface between the physical and numerical substructures dictates the type of formulation used for hybrid simulation. Depending on the nature of the problem, compatibility or equilibrium conditions can be satisfied. Accordingly, hybrid simulation can be conducted in displacement-based or force-based approaches.

### 2.3.1 Displacement-based hybrid simulation

It imposes strict kinematic compatibility conditions, and it is commonly used in computing the seismic response of structures. Due to its simplicity and suitability for broad applications, it is treated as the conventional method for hybrid simulation. Nevertheless, this approach has challenges when used with stiff test specimens, for which experimental error becomes unavoidable due to: a) the difficulty to control actuators when imposing small displacements, b) small errors in

the displacement command can result in large force discrepancies.

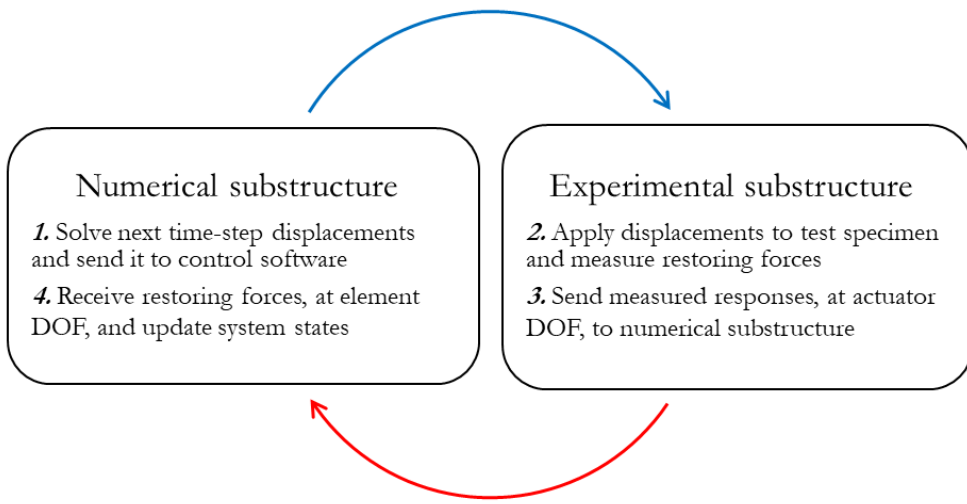


Figure 2-5: Displacement-based approach for hybrid simulation

### 2.3.2 Force-based hybrid simulation

It imposes strict dynamic equilibrium conditions at the interface boundary between the numerical and physical substructures (see Figure 2-6). This approach is useful for a hybrid simulation involving motion-induced loads, such as fluid-structure interaction. It is also suitable for hydrodynamic loads, namely tsunami, storm surge, breakwater, etc. where strict force (dynamic) equilibrium is preferred to kinematic compatibility (Nakata & Stehman, 2014). This formulation appears more qualified for hurricane and strong wind loads as well.

The force approach for hybrid simulation requires the dynamic force of actuators to be controlled in addition to the requirement for a robust force-based time-stepping algorithm. In general, Finite Element Analysis (FEA) is commonly conducted using displacement-based integration schemes. Therefore, force-based integration schemes need to be developed. Forouzan et al. (2017) developed an explicit force-based quadratic alpha method of numerical integration and applied it to a 3-DOF shear-type steel structure.

On the other hand, force control of actuators is challenging when compared to the traditional displacement control of actuators. The restoring force measured from a physical substructure is not noise-free due to friction, break-away forces on piston seals, and stick-slip phenomena during testing. In this approach, an actuator should be an inherent source of force, i.e., a low impedance system. However, an actuator is a high impedance device (good position control) and the presence of a stiff test structure may lead to a low proportional gain of the controller ( $F(\omega) = Z(\omega) \times V(\omega)$ , where  $Z(\omega)$  and  $V(\omega)$  are the impedance and velocity of an actuator, respectively). As the stiffness of a test structure increases, the response becomes oscillatory (Bousias, 2014). This approach can have large

force errors resulting from small gaps in actuator clevises and may induce brittle failure of a test specimen (Whyte & Stojadinovic, 2014). Besides, unlike the displacement control, the transformation of force from a global coordinate system to an actuator DOF does not yield a unique solution as in the case of the kinematic transformation (Bousias, 2014). Nevertheless, significant progress has been achieved in the last decade even though it has not been commonly adopted by researchers.

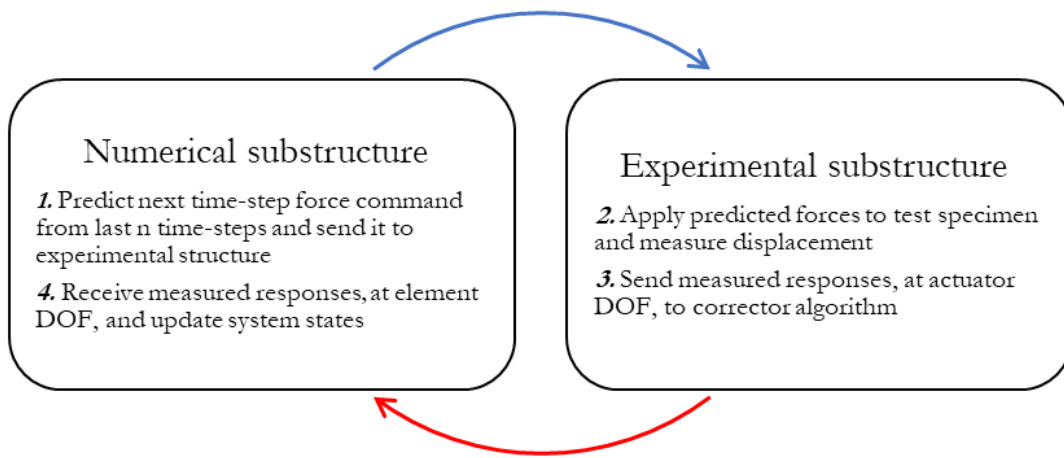


Figure 2-6: Force-based approach for hybrid simulation

## 2.4 Framework for hybrid simulation

The implementation of hybrid simulation has been problem-specific and stayed strongly dependent on the configuration of an experiment, numerical analysis software, actuator control, and data acquisition system employed in each testing facility. The development of a common framework for hybrid simulation was only recently been addressed with OpenFresco (Schellenberg et al., 2009) and UI-SimCor (Kwon et al., 2007). Schellenberg et al. (2009) recommend that such a framework should support various time-stepping algorithms, numerical modeling software, testing configurations (only actuator or shaking table, or actuator and shaking table), control systems (MATLAB and Simulink, LabVIEW, etc.), data acquisition systems, and communication protocols.

In general, two equivalent approaches can be used in developing a framework for hybrid simulation.

- a) **Structural analysis approach:** Hybrid simulation is considered as a finite element analysis whereby an experimental substructure is embedded as part of a reference structure under study.
- b) **Control system approach:** Hybrid simulation is treated as a feedback system whereby a physical substructure is assumed as a plant controlled by a computational driver.

An example of the first approach is the OpenFresco software (Takahashi & Fenves, 2006), which

is an object-oriented open-source framework software. It works as a middleware, bridging the communication between finite element software and control software. Its development was carried out in two steps:

1. Object-Oriented Analysis (OOA): This is the conceptual model that ensures the requirements of a common framework. It includes modeling physical substructures, generation of various command signals, conversion of measured signals appropriate for a numerical analysis program, ability to communicate with various control software and data acquisition hardware. Capability for speedy communication to help performing real-time execution and distributed hybrid testing is included as well.
2. Object-oriented model: It is a process of abstracting real-world objects into software classes and allowing data operations of one abstract class to remain hidden to other classes. OpenFresco has four abstract classes, namely the *experimental element*, *experimental site*, *experimental setup*, and *experimental control*. Its physical operations are therefore abstracted into four classes.

The three-tier software framework developed at the University of Berkeley, within the Network for Earthquake Engineering and Simulation (NEES), was designed to be modular and flexible. These characteristics allowed it to operate with various computational drivers from a top client tier. The 3<sup>rd</sup> tier in this framework is the laboratory control and data acquisition system that is responsible for driving a test specimen and collecting measured data to be returned to the computational drivers.

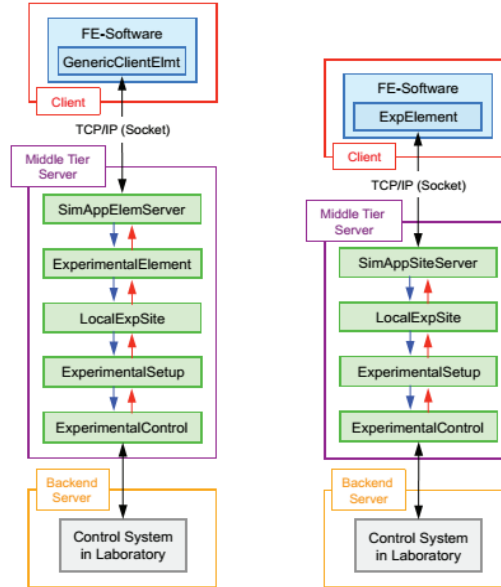


Figure 2-7: Two configurations of the NEES three-tier software architecture for hybrid simulation (after Schellenberg et al., 2009)

The top-tier and middle-tier represent the integration and middleware loop, respectively. For example, OpenSees can be used in the outer integration loop while OpenFresco bridges the

communication between OpenSees and a control software. Commonly, the top and middle tiers can reside in one computer, or they can be separated into two computers that are connected by a TCP/IP socket.

For local deployment, depending on the way the experimental element is defined, the OpenFresco framework has two possible configurations, as shown in Figure 2-7. In the first configuration, a generic client element is embedded into a finite element software using user-defined elements. Data exchange between the finite element software and OpenFresco middleware takes place through the embedded element. The generic client element requires the node number, the degrees of freedom that it is connected to, and the port to communicate through as input parameters (Schellenberg et al., 2009).

In the second configuration, an experimental element is added into the finite element software instead. This eliminates the need for the experimental element abstract class in the middleware. The drawback of the first approach is that users must rely on the existing elements of OpenFresco to represent an experimental element. Instead, in the second approach, the user can define an experimental element using resources from the finite element software. Thus, the second approach gives more flexibility in modeling an experimental element. In the case of geographically distributed testing, the middle-tier server is divided into two sections that are distributed across networks. This gives rise to a four-tier architecture. Herein, the implementation of OpenFresco for local hybrid testing is only addressed.

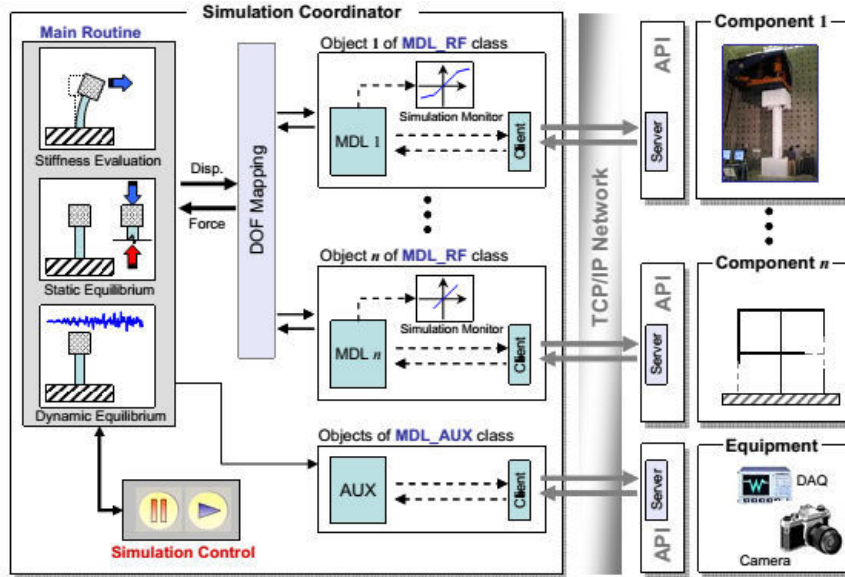


Figure 2-8: UI-SimCor architecture

The UI-SimCor (the University of Illinois Simulation Coordinator) software framework is another open-source, MATLAB-based, intuitive, simple, and efficient framework suitable for multi-site and multi-platform hybrid simulation tests (Kwon et al., 2007). It was developed at UIUC (the

University of Illinois at Urbana-Champaign), also within the NEES network. Although the initial focus of this framework was for distributed testing of structures, it has been successfully applied for many local hybrid tests. The excellent performance of UI-SimCor was demonstrated in the MISST (Multi-site-soil-structure-Foundation Interaction) project (Spencer et al., 2006) which accounted for soil-structure interaction of bridge piers in a distributed testing. The simulation coordinator is composed of two classes (Kwon et al., 2005):

1. MDL\_RF (restoring force module): It is an abstraction of structural components at distributed remote sites and handles routines such as time-integration, command generation, and measurement of restoring forces. New simulation tools and computational resources can be easily added to it. It can also serve as a means of communication among various remote sites using the ASCII or binary data format.
2. MDL\_AUX (auxiliary module): This class controls the experimental hardware except for actuators and sends pre-specified commands to remote sites for actions to be taken such as picture taking and DAQ triggering. It takes the role of interfacing programs of several computational drivers at remote sites to open a port for communication, impose displacements and send out restoring forces.

A shortlist of computational drivers, communication protocols, control, and data acquisition (DAQ) software that are supported by the two frameworks are presented in Table 2-1.

Table 2-1: Resources supported by OpenFresco and UI-SimCor

Type	<i>OpenFresco</i>	<i>UI-SimCor</i>
	Open-source	Open-source
Computational drivers	<ul style="list-style-type: none"> <li>✓ OpenSees</li> <li>✓ MATLAB/Simulink</li> <li>✓ OpenSees Navigator</li> <li>✓ UI-SimCor</li> <li>✓ ABAQUS</li> <li>✓ LS-DYNA</li> <li>✓ Ansys</li> </ul>	<ul style="list-style-type: none"> <li>✓ Zeus_NL</li> <li>✓ OpenSees</li> <li>✓ FEDEAS lab</li> <li>✓ ABAQUS</li> <li>✓ Any simulation tool in C++ or Fortran</li> </ul>
DAQ, control and communication	<ul style="list-style-type: none"> <li>✓ dSPACE</li> <li>✓ MTS</li> <li>✓ LabVIEW</li> <li>✓ National Instruments</li> <li>✓ SCRAMNet</li> <li>✓ Pacific Instruments</li> <li>✓ ADwin</li> <li>✓ TCP/IP socket</li> </ul>	<ul style="list-style-type: none"> <li>✓ OpenFresco</li> <li>✓ NTCP connection</li> <li>✓ MATLAB plug-in</li> <li>✓ TCP/IP socket</li> <li>✓ LabVIEW</li> <li>✓ All laboratory controls used in OpenFresco</li> </ul>

## 2.5 Time-stepping algorithms

Time-stepping algorithms for hybrid simulation can be classified as implicit or explicit methods

depending on whether the method requires information of the next time-step response to solve the current time-step increment or not. Recent developments in mixed methods were also implemented for hybrid testing (Mosqueda and Ahmadizadeh, 2008). Explicit algorithms need the current and last  $n$  states to solve the next time-step state. These methods are very efficient, fast, and easy to implement, but they are only conditionally stable. They become problematic in stiff problems because they require a very small time-step which could be prohibitive for hybrid simulation applications. Besides, classical explicit methods are non-iterative, one-step schemes, that are characterized by large unbalanced forces during nonlinear analysis. Additionally, they may not apply to structural systems having massless DOFs which can result in a singular mass matrix (Schellenberg et al., 2009). Nevertheless, the non-iterative nature of explicit methods makes them desirable for real-time hybrid simulation tests.

On the other hand, implicit algorithms are attractive for softening structures as well as stiff systems. However, implicit algorithms impose time constraints because the time spent by the numerical program in finding the iterative solution for a given time increment is indeterminate. Besides, the trial displacement may overshoot the target displacement; consequently, the actuator needs to unload the experimental substructure to correct this error. This loading and unloading can introduce unrealistic energy dissipation making response simulation inaccurate.

Hughes et al. (1979) proposed an implicit-explicit integration method for nonlinear mechanics. A similar study was conducted by Liu & Belytschko (1982) where the degrees of freedom (DOF) of a structure are divided into experimental and analytical DOFs. Likewise, to improve the limitation of explicit methods, a combined implicit and explicit method was studied by Mosqueda et al. (2007). In the latter, the integration method can improve the accumulation of errors of the explicit scheme and defaults to an explicit scheme when the solution does not converge.

Therefore, both the accuracy and stability of any explicit algorithm must be studied before applying it for hybrid testing. Period distortion and algorithmic damping are the criteria for evaluating the performance of a time-stepping algorithm (Hughes et al., 1979; Chopra, 2012). The integration algorithms are commonly studied in time-domain; nonetheless, the amplitude and phase of their frequency response, which is constructed using the discrete transfer function, can also be used to describe their time-domain properties (Muğan, 2003).

In the last two decades, several time-stepping algorithms, both explicit and implicit, that are tailored for hybrid simulation, have been developed. Some of the commonly used integration methods will be discussed subsequently.

### 2.5.1 Explicit integration scheme

To push the boundaries of hybrid simulation towards real-time hybrid simulation, important improvements have been made to the accuracy and unconditional stability of time-stepping algorithms. For example, the modified Newmark Explicit method (Shing & Mahin, 1987) was

developed from the original explicit Newmark method by adding frequency-proportional numerical damping. The scheme was found to be effective for nonlinear elastic structures in comparison to the initial-stiffness dependent viscous damping. Chang (1997) also developed a dissipative and second-order accurate explicit algorithm that is unconditionally stable. The method was developed for pseudo-dynamic testing and it was reported to have better accuracy compared to the explicit Newmark method. Another attractive method developed by Chen et al. (2009), termed as CR algorithm, allows trial displacement and velocity to be explicitly calculated. The pole mapping technique from the discrete control theory is utilized and the integration parameters can be chosen to achieve unconditional stability of linear elastic and nonlinear softening-type structures. However, the algorithm is only conditionally stable for nonlinear structures with stiffening behavior. Kolay & Ricles (2014) also proposed a generalized form for an explicit  $\alpha$ -method (KR- $\alpha$ ) that is unconditionally stable for structures with softening behavior. The controllable numerical damping of this method is governed by  $\rho_\infty$ . This method constitutes a one-parameter family of explicit methods which was developed by modifying the implicit generalized  $\alpha$ -method of integration thus inheriting its characteristics. The CR algorithm is therefore a special case of the KR- $\alpha$  algorithm that is obtained when  $\rho_\infty=1$  (zero numerical damping).

### 2.5.1.1 Explicit Newmark method

The general Newmark-beta method is defined by the discrete form of the equation of motion and the Newmark's finite difference formulas for the next time-step displacement and velocity is based on two weighting parameters,  $\beta$  and  $\gamma$ .

$$M\ddot{u}_{i+1} + C\dot{u}_{i+1} + P_r(\ddot{u}_{i+1}, \dot{u}_{i+1}, u_{i+1}) = P_{i+1} \quad (2.8)$$

$$u_{i+1} = u_i + \Delta t \dot{u}_i + \Delta t^2 \{(0.5 - \beta)\ddot{u}_i + \beta \ddot{u}_{i+1}\} = \tilde{u}_{i+1} + \Delta t^2 \beta \ddot{u}_{i+1} \quad (2.9)$$

$$\dot{u}_{i+1} = \dot{u}_i + \Delta t \ddot{u}_i (1 - \gamma) + \Delta t \ddot{u}_{i+1} \gamma = \tilde{\dot{u}}_{i+1} + \Delta t \ddot{u}_{i+1} \gamma \quad (2.10)$$

The explicit form of the Newmark method is therefore obtained when  $\beta=0$ . This results in the trial displacement  $\tilde{u}_{i+1}$  (displacement at the first iteration of an implicit Newmark method) to be equal to the final displacement.

$$u_{i+1} = \tilde{u}_{i+1} = u_i + \Delta t \dot{u}_i + \frac{\Delta t^2}{2} \ddot{u}_i \quad (2.11)$$

Substituting equations (2.9) and (2.10) in equation (2.8), the acceleration at the current time-step is obtained as:

$$M_{eff}\ddot{u}_{i+1} = P_{eff} \quad (2.12)$$

In equation (2.12),  $M_{eff}$  and  $P_{eff}$  are given by:

$$M_{eff} = M + \Delta t \gamma C \quad (2.13)$$

$$P_{eff} = P_{i+1} - P_r(\ddot{u}_{i+1}, \tilde{\ddot{u}}_{i+1}, \tilde{u}_{i+1}) - C\tilde{u}_{i+1} \quad (2.14)$$

At the end of the time-step,  $\Delta t$ , the velocity is updated using equation (2.9). If the effective mass matrix,  $M_{eff}$ , is diagonal, equation (2.12) can be solved for  $n$  uncoupled equations. At  $\gamma=0.5$ , the Newmark method inherits the properties of the central difference method which is second-order accurate and conditionally stable if:

$$\Delta t \leq T_n/\pi \quad (2.15)$$

where  $T_n$  is the smallest natural period of a structure. For second-order accuracy,  $\gamma \leq 0.5$ . The major drawback of the Newmark method is that it has zero numerical damping at  $\gamma=0.5$ . For values of  $\gamma$  greater than 0.5, too much numerical damping is introduced by the algorithm. This can overly damp the response of lower modes of a structure. Besides, the algorithm is no more second-order accurate. However, the acceleration-based method does not require the stiffness matrix to be calculated at each time-step. Thus, the method can be attractive for real-time hybrid testing of a structure that has a small natural frequency. Despite this, the use of the explicit Newmark method for nonlinear hybrid simulation tests, either softening or stiffening type, is limited due to its conditional stability.

### 2.5.1.2 CR integration algorithm

The properties of an integration algorithm and its corresponding discrete transfer function can be utilized in developing new integration schemes. The discrete transfer function of an integration method is the ratio of output to input in the Z-plane. The eigenvalues of the amplification matrix of the discrete transfer function represent its poles. The CR algorithm was developed using the pole-mapping technique to establish the values of its coefficients (Chae et al., 2013). The algorithm is explicit, unconditionally stable, and second-order accurate. The trial displacement and velocity responses are explicitly defined using two parameters,  $\alpha_1$  and  $\alpha_2$ .

$$\dot{u}_{i+1} = \dot{u}_i + \alpha_1 \Delta t \ddot{u}_i \quad (2.16)$$

$$u_{i+1} = u_i + \Delta t \dot{u}_i + \alpha_2 \Delta t^2 \ddot{u}_i \quad (2.17)$$

Considering a linear elastic SDOF structure, the equation of motion can be written as:

$$m\ddot{u}(t) + 2m\omega_n\xi\dot{u}(t) + m\omega_n^2u(t) = P(t) \quad (2.18)$$

Assuming the SDOF structure is at rest, a continuous transfer function between the output displacement and input force can be derived in the Laplace domain:

$$G(s) = \frac{U(s)}{P(s)} = \frac{1}{(s^2 + 2\xi\omega_n s + \omega_n^2)m} \quad (2.19)$$

The poles of  $G(s)$  are determined by solving its denominator. They can be shown to be equal to:

$$s_p = -\xi\omega_n \pm i\omega_n\sqrt{(1-\xi^2)} \quad (2.20)$$

However, the differential equation of motion of a structure is temporally discretized during

numerical analysis. Thus, the continuous  $G(s)$  function must be represented using the discrete Z-transform. A general Z-transform relating the output displacement to input force can be written as:

$$G(z) = \frac{U(z)}{P(z)} = \frac{n_r z^r + n_{r-1} z^{r-1} + \dots + n_1 z + n_0}{d_m z^m + d_{m-1} z^{m-1} + \dots + d_1 z + d_0} \quad (2.21)$$

where  $U(z)$  and  $P(z)$  are the discrete z-transforms of  $U(t)$  and  $P(t)$ , respectively;  $d_0, d_1, \dots, d_m$  and  $n_0, n_1, \dots, n_r$  represent the coefficients of the numerator and denominator of  $G(z)$ , respectively. The orders of the numerator and denominator are specified by  $r$  and  $m$  coefficients, respectively. The first-order Pade discretization (also known as Tustin's method) was utilized in approximating the exponential relationship between the continuous and discrete functions (i.e.,  $z = e^{s\Delta t}$ ).

$$z = \frac{1 + s \Delta t / 2}{1 - s \Delta t / 2} \quad (2.22)$$

Applying Tustin's transformation, the poles of the SDOF structure in the discrete z-domain can be derived as:

$$z_p = \frac{1 + \{-\xi \pm i\sqrt{(1 - \xi^2)}\} \omega_n \Delta t / 2}{1 - \{-\xi \pm i\sqrt{(1 - \xi^2)}\} \omega_n \Delta t / 2} \quad (2.23)$$

Likewise, the same discretizing formula is applied to equation (2.19) and  $G(z)$  becomes:

$$G(z) = \frac{\Delta t^2(z^2 + 2z + 1)}{\{(\omega_n^2 \Delta t^2 + 4\xi \omega_n \Delta t + 4)z^2 + (2\omega_n^2 \Delta t^2 - 8)z + (\omega_n^2 \Delta t^2 - 4\xi \omega_n \Delta t + 4)\}m} \quad (2.24)$$

The poles of  $G(z)$  are therefore derived from equation (2.24) (equivalent to equation (2.20)).

$$p_{1,2} = \frac{4 - \omega_n^2 \Delta t^2 \pm 4\sqrt{(\xi^2 - 1)}\omega_n \Delta t}{4 + \omega_n^2 \Delta t^2 + 4\xi \omega_n \Delta t} \quad (2.25)$$

Now, returning to the definition of the CR algorithm, the discrete transfer function  $G(z)$  can be derived by substituting equations (2.16) and (2.17) into the discretized form of equation (2.18).

$$G(z) = \frac{\Delta t^2(\alpha_2 z + \alpha_1 - \alpha_2)}{\{z^2 + (\alpha_2 \omega_n^2 \Delta t^2 + 2\xi \alpha_1 \omega_n \Delta t - 2)z + ((\alpha_1 - \alpha_2)\omega_n^2 \Delta t^2 - 2\xi \alpha_1 \omega_n \Delta t + 1)\}m} \quad (2.26)$$

Equating the discrete poles from equation (2.23) to the poles of equation (2.26), and solving for  $\alpha_1$  and  $\alpha_2$ , we get:

$$\alpha_1 = \alpha_2 = \frac{4}{4 + 4\xi \omega_n \Delta t + \omega_n^2 \Delta t^2} \quad (2.27)$$

For MDOF structures, Ricles & Chen (2008) have also shown that the coefficients can be derived as:

$$\boldsymbol{\alpha}_1 = \boldsymbol{\alpha}_2 = \frac{4\mathbf{M}}{4\mathbf{M} + 2\Delta t \mathbf{C} + \Delta t^2 \mathbf{K}} \quad (2.28)$$

where  $\mathbf{M}$ ,  $\mathbf{C}$ , and  $\mathbf{K}$  are the mass, damping, and stiffness matrices, respectively;  $\boldsymbol{\alpha}_1$  and  $\boldsymbol{\alpha}_2$  are vectors of integration coefficients.

### 2.5.1.3 KR- $\alpha$ integration algorithm

KR- $\alpha$  is a one-variable scheme derived from the implicit generalized-alpha method. It is explicit for both displacement and velocity and possesses controllable algorithmic damping. It was developed by transforming the two-variable implicit generalized-alpha method into an explicit method without altering its characteristics thus making it a candidate for RTHS tests. It is unconditionally stable for linear-elastic and softening-type nonlinear structures. Only the main principles of its derivation are discussed here but a detailed study can be found in Kolay & Ricles (2014). The KR- $\alpha$  algorithm is derived from the alpha-shifted equation of motion after specifying the spectral radius, a parameter that defines its numerical damping in the limit  $\omega_n \Delta t \rightarrow \infty$ . The trial displacement and trial velocity are defined in the same way as in the CR algorithm. The following equation describes the algorithm considering a MDOF structure subjected to an external excitation load vector  $\mathbf{P}(t)$  and the trial displacement and trial velocity are calculated using equations (2.16) and (2.17), respectively.

$$M\hat{\ddot{U}}_{i+1} + C\dot{U}_{i+1-\alpha_f} + KU_{i+1-\alpha_f} = P_{i+1-\alpha_f} \quad (2.29)$$

The weighting functions are determined from:

$$\begin{aligned} \hat{\ddot{U}}_{i+1} &= \boldsymbol{\alpha}_3 \ddot{U}_i + (\mathbf{I} - \boldsymbol{\alpha}_3) \ddot{U}_{i+1} \\ \dot{U}_{i+1-\alpha_f} &= \alpha_f \dot{U}_i + (1 - \alpha_f) \dot{U}_{i+1} \\ U_{i+1-\alpha_f} &= \alpha_f U_i + (1 - \alpha_f) U_{i+1} \\ P_{i+1-\alpha_f} &= \alpha_f P_i + (1 - \alpha_f) P_{i+1} \end{aligned} \quad (2.30)$$

where  $U, \dot{U}, \ddot{U}$  and  $P$  are the displacement, velocity, acceleration, and force vectors, respectively,  $\mathbf{I}$  is an identity matrix;  $\boldsymbol{\alpha}_1, \boldsymbol{\alpha}_2$  and  $\boldsymbol{\alpha}_3$  are the parameters of the integration scheme, each having  $n \times n$  dimension. The coefficient  $\alpha_f$  is the weighting parameter of this integration. The essential task in this approach is to determine the integration parameters. The algorithm starts by solving the initial acceleration for given initial conditions of displacement and velocity.

$$\ddot{U}_0 = M^{-1}[P_0 - C\dot{U}_0 - KU_0] \quad (2.31)$$

Considering the classical diagonal damping matrix and using the orthogonality property of modes of vibration, the nodal displacements are given by  $U = [\phi]\{Y\}$ , where  $\phi$  is the mode shape matrix and  $Y$  is the vector of modal coordinates. Then, the equation of motion can be expressed as  $n$  uncoupled equations.

$$M_G \hat{\ddot{Y}}_{i+1} + C_G \dot{Y}_{i+1-\alpha_f} + K_G Y_{i+1-\alpha_f} = [\phi]^T P_{i+1-\alpha_f} \quad (2.32)$$

Pre-multiplying the finite-difference formula by  $\phi^{-1}$ , we get:

$$\phi^{-1} \phi \hat{\ddot{Y}}_{i+1} = \phi^{-1} \phi \dot{Y}_i + \Delta t \phi^{-1} \boldsymbol{\alpha}_1 \phi \ddot{Y}_i \quad (2.33)$$

This reasoning is applied to obtain the next time-step modal coordinate response.

$$Y_{i+1} = Y_i + \Delta t \dot{Y}_i + \Delta t^2 \boldsymbol{\alpha}_2^* \ddot{Y}_i \quad (2.34)$$

$$\dot{Y}_{i+1} = \dot{Y}_i + \Delta t \alpha_1^* \ddot{Y}_i$$

$$\hat{Y}_{i+1} = \alpha_3^* \ddot{Y}_i + (\mathbf{I} - \alpha_3^*) \dot{Y}_{i+1}$$

where  $\alpha_1^* = \phi^{-1} \alpha_1 \phi$ ,  $\alpha_2^* = \phi^{-1} \alpha_2 \phi$  and  $\alpha_3^* = \phi^{-1} \alpha_3 \phi$  are the modal integration coefficients while  $M_G = [\phi]^T M[\phi]$ ,  $C_G = [\phi]^T C[\phi]$  and  $K_G = [\phi]^T K[\phi]$  are the diagonal matrices of mass, damping, and stiffness, respectively. For any mode  $j$  of the MDOF structure, the integration parameters can be written as:

$$\begin{aligned}\alpha_{1j}^* &= \frac{1}{1 + 2\gamma\xi_j\omega_j\Delta t + \beta(\omega_j\Delta t)^2} \\ \alpha_{2j}^* &= \frac{\left(\frac{1}{2} + \gamma\right)}{1 + 2\gamma\xi_j\omega_j\Delta t + \beta(\omega_j\Delta t)^2} \\ \alpha_{3j}^* &= \frac{\alpha_m + 2\alpha_f\gamma\xi_j\omega_j\Delta t + \alpha_f\beta(\omega_j\Delta t)^2}{1 + 2\gamma\xi_j\omega_j\Delta t + \beta(\omega_j\Delta t)^2}\end{aligned}\quad (2.35)$$

where  $\alpha_f$ ,  $\alpha_m$ ,  $\gamma$  and  $\beta$  are the parameters of the generalized-alpha integration. To ensure second-order accuracy, unconditional stability, and maximum numerical damping, the parameters  $\gamma$  and  $\beta$  are related by:

$$\begin{aligned}\gamma &= 1/2 - \alpha_m + \alpha_f \\ \beta &= 1/4(1 - \alpha_m + \alpha_f)^2\end{aligned}\quad (2.36)$$

Other than the need for high-frequency damping, energy dissipation of low-frequency modes can be controlled by choosing the  $\rho_\infty$ , as  $\omega\Delta t$  approaches infinity, for the three eigenvalues of the amplification matrix of the algorithm. If  $\rho_\infty=1$ , no numerical damping is introduced by the algorithm and the solution is identical to the CR algorithm. On the other hand, when  $\rho_\infty=0$ , the integration method achieves asymptotic annihilation where maximal numerical damping is produced. The integration parameters  $\alpha_f$  and  $\alpha_m$  can be related to  $\rho_\infty$  by minimizing the system energy. It should be noted that the relationships proposed by Kolay & Ricles (2014) may not be the most optimal solutions. Later, the same authors proposed an improved formulation (Kolay & Ricles, 2019).

$$\alpha_m = \frac{(2\rho_\infty - 1)}{\rho_\infty + 1}\quad (2.37)$$

$$\alpha_f = \frac{\rho_\infty}{\rho_\infty + 1}\quad (2.38)$$

### 2.5.2 Implicit integration scheme

Implicit time-stepping methods require the current time-step response to solve the equation of motion. They are unconditionally stable and ideal solutions for highly nonlinear complex structures and stiff problems. Implicit methods are iterative and require more than one function call per time-step. The first step in the implicit method is to predict the solution using an explicit expression and

correct it  $n$  times until convergence. Thus, the method is referred sometimes to as a predictor multi-corrector algorithm. The iterative solution of a nonlinear problem is commonly carried out through the Newton-Raphson method of solution. This method requires the tangent stiffness matrix at each iteration. It is prohibitive for hybrid simulation applications because of the intense communications between the numerical and experimental substructures.

Implicit methods are computationally demanding, and they can cause spurious loading-unloading cycles of the experimental substructure. Updating the tangent stiffness matrix to assemble it into the global stiffness matrix at each sub-step is computationally demanding and restoring forces measured at sub-steps are not noise-free. Moreover, the time of execution is not deterministic as the number of iterations is not fixed. Even though classical implicit methods are unconditionally stable and accurate under large time-steps, their implementation in RTHS is impractical if applied without any modifications.

The modified implicit Newmark method proposed by Schellenberg et al. (2009) was developed by reducing the displacement increments during the iterative process and fixing the number of iterations that are conducted at each time-step. The algorithm is termed as Newmark fixed-number of iterations or Newmark hybrid simulation. Reducing displacement increments satisfies the requirements for a continuously increasing displacement function. Besides, fixing the number of iterations enables determinism whereby real-time hybrid tests can be conducted. Two alternatives for the reduction of the displacement increment were proposed by Schellenberg et al. (2009). In the first approach, a reduction factor  $\theta$ , in the range  $[0, 1]$ , is directly applied to  $\Delta U$  solution at each sub-step. This approach improved the smoothness of the convergence path, but it is characterized by non-uniform displacement increments that can generate force oscillations during a hybrid test. Hence, it can only achieve good performance when used in combination with event-driven strategies. The second approach, hereinafter nominated as the Newmark Hybrid Simulation (NMHS) method, interpolates displacements for a fixed number of iterations using the Lagrange interpolation, based on the current time-step and the last  $n$  committed displacements.

Similarly, Chen & Ricles (2012) studied the characteristics of the implicit HHT- $\alpha$  method, developed by Hilber et al. (1977), by modifying it to have a fixed number of iterations. The algorithm was shown to be unconditionally stable for linear elastic structures, but conditionally stable for nonlinear softening or hardening structures. In this method, the command displacement in each sub-step is calculated using restoring forces of the last  $n$  sub-steps. The convergence error is minimized by correcting the restoring force and displacement at the end of each time-step. This method was reported to be accurate and stable when used in experimental tests (Jung & Shing, 2006, 2007). For brevity, only the derivation of the Newmark hybrid simulation algorithm is presented in this chapter.

### 2.5.2.1 Newmark hybrid simulation (NMHS)

The implicit Newmark method of integration (Newmark, 1959) is widely used for solving the differential equation of motion in earthquake engineering and structural dynamics. It is highly

accurate and unconditionally stable. It is iterative and suitable for numerical methods such as in Finite Element Analysis (FEA). The Newton-Raphson method, which is commonly employed for solving the iterative process, has a quadratic convergence property whereby displacement increments drop rapidly with each iteration. On the other hand, actuators are typically assigned the same amount of time interval for applying a displacement command. Hence, a rapidly decreasing displacement command results in a jerky and non-uniform movement of actuators. To overcome the above challenges, Schellenberg et al. (2009) developed the Newmark fixed-number of iterations, which is available in the library of the OpenSees-OpenFresco framework software.

The equation of motion and the equations defining the Newmark-beta method were already presented in the explanation for the explicit Newmark method; thus, only the iterative scheme is discussed here. Re-arranging the equation governing the Newmark-beta method, one gets:

$$\ddot{U}_{i+1} = \frac{\gamma}{\beta\Delta t} (U_{i+1} - U_i) - \left\{ \frac{\gamma}{\beta} - 1 \right\} \dot{U}_i - \Delta t \left\{ \frac{\gamma}{2\beta} - 1 \right\} \ddot{U}_i \quad (2.39)$$

$$\ddot{U}_{i+1} = \frac{\gamma}{\beta\Delta t^2} (U_{i+1} - U_i) - \frac{1}{\beta\Delta t} \dot{U}_i - \left\{ \frac{1}{2\beta} - 1 \right\} \ddot{U}_i \quad (2.40)$$

The equation of motion can also be written in the form of the unbalanced force vector,  $F$ , at the current time-step:

$$F(U_{i+1}) = M\ddot{U}_{i+1} + C\dot{U}_{i+1} + P_r(U_{i+1}) - P_{i+1} \quad (2.41)$$

Using the Newton-Raphson method, the above equation is solved through a Jacobian matrix,  $J$ , such as:

$$J(U_{i+1}^{(k)}) \Delta U^{(k)} = -F(U_{i+1}) \quad (2.42)$$

In structural dynamics, the Jacobian matrix and the vector unbalanced forces are referred to as the effective stiffness matrix and effective unbalanced force vector, respectively. Hence, we can write:

$$K_{eff}^{(k)} \Delta U^{(k)} = P_{eff}^{(k)} \quad (2.43)$$

The effective stiffness and effective unbalanced force at iteration  $k$  can be obtained by substituting equations (2.39) and (2.40) in equation (2.41).

$$\begin{aligned} K_{eff}^{(k)} &= c_3 M + c_2 C + c_1 K_t(U_{i+1}^{(k)}) \\ P_{eff}^{(k)} &= P_{i+1} - P_r(U_{i+1}^{(k)}) - M\ddot{U}_{i+1}^{(k)} - C\dot{U}_{i+1}^{(k)} \end{aligned} \quad (2.44)$$

where  $c_1=1$ ,  $c_2=\gamma/(\beta\Delta t)$ , and  $c_3=1/(\beta\Delta t^2)$ . The converged displacement at time-step  $i$  is adopted as the trial displacement at the first iteration of the time-step  $i+1$ . The velocity and acceleration responses at the first iteration are calculated from equations (2.39) and (2.40), respectively. In the classic implicit Newmark method, the increment in displacement at time-step  $i+1$  and sub-step  $k$  is calculated from:

$$\Delta U^{(k)} = solve \left\{ K_{eff}^{(k)} \Delta U^{(k)} = P_{eff}^{(k)} \right\} \quad (2.45)$$

However, the scaled iterative displacement increment in the NMHS method is calculated using Lagrange polynomials:

$$\Delta U_{scaled}^{(k)}(x) = \sum_{j=i+1-n}^{i+1} \{U_j L_{n,j}(x)\} - U_{i+1}^{(k-1)} \quad (2.46)$$

where  $U_j$  and  $U_{i+1}^{(k-1)}$  are the last  $j$ th committed displacement and the iterative displacement at the last sub-step, respectively;  $L_{n,j}(x = \frac{k}{k_{max}})$  is the  $n$ th order Lagrange polynomial at the  $k$ th iteration ( $k_{max}$  is the maximum number of iterations carried out in each time-step). The next step in this algorithm is to update iterative responses using the scaled displacement increment:

$$\begin{aligned} U_{i+1}^{(k)} &= U_{i+1}^{(k-1)} + c_1 \Delta U_{scaled}^{(k)} \\ \dot{U}_{i+1}^{(k)} &= \dot{U}_{i+1}^{(k-1)} + c_2 \Delta U_{scaled}^{(k)} \\ \ddot{U}_{i+1}^{(k)} &= \ddot{U}_{i+1}^{(k-1)} + c_3 \Delta U_{scaled}^{(k)} \end{aligned} \quad (2.47)$$

OpenFresco does not return the tangent stiffness of an experimental substructure because it is difficult to calculate the tangent stiffness from force measurements taken at a few locations of a test specimen. Hence, the Jacobian matrix is assembled using the tangent stiffness matrix of the numerical substructure and the initial stiffness matrix of the experimental substructure. The resulting integration method has nearly uniform and monotonic displacement increments.

### 2.5.3 Operator-splitting method

The alpha Operator-Splitting ( $\alpha$ -OS) integration method, first adopted by Nakashima et al. (1990), is one of the most common, non-iterative, and unconditionally stable techniques. It works using the prediction-correction principle to achieve improved stability and accuracy compared to other explicit methods. The  $\alpha$ -OS integration splits displacements and velocities into implicit and explicit terms, and it is unconditionally stable for nonlinear softening systems. The tangent stiffness of the experimental substructure is not required in this method. The above advantages have led to its wide use among the hybrid testing community. The algorithm was applied in real-time hybrid simulation tests (Bursi & Wagg, 2008). The  $\alpha$ -OS integration is available in the OpenSees framework. It has one parameter,  $\alpha$ , that is responsible for defining the numerical damping of the algorithm and it requires a linear algorithm for solving a system of equations. The value of  $\alpha$  has the interval [2/3, 1]; and when  $\alpha=1$ , it reduces to the family of the Newmark integration method.

In addition to the first  $\alpha$ -OS method, a similar integration algorithm called the generalized-alpha OS (termed as G $\alpha$ OS1) was also developed by Schellenberg et al. (2009). It combines the operator-splitting technique proposed by Hughes et al. (1979) and the generalized-alpha method of Chung & Hulbert (1993). However, when initial stiffness is used in this approach, it can lose its unconditional stability if significant geometric nonlinearities are accounted for using the corotational transformation. To improve the challenges of the first approach, a second method

called G $\alpha$ OS2 was developed. The latter uses a mixed stiffness matrix while calculating the restoring forces (Schellenberg et al., 2009). An alternative operator-separator scheme, based on the Generalized-alpha method of integration, was also proposed by Bonelli & Bursi (2004).

In the predictor phase of  $\alpha$ -OS, Newmark equations are used to predict the trial displacements,  $\tilde{u}_{i+1}$ , and trial velocities,  $\tilde{u}_{i+1}$ . The integration parameters are computed from:

$$\beta = \frac{(2 - \alpha)^2}{4}; \gamma = \frac{(3 - 2\alpha)}{2} \quad (2.48)$$

where  $\alpha \in [2/3, 1]$ ; and the alpha shifted equation of motion, which is used in constructing the  $\alpha$ -OS integration, reads:

$$M\ddot{U}_{i+1} + \alpha C\dot{U}_{i+1} + C(1 - \alpha)\dot{U}_i + \alpha P_r(U_{i+1}) + (1 - \alpha)P_r(U_i) = \alpha P_{i+1} + (1 - \alpha)P_i \quad (2.49)$$

The vector of restoring forces in the left-hand side of the equation (2.49) is estimated through the operator-splitting technique, based on the initial stiffness  $K_{in}$ , as:

$$P_r(U_{i+1}) \cong K_{in}U_{i+1} - K_{in}\tilde{U}_{i+1} + P_r(\tilde{U}_{i+1}) \quad (2.50)$$

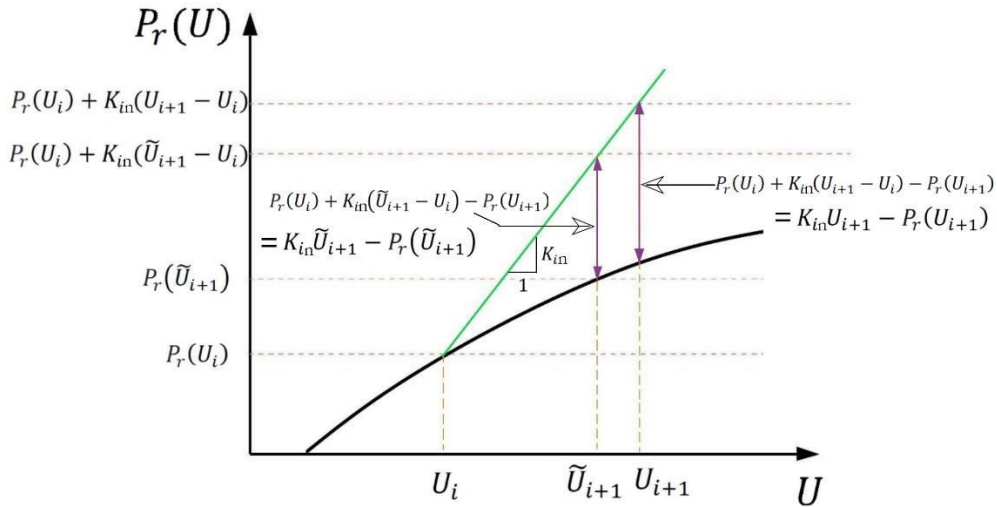


Figure 2-9: Approximation of nonlinear resisting forces in Operator-splitting integration

Equation (2.50) is derived from the approximation that the difference between the elastic and nonlinear restoring forces at the predictor displacement  $\tilde{U}_{i+1}$  is approximately equal to the difference between the elastic and nonlinear restoring forces at the actual displacement  $U_{i+1}$ . The graphical representation of this approximation is presented in Figure 2-9. Substituting equation (2.50) into equation (2.29) and using equation (2.30) (note that in the  $\alpha$ -OS scheme, also in HHT,  $\alpha_f = 1 - \alpha$  and  $\alpha_m = 0$ ), the displacement increment between the predictor and final displacement ( $\Delta U = U_{i+1} - \tilde{U}_{i+1}$ ) may be computed by solving:

$$K_{eff}\Delta U = P_{eff} \quad (2.51)$$

The next time-step displacement and velocity can be written as a function of  $\Delta U$ :

$$\begin{aligned}\dot{U}_{i+1} &= \frac{\gamma}{\beta(\Delta t)}(U_{i+1} - \tilde{U}_{i+1}) + \dot{U}_i + \Delta t(1 - \gamma)\ddot{U}_i \\ \dot{U}_{i+1} &= \frac{1}{\beta(\Delta t)^2}(U_{i+1} - \tilde{U}_{i+1})\end{aligned}\quad (2.52)$$

From the above formulation, one can derive the effective stiffness and effective restoring force:

$$\begin{aligned}K_{eff} &= c_3 M + \alpha c_2 C + \alpha c_1 K_i \\ P_{eff} &= \left\{ \begin{array}{l} \alpha P_{i+1} + (1 - \alpha)P_i - (1 - \alpha)K_{in}(U_i - \tilde{U}_i) - \\ \alpha P_r(\tilde{U}_{i+1}) - (1 - \alpha)P_r(U_i) - C \{ \alpha \tilde{U}_{i+1} + (1 - \alpha)U_i \} \end{array} \right\}\end{aligned}\quad (2.53)$$

where  $c_1 = 1$ ,  $c_2 = \gamma/(\beta\Delta t)$ , and  $c_3 = 1/(\beta\Delta t^2)$ . At the end of time-step  $i+1$ , responses can be then updated as:

$$\begin{aligned}U_{i+1} &= \tilde{U}_{i+1} + c_1 \Delta U \\ \dot{U}_{i+1} &= \tilde{\dot{U}}_{i+1} + c_2 \Delta U \\ \ddot{U}_{i+1} &= c_3 \Delta U\end{aligned}\quad (2.54)$$

During a hybrid test, using the  $\alpha$ -OS scheme, the trial displacement  $\tilde{U}_{i+1}$  is applied through an actuator and the measured force  $P_r(\tilde{U}_{i+1})$  is returned to the numerical program and the system states are updated using equation (2.54). To improve its accuracy, Ahmadizadeh & Mosqueda (2008) developed a method for estimating the tangent stiffness of an experimental element by transforming measurements into a coordinate system that reduces the size of the update-matrix. The proposed method was validated in a hybrid test comprising a highly nonlinear experimental substructure.

## 2.5.4 Accuracy and stability analysis of integration algorithms

### 2.5.4.1 Stability analysis

For linear-elastic systems, the stability analysis can be performed by studying the amplification matrix of the integration algorithm, or through the discrete control theory. In the latter, the discrete transfer function from input force to output displacement is first constructed and the roots of its characteristic equation dictate the stability properties of the algorithm.

In general, the next time-step response of a SDOF structure, under free vibration, can be written in a recursive form:

$$[u_{i+1} \ \Delta t \dot{u}_{i+1} \ \Delta t^2 \ddot{u}_{i+1}]^T = A[u_i \ \Delta t \dot{u}_i \ \Delta t^2 \ddot{u}_i]^T \quad (2.55)$$

The amplification matrix,  $A$ , can be derived from the relationship between the equation of motion and the discretization adopted in a time-step. For illustration, the amplification matrix for the KR- $\alpha$  integration method takes the following form:

$$A = \begin{bmatrix} 1 & 1 & \alpha_2 \\ 0 & 1 & \alpha_1 \\ (\omega\Delta t)^2 & 2\xi\omega\Delta t + (1 - \alpha_f)(\omega\Delta t)^2 & \frac{\alpha_3 + 2(1 - \alpha_f)\alpha_1\xi\omega\Delta t + (1 - \alpha_f)\alpha_2(\omega\Delta t)^2}{\alpha_3 - 1} \\ \alpha_3 - 1 & \alpha_3 - 1 & \alpha_3 - 1 \end{bmatrix} \quad (2.56)$$

The solution of the eigenvalue problem results in three eigenvalues,  $\lambda$ :

$$|A - \lambda I| = \lambda^3 - A_1\lambda^2 + A_2\lambda - A_3 = 0 \quad (2.57)$$

where  $I$  is a 3x3 identity matrix;  $A_1$ ,  $A_2$ , and  $A_3$  are the principal invariants of  $A$ , i.e., trace of  $A$ , sum of the principal minors of  $A$ , and determinant of  $A$ , respectively. To ensure a bounded response, the magnitude of the largest eigenvalue must be less than one. This condition should be true throughout the space of  $\Omega = \omega\Delta t$ , where  $\Omega$  is bounded between zero and infinity. The solution to the problem in the two cases can, therefore, be used in establishing the relationship between the spectral radius and  $\Omega$ . It is a general practice to conduct stability analysis at various levels of inherent damping. For a linear-elastic system, the KR- $\alpha$  method is unconditionally stable if the inherent damping is greater than zero.

The stability analysis of an integration algorithm for nonlinear systems can be also performed using the discrete control theory. In that case, the equation of motion is written in an incremental form which can be represented using a block diagram. Taking a small time-step, tangent stiffness  $k_t$  can be considered as constant. Hence, the incremental nonlinear restoring force becomes the product of  $k_t$  and an incremental displacement. The transfer functions that make up the block diagram are determined, and the closed-loop transfer function of the system is obtained. The poles of this transfer function are then examined by changing  $k_t$ . Eventually, the complete solution of the problem can be utilized in establishing the stability limit as a function of the ratio of tangent stiffness to initial stiffness.

As mentioned above, the explicit Newmark method is conditionally stable while the NMHS is unconditionally stable. The latter is recommended for stiff problems that are characterized by strong material and geometric nonlinearities. Such problems require well-converged equilibrium states at the end of each time-step. The KR- $\alpha$  and CR integration methods are unconditionally stable for linear and nonlinear softening-type structures. However, both algorithms are conditionally stable for stiffening-type structures. For example, the stability limit of the KR- $\alpha$  integration method for stiffening-type structures can vary depending on the spectral radius at infinity,  $\rho_\infty$  (Kolay & Ricles, 2014):

$$\begin{aligned} \frac{k_t}{k_i} &\leq 1 + \frac{4}{\Omega^2}; \quad \rho_\infty = 1 \\ \frac{k_t}{k_i} &\leq \frac{4}{3} \left(1 + \frac{2\xi}{\Omega}\right) + \frac{4}{\Omega^2}; \quad \rho_\infty = 0 \end{aligned} \quad (2.58)$$

where  $k_t$  and  $k_i$  are the tangent and initial stiffnesses, respectively. If  $\rho_\infty=1$ , the stability of KR- $\alpha$  is identical to that of the CR method. In equation (2.58), at maximum algorithmic damping and assuming zero inherent damping, the stability limit has improved by 1/3 at very large frequencies.

### 2.5.4.2 Accuracy analysis

In structural dynamics, the accuracy of a numerical integrator is commonly expressed in terms of numerical dissipation and dispersion. For any integration scheme, analytical derivation of the accuracy measure is difficult, and hence the general practice is to resort to the linear-elastic response of a SDOF structure under a free vibration (Kolay & Ricles, 2014). The solution of a free vibration problem in the discrete formulation can be written like an exact solution, which reads:

$$u(t) = e^{-\bar{\xi}\bar{\omega}_n t} (A \cos(\bar{\omega}_D t) + B \sin(\bar{\omega}_D t)) \quad (2.59)$$

where  $\bar{\omega}_D = \bar{\omega}_n \sqrt{1 - \bar{\xi}^2}$ ,  $\bar{\xi}$  and  $\bar{\omega}_n$  are the damped frequency, damping ratio and undamped natural frequency, respectively. The accuracy measure can be then evaluated as:

1. A measure of dispersion (Period Error, PE): The relative error of the natural period of a structure is calculated from the exact and equivalent discrete solutions of the natural period of the structure. It is calculated by  $PE = (\bar{T} - T_n) / T_n$ , where  $\bar{T}$  is the apparent natural period and  $T_n$  is the exact natural period of the structure.
2. A measure of dissipation (Numerical Damping, ND): It is the ability to introduce numerical damping to suppress the contribution of higher modes in the response of a structure. Nonetheless, the effect of this numerical damping should be very small or negligible in the lower modes; otherwise, the accuracy of the integration method may be compromised. The numerical damping  $ND$  is obtained from  $\bar{\xi} - \xi$ , where  $\bar{\xi}$  is the equivalent damping of the structure that combines the numerical and inherent damping characteristics and  $\xi$  is the inherent damping of the structure.

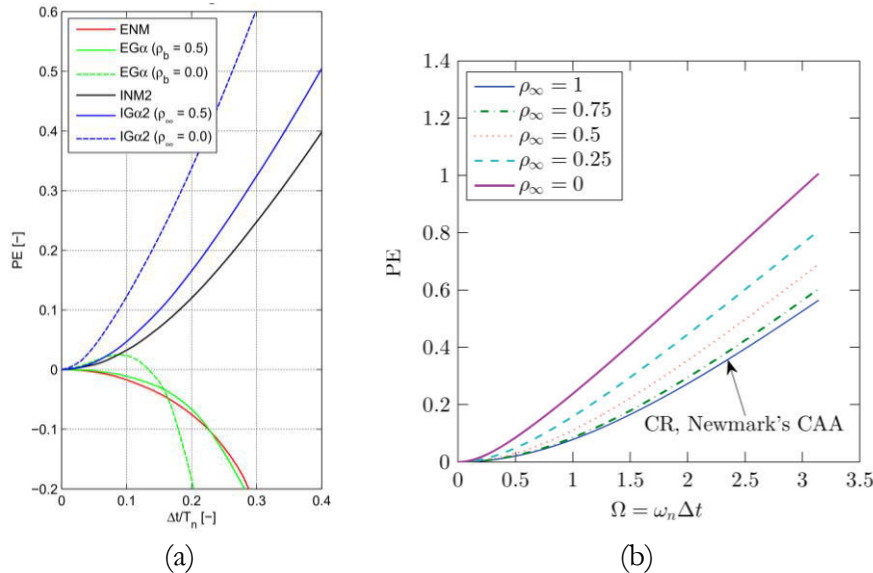


Figure 2-10: Period elongation (PE): (a) Explicit NM and NMHS(INM2) algorithms (Schellenberg et al., 2009) and (b) KR- $\alpha$  and CR algorithms (Kolay & Ricles, 2014)

In general, explicit methods such as the Newmark and explicit generalized-alpha methods shorten

periods, whereas all the implicit methods, including the operator-splitting method, lengthen periods (see Figure 2-10(a)). The NMHS algorithm (labeled as INM2 in Figure 2-10(a)) has better period elongation characteristics compared to the modified implicit Generalized-alpha method (IG $\alpha$ 2). The latter was proposed by Schellenberg et al. (2009) and it is not discussed in this chapter since it has a similar principle to the development of the modified implicit Newmark method.

The CR algorithm has identical dispersion characteristics to the implicit Newmark integration with average acceleration. The dispersion of KR- $\alpha$  increases with increasing numerical damping. when  $\rho_\infty=1$ , it achieves similar dispersion characteristics as that of the CR algorithm, as shown in Figure 2-10(b).

Both the explicit and implicit Newmark methods do not introduce numerical damping, as shown in Figure 2-11(a), whereas the generalized-alpha methods introduce numerical damping controlled by the spectral radius. In the explicit generalized-alpha method, as the stability limit approaches, the numerical damping increases faster than their implicit counterparts. Considering the KR- $\alpha$  integration, its effective damping increases as  $\rho_\infty$  gets smaller, but it can be less than the inherent damping, with increasing values of  $\Omega$ , for inherent damping greater than zero. This phenomenon explains why inherent damping may not be effective in suppressing the spurious contribution of higher modes. The presence of experimental errors in hybrid simulation is a potential source for the excitation of higher modes.

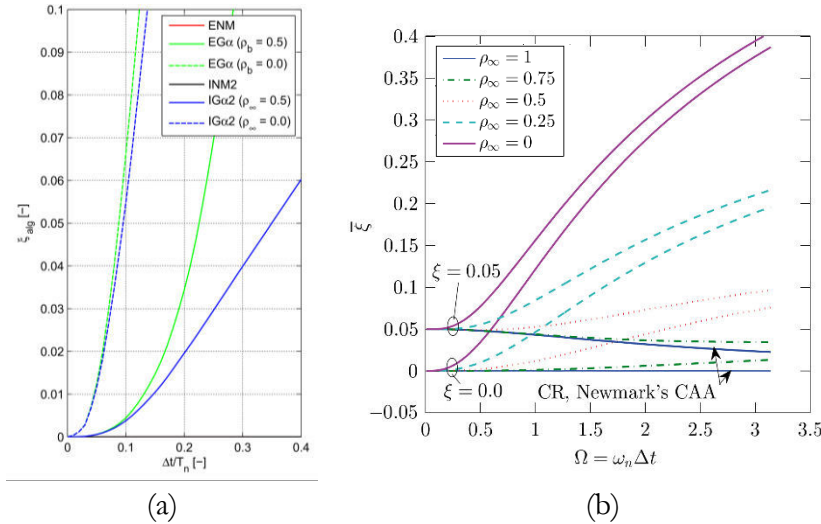


Figure 2-11: Numerical Damping: (a) Explicit NM and NMHS(INM2) algorithms (Schellenberg et al., 2009) and (b) KR- $\alpha$  and CR algorithms (Kolay & Ricles, 2014)

## 2.6 Experimental errors

In structural testing, the dynamics of a servo-hydraulic actuator, other mechanical components, and connections are the main sources of the inherent nonlinearity of a load transfer system. Besides, the

test specimen can behave nonlinearly. Generally, experimental errors can be categorized as systematic or random. In hybrid testing, a systematic error can be difficult to mitigate because it may propagate into the numerical program and grow exponentially. On the other hand, random errors have a stochastic nature. Noise of measurements is the main source of random errors. Systematic errors comprise time-delay and gain error. In a hybrid simulation test, system time-delay is the summation of the actuator's time-delay, computational delay, and communication delay (pure time-delay). Horiuchi et al. (1999) studied the effect of the actuator's time-delay in RTHS using the energy balance method. They showed that time-delay is equivalent to negative damping, meaning that energy is added to a system. If this negative damping exceeds the inherent damping of a structure, response simulation becomes unstable. In servo-hydraulic actuation, the communication delay is in the order of 1 ms, which is small as compared to the response delay (20-80 ms). Computational time-delay arises due to the sequential nature of a hybrid simulation test. In hybrid simulation tests, the loading history of an experimental substructure is not known *a priori*. Therefore, the time-delay of hybrid testing cannot be fully eliminated; rather, compensation techniques are used to reduce it. Before deeply exploring delay compensation methods, it is worth noting that no compensation method can replace the need for high-performance hardware and accurate control algorithms necessary for hybrid simulation.

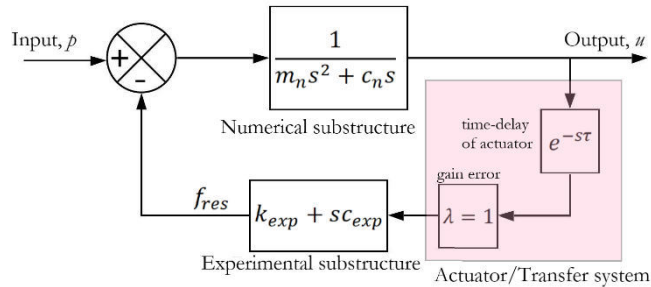


Figure 2-12: Block diagram of a hybrid simulation test

To demonstrate the precarious nature of an actuator's time-delay, a simulated hybrid test of a SDOF structure was conducted in LabVIEW software. In this example, the actuator's time-delay was modeled as a pure time-delay; one with 30 ms and another with 100 ms. Modeling actuator using a fixed time-delay is plausible for small frequency ranges, in practice, since time-delay is expected to remain constant at low frequencies. Here, the controller of the actuator is assumed to have no gain error,  $\lambda=1$ , in the frequency range of interest, which is consistent with the objectives of tuning servo-hydraulic actuators during hybrid simulation tests. To this end,  $\lambda=1$  was adopted. Nevertheless, when input motion to an actuator has a wide range of frequencies or it is operated beyond its performance limits (e.g., a high-velocity stroke of an actuator), the fixed time-delay assumption is not pragmatic. Actuator's variable time-delay can be improved using algorithmic damping. On the other hand, issues on the performance limit of actuators may only be rectified using a well-designed hydraulic system.

In Figure 2-12, the worst-case scenario for instability is achieved by experimentally modeling the full stiffness of the SDOF structure. Thus, the full stiffness and a portion of the viscous damping are modeled as the experimental substructures and the remaining portion of the SDOF structure was modeled numerically. For a time-invariant system with time-delay  $\tau$ , its dynamics under free vibration can be expressed in a state-space form as:

$$\begin{Bmatrix} \dot{u}(t) \\ \ddot{u}(t) \end{Bmatrix} = \begin{bmatrix} 0 & 1 \\ 0 & -c/m \end{bmatrix} \begin{Bmatrix} u(t) \\ \dot{u}(t) \end{Bmatrix} + \begin{bmatrix} 0 & 0 \\ -k/m & 0 \end{bmatrix} \begin{Bmatrix} u(t-\tau) \\ \dot{u}(t-\tau) \end{Bmatrix} \quad (2.60)$$

The state vector is given by  $u = [u(t) \dot{u}(t)]^T$ . Applying Laplace transformation to equation (2.60), the characteristic equation of the hybrid simulation test becomes:

$$c(s, e^{-s\tau}) = m_n s^2 + c_n s + (sc_{exp} + k_{exp}) e^{-s\tau} = 0 \quad (2.61)$$

The time-delay,  $e^{-s\tau}$ , can be represented by the Rekasius equation (Ebenbauer & Allgöwer, 2006) as:

$$e^{-s\tau} = \frac{1 - sT}{1 + sT} \quad (2.62)$$

where  $s = i\omega$  and  $\tau, T \in R^+$ . The characteristic equation is first mapped into a polynomial using Euler's theorem, then Routh's stability theorem is used to determine the critical time-delay,  $\tau_{crt}$  (Mercan & Ricles, 2007). The polynomial,  $q(T, s)$ , is the characteristic equation of the SDOF structure described above and it can be shown to be:

$$q(T, s) = m_n Ts^3 + (m_n + c_n T - c_{exp} T)s^2 + (c_n + c_{exp} - k_{exp} T)s + k_{exp} = 0 \quad (2.63)$$

After constructing the Routh's stability array from the characteristic polynomial, it can be shown that for some value of  $T$ ,  $q(T, s)$  has two unstable roots. The two unstable roots are determined from the Routh array at points where it crosses the imaginary axis. The roots are determined by solving the following equation:

$$k_{exp}(c_{exp} - c_n)T^2 + (c_n^2 - c_{exp}^2 - 2m_n k_{exp})T + m_n(c_{exp} + c_n) = 0 \quad (2.64)$$

Thus, hybrid testing of the SDOF structure, considering time-delay and a rate-dependent experimental substructure, the value of  $T$  related to the critical time-delay,  $T_{crt}$ , is the smallest of the two roots. We also know that equation (2.62) holds for  $s = i\omega$  if and only if:

$$\tau = \frac{2}{\omega} \{\tan^{-1}(\omega T) \pm k\pi\}; \quad \text{where } k = 0, 1, 2, \dots \quad (2.65)$$

The above equation can be transformed into a critical time-delay formulation by replacing variables with their critical values. Note that  $\omega_{crt}$  corresponds to  $T_{crt}$  and it is calculated by substituting  $T_{crt}$  in  $q(T, s)$  and solving for  $\omega_{crt}$  after replacing  $s$  by  $i\omega$ :

$$\tau_{crt} = \frac{2}{\omega_{crt}} \{\tan^{-1}(\omega_{crt} T_{crt} \pm k\pi)\}; \quad \text{where } k = 0, 1, 2, \dots \quad (2.66)$$

In equation(2.66), the critical time-delay  $\tau_{crt}$  is indirectly a function of the time-delay,  $\tau$ , of the actuator. Hence, the relationship between the critical time-delay and actuator time-delay can be evaluated at different viscous damping ratios, as shown in Figure 2-13.

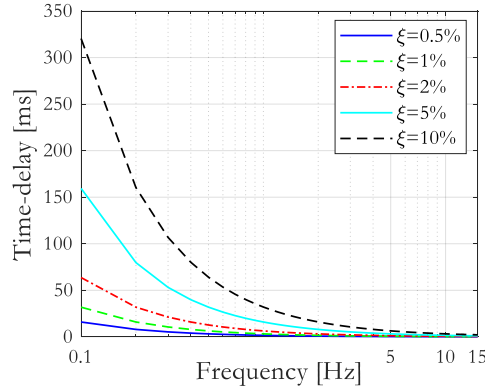


Figure 2-13: Critical time-delay of an actuator for a stable hybrid simulation test of a linear-elastic SDOF structure considering rate-dependent experimental substructure

The critical time-delay of an actuator decreases rapidly with an increasing frequency of a SDOF structure. At higher frequencies, the viscous damping  $\xi$  of the structure is less effective in preserving the stability margin since the critical time-delay of an actuator at large frequencies is small regardless of the structure's viscous damping. For illustration, considering a SDOF structure with 10 Hz of natural frequency, it becomes unstable at 1 ms and 4 ms time-delays when  $\xi=1\%$  and  $\xi=10\%$ , respectively. On the other hand, viscous damping significantly improves the stability margin in the frequency range [0, 1] Hz. For example, at 0.5 Hz of natural frequency, increasing the viscous damping ratio of the structure from 2% to 5% made the critical time-delay jump from 13 ms to 32 ms. Thus, the role of viscous damping cannot be ignored in reducing the detrimental effect of the time-delay of an actuator. This simulated study also reveals that the rate-dependency of the experimental substructure does not interfere with the stability margin of the structure. For a MDOF structure having a significant contribution of higher modes, these modes may trigger system instability because the critical time-delay is small at large frequencies.

Mercan & Ricles (2007) also addressed the stability of nonlinear SDOF structures by modeling system dynamics in Simulink. They found that the inelastic behavior of an experimental substructure has improved the stability margins. This is due to hysteretic energy dissipation of the test structure which offsets the effect of a time-delay. To model the variable time-delay of an actuator, such as the case of earthquake ground motion, they used a variable time-delay as opposed to the fixed time-delay assumption; and similar results were obtained. The only distinction in considering a variable time-delay is that it is more pragmatic and when stability limits are exceeded during analysis, even once, system instability may be triggered.

The focus of the above discussion was the stability of a structural system during hybrid simulation while, at the same time, the accuracy of response simulation can be influenced by amplitude error. Amplitude or gain error can result from incorrect setting of transducers, errors in control strategy, the noise of measured quantities, etc. Even though amplitude errors may not cause instability issues, studies conducted by Mercan & Ricles (2007) showed that it is worthwhile to study the accuracy of

hybrid simulation subjected to gain errors. Using bode plots of the transfer function of an elastic SDOF structure under amplitude error, considering rate-dependent and rate-independent cases, valuable information can be obtained on the characteristics of the resonant peak. Overshooting amplitude errors tend to extract energy from a system while undershooting errors adds energy to a system. Thus, both time-delay and undershooting amplitude errors add energy to a system. In practice, amplitude and time-delay errors of a servo-hydraulic actuator are found coupled in any experimental test, and there are only a few resources to decouple these errors. The common practice in hybrid simulation thus resorts to tuning a controller for optimal amplitude tracking followed by reduction of time-delay errors using compensation algorithms.

### 2.6.1 Error measurement and tracking indicators

Servo-hydraulic actuators are commonly employed in the experimental testing of structures and structural components. They have two main components: a servo-valve and a hydraulic actuator. There are several types of servo-valves available nowadays. Herein, a two-stage servo-valve (MOOG, 2002) is described, which corresponds to the servo-valve used in developing a software framework for hybrid simulation. A servo-valve controls the movement of oil to and from the chambers of a hydraulic actuator. Firstly, it receives electrical input from a controller unit. This electrical command is then applied to a coil that surrounds an armature thereby producing a torque on the armature (torque motor). In the first stage, a flapper is rigidly attached to the midpoint of the armature. The flapper extends through the flexure tube and passes between two nozzles, creating variable orifices between the nozzle tips and flapper. The torque produced by the armature causes the flapper to deflect, closing one of the nozzles, and diverts flow to the other side of a spool. This causes the spool to displace sideways while opening the flow of oil between the pressure (P) and return (R) ports. Besides, it opens the other two control ports (A and B ports in Figure 2-14) for the in-and-out movement of oil in the actuator chambers. Finally, the piston moves in the direction of equilibrium position and puts the actuator in motion whereby force is applied to a test

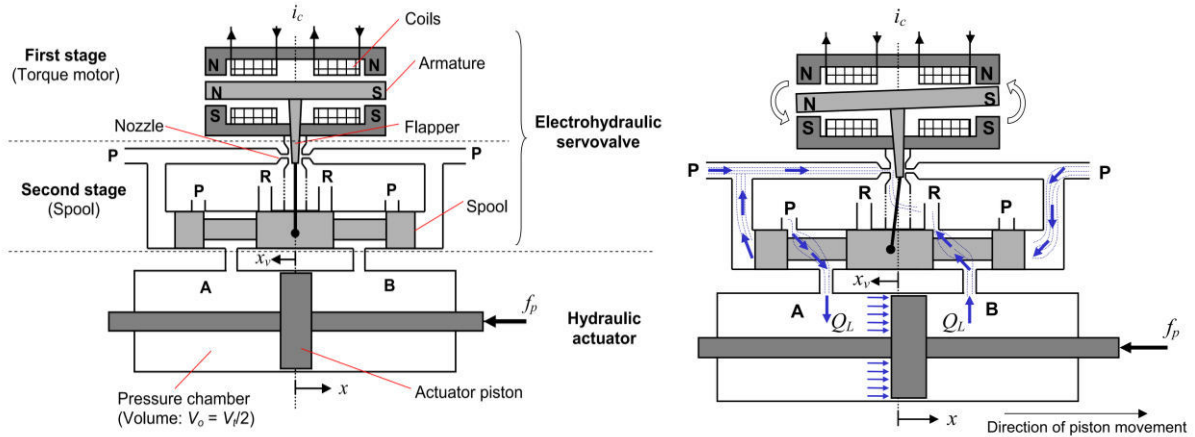


Figure 2-14: Two-stage servo-valve: neutral position (left) and displaced position (right)

structure. The displacement of the actuator that is measured by a transducer is then returned to the controller as a feedback signal. The error in the command displacement is calculated and the position of the actuator is adjusted by sending the error signal to the servo-valve.

The measured responses are highly dependent on the control strategy and controller gains. The feedback displacement is used to calculate the error signal, which is subsequently applied by the actuator. This process is repeated until a desired level of error is achieved or until the next time-step command is sent to the controller. The *response time* is the time required by the actuator to reach the desired position. It is also referred to as a response time-delay. This time-delay is a function of the servo-valve, controller, actuator dynamics, loading beam, and dynamics of a test specimen. For structural testing, servo-hydraulic actuators are commonly used due to their ability to apply large forces that cannot be realized using electric actuators. The latter are characterized by smaller time-delay and limited force capacity.

In RTHS, the identification of system time-delay, and tracking it periodically, is essential to adaptively compensate for the time-delay of an actuator. The coupling between time-delay and amplitude error can be simplified using the sub-space synchronization plot (SSP). It is constructed by plotting the command displacement in the horizontal axis and the measured displacement in the vertical axis. The slope of the plot gives the magnitude of the amplitude error. Plot inclination greater than  $45^\circ$  indicates an overshooting error whereas inclination below  $45^\circ$  is an indication of undershooting error. The direction of winding of the SSP plot can also be used to identify the nature of phase error. Clockwise direction of winding of the ellipse indicates a phase lead whereas anti-clockwise winding shows the presence of a phase lag (time-delay). Figure 2-15 shows a simulated time-delay of 100 ms between command and measured displacement signals and an amplitude error (undershoot) of 5%. The ellipse formed by the SSP winds in the anti-clockwise direction due to the phase-lag between the two signals. The linear fitting of the SSP plot has a milder slope compared to the  $45^\circ$  -line, thus indicating the presence of undershooting error.

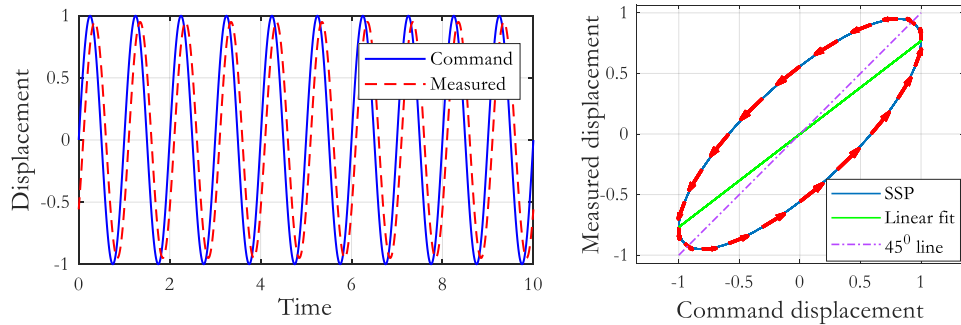


Figure 2-15: Phase-lag of measured displacement (left) and sub-space synchronization plot (right)

The identification methods discussed above allow the qualitative assessment of experimental errors. The quantitative assessment of experimental errors in hybrid testing is equally important, if not more. This assessment includes the estimation of the phase and amplitude errors between the

command and measured response quantities. Hence, error tracking indicators are discussed below.

Error tracking can be conducted online using indicators during a hybrid simulation. Despite being computationally demanding, the online estimation of error is useful to prevent equipment damage in uncontrolled tests. More importantly, it is essential during adaptive delay compensation. Error tracking can also be performed offline to verify the accuracy of a hybrid test. Several error tracking techniques have been developed up to date, the majority being in the time-domain and a few developments in the frequency domain. Some of these indicators are the Maximum Tracking Error (MTE), Root Mean Square (RMS) tracking error, Tracking Indicator (TI) (Chen & Ricles (2010), Chen & Ricles (2009)) and Energy Error (EE) (Mosqueda et al., 2007a, 2007b); Ahmadizadeh & Mosqueda, 2009). These indicators use a single parameter to describe the tracking error. The energy-based error indicator is different from the rest of the methods since it quantifies the global tracking error that accounts for errors in restoring force.

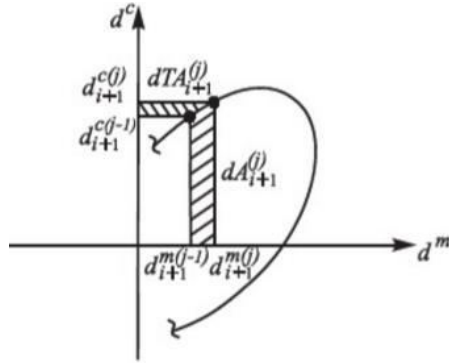


Figure 2-16: Definition for tracking indicator (TI)

On the other hand, TI calculates the local error between command and measured displacements. It uses the area enclosed in the SSP plot to quantify the tracking error of an actuator, as shown in Figure 2-16. The enclosed area is calculated as:

$$\begin{aligned} TI_{i+1}^j &= 0.5(A_{i+1}^j - TA_{i+1}^j) \\ A_{i+1}^j &= A_{i+1}^{j-1} + dA_{i+1}^j = A_{i+1}^{j-1} + 0.5\{(d_{i+1}^{c(j)} + d_{i+1}^{c(j-1)})(d_{i+1}^{m(j)} - d_{i+1}^{m(j-1)})\} \quad (2.67) \\ TA_{i+1}^j &= TA_{i+1}^{j-1} + dTA_{i+1}^j = TA_{i+1}^{j-1} + 0.5\{(d_{i+1}^{c(j-1)} - d_{i+1}^{c(j)})(d_{i+1}^{m(j)} + d_{i+1}^{m(j-1)})\} \end{aligned}$$

where  $A_{i+1}^j$  and  $TA_{i+1}^j$  are the enclosed area and complementary enclosed area at the  $j$ th sub-step of a ramp generator and the  $i+1$  step of a hybrid test. This algorithm was developed from the standpoint of a ramp generator applying command displacement in small increments. To decouple the amplitude and phase errors, Hessabi & Mercan (2007) proposed the Phase and Amplitude Error Indices (PAEI) method by deriving closed-form equations of the ellipse fitting the SSP plot. In most time-domain methods, a smaller amplitude of an error indicator signifies better performance. Nevertheless, these methods are dependent on the intensity of earthquake motion, therefore, a smaller value of an indicator does not necessarily mean good actuator performance. Large values of

TI and energy error indicators neither define poor actuator performance and they can be insensitive to errors (Chen & Ricles, 2010). To overcome the limitation of the time-domain approaches for error tracking, Guo et al. (2014) developed a Frequency Evaluation Index (FEI) for the assessment of actuator tracking in real-time hybrid simulations. In FEI, the time-delay of an actuator is estimated through the equivalent frequency method. It has a better quantitative assessment of the effect of an actuator's time-delay. Despite its improved performance, the FEI approach is only suitable for post-processing test results since it requires the entire data of a test for estimation. To improve the computational efficiency of this method, the data is decimated. This was performed with the aim of improving the efficiency of the frequency-based techniques for online error tracking capability. In 2014, Hessabi et al. (2014) proposed the so-called Frequency Domain Based (FDB) error indicator that is capable of uncoupling the amplitude and phase errors of an actuator. In order to use FDB error indicators for online tracking, the discrete Fourier spectra need to be calculated by Fast Fourier Transform (FFT) using a windowing technique. The effects of spectral leakage can be reduced through windowing functions such as Hamming. Table 2-2 summarizes the characteristics of all error tracking techniques discussed above.

Table 2-2: Properties of error tracking methods for real-time hybrid simulation

	<b>MTE</b>	<b>NRMSE</b>	<b>HSEM/ EEI</b>	<b>TI</b>	<b>PAEI</b>	<b>FEI</b>	<b>FDB</b>
Domain	Time	Time	Time	Time	Time	Frequency	Frequency
Error type	Local/ Global	Local/ Global	Global	Local	Local	Local	Local
Computing effort	Low	Low	Low	Low	High	Low	High
Decoupling experimental errors	General informati on only	Qualitative only	Identify the nature of phase error only	No	Yes	Yes	Yes
Applicability or Dependency	Response history dependent	Response history dependent	Structure/ experiment specific	Depends on command amplitude	Independe nt of command amplitude	Independe nt of command amplitude	Independe nt of command amplitude
Tracking	Offline	Offline	Offline	Online	Offline	Offline	Online

## 2.7 Delay compensation algorithms

It should be clear by now that delay compensation algorithms are imperative to achieve good actuator control for real-time hybrid simulations so that dependable responses can be determined. The time-delay of an actuator is important due to its destabilizing effect; therefore, its compensation is essential for accurate simulation of response. The assumption of a constant time-delay is not pragmatic; and the inherent nonlinear behavior of an actuator makes delay compensation even more complex. To improve the command tracking of an actuator, various delay compensation techniques

have been developed to date.

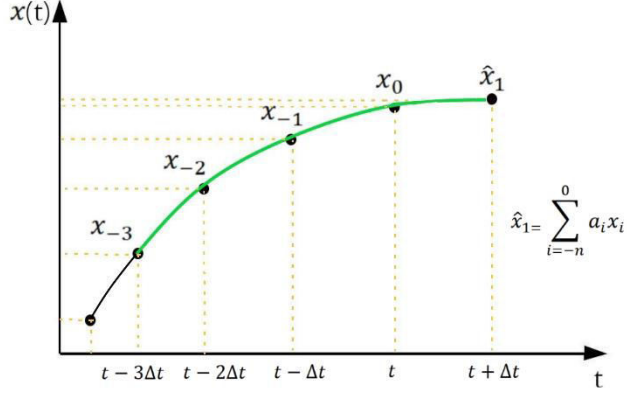


Figure 2-17: Third-order polynomial extrapolation

Horiuchi et al. (1999) introduced a third-order polynomial to predict the next time-step command displacement using the last three committed displacements. This approach is based on a constant time-delay assumption. It was applied to a hybrid experiment of a simple piping system supported on an energy absorber. The real-time hybrid test was in good agreement with a shaking table experiment of an identical structure. However, this technique performs well only when the prediction time is small compared to the fundamental period of a structure (relatively flexible structures). For structures having a small fundamental period, it may be difficult to ensure a stable experiment.

Darby et al. (2002) developed a technique for online estimation of time-delay and compensating for it. They estimated time-delay to be proportional to a feedback signal, i.e., a control error multiplied by two constant factors of proportionality. They examined the stability of linear and nonlinear single-actuator systems and the characteristics of twin-actuators controlling two degrees-of-freedoms. Zhao et al. (2003) proposed a velocity feedback compensation for accurately controlling the force applied by an actuator during Effective Force Testing (EFT). They showed that using EFT in combination with the nonlinear velocity feedback compensation, real-time dynamic testing can be conducted. The compensation process is independent of the nonlinearities of a test specimen. This technique was examined on a one-story steel structure undergoing nonlinear deformations; and the results were comparable with the output of a shake table experiment (Zhao et al., 2005, 2006). Shing et al. (2006) introduced a Discrete Feedforward Compensation (DFC) scheme to compensate for the time-delay between an actuator command and its response. In this scheme, the control error at the current time-step is assumed to be approximately equal to that of the last time-step. Consequently, the current time-step command is corrected by multiplying the control error of the last time-step by a gain factor. This scheme is useful when the proportional gain cannot be sufficiently raised because of stability concerns.

A model-based feedforward approach was proposed by Carrion et al. (2009) to compensate for actuator time-delay based on known structural properties of a test specimen and the excitation load.

This approach was used to evaluate the response of semi-active control in structures. They examined the characteristics of a magneto-rheological (MR) damper in hybrid tests. They have also studied simplified and complex modeling of an actuator's transfer function to be applied for feedforward compensation. They modified the inverse dynamics of an actuator transfer function to make the controller stable (Carrion & Spencer, 2007). This feedforward controller was implemented using the inverse dynamics of the system in series with a unit amplitude low-pass filter.

Chen (2007) proposed the adaptive inverse compensation scheme based on the first-order model of a servo-hydraulic actuator. The effectiveness of the proposed compensation method was examined in a large-scale real-time hybrid simulation test of a two-story four-bay moment-resisting frame equipped with MR dampers. The adaptive gains of this scheme need to be calibrated prior to conducting a hybrid test. The selection of optimal values for the adaptive gains can be challenging. Non-optimal adaptive gains reduce the performance of this scheme since inadequate delay compensation is performed. More recently, the Adaptive Time Series (ATS) compensation method was introduced by Chae et al. (2013). This approach updates its compensation parameters at each time-step of integration using the least-squares method. The main distinction of this method is that a user-defined adaptive gain is not required. The nonlinearities of a servo-hydraulic system and test specimen can be compensated throughout the duration of a hybrid simulation test. ATS has superior performance compared to the other existing compensation methods. In subsequent sections of this chapter, detailed discussions of selected compensation methods are presented. To help us to compare the existing compensation techniques, their characteristics are summarized in Table 2-3.

Table 2-3: Properties of delay compensation algorithms for hybrid simulation

Compensation method	PE <sup>1</sup>	VFFF <sup>1</sup>	DFF <sup>1</sup>	MBIC <sup>1</sup>	IC <sup>1</sup>	AIC <sup>1</sup>	ATS <sup>1</sup>
Need for calibration	Yes	Yes	Yes	Yes	Yes	Yes	No
Parameters to tune	3 (n=3)	4	1	Varies <sup>2</sup>	2	NA	NA
Initialization	NA	NA	NA	NA	NA	Yes (1)	Yes (3)
Limit setting	NA	NA	NA	NA	NA	Yes (1)	Yes (6)
Variable delay	Non-adaptive	Non-adaptive	Non-adaptive	Non-adaptive	Non-adaptive	Adaptive	Adaptive

### 2.7.1 Feedforward compensation

Feedforward compensation is an open-loop compensation scheme, as shown in Figure 2-18, whereby the controller does not use feedback response to control a system. It works by predicting

<sup>1</sup> PE: Polynomial extrapolation ( $n$  is the order of the polynomial); VFFF: Velocity feedback & feedforward; DFF: Discrete feedforward; MBIC: Model-based inverse compensation; IC=Inverse Compensation; AIC: Adaptive inverse compensation

<sup>2</sup> Depends on the degree of transfer function used in modeling the actuator dynamics

the ideal response of a system (Carrion & Spencer, 2007). System dynamics in Figure 2-18 refers to the combined dynamics of an actuator, servo-valve, and test-specimen. This controller does not have potential stability problems due to feedback signal as long as the controller and the system are stable. Generally, a feedforward controller augments a feedback controller by improving its slow response.

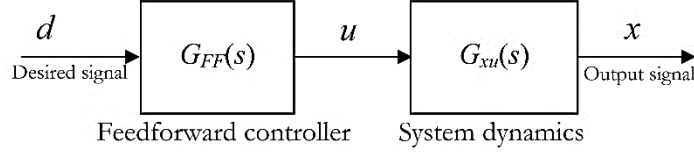


Figure 2-18: Block diagram of a feedforward controller

Under ideal conditions, the feedforward compensator cancels out the dynamics of the system resulting in a unit amplitude and zero phase characteristics between input and output signals. In this essence, the feedforward controller can be designed as pure inverse-dynamics of the system (Astrom & Bjorn, 1986). Therefore, the feedforward controller,  $G_{FF}(s)$ , can be expressed as:

$$G_{FF}(s) = G_{xu}^{-1}(s) \quad (2.68)$$

To successfully implement this control, one needs to make sure that the inverse of the system dynamics is causal and stable. The  $n$ th order approximation for the denominator of the transfer function, from the input command  $u$  to the measured displacement  $x$ , for a servo-hydraulic actuator can be written in the form of poles,  $p$ , and gain,  $K$ :

$$G_{xu}(s) = \frac{K}{\prod_{i=1}^n (s - p_{xu,i})} \quad (2.69)$$

where  $G_{xu}$  is the system dynamics. The inverse of the above equation is a derivative action whose magnitude increases without bound as frequency increases. The inverse of this transfer function cannot be used for a system with non-ideal conditions, i.e., with approximations. These approximations are inevitable since the system dynamics is typically developed using a linearized form of the true nonlinear characteristics of the servo-hydraulic actuators and test-specimen. In order to perform a stable control, Carrion & Spencer (2007) proposed a modified feedforward controller by placing the pure inverse of a system dynamics in series with a low-pass filter that has a unit gain. To make the modified inverse dynamics a proper controller, the order of the low-pass filter is defined to be equal to the order of the inverse dynamics. The *poles* of the low-pass filter are chosen to be the *zeros* of the inverse dynamics of the system multiplied by a modification factor,  $\alpha$ . If the pole modification factor is set to be greater than one, it makes the poles of the compensator large enough to interfere with the lower frequency dynamics of the system.

$$G_{FF}(s) = \alpha^n \frac{\prod_{i=1}^n (s - p_{xu,i})}{\prod_{i=1}^n (s - \alpha p_{xu,i})} \quad (2.70)$$

Depending on the value of  $\alpha$ , the behavior of the feedforward controller can be adjusted. When

$\alpha=1$ , the feedforward controller becomes one and no compensation is provided by the controller. When  $\alpha=\infty$ , the controller inherits the full characteristics of a pure inverse feedforward controller. Therefore, the optimal value for  $\alpha$  must maintain a balance between keeping the characteristics of the pure inverse feedforward controller, in the frequency range of interest, which corresponds to large values of  $\alpha$ , and enabling frequencies associated with the poles to be represented in the implementation of a digital controller with the sampling period used during a hybrid test (Carrion & Spencer, 2007). The latter can be achieved at small values of  $\alpha$ . The derivative action produced by the controller must be controllable. Consequently, for a target signal that is subjected to sudden changes, a smaller value of  $\alpha$  should be used to suppress the derivative action of the controller. Considering the first-order model for the actuator transfer function, which models the time-delay parameter only, it can be shown that the time-delay at lower frequencies can be reduced by an amount equal to the magnitude of  $\alpha$ . Carrion & Spencer (2007) reported that  $\alpha$  values in the interval 10-20 are adequate for reducing the time-delay of real-time hybrid simulation tests.

On the other hand, in Phillips & Spencer (2012), higher-order derivatives of improper inverses were evaluated directly by linearly extrapolating the relative acceleration using the Central Difference Method (CDM). They reported that this approach is more accurate than applying the low-pass filter approach discussed above since low-pass filters can introduce unwanted dynamics. Nevertheless, this approach is limited to servo-hydraulic system models of no zeros and three poles. Another alternative method that uses the Backward Difference Method (BDM) for calculating the discrete-time derivatives of improper inverse was developed by Phillips et al. (2014). This approach is easy, and flexible for implementation. In hybrid testing involving MR damper, Phillips et al. (2014) showed that the back-difference method is more accurate than the central-difference method when implementing improper inverses (see Figure 2-19).

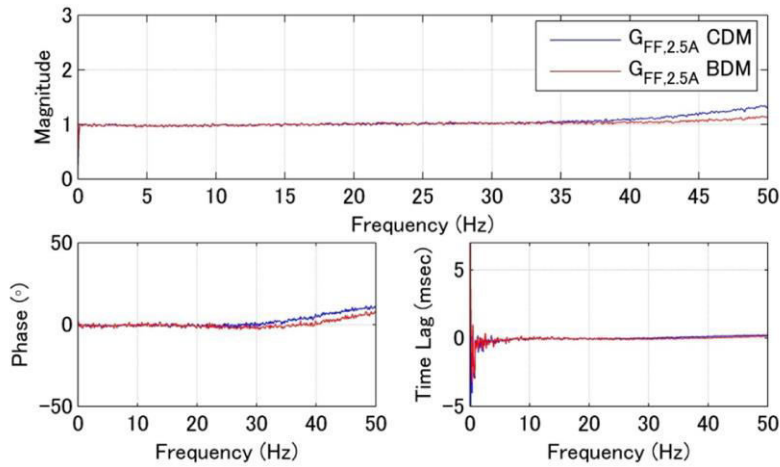


Figure 2-19: Feedforward control of MR damper using improper inverses constructed from BDM and CDM methods (after Phillips et al., 2014)

### 2.7.2 Adaptive inverse compensation

The Inverse Compensation (IC) method uses the model of a system to compensate for the unwanted dynamics of the system. It may be developed based on a constant time-delay principle or adaptive techniques. Chen & Ricles (2010) proposed the inverse compensation method assuming the first-order model for the servo-hydraulic system. In the early stage, inverse compensation was developed assuming a constant time-delay. However, the actual time-delay of an actuator is difficult to estimate accurately. Besides, it changes throughout the course of testing due to nonlinearities in the servo-hydraulic system and test-specimen.

In order to analyze its behavior, let us assume a ramp generator to interpolate the command displacement between the current and next time-steps. During a hybrid simulation, the ramp generator ensures a smooth response of an actuator and reduces the overshooting error of the command displacement. Considering the servo-controller sampling time  $\delta t$ , the time-step  $\Delta t$  is a multiple of  $\delta t$  taking a linear ramp generator. The command displacement sent to the actuator at the  $j$ th sub-step can be then expressed as:

$$d_{i+1}^{c(j)} = x_i + \frac{j}{n}(x_{i+1} - x_i); \text{ where } n = \Delta t / \delta t \quad (2.71)$$

Owing to the actuator's time-delay, the measured displacement  $d_{i+1}^{m(j)}$  lags the command displacement  $d_{i+1}^{c(j)}$ . Considering a state-of-the-art servo-controller, working at a clock speed  $\delta t$ , the actuator response can be idealized as a linear response, as shown in Figure 2-20. If  $\alpha$  is greater than one, the time duration that is allotted to the actuator to reach the desired command  $d_{i+1}^{c(j)}$  is exceeded, thus time-delay exist in the response of the actuator.

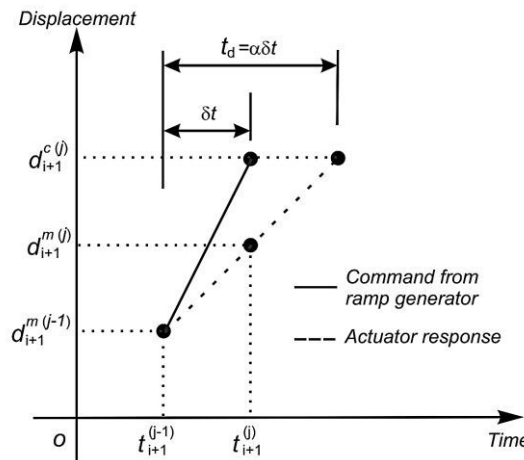


Figure 2-20: Actuator response under time-delay (after Chen & Ricles, 2010)

In Figure 2-20, the command and measured displacements are related by:

$$d_{i+1}^{m(j)} = d_{i+1}^{m(j-1)} + \frac{1}{\alpha} (d_{i+1}^{c(j)} - d_{i+1}^{m(j-1)}) \quad (2.72)$$

Applying the discrete z-transform to equation (2.72), the discrete transfer function from the output displacement,  $X^m(z)$ , to the desired (or command) displacement,  $X^c(z)$ , is obtained.

$$G_d(z) = \frac{X^m(z)}{X^c(z)} = \frac{z}{\alpha z - (\alpha - 1)} \quad (2.73)$$

In equation (2.73),  $z$  is the complex variable in the discrete domain and  $\alpha$  is the time-delay parameter, which is a function of the clock-speed of the controller. Subsequently, the discrete transfer function of the resulting inverse compensator,  $G_{IC}(z)$ , is given by:

$$G_{IC}(z) = \frac{X^p(z)}{X^c(z)} = \frac{\alpha z - (\alpha - 1)}{z} \quad (2.74)$$

where  $X^p(z)$  is the discrete transform of the predicted displacement that need to be sent to the servo-hydraulic actuator,  $d_{i+1}^{p(j)}$ , so that the time-delay of the actuator is fully compensated. Applying the inverse z-transform, the time-domain implementation of the inverse compensator can be derived as:

$$d_{i+1}^{p(j)} = \alpha d_{i+1}^{c(j)} - (\alpha - 1)d_{i+1}^{c(j-1)} \quad (2.75)$$

From the above equation, the inverse compensation proposed by Chen & Ricles (2010) can be simply interpreted as an extrapolation process using the last two commands. Thus, good actuator performance is dependent on the accurate estimation of the time-delay parameter,  $\alpha$ . Nonetheless, system nonlinearities make the accurate estimation of  $\alpha$  difficult. A constantly changing time-delay of the actuator response can potentially reduce the accuracy of this approach. To improve the performance of the inverse compensator the same authors presented an adaptive inverse compensation method. The adaptive inverse compensator  $G_{AIC}(z)$  reads:

$$G_{AIC}(z) = \frac{X^p(z)}{X^c(z)} = \frac{(\alpha_{est} + \Delta\alpha)z - (\alpha_{est} + \Delta\alpha - 1)}{z} \quad (2.76)$$

In equation (2.76),  $\alpha_{est}$  is the initial estimate of  $\alpha$  and  $\Delta\alpha$  is the evolutionary variable that defines the adaptive property to the inverse compensator. Chen & Ricles (2010) formulated  $\Delta\alpha$  in relation to the tracking indicator (TI), through an adaptive control law.

$$\Delta\alpha(t) = k_p \cdot TI(t) + k_I \int_0^t TI(\tau) d\tau \quad (2.77)$$

where  $k_p$  and  $k_I$  are the proportional and integral gains of the adaptive control law, respectively. When starting a hybrid test,  $\Delta\alpha$  is set to zero. In the Z-domain, equation (2.77) can be written as:

$$\Delta\alpha(z) = k_p \times TI(z) + k_I \times \frac{\delta t}{z - 1} \times TI(z) \quad (2.78)$$

The values of  $k_p$  and the ratio  $k_I/k_p$  are determined from numerical simulations by applying a predefined displacement history to the simplified model for the servo-hydraulic actuator. In the hybrid experiments conducted by Chen & Ricles (2010),  $k_I/k_p$  was set to be equal to 0.1 to reduce overshoot. This setting resulted in fast adaptation of a command signal. They also examined the robustness of the method by considering different estimates for  $\alpha_{est}$  at  $k_p$  values equal to 0, 0.2 and

0.4. The validation work of the adaptive inverse compensation was performed on a SDOF structure equipped with elastomeric damping. Using a predefined displacement, which was the expected displacement of the SDOF structure, accurate value for  $\alpha_{est}$  was determined in the frequency range of interest. Another two poor estimates for  $\alpha_{est}$  were then defined as  $0.5\alpha_{est}$  and  $1.5\alpha_{est}$ . At  $k_p=0$ , the simulation conducted using poor estimates of  $\alpha_{est}$  resulted in large values of TI, but, at  $k_p=0.2$  and  $k_p=0.4$ , the poor and accurate estimates of  $\alpha_{est}$  showed similar values of TI. Similar conclusion was also derived using the HSEM (Mosqueda et al., 2007a,b) metric for error tracking. For values of  $k_p$  greater than 0.4, no improvement was achieved on the performance of the actuator. Thus, it appears that optimal values for  $k_p$  are needed to ensure fast convergence and stable actuator performance. Overall, the adaptive inverse compensation is a candidate approach in improving the performance of an actuator in fast and real-time hybrid simulation tests. Nevertheless, recalling the dependency criterion of tracking indicators, discussed in section 2.6, TI may not be a reliable parameter for adaptive compensation because tracking errors evaluated from different intensities of ground motion may not be comparable due to its dependency on the amplitude of the command displacement (Guo et al., 2014).

### 2.7.3 Adaptive time series compensation

The time-delay and amplitude errors during a hybrid simulation test have evolutionary nature throughout the test duration. These changes depend on the amplitude of the load, the frequency content of the excitation, and the behavior of the test specimen. Considering a non-adaptive approach of a second-order compensator, it cannot capture these changes, giving rise to a poorly performing actuator. The Adaptive Time Series (ATS) compensator developed by Chae et al. (2013) is the adaptive implementation of the second-order compensator. It works by updating online the coefficients of the second-order compensator to account for the combined nonlinearity of the servo-hydraulic system and experimental substructure. The resulting compensation leads to better performance of the actuator. ATS can be categorized as an Adaptive Inverse Control (AIC) method (widely used in control engineering) since its formulation has the time-delay and amplitude errors that are used to model the inverse dynamics of a hybrid test.

If the output displacement,  $x$ , of a servo-hydraulic actuator has an amplitude error  $A$  and a constant time-delay  $\tau$  in relation to the input displacement,  $u$ , applied to an experimental substructure, which is illustrated in Figure 2-21, at time  $t$  we can write:

$$u(t) = \frac{1}{A}x(t + \tau) \quad (2.79)$$

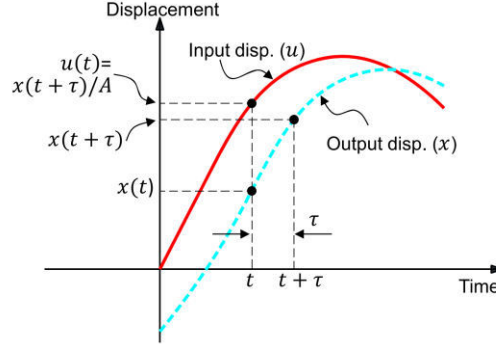


Figure 2-21: Input-output relationship for an actuator (after Chae et al., 2013)

If  $x$  is  $n$ -times differentiable at time  $t$ ,  $u(t)$  can be approximated using the Taylor series, which reads:

$$u(t) \cong \frac{1}{A} \left( x(t) + \tau \dot{x}(t) + \frac{\tau^2}{2!} \ddot{x}(t) + \dots + \frac{\tau^n}{n!} \frac{d^n x(t)}{dt^n} \right) \quad (2.80)$$

Consider a compensated displacement  $u_c$  that must be sent to an actuator so that the measured displacement matches the target displacement,  $x^t$ . Replacing  $u$  by  $u_c$  and the output displacement  $x$  by  $x^t$  in equation (2.79), the compensated displacement can be expressed in discrete form as:

$$u_c(t) = a_0 x_k^t(t) + a_1 \dot{x}_k^t(t) + a_2 \ddot{x}_k^t(t) + \dots + a_n \frac{d^n x_k^t(t)}{dt^n} \quad (2.81)$$

In the above equation,  $x_k^t$ ,  $\dot{x}_k^t$  and  $\ddot{x}_k^t$  are the displacement, velocity, and acceleration at the time  $t_k = k\Delta t$ , respectively. Here,  $k$  is the time index and  $\Delta t$  is the time-step size of the discrete-time domain. The coefficients of equation (2.81), herein referred to as compensation coefficients, are calculated by:

$$a_i = \frac{\tau^i}{i! A} ; \text{ where } i = 0, 1, 2, \dots, n \quad (2.82)$$

In a hybrid simulation test, the compensation coefficients are not available since the time-delay and amplitude error of a servo-hydraulic actuator are not known beforehand. In ATS, the compensation coefficients  $a_i$  are determined by minimizing the Least-Square Error (LSE) between the compensated and measured displacements collected from the last  $q\Delta t$  time duration (or  $q$  discrete time-steps). The objective function  $j_k$  for the LSE minimization in the interval  $[t_{k-q}, t_{k-1}]$  reads:

$$j_k = \sum_{i=1}^q (u_{k-i}^c - u_{k-i}^{est})^2 \quad (2.83)$$

where  $u_{k-i}^c$  is the compensated input displacement at time  $t_{k-i}$  and  $u_{k-i}^{est}$  is the estimated compensated displacement at the time  $t_{k-i}$ . The estimated compensated displacement at the time  $t_{k-i}$  is computed from the measured displacement  $x_{k-i}^m$ .

$$u_{k-i}^{est} = a_{0k} x_{k-i}^m + a_{1k} \dot{x}_{k-i}^m + a_{2k} \ddot{x}_{k-i}^m + \dots + a_{nk} \frac{d^n x_{k-i}^m}{dt^n} \quad (2.84)$$

From the LSE minimization in equation (2.83), the solution to the coefficients of the ATS compensator is derived as:

$$A = (X_m^T X_m)^{-1} X_m^T U_c \quad (2.85)$$

where  $A = [a_{0k}, a_{1k}, \dots, a_{nk}]^T$ ,  $U_c = [u_{k-1}^c, u_{k-2}^c, \dots, u_{k-q}^c]^T$  and the matrix of measured responses  $X_m$  is given by:

$$X_m = \begin{bmatrix} x_{k-1}^m & \frac{d(x_{k-1}^m)}{dt} & \dots & \frac{d^n(x_{k-1}^m)}{dt^{n-1}} \\ x_k^m & \frac{d(x_k^m)}{dt} & \dots & \frac{d^n(x_k^m)}{dt^n} \\ \vdots & \vdots & \ddots & \vdots \\ x_{k-q}^m & \frac{d(x_{k-q}^m)}{dt} & \dots & \frac{d^n(x_{k-q}^m)}{dt^{n-1}} \end{bmatrix} \quad (2.86)$$

Finally, the compensated input displacement can be determined using the coefficients of the ATS.

$$u_k^c = a_{0k}x_k^t + a_{1k}\dot{x}_k^t + a_{2k}\ddot{x}_k^t + \dots + a_{nk}\frac{d^n x_k^t}{dt^n} \quad (2.87)$$

Comparing equations (2.79) and (2.87) the first two compensation coefficients can be directly related to the amplitude and time-delay errors through:

$$A_k \cong \frac{1}{a_{0k}}, \tau_k \cong \frac{a_{1k}}{a_{0k}} \quad (2.88)$$

where  $A_k$  and  $\tau_k$  are the amplitude error and time-delay at time  $t_k$ , respectively. Commonly, servo-controllers are tuned to have a unit gain. Thus,  $A_k$  can be assumed to be one, making the time-delay of an actuator to be equal to  $a_{1k}$ . In equation (2.87), better accuracy of the estimated coefficients could be achieved if higher-order terms are used. However, higher-order time derivatives of the target displacement are not noise-free since noise is propagated from the experimental restoring force into the integration algorithm. Besides, for small time-delay, the contribution of higher-order derivatives is negligible. These reasons compelled Chae et al. (2013) to choose a second-order series while implementing ATS. To this end, the final expression of the compensated displacement reads:

$$u_k^c = a_{0k}x_k^t + a_{1k}\dot{x}_k^t + a_{2k}\ddot{x}_k^t \quad (2.89)$$

The derivatives of the target displacement can be obtained in many ways depending on the desired accuracy. Chae et al. (2013) adopted the backward finite-difference formula in calculating these derivatives.

$$\dot{x}_k^t = \frac{x_k^t - x_{k-1}^t}{\Delta t} \text{ and } \ddot{x}_k^t = \frac{x_{k-1}^t - 2x_k^t + x_{k-2}^t}{\Delta t^2} \quad (2.90)$$

Unlike the target displacement, the measured displacement is noisy. Therefore, applying the finite-difference formula for calculating the measured velocity and acceleration may lead to large errors in  $\dot{x}_k^m$  and  $\ddot{x}_k^m$ . Low-pass filters are used in reducing the higher frequency noise of the measured displacement. Nevertheless, the application of a low-pass filter introduces a phase lag between the target and measured displacements, which contradicts the aim of the delay compensator.

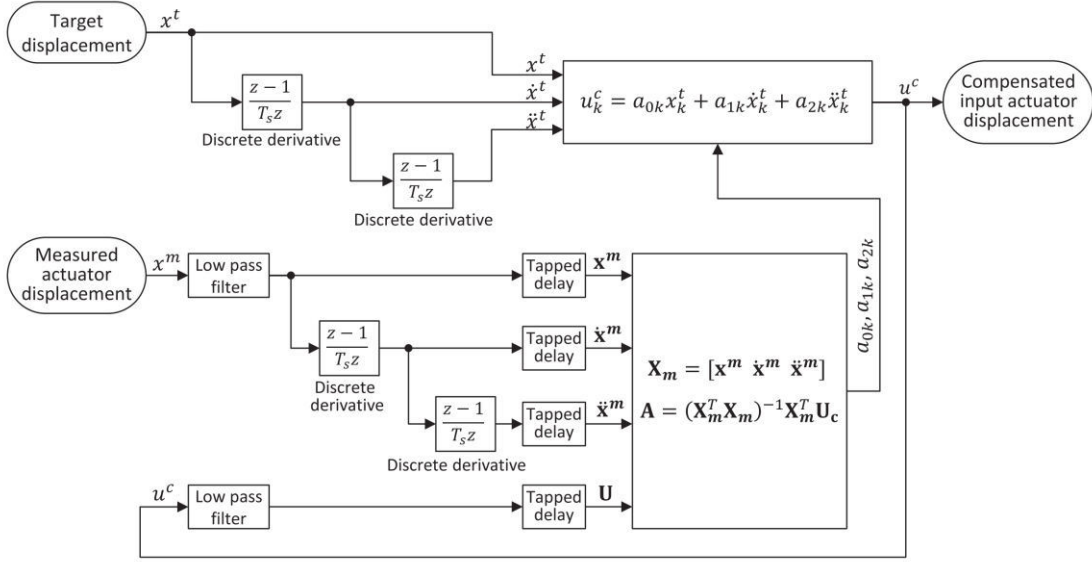


Figure 2-22: Simulink block diagram for ATS compensator (adopted from Chae et al., 2013)

In Chae et al. (2013), to synchronize the target and measured displacements, the former is low-passed while calculating the compensated displacement, meaning the actual compensation coefficients are determined from data collected in the interval  $[t_{k-q} - \phi, t_{k-1} - \phi]$ . Here  $\phi$  is the time-delay introduced by the low-pass filter. The tapped delay, shown in Figure 2-22, allows the collection of data while constructing the matrix given in equation (2.86).

Chae et al. (2013) adopted the sixth-order Butterworth filter, at 15 Hz cut-off frequency, during a real-time hybrid simulation test consisting of a moment-resisting frame and experimental element composed of a viscous damper. The cut-off frequency of the filter can be chosen depending on the participation of the modal frequencies of a structure. Before conducting a hybrid test, the compensator coefficients,  $a_{0k}$ ,  $a_{1k}$  and  $a_{2k}$ , must be initialized. The second-order compensation is used in estimating their initial values in an offline mode. Such second-order compensator is identical to ATS except of being an offline estimation. The estimation is conducted by applying a predefined Band Limited White Noise (BLWN) command displacement to an actuator. In Chae et al. (2013), the predefined displacement was constructed by combining two BLWN signals: one having large amplitude displacement and frequencies below 2 Hz, and another one having small amplitude displacement and frequencies in the interval 0-15 Hz. The nonlinearity of a servo-hydraulic actuator depends on the amplitude of a command displacement. Therefore, it is intuitive that the characterization displacement should have a comparable magnitude to the displacement imposed in the subsequent hybrid test. Nonetheless, to avoid premature damage of a test specimen when applying the characterization displacement, the maximum displacement must be limited. In doing so, the estimated initial values may not reflect the actual time-delay characteristics. Therefore, the adaptive scheme of ATS should be reliable in updating the compensation coefficients.

If the measured displacement is small, the noise to signal ratio can be high resulting in an ill-

conditioned  $X_m^T X_m$  matrix. This may result in the erroneous estimation of  $a_{0k}$ ,  $a_{1k}$  and  $a_{2k}$ . To mitigate this problem, Chae et al. (2013) defined the triggering command displacement of ATS to be 0.2 mm. Besides, better control of the adaptive compensator is achieved by fixing the maximum and minimum values of the compensation coefficients and limiting the rate of change of these coefficients. Chae et al. (2013) considered  $a_{0k}$  to be limited to [-30%, +30%] from the initial estimated value and its rate of change is limited to two per second (i.e.,  $\Delta a_{0k}/\Delta t \leq 2/1s$ ). The lower limits for  $a_{1k}$  and  $a_{2k}$  are typically set to zero while the maximum limit for  $a_{1k}$  can be assumed to have a 100% margin to the initial estimated value. A limit for the rate of change of  $a_{1k}$  is taken as 0.05 s/1 s since time-delay variation of 50 ms in 1 s can be considered as abnormal response behavior for an actuator. The maximum limit for  $a_{2k}$  can be obtained from equation (2.88) assuming zero gain error of an actuator and setting  $\tau_k = \tau_k^{max}$  resulting in  $a_2^{max} = (\tau_k^{max})^2/2$ . Using the same assumption, the rate of change of  $a_{2k}$  can be shown to be a product of  $a_{1k}$  and the rate of change of  $a_{1k}$  (i.e.,  $\Delta a_{2k}/\Delta t = a_{1k} \times \Delta a_{1k}/\Delta t$ ). Nevertheless, when the characteristics of the experimental substructure dictates, limit values discussed above can be altered. For example, for a highly nonlinear or stiff experimental structure or when strong control-structure interaction (CSI) prevails during hybrid simulation, appropriate limit values may differ from the limits provided by Chae et al. (2013). During hybrid testing, when limits are exceeded, the updating process is deactivated.

Dong (2015) suggested a triggering amplitude for ATS that is based on a Root Mean Square (RMS) value of the measured displacement and adopted a 1 mm RMS trigger. Kolay (2016) also found that ATS tends to amplify the high-frequency component of a structural response if  $a_1$  and  $a_2$  are set to large values. Hence, trial runs for tuning the upper limits of the compensation coefficients are handy prior to conducting a hybrid test. Additionally, putting too much restriction in the upper limits of ATS parameters may result in poor compensation in the frequency range of interest, which can eventually compromise the accuracy of a hybrid test. Herein, the ATS compensator is implemented with two small modifications. The first modification has to do with the triggering conditions whereas the second is related to the calculation of the higher-order derivatives of ATS.

## 2.8 Control algorithms for hybrid simulation

Accurate control of actuators is crucial for conducting hybrid simulation tests. Hydraulic actuators are inherently unstable mechanical devices that are characterized by a stiff oil-column frequency. To maintain the stability of hydraulic actuators some sort of control is required (Dyke et al., 1995). Actuator control can be conducted through position or force feedback. Generally, servo-hydraulic actuators are controlled in position due to their intrinsic high impedance property, meaning that they are designed to displace rigid bodies accurately. Besides, displacement control is typically less sensitive to experimental errors except with stiff test specimens. In the latter, a small displacement error can result in a notable force error. In this section, some of the common control algorithms used for structural testing, in hybrid simulation in particular, are discussed.

### 2.8.1 Proportional-Integral-Derivative controller

In hybrid testing, actuators are commonly controlled by feeding the measured displacement back to the servo-controller, commonly referred to as position control. In position control, the feedback displacement is used in computing the error signal,  $e$ . The error signal is computed as the difference between the command,  $u$ , and measured,  $x$ , signals each time the control loop is executed. Among many other closed-loop controllers, the Proportional-Integral-Derivative (PID) controller is often used for position control of actuators. The control rule for a PID controller reads:

$$i_c = K_p e + K_i \int e dt + K_d \frac{de}{dt} \quad (2.91)$$

where  $e$  is the error signal given by  $e = u - x$ . In the above equation,  $K_p$ ,  $K_i$  and  $K_d$  are the proportional, integral, and derivative gains, respectively; and  $i_c$  is the electrical command signal. Figure 2-23 shows the block diagram of a PID controlling the combined dynamics of an actuator and a test specimen through a displacement feedback loop.

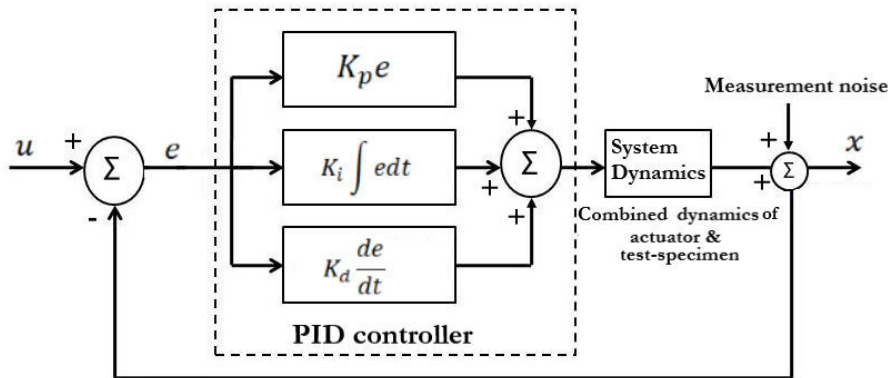


Figure 2-23:PID controller

The proportional gain reduces the error signal proportionally. When the integral and derivative gains are set to zero, the PID controller reduces to P-controller. This controller can result in a non-zero steady-state error to a constant input signal. The steady-state error can be reduced by increasing the proportional gain. However, large proportional gain increases the overshoot of the controller, eventually making the system unstable. Thus, the proportional gain needs to be limited to avoid instability issues. Several recommendations for setting the proportional gain can be found in control engineering (Ogata, 2009). On the other hand, the integral gain works to reduce the steady-state error of the control process. It integrates the error signal from committed iterations of the control loop and improves the tracking of input displacement without the need for high proportional gain. Likewise, the integral gain can cause oscillatory behavior leading to reduced stability of the system. The application of integral gain can be beneficial for pseudo-dynamic and slow hybrid testing. In real-time hybrid testing, the integral gain can be a source of potential instability, therefore, it is typically set to zero.

The derivative term works to reduce the transient behavior of a system response by adding control effort proportional to the derivative of the error signal. It increases system damping and improves the stability of actuation. However, the derivative action is sensitive to noise since noise is amplified during numerical differentiation thus leading to unstable control. Besides, experimental errors, including noise, can propagate into the numerical integration adding to the severity of using the derivative action. Consequently, the derivative action is rarely used in hybrid testing. Depending on the characteristics of an experimental substructure and the speed of a hybrid test, the PID gains can be defined. The gains of the controller define the category of a family of PID controllers, namely: Proportional only, Proportional-Integral, Proportional-Derivative, and PID controllers. In this work, a digital PID controller is developed for the uniaxial shaking table at LNEC, based on proportional and small integral gains to achieve the desired overshoot and settling time of the system response.

PID tuning is performed under open-loop or closed-loop conditions. Closed-loop tuning techniques can be implemented using the Ziegler-Nichols method, Modified Ziegler-Nichols method, Tyreus-Luyben method, and so forth (Ogata, 2009). Ziegler–Nichols methods have been widely used to tune PID controllers in process systems where the plant dynamics is not known. Other open-loop tuning techniques have been also applied to tune PID controllers. The common methods include the open-loop Ziegler-Nichols method and the Cohen & Coon method. The closed-loop tuning of the Ziegler-Nichols method assumes a one-quarter decay ratio (after a step change of a process, the amplitude ratio between subsequent oscillations equal to  $1/4$ ) as a design criterion for a PID controller. In this method, the proportional gain is raised until the output becomes oscillatory and the remaining gains are determined from Table 2-4, where  $K_{cu}$  and  $T_u$  are the critical proportional gain and period of oscillation, respectively. This control rule results in one pole, at the origin, and two zeros, in the negative axis at a distance four-times the period of oscillation. This trial-and-error method does not require the system model for tuning, but it can be oscillatory if the proportional gain is set in the proximity of marginal stability. The marginal stability of a PID controller can be improved using the modified Ziegler-Nichols method. On the other hand, open-loop tuning methods use the first-order transfer function to model a plant. In the Cohen & Coon method, the process reaction curve is determined from an open-loop test and the first-order model is applied to determine the PID gains. In general, for plants with third-order transfer function and higher, closed-loop methods give better results, considering set-point tracking and disturbance rejection of a PID.

Another important issue in PID feedback control is the integral windup. It is a phenomenon when a large change in setpoint occurs, the integral action accumulates a significant error during the rise-time resulting in excessive overshooting of the controller as the error is unwound. This situation happens when it is impossible to realize a command due to physical limitations, referred to as saturation. With the advancement of modern control systems and programmable logic controllers, it is much easier to prevent the integral windup either by limiting the controller output or using external reset feedback. The PID Virtual Instrument (VI) developed by the National Instruments

(NI), which is adopted in this work, uses the integral sum correction algorithm that facilitates anti-windup (National Instruments, 2016). In this algorithm, when the combined output of the proportional and integral actions exceeds the controller limit, the integral action is determined from the difference between the limit value and the proportional action.

Table 2-4: Ziegler-Nicholas rule for tuning PID controllers

Control method	Controller type	$K_p$	$K_i/K_p$	$K_D/K_p$
Ziegler-Nichols	P	$0.5K_{cu}$	-	-
	PI	$0.45K_{cu}$	$1.2T_u$	-
	PID	$0.6K_{cu}$	$0.5T_u$	$0.125T_u$
Modified Ziegler-Nichols	PID-some overshoot	$0.33K_{cu}$	$0.5T_u$	$0.33T_u$
	PID-no overshoot	$0.2K_{cu}$	$0.5T_u$	$0.33T_u$

## 2.8.2 Shaking table acceleration tracking

Substructuring test in a shaking table is a class of hybrid simulation that involves a shaking table test of a physical substructure while the numerical substructure is modeled in a computational software. Shaking tables can be used to conduct hybrid testing of structures if their control scheme can interface with external devices. Some of the potential applications include soil-structure interaction studies and the dynamic behavior of high-rise buildings (Horiuchi et al., 2000; Saouma & Sivaselvan, 2008; Zhang et al., 2017). However, unlike the conventional hybrid test, substructuring tests in a shaking table may require acceleration compatibility, directly or indirectly, at the boundary between numerical and physical substructures (Nakata & Stehman, 2014).

Horiuchi et al. (2000) and Igarashi et al. (2000) proposed the idea of conducting real-time hybrid testing using shaking tables. They demonstrated the proposed method by conducting hybrid experiments of a rigid mass and SDOF structure using a small shaking table. Igarashi et al. (2000) applied the proposed scheme for testing tuned mass-dampers in a shaking table while numerically simulating a SDOF structure. A great deal of research has been conducted on control issues related to substructuring tests in shaking tables (Neild et al., 2005; Stoten & Gómez, 2001). In Neild et al. (2005), an adaptive substructuring controller based on the Minimal Control Synthesis (MCS) has shown improved performance for displacement tracking of a shaking table during a RTHS test. Lee et al. (2007) used the inverse transfer function of a shaking table to improve the deviation in acceleration at the interface boundary of substructures when the upper part of the structure was modeled physically. Shao & Reinhorn (2012) also proposed a framework for physically modeling the middle part of a building while the top and bottom parts are modeled numerically. In their experiment, a shaking table was used to impose the base acceleration at the bottom of the physical model and the reaction force obtained from the upper part of the building was applied by an auxiliary actuator. Another approach for testing the lower part of a building, using inertial masses to apply force command at the interface boundary of substructures, was also proposed by Nakata & Stehman (2012). The approach that uses inertial mass to apply force falls under the class of

equivalent force control. Gunay (2014) implemented the Three-Variable Control (TVC) scheme, developed by the MTS Corporation, during a RTHS test of electrical disconnect switches using a shaking table. During the experiment, the insulator posts were physically tested, and the remaining part of the system was numerically modeled. To validate its effectiveness, the hybrid test was compared with a shaking table test of the full structure. Schellenberg et al. (2016) also conducted a shaking table hybrid test on a mid-level isolation system using the OpenFresco software framework. The isolation system and superstructure were physically modeled on a shaking table and the portion of the building below the isolation plane was numerically modeled. The superstructure element was built from a two-story steel frame resting on six triple-friction pendulum bearings. In Schellenberg et al. (2017), several experimental tests were also conducted by modeling triple friction pendulum bearings in the physical substructure while modelling several configurations of 2D and 3D buildings in the numerical substructure. Yang et al. (2015) studied the feasibility of three different ways, comprising (i) actuator only; (ii) shaking table only; and (iii) both shaking table and actuator, for conducting hybrid simulation tests using a single-span girder bridge case study.

Owing to the difficulty of conducting hybrid testing of soil-structure interaction in shaking tables, until recently no important advancements were made in this area of study. Zhang & Jiang (2017) accounted, numerically, for soil-structure interaction in a hybrid test of an equipment. To meet the demands of a real-time hybrid simulation, the finite element model of the soil, constructed in ANSYS software using the eight-node solid element thus comprising a large number of DOFs, was reduced to a few DOFs. The physical model was represented by a four-story one-bay steel frame superstructure and the equipment was attached to the roof of the steel frame. The hybrid test was conducted to give insight into the interaction of the equipment and soil through the structure. Dietz et al. (2015) took a similar approach by numerically modeling soil-structure interaction while a SDOF physical model was excited by a shaking table. The results of this experiment achieved good matching with a 1g shaking table test of the entire reference structure. In this hybrid test, the shaking table was controlled using a *Full State Compensation via Simulation (FSCS)* approach. The controller was developed using inverse dynamics and a full-state feedback control scheme.

The difficulty in shaking table control during hybrid testing is mainly due to the presence of important control-structure interaction. Nakata (2010) proposed a model-based control method termed as Acceleration Trajectory Tracking Control (ATTC). The controller is made from a feedforward controller, command shaping, Kalman filter, proportional-derivative displacement-based feedback controller, and intentional time-delay. The intentional time-delay was introduced between the shaking table command acceleration and actuator command displacement making the acceleration feedforward loop the driving source of the controller. The displacement feedback loop, shown in Figure 2-24, serves only to provide the stability (or prevent drift). The ATTC scheme was reported to have improved performance, over a wide range of frequency, compared to the conventional command shaping augmented displacement-based controller.

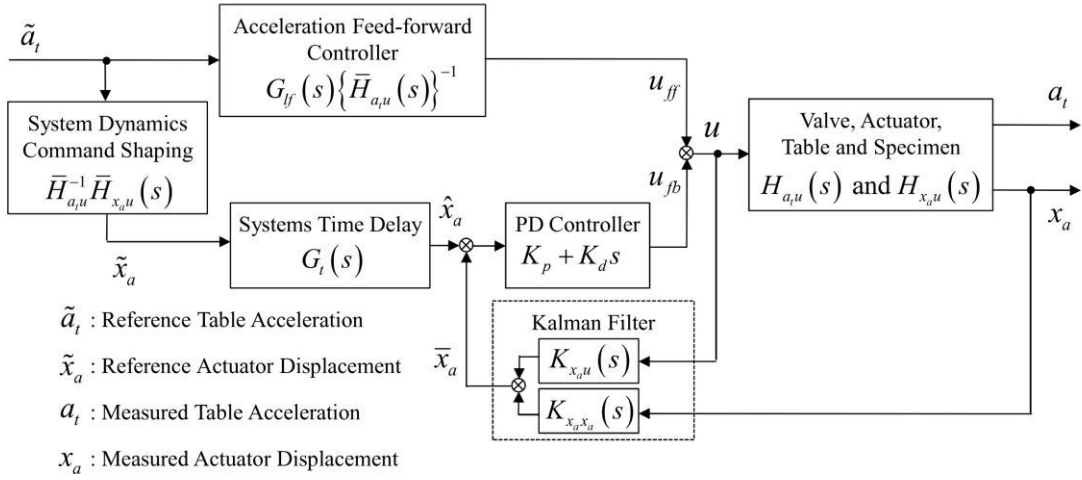


Figure 2-24: Block diagram of acceleration trajectory tracking control (after Nakata, 2010)

Phillips & Spencer (2012) presented another model-based feedforward-feedback controller for accurate tracking of command displacement during a RTHS test. Before applying this method, the transfer function from the input displacement to output displacement of the servo-hydraulic system was determined using a band-limited white noise input in the interval 0-50 Hz. This model-based feedforward-feedback method has demonstrated excellent performance during RTHS experiments conducted on a SDOF structure and a 9-story steel building.

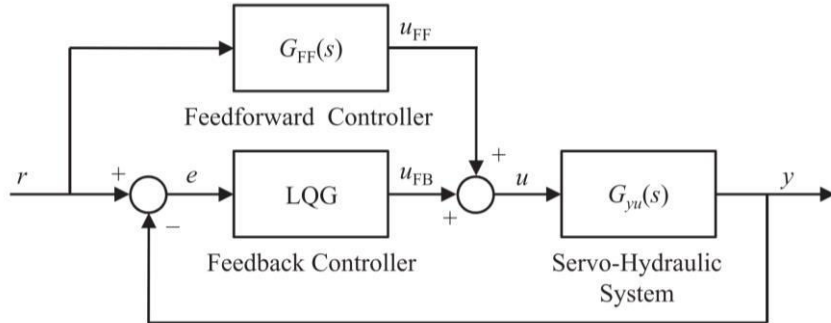


Figure 2-25: Block diagram of a feedforward-feedback controller (after Phillips & Spencer, 2012)

Similarly, Phillips et al. (2014) proposed a model-based multi-metric shaking table control strategy to improve acceleration tracking of a uniaxial shaking table, including its robustness to system nonlinearities. This method was aimed to address strong CSI during hybrid testing. The superior performance of this control scheme was demonstrated by comparing it with the Transfer Function Iteration (TFI) based offline tuning method, which is commonly used in shaking tables. In another effort to circumvent the lack of stability of a controller that uses direct acceleration feedback, Stehman (2014) introduced force feedback control of an actuator to provide stability to the shaking table thus preventing uncontrolled drift. The shaking table controller has two parallel closed loops:

an acceleration control loop and a force control loop. The gain in each loop corrects a reference variable. The two closed loops work independently but the output command is obtained by summing up the two displacement outputs. This approach is quite different from other conventional techniques employed in controlling a shaking table since no displacement feedback is utilized. However, this method requires additional hardware on the shaking table such as a spring element that serves as a reference value to the shaking table absolute position, producing forces proportional to the shake table position. This requirement is due to the stiff nature of actuators. The stiffness of the spring can be chosen based on the capacity of the load cell that measures the restoring forces.

### 2.8.2.1 Optimal acceleration tracking via a feedforward-feedback controller

Direct acceleration control of a shaking table is inherently unstable since it can drift even when acceleration is zero. Thus, the implementation of direct acceleration feedback control in shaking tables is very limited. In hybrid testing, a shaking table may be commanded by an acceleration command from a numerical substructure. Accurate tracking of this acceleration command is therefore important for the fidelity of the hybrid test. Phillips et al. (2014) developed optimal acceleration tracking for shaking tables using a model-based feedforward-feedback control scheme that utilizes acceleration and displacement feedbacks, as shown in Figure 2-26. In the offline operation of this controller, the target acceleration is converted to target displacement and the feedforward controller calculates a feedforward command  $u_{FF}$ . Instead of double integrating the desired acceleration to get displacement, a model-based conversion is employed in this scheme. This model-based conversion has provided a better prediction of the desired displacement in Nakata (2010).

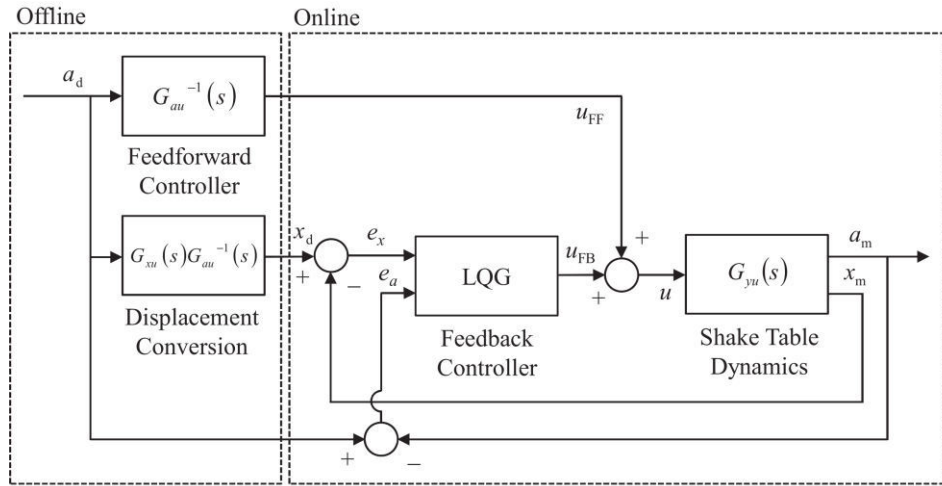


Figure 2-26: Model-based feedforward-feedback controller for acceleration tracking of a shaking table (after Phillips et al., 2014)

In this scheme, the transfer function of the system needs to be estimated, before conducting a

hybrid test, by applying a pre-defined command voltage to the shaking table. The inverse transfer function  $G_{au}^{-1}$  of the shaking table is then evaluated by fitting the Frequency Response Function (FRF) calculated from the input command voltage to the measured acceleration. In Phillips et al. (2014), two poles of the estimated  $G_{au}^{-1}$  are located at the origin, meaning the table drifts at low frequencies. To prevent shaking table from drifting, Phillips et al. (2014) high-pass filtered the desired acceleration to remove its low-frequency content without altering too much of its actual frequency content. For an accurate acceleration tracking of a shaking table that is characterized by nonlinearities (arising from test specimen, servo-hydraulic actuator, modeling errors, measurement noise, or combination of them), the feedforward controller can be augmented by a feedback controller. The Linear Quadratic Gaussian controller (LQG) on the other hand serves as a feedback controller to bring the deviation of the system states down to zero (Phillips et al., 2014). Using the principles of optimal control, the LQG is designed from a Linear Quadratic Regulator (optimal feedback control) and a Linear Quadratic Estimator (optimal state observer or commonly known as Kalman filter), which are independent of each other. Reformulating the system dynamics into deviation dynamics (error dynamics,  $\tilde{u} = u - \bar{u}$ ), the tracking problem is transformed to a regulator problem. Therefore, the input command voltage  $u$  to the servo-controller becomes:

$$u = \bar{u} + \tilde{u} = u_{FF} + u_{FB} \quad (2.92)$$

To improve the performance and robustness of the LQG controller, in the frequency range of interest, the dynamics of the deviation system is augmented by assuming a white Gaussian noise to model the system disturbance. A second-order shaping filter is applied to this noise such that the effect of high-frequency noise in the measured acceleration of the feedback control is reduced. The augmented state-space equation of the system deviation, represented by “~”, is eventually solved resulting in the optimal control gains.

$$\begin{aligned} \dot{z}_a &= Az_a + Bu_{FB} + E_a v_f \\ \tilde{y} &= Cz_a + w_f \end{aligned} \quad (2.93)$$

where  $z_a = [z_f \ \tilde{z}]^T$  and  $E_a = [E_f \ E]^T$  are the augmented state vector and the augmented system disturbance vector, respectively. In equation (2.93),  $v_f$  and  $w_f$  are the system disturbance and measurement noise (independent noises for acceleration and displacement), respectively; A, B, and C are the state, input, and output matrices, respectively. The disturbance vector E can be assumed equal to the input matrix B considering disturbance enters the system in the same way as the input (Phillips et al., 2014). The dynamics of the second-order shaping filter reads:

$$\begin{aligned} \dot{z}_f &= A_f z_f + E_f v \\ v_f &= C_f z_f \\ A_f &= \begin{bmatrix} 0 & 1 \\ \omega_f^2 & -2\xi_f\omega_f \end{bmatrix}; E_f = [0 \ 1]^T; \text{ and } C_f = [\omega_f^2 \ 2\eta_f\xi_f\omega_f] \end{aligned} \quad (2.94)$$

In equation (2.94),  $z_f$  is the state vector of the filter while the parameters  $\omega_f$ ,  $\xi_f$  and  $\eta_f$  control the frequency bandwidth, peak, and roll-off of the shaping filter. The disturbance  $v_f$  is a white

Gaussian noise,  $\nu$ , after passing through the second-order shaping filter. In LQG, the gain matrix of the regulator,  $k_{LQR}$ , is calculated in such a way that the system state returns to the origin (the controller tracks the setpoint in the context of tracking) by generating a control action. The solution for  $k_{LQR}$  is obtained by minimizing a cost function. Phillips et al. (2014) considered an output weighting for the cost function assuming full state feedback.

$$J_{LQR} = \frac{1}{2} \int_0^{\infty} \{ \tilde{y}^T Q_{LQR} \tilde{y} + u_{FB}^T R_{LQR} u_{FB} \} \quad (2.95)$$

where  $J_{LQR}$  is the cost function, and the matrices  $Q_{LQR}$  and  $R_{LQR}$  represent the output and input weighting matrices, respectively. The solution to equation (2.95) is determined by solving the algebraic Riccati equation to obtain a symmetric, positive definite matrix  $P$ :

$$A^T P + PA - [PB]R_{LQR}^{-1}[B^T P] + Q_{LQR} = 0 \quad (2.96)$$

Based on the weighting matrices chosen, the optimal gain  $K_{LQR}$  is calculated as:

$$K_{LQR} = R_{LQR}^{-1} B^T P \quad (2.97)$$

Finally, the control effort of the feedback controller is calculated as:

$$u_{FB} = -K_{LQR} z_a \quad (2.98)$$

To calculate the feedback control effort,  $u_{FB}$ , the augmented state vector of the system is first determined using the optimal state observer (Kalman filter). The augmented state-space equation of the system thus becomes:

$$\dot{\hat{z}}_a = A\hat{z}_a + Bu_{FB} + L_{Kal}(\tilde{y} - C\hat{z}_a) \quad (2.99)$$

where  $\hat{z}_a$  is the augmented state vector estimated using the Kalman filter and  $L_{Kal}$  is the optimal gain matrix of the Kalman filter. In equation (2.99),  $L_{Kal}(\tilde{y} - C\hat{z}_a)$  is the corrective term and  $\tilde{y} - C\hat{z}_a$  is the error vector between the measured and target output of the system. In multi-metric control, both the displacement and acceleration of a shaking table represent system outputs. Besides, the Kalman filter does not add time-lag to the system like other conventional filters. This makes it attractive for real-time hybrid testing.

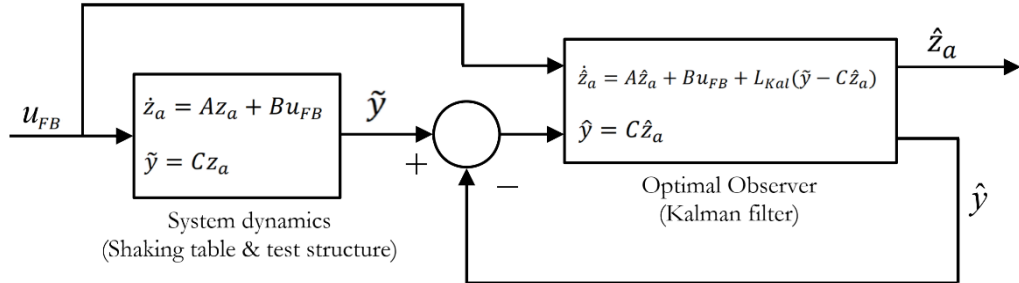


Figure 2-27: Optimal observer (Kalman filter)

Rearranging and grouping the prediction and correction terms of equation (2.99), the equation for the optimal observer can be written as:

$$\begin{aligned}\dot{\hat{z}}_a &= A_e \hat{z}_a + B_e [u_{FB} \ \tilde{y}]^T \\ \hat{y} &= C_e \hat{z}_a\end{aligned}\tag{2.100}$$

where  $A_e = A - L_{Kal}C_e$  and  $B_e = [B \ L]$ . The optimal gain of the Kalman filter depends on the relative value of the covariances of the process noise,  $Q_v\delta(\tau)$ , and measurement noises,  $R_w\delta(\tau)$ , of the system. Both are commonly assumed to be white Gaussian noises with zero mean and some covariance. The process noise, comprised of input noise and system uncertainties, is difficult to estimate by direct measurement and may require some tuning. The cross-covariance between the process and measurement noises is taken as zero since they are considered to be independent. The error covariance,  $P_e$ , is calculated as:

$$P_e = E[\{x(t) - \hat{x}(t)\}\{x(t) - \hat{x}(t)\}^T]\tag{2.101}$$

where  $E[\ ]$  is the expected value. Again, the algebraic Riccati equation is used to solve for the stationary error covariance, i.e.,  $\dot{P}_e=0$ . Minimizing  $P_e$  amounts to minimizing the mean-square of estimation error.

$$A^T P_e + P_e A - [P_e C^T] R_w^{-1} [C P_e] - E Q_w E^T = \dot{P}_e = 0\tag{2.102}$$

Depending on the choice of noise covariances, the optimal Kalman gain that minimizes the  $P_e$  can be then determined from:

$$L_{Kal} = P_e C^T R_w^{-1}\tag{2.103}$$

For discrete-time systems, the process of a Kalman filter is implemented using a prediction and correction comprising a prediction state, prior to measuring output, and a correction state, accounting for measured output. For time-invariant discrete systems, the procedure starts with the initialization of states,  $z$ , and the covariance matrix,  $P$ . The first step of the process is to predict system states. In the second step, the corresponding covariance matrix is calculated and the optimal gain matrix is estimated. This completes the prediction phase and the correction phase is put into action by updating the system states accounting for the measured output. At the end of the process, the estimate for the covariance matrix is updated as well. In this process, if the process and measurement noises are stationary, the error covariance and Kalman gain do not change, thus they do not need to be precomputed.

In the control and simulation module of LabVIEW software, the LQG controller is constructed using the Discrete Kalman filter function and the Linear Quadratic Regulator (LQR) VIs. These VIs have similar operations as explained above, but the implementation is slightly different. The Linear Quadratic Regulator (LQR) VI offers state or output weighing modes for minimizing the cost function. Likewise, the Discrete Kalman filter VI has several polymorphic instances for prediction, correction, and model checking. The default mode in this VI allows users to perform both prediction and correction (using prediction gain) and checks model parameters at the end.

### 2.8.3 Force control of actuators

As mentioned previously, actuators working under force feedback are potentially unstable due to the stiff oil-column frequency. Additionally, noise due to friction, stick-slip, breakaway forces on seals, backlash, and so on forth makes direct force control challenging. The first attempt in force control was made by Thewalt & Mahin (1987) when proposing the Effective Force Testing (EFT) technique as a means for conducting hybrid simulation. In EFT, the forces to be applied in the laboratory are known *a priori*. For a discretized model, the forces at each DOF can be obtained as a product of mass and ground acceleration. Subsequently, the force vector is then transformed into actuator DOFs. However, EFT cannot be used to conduct substructuring tests since the effective forces computed are still in the global DOF of the discretized nodes. It is unknown how much of the global force should be applied to an experimental substructure. Switch and mixed control strategies were also examined by Pan et al. (2005). They applied it on an eight-story two-span moment-resisting frame equipped with High Damping Rubber Bearing (HDRB) base-isolators. The HDRB was physically tested while the steel frame was numerically modeled in a finite element software. Each floor was represented by two DOF, one in the horizontal and another in the vertical direction. The vertical actuator was designed to switch between force and displacement control modes leaving the horizontal actuator to be controlled in displacement only. No coupling was considered between the two DOFs. The trial displacements of both actuators were computed using the alpha Operator-Splitting integration scheme and the force command to the vertical actuator was obtained as the product of the predicted displacement and the vertical elastic stiffness of the HDRB, assuming the bearings remain elastic in the axial direction. In the vertical direction, no displacement or measured force was feedback to the finite element software, rather the vertical trial forces obtained were considered as resisting forces. The approach taken by Pan et al. (2005) is accurate provided that the axial DOF remains elastic.

In another switch-control study conducted by Elkhoraibi & Mosalam (2007), the secant stiffness in the  $\alpha$ -OS integration scheme was used to compute trial forces. The secant stiffness matrix was diagonal since DOFs were considered to be uncoupled. The diagonal terms of the secant stiffness matrix at time-step  $n+1$  and iteration  $i$ ,  $k_{n+1}^i$ , were calculated as:

$$k_{n+1}^i = \frac{(\check{f}_{n+1}^{i-1} - r_n)}{(\check{u}_{n+1}^{i-1} - u_n)} \quad (2.104)$$

where  $\check{f}_{n+1}^{i-1}$  is the trial force at iteration  $i-1$  and time-step  $n+1$ ;  $r_n$  is the converged resisting force at time-step  $n$ ;  $\check{u}_{n+1}^{i-1}$  is the measured displacement at iteration  $i-1$  and time-step  $n+1$ ;  $u_n$  is the converged displacement at time-step  $n$ . The trial forces,  $\check{f}_{n+1}^i$ , were calculated using the implicit HHT integration method. Therefore, it can result in unrealistic loading and unloading cycles when applied to hybrid testing. To avoid this unrealistic energy dissipation, a reduction factor  $\lambda$  ( $\lambda < 1$ ) on the incremental trial force,  $\check{f}_{n+1}^{i+1} - \check{f}_{n+1}^i$ , was applied. The value of  $\lambda$  was tuned to get the desired output. Although the method is applicable only for structures with uncoupled DOFs, it has a wider application compared to the technique proposed by Pan et al. (2005). Nonetheless, it is difficult to

find structural models with uncoupled DOFs.

Sivaselvan et al. (2008) proposed an equivalent force control technique for actuators which is applicable to both effective force testing and real-time dynamic hybrid testing. In this technique, force control is conducted by controlling the actuator's displacement using an elastic spring (compliant system) of known stiffness that assumes the role of an oil spring. The proposed force control was executed by integrating it with a non-adaptive Smith-Predictor delay compensator. The restoring force of the compliant system, which can be measured by a load cell, is therefore indirectly controlled. The added compliance approach finds a way to work-around the mechanically stiff nature of an actuator making it a force-source. However, the spring must remain elastic throughout the duration of the hybrid test. Above all, it is only effective for elastic structural systems and the load transfer system must be represented as a pure time-delay. Besides, loss of force may also occur due to a poor connection between the actuator and compliant spring. More importantly, the capacity of this scheme to extend to large-scale testing could be hindered due to the limited energy-storage capacity of the compliant spring. As pointed above, when this approach is used in conjunction with a Smith-Predictor, response simulation of nonlinear experimental substructures can be erroneous since the compensator assumes elastic properties of the test structure. Besides, model deviations, or the time-delay of an actuator, cannot be compensated. Shao et al. (2011) applied this technique while developing a general framework for hybrid testing made from a shaking table and an auxiliary actuator.

Chae et al. (2018) combined the adaptive time series compensator with the compliant-system force control to accurately simulate the response of a nonlinear experimental substructure. This approach is referred to as D-ATS. The same authors also presented another approach for direct force control, termed as F-ATS, to mitigate difficulties in conducting displacement-based control of a stiff test structure. In the latter, force feedback is used instead of displacement feedback and the adaptive time series compensator operates under force compensation as opposed to displacement.

Furthermore, Kim (2011) developed a force control scheme based on the compatibility method of acquiring trial forces while the computational driver is working in displacement mode. He added a new abstract class to the OpenFresco software, by manipulating the experimental control object, enabling it to convert trial displacement, received from the computational driver, into trial forces. The OpenFresco ExperimentalSignalFilter (ESF) class was extended to handle this conversion. Methods introduced in the ESF include tangent-based (Broyden, BroydenFletcher-Goldfarb-Shanno (BFGS), Intrinsic and Transpose), and Krylov subspace compatibility methods. In this scheme, the control system imposes trial forces; and the measured forces and displacements are then returned to OpenFresco. The measured displacements are converted to measured forces in OpenFresco and eventually returned to the computational driver. The abstract classes are also equipped with filters to prevent noises from causing spurious updates. In the hybrid test conducted by Kim (2011), a predictor-corrector model for force control was adopted to bridge the clock-speeds between the integrator loop and the servo-control loop. Besides, Kim (2011) proposed an

equilibrium-based approach for analysis by programming a basic force-based FEA software in a MATLAB environment. However, the MATLAB program can only model a 1-D truss element, meaning it lacks diversity in terms of structural elements necessary for modeling structural systems. To accommodate both the softening and stiffening behavior of structural elements, switch control was also implemented by Kim (2011).

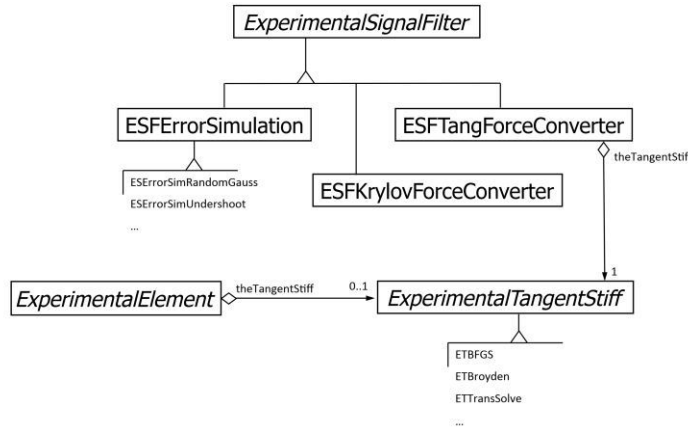


Figure 2-28: OpenFresco UML class diagram for computing tangent stiffness of an experimental element (after Kim, 2011)

### 2.8.3.1 Equivalent force control through added compliance

As mentioned above, Sivaselvan et al. (2008) proposed the equivalent force control method that combines a compliant system and the displacement control of an actuator. This approach is based on a “*series elastic actuators*” technique developed in robotics (Pratt et al., 2002). Generally, actuators are high impedance devices (mechanically stiff) designed for good position control (Sivaselvan et al., 2008), i.e., moving heavy loads accurately and quickly. Contrarily, force control requires a mechanically compliant system or a system with low impedance. In this technique, a spring element (compliant element) is attached in series to the actuator resulting in a low-impedance system. In related work, MTS developed a dual compensation scheme having displacement feedback in the primary loop and force feedback in the secondary loop. The MTS controller includes acceleration compensation to correct errors in measured forces. Going back, the impedance control strategy is commonly used in robotics to control force-displacement relationships. In the “*series elastic actuators*” technique, a flexible mechanism is incorporated between an actuator and the point of application of a load, considering non-resonant systems. During force feedback, the dynamics of the controlled structure is coupled with the actuator through velocity feedback. Hence, force control without velocity feedforward can be ineffective. From this standpoint, Shield et al. (2001) developed a velocity feedback compensation, by adding a positive feedback to the servo-valve, after compensating for the servo-valve dynamics. Such compensation is typically done through lead-lag compensators.

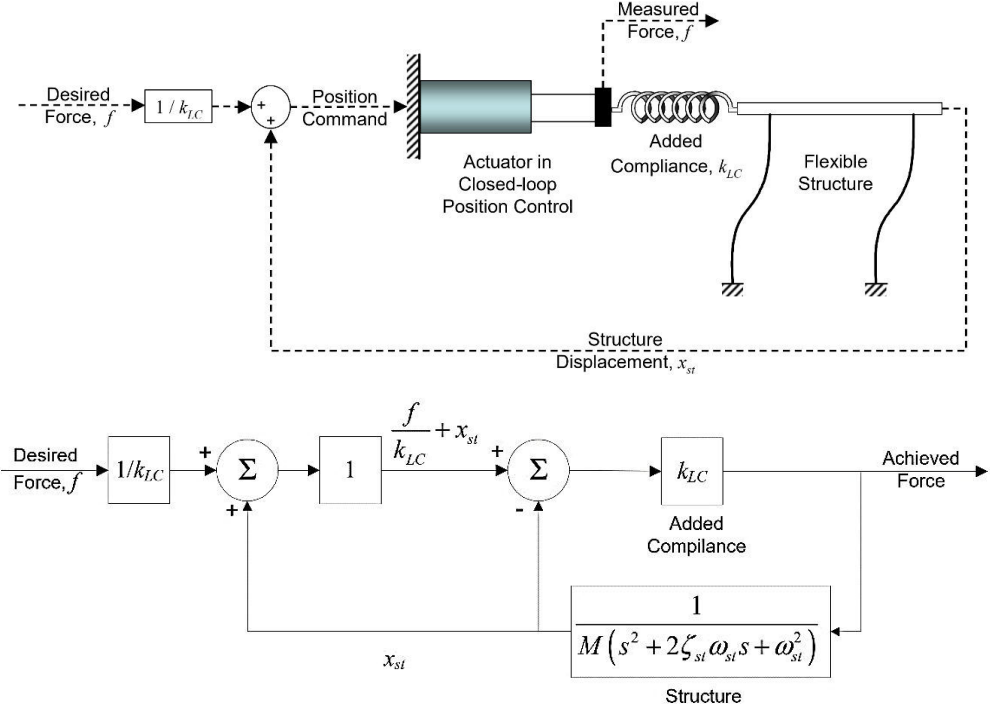


Figure 2-29: Dynamic force control using added compliance technique: physical model (top) and block diagram (bottom) (after Sivaselvan et al., 2008)

To illustrate equivalent force control using a compliance spring, let us consider first a rigid structure (infinite stiffness) connected to an actuator through a compliance spring. Assuming perfect disturbance rejection, consider a scenario where a force  $f$  is applied to the structure by an actuator. The compliance spring gets compressed by an amount  $f/k_{LC}$ , where  $k_{LC}$  is the elastic stiffness of the compliance spring; consequently, the actuator moves from its original position by a distance equal to  $f/k_{LC}$ . Now, imagine the structure is not rigid anymore and that it would move by a distance  $x_{st}$  after applying a force  $f$ . In the second scenario, the actuator needs to be commanded to a position  $f/k_{LC} + x_{st}$ . It is therefore clear now that one needs to predict the structure's displacement to command the actuator to  $f/k_{LC} + x_{st}$  position. This prediction (or compensation) can be done using the model of the structure or by feeding the measured displacement of the structure back to the actuator.

Combining the compensation from the structure's model and the feedback displacement, the Smith Predictor scheme is obtained. Accurate identification of the properties of a test specimen and transfer system (time-delay in particular) are necessary to tune the predictor. The compliance spring also becomes an additional control parameter. Care should be taken, because if the flexibility of the compliant spring is large, actuators may exceed their stroke limits.

In Sivaselvan et al. (2008), the proposed method was applied to a simple one-story shear building. The structure was tested considering two damping scenarios. Firstly, only inherent damping was

considered. Secondly, a dashpot was attached to the structure to increase the overall system damping. The controller was tuned to have a unit magnitude and a small time-delay. In the absence of the Smith Predictor compensator, the magnitude of the FRF of the output force was characterized by a sharp drop at the resonant frequency of the structure, in both scenarios. In the second scenario, when the Smith Predictor compensator was added to the controller, the output force achieved better characteristics at the resonant frequency of the structure. Nevertheless, the presence of Smith Predictor in the first scenario has only changed the characteristics of the output force slightly, mainly because of the low inherent damping of the structure and loss of force at the connections. To reduce this effect, Shao & Reinhorn (2012) proposed an additional positive feedback force which is a product of a damping coefficient and the measured relative velocity of the structure. However, a technique for estimating this damping coefficient does not exist to date.

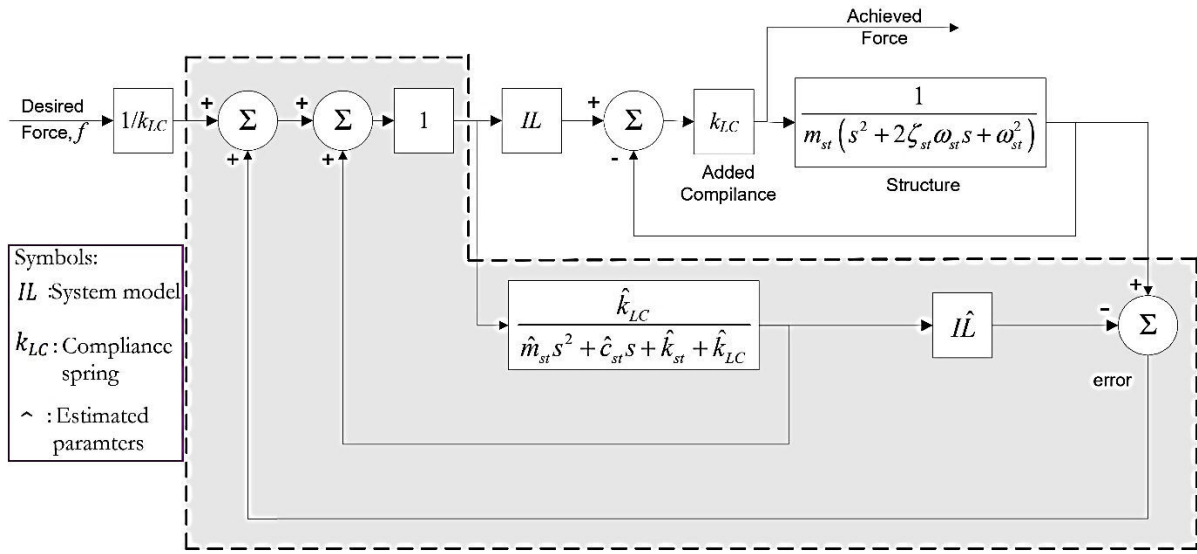


Figure 2-30: Smith Predictor compensation(after Sivaselvan et al., 2008)

Due to the potential of the added compliance approach, for controlling the actuator's force, Chae et al. (2018) implemented the added compliance approach using an adaptive compensation scheme. The adaptive time series compensator (Chae et al., 2013) was used to adaptively track and compensate system time-delay. The authors proposed two variations of the added compliance technique, one based on displacement (D-ATS) and another based on force (F-ATS), shown in Figure 2-31 and Figure 2-32. The working principle of D-ATS is similar to the conventional ATS except that it has three additional positive feedback loops.

Since velocity is not measured directly in structural testing, Chae et al. (2018) calculated the velocity estimate by summing up the derivative of the measured displacement, after low-pass filtering, and the integral of the measured acceleration, after high-pass filtering. The integration of the measured acceleration is performed in the duration of the time-delay of the actuator. Like the conventional ATS, the measured displacement of the actuator is also returned to the compensator to solve for

the next time-step compensated displacements,  $u_c$ , as shown in Figure 2-31.

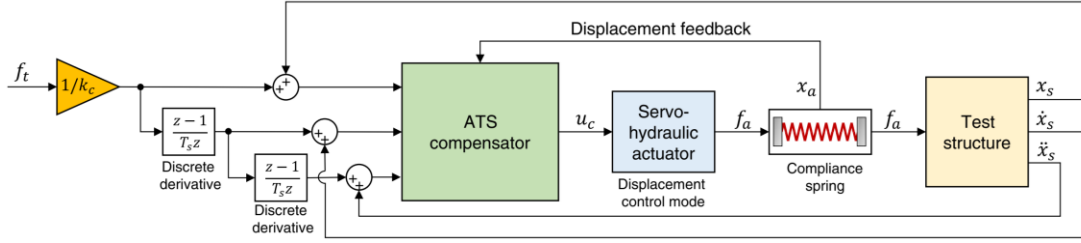


Figure 2-31: Block diagram of D-ATS (after Chae et al., 2018)

Unlike the existing ATS compensator, which is commonly used in a displacement control mode, in the F-ATS method, the controller is directly applied in force control mode, as shown in Figure 2-32. This scheme was intended for stiff test structures where displacement control can be erroneous. In the F-ATS, the target force and its derivatives are used in calculating the compensated force. The force measured from the compliance spring is the only feedback quantity needed in this scheme.

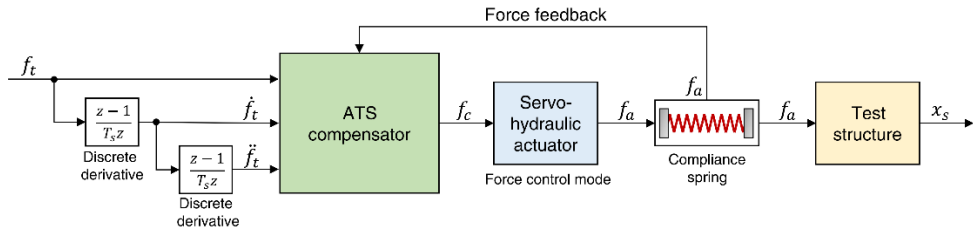


Figure 2-32: Block diagram of F-ATS (after Chae et al., 2018)

In fact, the stiffness of the compliance spring,  $k_{LC}$ , is not even required for this compensation. Nevertheless, the numerical model should be able to calculate target forces as opposed to displacement trials, typical of displacement-based analysis. Therefore, the F-ATS needs a force-based finite element software for its implementation.

In the first experiment, the D-ATS and F-ATS were experimentally tested using a SDOF structure consisting of a block of steel mass supported on roller bearings, a helical spring, and a magneto-rheological (MR) damper. Before validation tests, the nonlinearity of the test structure, derived from frictional forces, was estimated experimentally in the form of equivalent damping. Besides, the inertial force of the piston, which is measured by the load cell, was also compensated during these experiments. In the second experiment, the helical spring was replaced by a stiff steel bar. This test explored the force tracking capabilities of the axially stiff specimen using the D-ATS and F-ATS compensators by applying a predefined force history to the actuator. In both experiments, the D-ATS resulted in good force tracking whereas the F-ATS was less successful during the first experiment. This implies that the F-ATS is less attractive for effective force testing when the test structure is flexible. Nonetheless, the F-ATS has shown a remarkable performance when applied to the axially stiff specimen.

### 2.8.4 Prediction-correction methods for actuator control

In hybrid simulation tests, measured forces are returned to the numerical program at intervals of time depending on the speed of simulation and complexity of the test structure. This means the outer integration loop, which includes the time-stepping algorithm, should be synchronized with the clock speed of the controller. Thus, command displacements are applied to the actuator at short intervals of time in a deterministic manner. On the other hand, the numerical solution to the equation of motion can be time-consuming for nonlinear dynamic problems. Besides, data transmission is a potential source of time-delay. For example, the TCP/IP transmission protocol, which is a means of communication in the OpenFresco framework, has notable latency while transmitting data between a FEA software and control software. The time needed for the data transmission may not be constant, albeit small comparing to geographically distributed testing. To this end, the numerical integration and command generation processes must be synchronized. This can be performed using a predictor-corrector algorithm that ensures the parallel execution of the two tasks. This synchronizer predicts command signals deterministically (at the clock speed of the control system) to the actuator while the computational driver is solving the next time-step response. This prediction can be performed for a fixed duration or it can be adaptively changed. Once the target response is available in the control system, the algorithm starts correcting towards the target response. This continuous movement of actuators can significantly reduce the force relaxation effect prevalent in the hold-phase of the ramp-and-hold method. In the prediction-correction methods, if the numerical solution is not available at the control software within a pre-defined duration, the actuator may overshoot the target displacement. Thus, the algorithm switches to a slow-down phase. In this state, the actuator is slowed down smoothly to a stop state until the next time-step command is received.

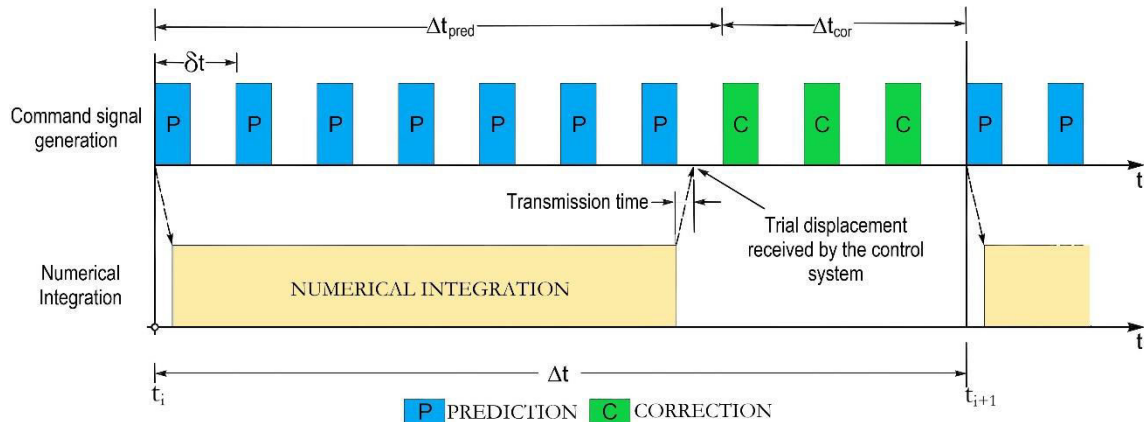


Figure 2-33: Sequence of execution in the predictor-corrector approach for synchronizing numerical integration and command generation (modified from Schellenberg et al., 2009)

The command displacements of an actuator can be predicted, for instance, using Lagrange polynomials. The prediction is based on committed displacements from the last  $n$  time-steps.

However, improved accuracy of prediction may be achieved using velocities and accelerations as well (Schellenberg et al., 2009). A more detailed discussion of the existing predictor-corrector algorithms is presented subsequently.

#### 2.8.4.1 Conventional algorithm

This algorithm was originally implemented by Nakashima & Masaoka (1999) where third-order Lagrange polynomials are adopted for the extrapolation and interpolation of command displacements to an actuator. The method has better accuracy at small values of  $\omega\Delta t$  (say  $\omega\Delta t < 0.5$ ). The authors achieved accurate velocities when using the third-order or fourth-order polynomials. Considering  $n$ th-order polynomial, the extrapolated displacements are calculated as:

$$d^p(x) = \sum_{k=-n}^0 d_k^{cm} P_{n,k}(x); \quad x \in [0, x_{max}] \quad (2.105)$$

where  $d_k^{cm}$  is the last  $k$ th time-step displacement received from, or committed by, the computational driver;  $P_{n,k}$  is the  $n$ th order predictor polynomial; and  $x$  is the fraction of the integration time-step,  $\Delta t$ . Also, the general formulation for the Lagrange polynomial  $P_{n,k}$  is given by:

$$P_{n,k}(x) = \prod_{\substack{i=0 \\ i \neq k}}^n \frac{x - x_i}{x_k - x_i} \quad (2.106)$$

The prediction is carried out until  $x_{max} = \Delta t_{pred}/\Delta t$ , where  $\Delta t_{pred}$  is the maximum duration for prediction (for example, 80% of the simulation time  $\Delta t$ ). The duration of prediction varies depending on the complexity of the numerical substructure, which dictates the time elapsed in solving the numerical substructure, as well as on the time-delay in data communication. For relatively simple structures, 60% of the simulation time can be conveniently used. If a long prediction period is adopted, the actuator can overshoot, deviating from its correct trajectory. Also, prediction using a lower-order polynomial (first-order or second-order), especially at large time-steps of integration, can distort the correct trajectory of displacement as well. The accuracy of predictors can be studied assuming the earthquake response of a structure as a sinusoidal vibration (Nakashima & Masaoka, 1999). The sinusoidal response is characterized by amplitude,  $A$ , and angular frequency,  $\omega$ . In discrete state, the response can be expressed as:

$$d_k^{cm} = A \sin(\omega t - \omega \Delta t(x - k)) \quad (2.107)$$

replacing  $d_k^{cm}$  in equation (2.105), the prediction formula is transformed into:

$$d^p(x) = \sum_{k=-n}^0 A \sin(\omega t - \omega \Delta t(x - k)) P_{n,k}(x) \quad (2.108)$$

$$d^p(x) = A R_d^p \sin(\omega t + \phi^p) \quad (2.109)$$

and,  $R_d^p$  and  $\phi^p$  can be derived from equation (2.108):

$$R_d = \sqrt{C_s^2 + C_c^2} \text{ and } \phi = \arctan(C_c/C_s) \quad (2.110)$$

$$C_c = - \sum_{k=-n}^0 \sin(\omega\Delta t(x-k))P_{n,k}(x)$$

$$C_s = \sum_{k=-n}^0 \cos(\omega\Delta t(x-k))P_{n,k}(x)$$

Comparing equations (2.109) and (2.105), the amplitude error,  $R_d^p$ , and phase-lag,  $\phi^p$ , are introduced into the true response by the prediction process. Increasing the integration time-step can result in loss of accuracy during the prediction process, hence, a small time-step must be adopted for accurate prediction. Displacements at the correction phase are calculated once the target displacement at the current time-step is available. Like the prediction phase, corrector displacements are calculated using third-order polynomials.

$$d^c(x) = \sum_{k=-n+1}^1 d_k^{cm} C_{n,k}(x); \quad x \in [0,1] \quad (2.111)$$

where  $C_{n,k}$  is the  $n$ th-order corrector polynomial. Using the assumption of a sinusoidal response, the interpolated corrector displacement is computed as:

$$d^c(x) = AR_d^c \sin(\omega t + \phi^c) \quad (2.112)$$

where  $R_d^c$  and  $\phi^c$  are the amplitude and phase-lag during the correction phase, respectively. The accuracy analysis of the corrector algorithm is identical to that of the predictor except for the predictor Lagrange polynomials that are replaced by the corrector Lagrange polynomials. However, the accuracy of the corrector is superior to that of the predictor because the corrector algorithm uses the current time-step displacement. For the sake of consistency, the same polynomial order is typically used for the predictor and corrector steps.

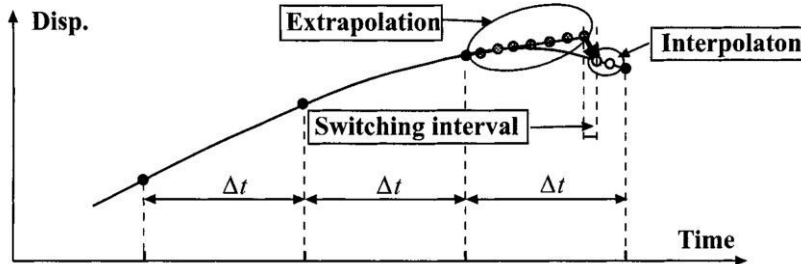


Figure 2-34: Velocity at switching interval of an extrapolation-interpolation algorithm (after Nakashima & Masaoka, 1999)

The difference between the last predicted displacement and the first corrector displacement, divided by time-interval of controller  $\delta t$ , can be taken as the velocity,  $v_s$ , at the interval when the algorithm switches from prediction to correction (switching interval). At the switching interval, shown in Figure 2-34, negative  $v_s$  can lead to undesired loading and unloading during the nonlinear response simulation of a test structure (Nakashima & Masaoka, 1999).

$$v_s = \frac{d^p(x = x_{max}) - d^c(x = 0)}{\Delta t} = AR_v \cos(\omega t - \phi^v) \quad (2.113)$$

where  $R_v$  and  $\phi^v$  are the amplitude and phase-lag of the switching velocity, respectively. Comparing the velocity at the switching interval to the true sinusoidal velocity,  $v = \text{Acos}(\omega t)$ , Nakashima & Masaoka, (1999) showed that first and second-order polynomials give rise to switching velocities with large amplification magnitude and phase-lead. The phase-lead may result in the unloading of the test structure when it is loaded towards its peak displacement. However, third and fourth-order polynomials have better characteristics as they have small magnitude of amplification. Nevertheless, they exhibit a significant phase-lag, especially under large prediction time-steps. The velocity phase-lag can cause undesired reloading of a test specimen when the switching interval occurs during the initiation of the unloading cycle. This effect is not detrimental since most structures are elastic during the unloading cycle. However, the phase-lead, prevalent when using the first or second-order polynomials, can seriously distort the response simulation of structures. Moreover, third-order polynomials have smaller magnitude amplification, at higher frequencies, compared to fourth-order polynomials; therefore, third-order Lagrange polynomials are recommended for predictor-corrector algorithms (Nakashima & Masaoka, 1999 and Schellenberg et al., 2009). Herein, the predictor-corrector explained above is referred to as the conventional method.

#### 2.8.4.2 Algorithm based on last predicted displacement

The conventional predictor-corrector algorithm explained above does not meet the requirements for  $C_0$ -continuity due to the discontinuous displacement at the switching interval. Besides, it does not meet the requirement for the accuracy of velocity. The need for  $C_1$ -continuity (continuity of the derivative at the switching interval) is less important as it may lead to unstable simulation. This instability is the result of a step-like jump at the switching interval where the high-velocity demand on the actuator causes an oscillatory motion. Although the step-like jumps can be alleviated by employing higher-order polynomials, it does not provide a definitive solution.

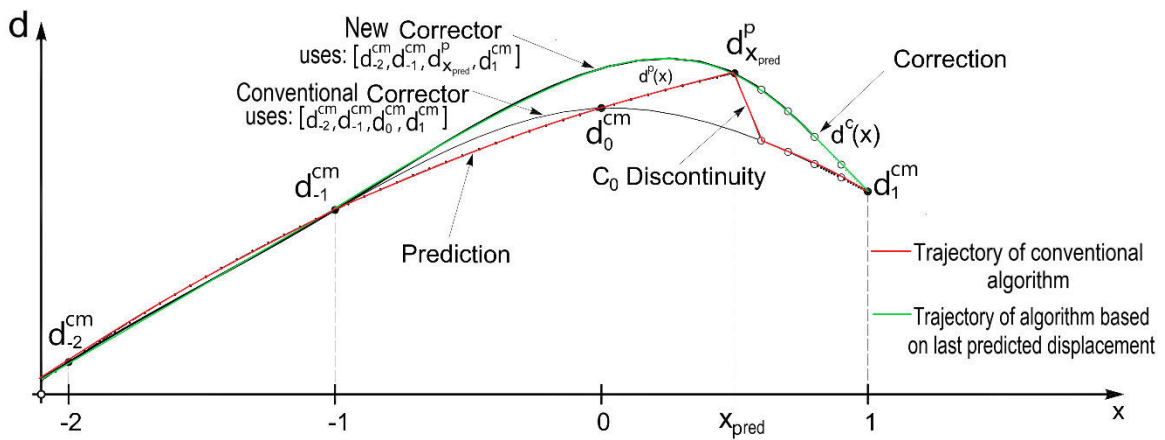


Figure 2-35: Algorithm based on last predicted displacement(modified from Schellenberg et al., 2009)

The algorithm based on the last predicted displacement, proposed by Schellenberg et al. (2009), essentially uses the last extrapolated displacement to replace the last committed displacement during the correction phase thereby making the predictor  $C_0$ -continuous. The predictor algorithm is

therefore identical to the conventional method whereas the corrector displacement is modified as:

$$d^c(x) = \sum_{\substack{k=-n+1 \\ k \neq 0}}^1 d_k^{cm} C_{n,k}(x, x_{pred}) + d_{x_{pred}}^p C_{n,x_{pred}}(x_{pred}); \quad x \in [0, 1] \quad (2.114)$$

where  $d_{x_{pred}}^p$  is the last predicted displacement and  $C_{n,x_{pred}}$  is the  $n$ th-order corrector polynomial at  $x = x_{pred}$ . The accuracy characteristics of this corrector algorithm are also examined considering a sinusoidal response of a test structure. The  $C_c$  and  $C_s$  coefficients of the amplitude error and phase-lag are now modified as:

$$\begin{aligned} C_c &= - \sum_{\substack{k=-n+1 \\ k \neq 0}}^1 \sin(\omega \Delta t(x - k)) C_{n,k}(x, x_{pred}) \\ &\quad - C_{n,k}(x, x_{pred}) \sum_{k=-m}^0 \sin(\omega \Delta t(x_p - k) P_{m,k}(x_{pred})) \\ C_s &= \sum_{\substack{k=-n+1 \\ k \neq 0}}^1 \cos(\omega \Delta t(x - k)) C_{n,k}(x, x_{pred}) \\ &\quad + C_{n,k}(x, x_{pred}) \sum_{k=-m}^0 \cos(\omega \Delta t(x_{pred} - k) P_{m,k}(x_{pred})) \end{aligned} \quad (2.115)$$

It is evident that this algorithm has a trade-off between the accuracy and the smoothness of the displacement trajectory at the switching interval. It is less accurate compared to the corrector algorithm implemented in the conventional method. This is mainly because the last predicted displacement, which already has the prediction error, is included in the interpolation process. However, the accuracy of this algorithm can be improved by limiting prediction errors using a small prediction time (small  $x_{pred}$ ). Overall, the reduced accuracy of the corrector algorithm is preferred over the disruptive property of the conventional algorithm since the oscillatory nature of the conventional algorithm can be problematic when combined with a responsive servo-hydraulic controller. Yet,  $x_{pred}$  is not a user choice only, but it is governed by the clock-speed of the controller (typically 1 kHz) and the simulation time-step. The simulation time-step of hybrid testing in turn depends on the complexity of the numerical substructure and the communication delay. Thus, the prediction-correction task may be a potential source of inaccuracy in hybrid testing. To address this problem, prediction-correction methods based on trial velocities and accelerations were explored by Schellenberg et al. (2009).

#### 2.8.4.3 Algorithm based on trial velocity

Prediction-correction using the last predicted displacement provides  $C_0$ -continuity, but the accuracy of its velocity needs to be improved further. Trial velocities can be used to improve the velocity accuracy of predictor-corrector algorithms. Several numerical integration methods, such as the Runge-Kutta integration, are explicit for velocities and displacements. However, trial velocities can be inaccurate in many integration methods. In the case where the trial velocity calculated by numerical methods is not capable of improving the velocity accuracy of the predictor-corrector

algorithm, it may be determined by differentiating the trial displacements instead. For numerical differentiation, Lagrange polynomials can also be employed. For brevity, only the algorithm that combines trial velocities and the last predicted displacement is discussed in this document. The predictor displacement obtained from the last  $n$  displacements and velocities uses a Hermite polynomial of order  $2n+1$ :

$$d^p(x) = \sum_{k=-n}^0 d_k^{cm} P_{2n+1,k}(x) + \sum_{k=-n}^0 d_k^{cm'} \hat{P}_{2n+1,k}(x); \quad x \in [0, x_{max}] \quad (2.116)$$

where  $d_k^{cm}$  and  $d_k^{cm'}$  are the last  $k$ th time-step displacement and velocity, respectively. In equation (2.116),  $P_{2n+1,k}$  and  $\hat{P}_{2n+1,k}$  are Hermite polynomials for displacement and velocity, respectively. Due to the availability of displacements and their time derivatives (velocities), Hermite polynomials will typically be more robust when compared to the Lagrange polynomials. Note that the Lagrange interpolation is a special case of Hermite interpolation where no derivatives are matched. Schellenberg et al. (2009) adopted third-order Hermite polynomials in his development. Likewise, the correction phase is conducted using trial displacements and velocities, including the last predicted displacement, and the corrector algorithm can only take a polynomial order of  $2n$ . To improve the efficiency of the corrector algorithm, Schellenberg et al. (2009) considered second-order Hermite polynomial. Consequently, the corrector displacement becomes:

$$d^c(x) = \sum_{\substack{k=-n+1 \\ k \neq 0}}^0 d_k^{cm} C_{2n,k}(x, x_{pred}) + \sum_{\substack{k=-n+1 \\ k \neq 0}}^0 d_k^{cm'} \hat{C}_{2n,k}(x, x_{pred}) + d_{x_{pred}}^p C_{2n,x_{pred}}(x, x_{pred}) \quad (2.117)$$

where  $C_{2n,k}$  and  $\hat{C}_{2n,k}$  are the Hermite polynomials for the displacement and velocity commands, respectively; and  $C_{2n,x_{pred}}$  is the Hermite polynomial for the displacement command at the end of the prediction phase. Assuming the trial velocities are obtained by numerical differentiation based on Lagrange polynomials, the general form of the derivatives is given by:

$$\begin{aligned} d_k^{cm'} &= \sum_{k=-n}^0 d_k^{cm} P'_{n,k}(x) \\ P'_{n,k} &= \sum_{\substack{i=0 \\ i \neq k}}^n \left\{ \frac{1}{x_k - x_i} \prod_{\substack{q=0 \\ q \neq (i,k)}}^n \frac{x - x_q}{x_k - x_q} \right\} \end{aligned} \quad (2.118)$$

Good estimates of velocities can be obtained using second-order or third-order numerical differentiation. Among the predictor-corrector algorithms, the algorithm which uses velocities and accelerations is the most accurate method when used with the last predicted displacement. The improved accuracy of the latter algorithm can be emphasized at large values of  $x_{pred}$ . Nonetheless, it can be oscillatory at large time-steps. On the other hand, considering algorithms that do not use the last predicted displacement, correctors that are based on velocities only are the most accurate. To limit the extent of information, the algorithm that uses velocities and accelerations is not presented in this thesis, but it is expounded in Schellenberg et al. (2009).

### 2.8.5 Simultaneous control of an actuator and shaking table

In the past few decades, hybrid simulation has marked important advancements in execution attracting a wide array of applications. Among them, the ability to conduct hybrid simulation tests of structures by simultaneously using a shaking table and an auxiliary actuator was investigated (Yang et al., 2015; Shao & Reinhorn, 2012). Yang et al. (2015) used the OpenSees-OpenFresco-Simulink-MTS hybrid testing platform in conducting a real-time hybrid simulation test of a single-span girder bridge using a shaking table and an actuator.

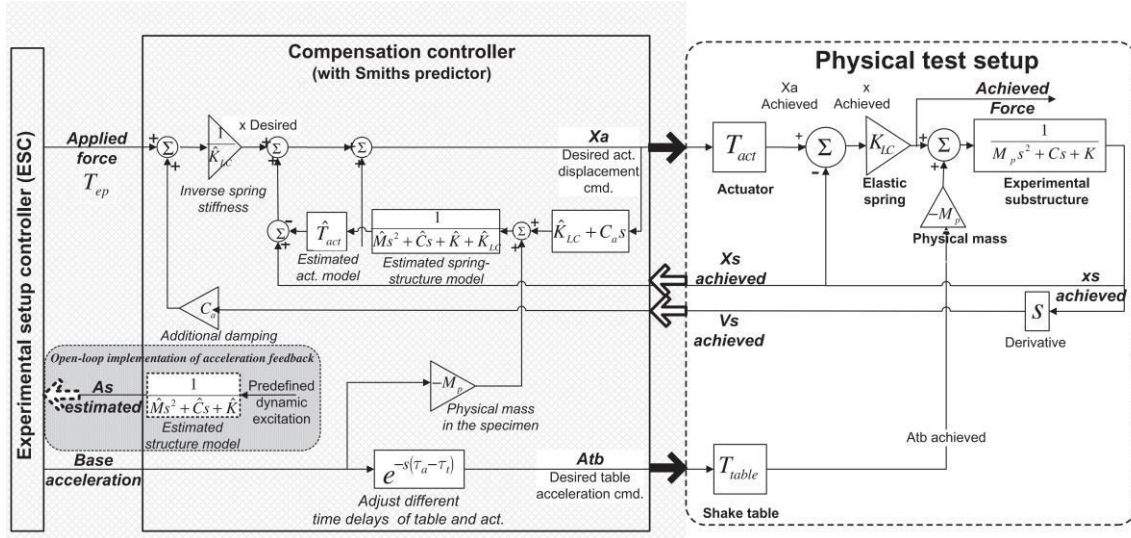


Figure 2-36: Flow diagram for hybrid testing using a shaking table and an auxiliary actuator when added compliance force control, based on Smith Predictor compensation, is adopted to control the auxiliary actuator (after Shao et al., 2012)

The reliability of the loading scheme was verified by comparing two hybrid tests performed on the same structure. The first scheme modeled a rubber bearing of the bridge piers as an experimental element whereas the second test step was made from an experimental element comprising the rubber bearing and bridge girder. Shao et al. (2012) developed a modular controller platform focusing on the force-based formulation for conducting hybrid testing. They presented a software framework capable of executing dynamic, pseudo-dynamic, and quasi-dynamic testing by combining a shaking table and an auxiliary actuator. Force-based control of the auxiliary actuator was also incorporated into their software framework which was accomplished through the equivalent force control method, based on the Smith Predictor compensation, developed by Sivaselvan et al. (2008). The integration of the equivalent force control scheme into this framework enabled the bottom part of a building to be modeled physically whereby the reaction force from the numerical substructure is the command driving the auxiliary actuator. The proof-of-concept of this scheme was performed on a pilot test constructed from a two-story shear frame structure made from steel.

In addition to the need for equivalent force control, the synchronous operation of a shaking table

and auxiliary actuator was addressed by Shao et al. (2012). The synchronicity of their motion is ensured by intentionally delaying one of them by the difference of their time-delays. This means, assuming the shake table response delay  $\tau_{ST}$  is larger than the auxiliary actuator  $\tau_a$ , the auxiliary actuator is delayed by an artificial delay equal to  $\tau_{ST} - \tau_a$ . This framework may enable physical testing of the soil-structure interaction of a building while the superstructure part is modeled in a numerical program. Its application may also be extended easily to bridge structures. The potential of this scheme is explored in detail in chapter five.

## 2.9 Summary

This chapter intended to present notable developments in the hybrid simulation technique from its initial inception to the present time. A brief history of hybrid simulation was presented first. After introducing the principles of hybrid simulation, the development of pseudo-dynamic testing, its challenges, and improvements, in getting where it is now, was explained. The issue of a common framework for hybrid simulation was highlighted while introducing and comparing the current frameworks for hybrid simulation.

Due to a large number of existing time-stepping algorithms, representative schemes for explicit, implicit, and operator-separator methods of implementation, and their characteristics, were discussed. The stability and accuracy of these algorithms were also examined since they play a major role in the accuracy of response simulation during hybrid simulation tests. Particular attention was given to explicit methods with algorithmic damping, which are attractive for real-time hybrid simulation tests.

After explaining the sources of experimental errors, both offline and adaptive approaches for delay compensation were discussed. The concept of critical time-delay in hybrid testing was introduced and its relationship to the physical substructure during a hybrid simulation was elaborated using a simulated study. The present tools for error tracking were also explored, and their pros and cons were highlighted. Especial emphasis was given to the tracking indicator (TI) approach, due to its simplicity and relevance for online application.

In this chapter, a detailed review of delay compensation techniques is also included. After discussing non-adaptive and adaptive techniques for delay compensation, two useful adaptive methods were examined in detail. Following a short discussion on adaptive inverse compensation, the development and implementation issues of adaptive time series compensator were explored and commented on.

Before addressing advanced control techniques of an actuator and shaking table, basic principles and tuning of a PID controller were presented. Some of the most challenging concepts in control engineering such as acceleration tracking of shaking tables and equivalent force control of actuators were also expounded. The former is indispensable in smart hybrid simulation tests involving shaking tables. Force-based control in hybrid simulation, its challenges and importance in hybrid tests, that physically model the lower part of a structure, was discussed by reviewing the literature.

The effort in bridging the clock speed between a numerical integration and the actuator motion, including data communication, through a continuous movement of actuators was also investigated in this chapter. Predictor-corrector algorithms using displacements only and algorithms using last predicted displacement were examined and compared. Besides, the accuracy boost gained by using velocities and accelerations in the predictor-corrector algorithms was briefly discussed.

At the end of this chapter, the challenges and solutions to hybrid testing involving an actuator and shaking table were explored using past experimental works. The prospect of physically modeling soil-structure interaction in hybrid simulation tests using the latter framework was finally pointed out.



## 3 Simulated Hybrid Testing of Structures-Applications

### 3.1 Introduction

In the last two decades, hybrid simulation has significantly improved, and test setups have become increasingly complex. Nevertheless, hybrid simulation continues to offer a versatile, dependable, and economically feasible solution for simulating the seismic response of structures. During a hybrid test, interface commands are computed by a numerical substructure and applied to an experimental substructure through actuators and/or a shaking table. At the end of each time-step, the numerical substructure receives the feedback force measured from the experimental substructure. Due to the inherent nature of the servo-hydraulic actuators, the feedback signal is not an exact match of the command. Time-delay of actuators and measurement noise are primarily responsible for this mismatch. In general, experimental errors can be classified as systematic and random errors. Systematic errors can accumulate thus making a hybrid test unstable. On the other hand, measurement noise is the prime source of random errors. A typical hybrid simulation platform comprises a control and data acquisition system, an experimental setup, and a numerical substructure model in a simulation program. This multi-component nature makes it prone to bugs or errors. Thus, it is prudent to test the hybrid simulation software and the data exchange between the components of the testing platform before conducting an actual hybrid test. This test is called simulated or virtual hybrid testing, also referred to as rehearsal testing.

In addition to the software error identification, virtual hybrid simulation can be used for tuning control algorithms and delay compensation methods which can potentially improve the accuracy of hybrid testing. Besides, parametric analysis can be easily conducted using simulated hybrid tests. These parametric tests can be used to investigate the robustness of some of the ingredients of hybrid simulation and explore domains of application for hybrid simulation, such as the cases presented herein. For example, stability analysis of a hybrid test can be conducted in a simulated environment since a large number of hybrid tests are required. Likewise, the effectiveness and robustness of time-stepping algorithms for hybrid testing can be studied. These studies can be more representative if true experimental conditions, that are prevalent during hybrid testing, are adequately captured and modeled. An exhaustive model might include controller dynamics, sensor noise, and actuator dynamics.

In hybrid testing, inaccurate response simulation may be tolerated if errors are within allowable margins, but unstable simulation must be avoided as it might result in damage to a test structure and testing facility. To fully understand the conditions of instability of substructuring tests, a reference structure is partitioned into numerical and experimental subdomains and analyzed parametrically. The prime importance of this study is to understand and solve the effects of instability during hybrid tests. Herein, virtual hybrid simulation tests are conducted by analytically

modeling the load transfer systems (servo-hydraulic actuator or shaking table) to obtain a frequency response function representation for the hybrid test. The Routh-Hurwitz method can be then used to analyze the stability conditions of any substructuring test using this frequency response function. The frequency response function was applied for the stability analysis considering linear SDOF systems. The stability analysis of nonlinear SDOF systems was also investigated by modeling the constituents of hybrid simulation in MATLAB/Simulink programming software.

The application of hybrid simulation to structural reliability and global sensitivity studies is another domain whereby simulated hybrid tests can be utilized as a proof-of-concept. The behavior of structures can only be estimated realistically taking into account the uncertainties in strength, support conditions, geometry, applied load, etc. (Stefanou, 2009). The collapse estimation of structures is the limit state of more interest to the engineering community because it is the ultimate scenario leading to loss of property and lives. Consequently, the collapse estimation of complex structures subjected to seismic action has been under thorough investigation in the last two decades. Much of the work done up to now is focused on structural reliability-based design, structural reliability analysis, reliability-based optimization, etc. Numerical tools, such as Finite Element Analysis (FEA) software, have been widely used because they can reasonably model the behavior of structural systems. Furthermore, the financial burden in performing experimental tests played a major role in the wide use of the Finite Element Methods (FEM). The FEM is essential during the analysis and design of structures; nevertheless, it may fail to capture the complex behavior of structures even though sophisticated tools are employed. On top of that, new structural elements or energy dissipation devices, that make part of a structure may not have their constitutive models readily available for modeling.

The prime concern in conducting the reliability analysis through numerical methods is the adequacy of the modeling capabilities of the FEA software. This may be addressed using hybrid simulation tests to substitute the FEM analyses. Dependable structural responses can therefore be obtained by testing the critical parts of a structure. Nevertheless, using experimental methods in reliability analysis presents a huge challenge since a limited number of experiments can only be performed. The surrogate modeling approach is a candidate solution to conduct reliability and sensitivity studies from a small number of experimental tests.

Recent advances in engineering enabled FEA software to be used for stochastic and parametric studies. As a result of this, the Finite Element Reliability Analysis (FERA) (Sudret & Der Kiureghian, 2002) and the Stochastic Finite Element Analysis (SFEA) (Haukaas & Der Kiureghian, 2005) were born to deal with the computation of failure probability and response probabilistic distribution. Other open-source frameworks, such as OpenSees, are customized to perform reliability analysis (McKenna, 2011).

The Monte Carlo Simulation (MCS) is commonly employed for generating samples during reliability analysis, and the FEA software runs repeatedly using the generated samples. Hence, a full description of the probabilistic distribution of structural responses can be obtained. To reduce the

computational cost of the MCS, simplified methods such as the First-Order Reliability Method (FORM) can be used to approximate the probability of failure based on a limit state function. However, the limit state function or performance function may not be available since it can be implicitly defined. Additionally, the FORM linearizes the limit function at an operational point, hence, its accuracy strongly depends on the degree of nonlinearity of the system. It is therefore not recommended for dynamic analysis of structures (Koduru & Haukaas, 2010). The Second-Order Reliability Method (SORM) is also seldom used for more accurate analysis although it is less efficient (Rackwitz, 2001). The efficiency of this approach may be improved by conducting the FORM followed by decomposing the limit-state function into additive univariate functions, at the most probable point, and applying the saddle-point approximation of failure probability (Zhang & Du, 2010).

Adopting surrogate models in approximating a response surface is another alternative in stochastic analysis. In SFEA, the PDF of a response function is represented intrinsically by expanding the response onto a basis of the probability space called the Polynomial Chaos (PC). This brought about the birth of the Polynomial Chaos Expansion (PCE) (Sudret, 2008). The great advantage of the PC-based finite element analysis is that the full randomness of the response is contained in a set of expansion coefficients, and the global sensitivity indices are obtained as by-products. Recently, this technique was applied for computing the global sensitivity indices in hybrid simulation tests (Abbiati et al., 2015).

In Chowdhury et al. (2009), the additive formulation for the Dimensional Reduction Method (DRM) was adopted to approximate a response surface of a containment structure. A *cut-off* function, which is the basis for this study, is evaluated at a finite number of points while interpolating at intermediate points. Most of the aforementioned SFEA techniques do not provide the entire probabilistic description of a response function. Zhang & Pandey (2014) developed a robust and efficient method for estimating variance-based global sensitivity indices using the *Multiplicative Dimensional Reduction Method (M-DRM)*. This method is a multiplicative form of the conventional DRM method. The  $k$ th moment of a response function is evaluated by optimizing the one-dimensional numerical integration of the  $k$ th moment of all the *cut-off* functions through the Gauss quadrature formulas. This limits the number of model evaluations carried out in computing the response moments and sensitivity indices. The M-DRM approach was also extended to estimate the full probabilistic distribution of a response function by minimization of an entropy function (Balomenos & Pandey, 2016). The Maximum Entropy (MaxEnt) principle maximizes the entropy subjected to constraints, specified as fractional moments, thereby estimating the most unbiased distribution. The probability distribution is then estimated from a few fractional moments of the response.

In this chapter, after introducing the principles of virtual hybrid testing, its applications are explored. Its capability spans from rehearsing hybrid tests (Schellenberg et al., 2019) to conducting robustness tests of existing time-stepping algorithms for hybrid simulation. You & Schellenberg (2017) have

also shown the potential of rehearsal testing for hybrid simulation using the OpenFresco framework. In this work, first, Virtual Hybrid Simulation (VHS) was applied to parametrically study the stability of hybrid simulation tests considering linear and nonlinear SDOF systems. Then, the robustness of time-stepping algorithms in the presence of experimental errors is investigated. The latter explores three common integration algorithms for hybrid simulation. Lastly, the scheme was utilized as a proof-of-concept for the reliability and global sensitivity studies in hybrid tests using the M-DRM principle. The proposed global sensitivity study was eventually validated through experimental tests.

## 3.2 Virtual Hybrid Simulation

Virtual hybrid simulation is the simulated form of true hybrid testing whereby the experimental substructure is also modeled in a numerical program. The experimental conditions during a hybrid test can also be emulated while conducting a virtual hybrid test. The hybrid simulation of a simple linear structure can be performed analytically by solving the equation of motion in any numerical software, e.g., MATLAB/Simulink. This simulated hybrid test can be conducted by deriving a closed-form equation (transfer function) describing the combined dynamics of the actuator, and the numerical and physical substructures. For a parametric study, the variables of this transfer function can be altered by changing the properties of the test structure, dynamics of the actuator, or both. In this chapter, the above approach is adopted to study the stability margins of the hybrid test of a SDOF structure.

On the other hand, the finite element software, such as the OpenSees-OpenFresco framework, can be used to perform the virtual hybrid testing. Unlike the transfer function method, the FEM approach allows complex structural systems to be represented (Schellenberg et al., 2019). Nowadays, conducting simulated hybrid tests before an actual experiment has become a common practice among researchers, thus offering insight into the anticipated outcomes from hybrid tests. It also allows researchers to identify and resolve software bugs. Furthermore, one can inspect errors in the numerical model, and the adequacy of control/compensation algorithms can be examined.

### 3.2.1 VHS through OpenSees-OpenFresco framework

The Open-source Framework for Experimental Setup and Control (OpenFresco) is an environment-independent software framework that serves as an interface between a finite element software and a control software. The *ExperimentalControl* class is one of the four abstractions of the OpenFresco software that is responsible for the communication between the finite element software and the control (including data acquisition) system (Schellenberg et al., 2009). A fully simulated hybrid test can be conducted using the *SimUniaxialMaterial* and *SimDomain* experimental control objects. The *SimUniaxialMaterial* models the experimental substructure by simulating the force that a load cell would measure in a laboratory. On the other hand, the *SimDomain* control

object makes all the OpenSees element, material, and section libraries available to OpenFresco (Schellenberg et al., 2007). The *SimFEAdapter* control object of OpenFresco is another tool for conducting a simulated hybrid test which is designed to couple two finite element programs. Many finite element software packages are highly specialized for modeling and analysis of particular engineering applications and may lack specific features needed to model the key attributes of a problem of interest. Thus, software packages can be combined taking advantage of their capabilities, eventually improving the accuracy of response simulation (Schellenberg et al., 2019). The latter approach is discussed in chapter five of the thesis in more detail.

The OpenFresco software framework also offers the *ExpSignalFilter* (ESF) objects that are used to modify responses that are going back and forth of a control system. The ESF has two class objects, as shown in Figure 3-1. The *ESSErrorSimulation* filter object is capable of modeling systematic (undershoot and overshoot) and random (Gaussian white noise) experimental errors. The filter object is declared using the *ctrlFilter* and *daqFilter* vectors while defining an experimental control object. Five parameters, namely displacement, velocity, acceleration, force, and time can be modified using the *ExpSignalFilter* object. The *ctrlFilter* is thus defined by a five-point vector using zeros and ones, mirroring the above five response parameters. Likewise, the *daqFilter* modifies measured responses before being returned to the numerical program.

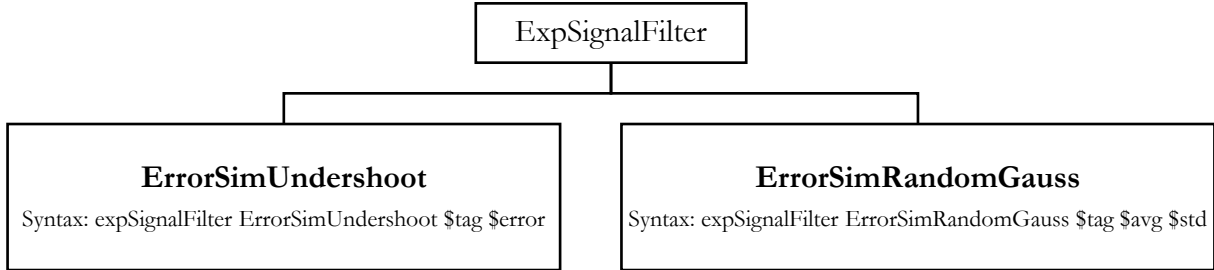


Figure 3-1: *ExpSignalFilter* object of the OpenFresco software

The response parameter at the output port of the *ErrorSimUndershoot* filter,  $d_i^{out}$ , is calculated by a piecewise function:

$$d_i^{out} = \begin{cases} d_i^{in} - error: & \text{if } d_i^{in} > d_{i-1}^{out} \\ d_i^{in} + error: & \text{if } d_i^{in} < d_{i-1}^{out} \\ d_i^{in} & : \text{if } d_i^{in} = d_{i-1}^{out} \end{cases} \quad (3.1)$$

Likewise, the output signal when applying the *ErrorSimRandomGauss* filter reads:

$$d_i^{out} = d_i^{in} + error(\text{avg}, \text{std}) \quad (3.2)$$

In the above equation, a randomly distributed Gaussian error is defined using the mean and standard deviation parameters (hereinafter as error parameters). The Box-Muller transformation generates the WGN using uniform deviates. The amplitude-dependent behavior of a servo-

hydraulic actuator, that arises from its inherent nonlinearity, combined with the nonlinearity of a test specimen can be therefore represented using the *ESFErrorSimRandomGauss* filter object of ESF (Tekeste et al., 2017b). The error parameters are typically estimated from identification tests conducted before starting a hybrid simulation test.

### 3.3 System identification of a uniaxial shaking table at LNEC

In structural testing, commands to substructures (as in the case of hybrid testing), or complete structural systems, can be effectively applied by a shaking table. The uniaxial shaking table (ST1D) at LNEC, shown in Figure 3-2, operating since the 1970s, is driven by a servo-hydraulic actuator capable of applying forces up to 200 kN (with an equivalent differential pressure of 165 bars). The shaking table can be operated either along the horizontal or the vertical axis; and it was originally controlled in position by an analog servo-controller, designed by MB Electronics, using a proportional gain. To facilitate the development of a software framework for hybrid testing, the servo-controller was replaced, herein, by a digital controller that uses the National Instruments (NI) hardware.

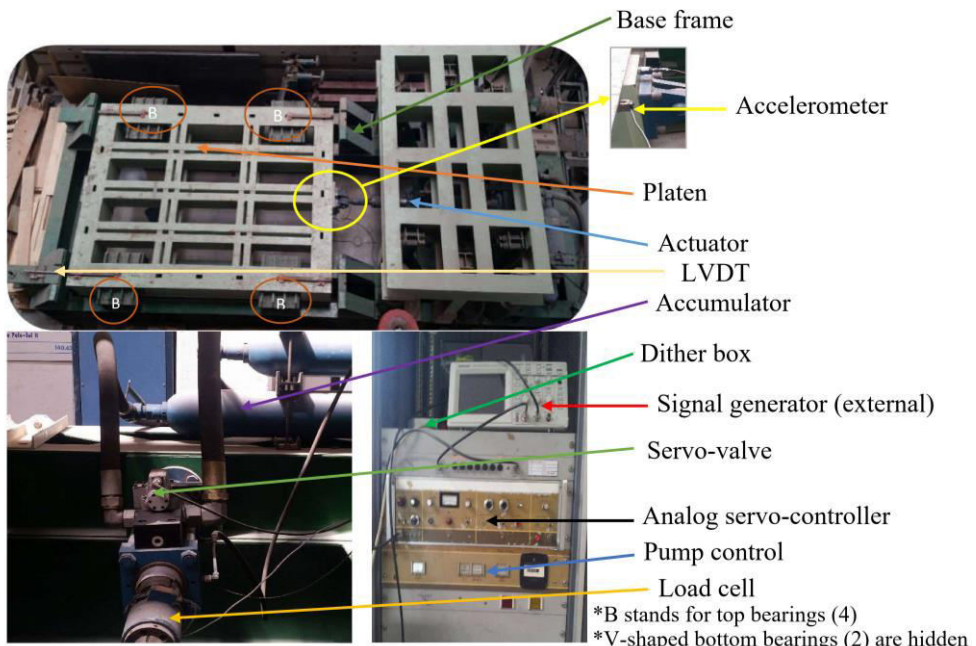


Figure 3-2: Uniaxial shaking table at LNEC

The ST1D is equipped with a rugged and moderate duty servo-hydraulic actuator, HAC450-8, manufactured by MB Electronics. The servo-hydraulic actuator has a 2-stage electro-hydraulic servo-valve from MOOG, model E072-014, whose rated oil flow is 152 l/min at a pressure drop of 1000 psi (68.9 bar). The ST1D is driven by two parallel pumps capable of delivering a total oil flow up to 242 l/min. The pumps are positioned on both sides of the axis of an electrical engine running at 380 V, 50 Hz, and 205 A, with a capacity of 150 HP and 1480 rpm. The oil flow received

from the pumps is also boosted by two diaphragm-type accumulators filled with nitrogen gas reaching 143 bar pressure. The platen has a useful horizontal area of  $2 \times 3 \text{ m}^2$  whereas the useful area in the vertical configuration is  $2.45 \times 1.45 \text{ m}^2$ . The platen is guided by roller bearings, located at the top and bottom sides, using THOMPSON chains. The two V-shaped rollers that are located on one of the longitudinal sides of the shaking table prevent its side movements.

### 3.3.1 Modeling shaking table dynamics

The analytical model for the ST1D system can be obtained by combining the analytical models of the controller, servo-valve (its dynamics and flow characteristics), hydraulic actuator (continuity and force balance equations), platen mass, and total damping of the system (Phillips, 2012; Carrion & Spencer, 2007). A payload (test specimen), which is rigidly attached to the platen, interacts with the dynamics of the ST1D resulting in the so-called Control-Structure Interaction (CSI). Firstly, the transfer function for the ST1D was developed without considering any payload (referred hereafter as the transfer function of a bare shaking table). In the presence of a payload, its dynamics can therefore be reproduced by simply incorporating the properties of the payload. For a payload that is rigidly attached to the shaking table, the CSI effect is caused by the interaction of the base shear force of the payload and the shaking table. This feedback force is incorporated into the transfer function of the bare shaking table when deriving the transfer function of the system comprising of a payload that is rigidly attached to the ST1D.

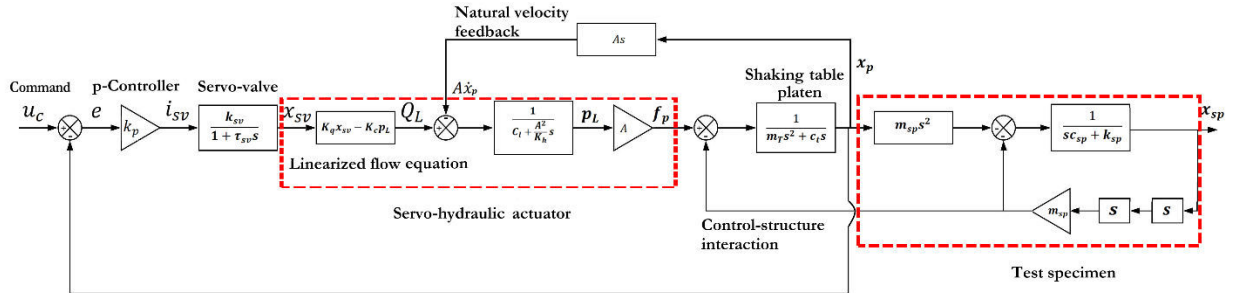


Figure 3-3: Schematic diagram of a shaking table system

Considering an elastic SDOF payload structure, the schematic diagram of the ST1D was developed first, as shown in Figure 3-3. The first-order transfer function was adopted in modeling the servovalve since it is adequate for the operational frequency of the ST1D (MOOG, 2002). The general nonlinear flow equation of the actuator is typically linearized near its operational point (origin) (Merrit, 1967), and the actuator can be represented by the first-order transfer function. The mass and damping characteristics of the platen were identified (hereinafter referred to as mechanical identification) using an experimental campaign that is explained subsequently. Under the bare shaking table condition, a fourth-order transfer function,  $G_{x_p u_c}$ , from the measured displacement to the command signal of the platen, can be derived from Figure 3-3. The transfer function has 4 poles and no zeros. On the other hand, in the presence of a SDOF payload, the transfer function is

characterized by 6 poles and 2 zeros. The transfer function  $G_{x_p u_c}$  can be shown to be:

$$G_{x_p u_c} = \frac{\frac{Ak_p k_{sv} k_q}{k_{pl}}}{Y_4 s^4 + Y_3 s^3 + Y_2 s^2 + Y_1 s + \frac{Ak_p k_{sv} k_q}{k_{pl}}} \quad (3.3)$$

where:  $Y_1 = c_t + \frac{A^2}{k_{pl}}$        $k_{pl} = K_c + C_l$   
 $Y_2 = \tau_{sv}(c_t + \frac{A^2}{k_{pl}}) + m_T^* + c_t \frac{A^2}{k_{pl} K_h}$        $K_h = \frac{4\beta_e A^2}{V_t} \text{ and}$   
 $Y_3 = m_T^* \tau_{sv} + \frac{A^2}{k_{pl} K_h} (m_T^* + \tau_{sv} c_t)$        $m_T^* = m_p + m_{sp}(1 + H_{sp})$   
 $Y_4 = \frac{A^2}{k_{pl} K_h} m_T^* \tau_{sv}$

where  $k_p$  is the proportional gain of the controller;  $k_{sv}$  and  $\tau_{sv}$  are the gain and time-delay parameters of the servo-valve transfer function, respectively;  $k_q$  and  $K_c$  are the valve flow gain and the valve pressure-flow gain, respectively;  $A$  and  $V_t$  are the area and total volume of the fluid under compression in the actuator, respectively;  $C_l$  is the total leakage coefficient of the piston;  $\beta_e$  is the effective bulk modulus of the system (including oil, entrapped air, etc.);  $k_h$  is the oil-column frequency of the actuator;  $m_p$  and  $m_{sp}$  are the mass of the platen and the SDOF structure, respectively; and  $c_t$  is the combined damping force of the actuator and the platen. The transfer function relating the displacements of the platen and the SDOF structure  $H_{sp}$  reads:

$$H_{sp}(s) = \frac{x_{sp}(s)}{x_p(s)} = \frac{-m_{sp}s^2}{m_{sp}s^2 + sc_{sp} + k_{sp}} \quad (3.4)$$

where  $k_{sp}$  and  $c_{sp}$  are the stiffness and damping of the SDOF structure, respectively. Considering the shaking table without a payload,  $m_T^* = m_p$ , otherwise  $m_T^* = m_p + m_{sp}(1 + H_{sp})$ .

### 3.3.2 Experimental identification of shaking table forces

The mechanical subsystem of ST1D includes the platen, lateral bearings, connecting rod, and actuator. The first objective of this study is to develop a simplified analytical model for the mechanical subsystem through an experimental test. Periodic signals were used during these experiments and the periodicity of the measured signals was the key in determining the inertial, damping, and elastic forces associated with the mechanical subsystem (Ozcelik et al., 2008). Hence, several sinusoidal (S) and triangular (T) input displacements, shown in Table 3-1, of varying frequency and amplitude, were used to determine these forces. We know that the force measured by a load cell is the resultant of inertial, damping, and elastic forces. Hence, we can write:

$$F_I(t) + F_D(t) + F_E(t) = F_A(t) \quad (3.5)$$

where  $F_I(t)$ ,  $F_D(t)$ ,  $F_E(t)$  and  $F_A(t)$  are the inertial, damping, elastic, and actuator forces, respectively.

During the test, the force applied by the actuator was measured by a LEBOW type load cell. Owing to the periodicity of the input signals, the measured force has point couples where any two of the three forces are equal and opposite, thus canceling each other. Consequently, the average of the measured forces at these coupling points gives the contribution of the remaining force component.

Table 3-1: Input signals for characterization of LNEC's uniaxial shaking table

Test	Frequency [Hz]	Displ <sub>max</sub> [cm]	Vel <sub>max</sub> [cm/s]	Acc <sub>max</sub> [% g]
S9	0.20	4.00	5.03	0.644
S15	0.50	4.00	12.57	4.024
S17	0.40	4.00	10.13	2.576
T3	0.20	1.00	0.80	NA
T5	0.40	1.00	1.60	NA
T6	0.50	1.00	2.00	NA
T8	0.10	4.00	1.60	NA
T20	0.10	4.00	4.00	NA
T22	0.10	8.00	3.20	NA
T23	0.05	8.00	6.40	NA

The identification work was conducted under the bare shaking table condition. As mentioned before, the shaking table transfer function, under any payload, can be then readily available. This is consistent with the objective of the thesis since the shaking table may be used in testing different structures during the validation phase of a hybrid simulation framework. Evidently, each test will have a unique transfer function due to the inherent control-structure interaction (CSI) effects. Consequently, identification of the shaking table is needed for each test when its transfer function is required for the implementation of the hybrid tests. Nonetheless, if the transfer function of the bare shaking table is determined, the CSI due to any payload can be easily reproduced.

The mechanical parameters of the ST1D can be obtained by fitting the estimated forces to mathematical models that are capable of representing the observed behavior. The following simplified models are considered in modeling the inertial, elastic, and damping forces, respectively:

$$\begin{aligned} F_I &= M\ddot{u}_x ; \text{ where } M = M_{Pl} + M_{act} \\ F_E &= Ku_x \\ F_D &= [F_\mu + C|\dot{u}_x|^\alpha]sign(\dot{u}_x) ; \text{ where } 0 \leq \alpha \leq 1 \end{aligned} \quad (3.6)$$

where  $M_{act}$  is the total mass of the moving parts of the actuator;  $u_x$ ,  $\dot{u}_x$  and  $\ddot{u}_x$  are the displacement, velocity and acceleration of the platen, respectively;  $K$  is the stiffness of the ST1D;  $F_\mu$  is the Coulomb friction force;  $C$  is the viscous damping constant; and  $\alpha$  is a dimensionless coefficient.

### 3.3.2.1 Elastic force

Since ST1D is supported on chain bearings, it may be practical to assume zero elastic force, but it may actually be estimated by applying a triangular displacement input to the shaking table (input signal which is characterized by constant velocity and zero acceleration steps). In this test, the measured acceleration has spikes at the instants when the direction of motion of the shaking table

is inverted. However, for the estimation of the elastic force, the platen must be in a steady-state motion (or constant velocity).

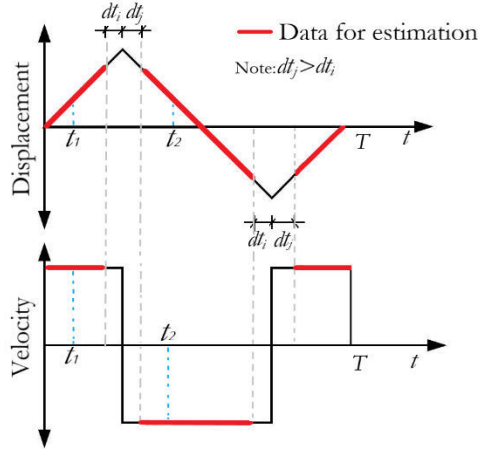


Figure 3-4: Estimation of elastic force using a triangular input displacement

To do so, samples for estimation were selected after an offset from the inversion of motion, indicated by the red line shown in Figure 3-4. The offset adopted in the interval after the inversion of the input signal is larger than before the inversion. This is mainly because the dynamic disturbance persists longer following the inversion of motion as opposed to approaching the inversion of motion. Consider two instances,  $t_1$  and  $t_2$ , in the triangular signal, satisfying the offset criteria, having equal and opposite velocities and equal displacements, the elastic force  $F_E$  can be determined as:

$$F_E(u_x(t_1)) = 1/2[F_A(t_1) + F_A(t_2)] = Ku_x(t_1) \quad (3.7)$$

$$u_x(t_1) = \frac{1}{2}[u_x(t_1) + u_x(t_2)] ; \text{ where } 0 < t_1 < T$$

Due to the inherent nonlinear behavior of actuators, the identification process was carried out by changing the amplitude and frequency of the triangular input signal. The characteristics of all the triangular input signals can be found in Table 3-1. As expected, the elastic force estimates from tests T5 and T6, shown in Figure 3-5, are approximately zero; nevertheless, some spurious estimates were obtained as a result of the low signal-to-noise ratio of the measured force.

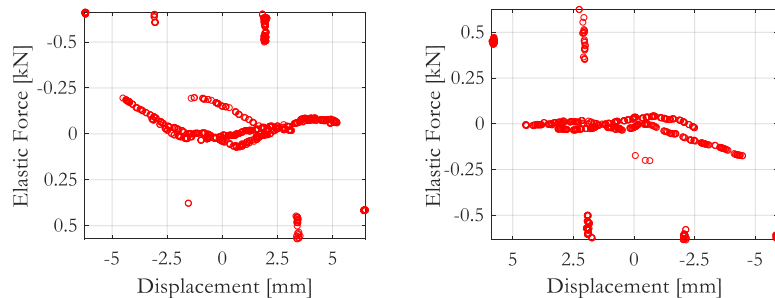


Figure 3-5: Elastic force estimates from T6 (right) and T5 (left) experiments

### 3.3.2.2 Inertial force

The effective horizontal mass of the ST1D has the contribution of the platen, connecting rod, and actuator. In other words, it is the total moving mass of the shaking table. It can be estimated from sinusoidal tests by identifying point couples that have equal and opposite velocities (considering zero elastic force).

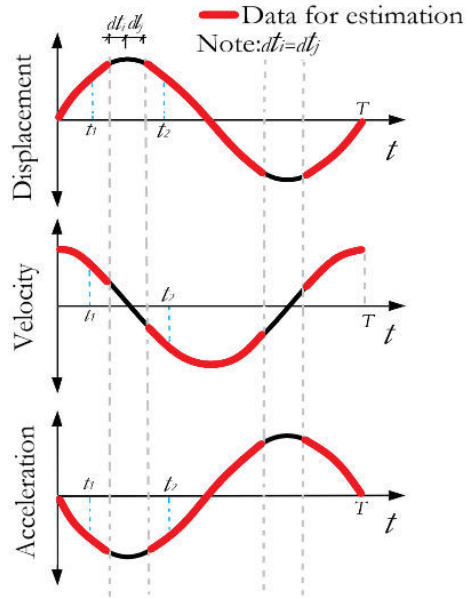


Figure 3-6: Mass estimation using sinusoidal input displacement

Take two instances,  $t_1$  and  $t_2$ , with opposite velocities, the inertial force is estimated from:

$$\begin{aligned}
 F_I(\ddot{u}_x(t_1)) &= \frac{1}{2}[F_A(t_1) + F_A(t_2)] = M\ddot{u}_x(t_1) \\
 \ddot{u}_x(t_1) &= \frac{1}{2}[\dot{u}_x(t_1) + \dot{u}_x(t_{2,opt})]; \text{ where } 0 < t_1 < T \\
 t_{2,opt} &= t_2 + \underbrace{\operatorname{argmin}_{\delta t}}_{\delta t} \{[\dot{u}_x(t_1) + \dot{u}_x(t_2 + \delta t)]\}; \text{ where } \delta t \in [-Tol, Tol] \\
 t_2 &= \begin{cases} T/2 - t_1 & \text{for } t_1 \leq T/2 \\ T - t_1 & \text{for } T/2 < t_1 < T \end{cases}
 \end{aligned} \tag{3.8}$$

The samples in the proximity of the inversion of motion (i.e., samples with velocities less than 5 mm/sec) were discarded from the estimation data. Here, a search algorithm was implemented in MATLAB for a reliable selection of samples. The samples with accelerations above the maximum acceleration of the input signal were eliminated first. In the next step, point couples were identified in such a way that, for the sample at time  $t$ , the velocity sum of the sample at time  $t$  and the samples in the interval  $[T/2-t-Tol, T/2-t+Tol]$  is minimized. The term tolerance ( $Tol$ ) in equation (3.8) refers to the duration before and after the time  $t_2$  in which the sample at time  $t_1$  searches to minimize the velocity sum. Three sinusoidal input signals of varying frequencies, shown in Table 3-1, were

adopted in estimating the inertial mass.

The mass of the shaking table that is evaluated at small accelerations (typically  $<0.2\% g$ ) is not reliable due to the small signal-to-noise ratio (Lanese, 2012). Similarly, estimates at larger accelerations and velocities might be inaccurate since the sinus signal gets distorted thus making the periodicity principle not applicable anymore. Hence, input signals were chosen, adequately, smaller than the ST1D's limiting velocity (20 cm/s).

The effective horizontal masses of the ST1D that are estimated from the sinusoidal tests are nearly identical, as shown in Figure 3-7. It is evident that mass estimation is prone to significant uncertainties at lower frequencies, but the overall estimate converges towards the average working accelerations of the ST1D. Therefore, the fidelity of the mass estimates may be approximated by a weighting function  $w_i = (1/f_i)^{-1}$ , where  $f$  is the frequency of the sinusoidal input. This weighting function is applicable as long as the amplitudes of the input signals are the same. Applying the weighing function to the mass estimates, the effective horizontal mass of the ST1D was found to be approximately 2.063 t.

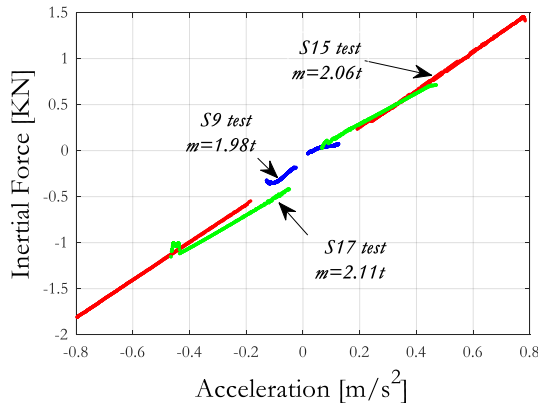


Figure 3-7: Effective horizontal mass estimates of LNEC's uniaxial shaking table

### 3.3.2.3 Dissipative force

The ST1D's dissipative force originates from the friction between the piston and actuator chamber as well as the friction of the bearings, where the platen is supported on. Unlike the inertial force, modeling the dissipative force is complex. Herein, the dissipative force is modeled as the sum of Coulomb friction and viscous damping forces. The forces that were measured during the sinusoidal experiments can be utilized also for estimating the dissipative force. It can be computed directly by deducting the inertial and elastic forces from the measured force (since both forces are already estimated). Likewise, the force measured during the triangular input signals can also be used to estimate the dissipative force. In the latter, experiments with large amplitudes did not yield reliable estimates, because the abrupt inversion of motion of the shaking table introduced undesired dynamics which reduced the fidelity of the estimates. In the post-processing phase, shown in Figure 3-8, similar procedures, as in the elastic force, were adopted in calculating the dissipative force.

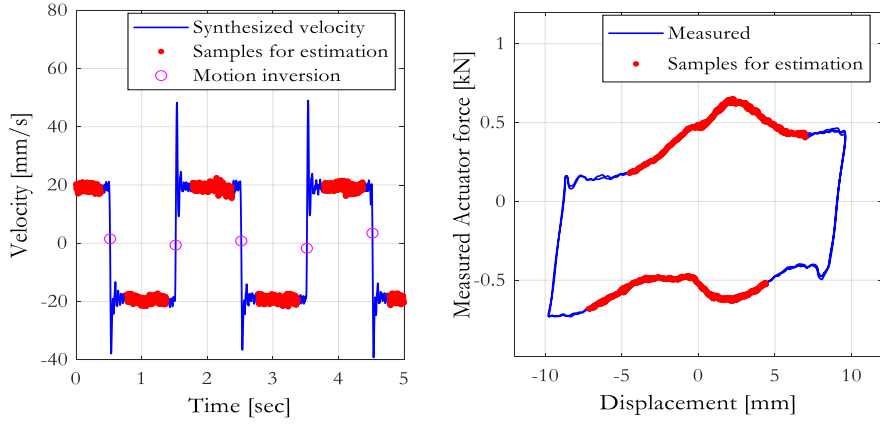


Figure 3-8: Choice of samples for estimating dissipative force: T6 test

Point couples (red points in Figure 3-8) having equal and opposite displacements were used for estimating the dissipative force. In this work, the velocity signal was synthesized from the displacement and acceleration measurements. For each experiment, the mean value of the dissipative force was estimated, considering positive and negative velocities, from seven triangular input signals.

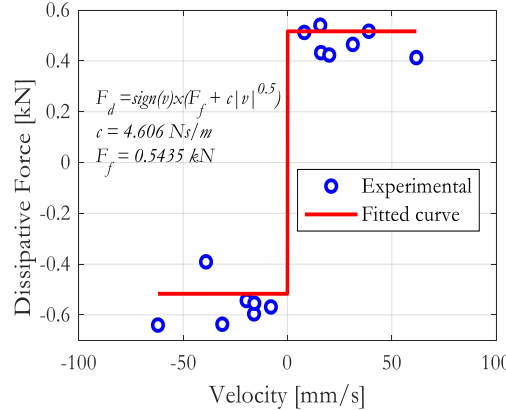


Figure 3-9: Curve fitting of LNEC's uniaxial shaking table dissipative force

The estimates were fitted to the proposed analytical equation after setting the lower boundaries of the model parameters to zero. The dissipative force was primarily governed by the Coulomb frictional force ( $F_f$ ) because friction is dominant at small velocities. It is noteworthy to mention that the standard deviation of the estimates is significant, as shown in Figure 3-9.

### 3.3.3 Identification of shaking table parameters

Now that the mechanical subsystem of ST1D is fully identified, the parameters of the transfer function of the uniaxial shaking table, derived from Figure 3-3, can be estimated using an experimental frequency response function (FRF). To compute this FRF, a Band Limited White

Noise (BLWN) displacement, in the frequency interval 0-50 Hz, was applied to the ST1D. Hence, the analytical transfer function and the experimentally derived FRF are used for the parametric identification of the shaking table. In the computation of the experimental FRF, the displacement signal was synthesized from displacement and acceleration measurements since accelerometers and LVDTs are not effective over the entire frequency range of the measured responses. From this standpoint, the synthesized displacement was evaluated at a cross-over frequency of 1 Hz.

Eventually, the FRF of the shaking table was fitted, parametrically, to equation (3.3). The parametric fitting was carried out in MATLAB using the constrained nonlinear least-square optimization algorithm. The result of this parametric identification is presented in Table 3-2. The fitted transfer function has four poles and no zeros. It is characterized by a small gain error (compared to ideal control) at small frequencies due to the difficulties in using the analog controller of the ST1D.

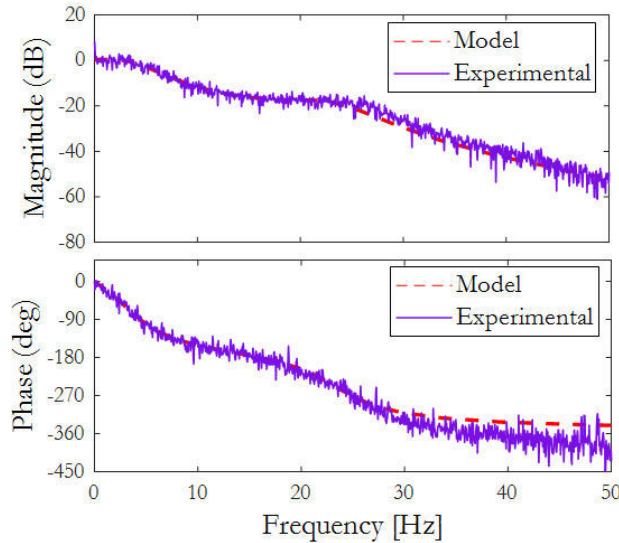


Figure 3-10: Curve fitting of the LNEC's uniaxial shaking table transfer function

The estimated transfer function of the shaking table is in good agreement, both in magnitude and phase, with the experimental FRF, as shown in Figure 3-10. The time-delay of the shaking table was found to vary between 50 ms, at frequencies below 5 Hz, and 20 ms, at frequencies greater than 20 Hz. The estimated time-delay of the shaking table is considerably large; it can thus introduce undesirable time-delay during hybrid simulation tests. Consequently, the development of delay compensation algorithms for ST1D is addressed in chapter four. Finally, the estimated parameters of the ST1D were validated using the S17 experiment, and the output displacement of the estimated model of the ST1D matches accurately the measured displacement, as shown in Figure 3-11.

To validate the proposed approach, i.e., reproducing the CSI effect resulting from a payload, the transfer function of the bare ST1D was modified by incorporating the dynamics of a payload. For simplicity, rigid and flexible SDOF payloads, with identical masses, were considered here. The natural frequency of the flexible SDOF structure was chosen to be 5 Hz, and it has a total mass of 2 t. Besides, the viscous damping of the structure was taken as 2%.

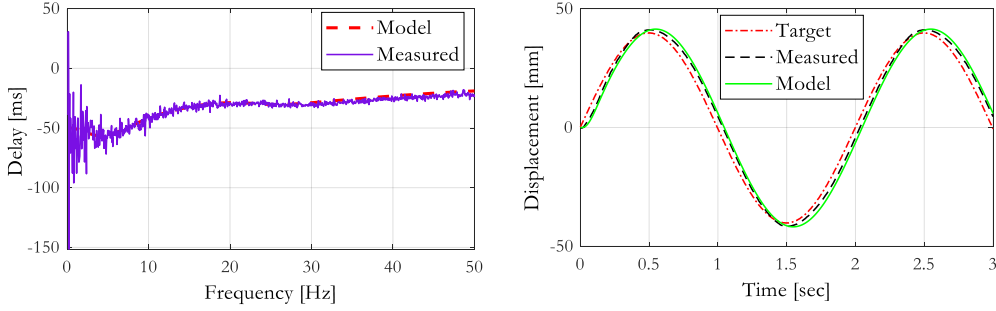


Figure 3-11: Curve fitting of time-delay (left) and validation of the estimated model of LNEC's uniaxial shaking table (right)

Table 3-2: Estimated parameters of LNEC's uniaxial shaking table

Component	Description	Parameter	Estimated values	Units
Servo-controller	P-gain	$k_p$	1.2993	V/cm
Servo-valve	Valve time constant	$\tau_{sv}$	0.0246	s
	Valve flow gain	$k_{sv}k_q$	1934.50	cm <sup>3</sup> /s/V
	Valve pressure gain & leakage factor	$k_{pl}$	1.67401e-7	m <sup>3</sup> /s/kPa
Actuator	Oil bulk modulus	$\beta_e$	193716.28	kPa
	Volume of oil in actuator's chamber	$V_t$	0.002659	m <sup>3</sup>
	Area of piston	$A$	0.012456	m <sup>2</sup>
Platen	Platen mass	$m_p$	1.9751	ton
	Total damping (actuator & platen)	$c_t$	5.7800	kNs/m

When the flexible SDOF structure is rigidly attached to the ST1D, the transfer system is characterized by a notch at its resonant frequency, shown in Figure 3-12, indicating the presence of CSI. In this scenario, the oil-column frequency of the shaking table transfer function remained unchanged. On the other hand, considering a rigid payload the oil-column frequency has a notable shift relative to the bare shaking table condition and it also has a relatively stiffer response.

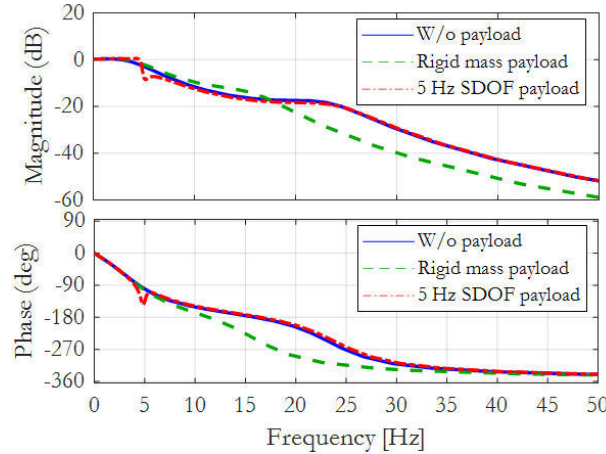


Figure 3-12: Control-structure interaction of LNEC's uniaxial shaking table

### 3.4 Choice of time-stepping algorithms for hybrid testing

The stability and robustness of time-stepping algorithms in the presence of experimental errors are of paramount importance during hybrid testing. It is therefore prudent to conduct a simulated hybrid test before an actual experimental to ensure that the selected integration method is appropriate. Besides, the adequacy of its parameters can be verified. Herein, three common time-stepping algorithms, namely the  $\alpha$ -OS, HHTH, and NMHS, are studied and compared with the Iterative Newmark Integration (INM) method. The HHTH and NMHS algorithms were derived from the original iterative schemes by fixing the number of sub-steps conducted at each time-step of a hybrid test.

The parametric study was conducted by changing the ground motion input, degree of nonlinearity of the test structure, magnitude and nature of experimental errors, parameters of the time-stepping algorithms ( $\alpha$  parameter in the case of  $\alpha$ -OS and the number of iterations in the cases of NMHS and HHTHS), and time-step of the response simulation.

#### 3.4.1 Application to a steel frame structure

The parametric study was conducted on a steel portal frame which has two columns that are pinned at the base. The properties of the portal frame were adopted from a hybrid test conducted by Schellenberg et al. (2008). Here, the simulated hybrid test of the steel frame was conducted by applying two earthquake records: El Centro N-S component (1940) and Kobe (1995). The input earthquakes were scaled to explore the elastic and inelastic properties of the steel frame.

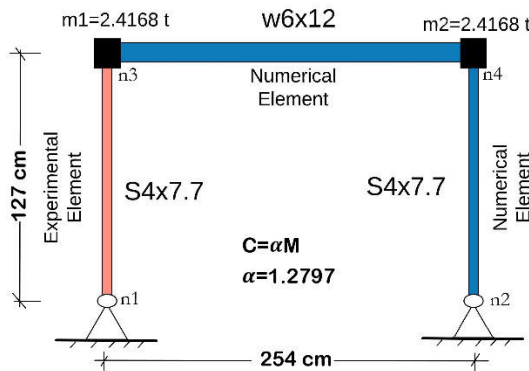


Figure 3-13: Steel portal frame case study

To test the robustness of the time-stepping algorithms, experimental errors were injected into the trial displacements going out to the experimental substructure. The effect of an undershooting error is mainly discussed here as it may lead to stability problems in hybrid testing.

The three integration schemes were compared using energy-based and force-based criteria. The first criterion uses the maximum Energy Error Indicator (EEI) evaluated by normalizing the energy

error in the equation of motion. It was derived by slightly modifying the Energy Balance Error (EBE) which was formulated by Filiault et al. (1994). Ahmadizadeh & Mosqueda (2009) also proposed the Hybrid Simulation Error Monitor (HSEM) for online monitoring of errors in hybrid testing. In HSEM, velocity is calculated from the first derivative of displacement response to maintain the kinematic relationship of system dynamics and thereby eliminating energy errors due to mismatching kinematics. However, this effect is significant only when considering the explicit Newmark method because trial displacements are not corrected. In the present parametric study, the prime focus are the operator-separator algorithms and the implicit algorithms with a limited number of iterations. In these algorithms, negligible errors were found in the kinematic relationship of the responses which strengthens the findings reported by the authors of HSEM. On the other hand, in EEI, velocity is computed by the finite element software; otherwise HSEM and EEI have the same formulation. At the  $k$ th time-step of analysis, the latter is calculated as:

$$EEI_k = \left\{ \frac{E_{I,k} - E_{D,k} - E_{H,k} - E_{T,k}}{E_{I,k} + E_{strain}} \right\} \times 100\% \quad (3.9)$$

where  $E_{D,k}$  is the viscous damping energy;  $E_{H,k}$  is the kinetic energy;  $E_{T,k}$  is the absorbed energy;  $E_{I,k}$  is the relative input (inertial) energy; and  $E_{strain}$  is the strain energy. The strain energy represents the elastic area of the force-displacement curve and it is evaluated using the initial stiffness,  $k_{int}$ , and yield displacement,  $u_y$ . In discrete form, the energy of a structure can be calculated using the trapezoidal rule of integration:

$$\begin{aligned} E_{I,k} &= E_{I,k-1} - \frac{1}{2} \{x_k - x_{k-1}\}^T [M] \{\ddot{x}_{g,k} + \ddot{x}_{g,k-1}\} \\ E_{H,k} &= \frac{1}{2} \{\dot{x}_k\}^T [M] \{\dot{x}_k\} \\ E_{T,k} &= E_{T,k-1} + \frac{1}{2} \{x_k - x_{k-1}\}^T \{r_k + r_{k-1}\} \\ E_{D,k} &= E_{D,k-1} + \frac{1}{2} \{x_k - x_{k-1}\}^T [C] \{\dot{x}_k + \dot{x}_{k-1}\} \\ E_{strain} &= \frac{k_{int} u_y^2}{2} \end{aligned} \quad (3.10)$$

where  $x_k$ ,  $\dot{x}_k$ ,  $\ddot{x}_{g,k}$  and  $r_k$  stand for the displacement, velocity, ground acceleration, and restoring force of the structure at the  $k$ th time-step of analysis, respectively; M is the mass matrix; and C is the damping matrix. The energy of the steel portal frame evaluated using the trapezoidal rule is presented in Figure 3-14 for illustration purposes.

Following the proposal from Ahmadizadeh & Mosqueda (2009), the stability threshold value for the EEI was taken as 15%. The second criterion is related to the residual force vector, which might also be a powerful indicator of the accuracy of a numerical solution. It monitors if the maximum absolute value of the residual force vector at each time-step (or sub-step) is within an acceptable range. This parameter is hereafter referred to as effective residual force ( $P_{eff}$ ). The L2 norm of the effective residual force is given by:

$$\left| P_{eff,i} \right|_2 = \max \left\{ \left| -M\ddot{u}_i - C\dot{u}_i - r(u_i) + M\ddot{u}_{g,i} \right|_2 \right\} \quad (3.11)$$

In the study conducted by Hashemi et al. (2017), a threshold value for  $\left| P_{eff,i} \right|_2$  equal to  $10^0$  was associated with the level of noise in measurements that requires filtering or changes in hardware. Nonetheless, it is not easy to fully comprehend this criterion since  $P_{eff}$  is a vector of residual forces. In Hashemi et al. (2017), the  $P_{eff}$  criterion is described as a good indicator of potential instability during a hybrid simulation. However, this criterion can be stringent for assessing the accuracy of time-stepping algorithms. From this standpoint, this criterion is not fully explored here.

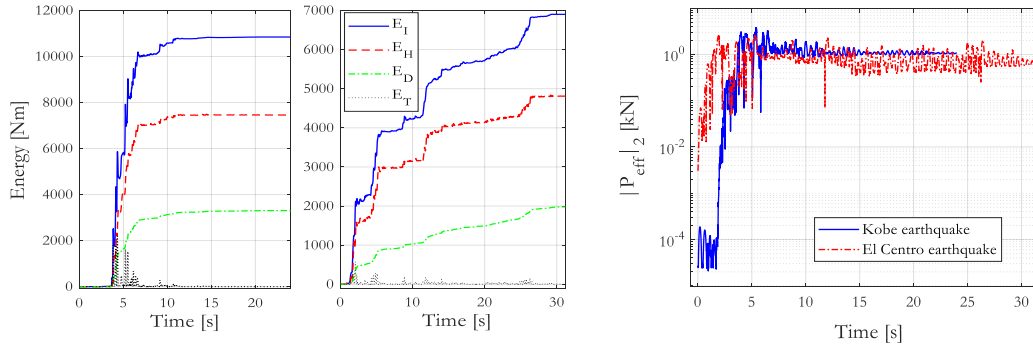


Figure 3-14 Energy plot of the steel portal frame, using the  $\alpha$ -OS integration, without experimental errors, subjected to Kobe earthquake scaled to 1.642 g PGA (left) and El Centro earthquake scaled to 0.478 g PGA (middle); and norm L2 of  $P_{eff}$  (right)

### 3.4.2 Results and discussions

The results of the parametric study are summarized as:

#### a) Effect of an experimental error on the accuracy of response simulation

To assess the effect of experimental errors during hybrid testing, the simulated hybrid test of the portal frame was executed using the  $\alpha$ -OS integration, taking  $\alpha=0.9$  and  $\Delta t=0.005$  s. The experimental error (undershoot), which is calculated using equation (3.1), was progressively increased until the initiation of instability.

The deviation in the lateral displacement of the portal frame increases exponentially with slight increments of the undershoot error, as shown in Figure 3-15. The erroneous simulation gives rise to negative EEI (adds energy to the system) in both earthquake records. Herein, undershoot error of the order of 1/200 of the maximum drift resulted in unstable simulation. During the inelastic response simulation, an increase in the experimental errors resulted in large deviations of the residual displacement. The main reason for this deviation is the non-iterative nature of  $\alpha$ -OS combined with the small numerical damping ( $\alpha=0.9$ ) of the algorithm. In the post-peak response, the frame has mild strength degradation; hence, experimental errors are less important to the

restoring force of the experimental element. This phenomenon is characterized by a large error of the lateral displacement and a small deviation of the EEI. This can be observed when the portal frame is subjected to the Kobe earthquake which has an equivalent ductility around six.

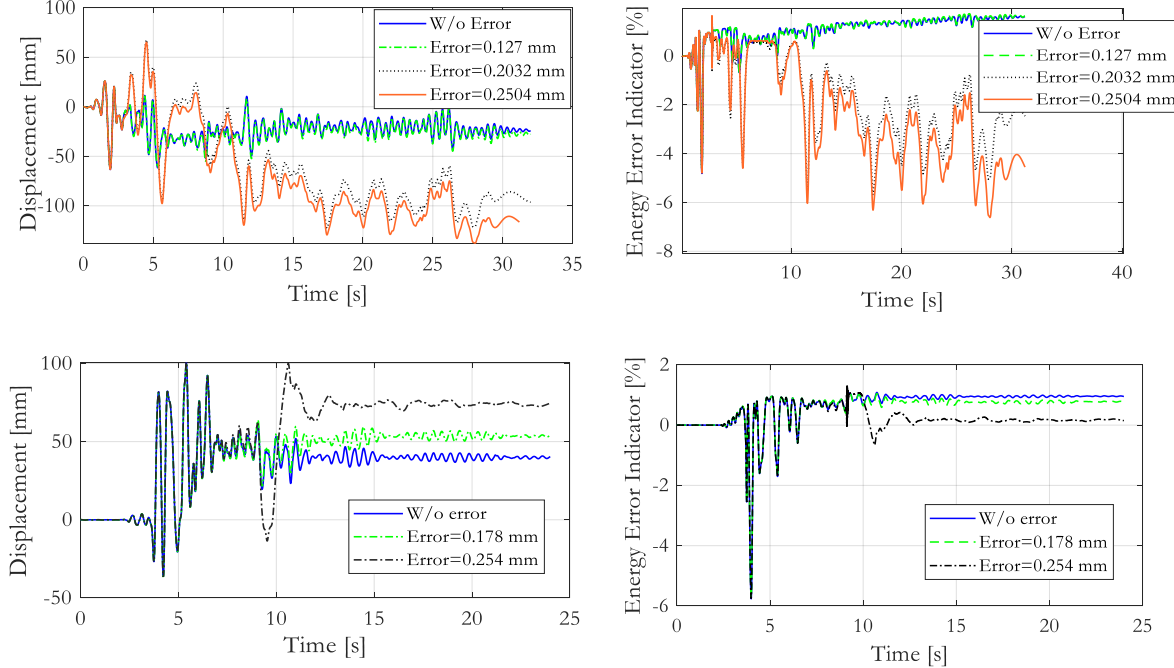


Figure 3-15: Lateral displacement and EEI of the steel portal frame subjected to the El Centro earthquake scaled to 0.478 g PGA (top row) and Kobe earthquake scaled to 1.642 g PGA (bottom row)

### b) Robustness of time-stepping algorithms to experimental errors

This section is dedicated to shed light on the robustness of time-stepping algorithms for hybrid simulation. Control errors and noise in data acquisition systems are inevitable during a hybrid test. The need for robust time-stepping algorithms is therefore crucial to reduce these effects from propagating into the numerical program. Hence, an ideal integration method must have numerical damping to suppress the contribution of higher modes that are liable to be excited during an experimental test.

The steel frame was subjected to a 0.2032 mm undershooting error. In addition to being attractive for fast and real-time hybrid simulation tests, the  $\alpha$ -OS scheme has shown satisfactory performance compared to other implicit methods, as shown in Figure 3-16. The EEI of  $\alpha$ -OS is intermediate between the NMHS and HHTHS method. The positive EEI of  $\alpha$ -OS integration may be advantageous in ensuring the balance between accuracy (zero EEI) and robustness in case of undershooting error (a positive energy reserve). Furthermore, the two iterative methods have significant positive EEIs which might be the result of the limited number of iterations.

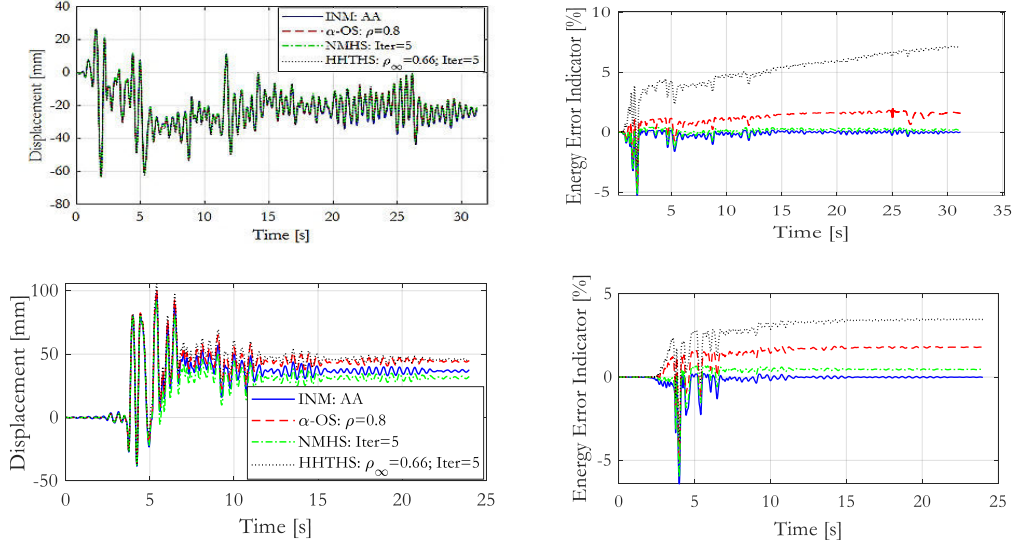


Figure 3-16: Lateral displacement and EEI of the steel portal frame subjected to the El Centro (top row) and Kobe (bottom row) earthquakes

### c) Selecting parameters of time-stepping algorithms

For brevity, only the effect of changing the parameters of  $\alpha$ -OS and NMHS are discussed in this work. Here, undershooting errors of 0.2286 mm and 0.1778 mm were applied to the El Centro earthquake and Kobe earthquake inputs, respectively. The  $\alpha$  parameter, bounded in  $[0.67, 1]$ , defines the numerical damping of the  $\alpha$ -OS method. The larger the numerical damping of a hybrid test the less sensitive it becomes to experimental errors. Nevertheless, the amount of numerical damping must be controlled as it might underestimate the response of lower modes of the structure. For a moderate level of undershooting error, say 0.1-0.5% of the maximum response,  $\alpha=0.8$  may be used.

In the case of NMHS, the number of sub-iterations carried out in a single time-step has little effect on the accuracy of the simulation. Looking at the results presented in Figure 3-17, 5-10 iterations appear reasonably adequate. However, during fast hybrid tests, a fewer number of iterations may be considered. On the other hand, the application of the implicit Newmark method (INM) for hybrid testing can be prohibitive since it is non-deterministic and incompatible with the path-dependent behavior of experimental substructures.

### d) Time-step of analysis

The effect of time-step size in hybrid testing was also studied considering the  $\alpha$ -OS integration (when  $\alpha=0.8$ ). First, the stability criterion for the time-step size,  $\Delta t$ , of the  $\alpha$ -OS integration was satisfied; therefore, any instability phenomena must be derived from the combined effect of its parameters and experimental errors. A rational approach for defining the experimental errors was adopted during this study, meaning the undershoot error is assumed to be proportional to  $\Delta t$ , i.e., as  $\Delta t$  gets smaller, the experimental error needs to get smaller as well. This approach preserves the total erroneous energy that is added to the test structure, thus, enabling the comparison among

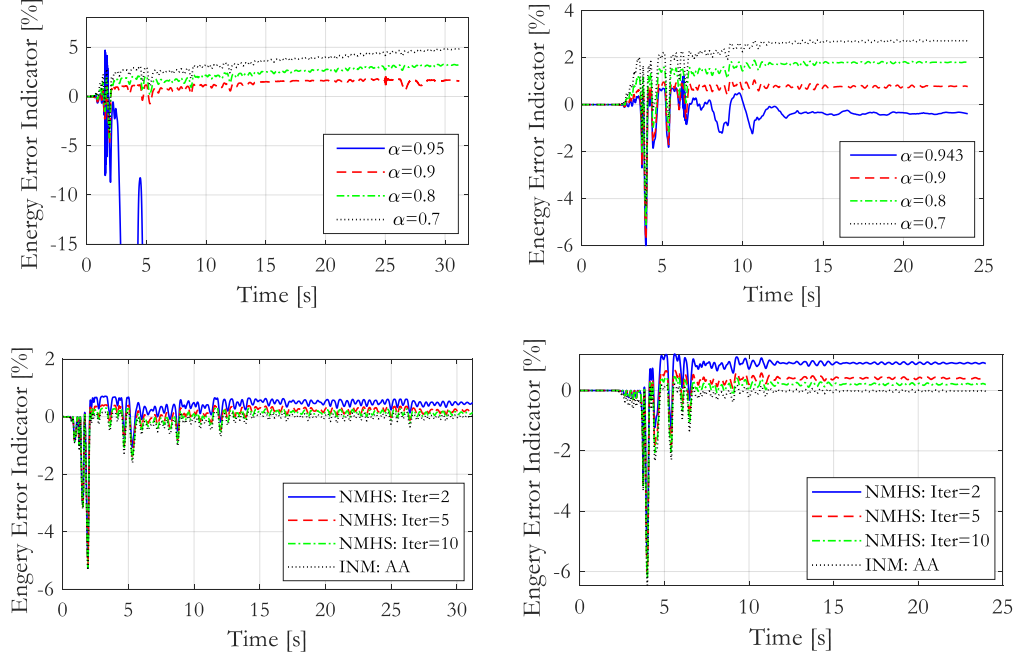


Figure 3-17: EEI of the steel portal frame using  $\alpha$ -OS and NMHS methods: subjected to the El Centro (left column) and Kobe (right column) earthquakes

hybrid tests of different  $\Delta t$ . Accordingly, the undershoot errors were calculated by dividing a constant undershoot error, which is 0.2032 mm when  $\Delta t=0.005$  s, by a time factor. The time factor is calculated as  $0.005/\Delta t$ , where  $\Delta t$  is the time-step of analysis. The benchmark response, denoted by an asterisk in Figure 3-18, was evaluated at  $\Delta t=0.001$  s without considering experimental errors.

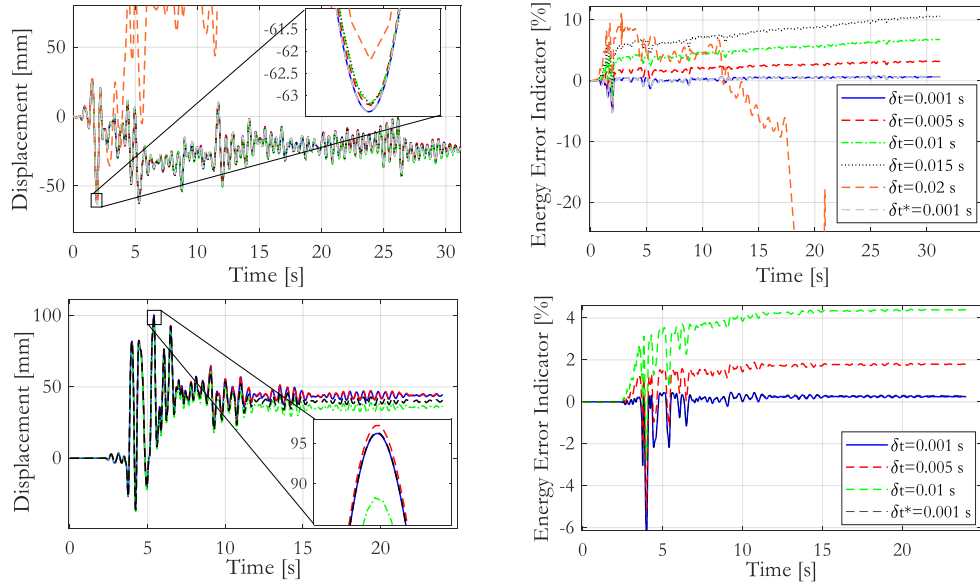


Figure 3-18: Lateral displacement and EEI of the steel portal frame, for various  $\Delta t$  of analysis, subjected to the El Centro (top row) and Kobe (bottom row) earthquakes

The simulations conducted by applying the El Centro (1940) and Kobe (1995) earthquakes reveal the benefit of using a small  $\Delta t$  in improving the accuracy of the hybrid simulation. Although the stability of a hybrid test is dictated more by the peak EEI, the overall accuracy is rather dependent on the residual EEI. The residual EEI reflects the cumulative energy error during a hybrid test and is thus more representative for evaluating the accuracy of a response simulation.

### e) Level of inelasticity/damage of a test structure

This study explores the relationship between the structure's inelasticity and the impact of experimental errors during a hybrid test. The deviation of the EEI and the normalized root-mean-square error (NRMSE) are used as error metrics, which are calculated from equations (3.12) and (3.13), respectively.

$$NRMSE = \frac{\sqrt{\frac{\sum(y - y_e)^2}{n}}}{\bar{y}} \quad (3.12)$$

$$\Delta EEI = EEI - EEI_e \quad (3.13)$$

where  $y$  and  $y_e$  are the structural responses (displacement or restoring force) under ideal experimental conditions (without experimental errors) and considering experimental errors, respectively. The same representation holds for  $EEI$  and  $EEI_e$ .

Figure 3-19 (a, b) presents the response of the steel frame, in the presence of an undershoot

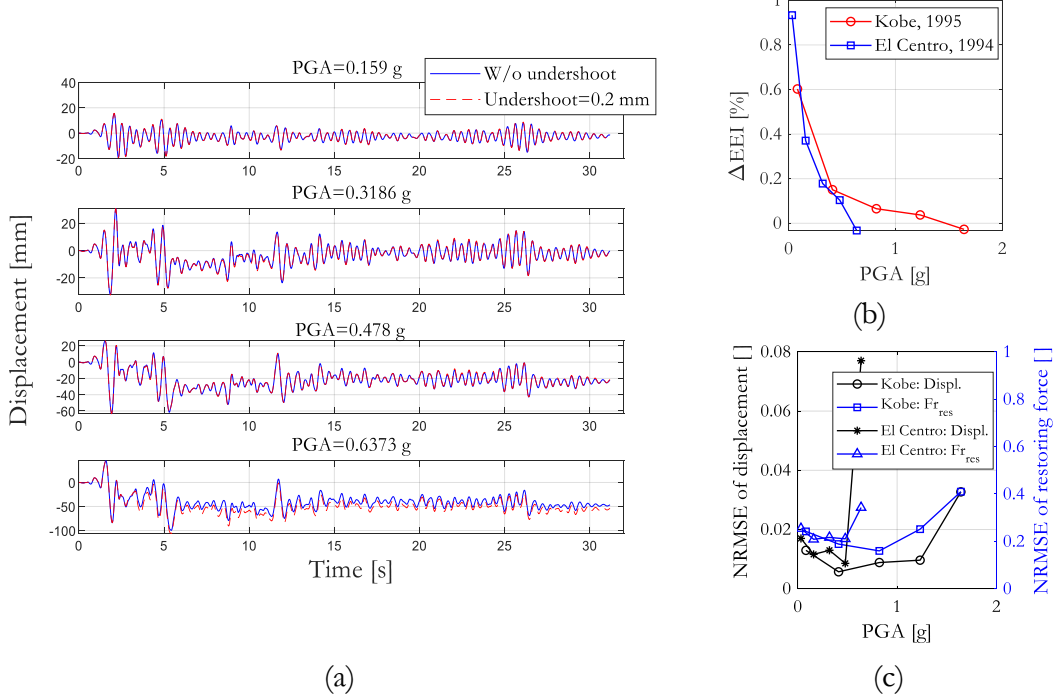


Figure 3-19: (a) Lateral displacement of the steel portal frame; (b)  $\Delta EEI$ ; (c) NRMSE of displacement and restoring force

error, with increasing level of intensity of the El Centro earthquake. The results show that the  $\Delta EEI$  diminishes as the structure is driven further into the post-peak branch of the capacity curve. This may be explained by the large hysteretic energy of the structure which absorbs the additional external energy. Likewise, the NRMSE of the lateral displacement, shown in Figure 3-19(c), tends to decrease as the structure approaches its plateau. In the post-peak curve, the NRMSE rebounds and increases again.

#### f) Overshooting versus undershooting errors

Although an overshooting error does not have a detrimental effect, it needs to be monitored during hybrid testing as it may reduce the accuracy of responses. This analysis, presented below, was performed without applying gravity loads to the structure since immediate numerical instability was recorded in the presence of an overshooting error. Besides, the NMHS algorithm with five iterations was selected for this analysis. When subjected to the El Centro earthquake, the EEI of the steel frame showed a notable difference between the control system undershooting as opposed to overshooting. Contrary, a very small difference in the EEI was attained when the Kobe earthquake was applied to the portal frame. Hence, the EEI appears to be dependent on the characteristics of the input ground motion.

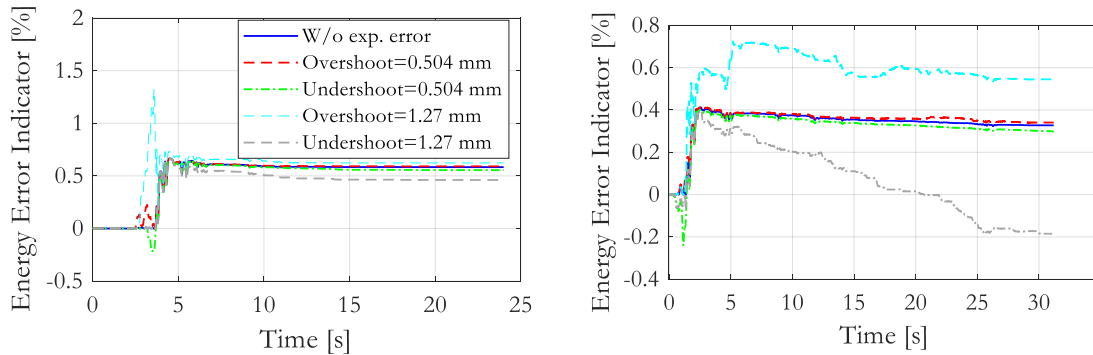


Figure 3-20: EEI of the steel portal frame, considering undershoot and overshoot experimental errors, subjected to El Centro (right) and Kobe (left) earthquakes

In summary, the EEI criterion for the assessment of the robustness of time-stepping algorithms in hybrid simulation was found very useful; nevertheless, it is important to consider additional error metrics that are less sensitive to uncertainties such as the record-to-record variability.

### 3.5 Stability analysis of linear and nonlinear SDOF systems in hybrid tests

Time-delay during a hybrid test may render it unstable, resulting in damage to a test specimen and equipment (Saouma & Sivaselvan, 2008). Hence, it is important to perform stability studies that can shed light on the development of efficient delay compensators. Conditionally stable time-stepping

schemes that are used in solving the equation of motion are also sources of instability. In this section, only instability issues that explicitly originated from experimental errors are addressed.

In Mercan & Ricles (2007), a simplified analytical study of the stability of hybrid simulation was conducted by modeling the time-delay of an actuator as a *pure delay*. However, time-delay can vary as a function of frequency; therefore, a realistic model for an actuator is essential in understanding the stability of hybrid testing. Herein, the stability analysis is conducted using the Routh-Hurwitz stability test because it can capture instability phenomena with a small computational cost. It is noteworthy to mention that this stability analysis is also intended to shed light on how to substructure a reference structure during hybrid testing from the standpoint of stability criterion.

### 3.5.1 Routh stability criterion for linear time-invariant systems

The Routh-Hurwitz stability criterion is a mathematical test for the stability of Linear Time-Invariant (LTI) control systems. The stability of a closed-loop system can be determined using the Routh-Hurwitz method without directly solving the closed-loop dynamics (Anagnos & Desoer, 1991). The principle of this technique relies on finding roots of the characteristic equation that fall in the right-half of the S-plane, i.e., roots with positive real parts which correspond to an unbounded response. The coefficients of the characteristic equation are first arranged in a square matrix called the *Hurwitz matrix*. The system is stable if and only if the sequence of determinants of its principal submatrices are all positive. Consider the closed-loop transfer function of a hybrid test,  $G(s)$ :

$$G(s) = \frac{N(s)}{D(s)} = \frac{\sum_{i=0}^n n_i s^i}{\sum_{i=0}^m d_i s^i} \quad (3.14)$$

where  $n_i$  and  $d_i$  are real constants and  $n \leq m$ . The first step is to factor out any roots at the origin to obtain the characteristic equation which reads:

$$d_m s^m + d_{m-1} s^{m-1} + d_{m-2} s^{m-2} + \dots = 0 \quad (3.15)$$

If the order of the resulting polynomial is at least two and if any coefficient  $d_i$  is zero or negative, the polynomial has at least one root with a non-negative real part. To obtain the exact number of roots with non-negative real parts, the process starts by setting the *Hurwitz matrix* as shown in Table 3-3.

Table 3-3: Hurwitz matrix

$s^m$	$d_m$	$d_{m-2}$	$d_{m-4}$	$d_{m-6}$	$d_{m-2i}$
$s^{m-1}$	$d_{m-1}$	$d_{m-3}$	$d_{m-5}$	$d_{m-7}$	$d_{m-2i-1}$
$s^{m-2}$	$c_0$	$c_1$	$c_2$	$c_3$	$c_i$
$s^{m-3}$	$e_0$	$e_1$	$e_2$	$e_3$	$e_i$
$\vdots$	$\vdots$	$\vdots$	$\vdots$	$\vdots$	$\vdots$
$s^0$	$f_1$				

where  $c_i$  and  $e_i$  are calculated as:

$$c_i = \frac{d_{m-1} \times d_{m-2i} - d_m \times d_{m-2i-1}}{d_{m-1}}; e_i = \frac{c_0 \times d_{m-2i-1} - c_i \times d_{m-1}}{c_0} \quad (3.16)$$

The first two rows are directly obtained from the characteristic polynomial given in equation (3.15), and the rest of the matrix is constructed according to the rule presented in equation (3.16). During the construction of the *Hurwitz matrix*, if any entry is zero, it is replaced by a very small number. If an entire row is zero, it signifies that the system has two real or complex roots that are equal and opposite. In this scenario, the row of zeros is replaced by  $dp/ds$  where  $p(s)$  is an auxiliary polynomial that is obtained from the values of the row just above the current row. For the stability test, only the first column of the *Hurwitz matrix* is used. *If the number of changes in the sign of the entries of the first column is zero, all roots are in the left half of the S-plane, hence the system response is bounded.*

### 3.5.2 Application to linear SDOF systems

The first step in the application of Routh's stability analysis to a hybrid test, composed of a shaking table and linear-elastic SDOF substructures, is to derive the closed-loop transfer function of the system. This transfer function is constructed by modeling the numerical substructure, the load transfer system (shaking table), and the experimental substructure, as shown in Figure 3-21.

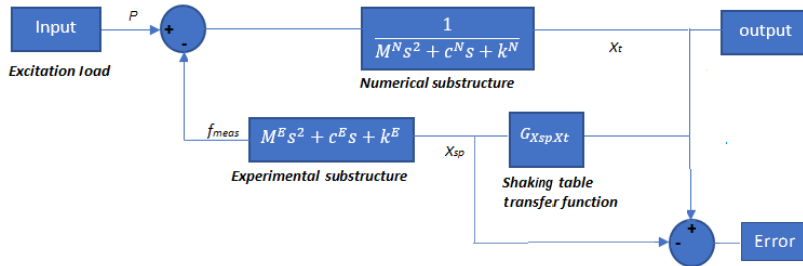


Figure 3-21: Schematic diagram of a substructuring test in a shaking table

The properties of the experimental substructure are incorporated into the transfer function of the bare ST1D, derived earlier in this chapter, to reproduce the CSI properties of the shaking table transfer function. Working out the closed-loop dynamics, which includes the numerical substructure as well, a transfer function with 6 poles and 4 zeros is obtained. The stability of this transfer function can now be examined.

The hypothetical test setup shown in Figure 3-22 was devised so that the displacement at the platen is equal to that of the test specimen. This test setup was conceived to be constructed from a rigid 3D truss and a rigid beam. The reference SDOF structure, 2 t of mass, has a fundamental frequency of 1 Hz and 2% of viscous damping. The experimental substructure models a portion of the structure's stiffness, damping, and mass. The mass, stiffness, and damping of the reference structure are therefore partitioned from 0 to 100%, between the experimental and numerical parts, in a grid space separated by 5%. Note that, in this test setup, a full shake table test can also be performed.

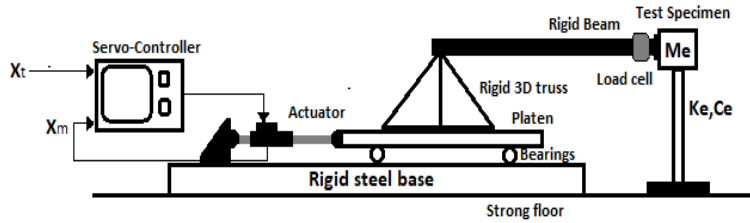


Figure 3-22: Hypothetical test setup of a SDOF structure in hybrid simulation

Several test setups were generated by changing any two of the SDOF properties while the third property is constant (i.e., 20x20 test setups). Stability contour plots between any two of these properties can therefore be generated. The inter-dependencies among the properties of the SDOF structure is intended to give a better understanding on how the stability of hybrid tests is ensured. Furthermore, the stability analysis was performed for different natural frequencies and viscous damping coefficients of the reference structure. It should be noted that the subsequent discussions of the results of the stability analyses are unique to the ST1D model and the properties of the SDOF considered in this study.

### 3.5.2.1 Results and discussions

The following conclusions can be made after closely studying Figure 3-23 and Figure 3-24:

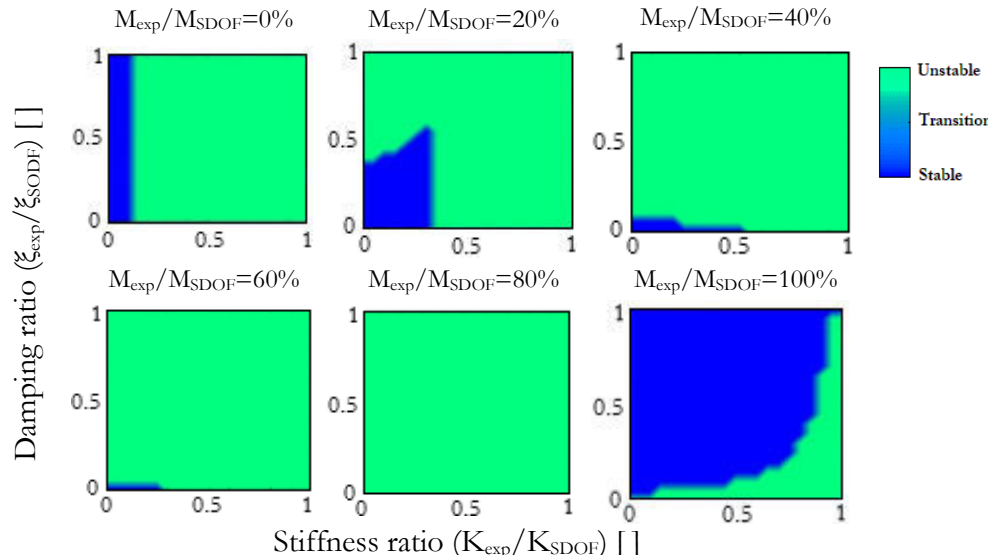


Figure 3-23: Stability contours of stiffness versus damping at constant  $M_{exp}/M_{SDOF}$

- In the contour plot for the stiffness versus damping, when the experimental mass,  $M_{exp}/M_{SDOF}$ , is in the interval 0-10%, the presence of experimental damping does not influence the stability of the hybrid test, i.e., the entire system damping can be modeled experimentally without risk of instability. As the experimental mass increases further, the stability of the hybrid test is only guaranteed for smaller experimental damping.

- ii. Increasing the experimental mass to 40%, the maximum stiffness that can be modeled experimentally increases too; however, it retracts as the experimental mass increases further. When  $M_{exp}=80\%$ , the test becomes unstable for any experimental stiffness and damping. However, an inverted-triangle zone of stability appears as the experimental mass reaches 100%. The top-right corner of this region represents a typical shaking table test.
- iii. In Figure 3-24, the influence of the SDOF structure frequency and damping is analyzed. An increase in the damping coefficient of the SDOF structure, while keeping a constant mass ( $M_{exp}=20\%$ ), results in an increase in the maximum allowed experimental damping. On the other hand, as the frequency of the reference SDOF structure increases, the stability of the hybrid test can only be kept by reducing the experimental stiffness. Furthermore, increasing the viscous damping of the SDOF structure permits larger portions of its stiffness to be experimentally modeled without the hybrid test becoming unstable.

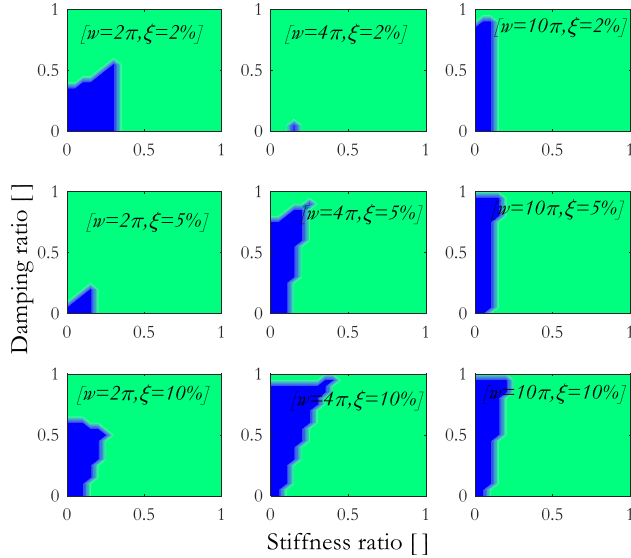


Figure 3-24: Stability contours of stiffness versus damping at  $M_{exp}/M_{SDOF} = 20\%$

To validate the reliability of the above stability test, a time-domain response simulation of the hybrid test was performed considering the stability contour between stiffness and damping, at 20% of the experimental mass. Two coordinates were selected from the stability contour: one in the stable zone and the other in the unstable zone; and the corresponding transfer functions were simulated in MATLAB software using a transient motion followed by a free-vibration tail.

The transient motion was prepared by scaling the El Centro earthquake (1940) to 0.3 g PGA. Besides, the coordinates ( $Crd$ ) were selected to be in the boundary between the stable and unstable regions, as shown in Figure 3-25. The response of the simulated hybrid test in the unstable coordinate ( $Unst_{ord}$ ), corresponding to  $K_{exp}=35\%$  &  $C_{exp}=20\%$ , and the stable coordinate ( $St_{ord}$ ), corresponding to  $K_{exp}=30\%$  &  $C_{exp}=20\%$ , matches the prediction made by Routh's stability test, i.e., response at  $St_{ord}$  is bounded; conversely,  $Unst_{ord}$  has an unbounded response.

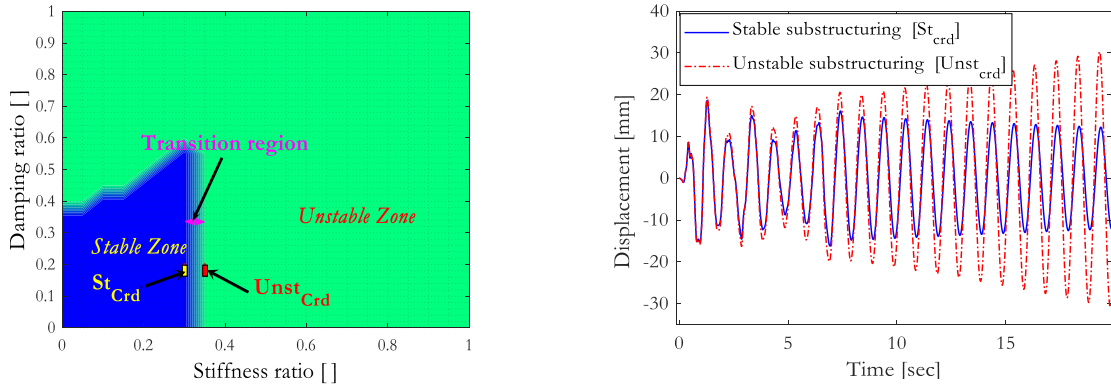


Figure 3-25: Validation of the Routh's stability test for stiffness versus damping contour at  $M_{\text{exp}}/M_{\text{SDOF}} = 20\%$

In the same manner, the following points can be concluded from the mass versus damping stability contour:

- i. In the stability contour plot for the mass versus damping, increasing experimental stiffness requires a reduction in the experimental damping so that the hybrid test becomes stable. At large experimental stiffness, approximately 40%, nearly any experimental mass renders the system unstable, as shown in Figure 3-26.
- ii. When the full mass of the SDOF is physically modeled, regardless of the experimental stiffness, the hybrid test can achieve stability. However, this is ensured only when minimum experimental damping is present, and the latter needs to increase proportionally to an increase in the experimental stiffness.

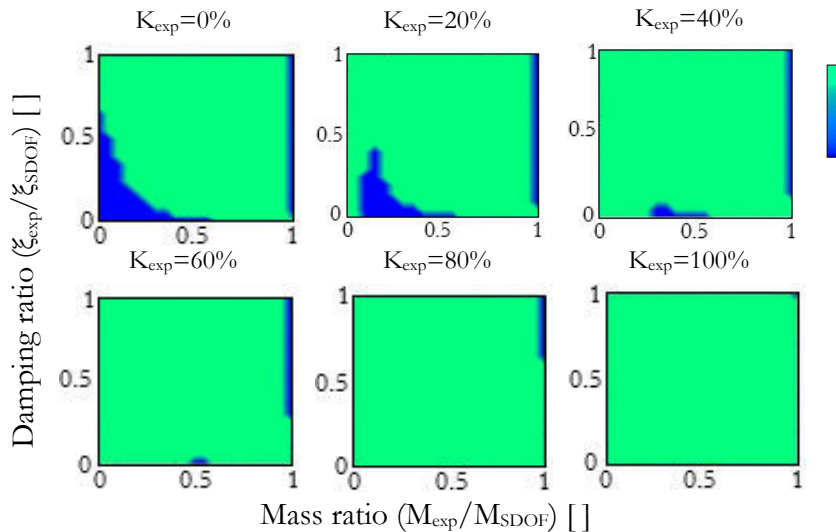


Figure 3-26: Stability contours of mass versus damping at constant  $K_{\text{exp}}/K_{\text{SDOF}}$

- iii. Increasing the viscous damping or natural frequency of the reference structure resulted in

completely different stability contours, as shown in Figure 3-27, which are complex to be interpreted. Nonetheless, increasing both quantities at the same time improved the stability of the hybrid test.

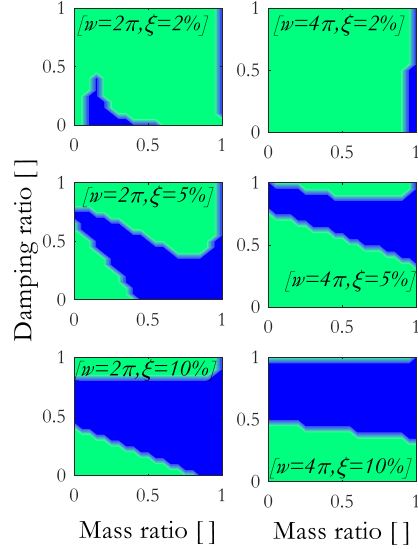


Figure 3-27: Stability contours plot of mass versus damping at  $K_{exp}/K_{SDOF} = 20\%$

The validation of the mass versus damping stability contour, at  $K_{exp}/K_{SDOF} = 20\%$ , was also conducted by taking the  $Unst_{ord}$  and  $St_{ord}$  coordinates. The Routh's stability method was again able to mimic the dynamic properties of the selected points, as depicted in Figure 3-28. The response at  $Unst_{ord}$  increases without bound whereas the response of the structure at the  $St_{ord}$  decays slowly.

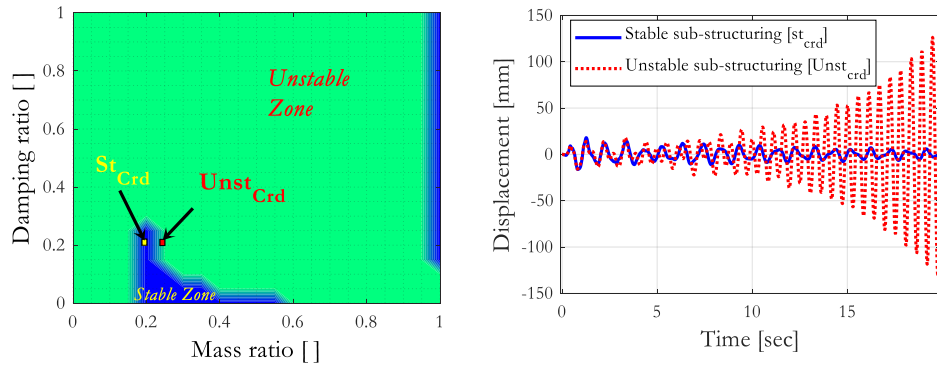


Figure 3-28: Validation of Routh's stability test for mass versus damping at  $K_{exp}/K_{SDOF} = 20\%$

Similarly, the stability contour for stiffness versus mass, at constant experimental damping, was explored. It was found that regardless of the amount of experimental damping, the stability contour remains the same except when the experimental damping reaches 100%. Besides, the maximum allowable experimental stiffness increases linearly as the experimental mass increases in the interval 0-30%. At full experimental mass, larger experimental stiffness is again admissible (see Figure 3-29).

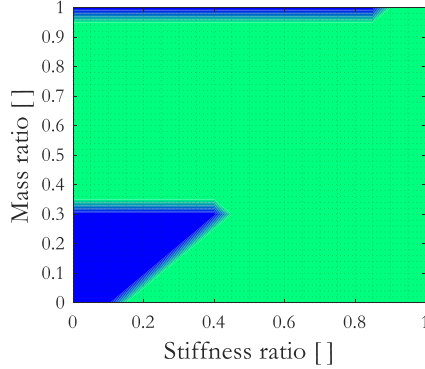


Figure 3-29: Stability contour of mass versus damping for all  $C_{\text{exp}}/C_{\text{SDOF}}$  but 100%

### 3.5.3 Application to nonlinear SDOF systems

The stability analysis of the linear-elastic SDOF structure, presented above, was extended to inelastic SDOF structures whereby the Bouc-Wen model represents the experimental substructure constitutive relationship. The Bouc-Wen hysteresis model is a nonlinear differential equation typically used to describe nonlinear hysteretic systems. The model can be visualized as two springs connected in parallel, as shown in Figure 3-30.

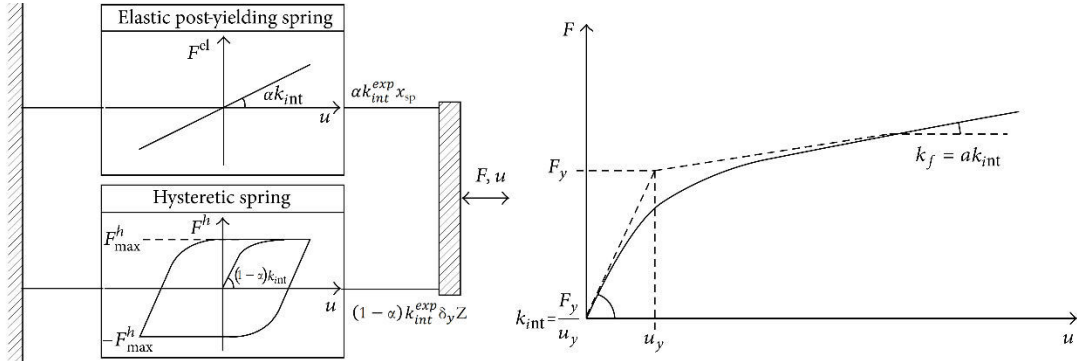


Figure 3-30: Idealization of the Bouc-Wen model

Considering the Bouc-Wen model of an experimental substructure, the nonlinear restoring force  $f_{\text{exp}}$  can be written as:

$$f_{\text{exp}}(t) = \alpha k_{\text{int}}^{\text{exp}} x_{\text{sp}}(t) + (1 - \alpha)k_{\text{int}}^{\text{exp}} \delta_y Z(t) + c^{\text{exp}} \dot{x}_{\text{sp}}(t) \quad (3.17)$$

$$\dot{Z}(t) = \dot{x}_{\text{sp}}(t) \left\{ A + \beta \times \text{sgn}(Z(t)\dot{x}_{\text{sp}}(t)) + \gamma |Z(t)|^n \right\} / \delta_y \quad (3.18)$$

where  $x_{\text{sp}}$  is the displacement of the experimental substructure;  $\delta_y$  is the yield displacement;  $\alpha$  is the ratio of the post-yield stiffness to the pre-yield stiffness;  $Z(t)$  is a dimensionless hysteresis parameter having zero initial condition;  $A$ ,  $\beta$ ,  $n$ , and  $\gamma$  are the Bouc-Wen parameters;  $k_{\text{int}}^{\text{exp}}$  and  $c^{\text{exp}}$  are the initial stiffness and viscous damping of the experimental substructure, respectively. The parameters  $\beta$  and

$\gamma$  control the size and shape of the hysteretic loop, respectively. Herein, to reduce the redundancy of the model parameters, the value of  $A$  was taken as one (Ma et al., 2004)

The simulated test was performed by analytically modeling all the elements of the hybrid test in MATLAB/Simulink, as shown in Figure 3-31. The solution to the Simulink model, which includes a linear-elastic numerical substructure, the transfer function of the ST1D, and the Bouc-wen model of the experimental substructure, was determined using the ode14x solver.

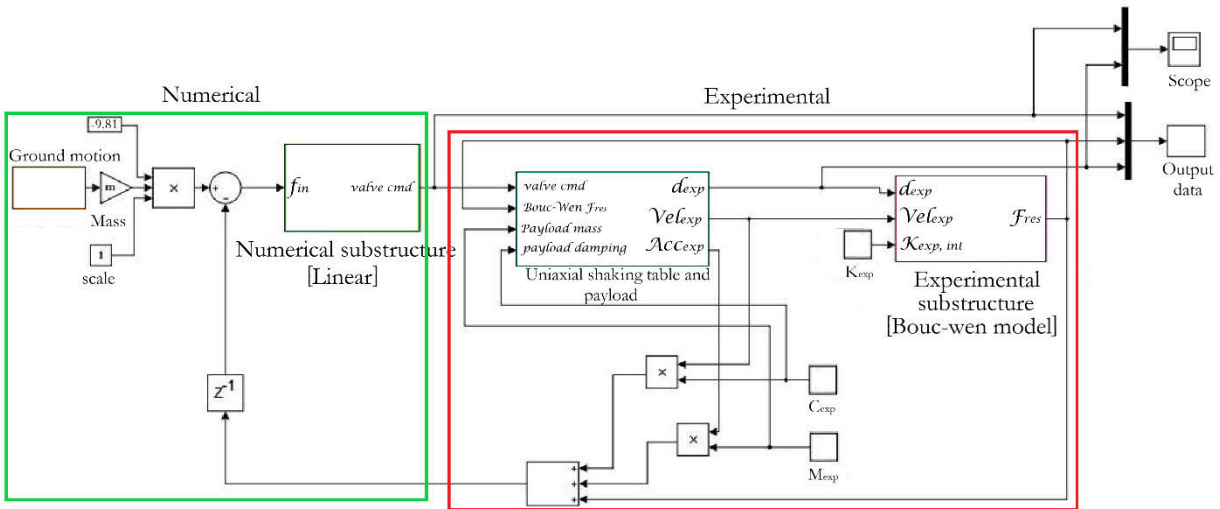


Figure 3-31: Simulink model for a simulated hybrid test of an inelastic SDOF structure using the Bouc-Wen hysteresis to model the experimental substructure

### 3.5.3.1 Results and discussions

The two coordinates,  $S_{t,rd}$  and  $U_{n,t,rd}$ , that were introduced to validate the Routh's stability test for the stiffness versus damping contour are again considered here. The coordinates' properties and the input motion that were used for the linear-elastic case were also adopted for the validation of the inelastic SDOF structure.

The displacement responses of the linear and nonlinear SDOF structures, shown in Figure 3-32, have interesting stability characteristics. In the linear-elastic SDOF structure, the hybrid test is unstable, but the response of the inelastic SDOF structure (with properties identical to the linear-elastic structure) is bounded. The main reason for this stable response is the hysteretic energy of the inelastic structure, meaning higher effective damping. This means that the stable region obtained in the linear-elastic case is now enlarged. This demonstrates the improved stability of structural systems once the inelastic level of response is reached.

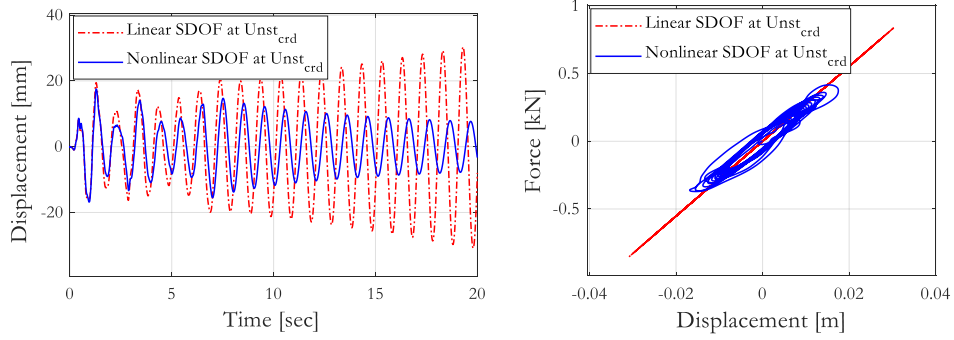


Figure 3-32: Comparing the stability of hybrid simulations of elastic and inelastic structures: displacement plot (left) and hysteresis plot (right)

From equations (3.17) and (3.18), it can be shown that the dimensionless variable,  $Z$ , attains its maximum value at  $Z_{\max} = [A/(\beta+\gamma)]^{1/n}$ . This dimensionless parameter serves as a measure of the degree of inelasticity. Thus, three cases were considered with an increasing degree of inelasticity, by changing the  $\beta+\gamma$  value, assuming the same yielding force. In detail, three sets of values:  $\beta=\gamma=0.25$ ;  $\beta=\gamma=0.5$ ; and  $\beta=\gamma=0.75$  were chosen to model the slightly inelastic, moderately inelastic, and strongly inelastic responses, respectively. Arguably, the limiting restoring force attained by the Bouc-Wen model can be written as a product of the absolute maximum yielding force,  $F_y$ , and  $Z_{\max}$ . Hence, we can express the inelasticity factor  $\rho$  as:

$$\rho = \max \frac{|f_r(t)|}{f_{max}} = \max \frac{|f_r(t)|}{F_y [A/(\beta + \gamma)]^{1/n}} \quad (3.19)$$

where  $f_r(t)$  is the restoring force of the experimental substructure at time  $t$ . From Figure 3-33, it can be concluded that the decay gradient is proportional to the degree of inelasticity,  $\rho$ , of the structure; therefore, as the level of damage of a structure increases, the risk for unstable hybrid simulation reduces proportionally.

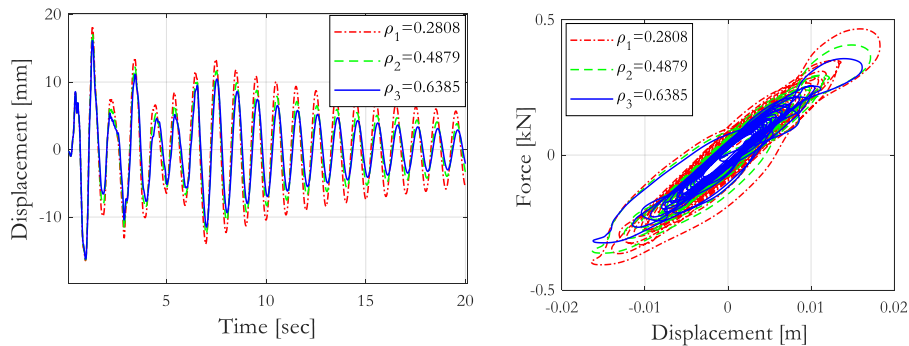


Figure 3-33: The effect of the degree of inelasticity of an experimental element in the stability of a hybrid test

## 3.6 Reliability and global sensitivity studies in hybrid simulation

### 3.6.1 Multiplicative Dimensional Reduction Method

For a realistic evaluation of the uncertainties in structural responses, probabilistic analysis is essential. In general, any response parameter can be represented as a function of several random parameters such as the material properties, geometric characteristics, and applied loads:

$$r = g(Z) \quad (3.20)$$

where  $Z$  the vector of random variables and  $r$  is the scalar response. Furthermore, the probability of failure can be defined using a limit-state equation, which reads:

$$p_f = 1 - F_r(g_c) \quad (3.21)$$

where the cumulative distribution,  $F_r$ , is calculated as:

$$F_r(g_c) = \int_0^{g_c} f_r(x) dx \quad (3.22)$$

where  $f_r$  is the Probability Density Function (PDF) of the response parameter  $r$ . The probabilistic formulation presented in equation (3.22) can be approximated using response surface methods, for instance, since it can be a complex function of random variables.

The conventional Dimensional Reduction Method (DRM) approximates a response function in the form of an addition (Xu & Rahman, 2004):

$$r = g(Z) \approx \sum_{i=1}^n g_i(z_i) - (n-1)g_0 \quad (3.23)$$

where  $g_i(z_i)$  is the  $i$ th cut-off function that is evaluated by changing the  $i$ th random variable while the rest of the random variables take their mean values. Therefore, it can be written as:

$$g_i(z_i) = g(c_1, c_2, \dots, c_{i-1}, z_i, c_{i+1}, \dots, c_{n-1}, c_n) \quad (3.24)$$

To simplify the computation of fractional moments, Zhang & Pandey (2013) derived the multiplicative formulation for the univariate approximation of a response function. This method is termed as Multiplicative Dimensional Reduction Method (M-DRM) and the response function is expressed as:

$$r = g(Z) \approx g_0^{(1-n)} \times \prod_{i=1}^n g_i(z_i) \quad (3.25)$$

### 3.6.2 Global sensitivity indices

The first and second statistical response moments of multi-degree of freedom (MDOF) dynamical systems, having random loads and random structural properties, are essential for describing the

effect of the uncertainty of input parameters on structural responses. Using the univariate M-DRM formulation and assuming independent random variables, the  $k$ th-order moment of a response function can be approximated by:

$$E[r^k] \approx E \left[ \left\{ g_0^{(1-n)} \times \prod_{i=1}^n g_i(z_i) \right\}^k \right] = g_0^{k(1-n)} \prod_{i=1}^n E [\{g_i(z_i)\}^k] \quad (3.26)$$

Using the above formulation, the mean and standard deviation can be derived as:

$$\mu_r = E[r] \approx g_0^{(1-n)} \prod_{i=1}^n E [g_i(z_i)] \quad (3.27)$$

$$\sigma_r = E[r^2] - \mu_r^2 \approx g_0^{2(1-n)} \prod_{i=1}^n E [\{g_i(z_i)\}^2] - \mu_r^2 \quad (3.28)$$

The expected value,  $E$ , is evaluated by numerical methods that can optimize the integration process. Depending on the type of distribution, the Gauss-Hermite, Gauss-Legendre, or Gauss-Laguerre quadrature formulations can be used. The Gauss-Hermite quadrature matches well with normal and lognormal distributions of a response parameter. On the other hand, the Gauss-Legendre and Gauss-Laguerre quadrature are used with the uniform and exponential distributions, respectively (Abramowitz & Stegun, 1972). Using the appropriate quadrature rule, the expectation operator,  $E$ , can be approximated by a finite number of integration points,  $L$ , as:

$$E[\{g_i(z_i)\}^k] = \int_{z_i} (g(z_i))^k f_i(z_i) dz_i \approx \sum_{j=1}^L w_j \{g_i(z_j)\}^k \quad (3.29)$$

where  $w_j$  and  $z_j$  are the  $j$ th weight and coordinate of the quadrature rule, respectively; and  $f_i$  is the PDF of the  $i$ th random variable. Substituting equation (3.29) into equations (3.27) and (3.28), the response moments can be written as:

$$\mu_r \approx g_0^{(1-n)} \prod_{i=1}^n \left( \sum_{j=1}^L w_j \{g_i(z_j)\} \right) \quad (3.30)$$

$$\sigma_r \approx g_0^{2(1-n)} \prod_{i=1}^n \left( \sum_{j=1}^L w_j \{g_i(z_j)\}^2 \right) - \mu_r^2 \quad (3.31)$$

In the same context, the variance-based global sensitivity analysis is the process of quantifying the contribution of a random variable to the total variance of a response function. The first-order sensitivity indices measure the effect of varying a random variable alone whereas the total sensitivity indices account for the interaction with other random variables as well. The analytical basis for the global sensitivity analysis came from ANOVA (Analysis of Variance) decomposition of a response variance. Although ANOVA decomposition is conceptually simple, the computation of variance components of a general response function is rather difficult because it involves a series of high

dimensional integrations (Efron & Stein, 1981). Therefore, minimizing the computational effort is a primary area of research in the variance-based global sensitivity analysis.

The Monte Carlo simulation is an effective method for global sensitivity analysis of a general response function. However, it is impractical in the context of hybrid testing. In this work, the M-DRM technique, an alternative to the conventional DRM method, was chosen to approximate the response function obtained from hybrid testing. The univariate M-DRM approximates a complex function of random variables by a product of one-dimensional functions, thus reducing the computational cost of calculating the variance-based global sensitivity indices. Besides, simple algebraic expressions can be derived for primary, joint variate, and total sensitivity indices, which are easy to use in practice (Zhang & Pandey, 2014). In the variance-based global sensitivity analysis, the general formulation for the first-order sensitivity index of a random variable  $i$  is given by:

$$S_i = \frac{V_i\{E_{-i}[r|Z_i]\}}{V(r)} = \frac{V_i}{V_r} \quad (3.32)$$

where  $S_i$  is the first-order sensitivity index of the random variable  $i$ ;  $V_i$  is the variance obtained by varying the random variable  $i$  alone and  $V_r$  is the total variance of the response  $r$ . Mirroring the above general formulation into the univariate M-DRM, the first-order sensitivity index can be shown to be:

$$S_i \approx \frac{\left\{ \sum_{j=1}^L w_j \{g_i(z_j)\}^2 \middle/ \left\{ \sum_{j=1}^L w_j \{g_i(z_j)\} \right\}^2 \right\} - 1}{\prod_{i=1}^n \left\{ \sum_{j=1}^L w_j \{g_i(z_j)\}^2 \middle/ \left\{ \sum_{j=1}^L w_j \{g_i(z_j)\} \right\}^2 \right\} - 1} \quad (3.33)$$

Theoretically, sensitivity indices must sum up to one. Extending this rule to the sensitivity indices that are derived from the M-DRM method, we can write:

$$\sum_{i=1}^n S_i + \sum_{i < j} S_{ij} + \sum_{i < j < k} S_{ijk} + \dots S_{123\dots n} = 1 \quad (3.34)$$

where  $S_{ij}$ ,  $S_{ijk}$ , etc., are the joint sensitivity indices. These joint-variate sensitivity indices can also be estimated using the M-DRM technique. Considering a bivariate problem, the joint sensitivity indices are calculated from:

$$S_{ij} = \frac{V_{ij}}{V_r} = S_i \times S_j \times \left\{ \prod_{i=1}^n \left\{ \frac{\sum_{j=1}^L w_j \{g_i(z_j)\}^2}{\left\{ \sum_{j=1}^L w_j \{g_i(z_j)\} \right\}^2} \right\} - 1 \right\} \quad (3.35)$$

where  $V_{ij}$  is the joint variance obtained by varying the random variables  $i$  and  $j$  at the same time. Likewise, the general formulation for the total sensitivity  $TS_i$  of random variable  $i$  is given by:

$$TS_i = \frac{E_{-i}\{V_i[r|Z_{-i}]\}}{V_r} = 1 - \frac{V_{-i}\{E_{-i}[r|Z_{-i}]\}}{V_r} \quad (3.36)$$

where  $Z_{-i}$  is the vector of random variables that contains all elements of  $Z$  except the  $i$ th random variable ( $z_i$ ). In the above equation, the term  $V_{-i}\{E_{-i}[r|Z_{-i}]\}$  refers to the variance reduction obtained by fixing all input variables except  $z_i$ . In Zhang & Pandey (2014), the M-DRM based approximation for the total sensitivity index  $TS_i$  is given by:

$$TS_i \approx \frac{1 - \left\{ \left( \sum_{j=1}^L w_j \{g_i(z_j)\} \right)^2 / \sum_{j=1}^L w_j \{g_i(z_j)\}^2 \right\}}{1 - \prod_{i=1}^n \left\{ \left( \sum_{j=1}^L w_j \{g_i(z_j)\} \right)^2 / \sum_{j=1}^L w_j \{g_i(z_j)\}^2 \right\}} \quad (3.37)$$

Considering lognormally distributed input variables, the coordinates of the  $L$ th-order Gauss-quadrature rule are utilized to calculate the input values. The  $i$ th input variable at the  $j$ th coordinate,  $x_i^j$ , is therefore obtained by transforming the lognormally distributed random variable ( $\mu_i^{LN}$ ,  $\sigma_i^{LN}$ ) into the Gauss-quadrature form, which reads:

$$\int_{-\infty}^{+\infty} e^{-z^2} f(z) dz = \sum_{i=1}^n w_i f(z_i) \quad (3.38)$$

Consequently, the Gauss-quadrature rule and lognormal distribution can be related by:

$$s_j = \frac{\ln x_i^j - \mu_i^{LN}}{\sqrt{2}\sigma_i^{LN}} \Rightarrow x_i^j = e^{(\sqrt{2}s_j\sigma_i^{LN} + \mu_i^{LN})} \quad (3.39)$$

where  $s_j$  is the  $j$ th coordinate of the  $L$ th-order Gauss integration. Likewise, if a normally distributed random variable ( $\mu_i^N$ ,  $\sigma_i^N$ ) is considered,  $x_i^j$  can be shown to be:

$$x_i^j = \frac{\sqrt{2}s_j\sigma_i^N + \mu_i^N}{\sqrt{\pi}} \quad (3.40)$$

### 3.6.3 Reproduction of full probabilistic distribution

The probabilistic definition of a response function is required for defining failure probabilities in the reliability analysis of structures. To this end, if the distribution type is not known beforehand, the construction of the observed probability density is needed. The Probability Density Function (PDF) of a response function can be constructed from an assumed distribution using its moments, mean, and standard deviation.

There are only a few studies, up to this date, addressing the reconstruction of a PDF using moments. The reconstruction of an M-determinate cumulative distribution employing mixtures, the first few moments being exactly the same as those of the target distribution, was proposed by Lindsay et al. (2000). This technique requires calculations of high-order Hankel determinants. Due to the ill-conditioning of the Hankel matrices, the method is not useful when a large number of moments need to be matched. On the other hand, heuristic methods that utilize an assumed PDF, although

simple, can be highly sensitive when approximating tail probabilities.

The reconstruction of an unknown density function using the Maximum Entropy principle, through ordinary and fractional moments, was studied by Inverardi & Tagliani (2003). Although the rate of convergence of this technique is not fully established, promising results were obtained in the past. The principle of maximum entropy (MaxEnt) states that by maximizing the entropy subjected to constraints supplied by the available information, i.e., fractional moments, the most unbiased probability estimate of a response is obtained (Inverardi & Tagliani, 2003).

Information about a large number of central moments can be contained in a few fractional moments (Pierluigi et al., 2005; Inverardi & Tagliani, 2003 and Milev et al., 2012). These fractional moments are incorporated into the M-DRM method for a reliable estimation of a distribution density function (Balomenos & Pandey, 2016). Nonetheless, the MaxEnt algorithm can experience numerical instability when a large number of fractional moments are used (Tagliani, 1999). Therefore, the M-DRM method that uses a small number of fractional moments, typically three or four, is adopted in this work.

Now, consider a distribution density function  $f_r$  of a structural response  $r$ . The  $\alpha$ th fractional moment can be calculated as:

$$E[r^\alpha] = M_r^\alpha = \int_r r^\alpha f_r(y) dr \quad (3.41)$$

The maximum entropy  $H[r]$  of the distribution  $f_r$  is given by:

$$H[r] = - \int_r f_r(z) \ln(f_r(z)) dz \quad (3.42)$$

Eventually, the maximization of the entropy function gives rise to the optimum coefficients for the fractional moments and Lagrange multipliers that are used to construct the estimated PDF,  $\hat{f}_r$ :

$$\hat{f}_r = \exp \left\{ - \sum_{i=0}^m \lambda_i z^{\alpha_i} \right\} \quad (3.43)$$

where  $\alpha = [\alpha_0, \alpha_1, \alpha_2, \alpha_3, \dots, \alpha_m]$  and  $\lambda = [\lambda_0, \lambda_1, \lambda_2, \lambda_3, \dots, \lambda_m]$  are the exponents of fractional moments and Lagrange multipliers, respectively. The optimal values of the exponents  $\alpha_i$  and coefficients  $\lambda_i$  are determined by minimizing the *Kullback-Leibler (kl)* divergence between the true( $f_r$ ) and estimated ( $\hat{f}_r$ ) PDFs, which can be implemented using the *simplex algorithm* (Balomenos & Pandey, 2016). Using the *simplex algorithm*,  $\alpha_i$  and  $\lambda_i$  can be minimized without prior knowledge of  $\alpha_i$ , as suggested by Zhang & Pandey (2013). However, the algorithm can converge to local minimum points because it is highly dependent on the initial value of these coefficients (Jeffrey et al., 1998).

Another approach, proposed by Van Coile et al. (2017), splits the optimization process into two steps. First, the optimization of the Lagrange multipliers is carried out using predefined fractional moments. Second, the *Kullback-Leibler* function is minimized using the output of the first step. For pragmatic reasons, the two-step optimization method is adopted herein and the fractional

coefficients, in the interval [-2, 2], are generated using the Latin Hypercube Sampling (LHS). In this work, the procedure explained above was implemented in the MATLAB software using the heuristic *Nelder–Mead* method (also called *dowhill simplex* method). The MATLAB algorithm can be summarized as:

### Step 1:

Considering a model with  $p$  random variables, define the number of fractional moments ( $m$ ), the Gauss-quadrature order ( $L$ ) and the number of iterations ( $n$ ) for the MaxEnt algorithm; and set  $j=1$ .

**while**  $j < n$

- i. Generate  $\boldsymbol{\alpha} = [\alpha_1, \alpha_2 \dots \alpha_m] \sim U(-2, 2)$  using the LHS
- ii. Initialize  $\boldsymbol{\lambda} = [\lambda_1, \lambda_2 \dots \lambda_m]$
- iii. Minimize the  $kl$  function:

$$kl = I(\alpha, \lambda) = \ln \left\{ \int_r \exp \left( - \sum_{i=1}^m \lambda_i z^{\alpha_i} \right) dy \right\} + \sum_{i=1}^m \lambda_i M_r^{\alpha_i} \quad (3.44)$$

$$M_r^{\alpha_i} = g_0^{\alpha_i(1-p)} \prod_{i=1}^p E [\{g_i(z_i)\}^{\alpha_i}] \quad (3.45)$$

- iv. Record  $kl$ ,  $\boldsymbol{\alpha}$ , and  $\boldsymbol{\lambda}$
- v. Increment  $j$  by 1

### Step 2:

**do**

Search for the global minimum of the  $kl$  vector,  $\mathbf{kl}$ , and the corresponding  $\boldsymbol{\alpha}$  and  $\boldsymbol{\lambda}$  parameters:

$$kl_{min} = \min\{\mathbf{kl}\} \quad (3.46)$$

Let us consider the response of a structure with  $p$  independent random variables, using the  $L$ th-order Gauss quadrature, all moments of the cut-off function can be determined from  $pL$  response evaluations. One additional evaluation of the response is also required at the mean values of the random variables. Subsequently,  $pL+1$  response evaluations, which translate into  $pL+1$  hybrid tests, are necessary to obtain the required moments of the response function.

#### 3.6.4 Application to a steel frame structure

The proof-of-concept of the proposed method was first conducted using simulated hybrid tests of a two-bay one-story steel frame structure shown in Figure 3-34 (Tekeste et al., 2019). All columns are pin-ended at the top so that only the translational DOF of the frame is controlled during the hybrid test.

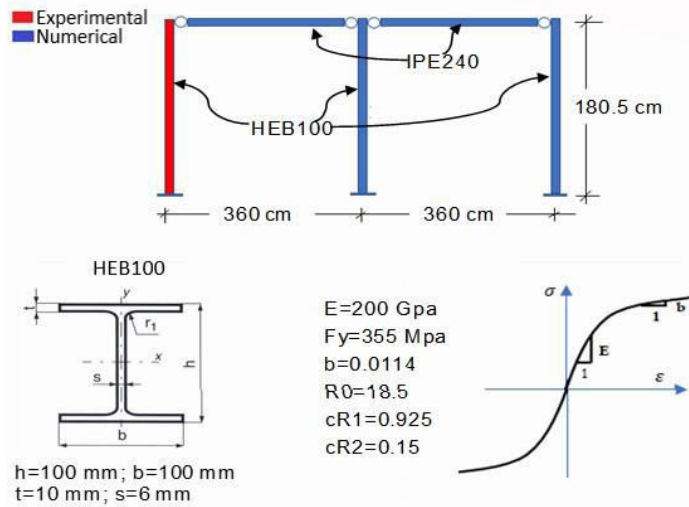


Figure 3-34: Steel frame structure and its column properties

One of the exterior columns of the steel structure was modeled as the experimental element while the remaining parts of the frame were numerically modeled in the OpenSees software. To mimic the experimental conditions, experimental errors were also included in the model. The experimental element was represented using the uniaxial material in the OpenFresco software, and its restoring force was obtained from the force-displacement constitutive relationship. The experimental error was added to the trial displacement using the *expFilterSignal* class. The response of the experimental element, modified by the simulated error, is then returned to the OpenSees software and the next time-step trial displacement is then computed. For the same reason discussed in the earlier case studies, the undershooting experimental error was chosen in this work (Mercan & Ricles, 2007; Tekeste et al., 2017a). The amplitude of the undershoot error was taken as 5% of the RMS value of the frame's lateral displacement.

The stiffness and viscous damping of the numerical elements of the steel frame were modeled as Random Variables (RV). To avoid the overestimation of the structure's damping, the mass-proportional approach was adopted since the OpenFresco framework does not return the tangent stiffness of the experimental element. Herein, the initial stiffness of the experimental column was estimated from hammer tests (a detailed explanation of the hammer test is presented in chapter 4). Besides, mass-proportional damping ensures that the two input parameters are independent of each other, which is the basis for the M-DRM approach (Zhang & Pandey, 2013). To realize the uncertainty in the stiffness of the frame, the elasticity modulus of the numerical element was varied instead since stiffness is directly proportional to the elasticity modulus. Furthermore, various levels of the response of the structure were examined by increasing the intensity of the input ground motion. In this study, the El Centro (1940), Northridge 260 (1994), and Kobe (1995) earthquake records were used as ground motion inputs to the steel frame structure. Besides, the adequacy of the M-DRM method was investigated by changing the coefficient of variation of the random parameters, as shown in Table 3-4.

Table 3-4: Coefficient of variation (CV) of random variables

	Stiffness [%]	Damping coefficient [%]
CV1	1	2
CV2	3	6
CV3	5	10
CV4	6.5	20

During the reliability analysis, the hybrid test was executed  $pL+1$  times, where  $p$  is the number of RVs and  $L$  is the number of Gauss-Hermite integration points. If  $L$  is odd, the central Gauss point has zero coordinate which corresponds to the median value. This causes the number of model evaluations to further reduce to  $p(L-1)+1$  (Van Coile et al., 2017). Therefore, for each combination

Table 3-5: Ground motion input for the implementation of the M-DRM in hybrid tests

Earthquake	$\Delta t$ [s]	Intensity of input motion		
		PGA1 [g]	PGA2 [g]	PGA3 [g]
El Centro (1940)	0.02	0.0909	0.1818	0.3030
Kobe (1995)	0.01	0.2464	0.4928	0.8213
Northridge 260 (1994)	0.01	-	-	0.4717

of earthquake record, ground motion scale factor, and coefficient of variation, the simulated hybrid test was executed 13 times, i.e., 2 random variables and seventh-order Gauss-Hermite quadrature result in 13 ( $2 \times (7-1)+1$ ) response evaluations. In each simulation, the mean, standard deviation, first-order sensitivity indices, and the total sensitivity indices were extracted for selected responses of the numerical and experimental elements. The benchmark for the M-DRM estimates was derived from the Monte Carlo based method. Five thousand model evaluations of the Monte Carlo were executed to derive the reference moments of the selected responses of the frame.

### 3.6.4.1 Choice of the Gauss-quadrature order

The accuracy and computational cost of the M-DRM method are strongly dependent on the choice of the number of integration points (or Gauss-quadrature order). Therefore, it is logical to select the optimal number of integration points for the finite integration. In turn, the number of response evaluations for a structure is directly proportional to the number of integration points. To examine this dependency, the M-DRM-based reliability analyses of the steel frame were executed by gradually increasing the number of integration points. The improvement in the error margin, using the Monte Carlo output as a reference, was then evaluated. A relatively smaller number of model evaluations were conducted since the objective of this study, at this stage, is only to evaluate the effect of the number of integration points on the M-DRM estimates. Consequently, 1000 and 5000 Monte Carlo based model runs were executed for the cases PGA1 and PGA3, respectively. During these analyses, no experimental errors were included as they might distort the true convergence characteristics of the sensitivity indices and relative error quantities. Besides, the coefficients of variation for the stiffness and damping were taken as 5% and 10%, respectively, and the steel frame was subjected to the El Centro (1940) earthquake record.

The global sensitivity indices of the frame's lateral displacement and shear force are plotted against the number of integration points in Figure 3-35. The convergence of the sensitivity indices is slow and oscillatory, but a reasonable convergence is achieved using 5-7 number of integration points. However, the relative error quantities of the estimates, compared to their MCS counterparts, are oscillatory. Nonetheless, a gradual descent of the relative error can be observed in Figure 3-36(a). An in-depth look at the results reveals that the odd number of integration points appears to yield a smaller error amplitude compared to the even number of integration points.

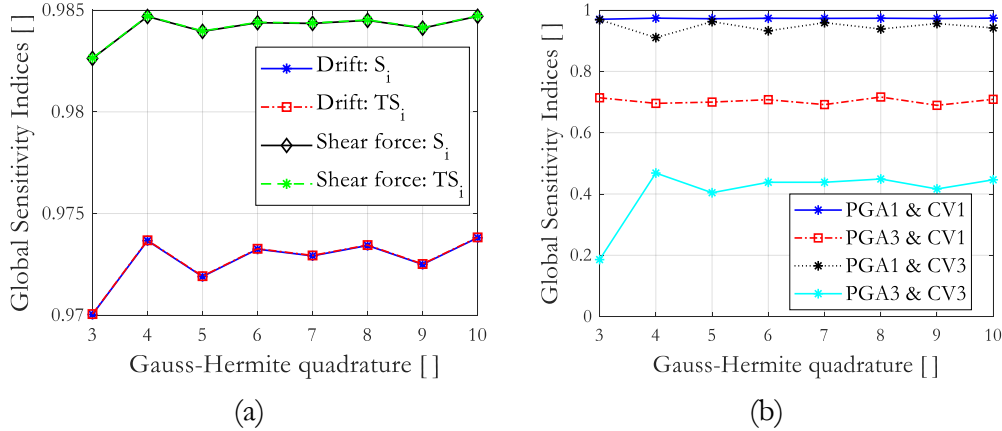


Figure 3-35: (a) First-order and total sensitivity indices versus the number of integration points for the PGA1-CV1 scenario; (b) first-order sensitivity indices of the maximum drift response by changing the CV of input variables and the PGA of the input motion

In Figure 3-35(b), the first-order global sensitivity indices of the maximum drift of the frame converge at five integration points, but the speed of convergence shows some dependence both on the intensity level of input motion and the variance of the input variables. Likewise, the first-order global sensitivity indices of the maximum drift and shear force, to the stiffness input of the structure,

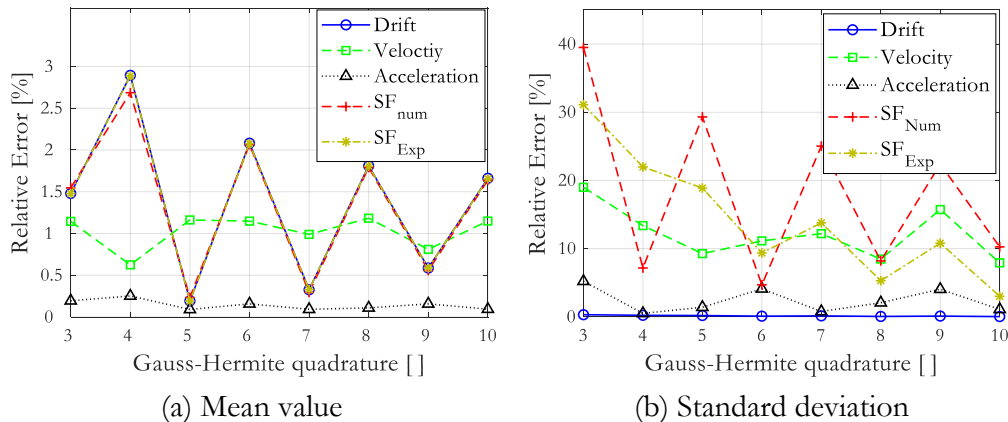


Figure 3-36: Relative error quantities versus the number of integration points for the PGA1-CV3 scenario

showed negligible improvements with an increase in the number of integration points. This is particularly true when the variances of the input variables are small (see Figure 3-35(b)). In the presence of the largest input variance (CV3) considered here, at all levels of the input motion, the oscillatory convergence prevails. This oscillatory behavior appears to be dominant when the structure is elastic.

The relative errors of the mean values of the velocity and acceleration responses, at the roof level of the steel frame, are smaller than 3%, as shown in Figure 3-36(a). However, for the Gauss quadrature below five points, significant errors in the standard deviation were obtained, as shown in Figure 3-36(b). These errors are more pronounced for the shear demand and velocity of the structure. When the structure becomes inelastic and the largest variances of the input parameters are considered (the PGA3-CV3 scenario), the relative error quantities of the first two moments of the frame structure are smaller than their elastic counterparts, as shown in Figure 3-37. Furthermore, the oscillatory convergence, observed when the frame was elastic, disappears, and the error amplitude becomes constant for integration points greater than 5. Selected results of the output of the analyses conducted here are presented in Table 3-6 and Table 3-7.

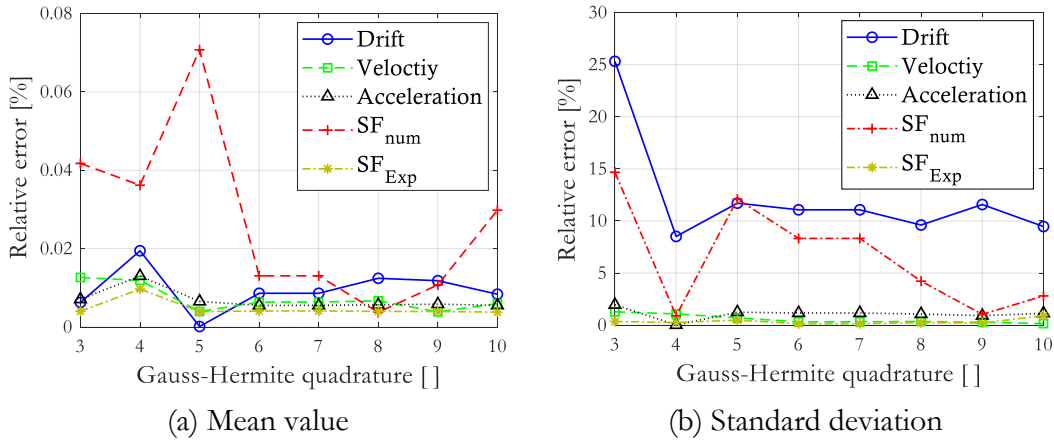


Figure 3-37: Relative error quantities versus the number of integration points for the PGA3-CV3 scenario

To conclude, although the fifth-order Gauss-quadrature is reasonably good for estimating the global sensitivity indices, the seventh-order Gauss-quadrature rule was chosen for the subsequent analysis. Herein, estimates from odd-sized integration points are only presented since they have favorable convergence properties in addition to the reduction in the number of model evaluations. The latter is consistent with the findings reported by Zhang (2013), on a corner peak function (Genz, 1987), where reliable sensitivity indices were obtained only after adopting a larger number of even integration points (Zhang & Pandey, 2014).

Table 3-6: Sensitivity indices of the maximum lateral displacement to the stiffness RV

CV1, PGA1	Gauss-Hermite integration points			
	n=3	n=5	n=7	n=9
Drift	0.9700	0.9719	0.9729	0.9725
Roof Acceleration	1.0000	0.9998	0.9999	1.0000
Shear Force	0.9700	0.9721	0.9731	0.9727

The PDF estimated, from the M-DRM formulation, using only three integration points failed to model the peak of the observed PDF. On the other hand, considering seven integration points, the mode of the PDF can be accurately captured. However, a slight mismatch in the tail of the PDF can be depicted in Figure 3-38.

Table 3-7: Sensitivity indices of different responses to the stiffness RV

CV1, PGA3	Gauss-Hermite quadrature				CV3, PGA3	Gauss-Hermite quadrature			
	n=3	n=5	n=7	n=9		n=3	n=5	n=7	n=9
Drift	0.7139	0.6999	0.6917	0.6893	Drift	0.1859	0.4041	0.4383	0.4164
Acceleration	0.4283	0.4364	0.4312	0.4285	Acceleration	0.6136	0.6370	0.6374	0.6367
Shear Force	0.9765	0.8445	0.8985	0.9763	Shear Force	0.8897	0.8843	0.8880	0.8908

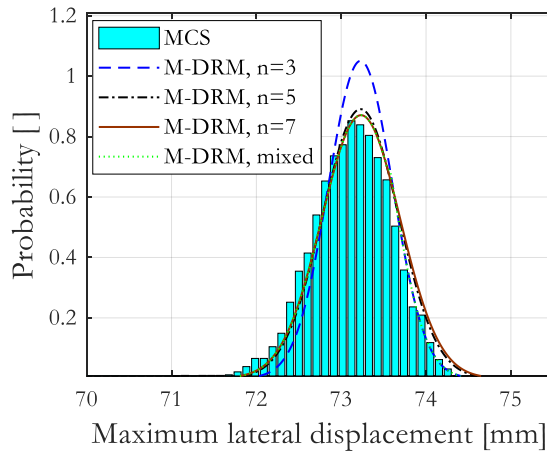


Figure 3-38: Comparison of PDFs estimated by the M-DRM and MCS methods for the PGA1-CV3 scenario

In Figure 3-38, the mixed M-DRM was obtained by constructing a mixed PDF, which is a piecewise equation built from the PDFs estimated using three and seven integration points. The mixed PDF matches the MCS result better than others. Thus, combining PDF estimates may also be considered in the future to narrow down discrepancies in the tail region. Nevertheless, it should be noted that the resulting PDF can be discontinuous, hence, it is not investigated any further.

The estimation of the probabilistic distribution of the maximum drift, presented in Figure 3-38, was conducted through the MaxEnt algorithm, using moments evaluated from the M-DRM method. However, it may also be pragmatic to estimate the PDF of a response function from the first two

moments, given the PDF is known beforehand. The additional burden in solving the fractional moments and the need to perform MaxEnt optimization can therefore be avoided. Here, the assumed-lognormal estimation of a PDF is performed using the first two integer moments of the M-DRM method. This simplified method is compared to the MaxEnt estimates in the subsequent discussions.

### 3.6.4.2 Results and discussions

#### 3.6.4.2.1 Case study one: Two RVs

In this case study, the stiffness and damping of the numerical substructure are the random variables of the steel frame while the experimental column is deterministic. The simulated studies, both the M-DRM and MCS, were conducted in MATLAB using the OpenSees-OpenFresco software framework as the analysis engine. First, input parameters are written into a Tcl file, and then the file is read in the master script of the OpenSees-OpenFresco. Here, the lateral displacement and shear force responses are mainly discussed. The first-order and total sensitivity indices are also examined thoroughly using different earthquake records, intensities of the input motion, and variances of the input variables.

The sensitivity indices of the maximum drift clearly show that the stiffness RV is the dominant parameter, as shown in Figure 3-39 and Figure 3-40. But the dominance of the structural stiffness reduces as the variance of the RVs increases, regardless of the intensity of the ground motion.

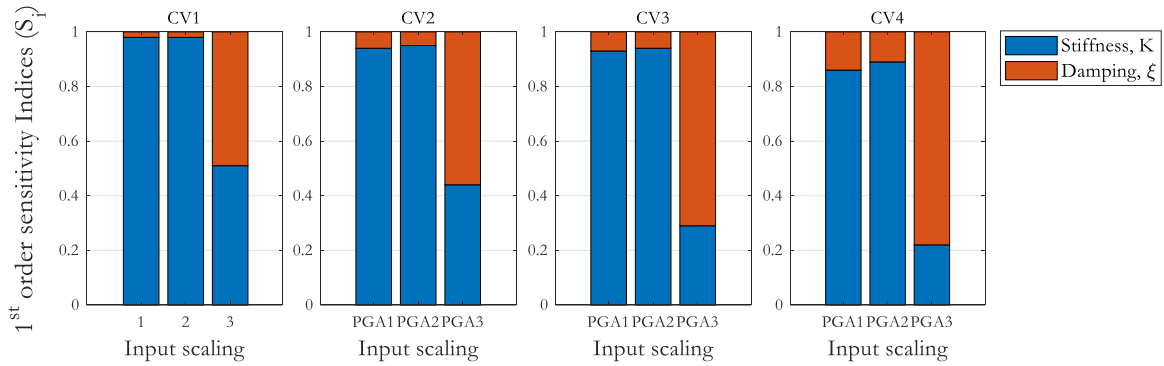


Figure 3-39: First-order sensitivity indices of the maximum drift response considering the El Centro earthquake input

In Figure 3-39, the maximum drift gains more sensitivity to the structural damping with increasing level of the input variances and increasing intensity of the El Centro (1940) input motion. Different observations were made when the steel frame was subjected to the Kobe (1995) earthquake (see Figure 3-40). Hence, the sensitivity indices are dependent on the characteristics of the earthquake records as well.

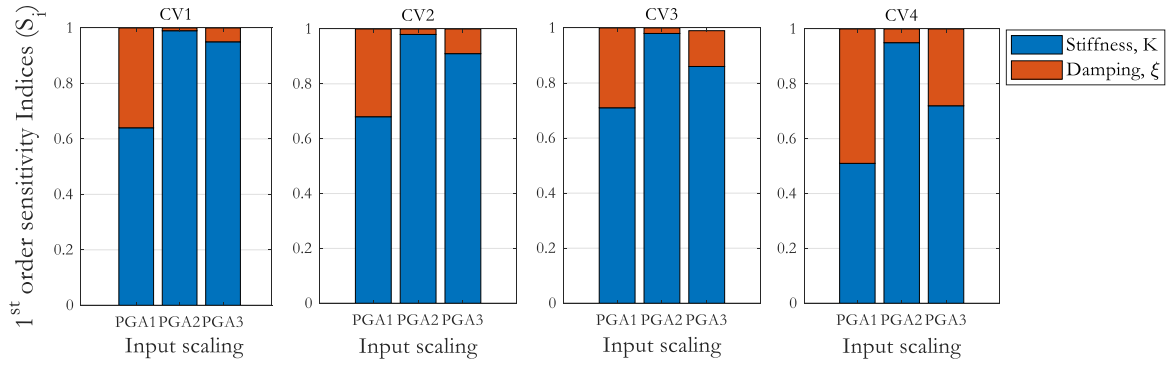


Figure 3-40: First-order sensitivity indices of the maximum drift response considering the Kobe earthquake input

In the current case study, the joint sensitivity indices of the maximum drift are very small, particularly for the low-to-medium variance of the input parameters. This absence of interdependence between the structural stiffness and damping is mainly attributed to the mass-proportional scheme adopted in modeling the structural damping.

On the other hand, the sensitivity indices of the maximum shear force of the experimental column resemble that of the maximum drift, as shown in Figure 3-41. Nonetheless, unlike the drift response, the sensitivity of the maximum shear force, to the structural damping, did not increase significantly with an increase in the intensity of the input motion. Contrary, the shear force of the experimental column appears to be more sensitive to changes in the variance of the RVs instead.

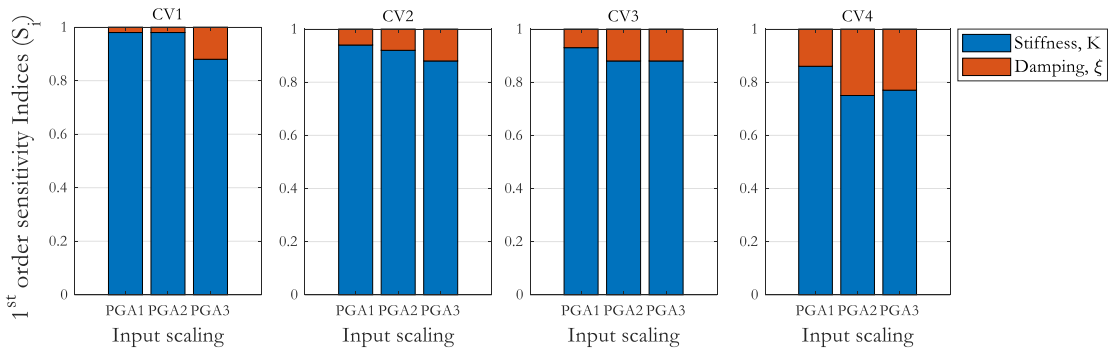


Figure 3-41: First-order sensitivity of the maximum shear force of the experimental column considering the El Centro earthquake input

Besides, it is also essential to look at the sensitivity of the higher-order kinematics, such as velocity and acceleration, as they may govern the restoring forces of experimental structures comprising rate-dependent devices. In the current case study, the relative roof acceleration of the steel frame is highly sensitive to its stiffness, when the intensity of the El Centro input motion is relatively low (i.e., PGA1 and PGA2, which correspond to the elastic and slightly inelastic responses, respectively). However, its sensitivity to the structural damping has a notable increase at the third intensity (PGA3) of the input motion, as shown in Figure 3-42. Furthermore, this increase gains more

amplitude as the variance of the RVs becomes increasingly larger.

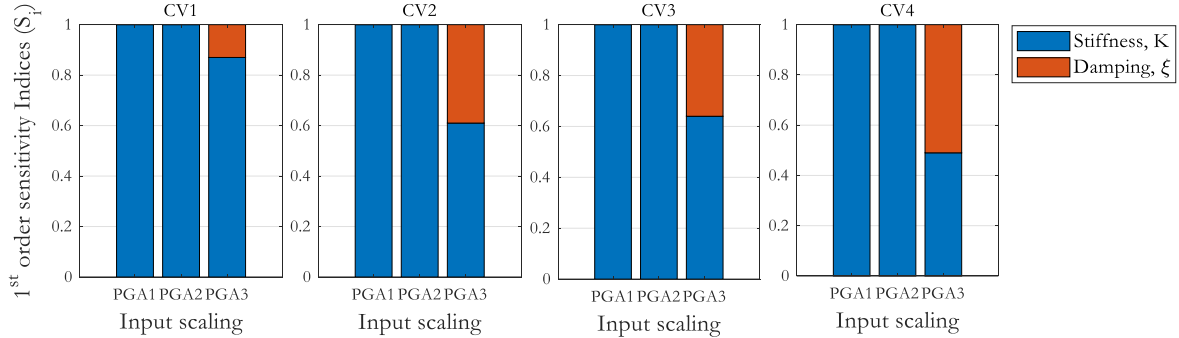


Figure 3-42: First-order sensitivity indices of the maximum roof acceleration considering the El Centro earthquake input

During the PDF estimation, using the MaxEnt algorithm, one thousand uniformly distributed samples were generated in the interval [-2, 2]. Each of these samples contains three coefficients of fractional moments (corresponding to three fractional moments). The Latin Hypercube Sampling (LHS) (Loh, 1996) was employed in generating these samples so as to ensure proper distribution of the fractional coefficients across all possible values, thus improving the sampling efficiency and computational cost. After evaluating the model at all the Gauss integration points, the fractional moments can be readily approximated using equation (3.45). Consequently, four sets, each one thousand, Lagrange multipliers are obtained as outputs. The first set of the LaGrange multipliers  $\lambda_0$  (the integral part of equation (3.44)) corresponds to  $\alpha_0$ , which is taken as zero in equation (3.43).

The MATLAB program records the  $k/l$  function calculated in each iteration, together with the estimated coefficients of fractional moments and Lagrange multipliers. The recorded data is then read in the subsequent step and the program searches for the global minimum of the  $KL$  vector. The  $\alpha$  and  $\lambda$  parameters that correspond to the global minimum of the  $KL$  vector become the optimal estimates to be used in equation (3.43). A tabular form of the procedure, applied to the current case study structure, is presented in Table 3-8.

Table 3-8: Application of MaxEnt to the maximum drift response for the PGA3-CV3 scenario considering the El Centro earthquake input

Trials	Generation			Estimation				
	$\alpha_1$	$\alpha_2$	$\alpha_3$	$\lambda_0$	$\lambda_1$	$\lambda_2$	$\lambda_3$	$k/l$
1	-1.7286	0.6809	0.7920	708.9957	-36.5016	-247.5749	130.0399	1.1380
2	0.9075	0.0008	-0.9908	708.9950	4.2485	-1152.1735	16844.9300	1.1303
:	:	:	:	:	:	:	:	:
555	<b>0.9212</b>	<b>1.5192</b>	<b>1.9087</b>	<b>654.2166</b>	<b>906.6320</b>	<b>-180.6437</b>	<b>20.6783</b>	<b>0.5521</b>
:	:	:	:	:	:	:	:	:
1000	-0.5491	-0.3650	-1.5010	708.9903	17638.1713	-11393.9442	454.8975	1.1475

The fractional moments corresponding to the three fractional coefficients can be now determined,

as presented in Table 3-9. In this case study, fractional moments fewer than three were able to capture the desired probabilistic distribution, nevertheless, it is recommended to use three or more fractional moments for dynamic analysis.

Table 3-9: MaxEnt estimates of the maximum drift for the PGA3-CV3 scenario considering the El Centro earthquake input

Fractional moments	$i$	0	1	2	3
3	$\lambda_i$	654.22	906.63	-180.64	20.68
	$\alpha_i$	-	0.9212	1.5192	1.9087
	$M_i$	-	52.3774	684.1610	3648.6819

Finally, the probabilistic density function of the maximum drift of the steel frame,  $r(z)$ , can be constructed using the above estimates, which reads:

$$r(z) = e^{-\{654.22 + 906.63z^{0.9212} - 180.64z^{1.5192} + 20.68z^{1.9087}\}} \quad (3.47)$$

Figure 3-43 shows that the PDF estimated by the MaxEnt algorithm matches the observed distribution (MCS) accurately. The assumed-lognormal distribution, which utilizes the mean and standard deviation estimates of the M-DRM method, is also in good agreement with the observed data. This suggests that the lognormal distribution can suitably model the maximum drift of the steel frame, nonetheless, we cannot generalize about the goodness of fit of the assumed-lognormal distribution as it may fail to capture distributions of complex nature, for example, the bimodal distribution.

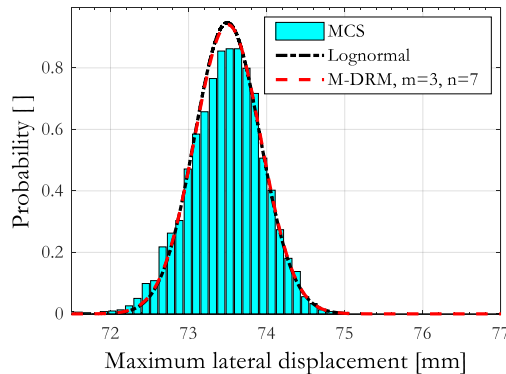


Figure 3-43: PDFs of the maximum drift estimated by the MCS, assumed-lognormal, and M-DRM methods for the PGA3-CV3 scenario considering the El Centro earthquake input

The Probability of Exceedance (POE) of the inter-story drift in structures is defined as the percent probability that the global drift limit is exceeded in 50 years. Both EC8 (sections 4.4.2.2 and 4.4.3.2) and AISC have two deformation criteria, namely the ‘second-order effect’ and the ‘inter-story drift’, that need to be satisfied for structures to comply with the limits stipulated by the respective norms.

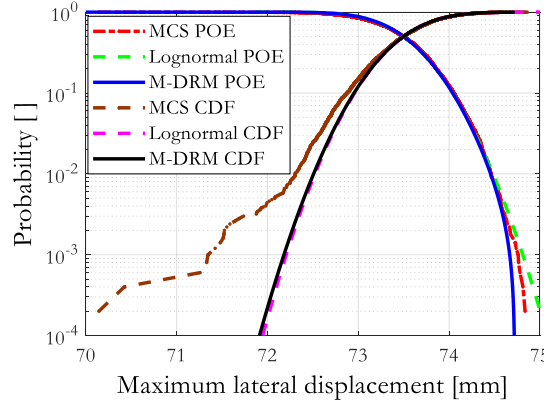


Figure 3-44: POE and CDF of the maximum drift for the PGA3-CV3 scenario considering the El Centro earthquake input

Considering I or II importance classes, EC8 stipulates the maximum drift ratio to be in the interval 1-2% of the floor's height depending on the ductility of cladding materials attached to the structural elements. However, the structural collapse of steel frames takes place at large drift ratios (Dimitrios, 2012). Assuming the collapse of the case study structure to occur at a drift ratio equal to 4.135% (74.63 mm of drift), the POEs were estimated as  $1.78 \times 10^{-3}$  and  $2.0 \times 10^{-3}$  by the MCS and the M-DRM, respectively. Besides, the POE estimated by the M-DRM was found to be accurate for probabilities as low as  $8.0 \times 10^{-3}$ , as shown in Figure 3-44, which can be interpreted as 99.2% of non-exceedance probability. Admittedly, the M-DRM estimates deviated from the observed cumulative distribution at low probabilities. Furthermore, the PDF constructed assuming lognormal distribution as well failed to model the tail of the probability distribution.

Table 3-10: Relative error of the maximum lateral displacement estimate of the M-DRM for the PGA3-CV3 scenario considering the El Centro earthquake input

$CV_k=5\%$	Maximum lateral displacement [mm]		
$\xi=2\%, CV_\xi=10\%$	MCS ( $5 \times 10^3$ trials)	M-DRM	Relative error [%]
Mean	73.4750	73.4988	0.0323
Standard deviation	0.4708	0.4213	10.495
Coefficient of variation	0.0064	0.0057	10.436

Compared to the POE, the relative error quantity appears to be a useful metric for comparison, because POE can be stringent in regions of mismatch. The relative errors presented in Table 3-10 proclaim the good agreement between the MCS and M-DRM estimates. The relative error metric of an  $i$ th moment is calculated as:

$$rel_{err}^i = \frac{|M_{M-DRM}^i - M_{MCS}^i|}{M_{MCS}^i} \quad (3.48)$$

where  $M_{MCS}^i$  and  $M_{M-DRM}^i$  are the  $i$ th observed and M-DRM moments, respectively.

The maximum shear force of the experimental column has a narrow distribution since the variance

of the input variables is comparatively small. Despite this, the MaxEnt algorithm was able to accurately capture its observed probabilistic distribution. Besides, the probabilistic distribution of the maximum base shear is in good agreement with the observed distribution, as shown in Figure 3-45. The moments estimated by the M-DRM are also in good agreement with the output of the MCS method, with relative error quantities  $rel_{err}$  less than 1%.

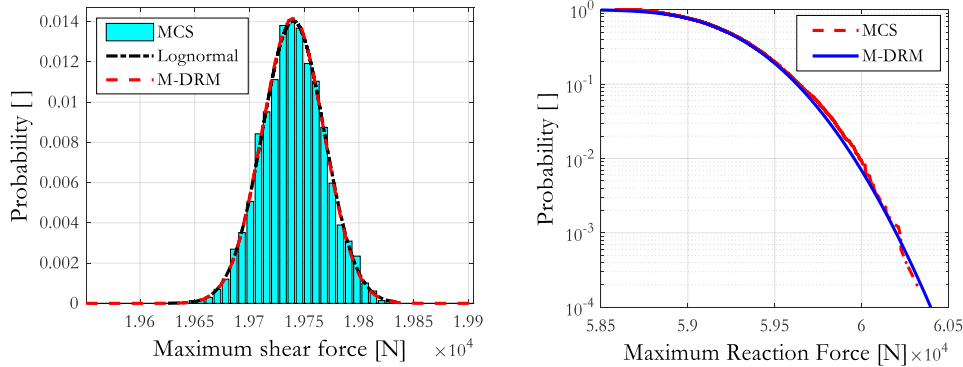


Figure 3-45: PDFs of the maximum shear force of the experimental column estimated by the MCS, assumed-lognormal and M-DRM (left); and POE of the total shear demand (right) for the PGA3-CV3 scenario considering the El Centro earthquake input

Initially, the MaxEnt algorithm gave an erroneous (overshooting) variance estimate but an accurate mean value of the maximum shear force of the experimental element. This erroneous estimation was the result of constraining the fractional moment coefficients in the interval [-2, 2]. After changing units of the maximum shear force to kilo Newton units, instead of Newton units, the problem could be resolved, because the shear force vector supplied to the MaxEnt algorithm became sufficiently small that the observed PDF can be accurately captured, as shown in Figure 3-46, using the fractional moments in the interval [-2, 2].

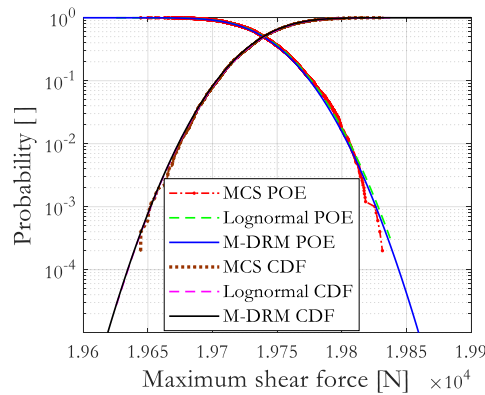


Figure 3-46: POE and CDF of the maximum shear force of the experimental column for the PGA3-CV3 scenario considering the El Centro earthquake input

Hence, it is advisable to work with a smaller amplitude of response quantities if the fractional coefficients are restricted to the interval [-2, 2], otherwise, an optimal interval must be defined. The

assumed-lognormal distribution shown in Figure 3-46 was also able to model the important characteristics of the observed PDF.

Table 3-11: Relative errors of the M-DRM estimates of the maximum shear force of the experimental column, for the PGA3-CV3, considering the El Centro earthquake input

$CV_k=5\%$ $\xi=2\%, CV_\xi=10\%$	Maximum shear force of experimental column [N]		
	MCS ( $5 \times 10^3$ runs)	M-DRM	Relative error [%]
Mean	19740.03	19739.54	0.0025
Standard deviation	28.4359	28.1894	0.8669
Coefficient of variation	0.1441%	0.1428%	0.9002

In the current case study, the maximum drift of the steel frame has a small variance (a narrow PDF). Thus, investigating a large variance of the maximum drift is necessary to attest the potential of the M-DRM technique. This was accomplished by changing the mean and coefficient of variation of the damping coefficient to be 5% and 20%, respectively. The remaining parameters were kept the same except that the Northridge 260 (1994) earthquake, scaled to 0.471 g PGA, was the input motion.

Table 3-12: MaxEnt estimates at  $\xi=5\%$ ,  $CV_\xi=20\%$ , and  $CV_k=5\%$  considering the Northridge 260 (1994) earthquake input scaled to 0.471 g PGA

PDF coefficients of the maximum lateral displacement [mm]					
Fractional moments	$i$	0	1	2	3
$m=3$	$\lambda_i$	594.6769	-53.196	-1.9469	25.9389
	$\alpha_i$		1.0606	1.5717	1.2739
	$M_i$		168.9	2005.7	474.3

The PDF estimated from the M-DRM method shows a remarkable agreement with the observed data, as shown in Figure 3-47. In this scenario, the M-DRM moment estimates of the maximum drift are exceptionally accurate (see Table 3-13). These errors are far small compared to errors

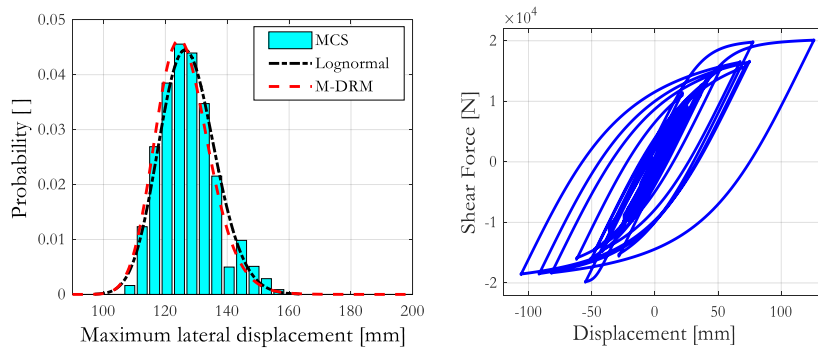


Figure 3-47: PDFs of the maximum drift, at  $\xi=5\%$ ,  $CV_\xi=20\%$  and  $CV_k=5\%$ , considering the Northridge earthquake, scaled to 0.471 g PGA, estimated by the MCS, assumed-lognormal and M-DRM methods (left); and the hysteresis of the experimental column at the median values of the RVs (right)

reported by Balomenos & Pandey (2016). Hence, in the presence of large input variance, the M-DRM method can yield reliable results as well. The assumed-lognormal distribution of the maximum drift was not able to accurately model the mode of the PDF, however, it approximately matches the shape of the observed distribution. On the other hand, the observed tail probabilities could not be accurately modeled by both methods.

Table 3-13: Relative error of the M-DRM estimates at  $\xi=5\%$ ,  $CV_\xi=20\%$  and  $CV_k=5\%$  considering the Northridge earthquake input scaled to 0.471 g PGA

$CV_k=5\%$ , $CV_\xi=20\%$ , $\xi=5\%$	Maximum lateral displacement [mm]		
	MCS ( $5 \times 10^3$ runs)	M-DRM	Relative error [%]
Mean	127.3875	127.3035	0.0659
Standard deviation	9.0941	9.0221	0.7917
Coefficient of variation	0.0714	0.0709	0.8392

Furthermore, although the PDF estimated using the M-DRM could not exactly match the peak and tail of the observed distribution of the maximum shear force of the experimental column, the first two moments were accurately determined. In this analysis, the columns reached a ductility ratio  $\mu>2$ . Although the overall shape of the observed PDF could be reproduced, the M-DRM estimate of the POE is slightly larger than the observed POE. Likewise, the M-DRM estimate of the POE of the right tail has a notable discrepancy compared to the observed values, as shown in Figure 3-48. Similar characteristics are displayed by the maximum drift POE estimates of the maximum drift (see Figure 3-49). The experimental errors that were added during the simulation may contribute to these deviations presented in Table 3-15.

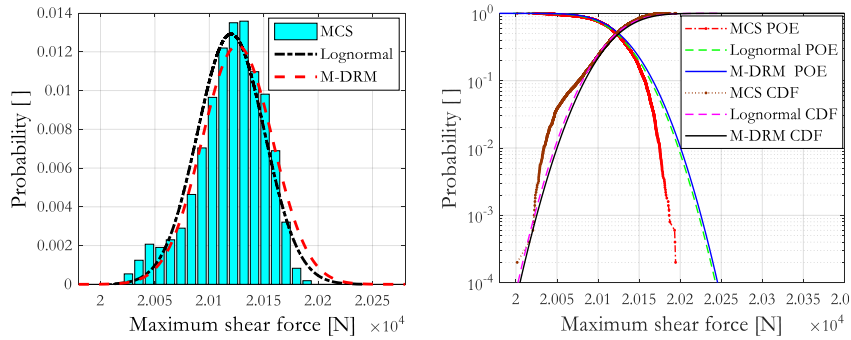


Figure 3-48: PDFs of the maximum shear force of the experimental column, at  $\xi=5\%$  and  $CV_\xi=20\%$ ,  $CV_k=5\%$ , considering the Northridge earthquake input, scaled to 0.471 g PGA, estimated by the MCS, assumed-lognormal and M-DRM methods (left); and POE and CDF estimates (right)

Table 3-14: MaxEnt estimates at  $\xi=5\%$ ,  $CV_\xi=20\%$  and  $CV_k=5\%$  considering the Northridge earthquake input scaled to 0.471 g PGA

PDF coefficients of the maximum shear force of the experimental column					
Fractional moments	$i$	0	1	2	3
$m=3$	$\lambda_i$	550.2808	3927.09	-41735.67	112112.16
	$\alpha_i$		1.6855	1.1278	0.5661
	$M_i$		157.5833	29.5374	5.4710

Table 3-15: Relative error of the M-DRM estimates at  $\xi=5\%$ ,  $CV_\xi=20\%$  and  $CV_k=5\%$  considering the Northridge earthquake input scaled to 0.471 g PGA

$CV_k=5\%$ ; $CV_\xi=20\%$ $\xi=5\%$	Maximum shear force of the experimental column [N]		
	MCS ( $5 \times 10^3$ runs)	M-DRM	Relative error [%]
Mean	20119.00	20122.40	0.0157
Standard deviation	31.288	32.360	3.4258
Coefficient of variation	0.0016	0.0016	~0%

Furthermore, the sensitivity indices of the maximum lateral displacement were found to be equally shared between the stiffness and damping coefficient due to the combined effect of the large intensity of input motion and the large variance of the damping coefficient. For brevity, the results of the sensitivity analysis are not presented here.

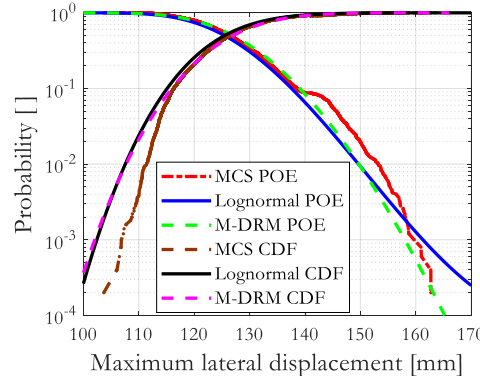


Figure 3-49: POE and CDF of the maximum lateral displacement at  $\xi=5\%$ ,  $CV_\xi=20\%$  and  $CV_k=5\%$  considering the Northridge earthquake input scaled to 0.471 g PGA

### 3.6.4.2.2 Case study two: Three RVs

In the first case study, the reliability and sensitivity of the steel frame, in simulated hybrid testing, were examined considering two random variables. To further explore the capability of the proposed technique, a second case study, which utilizes the same reference frame, is examined, subsequently, by modeling three random variables, namely stiffness, damping, and yield stress of the numerical elements. The coefficients of variation of all the random variables except the stiffness RV were assumed to be 10%, and the simulated hybrid tests of the steel frame were performed using the El Centro (1940) earthquake record.

Global sensitivity indices at the PGA1, PGA2, and PGA3 were estimated to appreciate the shift in the most critical RV, to the response of the frame, as the columns become increasingly inelastic. At the low intensity of the input motion (PGA1), all the response parameters studied, comprising the maximum lateral displacement and the maximum shear force of the numerical and experimental columns, were highly sensitive to the stiffness of the structure. However, at the intermediate level (PGA2), the columns start to yield, but the maximum drift remains very sensitive to changes in the stiffness of the structure. Contrary, the shear force of the numerical column becomes more sensitive to changes in the yield stress. On the other hand, the shear demand of the experimental column is sensitive to the stiffness of the structure, both in PGA1 and PGA2 intensities, because its initial stiffness is utilized throughout the analysis.

The order of sensitivity has completely changed when the large intensity of input motion (PGA3) was applied. The maximum drift response ( $\delta_{max}$ ) and the maximum shear demand of the numerical column ( $SF_{max}^{NumCol}$ ) became more sensitive to changes in the yield stress. The dominance of the initial stiffness on the shear demand of the experimental column ( $SF_{max}^{ExpCol}$ ) was also partially shared by the yield stress, as shown in Figure 3-50. The sensitivity of the structural responses to the damping of the structure is small, and its importance appears to, slightly, degrade with increasing intensity of input motion. Besides, the sensitivity indices of the total shear demand (total reaction force ( $SF_{max}^{Tot}$ )), which combines the characteristics of the experimental and numerical elements, closely resembles the pattern observed in the numerical columns. This signifies that the responses of the structure are primarily governed by the characteristics of the numerical elements. The above discussions are summarized in Figure 3-50.

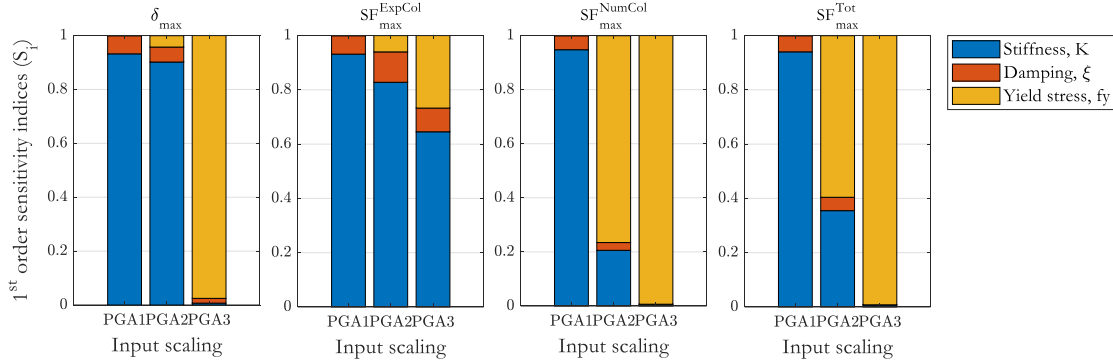


Figure 3-50: Global sensitivity indices of the steel frame at  $CV_k=5\%$ ,  $CV_\xi=10\%$  and  $CV_{f_y}=10\%$  considering the El Centro earthquake input

Table 3-16: Relative error of the M-DRM estimates considering the unscaled El Centro earthquake input

$CV_k=5\%$ , $CV_{fy}=10\%$ $\xi=2\%$ , $CV_\xi=10\%$	Maximum lateral displacement [mm]		
	MCS ( $5 \times 10^3$ runs)	M-DRM	Relative error [%]
Mean	73.5042	73.6811	0.2407
Standard deviation	2.5200	2.6886	6.6920
Coefficient of variation	0.0343	0.0365	6.4140

In the case study, the potential of the method in terms of relative error quantities and probability distribution fitting was also investigated. The M-DRM estimates of the first two moments of the maximum drift have relative errors smaller than 7%.

Table 3-17: MaxEnt estimates considering the unscaled El Centro earthquake

Fractional moments	$i$	Maximum lateral displacement [mm]			
		0	1	2	3
$m=3$	$\lambda_i$	274.5994	-7950276.90	15648030.17	-5272165.81
	$\alpha_i$		-1.6744	-1.7148	-1.6618
	$M_i$		7.56e-04	6.35e-04	7.97e-04

The optimal fractional coefficients, presented in Table 3-17, are all non-positive terms. Consequently, the corresponding moments are very small and the LaGrange multipliers are large; however, the estimated PDF function has a good agreement with the observed distribution. Besides, the PDF estimated by the M-DRM method has superior performance compared to the assumed-lognormal distribution, as shown in Figure 3-51.

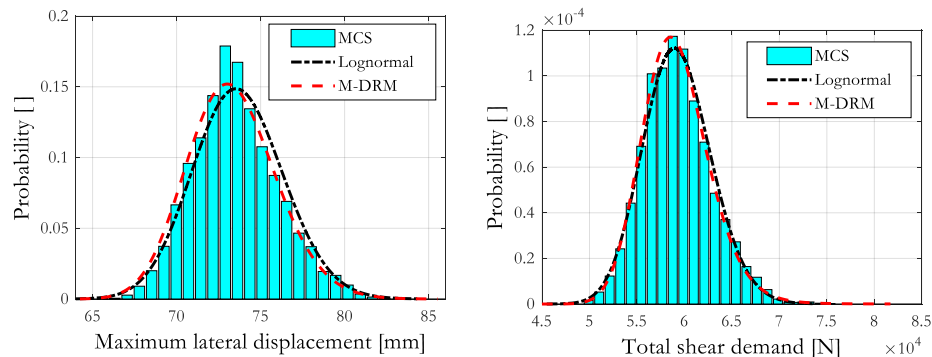


Figure 3-51: PDFs of the maximum drift (right) and maximum shear force (left) estimated by the MCS, assumed-lognormal; and M-DRM methods considering the unscaled El Centro earthquake input motion

Like the first case study, the observed PDF was assembled from  $5 \times 10^3$  model evaluations of the Monte Carlo method. The total shear demand of the steel frame, shown in Figure 3-52, was also accurately modeled by the M-DRM, with very small relative errors. The peak and tail of the observed

distribution are also in good agreement with the estimated PDF. Nonetheless, a closer look at the POE of the total shear demand could be beneficial to investigate the discrepancy between the estimated and exact probabilities.

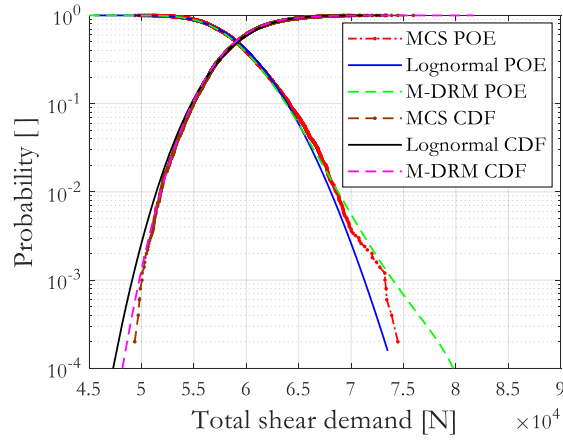


Figure 3-52: POE and CDF estimates of the total shear demand considering the unscaled El Centro earthquake input motion

Looking at the POE estimates, probabilities greater than  $10^{-3}$  of the total shear demand can be accurately estimated. Using the PDF estimate for the maximum drift, conformity with code provisions for the limit-state criterion can also be checked. For example, taking  $h/24$  as the drift limit, the POE estimate is  $2.382 \times 10^{-1}$  from the MCS,  $2.312 \times 10^{-1}$  from the M-DRM, and  $2.822 \times 10^{-1}$  from the assumed-lognormal distribution.

Table 3-18: Relative error of the M-DRM estimates considering the unscaled El Centro earthquake input motion

$CV_k=5\%$ , $CV_{f_y}=10\%$ $\xi=2\%$ , $CV_\xi=10\%$	Total shear demand [N]		
	MCS ( $5 \times 10^3$ runs)	M-DRM	Relative error [%]
Mean	59316	59266	0.0843
Standard deviation	3593.6	3573.4	0.5621
Coefficient of variation	0.0606	0.0603	0.4950

The effect of the number of iterations of the MaxEnt algorithm was also explored in this work to build confidence about the optimality of the number of iterations needed for efficient estimation. It should be noted that the coefficients of a PDF estimated from a different number of iterations may not be unique; however, the resulting PDFs are identical. Generalization about the optimum number of iterations, for the MaxEnt algorithm, cannot be made at this stage, but 1000 iterations may serve as a starting point for simple to moderately complex structures. The complexity of a problem may be quantified, qualitatively, by the number of structural members, the number of random variables, and the inelasticity level of structural members.

Furthermore, the number of fractional moments,  $m$ , necessary for estimating the probability density

function can only be selected by a trial-and-error method. Increasing the number of fractional moments may increase the accuracy of estimation while increasing the computational cost of the estimation. In general, fractional moments greater than three may be used to model non-traditional PDFs such as multimodal distributions. Nonetheless, using a large number of fractional moments may introduce spurious estimates; therefore, it is pragmatic to consider various  $m$  values and select one that best minimizes the  $k_l$  function (Inverardi & Tagliani, 2003). In this work, three fractional moments were found to be optimal for the case study structure.

### 3.6.5 Experimental validation of M-DRM in hybrid tests

#### 3.6.5.1 Introduction

All the discussions on the M-DRM modeling, until now, were derived from simulated studies and the Monte Carlo method was used in establishing a benchmark for comparing the outcomes of the M-DRM method. However, the experimental validation of the proposed reliability and global sensitivity studies in hybrid tests, which use the M-DRM technique, is interesting for future applications and, hence, extended here.

The experimental validation was carried out in a collaborative work using hybrid simulation experiments conducted by Abbiati et al. (2020). The experimental work was originally developed to validate global sensitivity analysis in hybrid tests using the sparse PCE modeling technique. In the experimental campaign, four random variables were chosen to define the uncertainty of the prototype structure. To use this experimental test for validating the M-DRM technique, the conflict in modeling the random variables needs to be resolved. In detail, the set of random variables generated during the PCE analysis are not identical to that of the M-DRM method. Therefore, the direct utilization of these hybrid experiments is not possible. Nonetheless, the outcomes of the PCE-based sensitivity study can be used as a benchmark for validating the M-DRM method.

#### 3.6.5.2 Case study structure

The prototype structure, shown in Figure 3-53, is a simply supported beam coupled with two linear-elastic rotational springs at the supports and a dashpot damper attached to the freely sliding support of the beam. The beam is subjected to a ground motion excitation  $a_g(t)$  acting on the y-axis. Two rotational masses at the supports,  $J_1=J_2=0.9 \text{ kgm}^2$ , and one translational mass at the right support,  $M=20,000 \text{ kg}$ , define the inertia of the prototype structure. To prevent the excitation of the axial mode of the structure, a large viscous damping,  $C=300,000 \text{ Ns/m}$ , was assigned to the dashpot.

The beam, 0.47 m long, made from an iron plate,  $E=100 \text{ GPa}$ , has a  $2 \times 200 \text{ mm}^2$  cross-sectional area. During the hybrid test, the full scale of the beam element ( $PS$ ) was experimentally tested while the two rotational springs ( $NS$ ) at the supports were numerically modeled. The hybrid tests were conducted at 50 time-scale factor; consequently, the inertia of the  $PS$  was incorporated into the numerical program. The support rotations of the prototype structure,  $u_1$  and  $u_2$ , and the translational

DOF,  $u_3$ , are retained by the hybrid model, as shown in Figure 3-53. The consistent mass matrix of the PS was condensed into the DOFs that are retained by the hybrid model. The inertial action of the ground motion is coupled to the rotational DOFs,  $u_1$  and  $u_2$ , through the off-diagonal entries of the reduced mass matrix.

The prototype structure is subjected to a pulse-like ground velocity characterized by  $V_p$  and  $T_p$  that represent its amplitude and period, respectively. The velocity-pulse is modulated by a pulse function made from a truncated cosine function of period  $\gamma T_p$ .

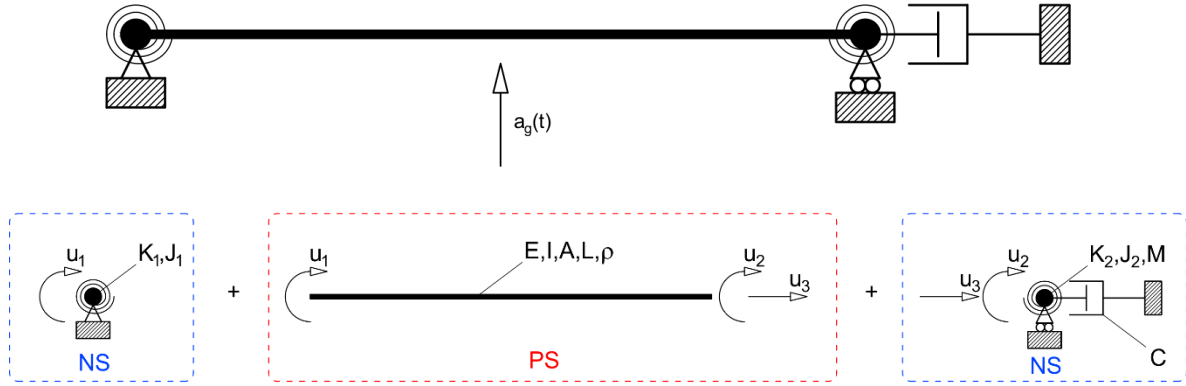


Figure 3-53: Substructuring the prototype structure into physical (PS) and numerical (NS) parts (after Abbiati et al., 2020)

The maximum velocity,  $V_p$ , of the pulse function occurs at  $t_{max,p} = \gamma T_p / 2$ . The first derivative of the velocity-pulse, which is an intuitive representation for a near-fault earthquake, defines the ground motion input  $a_g(t)$  (Abbiati et al., 2020). The equation for the velocity-pulse reads:

$$V_g(t) = \left\{ \frac{V_p}{2} \cos \left( 2\pi \left( \frac{t - t_{max,p}}{T_p} \right) + \nu \right) - \frac{D_r}{\gamma T_p} \right\} \left\{ 1 + \cos \left( \frac{2\pi}{\gamma} \left( \frac{t - t_{max,p}}{T_p} \right) \right) \right\} \quad (3.49)$$

In the above equation,  $\nu$  is the phase angle between the cosine wave and pulse function;  $D_r$  is the residual displacement at the end of the velocity pulse which is given by:

$$D_r = V_p T_p \frac{\sin(\nu + \gamma\pi) - \sin(\nu - \gamma\pi)}{4\pi^2(1 - \gamma^2)} \quad (3.50)$$

The velocity-pulse is defined for  $t \in [0, \gamma T_p]$ . Taking  $\gamma = 2$ ,  $t_{max,p} = \gamma T_p / 2$  and  $\nu = 0.1$  radians, the spectral acceleration of the velocity-pulse, at mean values of the random variables, can be determined as shown in Figure 3-54. The random variables of the hybrid model comprise two parameters of stiffness,  $k_1$  and  $k_2$ , and another two parameters of the input ground motion,  $V_p$  and  $T_p$ .

The global sensitivity analysis was evaluated considering the absolute maximum value of the support rotation,  $u_{1,max}$ , and the support moment,  $r_{1,max}$ . Hence, subsequent discussions of Sobol indices refer to the  $\{u_{1,max}, r_{1,max}\}$  response quantities. For the interval of random variables presented in

Table 3-19 and considering  $k_1 = k_2$ , the first bending mode of the prototype structure has periods between 0.45 s and 0.68 s. This interval coincides with the 0.66-2.0 s range of period of the carrier signal of the velocity-pulse (Abbiati et al., 2020). Therefore, the tuning between the period of excitation and the first vibration mode of the prototype structure affects the amplification of the  $u_1$  and  $r_1$  responses.

Table 3-19: Random variables of the hybrid model

Parameter	PDF type	Minimum value	Maximum value	units
$V_p$	uniform	3.5	4.5	m/s
$T_p$	uniform	0.5	1.5	s
$k_1$	uniform	20	120	Nm/rad
$k_2$	uniform	20	120	Nm/rad

A total of 200 hybrid tests were conducted using the samples generated by a Sobol sequence. This sample generation is therefore consistent with the PCE-based analysis but not with the M-DRM method. In the M-DRM technique, the Gauss-Legendre quadrature rule was adopted since it is suitable for uniformly distributed variables.

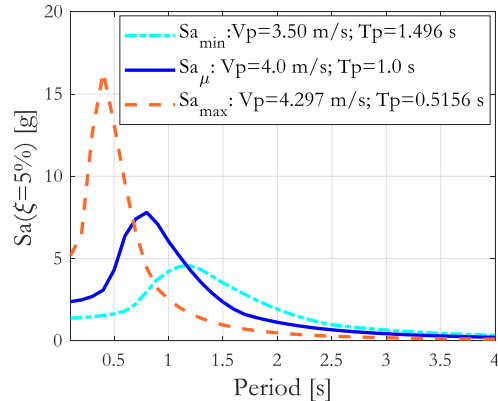


Figure 3-54: Spectral acceleration of the velocity-pulse function

### 3.6.5.3 Global sensitivity analysis through Polynomial Chaos Expansion

The Polynomial Chaos Expansion (PCE) can be simply described as a spectral decomposition method that projects a model response into a functional basis of orthonormal multivariate polynomials in the input variables (Berveiller et al., 2006). Sobol sensitivity indices are the by-product of the PCE modeling. They can be obtained by post-processing the coefficients of the PCE polynomials without additional computations (Sudret, 2008). The sparse PCE model is ideal to surrogate structural responses in hybrid testing since the method is closely related to the variance decomposition method. In Abbiati et al. (2020), the sparse adaptive least-squares minimization, based on the Least Angle Regression (LAR), was adopted in computing Sobol indices of  $u_{1,max}$  and  $r_{1,max}$ . In the PCE-based global sensitivity study conducted by Abbiati et al. (2020), 150 of those sample sets were used for training the four-disjoint PCE models while the remaining 50 were used

in the evaluation phase. Herein, the outcomes of the PCE-based analysis are presented in parallel to the M-DRM output in order to make the analogy between the two techniques.

### 3.6.5.4 Test setup

A stiff loading frame that is equipped with four electro-mechanical actuators was used to apply the two rotations,  $u_1$  and  $u_2$ , and the axial displacement,  $u_3$ , to the physical substructure. The test rig was designed to accommodate test specimens with a footprint of around  $200 \times 500 \text{ mm}^2$  and a thickness of 1-3 mm. The architecture adopted for executing the hybrid tests is portrayed in Figure 3-55. The same figure shows the physical substructure when mounted on the test rig. A detailed description of the software modules and the interfacing adopted between the servo-valve and control software can be found in Abbiati et al. (2020).

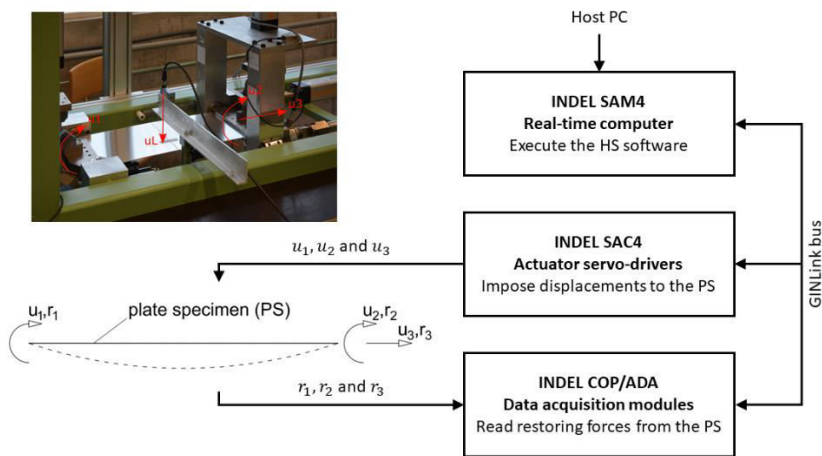


Figure 3-55: Test rig and software architecture for hybrid testing (after Abbiati et al., 2020)

At each time-step of the simulation (50 times the actual time-step), the numerical software (for details refer to Abbiati et al. (2020)) calculates the  $u_1$ ,  $u_2$  and  $u_3$  commands which are imposed on the plate specimen using the four actuators. The restoring forces measured by force transducers are then returned to the hybrid simulation software and the coupled equation of motion is solved. The detailed configuration of the test rig and the arrangement of actuators can be found in appendix 1.

### 3.6.5.5 Global sensitivity analysis using M-DRM method

The Global Sensitivity Analysis (GSA) was conducted using the M-DRM approach after evaluating the response of the hybrid model at cut-off points. The responses at the cut-off points, calculated from equation (3.24), can be combined using the multiplicative approach, presented in equation (3.25), while estimating the response of the hybrid model. In the absence of model responses at the cut-off points, which is the case in the current validation work, it can be estimated from a response surface model of the problem. Therefore, the PCE meta-model of the case study can be adopted for interpolating the responses needed for conducting the M-DRM GSA. Furthermore, noise was

added during the interpolation, consistent with the measurements during the hybrid tests. Nonetheless, the above statement is valid only if the model responses from the 200 tests are within a tolerable margin of error compared to the responses calculated using equation (3.25). In equation (3.25), the responses of the hybrid model at cut-off points are thus obtained by interpolation from the PCE meta-model. In this work, the response of the prototype structure at the cut-off points was interpolated using the UQLAB, a MATLAB toolbox for uncertainty quantification developed at ETH, Zurich (Stefano Marelli, 1996). At this stage, it is worth recalling that only the univariate approximation of the M-DRM was discussed until now, while the bivariate approximation of the M-DRM method was also used herein. For the sake of brevity, the formulation for the bivariate approximation is not included here, but it is expounded in Zhang (2013) and one can refer to it in appendix 2.

The responses of the hybrid model evaluated using the bivariate approximation are plotted in Figure 3-56 together with the univariate estimates. The univariate estimates of  $u_1$  and  $r_1$  achieved good matching with their corresponding measured quantities. The improvement in accuracy when using the bivariate estimation, which is depicted in Figure 3-56, is by far not comparable to the extra computational effort needed. In detail, the  $nN$  number of mechanistic model evaluations needed in the univariate M-DRM are small compared to the  $nN^2$  model computations of the bivariate M-DRM, where  $n$  and  $N$  are the number of random parameters of the hybrid model and the Gauss quadrature order, respectively. Hence, the univariate formulation of the M-DRM is considered in this validation work.

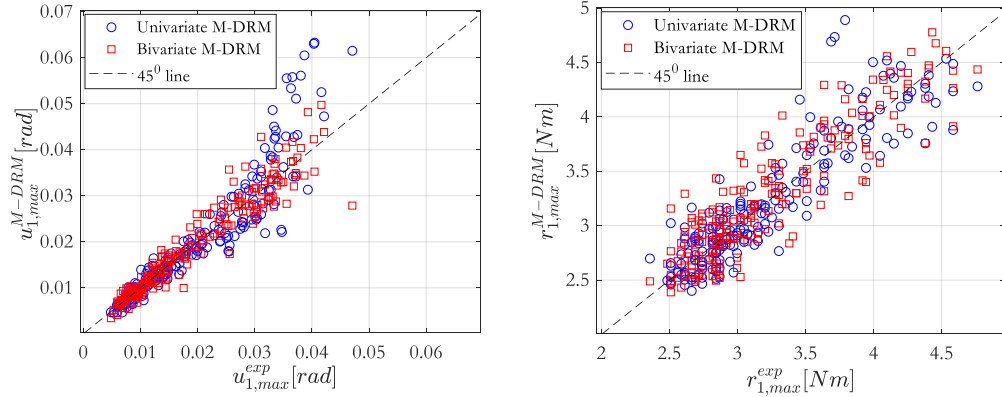


Figure 3-56: Comparison between measured and M-DRM estimates of  $u_{1,max}$  and  $r_{1,max}$  responses

### 3.6.5.6 Results of M-DRM method and comparison with PCE-based GSA

The first-order and total Sobol indices of the M-DRM method were computed for the interval of [3, 14] Gauss-Legendre order. The M-DRM estimates of the mean  $\hat{\mu}$  and variance  $\hat{\sigma}^2$  of  $u_1$  are presented in Figure 3-57 along with the PCE-based estimates. The results of the PCE meta-model are presented as a function of the number of hybrid experiments whereas the output of the M-

DRM is plotted against the order of the quadrature rule. Recalling the **Nn** rule, where  $n=4$ , the quadrature order can be converted into the number of hybrid experiments.

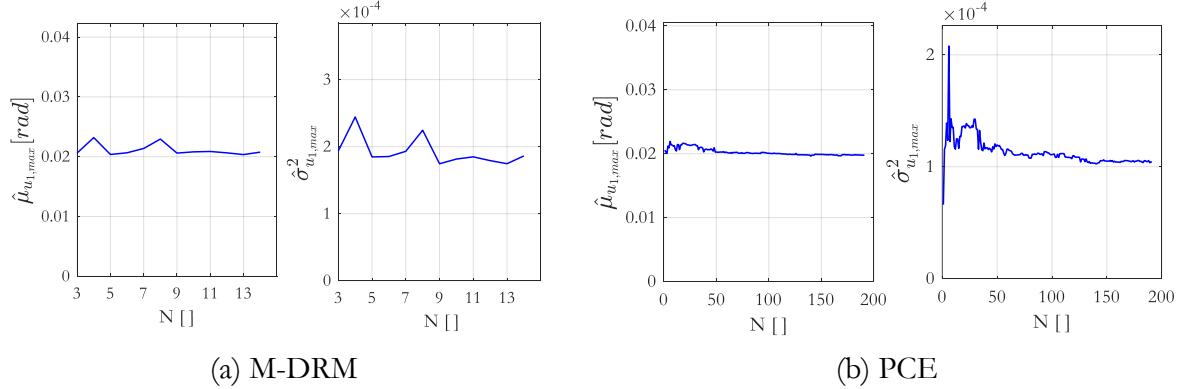


Figure 3-57: Convergence of the mean and variance estimates of  $u_{1,max}$  with increasing number of hybrid tests

In Figure 3-57, the mean value estimate,  $\hat{\mu}_{u_{1,max}}$ , of the M-DRM agrees well with the PCE estimate. On the other hand, the variance estimates of both methods are characterized by fluctuations, for a small number of experiments, and slow convergence; but the overall matching between them is reasonable. The same arguments are valid for the left-support moment  $r_1$  shown in Figure 3-58.

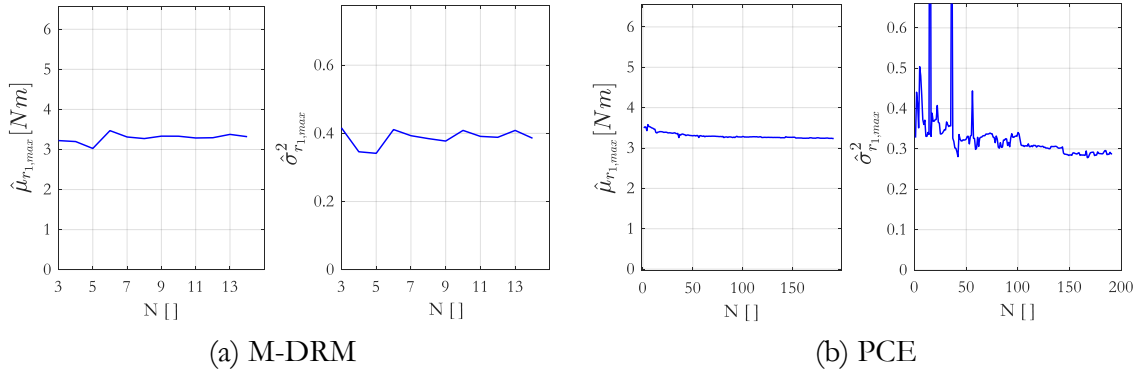
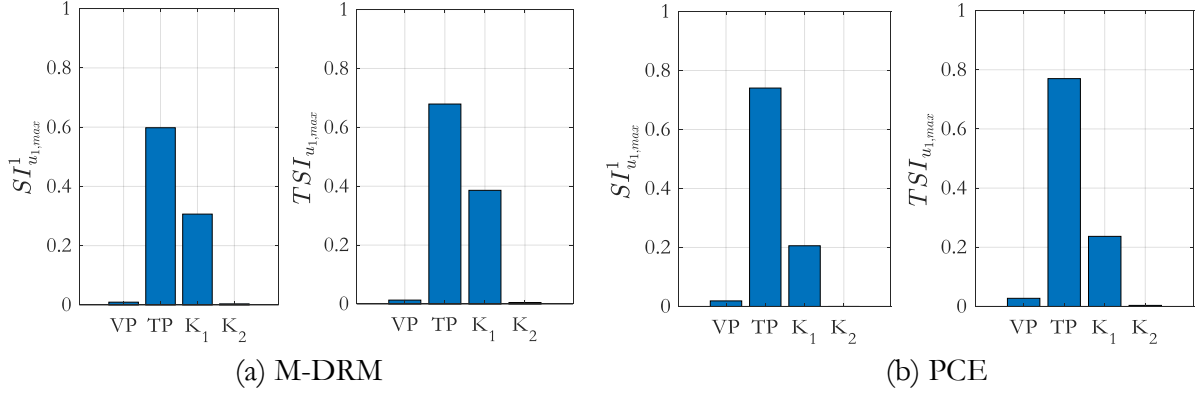


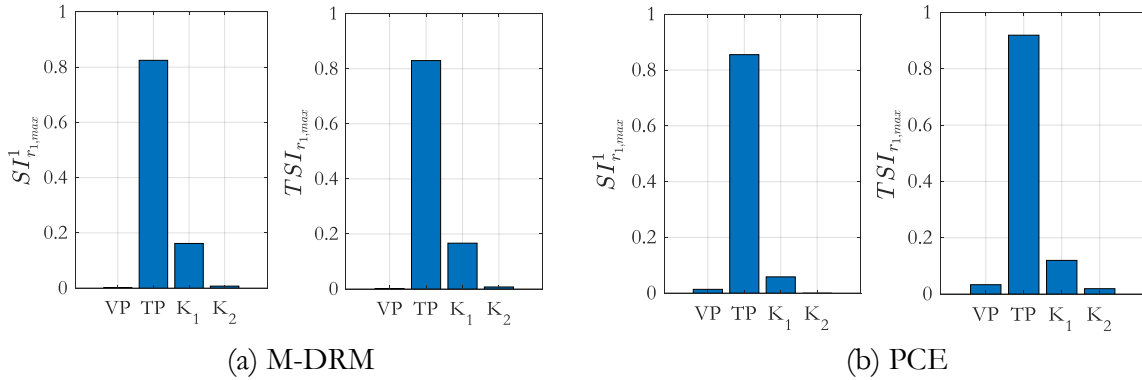
Figure 3-58: Convergence of mean and variance estimates of  $r_{1,max}$  with increasing number of hybrid tests

The size of the experiment was found to have a negligible effect on the convergence of the Sobol indices, estimated by the M-DRM, especially after the first 28 hybrid tests, which may be attributed to the interpolation of responses from the PCE meta-model. As shown in Figure 3-59, considering the seventh-order Gauss quadrature (equivalent to 28 hybrid tests), the first-order (*SI*) and total Sobol indices (*TSI*) calculated from the M-DRM method show small discrepancies compared to the PCE estimates.


 Figure 3-59: SI and TSI estimates of  $u_{1,max}$ 

The M-DRM estimate for the first-order sensitivity of the  $u_{1,max}$ , in relation to  $K_1$ , is larger than that of the PCE estimate, and the opposite is true concerning the period of the input motion, TP. The same argument is true for the TSI, except the discrepancies between the two methods are slightly smaller.

The SI and TSI of the maximum left-support moment, shown in Figure 3-60, that were evaluated using the M-DRM approach are in good agreement with the PCE estimates. Overall, the GSA of the M-DRM method can produce reasonable estimates in comparison to the Monte Carlo and PCE estimates with comparatively less computation cost, which translates into a smaller number of experimental tests.


 Figure 3-60: SI and TSI estimates of  $r_{1,max}$ 

To examine the underlying reason for the discrepancies between the M-DRM and PCE estimates, the PDFs of the  $u_{1,max}$  and  $r_{1,max}$  responses, determined from the M-DRM method, were fitted and compared to the responses obtained from the hybrid tests. In the fitting shown in Figure 3-61, the kernel density distribution (Lallich & Pastor, 2007) was utilized since a parametric distribution may not properly describe the data. The maximum support rotations,  $u_{1,max}$ , greater than 0.03 rad are overestimated in the univariate M-DRM method and the PDF is characterized by a heavy tail; herein lies the source of the discrepancies of the GSA results. Considering  $u_{1,max}$ , the bivariate M-DRM

has better accuracy compared to the univariate formulation, as shown in Figure 3-61. On the other hand, the univariate M-DRM estimates of the maximum left-support moment,  $r_{1,max}$ , are in good agreement with the experimental data except in the peak region. The bivariate M-DRM as well was not able to bridge this mismatch.

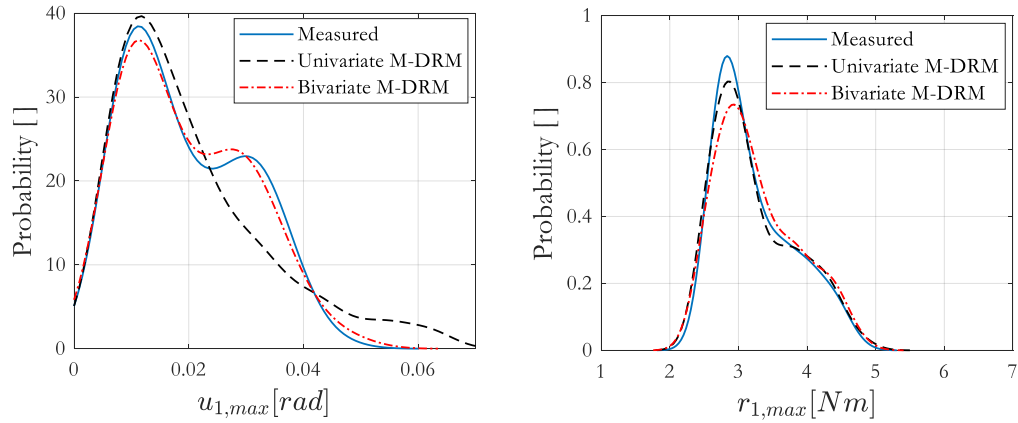


Figure 3-61: Comparing PDFs fitted to the univariate and bivariate M-DRM estimates against the PDF fitted to the measured responses

### 3.7 Summary

In this chapter, the concept of virtual or simulated hybrid testing was initially introduced. Then, an elaborate explanation of the OpenSees-OpenFresco software framework for conducting a simulated hybrid test was presented. The tools for modeling experimental errors within the OpenFresco framework were explained as well. In order to model experimental errors during the simulated hybrid testing, parametric identification of the LNEC's uniaxial shaking table was conducted. The actuator control loop, including a SDOF payload, was analytically modeled and the shaking table characteristics, such as mass, damping coefficient, and elastic force, were identified experimentally by applying periodic signals.

The remaining parameters of the closed-loop dynamics of the shaking table were estimated using the constrained nonlinear least-square optimization algorithm in Simulink. Eventually, a closed-form expression for the transfer function of the bare shaking table (without payload) was constructed by combining the estimates for the mechanical and servo-hydraulic parameters. Furthermore, the transfer function of the bare shaking table was developed so that it can be modified to reproduce the control-structure interaction of a SDOF payload. It was then applied to reproduce the laboratory conditions while conducting simulated hybrid tests. The subsequent parts of this chapter discuss three applications for the simulated hybrid testing.

First, its application in choosing time-stepping algorithms, including integration parameters, was addressed. In this work, simulated hybrid tests of a one-bay steel frame, pin-ended at the base, were

conducted by modeling experimental errors, and the Energy Error Indicator (EEI) was adopted to measure the accuracy of selected integration algorithms. Four integration algorithms were explored in this process, namely the Implicit Newmark,  $\alpha$ -OS, NMHS, and HHTHS. The  $\alpha$ -OS scheme was found to have acceptable EEI characteristics in addition to being attractive for fast and real-time hybrid simulation tests. Besides, a good choice of the  $\alpha$ -parameter was found to be essential for a better performance of the  $\alpha$ -OS integration. On the other hand, in the NHMS integration, increasing the number of iterations above five hardly improved the accuracy of the response simulation, while it seems to increase the computational cost. However, it is difficult to generalize on the latter since the iterations needed to solve the equilibrium equation are governed by the complexity of the structural systems.

The second application attempted to shed light on substructuring tests of linear and nonlinear SDOF structures from the standpoint of stability analysis. The simulated hybrid test was fully carried out in MATLAB/Simulink software by solving the equations of motion. The stability test of a linear SDOF structure, in a hybrid test, was performed by modeling it partly experimentally and partly numerically, while the ST1D's transfer function simulates the experimental conditions. The Routh's stability test was utilized to determine the portion of mass, stiffness, and damping of the SDOF that can be physically modeled without introducing system instability. Conditions for the unstable hybrid test of the structure, for different frequencies and damping ratios, were also explored considering the worst-case scenario for component substructuring. The stability test, which was performed in the frequency domain, was eventually validated by conducting simulations in the time domain.

Besides, the stability analysis was extended to inelastic SDOF structures. In the latter, the experimental substructure was modeled using the Bouc-Wen hysteretic model. The simulated studies reveal that inelastic structures can have improved stability conditions compared to their elastic counterparts.

In the third application, reliability and global sensitivity studies, that utilize hybrid testing, were investigated. The Monte Carlo simulation approach for structural reliability analysis, in hybrid testing, requires a large number of experimental tests, thus making it unrealistic. Thus, the M-DRM method was proposed to circumvent this difficulty. It approximates a structural response by a surrogate model enabling the computation of statistical moments with a limited number of experimental tests. Additionally, the full probabilistic distribution of the response can be estimated from fractional moments, obtained from the M-DRM method, using the Maximum Entropy principle (MaxEnt). In this technique, moments are evaluated by integrating cut-off functions using appropriate Gauss quadrature rules. Furthermore, global sensitivity indices are by-products of the estimation process and do not require additional model evaluation.

The proof-of-concept for this technique was carried out by performing simulated hybrid tests of a two-bay one-story steel frame structure. One of the outer columns of the structure was modeled as a physical element and the remaining parts were numerically modeled in the OpenSees software.

Firstly, the effect of the number of integration points of the Gauss-Hermite quadrature rule on the accuracy of the estimation was studied. Seven Gauss-Hermite quadrature points were found to be optimum after examining the convergence of sensitivity indices and moments. In the numerical studies that followed, two cases, namely two RVs, with two random inputs, and three RVs, with three random inputs, were studied. The reliability and global sensitivity studies of the two cases were conducted by gradually increasing the intensity of input motion and for different levels of uncertainty of the random input variables. In this work, the relative error of the M-DRM estimates, in comparison to the observed data (derived from the MCS approach) was used as an error metric. The relative error quantities between the two approaches revealed the superior performance of the proposed technique. Furthermore, the PDF estimated by the MaxEnt algorithm was found to be in good agreement with the observed distribution.

Finally, the M-DRM method was validated using data from actual hybrid tests of a simply supported beam, including elastic rotational springs at its supports. The validation work was conducted by taking advantage of the PCE meta-modeling and the output of the latter was used as a benchmark for the estimates of the M-DRM method. The proposed scheme was found to be in good agreement with the PCE estimates, thus reinforcing the findings of the simulated studies.



## 4 Development and Validation of a Software Framework for Hybrid Simulation

### 4.1 Development of a software framework for hybrid simulation

In the scope of this research work, two different schemes for hybrid simulation were developed at LNEC. They are integrated into a single software package, termed ‘LNEC-HS’, for ease of use. It was designed to have a state-machine operation, which promotes modularity and flexibility, using the Virtual Instruments (VIs) of the LabVIEW software. The framework software can be used to perform slow, fast, and real-time hybrid tests.

The first scheme of this software can be perceived as a three-loop architecture, as shown in Figure 4-1, comprising a control loop (innermost loop), a simulation coordinator (intermediate loop), and an integration loop (outermost loop). The innermost loop is dedicated to controlling a servo-hydraulic actuator or a shaking table. The intermediate loop interacts with the OpenFresco software through a TCP/IP protocol while continuously generating command displacements to the actuator. These commands are modified by a delay compensation algorithm before sending them to the actuator.

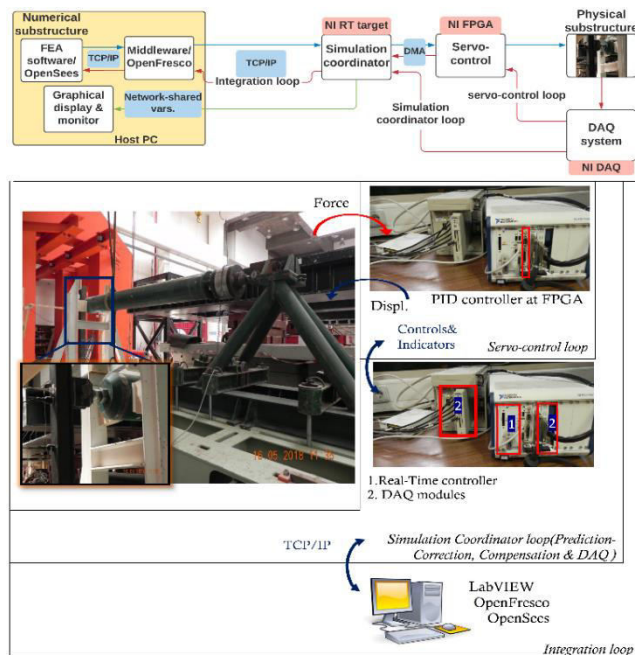


Figure 4-1: Three-loop architecture framework for hybrid simulation

The outermost loop, herein referred to as the integration loop, includes of the open-source finite element software framework, OpenSees, and the OpenFresco middleware that manages the

exchange of data between the numerical simulation and the simulation coordinator using the TCP/IP protocol. The integration loop receives the measured restoring force of the experimental substructure and advances the hybrid test one-step forward in time by solving the equilibrium equation.

The hardware for *LNEC-HS* software was constructed using the National Instruments (NI) embedded Real-Time (RT) controller, NI PXI-8106, and the National Instruments (NI) Field Programmable Gate Array (FPGA), NI PXI-7841R. The simulation coordinator was implemented in the RT controller while the FPGA module was programmed to execute the control algorithm. The data acquisition board, NI PXI-6289, records the actuator displacement, the acceleration of the test specimen, and the actuator force measured by the transducers. The NI PXI-8106 and the NI PXI-7841R modules are inserted into a chassis, NI PXI-1042Q, and communicate with each other through the Direct Memory Access (DMA). Despite the DMA FIFO providing a high throughput data transfer, the speedy transfer of small-sized data is essential during a hybrid test. Thus, direct communication, using control and indicator variables, was found to be effective in improving the computational efficiency of the framework software.

The building blocks of the software framework include a Real-Time VI (referred hereinafter as simulation coordinator VI), Host PC VI, and FPGA VI. The state-flow machine was primarily programmed to execute the simulation coordinator VI. Besides, this VI calls the FPGA VI at each time-step during a hybrid test. On the other hand, the Host PC VI provides a real-time display window for monitoring structural responses during the hybrid test. The sub-space synchronization and error tracking plots can also be monitored from the Host PC VI.

In a similar fashion, the second scheme, referred hereinafter as direct Hybrid Simulation (*directHS*), has a three-loop architecture, but it excludes the need for an external numerical simulation software. In fact, a simple numerical simulation program was developed using the LabVIEW software, and it was directly integrated into the simulation coordinator. This scheme eliminates the need for the OpenFresco middleware, thus allowing direct exchange of data between the computational driver and the simulation coordinator through local variables. Hence, no TCP/IP communication is used between the control software and the numerical simulation program. Nonetheless, the downside of this approach is that the computational driver was developed to model only two-dimensional linear-elastic shear frame numerical substructures. Therefore, it assumes that the numerical substructure must remain elastic throughout the hybrid test. In *directHS* scheme, two DOFs can be controlled using a shaking table, applying ground motion at the base, and an auxiliary actuator, applying interface force at the top part of the physical substructure. Thus, it is suitable for testing soft-story mechanisms in structures as well as for testing soil-structure interaction problems, where no or little structural nonlinearity is expected in the numerically simulated upper stories. It was conceived to improve the speed of a hybrid test, making it possible to perform real-time hybrid tests which are difficult to achieve using the first scheme. It is noteworthy to mention that the speed of execution of a hybrid test in this scheme may also be limited due to the clock-speed of the NI-RT controller.

During the validation work of *LNEC-HS* framework software, a cantilevered steel column, free to rotate at the top, was driven by a shaking table using a space truss and strut system in order to transfer the actuator's force to the experimental column.

#### 4.1.1 OpenSees software framework

The Open System for Earthquake Engineering Simulation (OpenSees) is an open-source Object-Oriented (OO) finite element software framework for simulating the seismic response of structural and geotechnical systems. It was implemented in the C++ programming language. The transparent and modular nature of the OpenSees software allowed many users to modify and/or develop modules devoted to performing specific tasks with little interaction with the rest of the framework. Hence, developers do not need to concern about the overall software implementation while making modifications or additions to a specific component, thus enabling them to focus on their areas of expertise (Fvenes et al., 2004).

The four principles of object-oriented programming are the building blocks of the OpenSees software. The concept of *abstraction* is the basic principle that focuses on the decomposition of real-life objects and procedures into modular components called classes. This concept allows developers to organize their modules into self-contained objects interacting with each other. The second principle is the concept of *encapsulation*. It restricts data sharing to methods that are responsible for returning and modifying the state of an object. The sole purpose of this principle is to protect data and its implementation procedure to obtain a flexible and extensible framework. The concept of *inheritance* is the third principle and prevents duplication of functionalities by facilitating inheritance of a functionality from base-classes to sub-classes. The last concept is the principle of *polymorphism*. Through this concept, the functionality of any method can be modified without changing the method itself. The sub-classes that make up the method are modified instead, since the actual operations are performed in sub-classes.

The four main components of the OpenSees framework for running a simulation are the *Model builder*, *Domain*, *Analysis*, and *Recorder*. The *Model builder* is responsible for constructing the objects of a model and adding them to the *Domain*. It can add or remove objects from the domain anytime during the analysis. The current time-step and previous time-step states of the model are kept and returned by the *Domain* object thus making it as the central object. This object is an aggregation of several other objects such as node, element, load pattern, single-point constraint, multi-point constraint, etc. Once the model is built, the *Domain* object is ready for analysis. The *Analysis* object then drives the model one time-step forward and returns the state of the model to the *Domain* object. The *Analysis* object has many sub-classes for conducting static analysis, eigenvalue analysis and transient analysis. On the other hand, the *Recorder* object monitors a user-defined parameter during the analysis process. Hence, the simulation results can be visualized and post-processed after the analysis.

#### 4.1.2 Middleware software

The Open Framework for Experimental Setup and Control (OpenFresco) has an object-oriented architecture with two abstractions for experimental objects. These experimental objects are the loading system (commonly servo-hydraulic actuators) and the control and data acquisition system. The loading system imposes boundary conditions such as displacement, velocity, acceleration, and force whereas the control system commands the actuators using target displacements received from a numerical program. The data acquisition (DAQ) object is responsible for recording measured responses from transducers.

The middleware software consists of four abstract classes. The *Experimental Setup* class transforms response quantities from the degrees of freedom of the experimental element into actuator degrees of freedom, using geometry and kinematics of the loading system. Transformations can be as simple as linear transformation (compatible with small displacements) or nonlinear algebraic transformations. The communication between a LabVIEW-based control program and the OpenFresco software is convened by defining control points. Typically, the control points that receive target displacements and control points that receive measured forces are defined separately. The *Experimental Control* class of OpenFresco is responsible for defining the control points, the direction of loading, and the actuator configuration. The *One-actuator* class of the *Experimental Control* was adopted in this work that is compatible with a two-point control of the simulation coordinator. On the other hand, the *Experimental Site* class facilitates the deployment of the OpenFresco software for geographically distributed hybrid tests.

The OpenFresco framework can interact with any finite element software as long as the software provides a means for modeling the experimental element. Here, the OpenSees software is primarily used as a computational software because it has a comprehensive library of materials and elements. Furthermore, new developments such as the implementation of new experimental elements are easy. To facilitate the integration of the OpenFresco framework and the OpenSees software, for hybrid testing, Tcl programming commands that are necessary for defining the OpenFresco's Experimental classes were developed by Schellenberg et al. (2009).

To allow proper communication between OpenSees and OpenFresco, the *Experimental Element* is added, as a new abstract class, into the existing *Element* class of the OpenSees, thus creating the interface between them (Schellenberg & Mahin, 2006). Through the inheritance principle, the *Experimental Element* inherits the properties of the *Element* class. The latter has a member function that assigns trial displacements, at element degrees of freedom, and returns restoring forces.

Throughout a hybrid test, the *Experimental Element* always returns the initial stiffness of the experimental element, because it is difficult to compute the tangent stiffness using forces that are measured only at a few points of the test specimen. Nevertheless, Kim (2011) estimated the tangent stiffness of an experimental element while studying the force-based hybrid simulation, by modifying the *ExperimentalSignalFilter* class. This filter class was originally designed to filter control and DAQ

response quantities as well as simulating experimental errors.

#### 4.1.3 Simulation coordinator VI

The operation of *LNEC-HS* software framework starts at this VI. It starts from the *Initialization* (also *Init*) state whereby all input parameters to a hybrid test are initialized. The summary of the tasks executed in this state is presented in Table 4-1. Once the main pressure that drives an actuator (or a shaking table) achieves a working pressure level (6.894 MPa), the user prompts to *Start-up* state by pressing a Hydraulic Service Manifold (*HSM*) button. The *Start-up* state allows the physical substructure to remain in the current position. This state is useful when stopping a hybrid test for various reasons and resuming a test after some time. In this state, among many other tasks, the control loop at the FPGA starts operating by pressing the *start-control-loop* button.

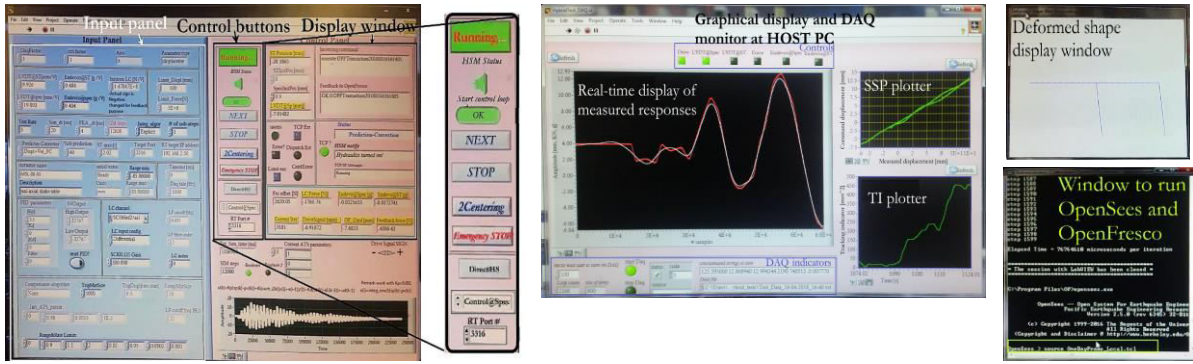


Figure 4-2: Graphical user interface (GUI) of LNEC-HS software framework

The current position of an actuator (or a shaking table) may need to be adjusted, before a hybrid test, so that the loading system is properly connected to the test structure. In addition, a hybrid test with an initial displacement may be of interest. For example, a hybrid test simulating the post-earthquake damage of a structure can be carried out after applying a residual drift.

Table 4-1: *Initialization* state

Initialization				
Previous state	Main function	Auxiliary function	Next state	Condition
N/A	<ul style="list-style-type: none"> <li>✚ Initializes:                             <ul style="list-style-type: none"> <li>➤ PID gains</li> <li>➤ Calibration data of transducers</li> <li>➤ TCP/IP parameters</li> <li>➤ Actuator data, etc.</li> </ul> </li> <li>✚ Transfers control parameters to FPGA</li> <li>✚ Resets and runs FPGA</li> </ul>	<ul style="list-style-type: none"> <li>✚ Disables:                             <ul style="list-style-type: none"> <li>➤ Actuator positioning</li> <li>➤ Next button</li> <li>➤ Stop button</li> <li>➤ Start-control-loop button</li> <li>➤ Emergency stop button</li> </ul> </li> </ul>	<i>Start-up</i>	<i>HSM</i> button

Table 4-2: *Start-up* state

<i>Start-up</i>				
Previous state	Main function	Auxiliary function	Next state	Condition
<i>Initialization</i>	<ul style="list-style-type: none"> <li>⊕ Starts the FPGA control loop</li> <li>⊕ Keeps an actuator in its current position</li> <li>⊕ Displays measurements</li> <li>⊕ Enables HS parameters:                             <ul style="list-style-type: none"> <li>➤ FE time-step</li> <li>➤ Delay compensator algorithm</li> <li>➤ PreCor algorithm, etc.</li> </ul> </li> </ul>	<ul style="list-style-type: none"> <li>⊕ Disables:                             <ul style="list-style-type: none"> <li>➤ PID gains</li> <li>➤ TCP/IP parameters</li> <li>➤ HS input data</li> <li>➤ Actuator data</li> </ul> </li> <li>⊕ Enables:                             <ul style="list-style-type: none"> <li>➤ Next</li> <li>➤ Stop</li> </ul> </li> </ul>	<i>Centering</i>	<i>Start-control-loop</i> and <i>Next</i> buttons
			<i>Stop</i>	<i>Stop</i> button

The *Centering* state was primarily designed to carry out the initial positioning of the actuator. During this operation, command displacements are applied in ramps at a rate of 0.5 mm/s. After a successful or an interrupted hybrid test, the software framework automatically returns to the *Centering* state. Then, the user can execute another hybrid test or terminate it. The *Next* button prompts the user to conduct more hybrid tests while the *Stop* button makes the actuator halt whereby the hydraulic pressure is dropped from high to low pressure, eventually to zero pressure. If the user is conducting more than one hybrid tests without interruption (software running continuously), the *TCP/IP port* number must be changed, from the front panel, in each test; this is because the TCP-listen VI reserves the active TCP/IP port for an extended amount of time after being closed. In the current implementation, the maximum number of sequential hybrid tests that can be executed using the middleware-based framework is limited to 16, for the economy of port utilization. At the end of this state, proper functioning of the FPGA module, DAQ system, and actuator position are checked against pre-defined limits and reported to the control panel, as shown in Table 4-3.

 Table 4-3: *Centering* state

<i>Centering</i>				
Previous state	Main function	Auxiliary function	Next state	Condition
<i>Start-up</i>	<ul style="list-style-type: none"> <li>⊕ Actuator positioning</li> <li>⊕ Records cell force offset</li> <li>⊕ Displays measurements</li> <li>⊕ Checks limits</li> <li>⊕ Launches DAQ at Host PC</li> </ul>	<ul style="list-style-type: none"> <li>⊕ Re-initializes:                             <ul style="list-style-type: none"> <li>➤ Limit intervals</li> <li>➤ TCP/IP error</li> <li>➤ Success button, etc.</li> </ul> </li> <li>⊕ Disables:                             <ul style="list-style-type: none"> <li>➤ Stop button</li> <li>➤ Next button</li> </ul> </li> </ul>	<i>Pre-run</i> or <i>Pre-directHS</i>	<i>Next</i> button
			<i>Start-up</i>	<ul style="list-style-type: none"> <li>⊕ <i>Stop</i> button</li> <li>⊕ Errors in the FPGA</li> <li>⊕ <i>Limit exceeded</i></li> </ul>

The *Pre-run* state was developed in support of the middleware-based scheme of the software. It creates a TCP/IP listener to connect to OpenFresco and initializes a group of queues that are necessary during the prediction-correction process of a subsequent state. The TCP/IP listener waits for a connection at a specified IP port for a duration of 3 s before timing-out.

Table 4-4: Pre-run state

Pre-run				
Previous state	Main function	Auxiliary function	Next state	Condition
<ul style="list-style-type: none"> <li>✚ Centering</li> <li>✚ DAQ VI launched</li> </ul>	<ul style="list-style-type: none"> <li>✚ Checks the FPGA and TCP/IP errors</li> <li>✚ Listens for TCP/IP connection</li> <li>✚ Saves configuration data into the Host PC</li> <li>✚ Creates queues for the PreCor state</li> <li>✚ Selects TCP/IP port</li> </ul>	<ul style="list-style-type: none"> <li>✚ Disables the DAQ sampling rate</li> <li>✚ Initializes control VIs of the PreCor state</li> <li>✚ Error handling</li> </ul>	PreCor	<ul style="list-style-type: none"> <li>✚ User prompt</li> <li>✚ No errors in FPGA &amp; TCP/IP</li> </ul>
			Stop	Errors in the FPGA and/or the TCP/IP connection

If the OpenFresco software fails to open the port within this time interval or the port is already reserved by the TCP/IP listener VI, the software automatically switches to the *Error* state. The exceedance of limits is also checked at the *Error* state to help make changes before starting a new hybrid test.

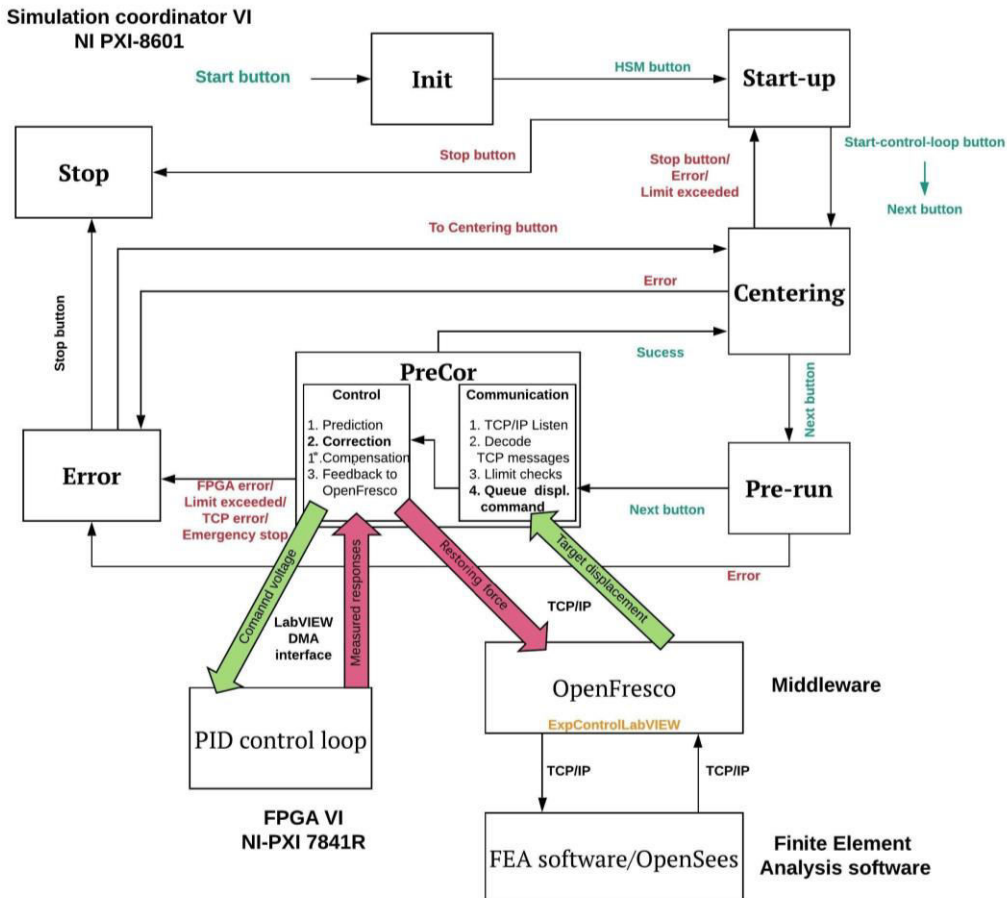


Figure 4-3: Schematic diagram of the middleware-based scheme of LNEC-HS software

The prediction-correction state (*PreCor*) is the most important and complex part of the software. The hybrid test is executed at this stage if all preceding states are completed without errors. The *PreCor* state can be decomposed into three blocks, namely communication/interface block, control and feedback block, and data acquisition block. The interface block allows the simulation coordinator VI to receive TCP/IP messages, from the OpenFresco software, decode the messages and check if the received commands are within the stroke limit of the actuator. In this block, the received command displacements are queued, and they are subsequently utilized during the correction phase of the control and feedback block. The control and feedback block of the *PreCor* state predicts actuator commands using displacements from the last three time-steps until the target displacement of the current time-step is available. The algorithm predicts displacements during the first 60% of the time-step size of the simulation; and corrects, towards the target displacement, during the remaining 40%. This default setting assumes that the target displacement can be available before 60% of the time-step. This process is explained in detail in a subsequent section.

On the other hand, the DAQ loop operates in parallel to the other two blocks. It is responsible for displaying measured responses during a hybrid test as well as sending them to the Host PC for saving. In this block, data is buffered for a duration of 0.1 s and it is routed to the Host PC through network-shared variables. The *PreCor* state also supports other auxiliary tasks as shown in Table 4-5.

 Table 4-5: *PreCor* state

<i>PreCor</i>				
Previous state	Main function	Auxiliary function	Next state	Condition
<i>Pre-run</i>	<ul style="list-style-type: none"> <li>✚ Continuous generation of commands via a prediction-correction process</li> <li>✚ Receives target displacement from the OpenFresco</li> <li>✚ Control-error compensation</li> <li>✚ Returns measured force and displacement to OpenFresco</li> <li>✚ Data acquisition</li> <li>✚ Sends measured responses to the Host PC</li> <li>✚ Tracks experimental errors</li> <li>✚ Stops a hybrid test in case of emergency</li> </ul>	<ul style="list-style-type: none"> <li>✚ Displays measured responses</li> <li>✚ Closes TCP/IP ports at the end of a test</li> <li>✚ Reports messages from the OpenFresco</li> <li>✚ Stops DAQ at the end of a test</li> </ul>	<i>Centering</i>	Successful hybrid test
			<i>Error</i>	<ul style="list-style-type: none"> <li>✚ TCP/IP error</li> <li>✚ Control error</li> <li>✚ Dispatch error (to OpenFresco)</li> <li>✚ Emergency stop</li> </ul>

The main function of the *Error* state is to maintain an actuator at its current position while the user decides to continue or terminate a test. The state-machine architecture allows the software to jump from the *PreCor* state to the *Error* state if the actuator's limits are exceeded, any control error is encountered, errors in the communication block occur or the *Emergency stop* button is switched on. From this state, the user can choose to stop the test or return to the *Centering state*.

Table 4-6: *Error* state

Error				
Previous state	Main function	Auxiliary function	Next state	Condition
<ul style="list-style-type: none"> <li>✚ <i>Pre-run</i></li> <li>✚ <i>PreCor</i></li> <li>✚ <i>Pre-directHS</i></li> </ul>	<ul style="list-style-type: none"> <li>✚ Keeps an actuator in its current position</li> <li>✚ Closes TCP/IP connection</li> <li>✚ Displays error source</li> <li>✚ Returns to <i>Centering</i> state</li> <li>✚ Stops a hybrid test</li> </ul>	<ul style="list-style-type: none"> <li>✚ Enables:                             <ul style="list-style-type: none"> <li>➢ Actuator parameters</li> <li>➢ Re-initialize the HS indicators</li> <li>➢ Displays sources of errors</li> </ul> </li> </ul>	<i>Centering</i>	<i>To-Centering</i> button
			<i>Stop</i>	<i>Stop</i> button

Input parameters of the test that may be responsible for the errors derived from the *PreCor* state may be adjusted after returning to the *Centering* state. This state re-initializes all the *PreCor* indicators making it ready for a new test. A schematic representation of the data flow and the interaction among the states of the middleware-based scheme of *LNEC-HS* is presented in Figure 4-3.

As pointed out earlier, the second scheme of *LNEC-HS* includes neither an external FEA software nor a middleware software. To operate this scheme of the software, the *directHS* button needs to be true, otherwise, the program defaults to the first scheme of the software. The two schemes of the software have similar data flow during their operation except for the *Pre-run* and *PreCor* states. When the *directHS* button is true, the software prompts the user from the *Centering* state to the *Pre-directHS* state. The latter has similar objectives as that of the *Pre-run* state. Here, preparatory actions are taken in support of the *directHS* state, whereby the hybrid test is executed. In the *Pre-directHS* state, the user is prompted to select a ground motion input file, in the form of acceleration and/or displacement time-history.

The middleware-free scheme of *LNEC-HS* was primarily developed for hybrid tests that model the lower stories of a shear building as a physical substructure. Hence, the input acceleration is directly applied to the physical substructure through a shaking table controller. This controller was designed to have acceleration tracking capabilities. Besides, a displacement controller is also available that can apply ground displacements to the shaking table. Both controllers operate in cascade to the PID control loop implemented in the FPGA VI.

 Table 4-7: *Pre-directHS* state

Pre-directHS				
Previous state	Main function	Auxiliary function	Next state	Condition
<i>Centering</i>	<ul style="list-style-type: none"> <li>✚ Prompts the user for input acceleration and/or displacement files</li> <li>✚ Definition of the numerical substructure and the parameters of the Newmark integration</li> <li>✚ Updates the control parameters</li> <li>✚ Records offsets in measurements</li> </ul>	<ul style="list-style-type: none"> <li>✚ Disables control parameters</li> <li>✚ Writes configuration file</li> <li>✚ Re-initializes indicators</li> <li>✚ Checks errors</li> </ul>	<i>directHS</i>	<i>Next</i> button
			<i>Error</i>	<ul style="list-style-type: none"> <li>✚ Errors</li> <li>✚ User declines a prompt</li> </ul>

Like the *PreCor* state, the *directHS* state has the control and data acquisition loops running in parallel. It also includes a numerical solver for a linear-elastic numerical substructure, based on the implicit Newmark integration. This state hosts two control loops, namely an equivalent force controller and the shaking table controller, mentioned above, as shown in Figure 4-4. The two control loops need to be synchronized during their parallel operation.

The equivalent force controller is responsible for applying the base shear force of the numerical substructure, computed by the numerical solver, through the auxiliary actuator. Two different algorithms are implemented for the equivalent force control, namely the Smith Predictor and ATS based equivalent force controllers.

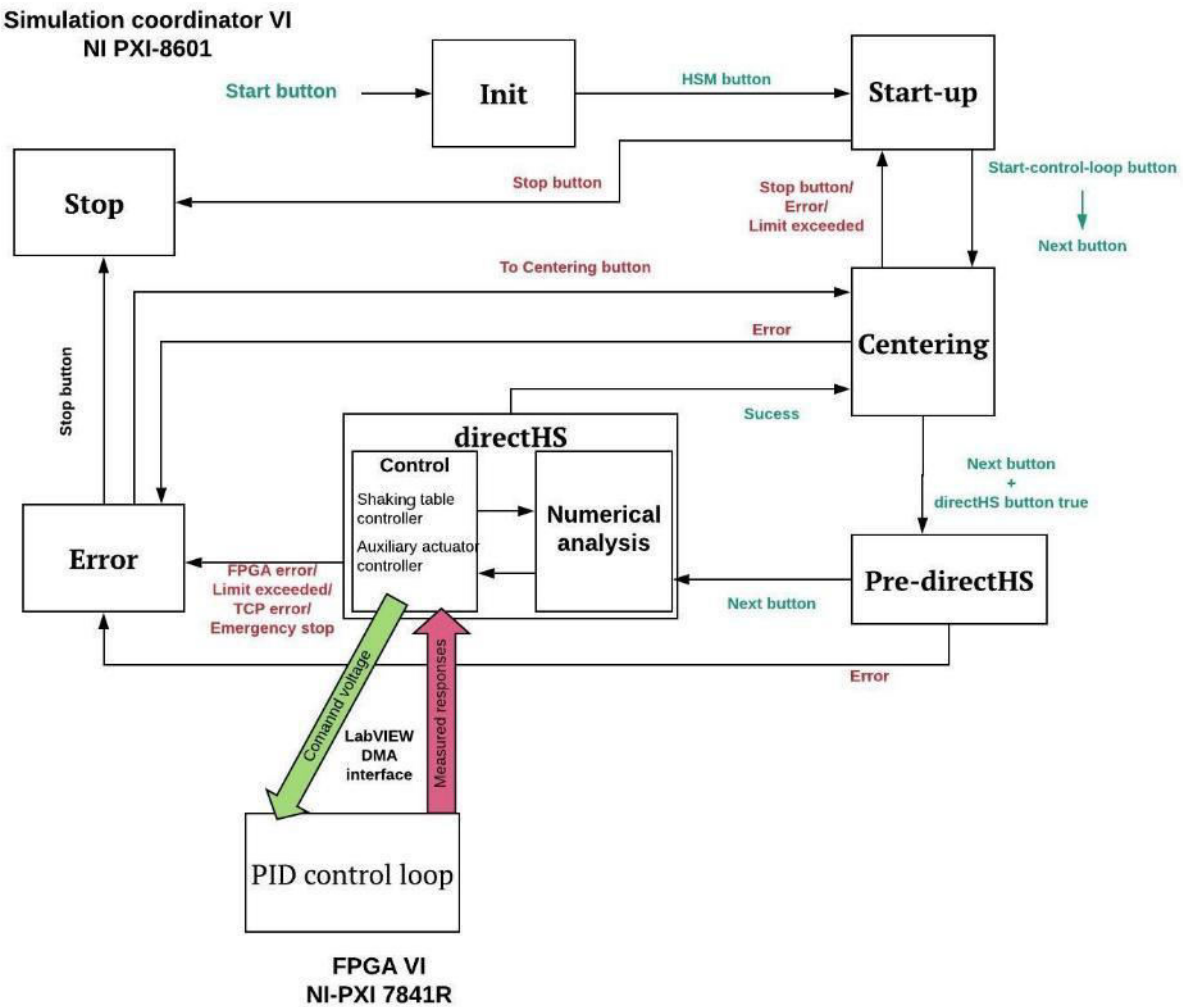


Figure 4-4: Schematic diagram of the middleware-free scheme of LNEC-HS software

A model-based controller is implemented in the shaking table controller, consisting of a Linear Quadratic Gaussian controller (LQG) and a feedforward controller, that works as a feedforward-feedback controller minimizing control errors in matching the input acceleration to the shaking

table. However, the tuning process of the LQG controller is not straightforward and, thus, an additional displacement-based controller was also implemented. Section 4.4 of this chapter enunciates the control algorithms developed in the *directHS* state. In the latter, the user needs to provide a ground displacement input file. This input file can be prepared offline by double integrating the acceleration history, after baseline filtering. A detailed discussion about the precautions needed for calculating ground displacement from acceleration records can be found in Boore (2001, 2002).

Table 4-8: *DirectHS* state

directHS				
Previous state	Main function	Auxiliary function	Next state	Condition
<i>Pre-directHS</i>	<ul style="list-style-type: none"> <li>✚ Shaking table control</li> <li>✚ Equivalent force control</li> <li>✚ Numerical solver</li> <li>✚ Data acquisition</li> <li>✚ Emergency stop</li> </ul>	<ul style="list-style-type: none"> <li>✚ Filtering and averaging acceleration measurement</li> <li>✚ Stops DAQ</li> <li>✚ Checks errors</li> </ul>	<i>Centering</i>	Successful hybrid test
			<i>Error</i>	<ul style="list-style-type: none"> <li>✚ Error indicators</li> <li>✚ Emergency stop</li> </ul>

#### 4.1.4 FPGA VI

The control algorithm of the software framework (innermost loop), which corresponds to a proportional–integral–derivative (PID), was implemented in the NI PXI-7841R FPGA target to achieve determinism and a high rate of execution. The PID algorithm works with a single-precision floating number necessary for the accuracy of position control. It uses the integral anti-windup scheme to overcome the accumulation of errors that can be caused by a large change in the setpoint. The algorithm also features a bump-less controller output for changes in the PID gains.

The load transfer system of the directHS scheme includes an actuator and a shaking table, thus two PID loops were implemented. They operate in parallel in the FPGA VI, one driving the auxiliary actuator and the other driving the shaking table, as shown in Figure 4-5. Two setpoint displacements are therefore sent to the control loop and two feedback displacements are acquired. The control loop has an execution speed of 5 kHz ( $2 \times 10^{-4}$  s). To reduce noise, the measured displacement is filtered by a low-pass second-order Butterworth filter, at 200 Hz cut-off frequency. When the software is operating under the middleware-based scheme, one of the two PID controllers is active and the second drive is disconnected physically.

The setpoints are checked against the actuators' stroke limits at the *RT host* and a Boolean indicator, *LimitExceeded*, is passed to the FPGA VI. The Boolean indicator defines if the PID loop must be executed or not. In the case of exceedance, the current position is sent to the drive signal and actuators are kept at their current position and, at the same time, the *RT host* switches to the *Error state*. To optimize the FPGA resources, the data acquisition from acceleration transducers (ENDEVCO) is also performed in the FPGA VI.

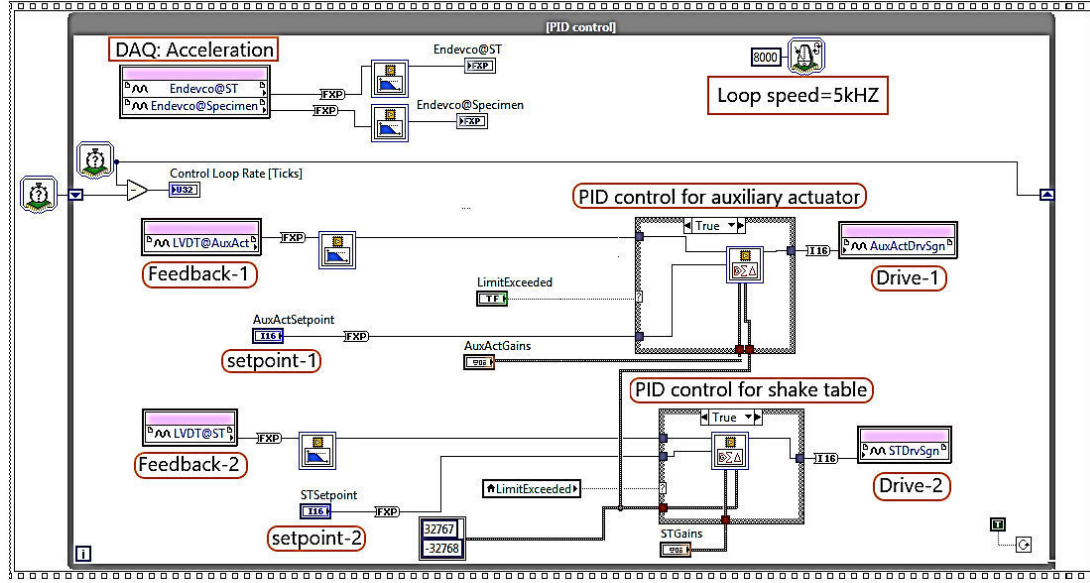


Figure 4-5: PID control loop at the FPGA VI

Generally, PID gains are tuned so that the output-input relationship of the controller has a unit amplitude in the frequency range of interest. In this work, a 10 mm square signal, 1 Hz frequency, was adopted for characterizing the step-response of the PID controller. During this test, the ST1D was rigidly attached to a mass-block weighing 600 kg. The proportional gain of the controller was adjusted to yield an overshoot error below 3% and a settling time of 44 ms. The integral gain was set to a very small value due to stability problems identified during the tuning process. The derivative term, in theory, facilitates convergence, i.e., reduces settling time. However, it can also result in excessive volatility—spikes in the output behavior of the controller, often termed *derivative kick*. Hence, the derivative gain was set to zero during the characterization work as well as in the subsequent hybrid test experiments.

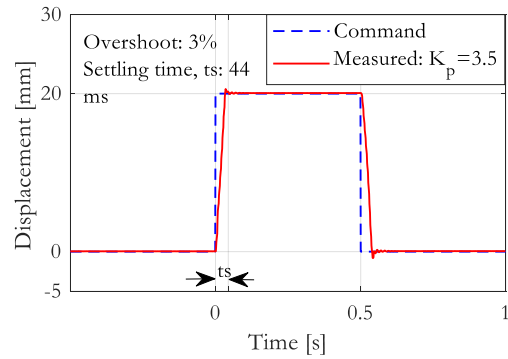


Figure 4-6: Tuning the ST1D's PID controller

A band-limited white noise, in the interval 0-20 Hz frequency, was applied in estimating the Frequency Response Function (FRF) of the ST1D. The characterization signal has a 1 mm RMS

value, and a 10% cosine-taper was applied at both ends for a smooth transition of the ST1D.

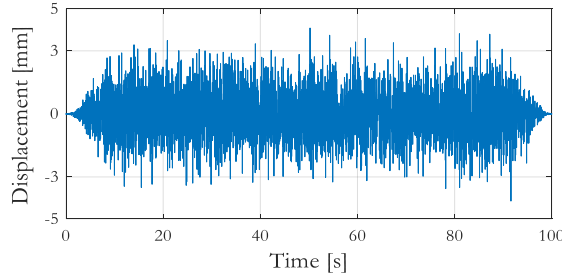


Figure 4-7: Characterization signal of the ST1D

In this characterization test, the ST1D's controller achieved a unit gain in the frequency interval 0–6 Hz, as shown in Figure 4-8, which is reasonably adequate for the current application. In the same figure, the coherence values indicate that the estimated FRF is reliable over the entire frequency range of interest. As shown in Figure 4-8, the FRF magnitude drops by 5 dB (more than half of the original magnitude) at 12 Hz; hence, the performance of the controller may need some improvement when stiff test structures are considered. Besides, the identified FRF is liable to changes due to CSI caused by test structures; therefore, adaptive compensation is indispensable.

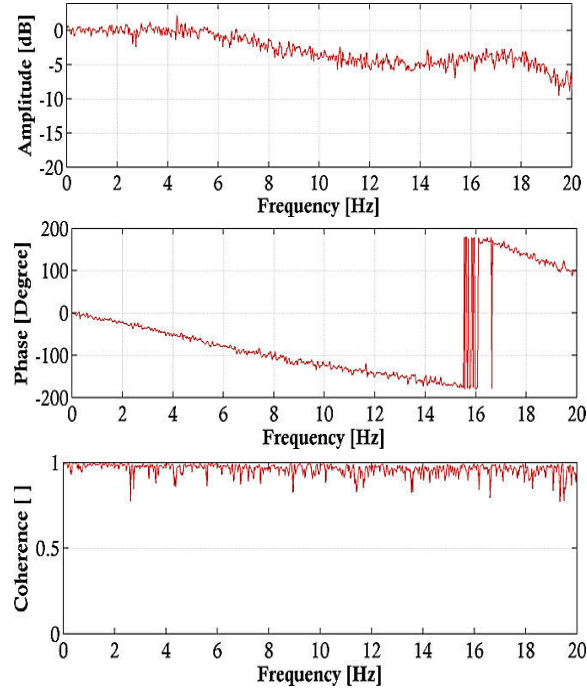


Figure 4-8: Frequency response function of the ST1D (after replacing the ST1D's analog controller by the NI PXI-7841R digital controller)

#### 4.1.5 TCP/IP interface

The communication block of the *PreCor* state was designed to exchange data with the OpenFresco framework via a TCP/IP network protocol. It enables the *RT host* to receive target displacements and send feedback responses to the FEA software. Herein, it is referred to as *LNTCP*. The *LNTCP* is a collection of LabVIEW VIs that ensure the proper transaction of responses, back and forth, between the simulation coordinator VI and the OpenFresco framework. The LabVIEW-based experimental control class of the OpenFresco sends TCP/IP data packets to the *LNTCP* and receives feedback forces. The communication starts with the definition of a *TCP listen VI* in the *Pre-run* state. Once the TCP/IP connection is established, the *TCP read VI* receives a command displacement and a *TCP write VI* sends intermediate replies and eventually a feedback force. A data packet, which has a variable-length tab-delimited ASCII format, is typically stored on a single line; and a newline serves as a message delimiter. A transaction identifier is included in every message so that the client-side can be asynchronous and multithreaded. The LabVIEW control class of the OpenFresco has a *propose-query-execute* mode of operation. In Figure 4-9, the schematic diagram shows the sequence of operations that are executed in a hybrid test where  $n$  is the number of steps in the test.

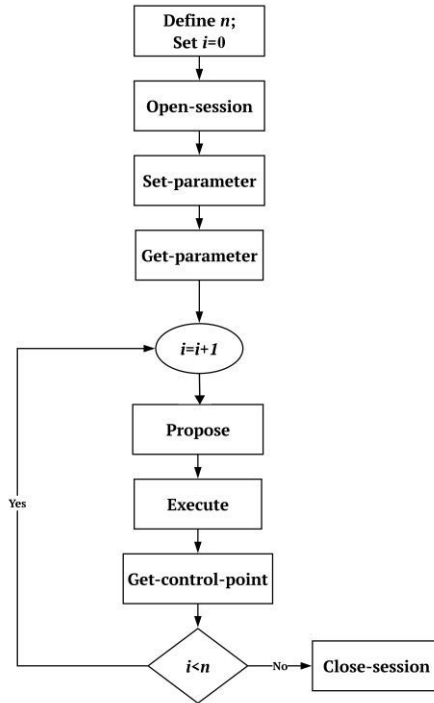


Figure 4-9: *LNTCP* dataflow

The Open-session message is received when a TCP/IP connection is established. The next two steps allow users to define and get parameters necessary for the subsequent communications in the *LNTCP*. These steps are optional, and they can be skipped by sending the 'OK' string back to the

OpenFresco framework. At each time-step of the integration loop, three mandatory steps, namely *Propose*, *Execute*, and *Get-control-point*, are executed. The message syntax of each step is important in decoding data packets received, from the OpenFresco, as well as sending feedback messages.

**Open-session:** It can be used to optionally initialize hardware or do any other system-specific work. The *LNTCP* application duly ignores it by sending the ‘OK’ string.

Receive syntax				Return syntax	
<i>Open-session</i>	<i>TransactionID</i>	<i>Parameter<sup>1</sup></i>	<i>Parameter<sup>2</sup></i>		OK

**Set-parameter:** This step mirrors the *Get-parameter* message. It is ignored by sending the ‘OK’ string as well.

Receive syntax				Return syntax	
<i>Set-parameter</i>	<i>TransactionID</i>	<i>ParameterName</i>	<i>Parameter</i>		OK

**Get-parameter:** This is mainly used for passing parameters to be used during a hybrid simulation test. This command is not used in the current implementation.

Receive syntax				Return syntax			
<i>Get-parameter</i>	<i>TransactionID</i>	<i>ParameterName</i>		OK	0	<i>ParameterName</i>	<i>Parameter</i>

**Propose:** This command can handle up to 12 control parameters depending on the number of *control points* supported by the application. In this research, a *two-point control* was developed, that has displacement as its only control parameter. Immediately after receiving this command, a separate loop in the *LNTCP* matches the command with the actuator metadata that was initially saved into the *RT host*. The actuator metadata comprise an actuator name, control point, geometry, parameter type, limit values, and so on forth. If the received data matches the actuator data, the proposed values are accepted, otherwise, it is rejected. In the receive-syntax, the entry *GeometryType* signifies the actuator’s axis of loading, which is a single character, x, y, or z. The entry *ParameterType* mirrors the control parameter, i.e., displacement, force, rotation, or moment; and the entry *Parameter* is a scalar floating-point number that represents the magnitude of the control parameter. No message is returned in response to the *Propose* command.

Receive syntax						
<i>Propose</i>	<i>TransactionID</i>	<i>{ControlPoint GeometryType}</i>	<i>GeometryType</i>	<i>ParameterType</i>	<i>Parameter<sup>1</sup></i>	<i>{ControlPoint GeometryType}</i>
		<i>ParameterType</i>		<i>Parameter<sup>2</sup></i> ...		
e.g., <i>Propose</i>	OPFTransactionIDTimeStamp		MDL-00-01	x	displacement	0.01

Note: The superscripts 1, 2, ..., indicate the number of control parameters.

**Execute:** This command message simply executes a previously accepted proposal. The same TransactionID that is used in the *Propose* and *Get-control-point* commands must be adopted. In the return phase of each command, the *LNTCP* uses a *Semaphore VI* which only allows a given command to be executed while blocking any other TCP threads to OpenFresco. The *TCP read VI* that is responsible for this operation was set to run at a higher level of priority.

**Get-control-point:** The *Get-control-point* command can support up to 12 control parameters as well.

It mirrors the *Propose* command and returns measured responses to the OpenFresco framework. The *LNTCP* was designed to handle two feedback parameters, i.e., displacement and restoring force measurements.

Receive syntax			Return syntax			
<i>Get-control-point</i>	<i>TransactionID</i>	<i>ControlPoint</i>	<i>OK</i>	<i>0</i>	<i>ParameterName</i>	<i>Parameter</i>
E.g., OK	0	OPFTransactionIDTimeStamp	x	displacement	0.01	x force -0.15

**Close-session:** The *Close-session* command is executed at the end of a hybrid test and it mirrors the *Open-session* command. This command does not perform any task in the current implementation.

Receive syntax			Return syntax	
<i>Close-session</i>	<i>TransactionID</i>	<i>Parameter<sup>j</sup></i>	<i>Parameter<sup>2</sup></i>	<i>Until next time!</i>

The LabVIEW plugin (*LNTCP*) was constructed using a command-reader loop, a limit-checking loop, and a replier loop. The *replier loop*, as its name indicates, displays the received and returned TCP data packets. The *command-reader loop* reads TCP data packets, received from the OpenFresco software, byte by byte, since TCP data is an anonymous sequence of bytes (Iniewski et al., 2008; Forouzan, 2010). Thus, data is collected byte by byte until the *EOL* (end of line) character is encountered, which marks the end of a message. The ASCII message is then parsed and enqueued into a *Command queue*.

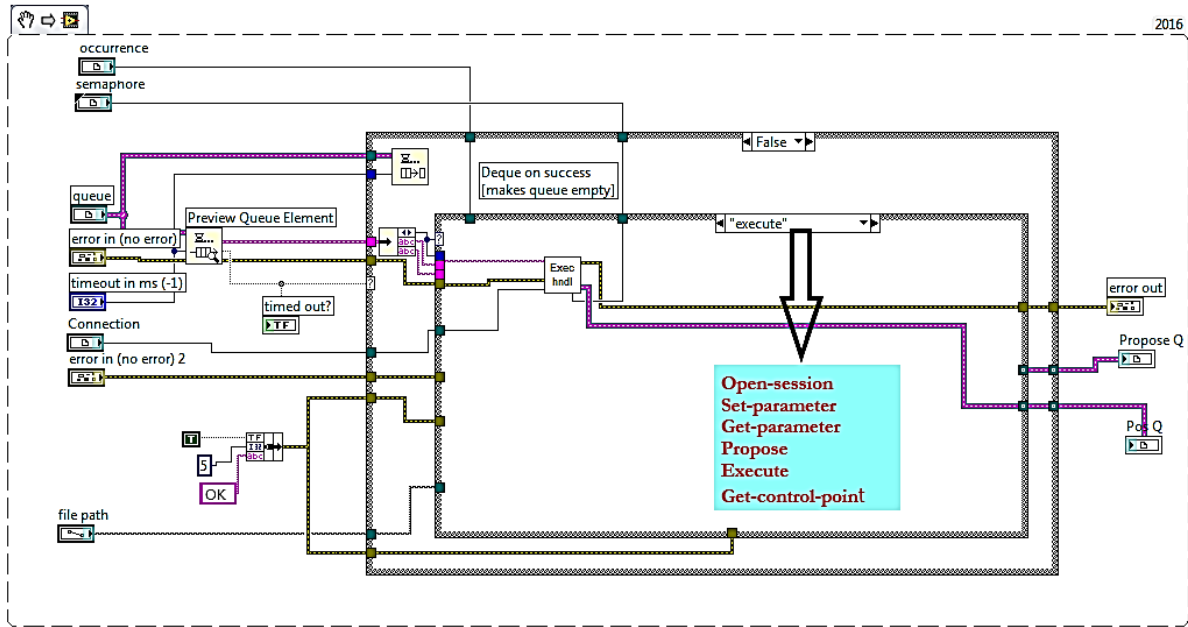


Figure 4-10: Implementation of the replier loop of the *LNTCP* for interfacing with the OpenFresco framework

The *limit-checking* and *replier loops* were programmed using case-structures, each case representing a unique step in the *LNTCP*. The data enqueued into the *command queue* is retrieved and a response is sent to the OpenFresco. As discussed earlier, at each step of the *LNTCP*, a LabVIEW semaphore

is acquired and released sequentially to avoid any thread collision. When the software prompts to execute the current time-step, the value of the control parameter is enqueued into a *Position queue*. The *Command queue*, at this stage, is emptied (or dequeued), as shown in Figure 4-10, and is ready to receive the next time-step control parameter. Then, a *PreCor queue* receives the target displacement of the current time-step from the *Position queue* and drives the correction phase of the prediction-correction process.

#### 4.1.6 Command generation and tracking

The timely interchange of target displacement and feedback force does not occur instantly, because a significant amount of time is spent during the TCP/IP communication. This phenomenon would force an actuator to move in a ramp-and-hold manner. This may cause force relaxation of the actuator, during the hold phase, thus reducing the accuracy of the simulation. This effect can be significant in fast hybrid tests that include strain-dependent physical substructures. To improve this limitation, continuous movement of an actuator is required during a hybrid test which can be performed using extrapolation-interpolation algorithms.

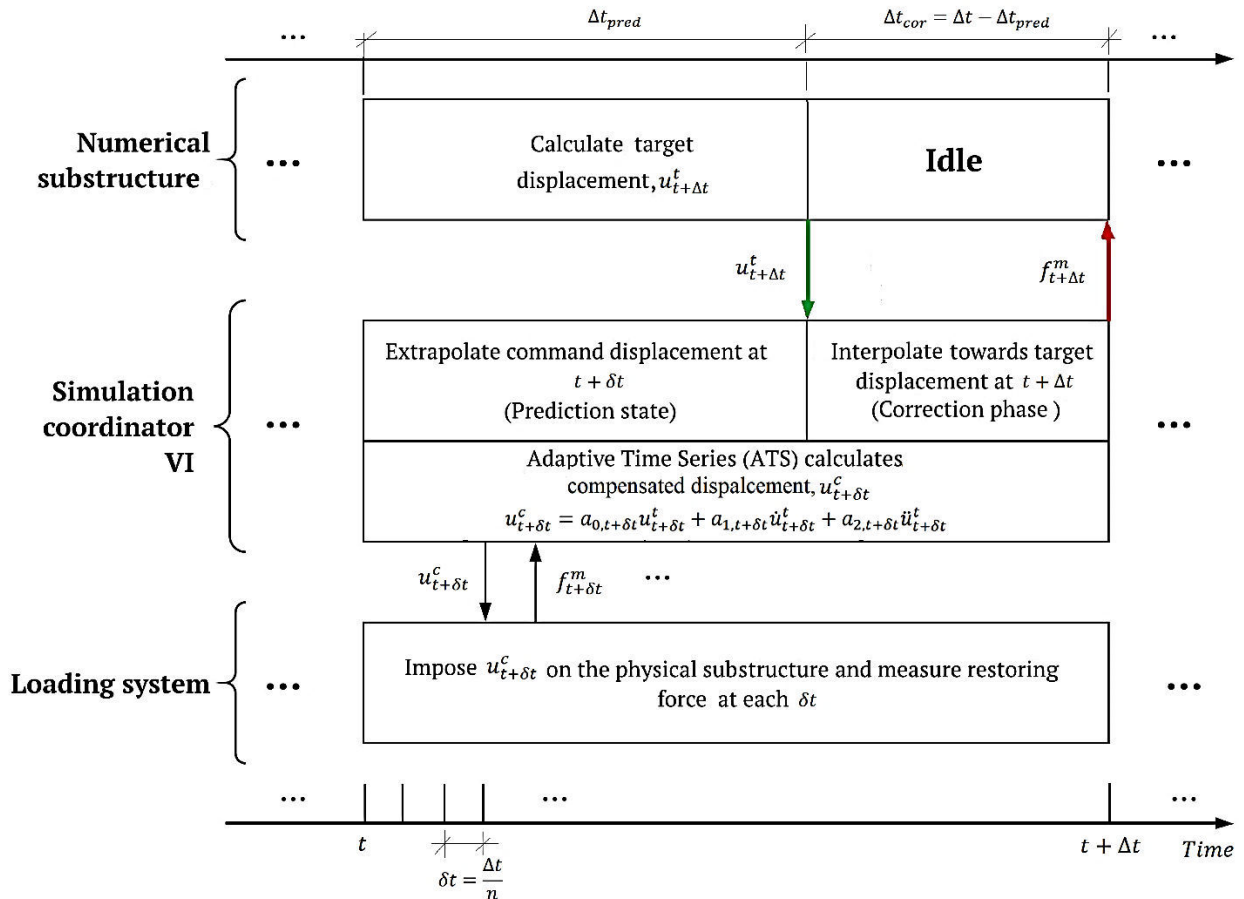


Figure 4-11: Schematic representation of dataflow in LNEC-HS software

The operation starts by applying extrapolated commands to the actuator while the finite-element software is solving the displacement at the current time-step. When the target displacement is available at the simulation coordinator VI, the algorithm interpolates towards it. The schematic diagram shown in Figure 4-11 gives a complete picture of the dataflow and interaction of the extrapolation-interpolation algorithm with the rest of the framework software.

The default period for the prediction (or extrapolation),  $\Delta t_{pred}$ , is 60% of the time-step and the remaining 40% is assigned to the correction (or interpolation) phase,  $\Delta t_{cor}$ . However, the duration of the extrapolation can be adjusted from the control panel. This input dictates the prediction phase shown in Figure 4-12. Theoretically, the response simulation of a structure with a large number of elements and/or significantly nonlinear properties takes a longer time, thus requiring a longer extrapolation period. In many cases, this additional time is anyway very small compared to the latency of the TCP/IP protocol, which therefore controls the speed of the test. For moderate-sized frames, the default setting adopted in this work is reasonable.

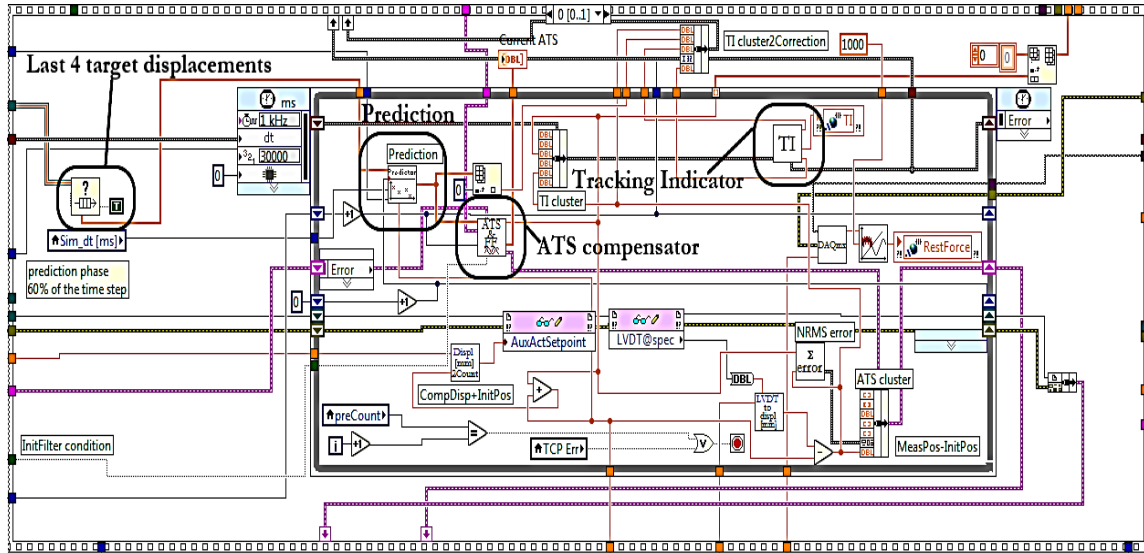


Figure 4-12: Implementation of the prediction loop of the simulation coordinator VI

Third-order Lagrange polynomials were implemented for extrapolating and interpolating actuator commands, following the footsteps of Nakashima & Masaoka (1999). Schellenberg et al. (2009) also adopted the same order for the Lagrange polynomials during an extrapolation-interpolation process using 80% of the simulation time-step for the extrapolation phase. In this work, three different extrapolation-interpolation algorithms are implemented.

The first method is based on displacements only, and the algorithm is characterized by a large discontinuity, step-like jump when it switches from the last predicted displacement to the first interpolated displacement. Hence, a high-velocity demand is imposed on the actuator. On the other hand, the second algorithm makes the displacement trajectory smoother. This is accomplished by including the last-predicted displacement in the interpolation process shown in Figure 4-13.

Nonetheless, it is not guaranteed to yield a continuous displacement path since it depends on the tuning of the controller. The third method seeks to improve the accuracy of the velocity of the actuator command using velocities and displacements for the extrapolation-interpolation process. However, many direct integration methods have less accurate trial velocities that can potentially impair the accuracy of this predictor-corrector algorithm. Thus, the algorithm implemented herein uses velocities, for the extrapolation-interpolation process, that are calculated by numerical differentiation using second-order Lagrange polynomials.

In the extrapolation process of the first algorithm, the last four target displacements (i.e.,  $[u_{t-3}, u_{t-2}, u_{t-1}, u_t]$ ) received from the numerical program are used for extrapolating the current time-step displacement. The prediction phase of the algorithm that uses the last-predicted displacement is identical to the first (conventional) method whereas the correction phase of the former includes the last-predicted displacement, i.e.,  $[u_{t-2}, u_{t-1}, u_{last,p}, u_{t+1}]$ , where  $u_{last,p}$  is the displacement predicted at  $\frac{\Delta t_{pred}}{\Delta t}$  fraction of the time-step. In addition, the extrapolation and interpolation of the algorithm that utilizes velocities were accomplished using third-order Hermite polynomials.

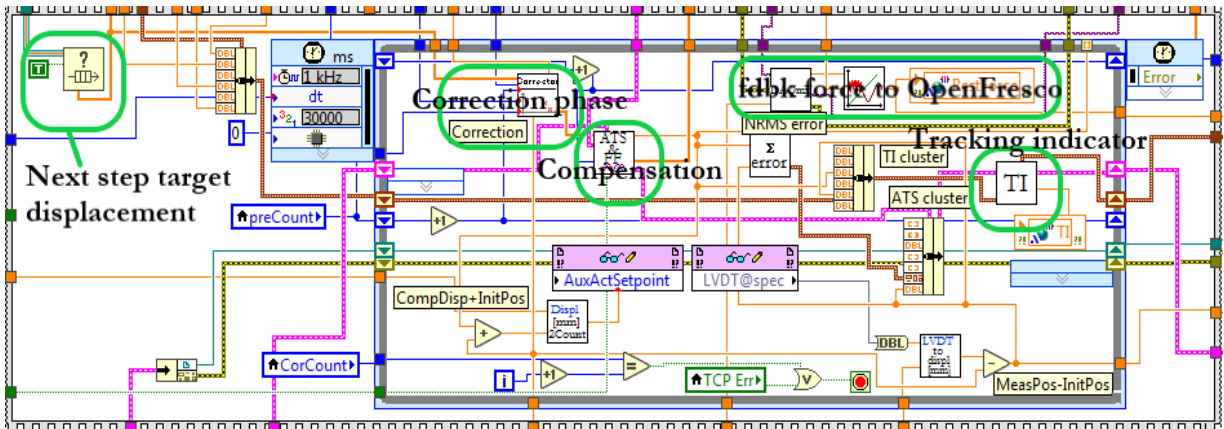


Figure 4-13: Implementation of the correction loop in the simulation coordinator VI

#### 4.1.7 Delay compensation

The phase and amplitude errors of a command displacement have evolutionary nature during a hybrid test since errors are dependent on the magnitude of the displacement command, excitation frequency, and tangent stiffness of the physical substructure. In general, offline compensation methods fail to account for these changes; hence, an adaptive method, whereby compensation parameters are evolutionary as well, is the core idea behind the Adaptive Time Series (ATS) technique. In ATS, compensation parameters are directly correlated to experimental errors, unlike in many other compensation schemes (Chae et al., 2013). The algorithm adopted in this research is slightly different from the original algorithm developed by Chae et al. (2013). The original ATS uses the Backward-Difference (BD) method to compute the target velocity and acceleration. Herein,

these derivatives the target displacement are calculated are calculated using third-order Lagrange polynomials.

Like the original ATS, initialization of the compensator parameters ( $a_0$ ,  $a_1$  and  $a_2$ ) is carried out by estimating the second-order compensator parameters in an offline test that uses a BLWN input. Besides, the compensator is triggered 1.024 s after initiating a hybrid test thus allowing the controller to build a compensation matrix that has 1024 data samples since the clock-speed of the command generation was set to 1 kHz.

Furthermore, potential instability can occur if the compensation matrix is ill-conditioned. This may happen when starting or ending a hybrid test since the measured displacement has a low signal-to-noise ratio. This may result in abrupt changes in the compensation parameters, which can eventually lead to unstable simulation. To resolve this issue, Chae et al. (2013) suggested stopping to update the compensation parameters if the peak measured displacement, in a 1 s window, is below a threshold displacement. In Dong (2015), a threshold value based on the RMS value of the measured displacement was found to have a better performance. Accordingly, herein, the initial values of the compensation parameters are kept current if the RMS value of the measured displacement, which is computed from a 1.0 s window, is smaller than 1 mm. The threshold value is designed to be adjustable because different transducers have different noise levels. Also, the performance of the loading system, especially the actuator, influences the threshold required, meaning state-of-the-art hardware may require a smaller threshold value. In this work, the ATS compensator was implemented in LabVIEW, as presented in Figure 4-14.

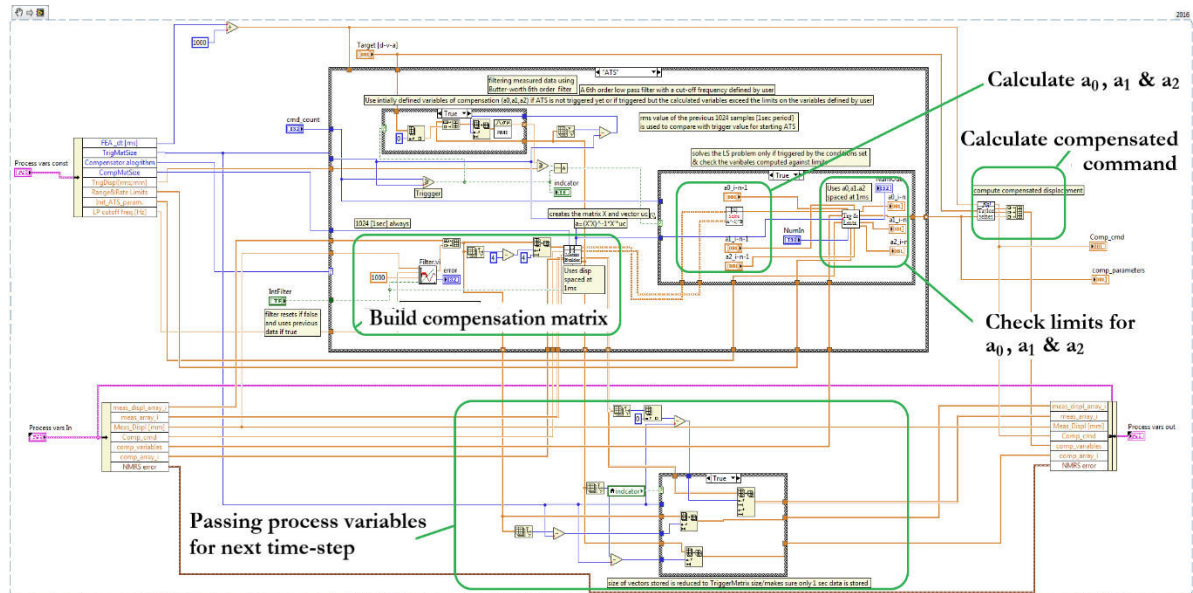


Figure 4-14: Implementation of the Adaptive Time Series (ATS) compensator in the simulation coordinator VI

To achieve a stable compensation, the compensation parameters are limited within intervals. The

range for  $a_0$  is derived from the maximum expected gain error. Herein,  $\pm 30\%$  margin from the initial value was adopted. The range for  $a_1$  is calculated from the maximum actuator time-delay using the initial parameters estimated. The maximum actuator delay,  $\tau_{max}$ , can be computed directly from  $a_1/a_0$  (assuming no gain error). The range for  $a_1$  is therefore set assuming  $\pm 100\%$  margin from the initial value. Similarly, the maximum value of  $a_2$  is determined from  $\tau_{max}^2/2$ ; hence, its range becomes  $[0, \tau_{max}^2/2]$ . In a case study, presented subsequently, for the validation of *LNEC-HS* software framework, a time-delay smaller than 2 ms was estimated after tuning the controller gains properly; however, it resulted in a significant overshoot error, which needs be compensated.

Additionally, the rates of change of the compensation parameters are also restricted depending on practical values that are supported by the servo-hydraulic actuators. The values proposed by Chae et al. (2013) were also adopted in this work. Since large values of  $a_1$  and  $a_2$  may amplify the higher frequency content of a structural response, trial runs for tuning the upper limits of the compensation parameters can be useful prior to conducting a hybrid test. On the other hand, putting too much restriction in the upper limits of the ATS parameters may equally result in poor compensation, which can eventually compromise the accuracy of the response simulation.

The Backward-Difference (BD) method for calculating derivatives, used in the original ATS, has a first-order error to the exact solution. In the original implementation of ATS, considering  $\Delta t$  for the clock-speed of the controller, the target velocity and acceleration are calculated as:

$$\dot{x}_t = \frac{(x_t - x_{t-N\Delta t})}{\Delta t}; \quad \ddot{x}_t = \frac{(x_t - 2x_{t-N\Delta t} + x_{t-2N\Delta t})}{(\Delta t)^2} \quad (4.1)$$

where  $N$  and  $\Delta t$  are the number of sub-steps in a time-step and the time-step duration, respectively. Replacing the BD formula in the second-order Taylor series and transforming the entire equation into the discrete z-transform, the discrete transfer function,  $G_{ATS}$ , from the target displacement,  $x_t$ , to the output compensated displacement,  $x_c$ , can be expressed by:

$$G_{ATS}(z) = \frac{x_c(z)}{x_t(z)} = \frac{1}{\Delta t^2 z^{2N}} \{q_2^{BD} z^{2N} + q_1^{BD} z^N + q_0^{BD}\} \quad (4.2)$$

where:

$$\begin{aligned} q_2^{BD} &= a_0 \Delta t^2 + a_1 \Delta t + a_2 \\ q_1^{BD} &= -a_1 \Delta t - 2a_2 \\ q_0^{BD} &= a_2 \end{aligned} \quad (4.3)$$

and  $a_0$ ,  $a_1$  and  $a_2$  are the compensation parameters. On the other hand, considering third-order Lagrange polynomials for computing the first and second-order derivatives of a displacement command, as adopted herein, the discrete transfer function,  $G_{ATS}$ , from the target displacement,  $x_t$ , to the output compensated displacement,  $x_c$ , can be expressed as:

$$G_{ATS}(z) = \frac{x_c(z)}{x_t(z)} = \frac{1}{\Delta t^2 z^{3N}} \{q_3^{LP} z^{3N} + q_2^{LP} z^{2N} + q_1^{LP} z^N + q_0^{LP}\} \quad (4.4)$$

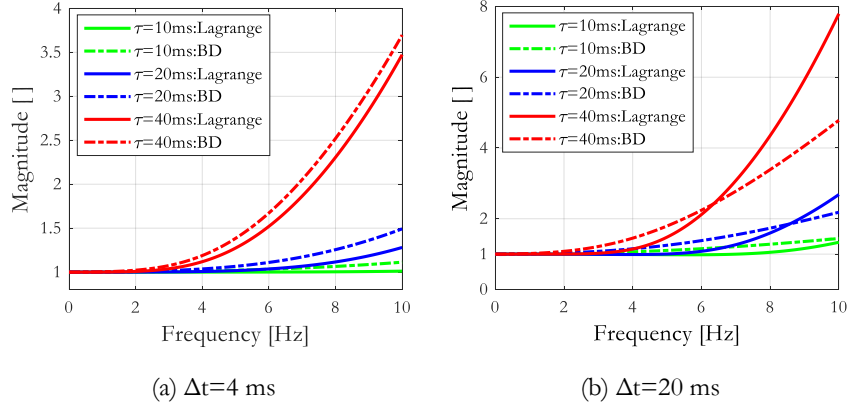
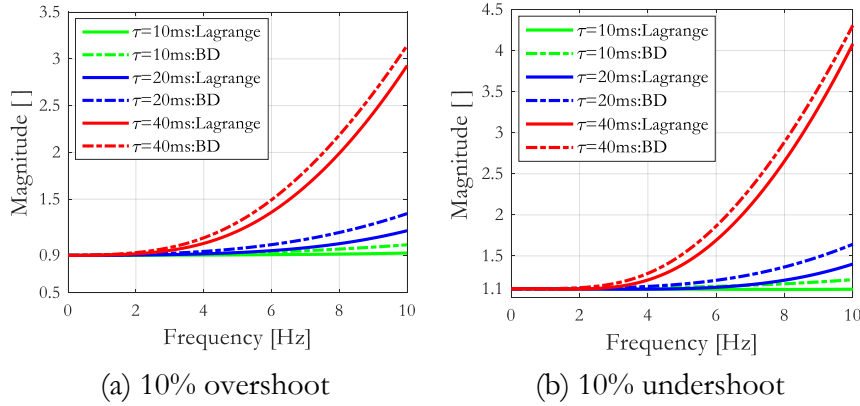
where:

$$\begin{aligned}
 q_3^{LP} &= a_0\Delta t^2 + \frac{11}{6}a_1\Delta t + 2a_2 \\
 q_2^{LP} &= -\frac{18}{6}a_1\Delta t - 5a_2 \\
 q_1^{LP} &= +\frac{9}{6}a_1\Delta t + 4a_2 \\
 q_0^{LP} &= -\frac{2}{6}a_1\Delta t - a_2
 \end{aligned} \tag{4.5}$$

In general, the target displacement is less noisy, thus higher frequency effects are less detrimental. Therefore, the choice for computing the derivatives of the target displacement can be assumed to be solely dependent on the accuracy criteria. From this standpoint, the accuracy of the ATS compensator that uses third-order Lagrange polynomials can be compared to the original implementation of ATS. The compensation parameters were varied to reflect the gain and delay errors that are calibrated to actual experimental tests. Accordingly,  $a_1$  and  $a_2$  parameters were varied to yield time-delays in the interval [20, 40] ms. This simulation study assumes a constant time-delay throughout a hybrid test, which is reasonable for comparing the two approaches if appropriate grid-spacing for the time-delay is considered (herein, for simplicity, the comparison was made at 10, 20, and 40 ms). As pointed out earlier,  $a_0$  is directly related to the gain error. Thus, cases without gain error and with  $\pm 10\%$  gain error were considered and superimposed with the presence of a time-delay of the actuator.

At a small time-step size, say 4 ms, the magnitude of  $G_{ATS}$  is close to one for the time-delay of an actuator in the order of 10 ms, as shown in Figure 4-15. For time-delays greater than 20 ms, the compensator overshoots as frequency increases. For example, when the time-delay of an actuator is 40 ms, the target displacements of a test structure vibrating at 10 Hz frequency can be amplified by a factor as large as 3.5. Overall, the ATS based on Lagrange derivatives is shown to have superior performance to that which is based on the BD method, as shown in Figure 4-15, especially when the time-step size is small. With an increase in the time-step (at 20 ms), at relatively lower frequencies (below 6 Hz), the performance of the Lagrange method is superior to the BD approach. On the other hand, for frequencies greater than 6 Hz, the performance of the Lagrange method appears to deteriorate with an increase in the time-delay of the actuator.

In Figure 4-16, the characteristics of the compensator in the presence of undershoot and overshoot errors are presented. Consistent with the conclusions made in Chapter three, simulation results confirm the additive nature of the undershoot error and the time-delay of an actuator.


 Figure 4-15: Magnitude of  $G_{ATS}$  without gain error

 Figure 4-16: Magnitude of  $G_{ATS}$  in the presence of gain error for a time-step of 4 ms

It is recalled that the theoretical relationship,  $a_2 = (a_1)^2/2$ , was adopted in defining the compensation parameters during the construction of  $G_{ATS}$ . However, the parameters of the compensator are estimated by minimizing the least square error between the compensated and measured displacements, meaning the true compensation parameters may not be necessarily related according to the theoretical expression. Considering  $a_2 < (a_1)^2/2$ , simulation results showed that the compensator has comparatively smaller overshoot errors especially when time-delay is significant. This entails the need for carefully monitoring the parameters of the ATS compensator during a hybrid test.

#### 4.1.8 Tracking indicator for hybrid testing

The Tracking Indicator (TI) metric is obtained from the area enclosed in the plot between command displacement, in the vertical axis, and the measured displacement, in the horizontal axis (Mercan & Ricles, 2009). The complementary and enclosed areas are used to compute the area enclosed in the plot. In *LNEC-HS* software, TI can be monitored online, from the GUI of the software, with a refresh rate of 0.1 s, to help identify errors during a hybrid test. A positive rate of change of TI indicate the measured displacement lagging behind the command displacement, where energy is

added into the hybrid simulation, while a negative rate of change correspond to the measured displacement leading the command displacement (Chen & Ricles, 2010). Despite the coupling between the time-delay and gain error, herein, the SSP plot, combined with the TI, is used both to quantify the control error and identify which of the two errors is dominant. For illustration, if the linear fitting of the plot is close to the  $45^\circ$  while the TI indicator is large, it can be interpreted as the time-delay being dominant in the control error.

Furthermore, the clockwise direction of winding of the SSP plot indicates a phase-lead while anti-clockwise winding indicates a phase-lag, and the plot inclination below  $45^\circ$  signifies an undershooting error while its inclination above  $45^\circ$  signifies an overshooting error. The Phase and Amplitude Error Indicator (PAEI) method for error tracking, which was proposed by Hessabi and Mercan (2007), uncouples the two errors using a Least squares solution for the ellipse equation of the SSP plot. This method was not implemented in *LNEC-HS* software because it needs a significant share of computational resources for operating it online.

#### 4.1.9 Data acquisition and transducers

The data acquisition block of the framework records data from Linear Variable Displacement Transducers (LVDTs), a load cell, and accelerometers. The 68-pin shielded connector block, NI SCB-68, connects the FPGA module to several signal conditioners. The RDP600 signal conditioner rack uses the RDP 611 module for conditioning analog signals from the LVDTs and load cell. Likewise, the measurements from the ENDEVCO accelerometers were obtained using a separate analog conditioner.

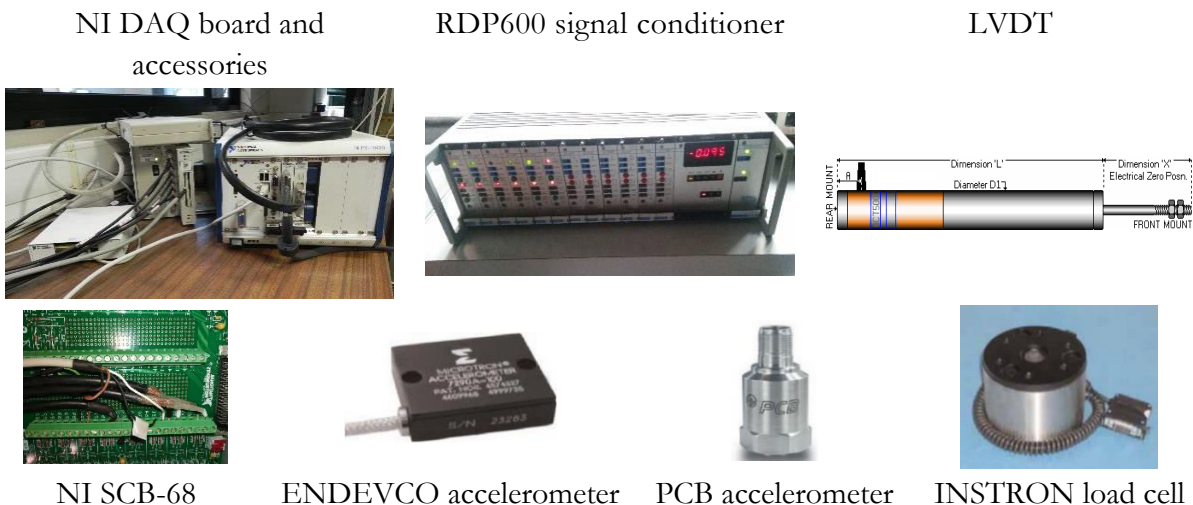


Figure 4-17: Transducers and data acquisition hardware for hybrid simulation

Before experimental testing, sensors are all calibrated whereby offsets and scale factors of an engineering unit to electrical command (voltage) are calculated, as shown in Figure 4-18. The

INSTRON load cell, 500 kN capacity, was calibrated in a compression machine, and the RDP type LVDTs were calibrated using a digital meter.

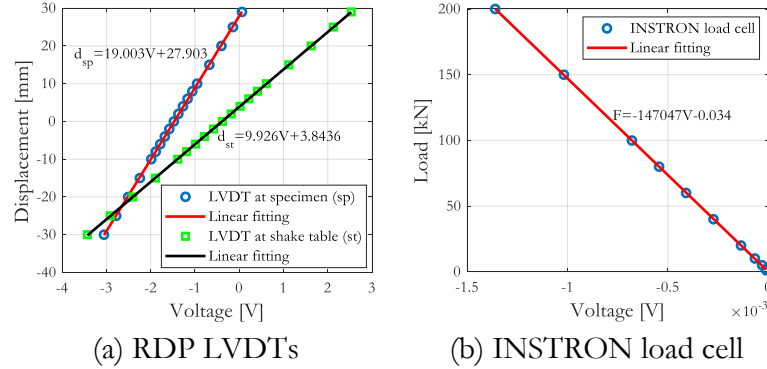


Figure 4-18: Calibration of transducers

The NI Data Acquisition (NI DAQ) board is integrated into the simulation coordinator VI for acquiring and buffering data. It buffers 100 measurements from each transducer before transferring it to the Host PC, as shown in Figure 4-19, thus reducing the computational load of the simulation coordinator VI during the prediction-correction state. The frequency of data acquisition can be adjusted from the front panel of the software. In the current implementation, data acquisition faster than 1 kHz frequency cannot be adopted due to hardware limitations.

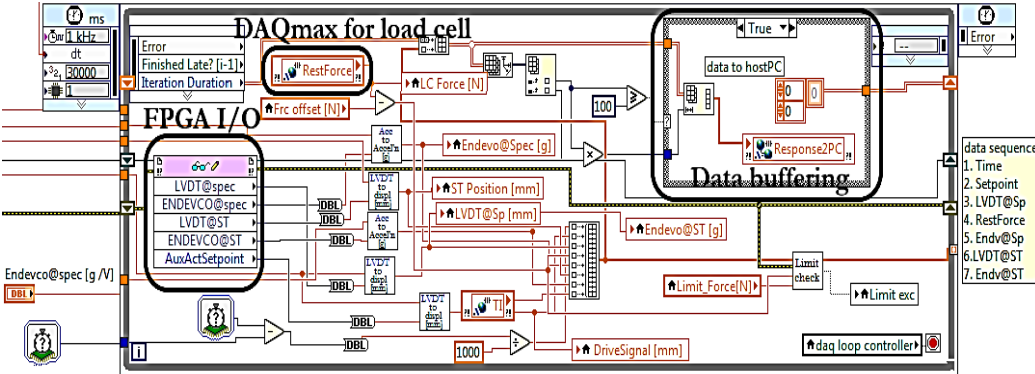


Figure 4-19: Implementation of data acquisition loop in the simulation coordinator VI

## 4.2 Validation of LNEC-HS software through hybrid tests

### 4.2.1 Case study

A two-dimensional steel Moment-Resisting Frame (MRF) structure, shown in Figure 4-20, was considered for validating the software framework. The steel structure is a two-bay, each 3.6 m wide, one-story steel frame with rigid beams, which is half-scale model of the prototype structure. The outer column (labeled as 'Exp') was chosen to be the experimental element and the remaining part

was modeled numerically in the OpenSees finite element software. Each column, 1.8 m in height, has a fixed-end connection at the base and it is hinged at the connection to the beam. The hinge boundary condition was introduced so that only the horizontal DOF of the experimental element is controlled during the hybrid test, which uses the actuator control setup.

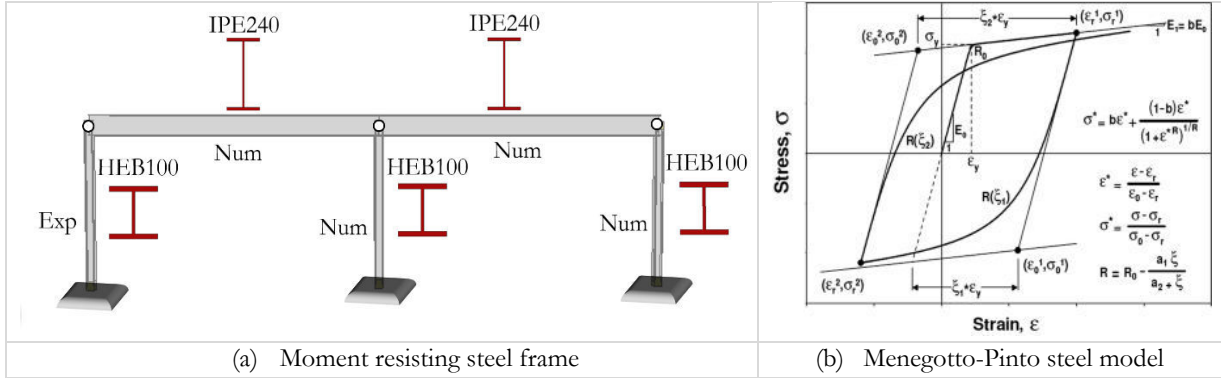


Figure 4-20: Case study structure for validating LNEC-HS software

All columns of the steel MRF are HEB 100 profiles, grade S355 steel, and the beam elements are made from the same grade of steel but IPE 240 profiles. The fiber element approach was adopted in modelling the numerical elements in the OpenSees software. The columns and beams of the structure were modeled using the Menegotto-Pinto (Steel02) constitutive model of steel. The beam elements were considered as elastic members. On the other hand, the force-based model for distributed plasticity, with five integration points, was adopted for the columns. The OpenSees-OpenFresco implementation of the hybrid test can be found in appendix 3.

#### 4.2.2 Test setup

The LNEC's uniaxial shaking table was used as an actuator for conducting the hybrid tests of the steel frame. The experimental column (test specimen) is welded to a steel base, at the bottom, and it is connected to a steel strut at the top, as shown in Figure 4-21. The loading strut is connected to the INSTRON load cell at its rear end, measuring restoring forces of the test specimen. In this test setup, the motion of the platen of the shaking table is transferred to the strut through a rigid space truss. The base frame of the shaking table and the steel base of the test specimen are also attached to the strong floor through a bolt and nut system.

To prevent undesired action on the test specimen other than the horizontal displacement, the out-of-plane motion of the steel strut was restricted through a guiding frame, as shown in Figure 4-21. Two Polytetrafluoroethylene (PTFE) boards reduce the friction at the interface between the steel strut and the guiding frame.

The command displacement generated from the predictor-corrector algorithm is first converted to an equivalent voltage output (0-10 V) and it is applied to the servo-valve of the actuator that drives the shaking table. In turn, the shaking table drives the experimental column through the

assembly of the space truss and the steel strut. In this setup, to achieve good matching between the displacement command and the displacement measured by the *LDVT@SPEC* (see Figure 4-21), the feedback displacement of the PID controller is returned from the latter.

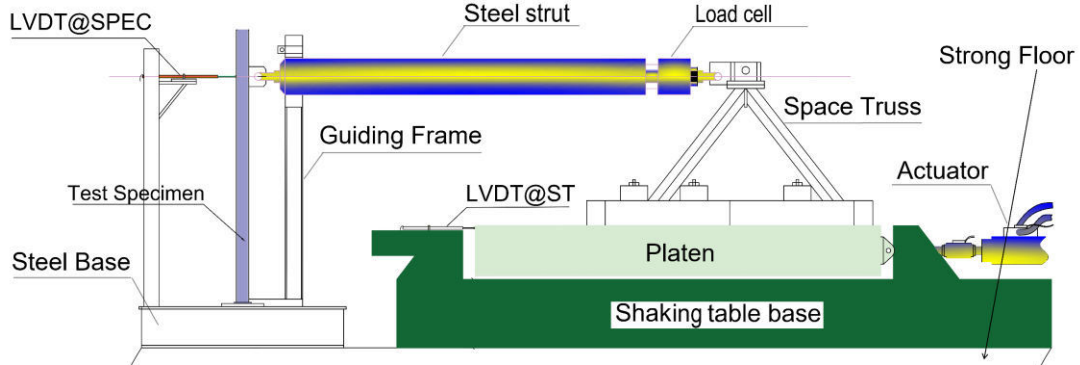


Figure 4-21: Schematic of setup for hybrid simulation

The sudden drop in the displacement measured by the *LDVT@SPEC*, near the peak response, shown in Figure 4-22(left), indicates the presence of small gaps at the connections of the test setup. From the hysteresis plot in Figure 4-22(right), we can see that a 0.1 mm gap exists between the displacements that are measured at the column and at the shaking table. Hence, all joints in the test setup, namely the connection between the steel strut and the space truss, the connection between the space truss and the platen, and the connection between the steel strut and the test specimen were all tightened after careful inspection.

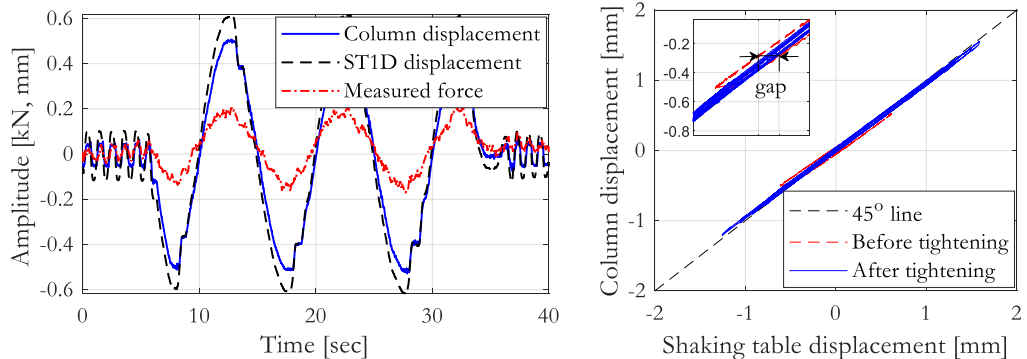


Figure 4-22: Identification of gaps in the test setup (left); and displacement of the experimental column versus displacement of ST1D (right)

As mentioned before, OpenFresco software does not return the tangent stiffness of an experimental element. Hence, an accurate estimation of the initial stiffness of the experimental substructure is important to improve the fidelity of the hybrid test. In this work, the modal frequencies of the steel column were identified using an instrumented hammer test and these frequencies were used to estimate the initial stiffness of the steel column.



Figure 4-23: Modal identification of the experimental substructure using impulsive excitation (hammer test)

The steel column was divided into six equal sections, M1-M6, spaced at 30 cm, from the base to the height where the column and the strut are connected, thus leaving a free height of 37.5 cm. Six sensitive PCB accelerometers, each with 0.5 g capacity and attached to one of the measurement points, were attached to one of the flanges of the HEB 100 steel column. Hammer impacts were then conducted on the opposite flange, in a roving manner, at the height of the accelerometers, resulting in six hammer tests, H1-H6. The hammer has a rigid head, and it is connected to a PCB accelerometer of 50 g capacity. Each hammer test was designed to have six impacts that are spaced by a 10 s idle time. The 10 s window size was selected after experimenting with the damp-out time of the acceleration measurements. This idle time prevents the overlapping of acceleration measurements from neighboring impacts. During this test, measured data was acquired at 1 kHz sampling frequency.

The FRFs of all impact tests were computed after filtering measured accelerations with a low-pass Butterworth filter at 50 Hz cut-off frequency. The modal frequencies and modal damping coefficients were determined using the Enhanced Frequency Domain Decomposition (EFDD) and Canonical Variate Analysis (CVA) methods of Operational Modal Analysis (OMA), i.e., assuming an output-only measurement. Nevertheless, system identification through the Experimental Modal Analysis (EMA) approach, considering input-output measurements, is more adequate in this case since the external force applied to the column was significant. Accordingly, the EMA estimates were also computed by superimposing the FRFs from all measurement points and all test setups. The estimates obtained from OMA were found to be in good agreement with those of the EMA approach. Eventually, the fundamental frequency was estimated to be 18.24 Hz (refer to Figure

4-24). This indicates the presence of a semi-rigid connection between the steel-base and the strong floor because the theoretical fundamental frequency of the column is 25.08 Hz. Therefore, the initially rigid-base model of the experimental column was modified to a pin-ended connection with a rotational stiffness defined by a rotational spring,  $K_\theta$ , as shown in Figure 4-24(right).

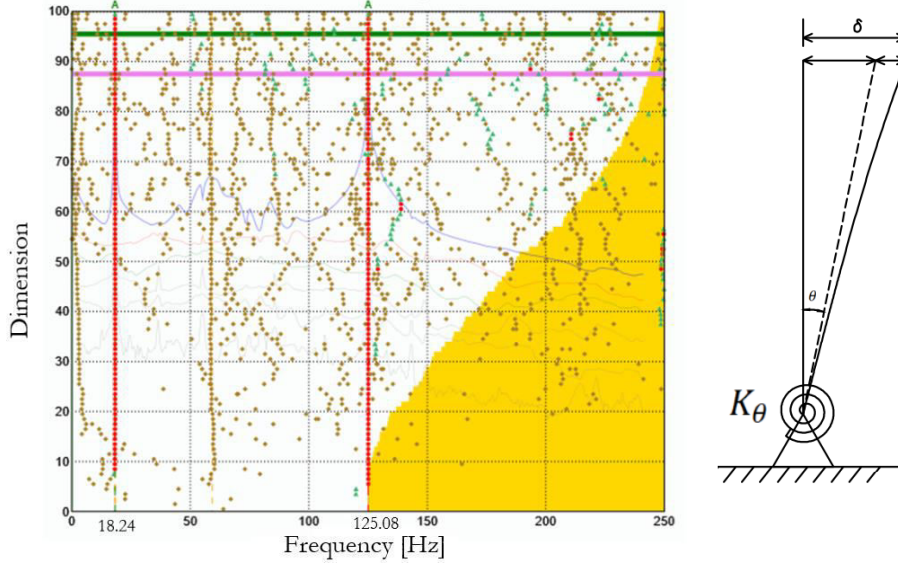


Figure 4-24: Column identification using Canonical Variate Analysis (left); and modeling the semi-rigid base connection of the experimental setup (right)

To estimate the rotational spring stiffness, the first and second modal frequencies of the semi-rigid model of the experimental column were matched to their corresponding experimental frequencies using a trial-and-error method, which resulted in  $K_\theta$  equal to 1942 kNm/rad. The comparison between the characteristics of the steel column estimated from the experimental system identification and from the numerical modal analysis is presented in Table 4-9. The stiffness matrix,  $K_{expElmt}$ , of the updated model of the column was then determined, and it was used in defining the stiffness matrix of the BeamColumn experimental element that models the steel column in the OpenFresco framework:

$$K_{expElmt} = \begin{bmatrix} 288090.00 & 0 & 0 \\ 0 & 282.075 & -617.33 \\ 0 & -617.33 & 1322.45 \end{bmatrix} \text{ kN, m}$$

Table 4-9: Modal identification results and model updating of the experimental substructure

Mode	Frequency [Hz]			Damping [%]
	Theoretical	Experimental [EMA/OMA]	Updated model	
1	25.08	18.24	18.25	0.27
2	148.76	125.08	124.87	0.18

To build a benchmark for the subsequent hybrid simulation tests, a pure numerical model of the steel structure was prepared in the OpenSees software. In this model, the rotational spring of the

experimental column was represented using the zero-length element and the rotational restraint, along the major axes, of the base node of the force-based inelastic beamColumn element was released. All columns were modeled using the Steel02 constitutive model.

The strain hardening ratio of the Steel02 constitutive model was computed from the principles of the Continuous Strength Method (CSM) developed by Yun & Gardner (2017). It is a strain-based approach that predicts section capacity more accurately compared to other international design guidelines. It uses a quad-linear curve to define the stress-strain backbone of steel. In this approach, the strain hardening ratio,  $b$ , is determined by:

$$b = \frac{(f_u - f_y)/(C_2 \varepsilon_u - \varepsilon_{sh})}{E} \quad (4.6)$$

and the ultimate strain  $\varepsilon_u$ , strain hardening  $\varepsilon_{sh}$ , and the slope of the 3<sup>rd</sup> branch,  $C_2$ , are calculated as:

$$\begin{aligned} \varepsilon_u &= 0.6(1 - f_y/f_u), \quad \text{but } \varepsilon_u \geq 0.06 \\ C_2 &= \frac{\varepsilon_{sh} + 0.4(\varepsilon_u - \varepsilon_{sh})}{\varepsilon_u} \\ \varepsilon_{sh} &= 0.1 f_y/f_u - 0.055, \quad \text{but } 0.015 < \varepsilon_{sh} \leq 0.03 \end{aligned} \quad (4.7)$$

where  $E$  is the steel modulus, 210 GPa;  $f_y$  and  $f_u$  are the yield stress and the ultimate stress of steel, respectively.

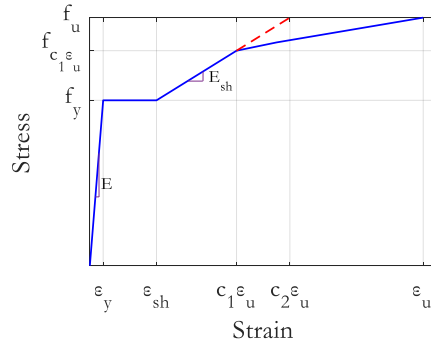


Figure 4-25: Quad-linear stress-strain curve for hot-rolled steel (Yun & Gardner, 2017)

In addition to the accurate representation of the initial stiffness of the experimental column, the reliable estimation of the initial parameters of the ATS compensator is essential. It is accomplished by identifying the parameters of the second-order compensator from an experiment. Herein, a compound signal was prepared by superimposing a 10 mm amplitude White Gaussian Noise (WGN), in the interval 0-1 Hz frequency, and a 2 mm amplitude WGN, in the interval 0-20 Hz frequency. The input signal was sampled at 50 Hz frequency and it was applied to the ST1D without the strut and truss assembly, because the result of this identification was envisaged to be used in other hybrid tests that use the same test rig.

In the second-order estimation, the measured acceleration was directly utilized after applying a high-pass Butterworth filter and the velocity response was synthesized from the measured displacement

and acceleration at 4 Hz crossover frequency. The measured displacement is cropped at the start and end to prevent ill-conditioning of the estimation matrix. At the end, the command and measured displacements were finally filtered through a 20 Hz low-pass Fourier filter.

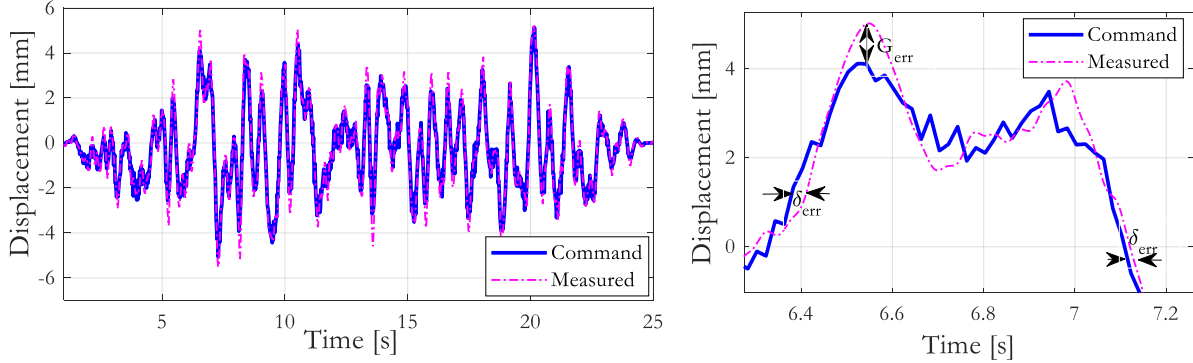


Figure 4-26: Command versus measured displacement of the ST1D subjected to the WGN input (left) and a closer view on the time-delay,  $\delta_{err}$ ; and the gain error,  $G_{err}$  (right)

In this experiment, the second-order parameters were obtained as  $a_0=0.9066$ ,  $a_1=0.0015$  s and  $a_2=9.95e-5$  s<sup>2</sup>. These parameters are equivalent to having a time-delay equal to 1.65 ms and an overshooting error of 10.3%. The identification work was performed at  $k_p=3.5$  and  $k_I=0.001$ . It should be noted that changing the PID gains of the controller can significantly alter the compensation parameters. In this work, the same PID gains were adopted during the validation of LNEC-HS.

#### 4.2.3 Rehearsal experiment for hybrid simulation

The first step in any hybrid testing is to ensure proper functioning of all software components. Any software bugs need to be detected and addressed at this stage of a hybrid test. Failure to do so can damage a test specimen prematurely. Furthermore, the adequacy of the control/compensator algorithms can be assessed. Therefore, a rehearsal hybrid test, also called *open-loop* hybrid test, is conducted by returning simulated restoring forces of the test specimen into the finite-element software. The loading system is left inactive by disconnecting the drive signal to the actuator or a small drive signal may be applied to the test specimen. In the former, software bugs and communication issues can be identified whereas, in the latter, the performance of a control/compensation algorithm can be examined after comparing the target and measured displacements, as shown in Figure 4-27(right). Note that the latter must be conducted at a low excitation level. In rehearsal hybrid tests, the experimental element is essentially elastic; consequently, the simulated restoring forces are proportional to the target displacements.

The *open-loop* hybrid test of the steel frame was conducted by scaling the El Centro (1994) earthquake to 0.03 g PGA. Figure 4-27 shows that the lateral displacement of the steel frame from the *open-loop* hybrid test is in good agreement with the numerical solution. This ensures that the software part of

the developed framework is operating properly. Besides, control errors were identified in the rehearsal test, thus slight adjustments were made to the compensation parameters.

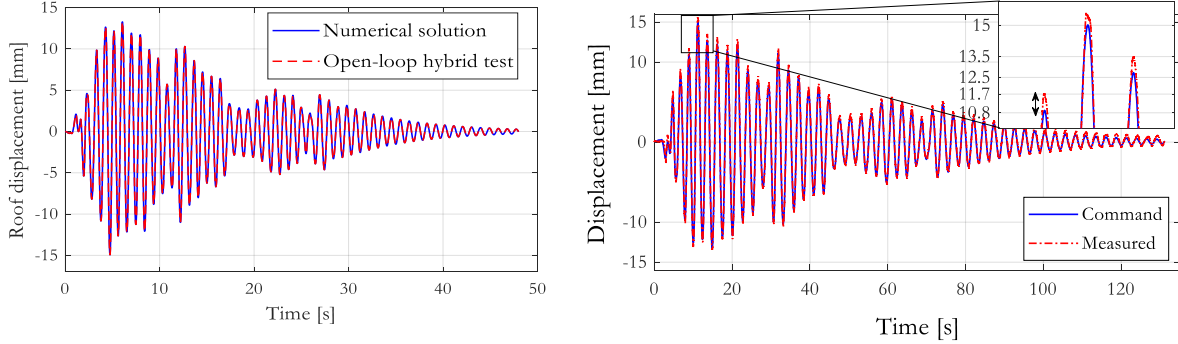


Figure 4-27: Comparing roof displacements between open-loop hybrid test and purely numerical analysis of the case study structure (left); and identification of control errors in the open-loop hybrid test (right)

#### 4.2.4 Hybrid test experiment

The term *closed-loop* hybrid test refers to a hybrid test which is conducted by returning the measured restoring forces to the computational driver. In addition to the rehearsal test, performing a *closed-loop* test at a low excitation level helps in pointing out errors in the feedback force. The experimental column is again strictly elastic during this additional rehearsal test. In this validation work, such tests revealed a small signal-to-noise ratio of the measured restoring force, which is inevitable as long as the excitation is low. Here, the level of noise was useful in deciding the level of filtering needed for the measured force returned to the computational driver. For brevity, the results of this rehearsal test are not discussed in this chapter. Instead, the results of a closed-loop hybrid test are discussed in subsequent paragraphs.

In this simulation, the fundamental frequency of the steel frame was calculated to be 1.08 Hz and mass-proportional damping, considering  $\xi=2\%$ , was applied to the structure. Based on the deductions made in chapter two, the  $\alpha$ -OS integration algorithm, considering  $\alpha=0.9$ , was chosen in this hybrid test. The steel frame as subjected to the El Centro input motion and the time-step of the analysis in OpenSees was set to 4 ms ( $\delta t_{FE}$ ). The ATS compensator was activated during this hybrid test in addition to the prediction-correction process. At the end of the response simulation, the true speed of the hybrid test,  $\delta t_{sim}/\delta t_{FE}$ , evaluated to be 27.8. In general, hybrid tests that are conducted at speed ratios 20-50 can be regarded as fast; thus, the *closed-loop* hybrid test conducted here can be classified as a fast hybrid test. Herein, a second-order low-pass Butterworth filter, 4 Hz cut-off frequency, was adopted to limit the level of noise in the measured restoring forces.

As shown in Figure 4-28(left), the controller algorithm overshoots (by as large as 20%) the target displacements during the hybrid test. This overshoot resulted in approximately 1 kN maximum

error in the restoring force (nearly 25% of the maximum restoring force). However, no important error propagation was observed since the hybrid test has small experimental errors towards the end of the test (see Figure 4-29(right)).

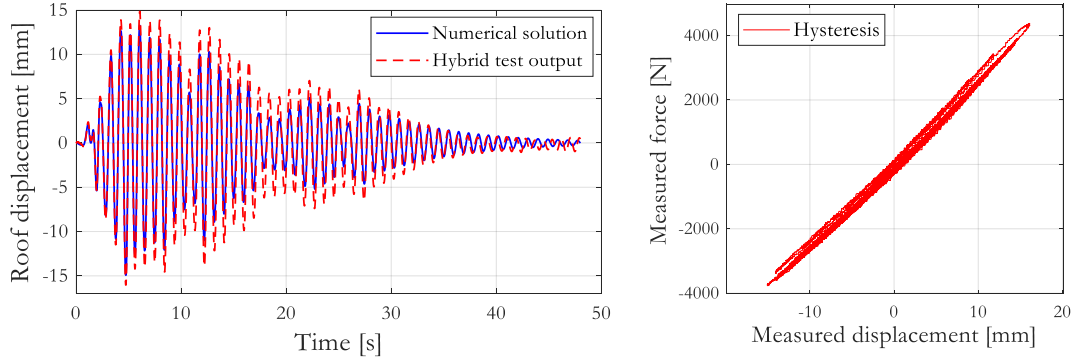


Figure 4-28: Comparing roof displacement between the actual hybrid test and the purely numerical analysis of the case study structure (left); and hysteresis loop (right)

The overshooting observed during the experimental test can be the result of higher mode excitation of the test frame. In detail, the excitation of the second and third modes of the frame, which are 33 Hz and 41 Hz, respectively. This reasoning agrees well with the frequency response of the lateral displacement shown in Figure 4-29.

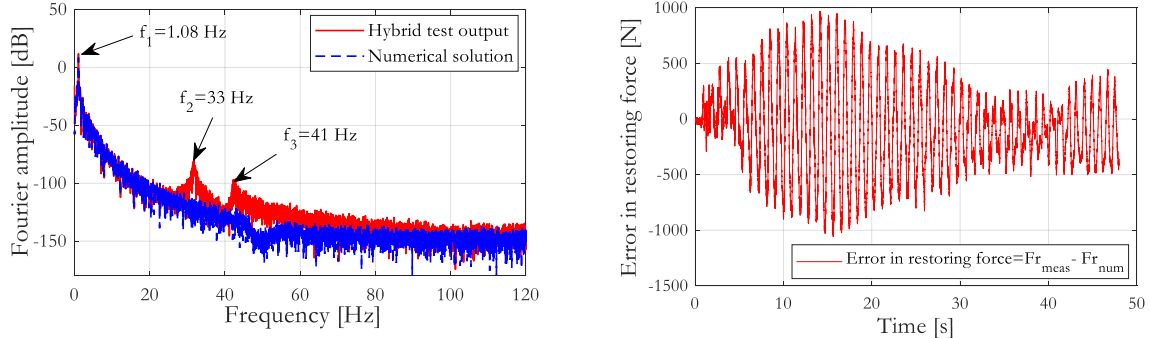


Figure 4-29: Comparing the Fourier amplitude of the roof displacement between the actual hybrid testing and the purely numerical analysis (left); and error in restoring force obtained by comparing the numerical and measured forces (right)

To conclude, better results may be obtained by increasing the numerical damping. Besides, adjusting the coefficients of the ATS compensator would be beneficial, especially the parameter related to gain error, to reduce the overshoot errors of the controller.

## 4.3 Advanced control strategies for substructuring in shaking table tests

### 4.3.1 Introduction

In substructuring tests, the control variable is dictated by the compatibility or equilibrium condition that is enforced at the boundary between the numerical and experimental substructures. Displacement often serves as a command to servo-hydraulic actuators since satisfying the displacement compatibility, at the interface boundary, is reasonable when the inertia effect of an experimental substructure is very small compared to its numerical counterpart. Nevertheless, hybrid tests involving significant inertia effects of the experimental substructure may need the compatibility of both accelerations and displacements to be enforced at the interface boundary to ensure accurate reproduction of inertial forces. However, direct control of shaking table acceleration is inherently unstable because the table's position cannot be determined accurately. After all, zero acceleration command does not necessarily mean that the table is static. In other words, the pole located at the origin is unobservable in acceleration measurements, which makes the system uncontrollable. Nonetheless, acceleration control is commonly performed by converting accelerations to displacements. On the other hand, advanced control methods use displacement-based control coupled with acceleration tracking capabilities, which is the focus of this work.

Considering a hybrid test of a base-isolation system, located at the mid-height level of a building, and the part of the building above the base isolation is represented physically, the acceleration input to the physical substructure, which can be applied through a shaking table, need to be controlled. The remaining parts of the structure below the base isolation are represented in a numerical simulation program. In this scenario, the experimental substructure can have a significant share of the inertial action. In such hybrid test, the measured shear force at the isolation level is applied to the numerical substructure while the absolute acceleration at that level, obtained from the numerical substructure, serves as the input acceleration to the experimental substructure. A similar scheme was attempted by Schellenberg et al. (2016) using absolute displacements instead of accelerations. They applied it to a mid-level seismic isolation system made from Triple Friction Pendulum (TFP) bearings. In this scheme, it is necessary to ensure that the inertial and damping forces are accurately reproduced.

In the past, several attempts have been done in improving acceleration tracking capabilities of shaking tables without direct acceleration feedback (Luco et al., 2010; Stehman & Nakata, 2016; Gunay S., 2014; Zhang et al., 2015; Fermandois & Spencer, 2017; Phillips et al., 2014). These studies aimed to achieve good matching between the input and measured acceleration in conventional shaking table tests. Besides, a hybrid test that needs acceleration matching has an additional challenge since errors of the target acceleration enter the numerical solution and get propagated.

Consequently, errors may increase exponentially resulting in an erroneous and/or unstable response simulation.

The Transfer Function Iteration (TFI) technique has been a favorite choice among laboratories for matching the acceleration input in shaking table tests. This technique employs an iterative offline correction procedure using the linearized transfer function of a shaking table and control errors. It is simple and effective in shaking table tests, especially for low-intensity input motion; nonetheless, it cannot be used for online applications such as hybrid testing. Afterall, it may result in premature failure of a test structure since the target acceleration has to be applied multiple times. Owing to nonlinearities in a test structure and/or a shaking table, the feedforward compensation alone is not a candidate for online acceleration tracking as well (Phillips, 2012; Phillips et al., 2014). A feedback control, based on the Linear Quadratic Gaussian controller (LQG), coupled with the feedforward compensator has been satisfactory in improving control errors due to system nonlinearities caused by model deviation and measurement noise (Phillips et al., 2014). This controller is termed as *feedforward-feedback* controller. Herein, the acceleration tracking of a shaking table in hybrid testing and its implementation in the NI real-time target and FPGA hardware is presented. Much attention was given to the improvement in the accuracy of acceleration tracking by controlling the displacement command to a shaking table. This objective was implemented using the *feedforward-feedback* controller.

On the other hand, if the nature of the problem or substructuring scheme demands equilibrium conditions to be enforced at the interface boundary, the target force to be applied by an actuator needs to be matched. Hybrid testing of stiff elements is a good example of this case. However, force control using servo-hydraulic actuators is challenging due to their large impedance. Indirect control of a force command is therefore employed, where the actuator, which is attached to a compliance spring, is controlled using a displacement command. In this scheme, the displacement command must be accurately compensated. Again, this brings us to the requirement for an advanced control strategy whereby good force matching is only expected after compensating the combined dynamics of the servo-hydraulic actuator and the test structure.

Consider now a substructuring test in a shaking table, whereby the lower part of a shear building is the physical substructure while the upper part is numerically modeled. In this scenario, the shear force obtained from the numerical substructure, at its base, is applied to the top of the physical substructure through an additional actuator that is controlled in force. This can be performed through the equivalent force control approach using added compliance. In this technique, a force command is matched, indirectly, by controlling an equivalent displacement, which is governed by the compliant system connected to the actuator. The Smith-predictor controller is a non-adaptive model-based technique for compensating the time-delay of a system (Sivaselvan et al., 2008). The application of this control scheme is difficult in the presence of nonlinearities of a test structure and/or a loading system. To overcome this challenge, the ATS compensator has been explored recently (Chae et al., 2018). In this study, both the model-based and adaptive approaches of the

equivalent force control are implemented in *LNEC-HS* software, and the model-based scheme was examined in a parametric study. Towards the end of this chapter, the implementation of the advanced control approaches in the *directHS* state are discussed. The synchronization between the feedforward-feedback controller of the shaking table and the equivalent force controller of the additional actuator is addressed as well.

#### 4.3.2 Robustness test of a feedforward-feedback controller

In chapter three, control-structure interaction (CSI) was shown to have a notable influence in the dynamics of the ST1D, consistent with the findings of Conte & Trombetti (2000). Thus, for accurate model-based control, a reliable estimate of the shaking table transfer function must be used, meaning its system identification needs to be conducted.

Before using the feedforward-feedback controller for experimental tests, the algorithm was studied in simulation mode by examining the acceleration tracking of a shaking table test of a two-story shear building made from steel. The transfer function of the uniaxial shaking table at the University of Illinois (Phillips et al., 2014) was adopted since the prime objective of this study is to explore the robustness of the controller. The transfer function, shown in Figure 4-30, was derived by applying a band-limited white noise, 0–20 Hz frequency, to the shaking table, with the steel frame rigidly attached to it. The first and second modal frequencies of the structure are 1.67 Hz and 4.63 Hz, respectively, and their corresponding damping ratios are 0.15% and 0.10%, respectively. The transfer function, given in equation (4.8), was originally derived from the input voltage signal, RMS value equal to 0.4 V, and the measured acceleration, units of m/s<sup>2</sup>. Assuming a 1:1 ratio between the voltage and displacement commands, the transfer function can be expressed as a function of the output acceleration and the displacement command, i.e.,  $\ddot{x}_m/x_{cmd}$  has m/s<sup>2</sup>/m units.

$$G_{a_m u_c} = \frac{\ddot{x}_m}{x_{cmd}} = \frac{9.733s^7 + 859.7s^6 + 9102s^5 + 7.726e05s^4 + 9.347e5s^3 + 7.039e7s^2}{s^7 + 89.98s^6 + 6806s^5 + 2.314e5s^4 + 5.422e6s^3 + 1.397e8s^2 + 4.996e8s + 1.156e10} \quad (4.8)$$

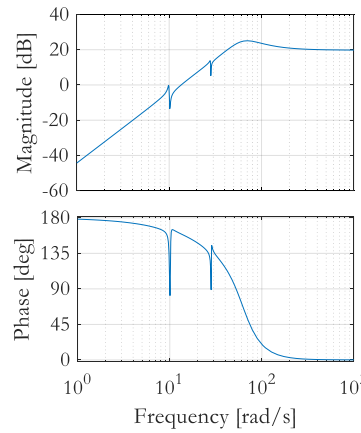


Figure 4-30: Transfer function of the uniaxial shaking table at the University of Illinois when rigidly attached to a two-story shear building (from Phillips et al., 2014)

To examine the robustness of the controller, a random Gaussian noise was added to the feedback loop to mimic the system disturbance. The Gaussian noise has zero mean and a standard deviation equal to 10% of the peak value of the target acceleration. The simulated study was carried out using the feedforward-feedback controller implemented in the simulation coordinator VI of *LNEC-HS* software. The following earthquake records were used as input accelerations to the uniaxial shaking table during this simulated study.

- a. El Centro earthquake, 1940 (0.2984 g PGA)
- b. Kobe earthquake, 1995 (0.2758 g PGA)
- c. Landers earthquake, 1992 (0.2736 g PGA)

The feedforward-feedback control algorithm was implemented in the NI-RT target using the built-in VIs available in the control and simulation module of LabVIEW. The LQG feedback controller is designed to work in cascade with the PID controller of the ST1D. The maximum clock speed of the LQG control loop was limited to 500 Hz whereas the clock speed of the PID controller was set to 5 kHz, i.e., when the LQG controller executes one acceleration command, ten iterations of displacement feedbacks are completed in the PID loop. After every ten iterations of the PID loop, measured acceleration is returned to the LQG control loop and the acceleration error is used in generating a correction signal. This correction command, which is internally converted into displacement, is again applied through the PID controller. This process is repeated  $n$  times, where  $n$  is the ratio of the time-step of the hybrid simulation to the clock speed of the LQG loop. For example, if the time-step of an accelerogram is 10 ms, 5 iterations of the LQG loop and 50 iterations of the PID loop are executed at each time-step.

Alongside, the feedforward control was simply implemented using the *transfer function* VI that takes a target acceleration and the transfer function of the uniaxial shaking table  $G_{a_m u_c}$  as its inputs, and calculates the feedforward displacement  $u_{FF}$ . To improve the instability phenomenon, the target acceleration is passed through a low-pass filter constructed from the  $G_{a_m u_c}$ .

On the other hand, the LQG feedback controller was constructed using the *Discrete Kalman filter* VI and *Linear Quadratic Regulator (LQR)* VI. The deviation in the measured states is feedback to the Kalman filter whereby optimal gains are calculated to accurately estimate the states of the system. Herein, the states of the shaking table include displacement, velocity, and acceleration. The estimated states are then returned to the *LQR* VI and the feedback command,  $u_{FB}$ , is determined. Eventually, the sum of the  $u_{FB}$  and  $u_{FF}$  is applied to shaking table as input command.

Accurate estimation of the R-matrix of the *Discrete Kalman filter* VI must be consistent with the magnitude of the measurement noise. This can be observed by changing the R-matrix for the same magnitude of noise. Therefore, the entries of the R-matrix can be estimated from acceleration measurements by applying zero input voltage to the shaking table. On the other hand, the Q-matrix, which represents the uncertainty in the modeling process (process noise), is difficult to estimate. It is therefore defined by a trial-and-error method.

In this study, the pole modification factor of the feedforward controller was set to one since equation (4.8) is causal. Besides, the covariance matrix of the measurement noise (R-matrix, which is square matrix with a dimension equal to the size of the output) of the Kalman filter was set to 0.1 and the covariance matrix of the process noise (Q-matrix, which is also a square matrix with a dimension equal to the number of states in the system) was defined by choosing the diagonal terms,  $d_1, d_2, \dots, d_n$ , of  $Q_{Kal}$ :

$$Q_{Kal} = \begin{bmatrix} d_1 & 0 & 0 & 0 & 0 & 0 & 0 \\ d_2 & 0 & 0 & 0 & 0 & 0 & 0 \\ d_3 & 0 & 0 & 0 & 0 & 0 & 0 \\ d_4 & 0 & 0 & 0 & 0 & 0 & 0 \\ d_5 & 0 & 0 & 0 & 0 & 0 & 0 \\ d_6 & 0 & 0 & 0 & 0 & 0 & 0 \\ d_7 & 0 & 0 & 0 & 0 & 0 & 0 \end{bmatrix} \quad (4.9)$$

In the *LQR VI*, two weighting matrices are necessary for solving the optimal gains from the *Riccati* equation. The Q-matrix of the *LQR VI* penalizes the state vector (or output vector) in the cost function whereas the R-matrix penalizes the input vector of the system. It should be noted that the R and Q-matrices of the *LQR VI* should not be confused with those of the *Discrete Kalman filter VI*, mentioned above. To distinguish them  $R_{LQR}, R_{Kal}, Q_{LQR}$  and  $Q_{Kal}$  are introduced herein. The  $R_{LQR}$  and  $Q_{LQR}$  matrices dictate the balance between the *control effort* and the *speed of response*. Both matrices are symmetric and positive semi-definite.

In general, increasing the magnitude of the  $Q_{LQR}$  allows the system to respond faster, which is favorable for real-time testing conditions and the  $R_{LQR}$  defines the cost of actuation (control effort) while an increase in the magnitude of the  $R_{LQR}$  reduces the control effort (expensive control strategy). Hence, the two matrices must be tuned to achieve an acceptable trade-off between the desired overshoot and rise-time characteristics (performance) and control effort of the controller are achieved.

In the first phase of the simulated study, the test specimen was elastic. The  $R_{Kal}$  and  $Q_{Kal}$  matrices were set to constant values whereas the  $R_{LQR}$  and  $Q_{LQR}$  matrices were varied to achieve a stable output. Since no model deviations were introduced at this stage, the pole factor of the feedforward controller was set to one. When setting the amplitude of the  $R_{LQR}$  below  $10^{12}$ , the feedback control becomes unstable, but it was found to be insensitive to the rest of the other input matrices. The cut-off frequency of the Butterworth filter that was used for filtering the output responses is 5 Hz. Likewise, during the computation of spectral densities, the structural responses were filtered at 20 Hz cut-off frequency to elucidate control errors at large frequencies. Furthermore, a high-pass filter, 0.25 Hz cut-off frequency, was applied to the input acceleration, before applying to the case structure, to remove its DC content. The following points explore the influence of the noise matrices of Kalman filter and the weighting matrices of LQR on the feedforward-feedback controller:

1. Taking  $R_{Kal}$  and  $R_{LQR}$  to be 0.1 and  $10^{14}$ , respectively, the controller has favorable characteristics, with comparatively small RMS error. The large magnitude of  $R_{LQR}$  may

indicate a small control effort; however, the effect of its magnitude on the level of the control effort is not clear. In this setting, the measured and target accelerations are in good agreement in the interval 0-10 Hz frequency, as shown in Figure 4-31. Nonetheless, significant control errors prevail above 10 Hz. Here, the entries of the  $Q_{LQR}$  matrix were set below one, and the diagonal terms of the  $Q_{Kal}$  were defined, from top to bottom, to be in [-1 5] interval of the natural logarithm.

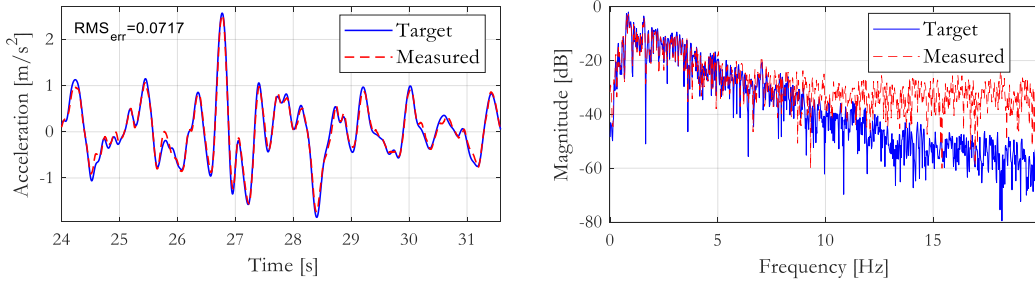


Figure 4-31: Performance of the LQG controller when  $R_{LQR}=10^{14}$  and  $R_{Kal}=0.1$

2. The parameter  $Q_{Kal}$  may be set as a unit matrix, although the first few entries can be slightly changed for a minimal improvement of the control characteristics. Nevertheless, it is pragmatic to adjust these parameters depending on the states of the system that make up the transfer function. The comparison between target and measured accelerations, when the test setup is subjected to the Landers record, shown in Figure 4-32, presents a comparable level of control error as the one observed in Figure 4-31.

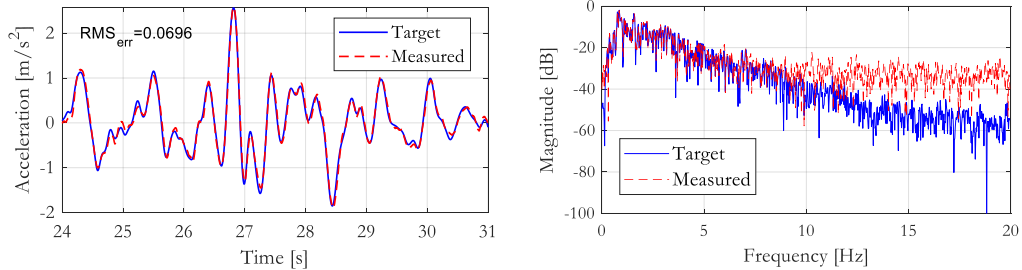


Figure 4-32: The performance of LQG controller when  $Q_{Kal}$  is a unit matrix

3. When the frame structure becomes inelastic, the RMS value of control error has increased because the properties of the damaged structure are not tuned to the controller anymore. Besides, the adaptive process of the LQG controller is too slow to correct this model deviation. In this simulation, the process noise was taken as a unit matrix.

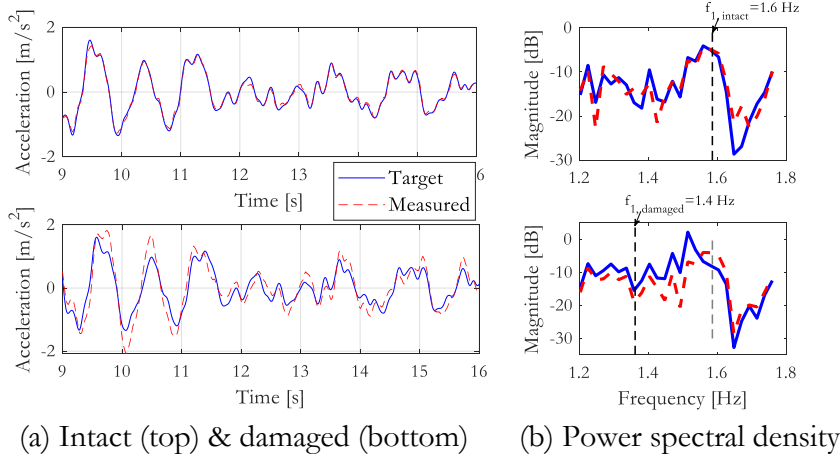


Figure 4-33: Acceleration tracking of a feedforward-feedback controller applied to a nonlinear structure in a substructuring test using a shaking table

4. A pole factor of 10 may be justifiable for limiting instability issues when a noncausal transfer function is adopted to model the system dynamics. The significance of the pole factor is more pronounced with erroneous system modeling and/or in the presence of model deviations.
5. The effect of delaying the feedback controller (i.e.,  $u_{FF}$  leads  $u_{FB}$ ) was also examined by comparing the performance of the controller with and without delaying the feedback control. A negligible discrepancy was recorded between the two approaches as opposed to the findings of Nakata (2010). However, extensive studies need to be performed to generalize this effect. The default setting of *LNEC-HS* software has zero delay.

The model deviation, which is apparent during the damage of the case structure, may be accounted by reducing the modal frequencies of the structure. Herein, the 1<sup>st</sup> and 2<sup>nd</sup> modal frequencies of the intact structure were reduced by multiplying 0.86 and 0.95 factors, respectively. In this study, all the three earthquake records were applied. However, only the results obtained using the El Centro earthquake are presented, since the others lead to similar conclusions. It is clear from Figure 4-34 that control errors are amplified because of the model deviation.

This simulation was performed at 20 ms time-step; consequently, the capacity of the feedback controller in suppressing these errors was not fully exploited since only a limited number of iterations of the LQG loop can be performed. The maximum possible clock-speed of the LQG loop during this study was 5 ms; hence four acceleration corrections were conducted at each time-step.

To explore further the robustness of the feedback controller, the time-step size of the simulation was made larger so that the number of corrective iterations of the feedback controller is relatively larger. Considering the Landers earthquake input and a time-step equal to 100 ms, which is

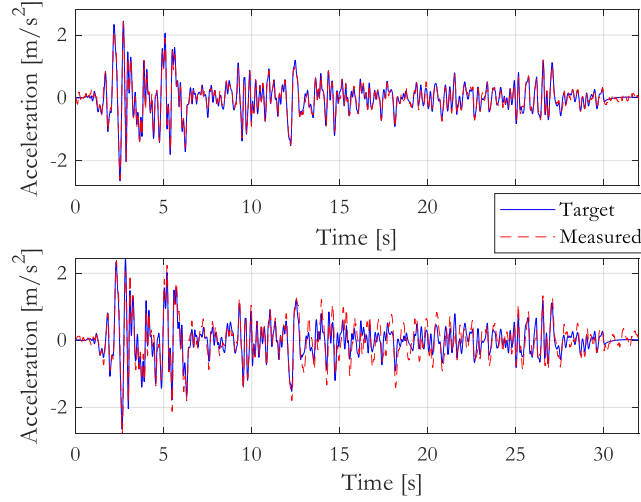


Figure 4-34: Target versus measured acceleration during a shaking table test of a two-story shear building using a feedforward-feedback controller: Intact structure (top) and damaged structure (bottom)

equivalent to an experimental test ten times slower than a real-time test, an excellent matching between the target and measured accelerations of the test structure can be achieved (see Figure 4-35). Hence, it can be concluded that the clock-speed of the LQG controller, relative to the time-step of a hybrid simulation, is relevant for the accuracy of the controller. Therefore, the clock-speed of the LQG control loop of *LNEC-HS* software was upgraded to 2 ms.

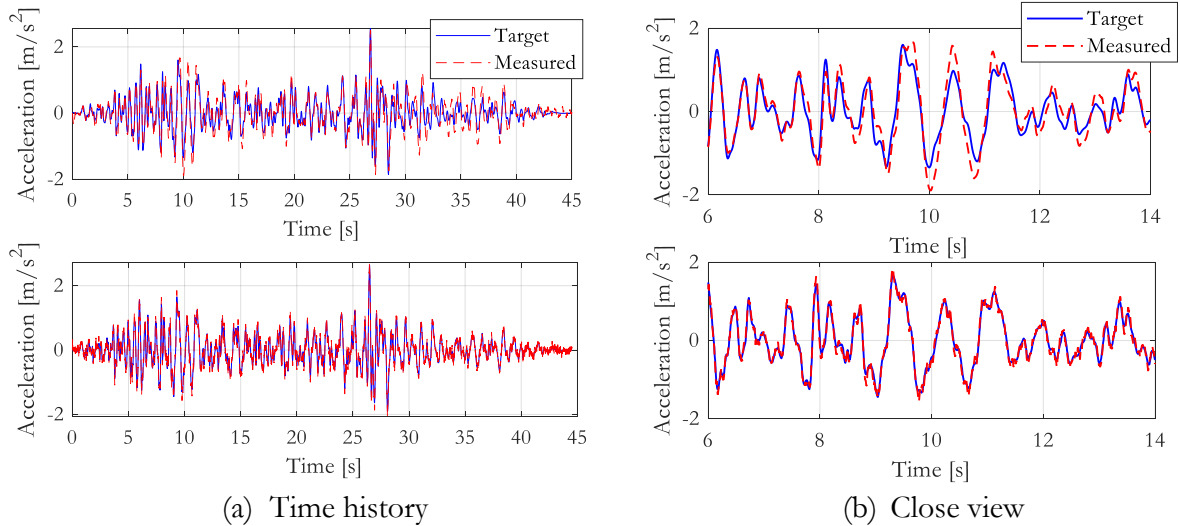


Figure 4-35: Performance of acceleration tracking of the LQG controller as a function of the number of feedback corrections:  $\Delta t_{\text{sim}}=10$  ms (top) and  $\Delta t_{\text{sim}}=100$  ms (bottom)

### 4.3.3 Equivalent force control through added compliance

In this section, the equivalent force control of actuators is explored due to its importance in simulating soil-structure interaction (SSI) in a substructuring test that models the lower portion of a reference structure as an experimental substructure. Such a test is idealized to have a steel frame structure that is erected on the soil deposit, contained inside an equivalent shear beam (ESB) container. In this test setup, the ground motion input is applied at the base of the flexible soil-container while a force command, which is obtained from the numerical substructure, is applied to the steel frame, at the interface boundary between the two substructures, using an auxiliary actuator.

Considering a two-story frame structure, which behaves as a shear building, with a shallow foundation resting on a dry sandy deposit, the physical substructure corresponds herein to the first story of the frame and the foundation soil. The ground motion of the reference structure can be applied through a shaking table at the base of the ESB container. The latter is assumed to be firmly attached to the shaking table.

As discussed previously, actuator control using a direct force feedback is unstable due to the stiff oil-column frequency. Furthermore, noise from friction, stick-slip, breakaway forces on seals, backlash, and so on forth makes force control challenging. Considering the experimental setup for the conceived SSI hybrid testing, we can write:

$$M_e \ddot{u}_e + C_e \dot{u}_e + K_e u_e = -\underbrace{M_e \ddot{u}_g}_{F_{ST1D}} + \underbrace{C_n \dot{u}_{ne} + K_n u_{ne}}_{F_{act}} \quad (4.10)$$

where  $F_{act}$  and  $F_{ST1D}$  are the interface shear force and the inertial force of the physical model, respectively; terms with the subscript “ne” pertain to the kinematics of the interface boundary. Force control of the auxiliary actuator is thus required to match  $F_{act}$  at the interface boundary. In direct force control, experimental errors may enter the numerical substructure making response simulation erroneous. Besides, a strong coupling is likely to occur between the shaking table and the auxiliary actuator, particularly when the auxiliary actuator is controlled using direct force feedback. The undesired dynamics that arise from this coupling can adversely affect the performance of the controllers.

Among the few studies that were conducted in the past, Stehman (2014) proposed a controlled mass approach for controlling the force using actuators. In this method, the force command from a numerical substructure is first converted into an equivalent acceleration and integrated twice to get the displacement command. Before applying it to the actuator, it is passed through a high-pass filter. However, this scheme could not be realized due to instability issues. Moreover, this control approach is dependent on the amplitude of the input ground motion as well as on the geometry and configuration of the experimental substructure. Another attempt from the same author uses a direct force control approach. In this approach, the auxiliary actuator has two controllers, and the shaking table is controlled in displacement mode. One of the controllers of the auxiliary actuator was built to achieve reference tracking and disturbance rejection objectives while the other

controller is dedicated to reducing the coupling between the shaking table and the actuator. In this scheme, the shaking table is independent of the dynamics of the auxiliary actuator since it is controlled in displacement. This technique has a decoupling algorithm to decouple the dynamics of the shaking table and the actuator. To the knowledge of the author, this approach was also not successfully applied in a hybrid test due to stability issues. However, this technique could be improved in the future if efficient decoupling mechanisms could be developed.

In the “*series of elasticity*” technique (Pratt et al., 2002), a flexible spring is attached in series to an actuator to turn it into a low-impedance system. Assuming perfect disturbance rejection and perfect displacement matching over the frequency range of interest, the actuator is commanded to the summation of the compression/extension of the spring element and the displacement of the test structure (Sivaselvan et al., 2008). The force applied to the test structure is therefore indirectly controlled:

$$x_{cmd} = F_{act}/K_{ac} + x_{st} \quad (4.11)$$

where  $x_{cmd}$ ,  $x_{st}$  and  $K_{ac}$  are the displacement command to the actuator, displacement of the test structure, and stiffness of the compliance spring, respectively. In equation (4.11),  $F_{act}/K_{ac}$  is the deformation of the compliance spring. This equivalent force control can be implemented using adaptive and non-adaptive approaches. The non-adaptive approach uses a model predicted displacement and the value of  $F_{act}/K_{ac}$  is calculated offline. The implementation of the two approaches is presented in the subsequent sections of this chapter.

#### 4.3.3.1 Equivalent force control using the Smith Predictor compensator

In this subsection, the equivalent force control of a SDOF structure, shown in Figure 4-36, that makes use of the Smith Predictor compensator, is explored in the frequency domain. Considering the first-order model of an actuator, the combined transfer function of the experimental element and the compensator was derived; and the accuracy of the force control, with and without using the Smith Predictor controller, was investigated. Besides, the sensitivity of the force control to errors in modeling the stiffness of the SDOF, errors in stiffness of the added compliance, and the

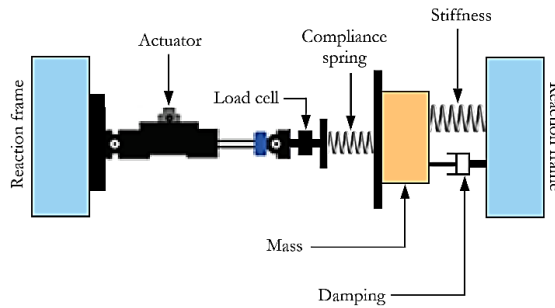


Figure 4-36: Equivalent force control of a SDOF structure using added compliance presence of time-delay of the actuator were investigated to help us examine its robustness. This

study applies the perturbation technique to model the parameters mentioned above based on their practical limits.

The concept of the Smith Predictor is simply to “*make the controller aware of the time-delay and endowed it with patience to wait it out*” (Sivaselvan et al., 2008). The application of the Smith Predictor compensation to the equivalent force control was proposed by Sivaselvan et al. (2008) assuming that the inner loop dynamics of an actuator can be modeled as a pure time-delay.

Consider a standard feedback control system that has an inner-loop controller of a test specimen. Due to the presence of the actuator dynamics, some undesired behavior is added into the system, which can be canceled out by feeding back both the predicted response of the test specimen and the characteristics of the actuator. However, the model used to predict the test structure may be erroneous, thus hindering full compensation. The above concept is illustrated in the schematic diagram shown in Figure 4-37.

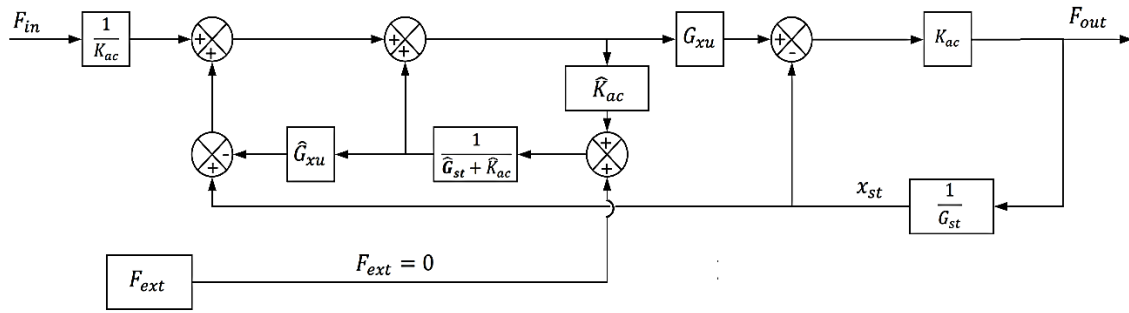


Figure 4-37: Schematic diagram of the equivalent force control of a SDOF structure through the Smith Predictor compensator<sup>3</sup>

From Figure 4-37, the combined dynamics of the system (controller and test structure), with and without Smith Predictor, can be derived as shown in equations (4.12) and (4.13), respectively. These transfer functions represent the ratio between the force measured at the spring and the command force to the actuator:

$$\frac{F_{out}(s)}{F_{in}(s)} = \frac{G_{xu} k_{ac}}{\hat{k}_{ac} \left\{ 1 + \frac{(1 - G_{xu}) k_{ac}}{G_{st}} \right\}} \quad (4.12)$$

$$\frac{F_{out}(s)}{F_{in}(s)} = \frac{G_{xu} k_{ac}}{\hat{k}_{ac} \left\{ 1 + \frac{(1 - G_{xu}) k_{ac} \hat{G}_{xu} - \hat{k}_{ac} (1 - \hat{G}_{xu}) (G_{st} + k_{ac})}{G_{st} \hat{G}_{st}} \right\}} \quad (4.13)$$

where \$k\_{ac}\$, \$G\_{xu}\$, and \$G\_{st}\$ are the stiffness of the added compliance, the first-order model of the actuator, and the transfer function of the experimental substructure (i.e., \$m\_{st}s^2 + c\_{st}s + k\_{st}\$),

<sup>3</sup> In Figure 4-37, \$F\_{ext}\$ refers to any external loading such as the inertial load applied by a shaking table during a hybrid test which includes a shaking table and an auxiliary actuator. To examine the performance of the equivalent force control, which uses Smith Predictor, independent of any external action, it was taken to be zero.

respectively. Herein, the estimated variables are represented by a hat sign. The SDOF structure was assumed to have 50 kg of mass, a fundamental frequency of 2 Hz, and a viscous damping of 2%. The first-order transfer function of the actuator,  $G_{xu}$ , was assumed to have a 5 ms time-delay and a unit amplitude. Besides, the compliance spring was chosen to have 76% of the structure's stiffness.

In the frequency domain analysis, when the Smith Predictor compensator is not deployed, the amplitude of the  $F_{out}/F_{in}$  has an abrupt drop at the natural frequency of the structure. This abrupt drop in the response function gets smaller as the inherent damping of the structure increases. Considering ideal modeling conditions, i.e., the true values of the system parameters are equal to their corresponding estimated values, the amplitude and phase characteristics of the  $F_{out}/F_{in}$  are examined in Figure 4-38. Deploying the Smith Predictor compensator in the equivalent force control loop has evident improvement in the characteristics of the  $F_{out}/F_{in}$ . Nonetheless, ideal conditions for modeling the system dynamics are not realistic; therefore, the impact of model deviation and/or incorrect modeling (actuator, test specimen, and compliance spring) on the performance of the compensator are explored here. This includes the effect of the inherent damping of the structure on the performance of the controller shown in Figure 4-38.

Considering the estimated time-delay of the actuator,  $\hat{G}_{xu}$ , to be 3 ms instead, full compensation of control errors was not achieved. In Figure 4-38, the transfer function built from the estimated parameters is referred to as a *non-ideal Smith Predictor*. The level of control error caused by the erroneous modeling of the time-delay of the actuator is therefore important.

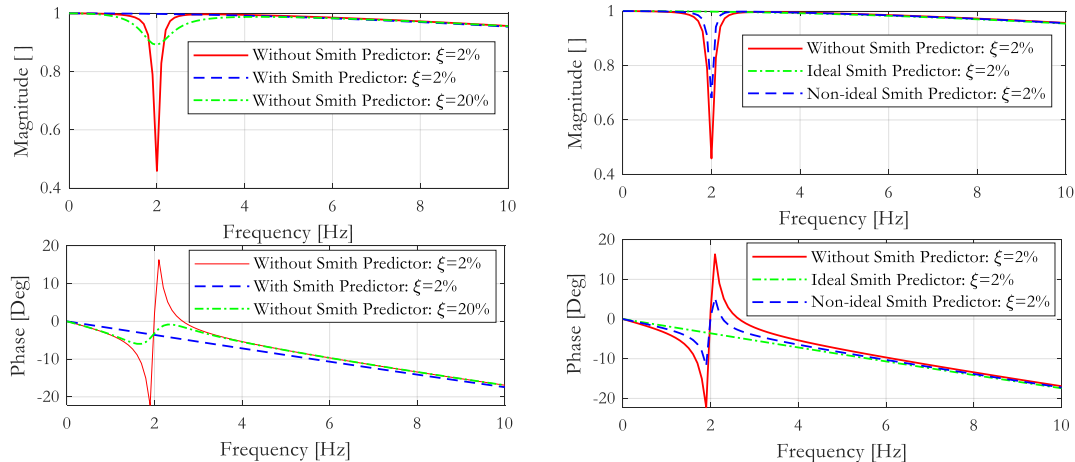


Figure 4-38: Performance of equivalent force control using Smith Predictor compensation (left) and its robustness to model deviations (right)

The following points summarize the results obtained from the robustness analyses conducted in this work.

- Overestimating the structure's stiffness,  $K_{st}$ , results in an abrupt drop of the amplitude of the  $F_{out}/F_{in}$ , at the natural frequency of the structure, and an overshooting peak just after

its natural frequency. Contrarily, underestimating the stiffness,  $K_{st}$ , gives rise to an exact opposite scenario, as shown in Figure 4-39(left). In the latter, the magnitude of the overshoot error, at the natural frequency of the structure, is larger than the abrupt drop of the  $F_{out}/F_{in}$  that was observed in the former. Therefore, overestimation of the structure's stiffness is less detrimental to the performance of the equivalent force control when compared to underestimating the structure's stiffness.

- Unlike the erroneous modeling in  $K_{st}$ , the effect of errors in modeling the viscous damping of the experimental substructure is nearly negligible. In Figure 4-39(right), in which the scale of the magnitude plot is very limited, the two peaks change polarity abruptly and the characteristics of the frequency interval between the peaks is equally affected. When the viscous damping is underestimated, the output force overshoots at the natural frequency of the structure.

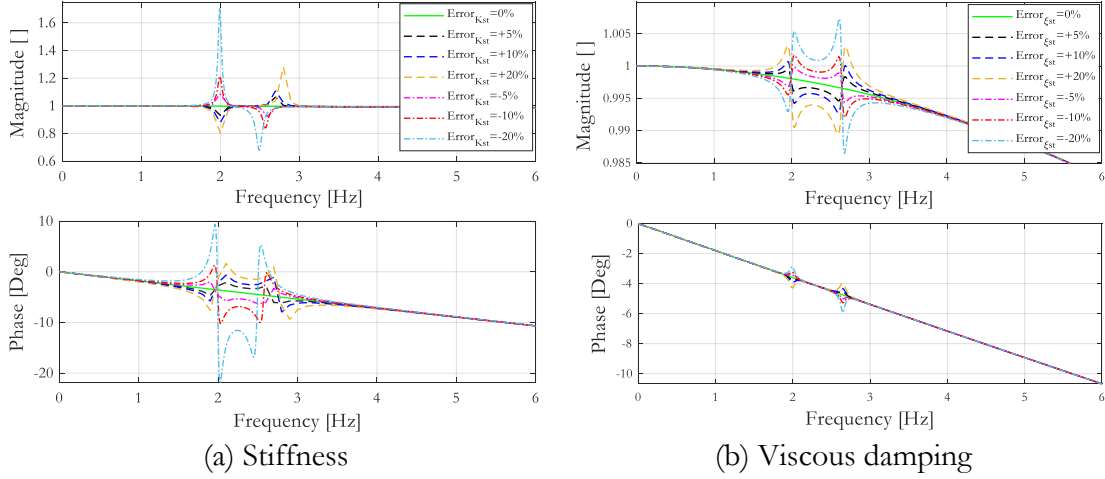


Figure 4-39: Performance of the equivalent force control, using the Smith Predictor compensation, to erroneous modeling of the experimental substructure

- On the other hand, overestimating the stiffness of the compliance spring,  $k_{ac}$ , makes the force output undershoot in the entire frequency range, as shown in Figure 4-40(left). The level of reduction in the force output is equivalent to the error in modeling the compliance spring. Conversely, underestimating the compliance spring causes the force to overshoot its exact amplitude. The system dynamics in the above two scenarios are also characterized by peaks after the natural frequency of the structure. The former rising abruptly while the latter plummets abruptly, both towards the unit amplitude. Even though, it appears that errors in modeling  $k_{ac}$  have significant effects, this parameter can be accurately characterized before attaching it to an actuator.
- In the cases of underestimation and overestimation of the actuator's true time-delay,  $\tau_{xu}$ , the output force undershoots and overshoots, respectively. Considering the same amplitudes of overestimation and underestimation errors in modeling  $\tau_{xu}$ , the errors in the

output force of the former stands out, as shown in Figure 4-40(right). However, the latter undershoots, as opposed to the former, hence, it may be more detrimental.

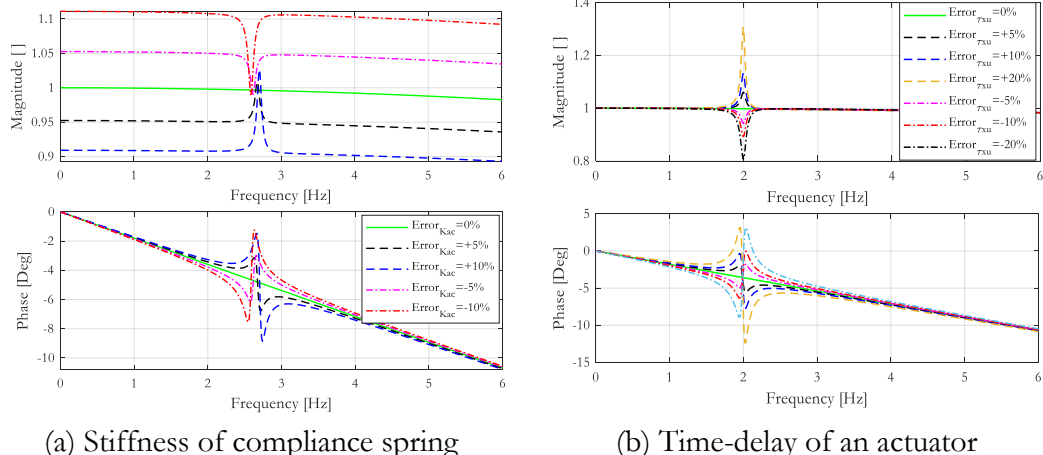


Figure 4-40: Performance of the equivalent force control, using the Smith Predictor compensation, to erroneous modeling of the load transfer system

In the pilot experimental test conducted by Sivaselvan et al. (2008), they concluded that the hybrid test was less sensitive to the accuracy of the parameters of the controller when the added compliance is made more flexible. The findings of this work reinforce the conclusion of the authors, as shown in Figure 4-41. However, increasing the flexibility of the compliance spring increases the stroke demand of the actuator. Hence, the stroke limit of a transfer system should also be considered while designing the properties of the compliance spring.

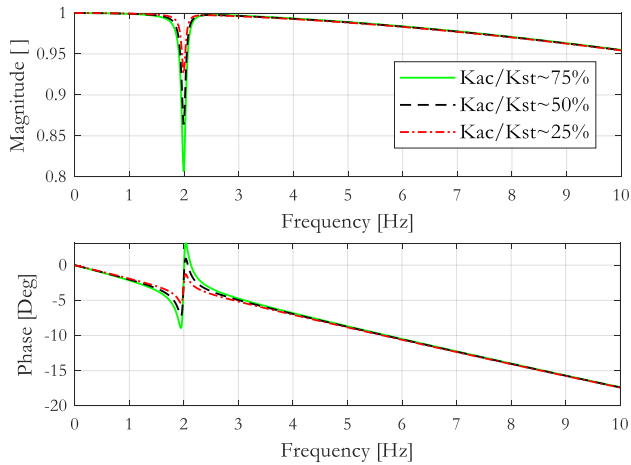


Figure 4-41: Performance of the equivalent force control, using the Smith Predictor compensation, as a function of the flexibility of the compliance spring

Additionally, a flexible compliance spring can make the tuning process of a controller easier such that it is less sensitive to the control-structure interaction between the load transfer system and the

test structure. The implementation of this controller therefore seeks a balance between the stroke limit of the actuator and the flexibility of the added compliance spring. Note that Figure 4-41 was evaluated assuming an underestimation error in  $\tau_{xu}$  of -20%.

The equivalent force control technique offers an easier solution to apply forces at the interface boundary of a simple experimental substructure. As discussed in the introduction, the need for substructuring, experimentally, the lower part of a structure may enforce equilibrium boundary conditions to be satisfied. Likewise, when soil-structure interaction is physically represented in hybrid tests, it may require forces, that are calculated by the numerical substructure, to be applied at the interface boundary. The equivalent force control may therefore be used in the above two cases.

The equivalent force control approach has not been thoroughly investigated up to date. In the frequency-domain analysis, presented above, important observations were made; nonetheless, it is valuable to examine the performance of the control approach during the seismic response evaluation of a structure. From this viewpoint, the control approach was implemented in a virtual hybrid simulation framework using MATLAB/Simulink.

A two-story linear-elastic shear building, shown in Figure 4-42, was used as a case study structure in this simulation. In the frequency-domain analyses, when the test structure has large inherent damping, the Smith Predictor control has shown better performance. To explore the performance of the controller under unfavorable conditions, a low Rayleigh damping ( $\xi=2\%$ ) was adopted in modeling the viscous damping of the structure.

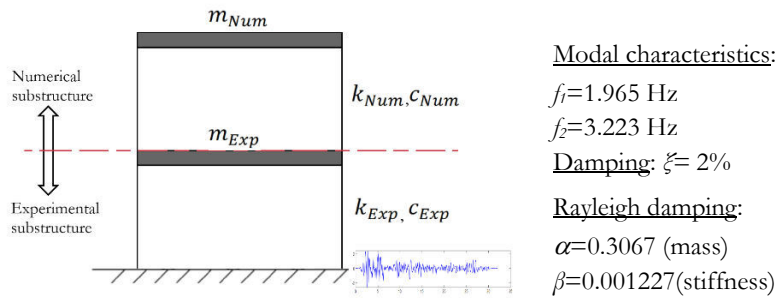


Figure 4-42: Substructuring test with the lower part of a shear building as the physical part

The solution to the numerical substructure was performed through the implicit Newmark method of integration. The interaction between the numerical and experimental substructures, including the load transfer system, were all modeled in Simulink, as shown in Figure 4-43.

The virtual “experimental substructure” block in Figure 4-43 models the first story of the structure, subjected to a base motion of a shaking table while the interface force (base shear of the numerical substructure) is applied by an auxiliary actuator. In these analyses, the shaking table was assumed to have ideal control performance, meaning the input and measured accelerations at the base of the experimental substructure are equal. This assumption disregards the coupling between the two

controllers and allows to isolate errors that are derived from the equivalent force control of the auxiliary actuator.

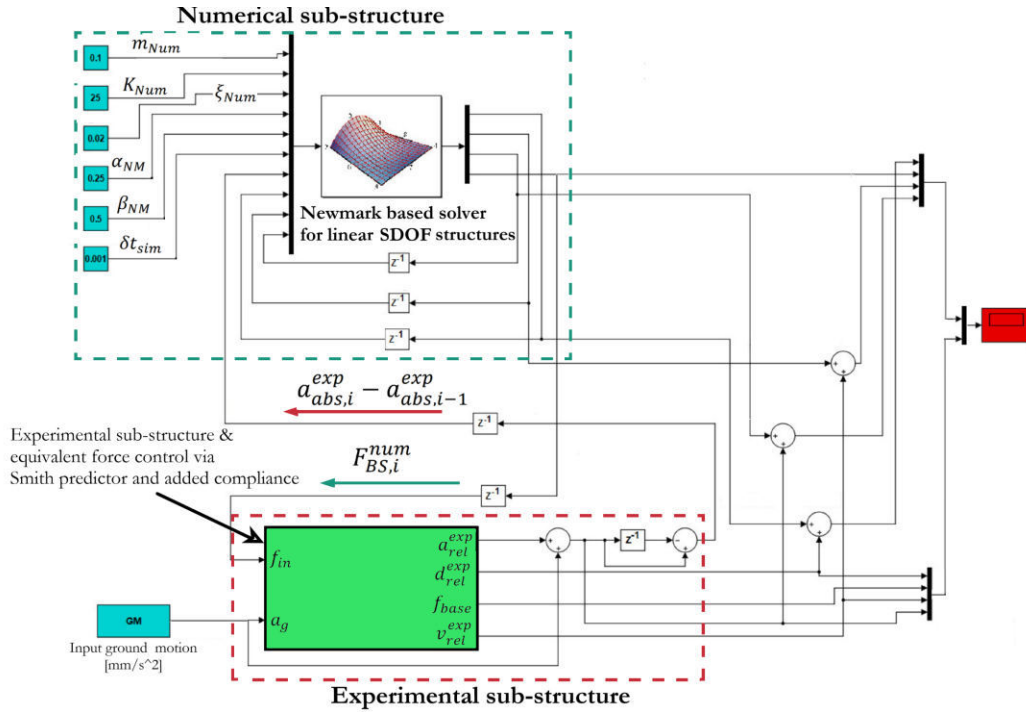


Figure 4-43: Simulink block diagram for a simulated hybrid test of a two-story shear building including the equivalent force control based on the Smith Predictor controller

Twelve earthquake records were chosen from the PEER NGA-West2 strong motion database and they were all scaled to  $0.49 \text{ m/s}^2$  acceleration at the first natural frequency of the structure (i.e.,  $\text{Sa}(T_1)=0.49 \text{ m/s}^2$ ), as shown in Figure 4-44, and the time-step of the response simulation was set to 1 ms. First, the analysis was carried without deploying the Smith Predictor compensator. The same analysis was then repeated by deploying the compensator. The structural responses from the two analyses were then compared.

In general, response simulation in the presence of the Smith Predictor compensator improved the overall accuracy of the substructuring test. For instance, the roof displacement of the structure when subjected to the Kobe (1995) earthquake, scaled to  $\text{Sa}(T_1)$  of 0.25 g (taken to be larger than  $0.49 \text{ m/s}^2$  so as to examine the potential of the compensator considering important displacements),, agrees well with the analytical (exact) solution, as shown in Figure 4-45, thus justifying the importance of using the compensator.

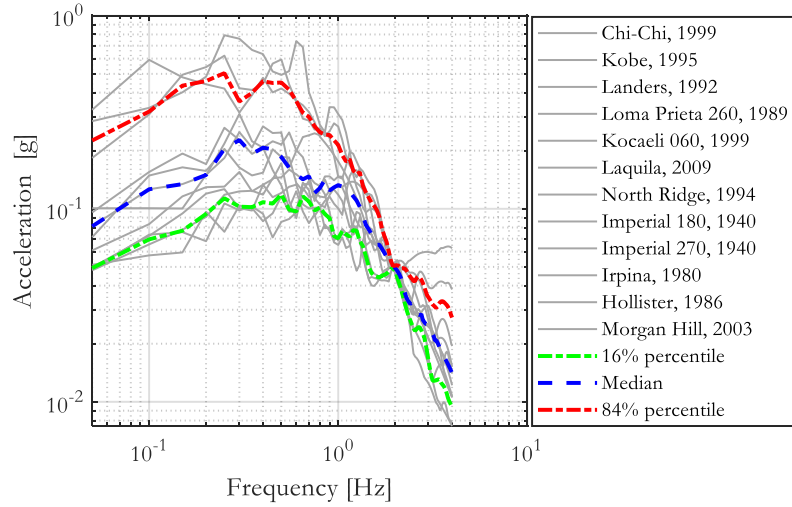


Figure 4-44: Ground motion suite and scaling

Herein, the analytical solution of the entire structure was used as a benchmark for calculating errors of the substructuring approach. Structural responses were first evaluated with and without the Smith Predictor compensator, then the normalized root-mean-square error (NRMSE) was calculated relative to the benchmark responses. The displacement, acceleration, and base shear responses at the interface boundary (I) and at the roof of the structure (T) were examined from these analyses.

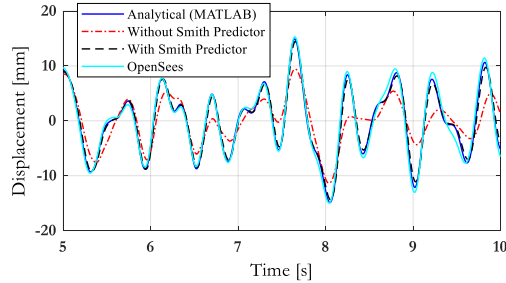


Figure 4-45: Top displacement of the shear building subjected to Kobe (1995) earthquake

As shown in Figure 4-46, when the Smith Predictor was deployed during the analyses, notable improvements in the NRMSE values of the drift, both at the interface boundary ( $Disp_I$ ) and the top story ( $Disp_T$ ), and shear force responses, including the interface force ( $Frc_I$ ) and the total base shear ( $BaseSF$ ), were obtained. Besides, the reduction in the NRMSE of the acceleration that is recorded at the interface boundary ( $Acc_I$ ) proclaims the successful force tracking capabilities gained using the compensator.

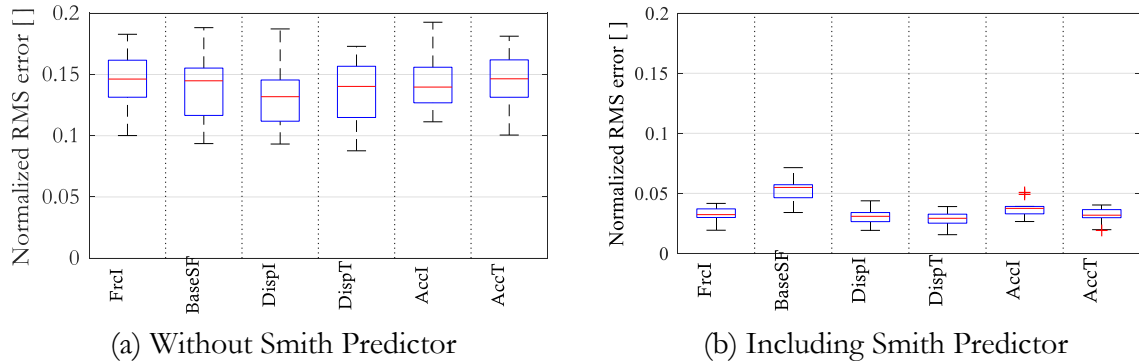


Figure 4-46: NRMSE of structural responses in substructuring tests involving the equivalent force control of actuator, with and without the Smith Predictor compensation<sup>4</sup>

#### 4.3.3.2 Adaptive method for equivalent force control

The Smith Predictor compensator is a non-adaptive control approach, thus limited to elastic experimental substructures. Contrary to this, an experimental structure in hybrid testing is expected to have a complex behavior which justifies the need for conducting such tests. On the other hand, non-adaptive compensation when used for nonlinear response simulation during hybrid testing can have detrimental effects on the fidelity of structural responses. Most importantly, adopting Smith Predictor compensation for a hybrid test involving soil-structure interaction, modeled physically, can be problematic since the response of the physical substructure is potentially nonlinear from the onset of the test. Thus, the chances of a poorly performing compensator can be high. Aside from that, some of the actuator's force may be dissipated at the connection between the compliance spring and the actuator. (see Sivaselvan et al., 2008). This can aggravate the performance of the compensator. In conclusion, the above reasoning justifies the need for an adaptive scheme for compensating the dynamics of a load transfer system during equivalent force control.

In the past, several adaptive techniques for displacement compensation of servo-hydraulic actuators have been developed and applied to hybrid simulation tests. In *LNEC-HS* software, the Adaptive Time Series (ATS) compensator was implemented with slight improvements (see section 4.1.7 for details). Hence, it is ideal to utilize the ATS compensator for the equivalent force control approach as well. The displacement-based ATS (D-ATS) compensator, applicable to equivalent force control, developed by Chae et al. (2018) is similar to the algorithm implemented in *LNEC-HS* software. In the pilot test conducted by Chae et al. (2018), the D-ATS has shown good tracking capabilities of absolute forces up to 2 kN. To the knowledge of the author, the D-ATS compensator has not been applied to hybrid testing of structures, but its adaptation is envisaged to be straightforward. To this end, the D-ATS compensator was integrated into the *directHS* state and operates with a velocity

<sup>4</sup> The central (red) line of the box plot, shown in Figure 4-46, indicates the median value whereas the top and bottom edges of the box indicate the 25<sup>th</sup> and 75<sup>th</sup> percentiles, respectively. The whiskers (black dotted lines) extend to the most extreme data not considered as outlier and the outliers are plotted using the '+' symbol.

response synthesized from displacement and acceleration measurements. In this compensator, the displacement, velocity, and acceleration of the test structure are returned into the control loop. In the current implementation, these kinematic quantities of the test structure are calculated through Lagrange differentiation.

## 4.4 Implementation of a middleware-free framework

It is recalled that the middleware-based scheme of *LNEC-HS* software is one of the approaches developed in the scope of this thesis. The second scheme of this framework software, the *directHS* one, also emulates the three-loop configuration but excludes any middleware software. Herein, a simple computational driver, programmed in LabVIEW, was integrated into the simulation coordinator of the framework. The second scheme does not require the OpenFresco middleware, meaning no TCP/IP communication is needed. Data is directly shared between the computational driver and the simulation coordinator through the local variables. However, the computational driver was designed to model only 2D linear-elastic shear building type of structures. This approach is suitable for SSI substructuring in shaking table tests where the soil medium and the lower stories of a shear building are physically modeled while the upper stories, presumably elastic, are modeled by the computational driver.

The middleware-free scheme includes the feedforward-feedback controller as well as the equivalent force controller explained above that are working in cascade with PID controllers. Likewise, the computational driver is executed in the *directHS* state of the software, together with the above controllers. Due to the sequential nature of the operation of the computational driver and the control block, the stacked-sequence structure in LabVIEW is suitable. This allows a strictly sequential implementation of the numerical and experimental substructures, which avoids the need to synchronize the numerical program with the control block. The data acquisition, limit checking, and emergency stop operations of the middleware-free framework share the resources of the middleware-based scheme.

### 4.4.1 Numerical simulation program

The numerical program, that was implemented in the *directHS* state, was designed to solve linear-elastic MDOF shear building models as stated above. In the Host PC, users must define the mass, stiffness, and damping matrices of the numerical substructure beforehand. The numerical program, which is based on the average acceleration scheme for Newmark integration, solves the equation of motion using the mass, stiffness, and damping matrices of the numerical substructure, as shown in Figure 4-47. It takes the absolute accelerations, measured at the top of the experimental substructure (interface boundary), as the input ground motion to the numerical substructure.

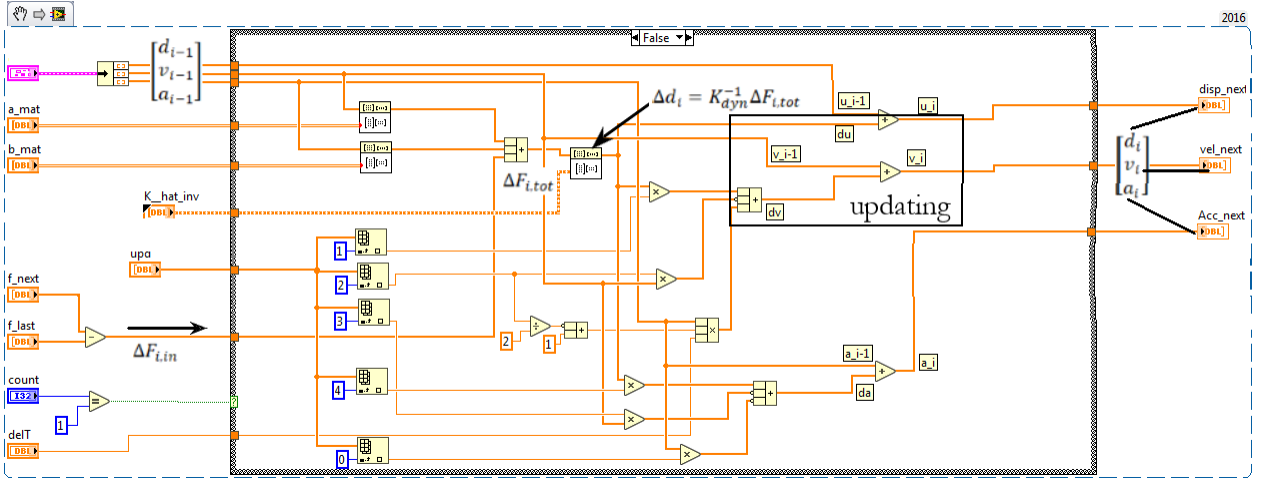


Figure 4-47: Newmark-based numerical program for linear-elastic MDOF shear building structures

The *directHS* state was designed to initiate a hybrid test immediately after a user agrees to a prompt message. Before this state, the coefficients of the integration algorithm and the dynamic stiffness of the numerical substructure are calculated in the *pre-directHS* state and then passed to the *directHS* state.

## 4.4.2 Implementation of advanced control algorithms

### 4.4.2.1 Feedforward-feedback controller

In this work, the advanced control algorithms, discussed above, were implemented in LabVIEW using built-in VIs from the real-time target tools. The feedforward-feedback was implemented using the control-and-simulation module and operates in cascade with the PID controller programmed in the FPGA. The communication between the RT target and the FPGA is bridged using the Direct Memory Access (DMA).

At the end of the *pre-directHS* state, the user is prompted to select an acceleration file to be applied by the shaking table. The input parameters to the *LQG+FF* VI, shown in Figure 4-48, where all the processes of the feedforward-feedback controller are executed, include the target and measured accelerations. Besides, the combined transfer function of the shaking table and the test specimen, which is determined from the measured acceleration to the input displacement,  $\ddot{x}_m(s)/x_{cmd}(s)$ , together with the measurement noise, the process noise, and the weighting matrices of the LQG controller are all defined and feed to the *LQG+FF* VI. Alternatively, these quantities can also be defined in the Host PC and shared to the RT target through Network-Shared variables.

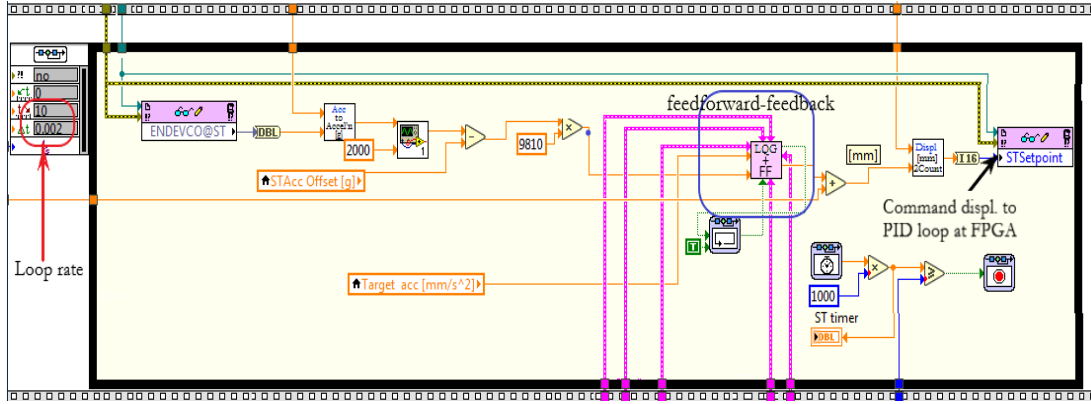


Figure 4-48: Implementation of acceleration tracking using a feedforward-feedback controller

The feedforward and feedback controllers contribute to the final set-point of the PID controller, as shown in Figure 4-49. The pole modification factor of the feedforward controller can be defined in the input panel (the default value is one).

The feedback controller implemented herein comprises three VIs, namely *Discrete Kalman filter*, *linear quadratic regulator* (LQR), and a matrix-product operator. The deviations in the states of the system are feedback to the Kalman filter whereby an optimal gain matrix,  $L_{Kal}$ , that is necessary for the accurate estimation of the states of the system,  $\hat{X}_{est}$ , is determined.

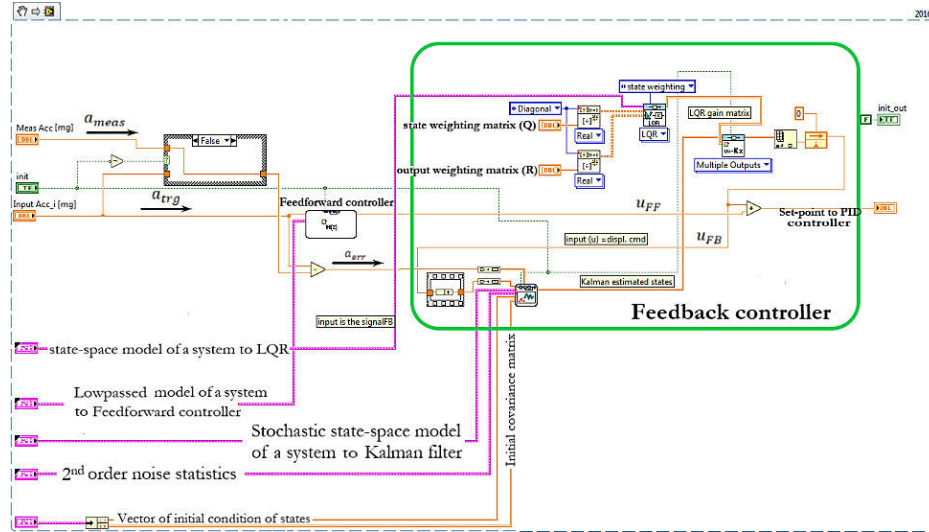


Figure 4-49: Implementation of a feedback control using Linear Quadratic Gaussian controller

Furthermore, the LQR controller receives the system model, the estimated states of the system, and the output weighing matrices and solves for an optimal gain matrix,  $K_{LQR}$ . The feedback command,  $u_{FB}$ , is then determined through the matrix-product operator as:

$$u_{FB} = K_{LQR}\hat{X}_{est} \quad (4.14)$$

Finally, the sum of feedforward and feedback displacement commands are sent as a set-point to the PID controller. The implementation of the LQG feedback controller is illustrated in Figure 4-49.

#### 4.4.2.2 Displacement control of a shaking table with offline adaptation

The additional displacement controller that was developed for tracking the acceleration of a shaking table is identical to a PID position controller except the target displacement is prepared beforehand by an offline adaptation process. The first step is to double integrate the acceleration record to get an equivalent target displacement to be applied to the shaking table. Before the adaptation work, blocks of mass, which correspond to the weight of the test structure, are rigidly attached to the shaking table, and the output-input FRF is computed by applying the target displacement to the shaking table. The blocks of mass are typically distributed to mimic the actual mass distribution of the test structure.

The inverse of the FRF is then applied to the target displacement to obtain the drive signal to the test rig (including a shaking table and the test structure). The displacement error between the target and measured quantities is then used to iteratively correct the input displacement to the shaking table. At the end of the iterative process, a good agreement between the target and measured displacements must be ensured. Besides, the measured acceleration should be closely comparable to the target acceleration. A detailed description of the adaptation process can be found in Duque & Bairrao (2000).

#### 4.4.2.3 Equivalent force control through added compliance

Two approaches for the equivalent force control were implemented in the middleware-free scheme of *LNEC-HS* software. As pointed out earlier, the equivalent force control which is based on the Smith Predictor compensation is only useful for physical substructures that are envisaged to remain elastic throughout a hybrid test. On the other hand, the ATS-based equivalent force control is applicable to nonlinear physical substructures. For brevity, only the implementation of the ATS-based equivalent force controller, in the *directHS* state, shown in Figure 4-50, is presented herein. The implementation of the Smith Predictor compensation is expounded in Shao & Reinhorn (2012).

In the ATS-based equivalent force controller, at each time-step, the target force is converted to an equivalent displacement depending on the stiffness of the compliance spring. The target displacement is then determined using the equivalent displacement and its first two derivatives, with the compensation parameters ( $a_0$ ,  $a_1$  and  $a_2$ ) multiplying those quantities to obtain the target displacement.

The displacement and acceleration measurements obtained from the physical substructure must be filtered before they are returned to the controller. Besides, the relative quantities of the absolute

measured responses are required by this controller. These relative quantities are also needed when synthesizing the velocity response. For synthesizing the velocity response of the test structure, a cross-over frequency can be defined from the control panel (the default setting is 2 Hz).

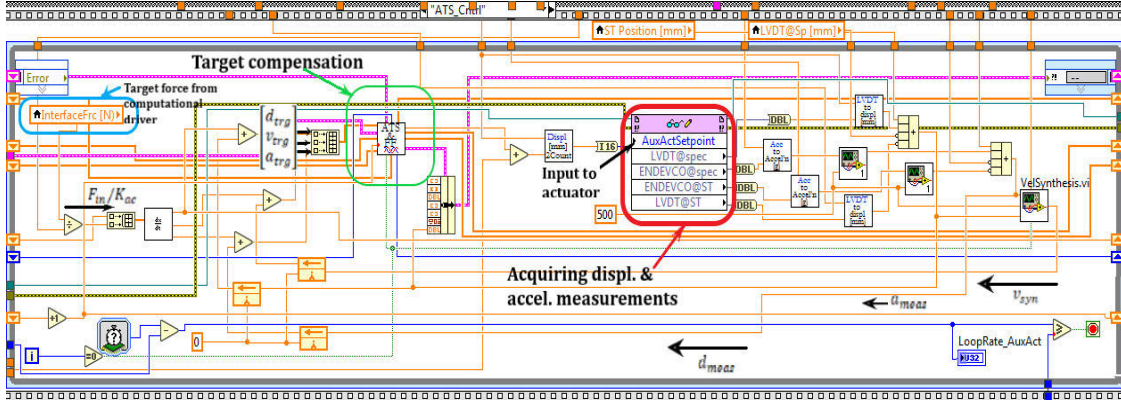


Figure 4-50: Implementation of equivalent force control using the Adaptive Time-Series (ATS) compensator

The initial and limit values of the compensation parameters can also be defined in the input panel of the software. However, the tracking indicator, which is part of the middleware-based approach, is not included in this implementation in order to optimize the clock speed of the control loop.

## 4.5 Summary

In this chapter, the development and validation of a software framework for hybrid simulation, which was carried out at LNEC, was presented. The conceived three-loop architecture of the framework was introduced, and its implementation using the state-machine design in LabVIEW software, utilizing the NI real-time controller and FPGA hardware, was explained in a stepwise manner. The flexibility and modularity offered by this software framework were highlighted and their implication in extending the framework in the future was discussed. The developed software, *LNEC-HS*, was designed to operate with and without a middleware software (OpenFresco). The middleware-based scheme of the software and the underlying processes of the TCP/IP communication block of the software were elaborately discussed. The predictor-corrector approach for continuous generation of commands for the actuators, delay compensation, and error tracking algorithms, which were developed as part of the simulation coordinator VI, were presented in chronological order of their execution. Furthermore, the performance of the ATS compensator was improved using the Lagrange differentiation instead of its original formulation, i.e., backward-differentiation. The importance and merits of the middleware-free scheme, comprising a simple numerical program inside the simulation coordinator VI, and its implementation in *LNEC-HS* software were also extended.

The validation of the software framework was performed by conducting a hybrid test of a two-bay

steel moment-resisting frame. The testing conditions and the test setup of the hybrid test, which uses LNEC's uniaxial shaking table, were presented; and the modelling of the numerical substructure, in the OpenSees software, was discussed stepwise. The experimental identification of the physical substructure (a steel column) was carried out, and the initial parameters of the ATS compensator were estimated by applying a noise signal to the shaking table. First, rehearsal tests that are necessary to ensure the proper functioning of the software and other laboratory devices were performed and examined. After the successful rehearsal tests, the actual hybrid test of the steel frame was performed and the output of the test was examined, including errors in matching the displacement command to the shaking table.

Furthermore, the principles and the implementation of advanced model-based control strategies for substructuring tests in shaking table platforms were investigated. These control strategies include acceleration tracking of a shaking table and equivalent force control of an actuator. Initially, the need for system identification of a shaking table, in support of the model-based control strategies, was elucidated. The implementation of a feedforward-feedback controller in LabVIEW software was then briefly discussed to help the reader understand the simulated studies that were presented afterward. The simulated hybrid tests examined the robustness of the feedforward-feedback controller as well as the choice of its parameters. These studies also revealed that system nonlinearities can have a notable effect on the accuracy of this controller. The need for an adequate number of corrective iterations of the controller, that must be executed for each input command, was highlighted. The optimum number of iterations was found to vary depending on the level of damage to the physical substructure.

Additionally, the adequacy of the equivalent force control of an actuator, which uses the added compliance approach, was explored, both in frequency and in time domains, when the controller is used in combination with the Smith Predictor compensator. The effectiveness of the Smith Predictor compensation in reducing control errors was demonstrated in both domains. The robustness of this compensator to errors in modeling the properties of an experimental substructure and to errors in modeling the properties of an actuator were also investigated. Briefly, some of the interesting outcomes of the frequency-domain analyses comprise: (a) large errors in modeling the time-delay of an actuator can erode the performance of the compensator; (b) errors in modeling the viscous damping of a lightly-damped experimental structure has minor implications whereas a structure with large damping has small tracking errors even without the Smith Predictor; and (c) increasing the flexibility of the compliance spring improves the performance of the force controller but also increases the stroke demand of an actuator, thus requiring a trade-off.

The time-domain parametric analyses of the controller were performed considering a two-story shear building subjected to a ground motion suite; hence, they shed light on the performance of the controller in evaluating the seismic response of structures. The shear building, which was partitioned to have the first story as the physical substructure, was analyzed using a MATLAB/Simulink program. In this work, a Simulink program for the equivalent force control

approach was developed which communicates with a Newmark-based solver of the numerical substructure. The simulated hybrid tests were conducted with and without deploying the Smith Predictor compensator, and the reduction in the NMRSE of the displacements and forces, at the interface boundary between the two substructures, when using the Smith Predictor were examined. The output of these studies revealed that the controller is sensitive to system nonlinearities and/or inaccurate modeling. To avoid this problem, the adaptive time-series (ATS) compensation was also examined and implemented in the proposed software, thus accounting for model deviations due to nonlinear response during the equivalent force control.

Finally, the implementation of the middleware-free scheme of *LNEC-HS* software was expounded. The implementation of the numerical program in the simulation coordinator of the software, its advantages, and its limitations were discussed. The main advantages of this scheme include the speedy execution of a hybrid test and therefore its potential in conducting SSI testing in hybrid simulation. Besides, the limitations of the developed numerical program were highlighted. The implementation of the feedforward-feedback control for an acceleration tracking of a shaking table was also explained. Finally, the implementation of the ATS-based equivalent force control of an actuator was described.

## 5 Soil-Structure Interaction Testing in Hybrid Simulation

### 5.1 Introduction

Damage on a structure due to an earthquake depends on the ground motion, the characteristics of the foundation soil, and the structure itself. The characteristics of the ground motion are governed by the complex source features, wave propagation, and local site conditions. On the other hand, the characteristics of the underlying foundation soil play an important role in altering the incident seismic waves. Moreover, the soil medium interacts with the superstructure in a complex way. Nevertheless, in conventional seismic design, it is common for structural engineers to assume fixed-end boundary conditions during analysis and design of structures (may approximate foundation in stiff or rocky soil), thus neglecting the interaction between the foundation soil and the structure.

Nonetheless, with the growing interest in performance-based seismic design, the benefits of including SSI in the evaluation for the seismic response of structures has been lauded (Mekki et al., 2014). SSI analysis has become important with the advent of engineering structures in massive constructions on soft soils such as nuclear power plants, concrete dams, underground structures, and bridges. In recent years, damage caused by earthquakes, such as the Kobe (1995) earthquake, highlighted the importance of the properties of foundation soil on the seismic behavior of a structure (Mylonakis et al., 2006).

SSI analysis is simply the result of the interaction between soil and structure, where the soil medium deforms by inertial forces of the structure that are transmitted through the structural foundation while the foundation input motion (different from the free-field motion) is driving the superstructure (Gazetas, 1991; Trifunac et al., 1999). The action of the forces which are transmitted from the structure to the foundation soil is termed as *inertial interaction*. On the other hand, the foundation input motion is the result of the bed-rock motion interacting with the soil and structural foundation, in what is referred to as *kinematic interaction*. It comprises base-slab averaging, effects of embedment, and scattering of incident waves.

Base-slab averaging is the result of inclined or incoherent incident waves whereby the base-slab translational motion at high frequencies is reduced relative to the free-field motion. The ‘embedment effect’ results in the reduction of the ground motion intensity with the depth of the foundation, affecting more significantly the high-frequency components of the ground motion. For structures resting on shallow foundations, the kinematic interaction is usually small, and it may be ignored. Hence, the free-field motion is adopted as the input excitation.

In what concerns inertial interaction, at low levels of shaking the dominant effects consist of period elongation and increase in radiation damping. In general, period elongation is more important in stiff and slender structures resting on soft soil where rocking dominates. However, the increase in

the system damping is more pronounced in the case of stiff and stocky structures resting on soft soil for which horizontal translation is the dominant response. Contrarily, under strong shaking, the nonlinear response becomes dominant, leading to excessive displacements and rotations at the foundation level.

The inertial interaction in the equivalent-linear elastic domain is primarily governed by the compliance of the foundation, period of the structure, and soil type (Gazetas, 1991; Trifunac et al., 1999). The inertial interaction of a SDOF structure resting on a rigid foundation can be approximately studied by modeling the foundation through uncoupled horizontal and rocking impedances comprising the static stiffnesses,  $K_x$  and  $K_\theta$ , and radiation damping coefficients,  $C_x$  and  $C_\theta$ , as shown in Figure 5-1. The material damping (soil hysteretic damping),  $\xi_s$ , models the hysteretic energy dissipation of the soil deposit.

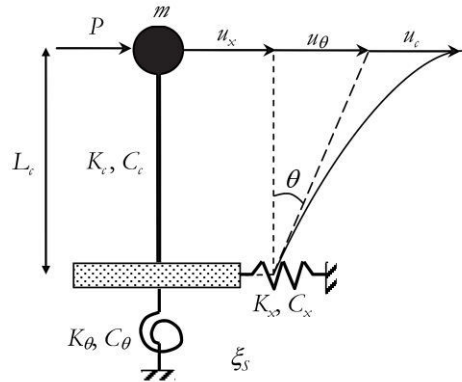


Figure 5-1: Soil-structure interaction of a SDOF structure (after Correia, 2011)

A closed-form expression for the equivalent period and damping of the SDOF structure can be derived from these impedances. Consequently, the period elongation of the SDOF structure can be shown to be approximately equal to:

$$\frac{\tilde{T}}{T_c} = \sqrt{1 + \frac{K_c}{K_x} + \frac{K_c L_c^2}{K_\theta}} \quad (5.1)$$

where  $\tilde{T}/T_c$  is the period elongation, and  $T_c = 2\pi\sqrt{m/K_c}$  is the period of the fixed-base SDOF structure. Likewise, the effective damping of the SDOF structure can be approximated by:

$$\tilde{\xi} = \frac{\xi_c}{\left(\tilde{T}/T_c\right)^2} + \left[1 - \frac{1}{\left(\tilde{T}/T_c\right)^2}\right]\xi_s + \frac{\xi_x}{\left(\tilde{T}/T_x\right)^2} + \frac{\xi_\theta}{\left(\tilde{T}/T_\theta\right)^2} \quad (5.2)$$

where  $T_x = 2\pi\sqrt{m/K_x}$  and  $T_\theta = 2\pi\sqrt{m/K_\theta}$  are fictitious periods calculated assuming that the only source of foundation-structure flexibility to be the translational and rotational impedances, respectively. The period elongation and additional damping effects of including the SSI response might mislead into assuming smaller acceleration and stress in the structure and foundation.

Nonetheless, it should be noted that the oversimplified perception, which develops on the beneficial role of including SSI effects during response simulation, may result in unsafe design (Mylonakis & Gazetas, 2000). Thus, careful assessment of both the soil conditions and the ground motion is crucial to the significance of SSI effects during response simulation of a structure.

The relationship between the properties of fixed-base and flexible-base SDOF oscillators may be described through dimensionless parameters such as the aspect ratio  $h/r$ , soil Poisson ratio  $\nu$ , soil hysteretic damping  $\beta$ , and  $\sigma$  and  $\bar{m}$ , which are given by:

$$\sigma = \frac{V_s T}{h}; \bar{m} = \frac{m}{\rho \pi r^2 h} \quad (5.3)$$

where  $V_s, T, h, m, r, \rho$  are the effective shear-wave velocity, period of vibration, height of the superstructure, mass of the superstructure, radius of the circular footing, and density of the soil, respectively. The dimensionless parameters  $\sigma$  and  $\bar{m}$  represent the soil-to-structure relative stiffness and the relative mass of the structure to the soil medium, respectively. For typical building structures resting on soil or weathered rock,  $\sigma$  is greater than 2 and  $\bar{m}$  is bounded in [0.1, 0.2]. A representative value of  $\bar{m}=0.15$  is recommended for buildings (Veletsos & Meek, 1974). Considering a rigid circular foundation on the surface of a viscoelastic half-space, Veletsos & Nair (1975) derived the analytical solutions of  $\tilde{T}/T_c$  and  $\xi$ , as shown in Figure 5-2.

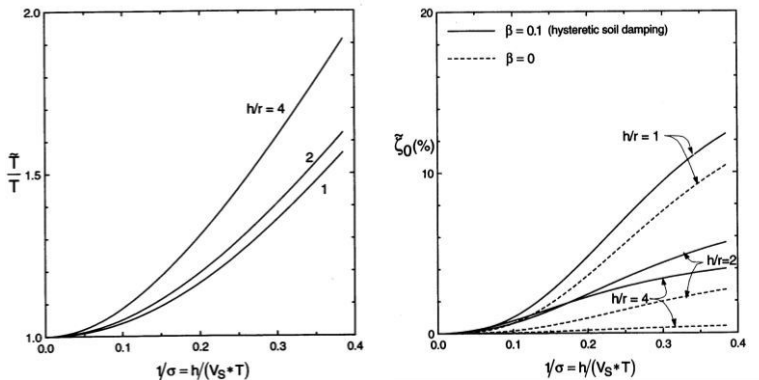


Figure 5-2: Period elongation and damping ratios of a SDOF structure taking  $\nu=0.4$  and  $\bar{m}=0.15$   
(after Veletsos & Nair, 1975)

As depicted in Figure 5-2, period elongation is negligible for flexible structures supported on stiff foundation soil. For stiff structures that are supported on soft soil (large values of  $1/\sigma$ ), soil-structure interaction can result in a notable period elongation. Such period elongation can be significant in slender structures (large  $h/r$  ratio) which can produce large over-turning moments. The effective damping,  $\xi$ , of stiff and stocky structures resting on soft soil is large – with a significant portion being the result of radiation damping. Conversely, in slender structures, the hysteretic damping of soil is the main source of the overall damping. This indicates that the horizontal movements of the foundation dissipate more energy through radiation damping than a rocking foundation.

Considering the effect of the mass of the structure, period elongation in massive structures is larger than in light structures and the opposite is true for damping. The latter is eminent for stiff structures resting on soft soil. Nonetheless, the influence of mass is negligible for structures resting on rocky or stiff soil.

Furthermore, SSI alters the base shear of structures depending on the period elongation of the system and its equivalent damping. Considering a smooth response spectrum like the typical design spectrum or a uniform hazard spectrum (UHS), in structures whose fundamental period is smaller than the period of the peak spectral response (mainly stocky structures), period elongation gives rise to an increase in base shear. Contrarily, period elongation of structures whose dominant periods are larger than the period of the peak spectral response typically results in a reduction of the base shear.

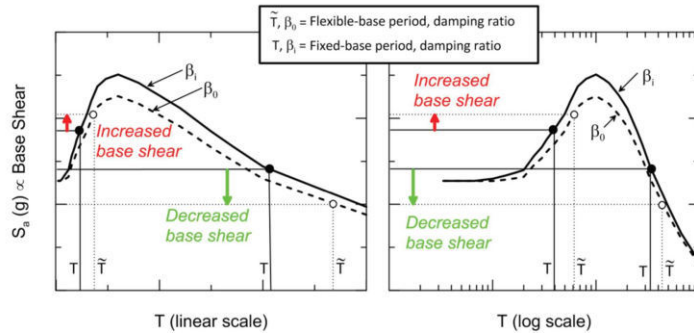


Figure 5-3:Effect of soil-structure interaction in the base shear of a structure (adopted from NIST, 2012)

In summary, SSI may result in an important energy dissipation at the foundation level, reducing structural damage whilst resulting in larger overall peak deformations and possibly also larger residual deformations. This reduction in structural damage may be exploited as long as the residual deformations of the foundation are limited. Besides, post-earthquake self-centering capabilities may also be exploited by accounting for the SSI effects in structures.

In continuation to the development of the middleware-free scheme of *LNEC-HS*, which is intended for hybrid tests involving SSI effects, this chapter discuss the background information for soil-structure interaction, including few experiments from the literature. A rehearsal hybrid test is also conducted which can be useful for designing a hybrid experiment as well as to foresee the outcome of the experiment. At the end of this chapter, the implementation of SSI hybrid testing in *LNEC-HS* software framework is discussed and it is investigated in a virtual simulation.

## 5.2 Numerical modelling of soil-structure interaction

Soil-structure interaction analysis can be performed through direct and indirect (substructure) methods. In the direct method, the complete characteristics of the soil and structure must be

modeled; hence, it requires accurate and efficient modeling tools to account for both. It can be carried out in a 2D or 3D model including the structural elements, the soil medium (as a continuum), the transmitting boundaries at the limits of the soil medium, and the foundation-soil interface elements, as shown in Figure 5-4.

The spatial discretization of the soil medium and the boundary elements should be carefully chosen. Additionally, the constitutive rules for the viscoelastic linear and nonlinear behavior of the soil elements are major ingredients of the direct approach for SSI analysis (Wolf, 1985). Here, the equations governing the soil-structure system, subjected to an earthquake motion, are solved in a true nonlinear analysis in a stepwise manner. Despite the potential of this method, the choice for the constitutive rules of soil, as well as calibrating its parameters, can be difficult. This means, modeling accurately the true nonlinear soil response and wave propagation can be challenging. Besides, modeling the nonlinearities at the interface between the soil and foundation, such as uplift and contact degradation, can be an arduous task. Due to these difficulties, this approach is not commonly practiced in engineering design, and it is seldom used for verification purposes. Moreover, performing parametric studies through the direct approach can be problematic due to its onerous computational cost.

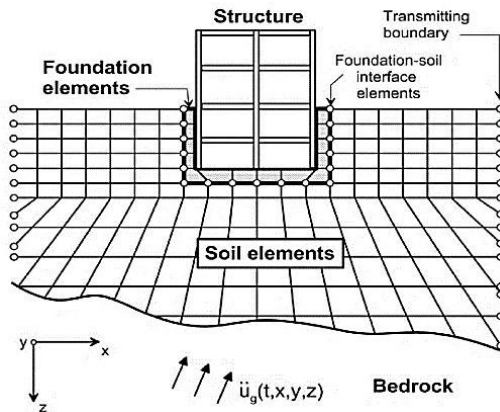


Figure 5-4: Direct approach for analyzing soil-structure interaction effects (adopted from NIST, 2012)

A relatively simple approach for the SSI analysis makes use of the superposition principle that decomposes the analysis process by solving the kinematic and inertial interaction effects separately, as shown in Figure 5-5. This approach gives rise to the substructure method for SSI analysis. It may not capture the full nonlinear behavior of soil, nonetheless, it gives a reasonable estimation of the dynamic response of elastic structures, for example, nuclear power plants (Kausel et al., 1978). In the first step, the effects of the kinematic interaction are accounted, resulting in the determination of the Foundation Input Motion (FIM),  $\ddot{u}_{FIM}$ . It is calculated by performing wave-propagation analyses on a system comprising the soil medium and a massless foundation (modeling its actual stiffness), subjected to an earthquake input motion,  $\ddot{u}_g$ , at the boundary of the soil. At this stage, the impedance functions of the foundation may also be determined. In the subsequent step, the

effects of the inertial interaction are calculated by analyzing the superstructure subjected to the foundation input motion, and the soil system is represented by its impedances. In this analysis, the total mass of the structure and its foundation are modeled.

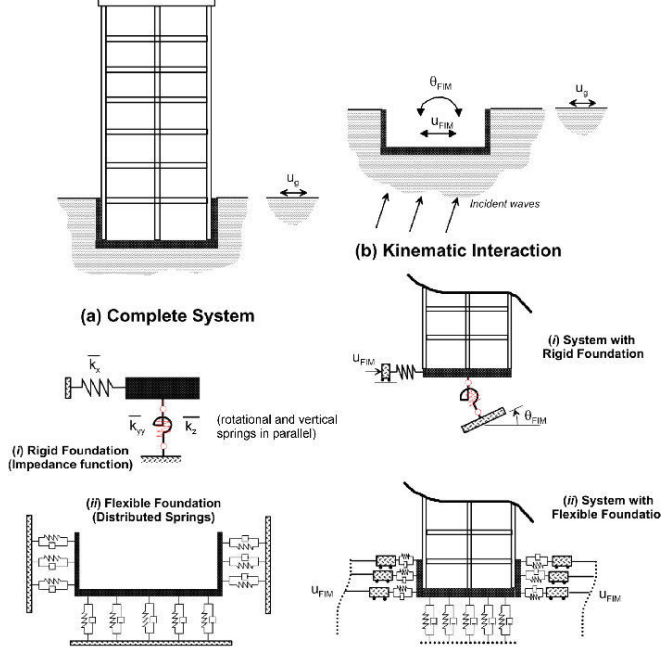


Figure 5-5: Substructure approach for analyzing soil-structure interaction effects (adopted from NIST, 2012)

The foundation impedance matrix is a complex frequency-dependent entity that is characterized by a real part, representing the dynamic stiffness and inertia of soil, and an imaginary part, which models its energy dissipation properties. The complex-valued impedance function,  $K^*$ , reads:

$$K^* = \bar{K} + i\omega C = K(k(\omega) + 2i\xi) \quad (5.4)$$

where  $\bar{K}$  is the dynamic stiffness;  $C$  is the system damping;  $\omega$  is the excitation circular frequency;  $K$  is the static stiffness;  $k(\omega)$  is a dimensionless frequency-dependent coefficient; and  $\xi$  is the damping coefficient. The imaginary part of equation (5.4) is commonly expressed using  $ia_0c$ , where  $a_0$  and  $c$  are the dimensionless terms of frequency and damping, respectively, and the dimensionless frequency is given by:

$$a_0 = \frac{\omega r}{V_s} \quad (5.5)$$

where  $r$  is the characteristic length of the structural foundation.

The foundation impedances can be directly represented from an assumed mass-spring-dashpot system, but they are commonly taken from the literature. For example, the closed-form solutions for calculating the dynamic impedance and damping of arbitrary shaped shallow foundations,

resting on homogeneous half-space, developed by Gazetas (1991) are presented in Table 5-1 and Figure 5-6 (Pais & Kausel, 1988; Mylonakis & Gazetas, 2000). For a time-domain analysis, the frequency-dependent behavior of the impedance function must be replaced by frequency-independent components such as the mass-spring-dashpot elements in the *lumped-parameter* models.

Table 5-1: Closed-form expressions for stiffness and radiation damping of arbitrarily shaped shallow foundations on homogenous half-space (after Gazetas, 1991)

Vibration mode	Static stiffness, $K$	Dynamic stiffness coefficient, $k$ ( $0 \leq a_0 \leq 2$ )	Radiation dashpot coefficient, $C$
Vertical ( $z$ )	$K_z = [2GL/(1 - \nu)][0.73 + 1.54\chi^{0.75}]$ with $\chi = A_b/4L^2$	$k_z = k_z(L/B, \nu; a_0)$	$C_z = (\rho V_{La} A_b) \cdot \bar{c}_z$ where $\bar{c}_z = \bar{c}_z(L/B; a_0)$
Horizontal ( $y$ ) (lateral direction)	$K_y = [2GL/(2 - \nu)][2 + 2.50\chi^{0.85}]$	$k_y = k_y(L/B; a_0)$	$C_y = (\rho V_s A_b) \cdot \bar{c}_y$ where $\bar{c}_y = \bar{c}_y(L/B; a_0)$
Horizontal ( $x$ ) (longitudinal direction)	$K_x = K_y - [0.2/(0.75 - \nu)]GL[1 - (B/L)]$	$k_x \approx 1$	$C_x = \rho V_s A_b$
Rocking ( $rx$ ) (about the longitudinal, $x$ -axis)	$K_{rx} = [G/(1 - \nu)]I_{bx}^{0.75}(L/B)^{0.25}[2.4 + 0.5(B/L)]$	$k_{rx} \approx 1 - 0.20a_0$	$C_{rx} = (\rho V_{La} I_{bx}) \cdot \bar{c}_{rx}$ where $\bar{c}_{rx} = \bar{c}_{rx}(L/B; a_0)$
Rocking ( $ry$ ) (about the lateral, $y$ -axis)	$K_{ry} = [3G/(1 - \nu)]I_{by}^{0.75}(L/B)^{0.15}$	$\nu < 0.40: k_{ry} \approx 1 - 0.26a_0$ $\nu \approx 0.50: k_{ry} \approx 1 - 0.26a_0(L/B)^{0.30}$	$C_{ry} = (\rho V_{La} I_{by}) \cdot \bar{c}_{ry}$ where $\bar{c}_{ry} = \bar{c}_{ry}(L/B; a_0)$
Torsion ( $r$ )	$K_r = 3.5GI_{bx}^{0.75}(B/L)^{0.4}(I_{bx}/B^4)^{0.2}$	$k_r = 1 - 0.14a_0$	$C_r = (\rho V_s I_{bx}) \cdot \bar{c}_r$ where $\bar{c}_r = \bar{c}_r(L/B; a_0)$

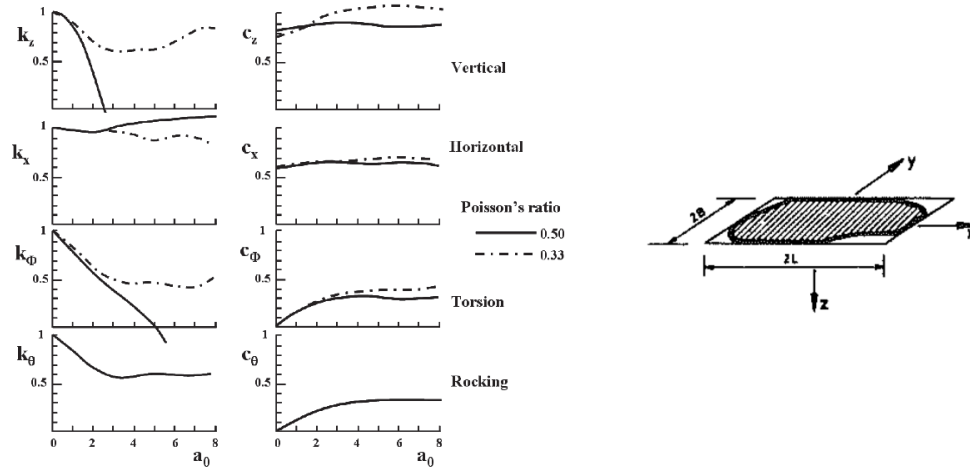


Figure 5-6: Coefficients for dynamic stiffness and damping for arbitrarily shaped shallow foundations on homogenous half-space (after Gazetas, 1991)

The *lumped-parameter* models are typically designed as spring-dashpot-mass systems, as shown in Figure 5-7, that are capable of representing the frequency-dependent behavior of impedance functions (Wolf, 1989). Wolf & Deeks (2004) have also introduced the concept of wave propagation in truncated cone models, from which any *lumped-parameter* model can be generated.

It should be noted that the substructure method, in many cases, can be simplified by neglecting the kinematic interaction thus using the free-field ground motion during analysis. In this case, the soil-structure interaction effects are expressed by the inertial interaction only. Generally, buildings

without large foundation slabs (small slab averaging effect), that are founded on shallow footings and horizontally layered soil deposits, subjected only to vertically propagating shear waves, have negligible kinematic interaction in comparison to the inertial interaction. Thus, the SSI analysis may be reduced to the analysis of a building resting on a compliant foundation subjected to the free-field ground motion (Correia, 2011).

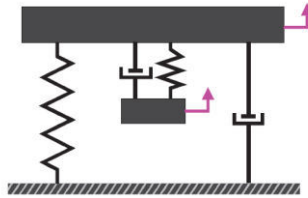


Figure 5-7: Spring-dashpot-mass model for a rocking footing (after Correia, 2011)

Other simplified methods such as *Newton's sliding block* and the *Beam on Nonlinear Winkler Foundation (BNWF)* have also been adopted for modeling soil-structure interaction. In the *Newton's sliding block* analysis, the deformation of soil is estimated by a sliding block technique (Sarma & Iossifelis, 1990), using forces obtained from an equivalent-linear SSI analysis. The failure surface is defined by the bearing strength of the soil deposit. This approach fails to model several nonlinearities of the soil-structure interaction; therefore, it is not adequate for accurately describing it.

The BNWF approach for modeling SSI, which was originally developed for pile foundations, has been extended to model shallow foundations. This model is constructed from a series of simple nonlinear springs and dashpots. The controlling parameters of the BNWF model, applied to shallow foundations, were extensively calibrated using centrifuge and 1g shaking table tests (Gajan & Kutter, 2007). The stiffness of the springs (subgrade reaction) is not only determined by the soil properties but also depends on the frequency of the structure, level of strain in the soil, and foundation properties.

### 5.2.1 Beam on Nonlinear Winkler Foundation

In this model, a series of one-dimensional nonlinear springs are distributed across the soil-foundation interface thus capturing, among others, the moment-rotation behavior. The vertical nonlinear springs are modeled by coupling the foundation impedances with gapping and dashpot elements. Raychowdhury & Hutchinson (2009) implemented the BNWF model in the OpenSees software framework using the elastic beamColumn elements, representing the foundation elements, and decoupled zero-length nonlinear spring elements that model the soil-foundation behavior.

The OpenSees model for the BNWF has three uniaxial spring element types, as shown in Figure 5-8, namely  $q-z$  springs, a  $p-x$  spring, and a  $t-x$  spring. The  $q-z$  springs model the vertical load-displacement behavior using the *QzSimple2* material. The  $p-x$  spring models the horizontal passive load-displacement behavior using the *PxSimple1* material. The  $t-x$  spring models the horizontal

shear-foundation sliding behavior using the *TxSimple1* material. The mathematical models of these springs were modified versions of the nonlinear springs that were originally developed for pile foundations (Boulanger et al., 1999).

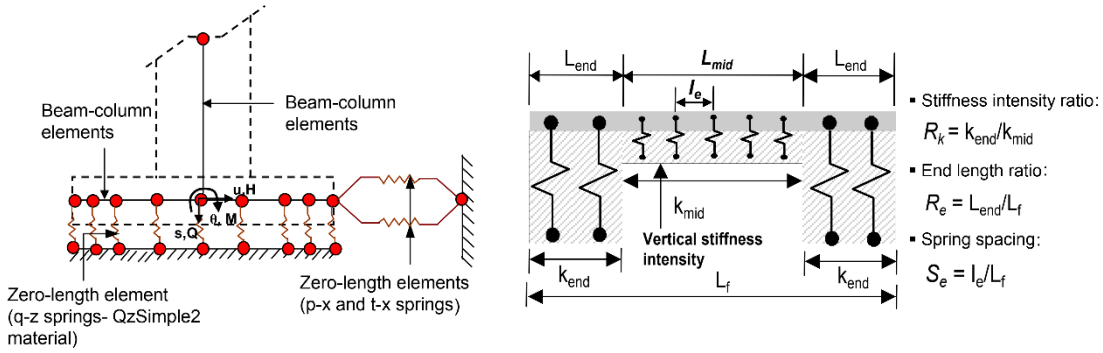


Figure 5-8: Implementation of the Beam on Nonlinear Winkler Foundation (BNWF) model in the OpenSees software (after Raychowdhury & Hutchinson, 2009)

### 5.2.1.1 Mechanistic springs of the BNWF model

The backbone curves of the materials used in the BNWF model are characterized by a linear-elastic region followed by a nonlinear region, where each material is designed to capture both the elastic far-field and nonlinear near-field effects. The familiar Masing rules are applied during the unload-reload operation of the hysteretic curves. Due to the unidirectional behavior of the springs, the concepts of plastic potential and flow rule are applicable but not fundamental. The backbone curve of the *QzSimple2* material is defined by an ultimate load in the compression side and a fraction of its ultimate load defines the tension resistance. The *PxSimple1* material is characterized by a pinched hysteretic model that was envisioned to capture the passive resistance, horizontal stiffness, and gaping effect of embedded foundations. This material model can suitably account for the gapping of a foundation during unloading on the opposite side of it (Raychowdhury, 2008). On the other hand, the *TxSimple1* has a large stiffness and “fat” hysteresis to capture the frictional resistance at the soil-footing interface. The backbone curves for the three materials are similar except for the parameters that control their shape; hence, only the formulation for the *q-z* spring is presented herein.

The linear-elastic portion of the backbone curve of the *q-z* spring, which is governed by its initial stiffness,  $k_z$ , reads:

$$q = k_z z \quad (5.6)$$

where  $q$  and  $z$  represent the spring force and vertical deformation, respectively. The upper limit of the elastic curve,  $q_0$ , is determined from the product of  $C_r$  and the ultimate load capacity,  $q_{ult}$ . The parameter  $C_r$  controls the range of the elastic branch. The ultimate load capacity of the *QzSimple2* material can be calculated using the Terzaghi (1943) equation of bearing capacity and the bearing capacity factors for depth, shape, and inclination may be determined from equations derived by

Meyerhof (1963), for instance. Likewise, the ultimate lateral load capacity is calculated considering a linearly varying pressure distribution whereas the general equation for shear resistance of a foundation is applied in determining the ultimate capacity in sliding.

On the other hand, the post-yield region of the backbone curve of the *QzSimple2* material is governed by:

$$q = q_{ult} - (q_{ult} - q_0) \left[ \frac{c \cdot z_{50}}{c \cdot z_{50} + |z - z_0|} \right]^n ; |z| > z_0 \quad (5.7)$$

where  $z_{50}$  is the foundation vertical displacement when 50% of  $q_{ult}$  is mobilized;  $z_0$  is the displacement at  $q_0$ ;  $c$  and  $n$  are constants that control the post-yield shape of the backbone curve. The mechanistic springs capture the near-field effect using a nonlinear spring and a gap component. The latter is a parallel combination of closure and drag springs, as shown in Figure 5-9.

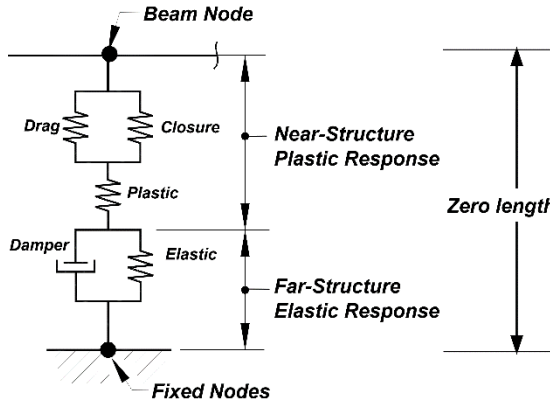


Figure 5-9: Conceptual diagram for mechanistic springs of the BNWF model (after Boulanger et al., 1999)

The closure spring, rigid in compression but very flexible in tension, has a bilinear elastic curve (Raychowdhury, 2008); and the nonlinear drag spring is governed by:

$$q_d = C_d q_{ult} - (C_d q_{ult} - q_0^d) \left[ \frac{z_{50}}{z_{50} + 2|z^g - z_0^g|} \right]^n \quad (5.8)$$

where  $q_d$  is the drag force on the closure component and  $C_d$  is the ratio of the maximum drag force to the ultimate capacity of the  $q$ - $\zeta$  spring. At the start of a current loading cycle,  $z_0^g = z^g$  and  $q_0^d = q_d$ . The drag spring returns a constant force in the gap zone but remains inactive when the gap closes. Figure 5-10 shows the cyclic response of the three materials when subjected to a sinusoidal displacement. The asymmetric behavior of the  $q$ - $\zeta$  spring prevails due to its small capacity in tension. The same figure shows the symmetrical and pinched behavior of the  $p$ - $x$  spring as well as the fat and symmetrical hysteretic curve of the  $t$ - $x$  spring.

To model an SSI problem using the BNWF approach in the OpenSees software, the following parameters are needed:

1. Radiation coefficient,  $c_{rad}$ : Models the dashpot coefficient, shown in Figure 5-9, that

accounts for the radiation damping. This parameter is highly dependent on the footing shape, aspect ratio, embedment depth, and soil stiffness. Closed-form expressions for this parameter can be obtained in Gazetas (1991).

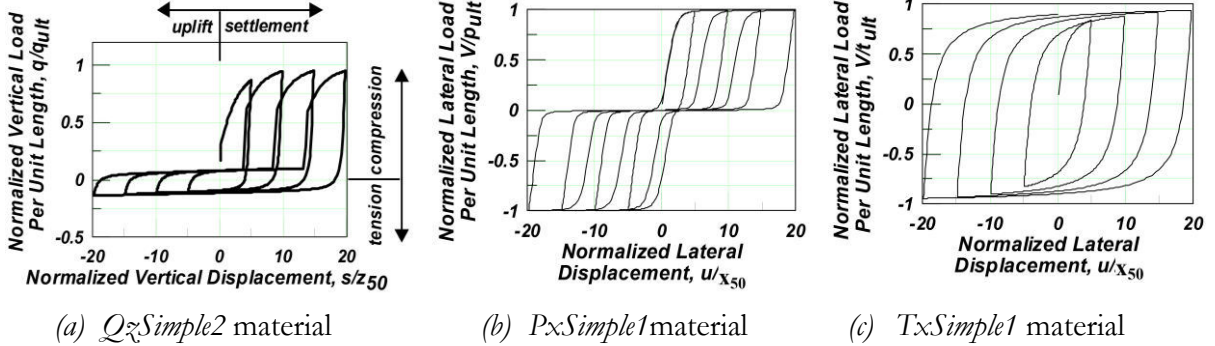


Figure 5-10: Cyclic response of the  $Q_z$ Simple2,  $P_x$ Simple1, and  $T_x$ Simple1 materials (after Raychowdhury & Hutchinson, 2009)

2. Tension capacity,  $T_p$ : It is the ratio of tension capacity to the bearing capacity of soil. This parameter can take values in the interval [0, 10%] (Raychowdhury & Hutchinson, 2009).
3. Distribution of vertical stiffness: BNWF uses  $R_k$ ,  $R_e$  and  $S_e$  (see Figure 5-8) parameters that are typically defined to ensure a higher reaction at the footing-end as the footing rocks. ATC-40 (1996) recommends the end-length  $L_{end}$  to be B/6; others suggest the end-length to be a function of the aspect ratio of the footing (Harden & Hutchinson, 2009).
4. Shape parameters of the constitutive laws [ $C_r$ , c and n]: These parameters are hard-wired to the OpenSees software, i.e., they are not specified by users. They are determined by calibrating the model using experimental data from tests.

### 5.2.1.2 Performance evaluation of BNWF using experimental tests

Raychowdhury & Hutchinson (2009) examined the performance of the BNWF model using experimental data obtained from soil-structure interaction tests, at 20 g centrifugal acceleration, conducted by Gajan et al. (2003a, 2003b) (SSG01, SSG02, SSG03, and SSG04 experiments) and Rosebrook & Kutter (2001a, 2001b, 2001c) (KRR01, KRR02, and KRR03 experiments). The experiments include strip footings, supporting shear walls resting on sandy and clayey soil, and square footings, supporting bridge columns resting on sandy soil. The experiments were chosen to evaluate its performance during quasi-static cyclic tests as well as dynamic tests. The dynamic tests were performed by applying earthquake ground motions at the base of the centrifuge models. The strip foundations were tested under a vertical safety factor (FSv) in the interval [2, 14] whereas the tests on the bridge foundation were conducted for FSv ranging from 17 to 31.

The centrifuge tests of the strip foundations were mostly conducted on a fine-grained dry Nevada sand, characterized by Dr=80%. Few experiments were also performed on the muddy soil of the San Francisco Bay, with undrained shear strength  $C_u=100\pm10$  kPa. The strip footing adopted

during the SSI experiments had  $2.8 \times 0.65 \text{ m}^2$  plan dimensions. Both surface and embedded footings, with D/B equal to one, were considered in the experimental study.

In the numerical model, the shear wall elements and the structural foundation were represented by elastic beamColumn elements and the static load was applied at the height defined in the experiments. The vertical springs were spaced at 2% of the total length (i.e.,  $l_e/L_f=2\%$ ) of the footing and a tension capacity equal to 10% of the compressive strength was adopted. The stiffness of the end region of the foundation was taken as 2.5 times the stiffness of the middle region, i.e.,  $R_k=2.5$ ; and the end-region ( $R_e$ ) was assumed to have 10% of the total length of the footing. Besides, two nonlinear lateral springs provide the sliding and friction resistance of the footing.

The maximum moment, shear force, rotation, and settlement of the strip foundation obtained from the experiments and numerical analysis were in good agreement. The mean deviations of these responses were found to be 9%, 16%, 14%, and 11%, respectively. Nonetheless, sliding was underpredicted in most cases, with a mean deviation of 44%, because the decrease in shear capacity obtained by increasing the moment demand cannot be captured due to the lack of coupling between the vertical and horizontal springs of the model. From the standpoint of performance-based design in earthquake engineering, residual displacements at the end of an earthquake excitation are important. Residual rotations calculated by the BNWF model were found to have very small discrepancies, in comparison to the experimental results, but sliding has large deviations. Contrarily, the residual settlement of the strip foundation has a minimal deviation in most of the studied cases. The above discussion is succinctly summarized in Figure 5-11.

In the experiments that were conducted on embedded square-footings, supporting bridge columns, the same Nevada sand was utilized again (Ugalde et al., 2007). The prototype structure, a single column bent, was scaled and modeled as a “lollipop” during these experiments. Bridge structures are typically designed to minimize vertical displacements, consequently, large values of FS<sub>v</sub> were adopted during the experiments. The BNWF model was evaluated from the dynamic tests of the lollipop structure subjected to moderate intensity earthquake ground motions obtained by scaling the Tabas (1978) and Loma Prieta (1989) earthquakes. The numerical model of the square footing was chosen to have the end length equal to 16% of the total length (Harden et al., 2005), and the end region was set to be five times stiffer than the middle region.

The bridge column and the structural foundation were modeled using elastic elements. The input acceleration to the numerical model was taken directly from the free-field acceleration recorded during the centrifuge experiments at the level of the base of the foundation. In this manner, the minimal kinematic interaction inherent in the experiments can be reproduced in the numerical analysis as well.

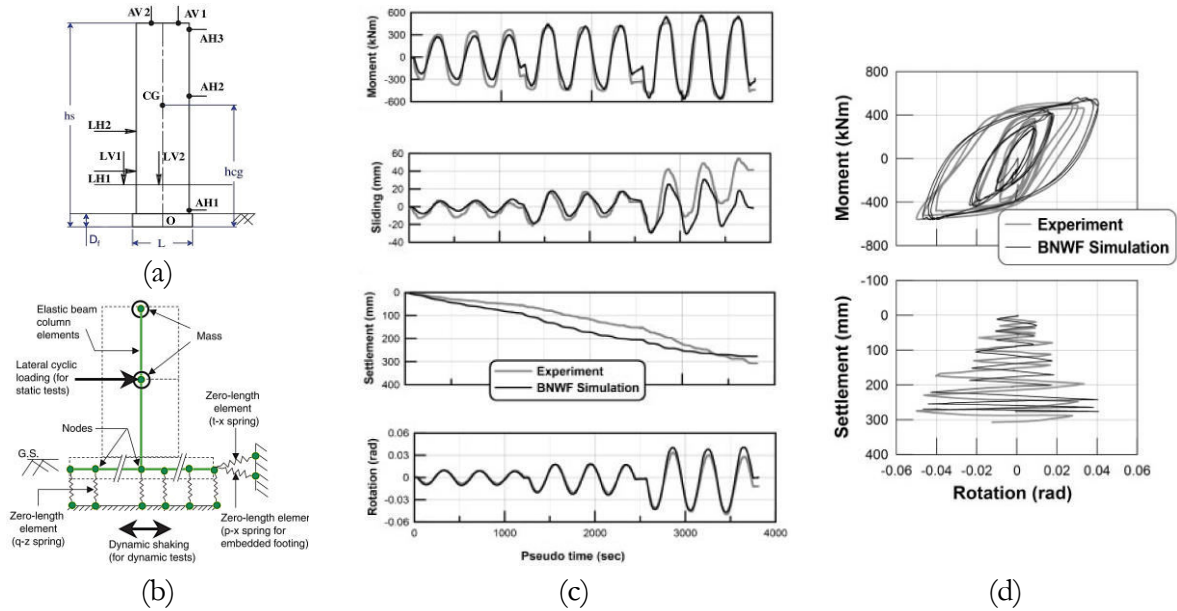


Figure 5-11: Dynamic testing of a shear wall resting on a strip footing, reference to SSG04-06 experiment (Gajan et al., 2003a): (a) prototype; (b) numerical modeling using the BNWF approach; (c) experimental versus numerically obtained responses; (d) moment-rotation plot (top) and settlement-rotation plot (bottom) (after Raychowdhury & Hutchinson, 2009)

The moment response, rotation, and settlement of the square footing, obtained from experiments and numerical simulations, are presented in Figure 5-12. To account for the foundation settlement at the start of an event, caused by a previous loading event, an initial displacement was applied to the numerical model. Like in the case of the strip footing, the BNWF model was able to reproduce the maximum values of the above responses. In general, a good agreement between the experimental results and the numerical simulations was achieved and the errors of the maximum moment, rotation, and settlement demands were 21%, 36%, and 20%, respectively. In other few experiments, the numerical model underestimated the moment capacity because the model does not account for the contribution of the side friction on the moment capacity of the foundation. Besides, the actual vertical capacity of soil increases above its theoretical value as the soil settles deeper, thus becoming denser. The lateral resistance of a foundation may also be greater than the theoretical estimate due to settlement.

Despite its simplicity and prediction capabilities, the BNWF approach was reported to be highly dependent on the calibration of its model parameters. It does not account for the kinematic interaction, being thus only suitable for structures supported on shallow foundations. Besides, due to its decoupled DOFs, it can underestimate the energy dissipation capability of foundations. This technique also exhibits strong variability of response for varying soil types. Furthermore, its limitations in capturing the sliding effect can generate important discrepancies compared to the 3D continuum approach. Hence, the BNWF approach is deemed to be only suitable for structures, supported on shallow foundations, with dominant rocking action.

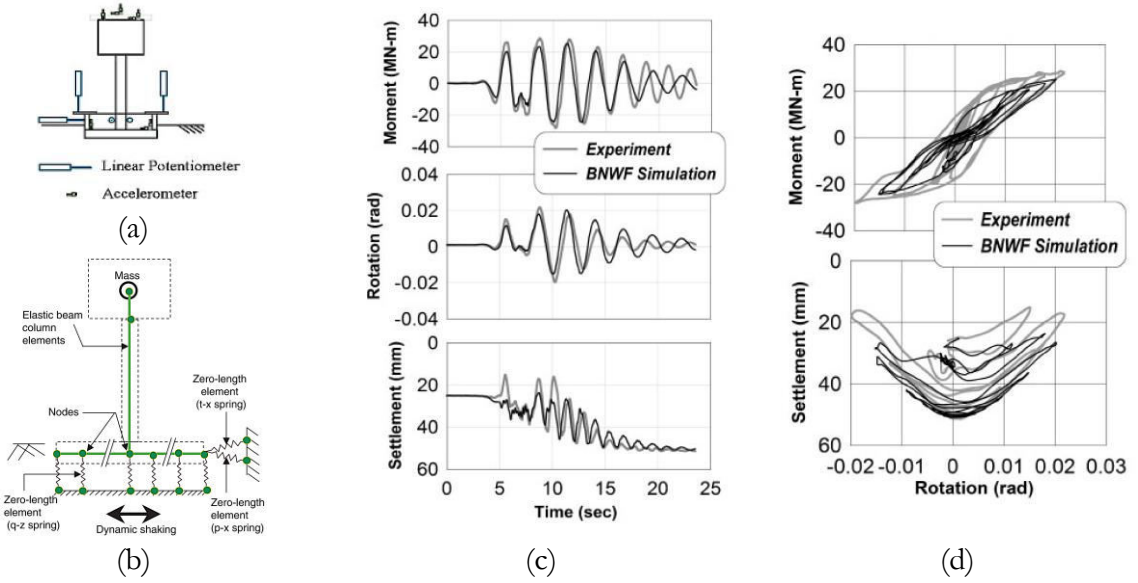


Figure 5-12: Dynamic testing of a bridge column supported on a square foundation, reference to JAU01–E08 experiment (Ugalde et al., 2007): (a) Test setup and instrumentation; (b) numerical modeling using the BNWF approach; (c) experimental versus numerically obtained responses; (d) moment-rotation plot (top) and settlement-rotation plot (bottom) (after Raychowdhury & Hutchinson, 2009)

### 5.2.2 Macro-element approach for soil-structure interaction analysis

Simplified models for analyzing soil-structure interaction are commonly used to avoid the computationally heavy 3D continuum approach. The integration of these simplified methods in the performance-based earthquake engineering approach is therefore essential. Nonetheless, there is a significant compromise in the accuracy of responses obtained from these methods. In the last two decades, the tradeoffs between the accuracy and computational cost of many simplified approaches have been thoroughly investigated. In this context, the macro-element method for soil-structure interaction analysis has been advocated to be a more advanced and reliable approach (Chatzigogos et al., 2009).

The macro-element approach is a simplified representation of the combined properties of soil and structural foundation by a single joint element that connects the center of mass of the foundation and superstructure. The detailed properties of the elements that make up both the soil medium and the structural foundation are usually not available. However, the macro-element can model the elastic far-field effects as well as the geometric and material nonlinearities exhibited in the near-field region. In detail, the partial foundation uplift and the associated contact degradation, soil plasticity, elastic behavior of soil, and radiation damping can be represented conveniently. For the application of deep foundations such as piles, the geometric nonlinearity occurs due to pile gapping instead of uplift. In the macro-element concept, based on plasticity theory, the global behavior of a foundation

element is formulated in terms of generalized displacements and forces.

The development of the macro-element approach dated back to the early 1990s by Nova & Montrasio (1991). In the early stage, the approach was limited to strip footings and static loading. Notable developments of the macro-element approach, following its conception, comprise the inclusion of geometric nonlinearity, enabling dynamic analysis, coupling system nonlinearities, and application to other footing types (Cremer et al., 2001, 2002; Chatzigogos, 2007 and Chatzigogos et al., 2009, 2010).

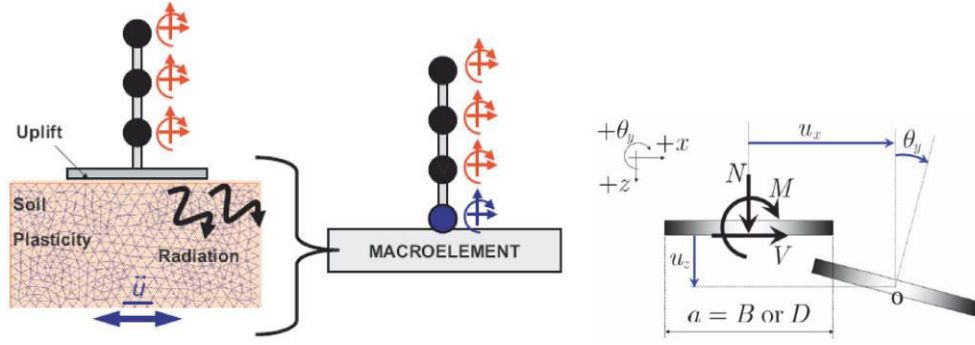


Figure 5-13: Macro-element approach for modeling soil-structure interaction (after Chatzigogos et al., 2009)

In this approach, the ultimate load is defined by a surface of bearing strength; and an elliptical bounding surface describes the soil plasticity (Chatzigogos, 2007). It accounts for the coupled nonlinearities prevalent during SSI analyses. In general, when a footing element is subjected to a small vertical force, the elastic soil behavior and the geometric nonlinearities due to uplift are dominant. The uplift mechanism of a macro-element may be represented by a phenomenological nonlinear and reversible model, without energy dissipation properties. At significantly large vertical forces, the soil plasticity kicks in and the two nonlinear mechanisms get coupled providing the surface for the ultimate load.

The equations of the macro-element approach are written in the form of generalized forces  $Q$  and displacements  $q$  (Chatzigogos et al., 2009), which are typically normalized as:

$$Q = \begin{bmatrix} Q_N \\ Q_V \\ Q_M \end{bmatrix} = \begin{bmatrix} N/N_{max} \\ V/V_{max} \\ M/M_{max} \end{bmatrix}; q = \begin{bmatrix} q_N \\ q_V \\ q_M \end{bmatrix} = \begin{bmatrix} u_z/D \\ u_x/D \\ \theta_y \end{bmatrix} \quad (5.9)$$

where  $N_{max}$  and  $D$  are the maximum vertical force and the diameter of a circular footing, respectively. In this approach, the relationship between incremental forces and displacements is expressed as:

$$Q = K \times q \Rightarrow \begin{bmatrix} \dot{Q}_N \\ \dot{Q}_V \\ \dot{Q}_M \end{bmatrix} = \begin{bmatrix} \kappa_{NN} & \kappa_{NV} & \kappa_{NM} \\ \kappa_{VN} & \kappa_{VV} & \kappa_{VM} \\ \kappa_{MN} & \kappa_{MV} & \kappa_{MM} \end{bmatrix} \begin{bmatrix} \dot{q}_N \\ \dot{q}_V \\ \dot{q}_M \end{bmatrix} \quad (5.10)$$

where the entries  $k_{ij}$  (i.e., i, j=N, M or V) represent the elements of the normalized stiffness matrix,  $K$ . The latter can be derived using the work done by the forces and displacements:

$$K = \begin{bmatrix} (D/N_{max})K_{NN} & (D/N_{max})K_{NV} & (1/N_{max})K_{NM} \\ (D/N_{max})K_{VN} & (D/N_{max})K_{VV} & (1/N_{max})K_{VM} \\ (1/N_{max})K_{MN} & (1/N_{max})K_{MV} & (1/DN_{max})K_{MM} \end{bmatrix} \quad (5.11)$$

and  $K_{ij}$ , where i, j=N, M, or V, represent the elements of the footing's stiffness matrix. In the work developed by Chatzigogos et al. (2009), the macro-element approach assumes undrained conditions for loading, where the soil takes the Tresca strength criterion with an associated plasticity model. Besides, the curve for the uplift mechanism was envisioned to model the apparent reduction in the foundation stiffness during uplift. Here, the ultimate surface does not define the yield surface of the plasticity model. Instead, the ultimate surface is obtained as the combined effect of the plasticity model and the uplift mechanism.

The macro-element approach can be represented by a simple rheological model allowing the incremental displacement to be decomposed into elastic and plastic parts, as shown in Figure 5-14(a). The model proposed by Chatzigogos et al. (2009) follows the assumption made by Cremer et al. (2002) where the horizontal force has no influence whatsoever on the uplift mechanism. Therefore, the elastic part of the rheological model is formulated considering  $Q_N$  and  $Q_M$  (see Figure 5-14(c)). Before the initiation of the uplift mechanism, the response is linear elastic and thus only dependent on the elastic impedances. At this stage, the coupling terms can be ignored if the foundation, with a flat base, is fully in contact with the soil surface.

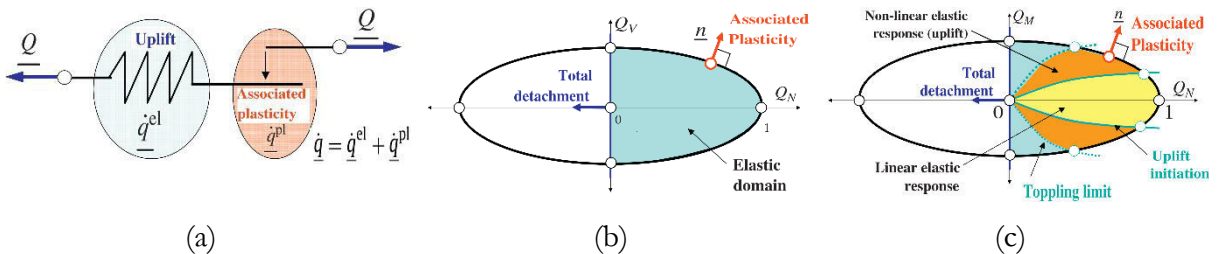


Figure 5-14: (a) Rheological model for macro-element method; (b)  $Q_N$ - $Q_V$  plane; (c)  $Q_N$ - $Q_M$  plane (after Chatzigogos et al., 2009)

When the normalized moment is larger than the moment for uplift initiation  $|Q_{M,0}|$ , the elastic tangent stiffness is determined by fixing the vertical force and progressively increasing the applied moment until the structure topples. For a strip footing, two approximations, presented in equation (5.12), are made, one for the  $Q_M - q_M^{el}$  relationship and another for the coupling between the vertical force and  $Q_{M,0}$ .

$$\begin{aligned}\frac{Q_M}{Q_{M,0}} &= 2 - \frac{q_{M,0}^{el}}{q_M^{el}}; |Q_M| > |Q_{M,0}| \\ \dot{q}_N^{el} &= -\frac{1}{2} \left( 1 - \frac{q_{M,0}^{el}}{q_M^{el}} \right)\end{aligned}\quad (5.12)$$

where  $q_{M,0}^{el}$  is the elastic normalized rotation angle corresponding to the moment during uplift,  $Q_{M,0}$ . Chatzigogos et al. (2009) assumed the coupling between uplift and the vertical DOF to be derived from the  $K_{NM}$  and  $K_{MN}$  terms without reducing  $K_{NN}$ . This assumption can therefore be used to drive the  $K_{MM}$  and  $K_{MN}$  entries of the tangent matrix, based on the initial stiffness matrix. The authors also adopted the same assumption while deriving the elastic tangent stiffness of a circular foundation.

The bending moment for uplift initiation  $Q_{M,0}$  is related linearly to the vertically applied force, and  $Q_{M,0}$  is taken as one-sixth and one-fourth of the normalized vertical force for circular footings (Cremer et al., 2001) and strip footings (Wolf, 1989), respectively. Several closed-form expressions for the elastic tangent stiffness have been developed in the past focusing on strip and circular foundations (Chatzigogos et al., 2009; Wolf, 1989). Wolf (1989) also proposed the elastic tangent stiffness of circular footings to be determined by preserving the diagonal matrix but reducing the diagonal entries  $K_{NN}$  and  $K_{MM}$ . Correia & Paolucci (2021) have redefined the macro-element uplift response in a more physically coherent framework.

In the soil plasticity model, the bounding surface is defined by an ellipsoid, centered at the origin in the space of forces (Chatzigogos et al., 2009). The bounding surface equation reads:

$$f_{BS} = \underline{Q} = Q_N^2 + \left( \frac{Q_V}{Q_{V,max}} \right)^2 + \left( \frac{Q_M}{Q_{M,max}} \right)^2 = 1 \quad (5.13)$$

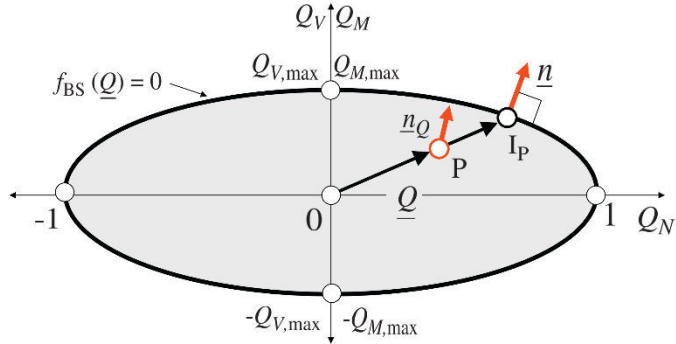


Figure 5-15: Bounding surface for the hypoplastic model in the macro-element modeling  
(after Chatzigogos et al., 2009)

The bounding surface determines the pure loading, unloading, and neutral loading cases, and provides the direction of the incremental displacement. The plastic modulus is also defined through the bounding surface. Plastic displacements are developed during the pure loading and reloading cases only and it is a function of a scalar distance,  $\lambda$ , between the current state (point  $P$  in Figure

5-15) and its image point on the bounding surface,  $I_p$ . The latter is the image point of  $P$ , a point inside the bounding surface, which is defined by the radial mapping rule:  $I_p = \{\lambda P | I_p \in \partial f_{BS} \& \lambda \geq 1\}$ . Chatzigogos et al. (2009) also proposed an isotropic, more complex formulation, for the plastic modulus adding parameters for describing the history of loading and the loading path. Eventually, the coupling of both nonlinear mechanisms is considered. It is recalled that the uplift moment is assumed to vary linearly with respect to the vertical force, which is not true. Cremer (2001) developed an *ad hoc* approximation for the elastic tangent stiffness  $K_{MM}$ , in the form of an exponential function, based on the vertical force, including a calibration parameter that depends on the shape of the foundation. Once again, Correia & Paolucci (2021) have redefined the macro-element bounding surface plasticity formulation in a more physically coherent framework, where cyclic evolution of the response and general loading conditions arise naturally.

Other complex mechanisms such as the second-order effect caused by the degrading contact area of a footing were also investigated by Gajan & Kutter (2007) and included in the macro-element response by Correia & Paolucci (2021).

Furthermore, the neutral loading of both nonlinear mechanisms, in the macro-element modeling of Chatzigogos et al. (2009), needs to be specified. The foundation-soil contact area is maintained under the combination of moment and vertical force during the uplift mechanism. Likewise, neutral loading in the hypoplastic model is ensured when the force state follows the path of the ellipsoid.

Again, the most rigorous and complete solution for the SSI analysis can still be conducted by dividing the problem into near-field and far-field analyses. The far-field analysis, which is assumed elastic, can be used to represent the wave propagation in the soil medium. The wave propagation analysis is usually conducted using finite element, spectral element, or boundary element methods. On the other hand, the near-field analysis accounts for all the geometric and material nonlinearities of the soil-footing response.

### 5.3 Experimental methods for soil-structure interaction

In the last two decades, with the growing interest in soil-structure interaction analysis, important experimental tests, utilizing the 1g shaking table and centrifuge, have been conducted for nonlinear response analysis of shallow foundations subjected to static and dynamic loads. Among the most relevant ones are: centrifuge tests on shear walls that were conducted at the University of California, Davis (Gajan et al., 2005), shaking table experiments conducted at the Public Works Research Institute (PWRI) in Japan (Shirato et al., 2008), an experimental test on a shallow foundation with eccentric loading (Maugeri et al., 2000) and a quasi-static shaking table test conducted by the Joint Research Center (JRC) in Ispra, Italy (SERIES, 2011). In other tests, Liu et al. (2013) conducted centrifuge tests on a steel frame supported on sandy soil and examined the relative yielding of structural elements and foundations. They advocated the concept of energy dissipation through foundation rocking motion to be accepted in the civil engineering community. A detailed summary

of recent experimental tests on soil-structure interaction can be found in Pecker et al. (2012).

### 5.3.1 Centrifuge and 1g shaking table tests

In this section, some of the most relevant experimental tests involving soil-structure interaction in the literature are explored.

- i. CAMUS IV, TAMARIS, CEA, Saclay, France (Combescure & Chaudat, 2000):

In the CAMUS 1g shaking table test, four experiments were conducted on four large-scale five-story shear wall buildings. The four shear buildings, 1/3 scale of the prototypes, which were constructed with different steel reinforcement and boundary conditions, were subjected to in-plane earthquake loading of increasing amplitude. Three of those buildings were fixed at the base while the fourth building was placed on a sand bed, as shown in Figure 5-16. The sand was filled to a container having 4x4 m<sup>2</sup> plan dimensions and 40 cm depth, and the footing was allowed to rotate and uplift freely. During the testing campaign, natural and synthetic accelerograms, of increasing intensities, prepared according to the French norm, PS92, for the design of earthquake-resistant structures, were used. In this test, when moments surpassed 150 kNm, the uplift mechanism isolated the footing element from the soil and limiting the loading transferred to the foundation even as the level of shaking becomes larger. The maximum rocking angle increased with increasing intensity of loading but the residual rocking angle, for the low and high intensities of shaking, remained close to zero, which could be attributed to the self-centering effect of the uplift phenomenon. In this test, the coupling between the foundation uplift and soil-plasticity was apparent from the accumulation of settlements after each heave, making the area enclosed in the

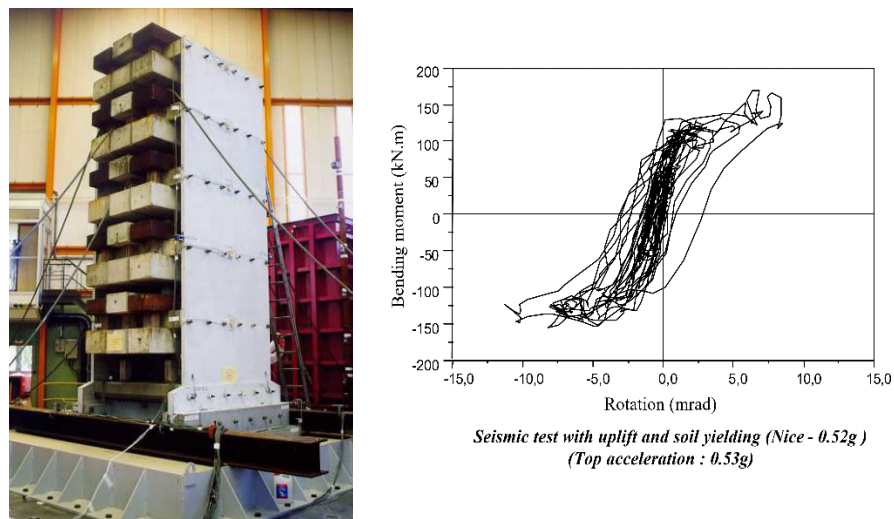


Figure 5-16: CAMUS IV test setup and moment-rotation response (from CEA, 2000)

M-θ hysteresis curve larger. Figni et al. (2012) used the results of this testing campaign for calibrating the parameters of a macro-element that is applicable to shallow foundations on dense

sand.

- ii. Centrifuge test at the NEES facility, UC Davis, USA (Gajan et al., 2005; Chang et al., 2007; Liu et al., 2013):

The centrifuge tests conducted by Chang et al. (2007), at the UC Davis facility, were applied to the mixed frame and wall structures shown in Figure 5-17. They have one-bay or two-bays, inside a rigid container, with  $1.76 \times 0.9 \text{ m}^2$  plan dimensions, mounted on a centrifuge. The centrifuge tests were conducted at 20 g, which is equivalent to a prototype 20 times larger than the model. Some of the experiments were carried out by applying slow cyclic loading, using an actuator, and others were conducted under dynamic base shaking.

Most of the tests were conducted on sandy soil, but one test was also performed on clayey soil. The steel columns of the two structures were supported on square footings whereas the wall is supported on a rectangular footing. A single mock-up was used for several tests by introducing fuses in the structure. During the test, the residual rotation (clockwise) of the strip footing of the one-bay frame was much smaller than the residual rotation (counter-clockwise) of the square footing whereas all footings of the two-bay frame rotated in the clockwise direction.

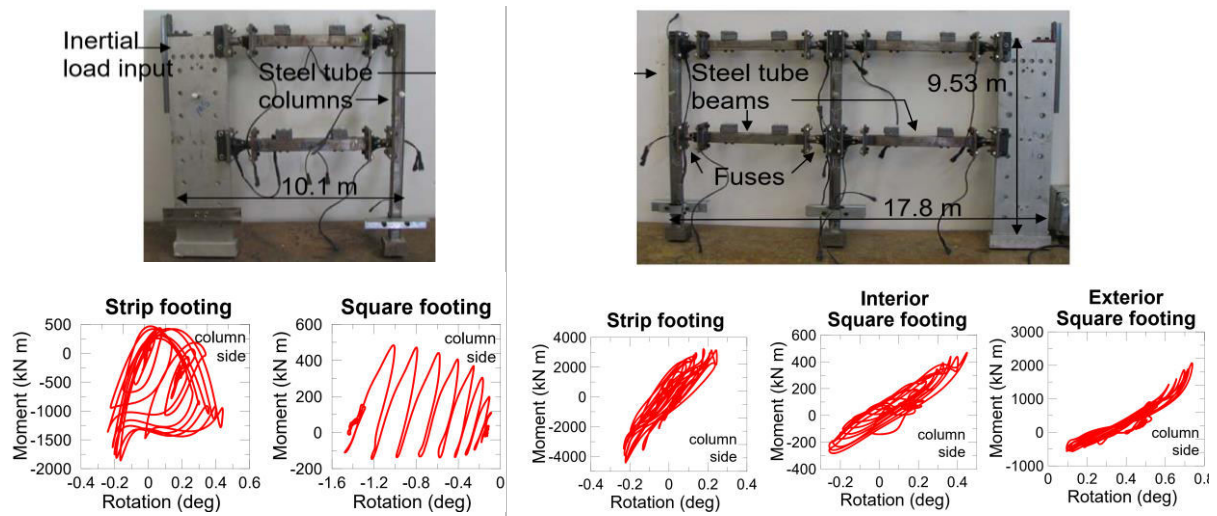


Figure 5-17: Centrifuge test of a mixed steel-concrete structure, at UC Davis, subjected to a dynamic base input scaled to 0.65 g PGA (after Chang et al., 2007)

In Gajan et al. (2005), centrifuge tests, at 20 g acceleration, were also conducted on rigid shear wall superstructures, supported on strip footings, subjected to vertical loading in addition to a slow cyclic lateral loading or a dynamic base shaking (see Figure 5-18). Most of the experimental tests were conducted on dry sandy soil. The experiments revealed a chain of interdependencies between the foundation uplift and soil yielding.

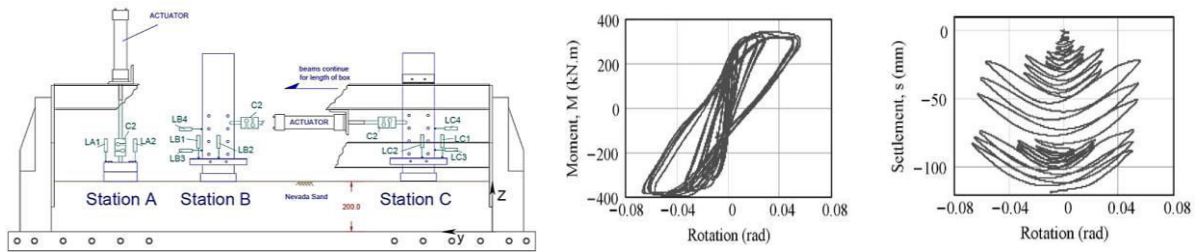


Figure 5-18: Centrifuge test of a shear wall structure, at UC Davis, under static cyclic and dynamic loadings (shows the results of SSG02 experiment) (after Gajan et al., 2005)

Using the same test rig, Liu et al. (2013) conducted a centrifuge test in three two-story one-bay steel frame structures founded in sandy soil. The structures were designed with similar layouts but different combinations of the foundation size and yield strength of the structural elements. The test rig was shaken with a single earthquake motion so that responses of the different models can be compared. Among the three structural configurations tested, the so-called balanced design resulted in a well-behaving system whereby the ductility demand of the structural components was appreciably reduced. In the balanced design approach, the foundation rocking yields at the same load as that of the structural elements (governed by structural fuses). On the other hand, the model that was designed according to the restrained rocking philosophy placed a large ductility demand on the structure, as shown in Figure 5-19.

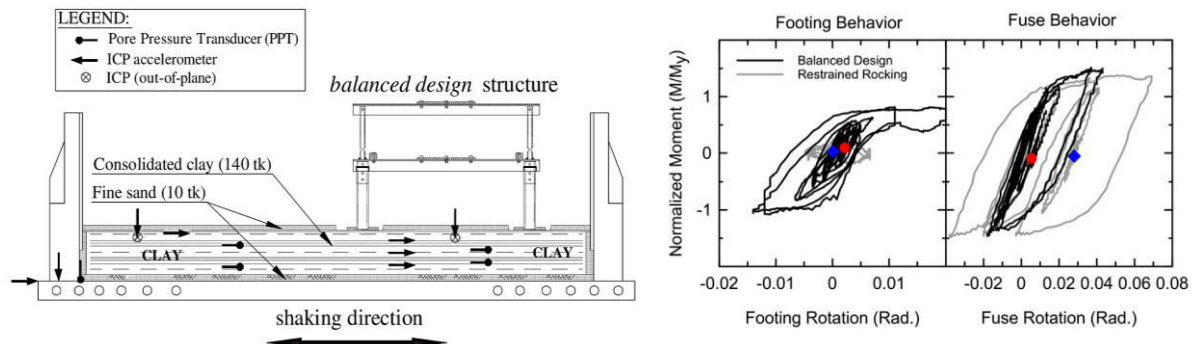


Figure 5-19: Restrained rocking and balanced design approaches for a steel frame in centrifuge tests at UC Davis (after Liu et al., 2013)

### iii. TRISEE, ELSA, JRC, Ispra, Italy (Faccioli et al., 1998; Negro et al., 2000):

The test setup for this experimental campaign was a square footing, 1 m in size, subjected to cyclic forces and moments at the top; and the nonlinear structure-foundation interaction was studied. A constant vertical force was maintained throughout these tests. The characteristics of the square footing were studied considering loose (LD) and dense (HD) sands. The sandy soil was contained in a large concrete caisson having  $4.6 \times 4.6 \text{ m}^2$  plan dimensions and 4 m height. The plastic response of the sandy soil started too early during those tests. The test phases included: (i) gradual increase of horizontal sine-like pulses until the onset of nonlinearity (corresponds to 5% of the vertical load);

(ii) application of earthquake-like horizontal force (does not exceed 20% of the vertical load) and overturning moment, maintaining compression everywhere across the soil-foundation interface; and (iii) application of sine-like displacement pulses until the ultimate resistance of the foundation. In phase III, shown in Figure 5-20, the settlement accumulated in the dense sand has sudden peaks resulted from the heaving action while the loose sand is characterized by a plastic sinking response that cancels out the uplifting action of the foundation.

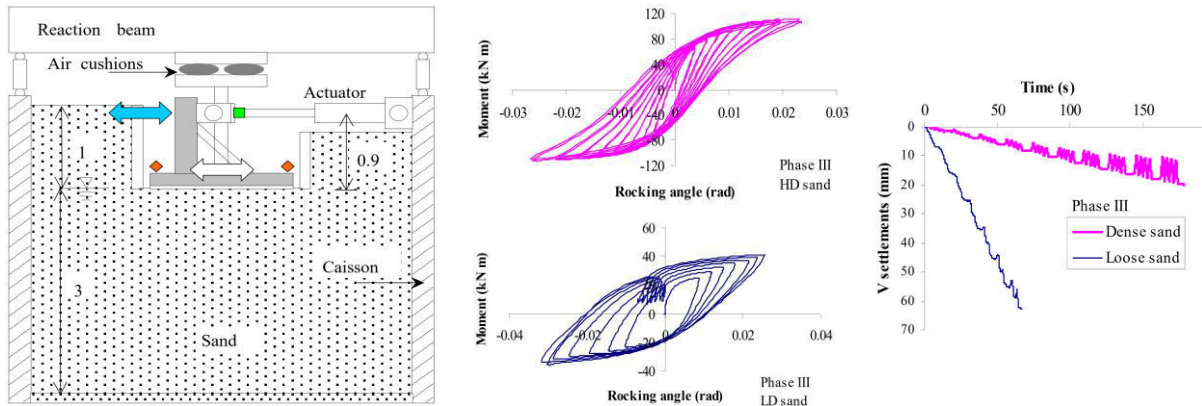


Figure 5-20: TRISEE test: Test rig (left) and results of phase III of the test (right) (after Faccioli et al., 1998)

iv. Public Work Research Institute (PWRI), Japan (Shirato et al., 2008):

The 1g shaking table tests conducted at the foundation engineering laboratory PWRI comprised of a square-shaped shaking table, 8 m in size, a laminar shear box having  $4 \times 4 \times 2.1 \text{ m}^3$  dimensions, a dry sandy soil which was filled up to 2 m height of the laminar box, and a bridge pier superstructure. The model was constructed from a steel rack at the top, a square footing, and a rigid I-beam connecting the two parts. The pier model was placed in the sand deposit contained in the laminar box. The latter was attached to the shaking table, where the earthquake motion was applied.

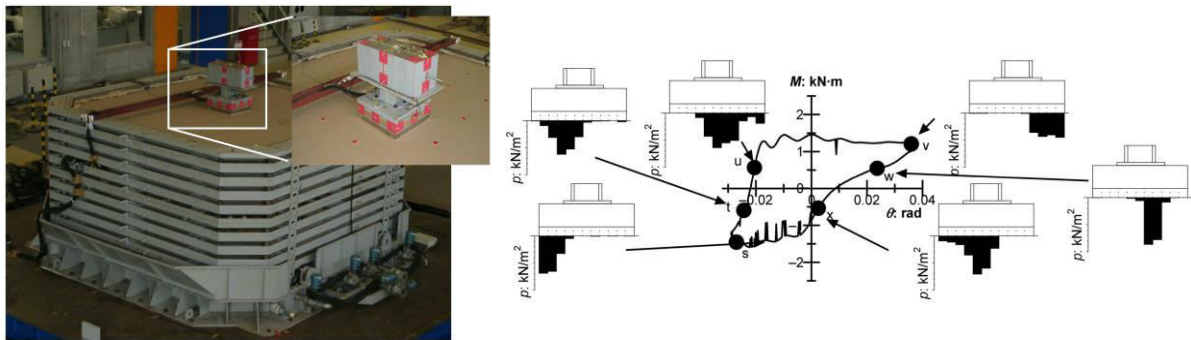


Figure 5-21: 1g shaking table tests of a pier model, at the PWRI laboratory: Test rig (left) and pressure distribution under Kobe (1995) earthquake input, scaled to 0.568 g PGA (right) (after Shirato et al., 2008)

The experimental tests of the pier model were conducted by applying monotonic and cyclic loads. The static safety factor FS<sub>v</sub> of the foundation was estimated around 29, implying a large soil bearing capacity compared to the weight of the structure. The pressure distribution of the foundation was investigated during these tests by measuring interface compressive stresses at multiple locations. A significant coupling between the uplift mechanism and soil plasticity was also observed in these tests. A reduction in the effective width of the foundation, which translates into the apparent stiffness degradation, can be observed in the moment-rotation diagrams, shown in Figure 5-21.

### 5.3.2 Hybrid testing

Soil-structure interaction analysis through hybrid testing has not been thoroughly investigated, even though its viability was sought in the early 1990s. Such analysis can be performed in a hybrid simulation framework either: (i) by modeling the SSI numerically while the superstructure is modeled physically; or (ii) by physically modeling the SSI while the superstructure is represented numerically. The first approach can be performed using the conventional method for hybrid testing. Consequently, several research studies were conducted, in the past, using this approach. In the second approach, the SSI hybrid test can be conducted by applying an earthquake excitation to the soil and foundation assembly, through a shaking table, while the interface commands, at the boundary between the two substructures, are imposed using additional actuators. Such laboratory testing has proven to be challenging. First, the deployment and operation of a large soil container have their own complexity. Besides, the need for controlling a shaking table and an auxiliary actuator at the same time, and their synchronization, makes the task more problematic.

The first application of hybrid simulation to the nonlinear seismic soil-structure interaction analysis was implemented by Toki et al. (1990). Toki and co-workers developed an algorithm called *HENESSI*. In this algorithm, a complex frequency-dependent stiffness matrix of the system is first determined, and the time-dependent pseudo-force is then calculated using the Hilbert and inverse Fourier transformations. The latter was originally used in decomposing the equations of motion into the initial, nonlinear, and time-rate-dependent characteristics of a system (Toki et al., 1990). The algorithm was applied in a pseudo-dynamic test which models the soil-structure interaction as a numerical substructure. A similar approach was followed during the development of SSI hybrid testing by Ohtomo et al. (2003), at the Central Research Institute of Electric Power Industry (CRIEPI). They took a nonlinear finite element analysis approach to study the seismic performance of in-ground structures (Saouma & Sivaselvan, 2008) and their test results were compared against a shaking table test conducted on a reinforced concrete box culvert embedded in a laminar soil box.

The first approach for the SSI hybrid testing was utilized by many other researchers (Wang et al., 2011; Dietz et al., 2015; Chang & Kim, 2019; Zhou et al., 2014). This approach requires an accurate numerical model of the soil domain; consequently, a large number of soil elements may be needed. Eventually, the speed of response simulation, during hybrid testing, may be limited. To circumvent this, Wang et al. (2011) used a two-DOF lumped-parameter model for the soil medium. Likewise,

a reduced model of soil, considering 60 Ritz vectors, was applied in a hybrid test conducted by Zhang & Jiang (2017). The latter was applied to an equipment–structure–soil interaction system. The physical model was made of a four-story one-bay steel frame and the equipment, attached to the roof of the structure; the base of the model was rigidly anchored to a shaking table. To compensate for the shaking table dynamics, Zhang and co-workers used the Inverse Dynamic Compensation via Simulation (IDCS) algorithm, based on a 4<sup>th</sup> order transfer function estimated from a pre-test identification experiment. During the hybrid test, the effect of the linear behavior of soil on the equipment was simulated.

In another SSI hybrid test, which uses the first approach, shown in Figure 5-22, the Multi-Site Soil-Structure-Foundation Interaction Test (MISST), performed by Spencer et al. (2006), investigated the structural and geotechnical aspects of a bridge structure. The prototype structure is a bridge located in the Santa Monica Freeway, California, that was severely damaged during the Northridge earthquake in 1994. The MISST project builds on the early work of the Multi-Site Online Simulation Test (MOST) framework (Spencer et al., 2004).

During the hybrid test, two piers of the bridge structure were tested physically, at different sites, one at the University of Illinois at Urbana-Champaign (UIUC) and another at the Lehigh University. Both piers are 1/2 scale models of their prototypes, and the SSI between the foundation and soil medium was modeled analytically at the RPI facility. The UI-SimCor software coordinator was responsible for the seamless coordination and communication among the three sites. During the hybrid test, the full mass of the structure was assigned to the deck to enable static conditions when testing the piers. Hence, the dynamic response of the bridge is determined from the analytical model of the deck. Two ground motions recorded during the Northridge earthquake were used in driving the hybrid model. Even though the hybrid test was carried out by modeling the SSI in a numerical program, the successful completion of this project has strengthened the collaboration among the structural and geotechnical laboratories in improving response simulation of structures.

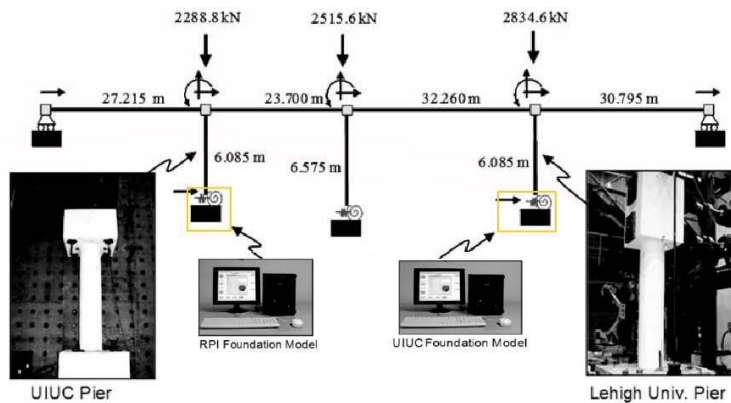


Figure 5-22: Multi-Site Soil-Structure-Foundation Interaction Test (MISST) (adopted from Saouma & Sivaselvan, 2008)

First of its kind, Stefanaki et al. (2015) performed an innovative hybrid test where a physical model

of soil-structure interaction was tested in a laboratory. The objective of the experimental test was to demonstrate the proof-of-concept of a hybrid test involving a physical model for SSI. The experimental substructure was made from a pile-group foundation, 3.05 m in height, embedded in saturated soil contained in a 7 m high laminar box, as shown in Figure 5-23.

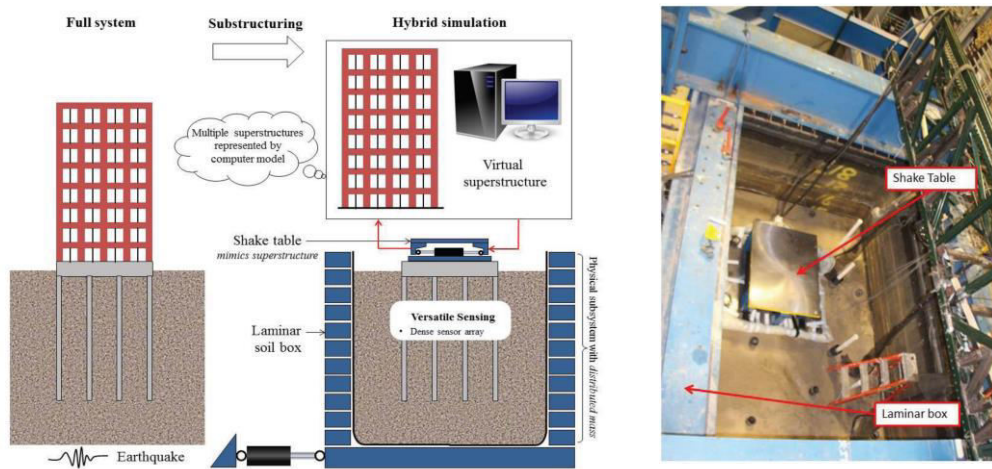


Figure 5-23: Hybrid simulation involving a physical model for soil-structure interaction  
(after Stefanaki et al., 2015)

The interface conditions were applied by a small shaking table that mimics the numerical substructure (i.e., the superstructure). The bedrock input motion to the model was applied, at the base of the laminar box, as a one-dimensional seismic excitation. To improve the stability robustness and to simplify the control design process, the impedance of the actuator, which applies the interface condition, was matched to the impedance of the superstructure (Verma & Sivaselvan, 2019).

Before installation, to ensure sufficient axial capacity in the steel pipes that represent the pile foundation, a Cone Penetration Test (CPT) was conducted. The small shaking table was placed at the top of the pile group, supported on a steel base plate. The experimental setup was highly instrumented comprising string potentiometers, in the laminar box, strain gauges, both in the laminar box and at the corner piles, accelerometers, placed in all three directions, and pore pressure transducers, throughout the depth of the soil. Interestingly, the small shaking table was also instrumented with load cells including differential pressure transducers in the actuators.

The hybrid tests were conducted by applying harmonic waves. A rigid-structure case, without interface conditions, was also investigated. The response of different superstructures was generated at a constant frequency by changing the amplitude and phase, relative to the base excitation, of the small shaking table. Eventually, the test output was used to study soil liquefaction considering the various superstructures. These hybrid tests shed light on the response of various superstructures under soil liquefaction, but, most importantly, have demonstrated the viability of the second approach for hybrid simulation in SSI problems.

## 5.4 Hybrid simulation in shaking table tests — application to SSI

### 5.4.1 Hybrid simulation tests in a shaking table

In a hybrid test that includes a shaking table, involving a physical model for SSI, the base excitation may be applied at the base of the soil-structure assembly through a shaking table while the interface force is applied using an auxiliary actuator. Let us consider, for example, a shear building having  $n$  stories where the first floor and the foundation soil are modeled physically in a shaking table. The remaining  $n-1$  top floors are therefore modeled in a numerical program.

The hypothetical experimental substructure shown in Figure 5-24 can be approximated as a SDOF structure, neglecting the soil dynamics, subjected to forces applied by the shaking table,  $F_{ST}$ , and the actuator,  $F_A$ . The sum of the two forces is therefore the total dynamic force applied to the test specimen. Hence, we can write:

$$M_e \ddot{u}_e + C_e \dot{u}_e + K_e u_e = -\underbrace{M_e \ddot{u}_g}_{F_{ST}} + \underbrace{\sum_{i=2}^n \dot{u}_{i,abs} M_{i,n}}_{F_A} \quad (5.14)$$

The variables with subscript ‘e’ represent the experimental substructure (note that the damping, c, and stiffness, k, of the SDOF include the foundation compliance; perhaps, the influence of the soil container may as well be added to make equation (5.14) more representative). The force command to the auxiliary actuator,  $f_i$ , is the base shear of the numerical substructure. It can be calculated as the sum of the absolute inertial forces of the upper  $n-1$  stories.

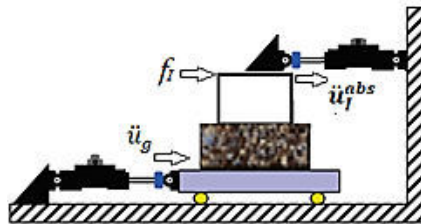


Figure 5-24: Idealization of a test rig for soil-structure interaction test in hybrid simulation

Although the scheme depicted in Figure 5-24 is challenging, it can accurately satisfy the boundary conditions of the problem at hand. In Shao & Reinhorn (2012), the total dynamic force is divided, conveniently, between the shaking table and the auxiliary actuator. Such force splitting offers an opportunity for a simplified approach where the shaking table alone can be used to apply the above two forces. To realize this, the actuator force,  $f_i$ , needs to be converted, online, into an equivalent acceleration of the shaking table during a hybrid test. Accordingly, equation (5.14) can be reformulated as:

$$M_e \ddot{u}_e + C_e \dot{u}_e + K_e u_e = -M_e \underbrace{\left( \ddot{u}_g + \left\{ \sum_{i=2}^n \ddot{u}_{i,abs} M_{i,n} \right\} / M_e \right)}_{\ddot{u}_{eq,ST}} \quad (5.15)$$

where  $\ddot{u}_{i,abs}$  is the absolute acceleration of the  $i$ th floor level;  $M_{i,n}$  is the  $i$ th floor mass; and  $M_e$  is the experimental mass (first-floor mass). In Shao & Reinhorn (2012), the equivalent acceleration of the shake table,  $\ddot{u}_{eq,ST}$ , was determined offline from an estimated acceleration response, and it was then double integrated since the shaking table was commanded in displacement. As discussed in the fourth chapter, direct acceleration feedback is unstable but indirect methods, such as the advanced shaking table control algorithm developed herein, are useful. The scheme represented in equation (5.15) does not require an additional actuator but its response simulation can be erroneous, according to Shao & Reinhorn (2012). These errors were primarily attributed to the lack of robust acceleration tracking of the shaking table. Besides, this formulation may not be applicable, again neglecting the soil dynamics, when the experimental substructure has more than one story because it is unknown how to determine the equivalent acceleration input to the shaking table,  $\ddot{u}_{eq,ST}$ .

#### 5.4.2 Soil container in 1g shaking table tests

In 1g shaking table tests, a model identification of the test specimen is crucial before conducting the hybrid test. The identified model can therefore be used in the model-based controller of the shaking table. The same is true for an auxiliary actuator. In geotechnical experimental testing, to model the boundary for the far-field soil medium, a flexible container is often used. However, reproducing the true boundary conditions of the prototype is difficult due to the end walls of the soil container. The walls of the soil container may give rise to strain and deformation incompatibilities between the model and the prototype. Besides, wave reflections from the walls can alter the seismic input motion that reaches the superstructure (Carvalho et al., 2010).

Soil containers are typically designed to match the dynamic properties of a soil deposit. The matching is performed for an intermediate range of strains expected in the soil deposit. LNEC's soil container was designed according to the Equivalent Shear Beam (ESB) philosophy of Zeng & Schofield (1996). It has  $2.0 \times 0.75 \times 1.75 \text{ m}^3$  dimensions and it was constructed as a flexible shear-stack of alternating aluminum frame and rubber-like elastomeric layers. The internal dimensions of the container are covered by a thin aluminum sheet with a slim layer of sand glued to it. The flexible container permits longitudinal shearing whereas its displacement in the transverse direction is restricted by braced columns that are placed very close to the longitudinal walls of the container.

During the identification test conducted by Carvalho et al. (2010), the frequency of the soil and container system was estimated to be 10.5 Hz, and the damping equal to 17%. The identification was conducted using a white noise input, with  $0.016 \text{ m/s}^2$  maximum acceleration, when the container was filled with dry sandy soil (SP-49 sand, which is a commercial sand from Sibelco, Lda). The sand has  $16.5 \text{ kN/m}^3$  specific weight,  $47^\circ$  angle of friction, and 38.2 MPa of average shear

modulus. The latter was calculated at mid-height of the soil deposit contained in the ESB container. An increase in the intensity of base shaking may slightly alter the frequency of the soil-container assembly (Carvalho et al., 2010). The filling process of soil, typically using a sand pluviator, during an experiment is also important. It is often performed to achieve homogeneity of the soil fill. In Carvalho et al. (2010), the filling was done by gradually reducing the flow rate of sand entering into the soil container.

#### 5.4.3 Pre-test identification and test setup

As discussed above, the prime objective of the system identification, in the context of the SSI hybrid testing in shaking tables, is for control purposes. In addition, the identified model can be used to convert an acceleration command of a shaking table into an equivalent displacement. Furthermore, it can serve to model control errors while conducting simulated studies.

Using the LNEC's uniaxial shaking table (ST1D) for a hypothetical SSI hybrid test and recalling the system transfer function of the ST1D, without payload, from chapter three, the properties of the joint soil-container (obtained from Carvalho et al. (2010)) can be simplified as a SDOF structure, as shown in Figure 5-25. Therefore, the transfer function of the bare ST1D can be modified to mimic the control-structure interaction (CSI) effects due to the SDOF structure. That was in fact the main idea of the parametric characterization of the ST1D, presented in chapter three, i.e., identifying the parameters of its transfer function so that it can be easily modified later to include rigid or flexible SDOF structures attached to it.

Therefore, combining the transfer function of the ST1D and the characteristics of the equivalent SDOF structure, the transfer function of the shaking table from the displacement command to the measured acceleration of the ST1D's platen,  $G_{a_p u_c}$ , can be derived, as shown in Figure 5-26. The abrupt drop of magnitude, near the natural frequency of the SDOF structure (10.5 Hz), shows the influence of CSI. In Figure 5-26, the relationship between the acceleration at the soil surface,  $a_{top}$ , and the displacement command are also presented. Besides, transfer functions of displacement measurements,  $x_p$  and  $x_{top}$ , are included in the plot.

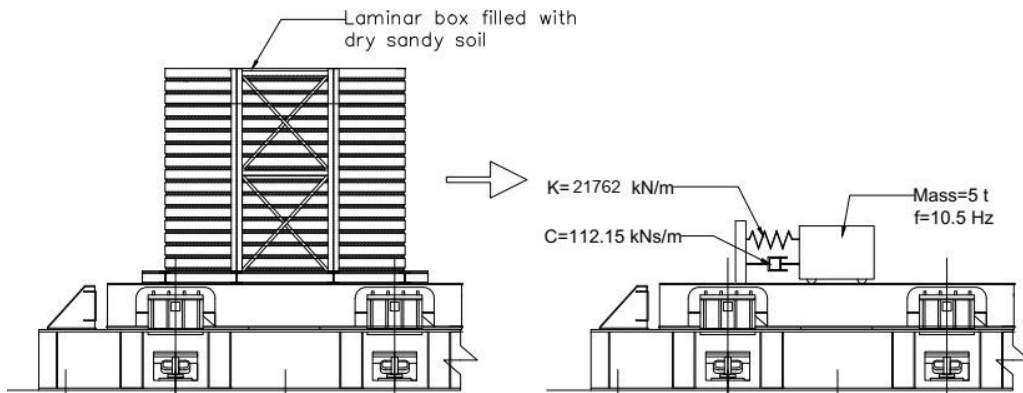


Figure 5-25: Idealization of a soil-container assembly as a SDOF in a shaking table test

This transfer function can be then readily used in the model-based controller of the ST1D. It can also be used to convert the acceleration input into a displacement command in the feedforward controller of the shaking table that is explored in chapter four. The latter approach was reported to have a better performance in Phillips et al. (2014).

Combining the tools developed up to now, hybrid testing of a shear building, including its SSI effects, can be performed. The substructuring scheme is thus envisioned to have the lower story as the physical substructure while the remaining top floors, which are essentially elastic, are represented analytically.

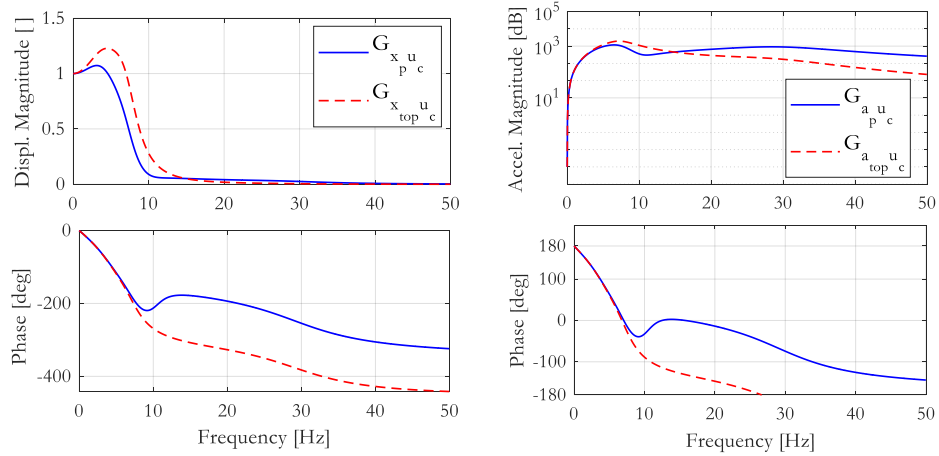


Figure 5-26: Transfer functions from the displacement command to the measured displacement and acceleration of the ST1D that is attached to a laminar box filled with dry sandy soil (SP-49 type)

#### 5.4.4 Rehearsal for soil-structure interaction test in hybrid simulation

Rehearsal tests for hybrid simulation are commonly performed to ensure software bugs and test setup anomalies do not hinder accurate simulation of structural responses. Hybrid simulation tests in a shaking table, also involving SSI, can benefit greatly from such rehearsal tests, because it can be challenging to perform an immaculate hybrid test in a complex test rig comprising of a shaking table, an additional actuator, and a test structure that is erected on a soil deposit. This is one of the objectives of the rehearsal test conducted herein. Besides, rehearsal tests may be useful also while designing SSI hybrid tests. To this end, the case study presented here is intended to show the capacity of a rehearsal test in predicting results anticipated during an actual hybrid testing. Rehearsal tests are expected to have a better fidelity of prediction if the experimental conditions are modeled. This can be achieved by modeling the characteristics of the load transfer system, as attempted herein.

#### 5.4.4.1 Case study

The bridge structure considered in this study constitutes part of the under-crossing of the I-10 freeway, Los Angeles, which was damaged during the Northridge earthquake in January 1994. The Collector-Distributor 36 forms a part of a pair of off-ramps from the eastbound carriageway at the intersection of I-10 with La Cienega-Venice which was constructed between 1992 and 1995. The RC bridge, made from a continuous three-celled box-girder deck, is first carried over to a two-column bent, then followed by three single-column bents, and ends on an abutment consisting of a vertical wall. The structure is located 25 km south-east of the epicenter of the earthquake.

The damage experienced by this bridge during the earthquake event was interesting. No visible damage was observed in the deck and abutment. On the other hand, the level of damage on the bridge piers varies greatly, with the left-most pier (pier-1) in Figure 5-27 being the most damaged of all. The middle pier, which is the longest pier, experienced minor damage characterized by slight spalling of concrete at the connection to the deck.

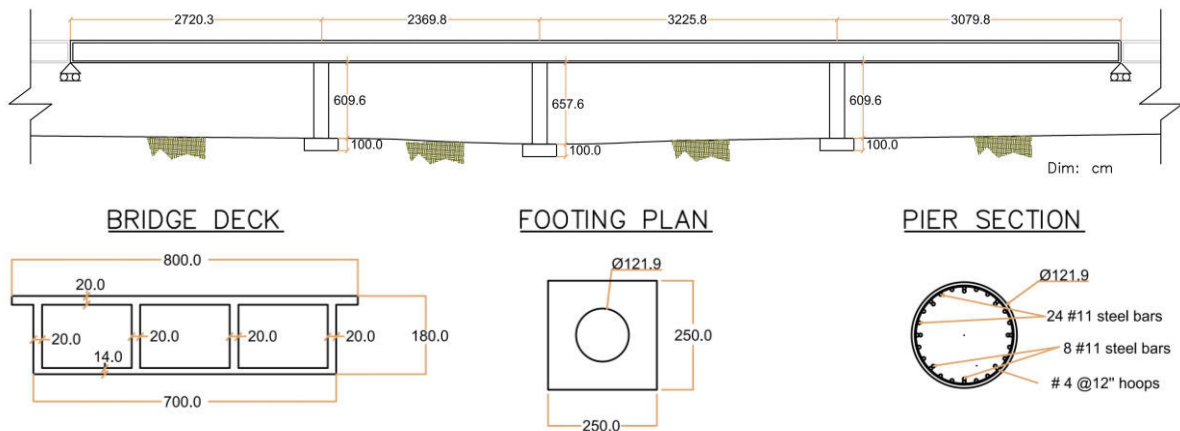


Figure 5-27: Details of the Collector-Distributor 36 under-crossing, Los Angeles, USA

As shown in Figure 5-28, pier-1 failed in shear, heavily cracked, with buckling of reinforcement bars and complete crushing of concrete. The symmetrical buckling of rebars and the opening of hoops make this failure spectacular. The interesting response of this RC bridge motivated researchers to study it both numerically and experimentally. In Broderick & Elnashai (1995), the dynamic nonlinear analysis of the structure was conducted considering three different modeling alternatives. They investigated the influence of boundary conditions at the foundations, abutments, and deck hinges. Great attention was paid to the discrepancies of the boundary conditions of the model between the design drawings and field observations.

As mentioned before, the bridge structure was also studied by conducting a geographically distributed hybrid simulation (Spencer et al., 2006). In this hybrid test, the structure was assumed to have three piers, as shown in Figure 5-27, in order to utilize the NEES participating laboratories. The interaction between soil and piers was modeled numerically as horizontal springs, with an

estimated stiffness of 2034.97 MN/m (to the knowledge of the author, there is no publicly available information about the properties of the foundation soil).

In this work, the modeling conditions assumed in the MISST test were fully adopted, except for the soil-foundation-structure interaction which was modeled using the BNWF approach. Herein, all piers were assumed to have a shallow foundation, 2.5 m x 2.5 m plan dimensions, and different classes of the foundation soil were considered according to the EC8 – Part 1 (2004) (EN 1998-1:2004, Table 3.1) provisions. The properties of these soil classes were also taken from the EC8 – Part 5 (2004) recommendations in the absence of specific measurements (EN 1998-5:2004, Table 4.1).



Figure 5-28: Damage of pier-1 (leftmost pier) of the Collector-Distributor 36 during the Northridge (1994) earthquake (after Spencer et al., 2006)

#### 5.4.4.2 Modeling

The OpenSees-OpenFresco framework for the coupled finite-element approach was adopted to conduct the rehearsal hybrid test of the bridge structure. The mass of the bridge deck was lumped at nodal points and the axial forces were applied at the top of the piers. The deck was modeled as an elastic beam element since no visible damage was observed during the earthquake event. On the other hand, fiber modeling using a single nonlinear force-based element, with 5 integration points, was adopted to model each pier. Herein, the soil-structure interaction assumes the BNWF modeling philosophy, which is readily available in the OpenSees library.

The substructuring of the bridge structure, shown in Figure 5-29, was performed so that SSI is included in the physical substructure. Accordingly, the foundation of the highly damaged pier (pier-1) was chosen to be the hypothetical physical model (slave program) and the remaining elements of the bridge were represented in the OpenSees software (master program). As shown in Figure 5-29, the BNWF approach was used in modeling the SSI of pier-2 and pier-3 as well.

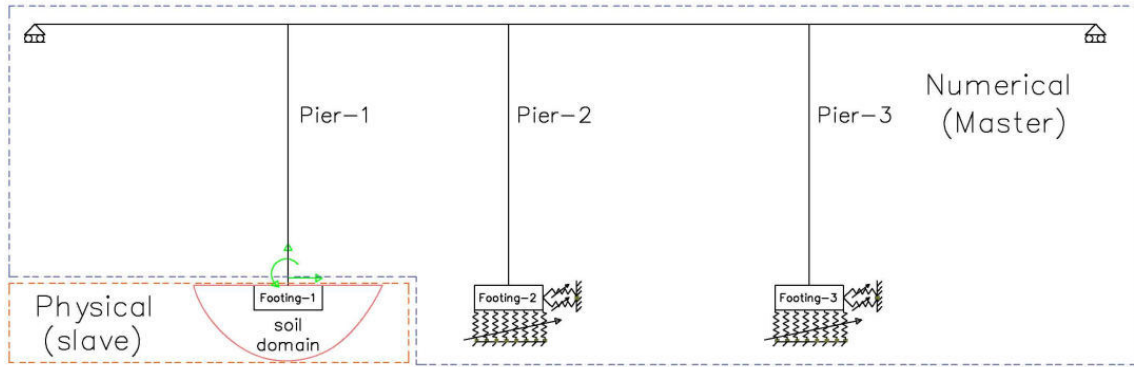


Figure 5-29: Substructuring scheme

In the test rig shown in Figure 5-30, command displacements  $u_1$ ,  $u_2$ , and  $u_3$  are calculated from the target commands  $u_{f,h}$ ,  $u_{f,v}$ , and  $\theta_f$  according to the actuators' configuration. In a true hybrid test, the foundation element may be scaled using the gravity similitude rule since its response is strongly influenced by the vertical action. As mentioned above, the simulated hybrid test uses the coupled finite element approach, meaning the *simFEadapter* control class of the OpenFresco framework can be used to interface the numerical and physical subassemblies.

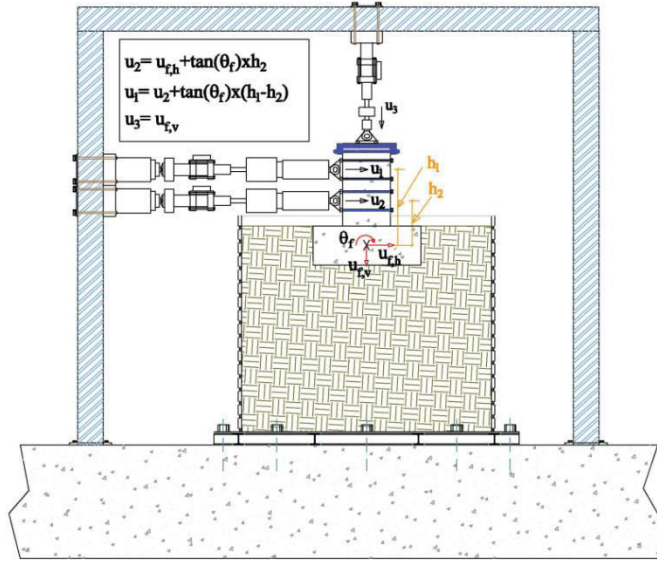


Figure 5-30: Hypothetical test rig for laboratory testing of SSI in hybrid simulation

For consistency, the properties of concrete and steel reinforcement were taken directly from the values reported in the MISST project. The Concrete04 uniaxial material models the properties of concrete. This material uses the Popovics curve (Popovics, 1973) in compression and it is characterized by a linear exponential decay in tension. The concrete has 35 MPa and 1.9 MPa of compressive strength and tensile strength, respectively. For unloading and reloading in compression, the uniaxial material uses the Karsan & Jirsa (1969) relationship to account for

stiffness degradation. The properties of the confined concrete of the pier cross-section are determined as per Mander et al. (1989). The steel02 material, corresponding to the Giuffre-Menegotto-Pinto model (Menegotto & Pinto, 1973), was employed to model the reinforcement bars. This material has a bilinear backbone and it accounts for the Bauschinger effect, which contributes to the gradual stiffness degradation of rebars under cyclic loading. It also has isotropic hardening in compression and tension.

The BNWF model simulates the inertial interaction at the interface between the foundation and soil. To explore the significance of soil-type in soil-structure interaction, the response simulation was carried out considering soil classes B and C, presented in Table 5-2, that are defined through the EC8 guidelines. In this work, the foundation soil was assumed to have a 1 m of embedment depth and soil densities in the interval 16-20 kN/m<sup>3</sup>. The initial shear modulus of soil in the BNWF model can therefore be calculated as:

$$G_{max} = V_s^2 \rho \quad (5.16)$$

where  $\rho$  and  $V_s$  represent the soil density and the shear wave velocity of the ground, respectively. According to the NIST (2012) recommendation, the vertical springs of the BNWF model were distributed considering  $R_k=2.0$ . Both the end-length ratio and the spring spacing were assumed to be 0.1, thus 13 nonlinear springs are used to model the vertical and rotational DOFs. Another two nonlinear springs, attached sideways, model the horizontal DOF. The foundation bearing capacity was determined from the equations developed by Meyerhof (1963) and the tension capacity of the soil was assumed to be 10% of the compressive strength.

Table 5-2: Foundation soil considered for the bridge case study

Soil class	Soil type	$\rho_{soil}$ [kN/m <sup>3</sup> ]	V <sub>s</sub> [m/s]	$G_{max}$ [Mpa]	$G^5$ [Mpa] <sup>5</sup>	$S_u$ [kPa]	$\Phi$	$\xi_{rad}$
B	Sand	20	360	264.2	132.1	-	45°	0.05
C	Sand	18	200	73.40	36.7	-	30°	0.05
C	Stiff clay	18	200	73.40	36.7	150.0	-	0.05

In the finite-element coupling scheme, the constituents of the numerical substructure were implemented in the master program while the hypothetical physical substructure was modeled in the slave program. The *SimFEadapter* control interfaces the master and slave programs. In the master program, the super-element was represented by the *experimental two-node link element*, shown in Figure 5-31, which is defined by a stiffness matrix derived by applying a unit displacement at one interface DOF of the slave subassembly while the remaining DOFs are restrained. The adapter element is usually taken to be 1000 times stiffer than the slave structure. Herein, the diagonals of the stiffness matrix of the adapter element were taken to be  $10^{12}$  (in [N, m] units).

<sup>5</sup> According to the EC8 – Part 5 (2004) (EN 1998-5:2004, Table 4.1) guidelines, for  $a_g S > 0.3$  g,  $G/G_{max} = 0.36(\pm 0.2)$ . Here,  $G/G_{max}$  was taken as 0.5.

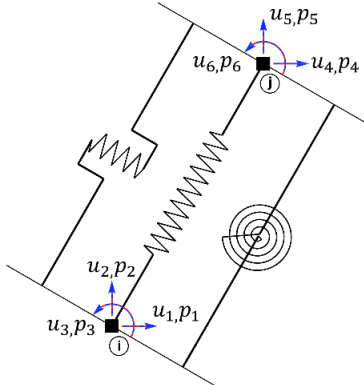


Figure 5-31: Experimental two-node link element (*EETwoNodeLink*) of the OpenFresco framework (after Schellenberg et al., 2009)

The Average Acceleration (AA) formulation of the implicit Newmark integration was adopted in the master program whereas a static integration was chosen on the slave side. The displacement commands of the three DOFs ( $u_{f,h}$ ,  $u_{f,v}$ , and  $\theta_f$ ), received from the master program, are applied to the slave subassembly; and restoring forces are returned. For brevity, only the transaction of displacements and forces using adapter elements is explained here (see Schellenberg et al. (2019) for more details about the finite-element coupling approach).

The communication between the slave and master subassemblies is executed through the OpenFresco framework by defining a super-element, in the master program, and an adapter element, in the slave program. These interface elements connect the two subassemblies. Herein, the finite-element subassemblies were both modeled in the OpenSees software. The following sequence of operations and data exchange, illustrated in Figure 5-32, are performed in each time-step of the analysis:

*Step 1:* The master integration method prescribes a global trial displacement vector of the super-element,  $\mathbf{u}_{\text{super}}$ , for all its degrees of freedom.

*Step 2:* The trial displacement vector is then sent to the OpenFresco middleware using a TCP/IP socket. The experimental site and experimental setup objects are used to transform and store the trial displacement vector. The *NoTransformation* experimental setup was adopted in this work since there is no true test rig involved. Hence, displacements and resisting forces of the two-node link element are directly applied to the slave subassembly.

*Step 3:* The Experimental control class provides a connection to the adapter element in the slave subassembly. The trial displacement vector is transferred to the *SimFEadapter* experimental control object through the TCP/IP socket. The adapter element then calculates a resultant displacement vector by combining the received trial displacement  $\mathbf{u}_{\text{super}}$  with its own elemental displacements. Subsequently, the force vector of the adapter element  $\mathbf{P}_{\text{adpt}}$ , which provides input to the slave program for assembling the unbalanced forces, is updated and returned to the slave subassembly.

Note that  $\mathbf{P}_{\text{adpt}}$  is the resultant force vector due to the deformations of the adapter element as well as the imposed displacements.

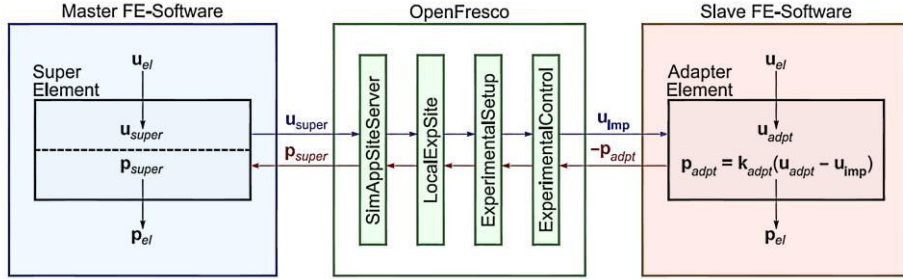


Figure 5-32: Data exchange in finite-element coupling approach of the OpenFresco framework (after Schellenberg et al., 2019)

*Step 4:* Once the solution to the equilibrium problem of the slave subassembly has converged, the opposite of the resultant force vector ( $-\mathbf{P}_{\text{adpt}}$ ) is returned to the *SimFEAdapter* experimental control via the TCP/IP socket. Similar operations of storage and transformation can be carried out on the resultant force vector using the experimental site and experimental setup modules of OpenFresco.

*Step 5:* The simulation application server (*SimAppSiteServer*) then returns the force vector to the super-element in the master program, again using the TCP/IP socket. The force vector is eventually returned to the master integration and the next time-step trial displacement vector is determined. The above five steps are therefore repeated at each time-step of the analysis. More information on the implemented rehearsal hybrid test can be found in Appendix 4.

To build an exhaustive model, control errors in matching the command displacements can be included. It is common to tune an actuator to have zero gain error in a relatively narrow frequency interval of interest. However, full compensation of the time-delay error of the actuator may not be achieved. From this standpoint, the actuator's transfer function may be represented by a unit amplitude and a time-delay  $\tau$ . Now, consider a measured displacement  $x(t)$  has  $\tau$  time-delay relative to a displacement command  $u(t)$ ; the error signal,  $Err(t)$ , reads:

$$Err(t) = x(t) - u(t) = x(t) - x(t + \tau)/A \quad (5.17)$$

where A is the coefficient of the amplitude error, which is one in this case. Using the second-order Taylor expansion, the error signal can be simplified as:

$$Err(t) = -\dot{x}(t)\tau - \ddot{x}(t)\tau^2/2 \quad (5.18)$$

This error signal can be evaluated assuming a sinusoidal response given by  $x(t) = a \times \sin(\omega_s t)$  where  $a$  and  $\omega_s$  are the amplitude and circular frequency, respectively. Applying Laplace transformation to both sides of equation (5.18), we can write:

$$Err(s) = \frac{a\tau\omega_s}{s^2 + \omega_s^2} \left\{ \frac{\tau\omega_s^2}{2} - s \right\} \quad (5.19)$$

The constant time-delay of the actuator, which is the basis for the above derivation, is obtained considering the limit of the time-lag of the system as the frequency approaches to zero. Thus, as  $s$  approaches to zero, equation (5.19) reduces to:

$$\underbrace{Err(s)}_{s \rightarrow 0} \approx \frac{a\omega_s\tau^2}{2} \quad (5.20)$$

The above formulation allowed us to convert the time-delay error  $\tau$  to an equivalent undershoot error consistent with error modeling in the OpenFresco framework. To this end, the undershoot error, defined using the *ExpSignalFilter* class of the OpenFresco framework, can be calculated using the first natural frequency of the bridge structure and the constant time-delay of the actuator. However, applying undershoot errors in the OpenSees-OpenFresco software framework while performing gravity analysis can cause convergence problems due to the stiff nature of the axial loading. During the MISST experiment, control errors were negligible which might be attributed to its slow execution. For consistency, no control errors are applied as well in this work.

During the coupled analysis, two records of the Northridge (1994) earthquake were used as input ground motions. The first record is part of the strong motion data collected at Santa Monica City Hall station (referred to as EQ1) and it has 0.37 g PGA. The second earthquake, which has 0.58 g PGA, was recorded at New Hall Fire Station (referred to as EQ2). From their spectral properties, shown in Figure 5-33, the second earthquake has a strong driving force since the first natural frequency of the bridge structure has periods in the interval 0.25-1.0 s. The lower end of this period interval corresponds to fixed-end conditions of the piers while the upper end of the interval is the result of considering compliant foundations.

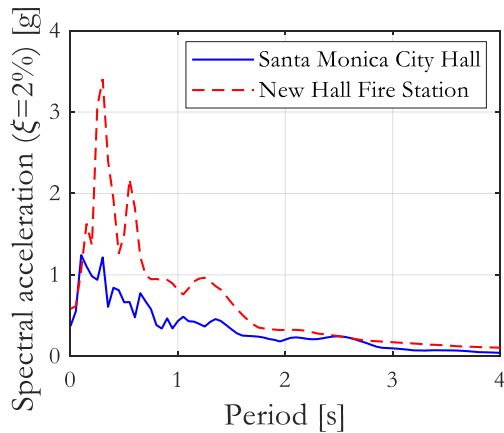


Figure 5-33: Spectral accelerations of the Northridge (1994) earthquake recorded at two different stations

#### 5.4.4.3 Results and discussions

Before performing the simulations, the capacity and period elongation of the bridge structure were explored considering fixed and flexible supports for the piers. The flexible supports are governed by the properties of the foundation soil. In addition to the soil types presented in Table 5-2, the SP-49 sand, characterized through experimental tests at LNEC, is considered in this study since its full characteristics are known.

In Figure 5-34, the capacity curves of the bridge structure in the longitudinal direction for different support conditions and different foundation soils are presented. Considering class B foundation soil, the capacity of the bridge to resist horizontal loads is reduced by 12.5%, compared to the fixed support condition, and it has a period elongation  $\tilde{T}/T=1.53$ . Likewise, the class C soil type (sand or clay) has shown a 37% reduction in the capacity of the bridge. In the latter, the period elongation of the bridge structure that is supported on the clayey soil is greater than that of the sandy soil, as shown in Figure 5-34. The capacity of the bridge structure that is supported on the SP-49 sand is somehow intermediate between the soil classes B and C.

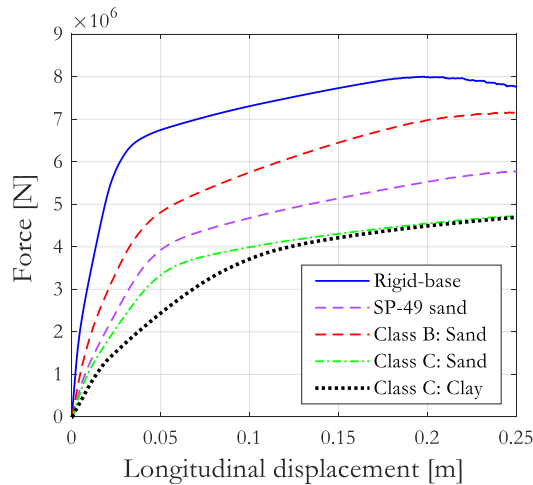


Figure 5-34: Capacity curves of the Collector-Distributor 36 under-crossing considering different boundary conditions and classes of the foundation soil

More importantly, the implementation of the substructuring scheme, which uses the coupled finite-element approach, was validated by comparing the modal properties and the capacity curves obtained from the coupled and non-partitioned (monolithic) modeling approaches. In this validation, the SP-49 sand was taken as the foundation soil.

In the first place, the modal properties of the substructured (coupled) problem were found to be in good agreement with that of the monolithic structure (see Table 5-3). Furthermore, as shown in Figure 5-35, the capacity curves of the bridge that are evaluated from the two approaches are nearly identical, indicating that the boundary conditions are accurately satisfied.

Table 5-3: Vibration modes of the case study bridge

Mode	Period of vibration [s]			
	MISSST experiment	Fixed base	SP-49 sand as the foundation soil	
			Monolithic	Substructured
1	0.3710	0.2855	0.5315	0.5386
2	0.0768	0.0682	0.0692	0.0692
3	-	0.0370	0.0374	0.0374

Furthermore, this validation work, performed between the substructured and monolithic numerical models, may be extended to validate this substructuring approach against an experimental method because the monolithic BNWF model can reproduce experimental results (reasonable agreement to be specific) as discussed in section 5.2.1.2. Thus, comparable results between experiments and the substructured simulation may be assumed.

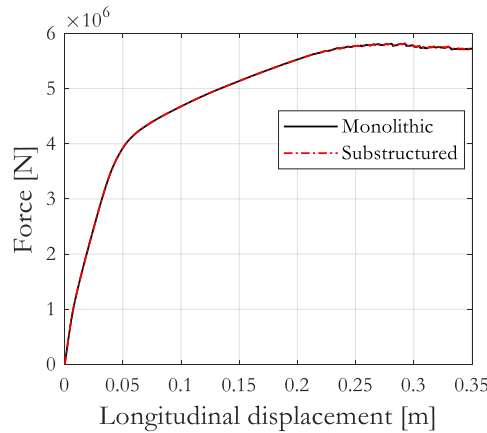


Figure 5-35: Capacity curves from monolithic and substructured modeling approaches

Consistently with the chronology of the load applied during the MISSST experiment, two different response analyses were carried out. First, the analysis was conducted by applying EQ1 input motion, scaled by 1.5. In the second analysis, the bridge structure was subject to EQ1, scaled by 1.5, followed by EQ2. The input motion adopted in the first analysis mimics the first phase of the MISSST experiment whereas the second analysis emulates the full experiment.

In the subsequent discussions, the response of the bridge structure to the first record, considering the SP-49 soil, is presented first. Then, the response of the bridge under the combined record is explained. Lastly, the response of the bridge is examined considering a class C type of clayey foundation soil.

### ANALYSIS-1: The bridge's response to EQ1 scaled by 1.5

At this stage of the analysis, the bridge attained a maximum drift ratio of 1%, which is well below the capacity of the bridge. The M-θ curves of all footings, shown in Figure 5-36(c), indicate that the foundation soil is essentially elastic during this phase of loading. Furthermore, in the hysteresis

curve of the bridge (see Figure 5-36(b)), no stiffness degradation is visible, thus minimal or no structural damage occurred to the piers.

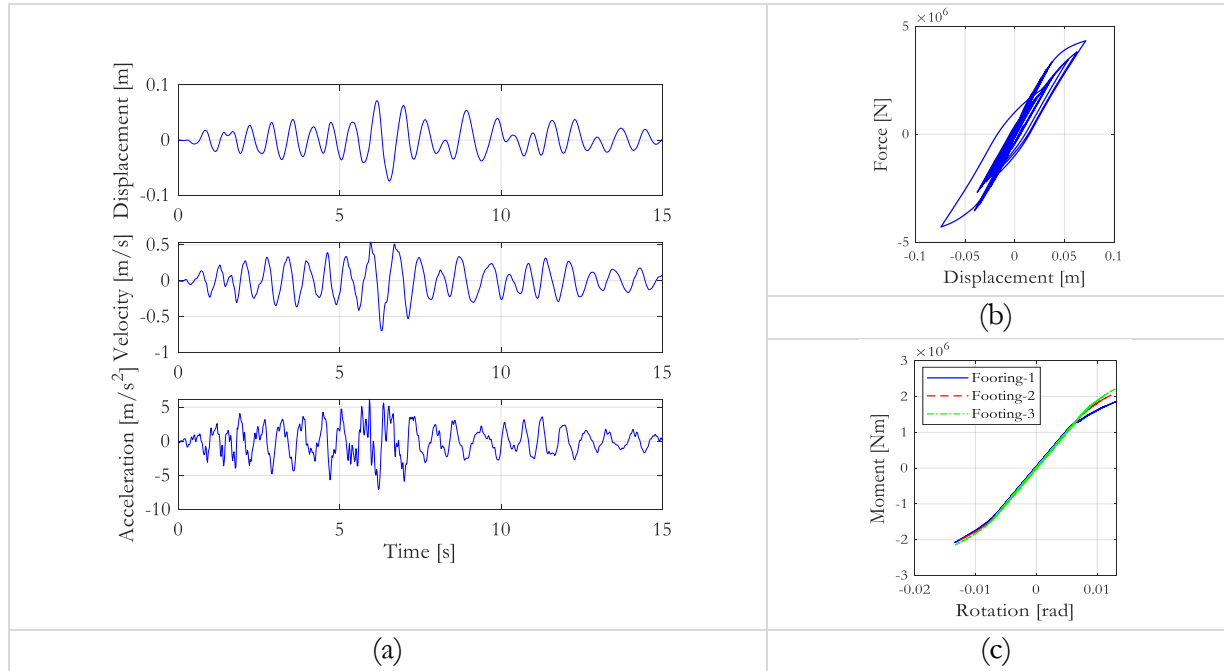


Figure 5-36: The response of the bridge that is founded on the SP-49 sand; and subjected to the Northridge (1994) earthquake, recorded at the Santa Monica City Hall station, scaled to 0.55 g PGA: (a) Pier-1 responses; (b) F- $\delta$  plot; (c) M- $\theta$  plot of the bridge footings

At this stage of the MISST experiment, minor flexural cracks at the base of both the experimental piers (Pier-1 and Pier-3) and a small shear crack at the mid-height of Pier-1 were observed, and the maximum drift of Pier-1 was 24 mm, which is way below the drift recorded in this analysis (see Figure 5-36(a)). This implies that the soil properties, or the SSI model in general, adopted during the MISST experiment were stiffer than that of the current work, which was also visible in the frequencies presented in Table 5-3. In the MISST experiment, the SSI was represented by a horizontal spring assuming the rotational DOF of the foundation to be fixed. This assumption can explain the small drift of Pier-1 that was recorded during the experiment.

Moreover, the rocking action of the foundation elements, shown in Figure 5-37, was found to be dominant in this phase of the analysis because of the large vertical factor of safety (FSv). Herein, the FSv of the foundation soil (SP-49 sand) was estimated to be 49, which is generally large for typical buildings and bridges.

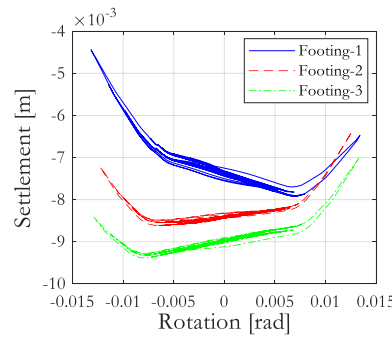


Figure 5-37: Rotation-settlement plot of the bridge's foundation

#### **ANALYSIS-2: The bridge's response to the full input motion of the MISST experiment**

In this simulation, the bridge structure, founded on the SP-49 foundation soil, was subjected to a ground motion built by concatenating EQ1, scaled by 1.5, and EQ2. In the MISST experiment, the two  $\frac{1}{2}$  scale piers that were used in the first phase of the hybrid test were reused during the second phase of the hybrid test, where EQ2 is the input motion, since no significant damage was registered during the first stage of the test. Here, a free vibration portion (zero acceleration), shown in Figure 5-38, was added between the two records so that the bridge's response during the first stage of the test is fully damped out before applying EQ2. In this manner, the actual loading conditions of the MISST experiment can be reproduced.

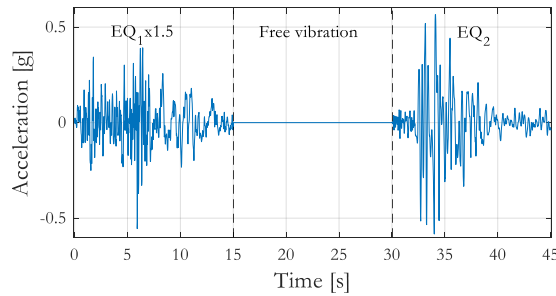


Figure 5-38: Input ground motion for evaluating the complete response of the bridge

As shown in Figure 5-39(b), EQ2 is comparatively demanding; consequently, large deformations of the piers were recorded. Nevertheless, the soil deposit did not suffer important damage due to the large ultimate capacity of the SP-49 sand, as shown in Figure 5-39(c). Consequently, at the end of the response simulation, only small residual deformations were observed in the piers.

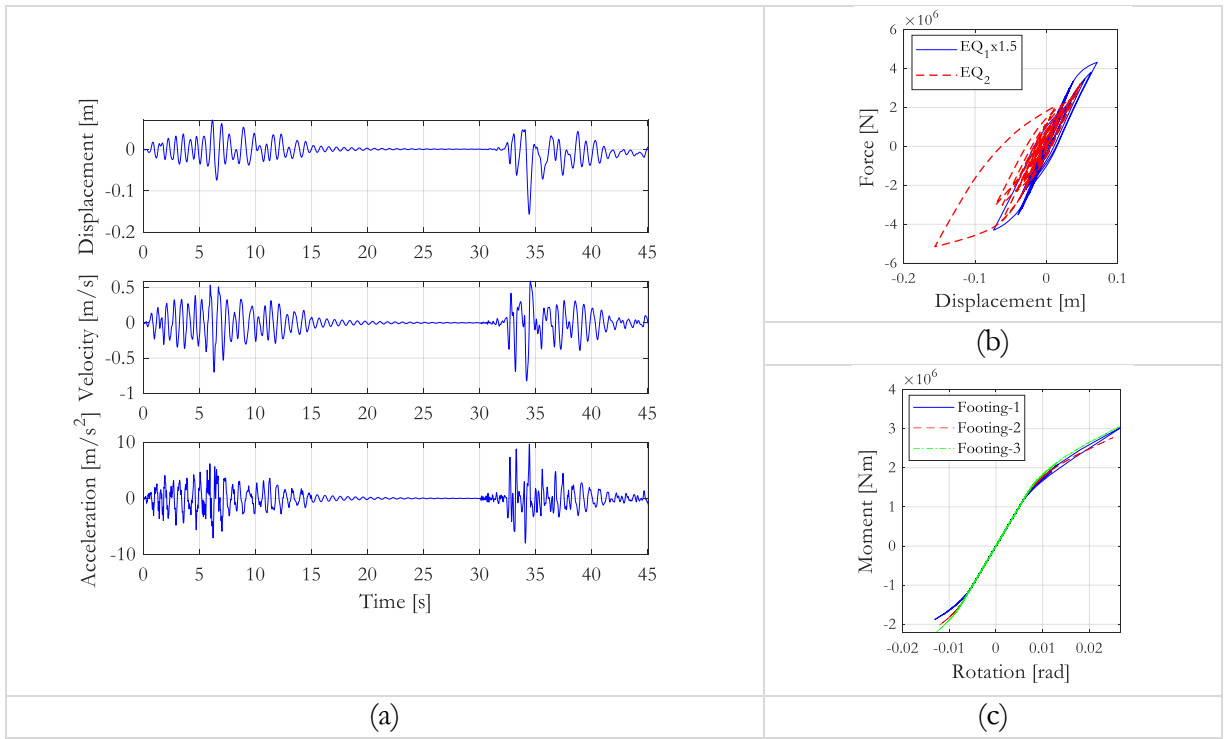


Figure 5-39: The response of the bridge that is founded on the SP-49 sand; and subjected to the Northridge (1994) earthquake, recorded at the Santa Monica City Hall station, scaled to 0.55 g PGA, followed by the unscaled Northridge earthquake, recorded at the New Hall Fire Station, 0.58 g PGA: (a) Pier-1 responses; (b) F- $\delta$  plot; (c) M- $\theta$  plot of the bridge footings

Following the initial settlement of the bridge structure, due to gravity loads, the input ground motion caused very small vertical displacements, as shown in Figure 5-40. Owing to the unsymmetrical displacement of the piers, all footings are also characterized by mostly one-sided uplifting.

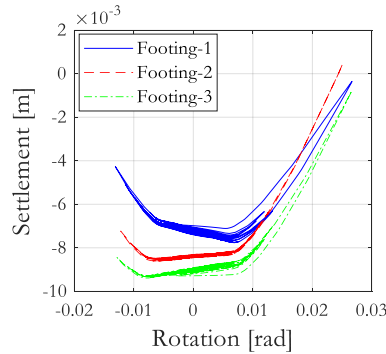


Figure 5-40: Rotation-settlement plot of the bridge's foundation

### ANALYSIS-3: Bridge's response considering clayey foundation soil

In this analysis, a different soil type was explored. The bridge foundation was assumed to be a clayey soil, class C according to EC8. The  $\tilde{T}/T$  of this model is 1.89 and the vertical factor of safety is 2.69. The bridge structure was subjected to the ground motion shown in Figure 5-38.

In the first phase, i.e., when applying EQ1 scaled by 1.5, the energy dissipated by the hysteretic response is small, but important energy dissipation was achieved while applying the EQ2 input. In the latter, significant energy was also dissipated by the foundation soil, which can be depicted from the moment-rotation curve shown in Figure 5-41. Furthermore, as shown in Figure 5-42, the bridge footings have significant vertical displacements. This is attributed to the small vertical safety factor of the clayey foundation soil.

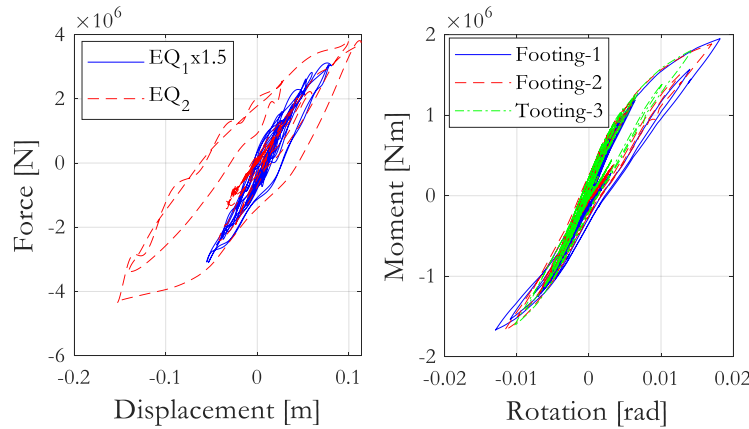


Figure 5-41: The response of the bridge that is founded on class C type of clayey soil; and subjected to Northridge (1994) earthquake, recorded at the Santa Monica City Hall station, scaled to 0.55 g PGA, followed by the unscaled Northridge earthquake recorded at the New Hall Fire Station, 0.58 g PGA: F- $\delta$  plot (left) and M- $\theta$  plot of the bridge footings (right)

In the rocking and vertical displacements of all footings, shown in Figure 5-43, important uplifting phenomena of the bridge foundation can be observed during the EQ2 record as the bridge is driven to large lateral displacements.

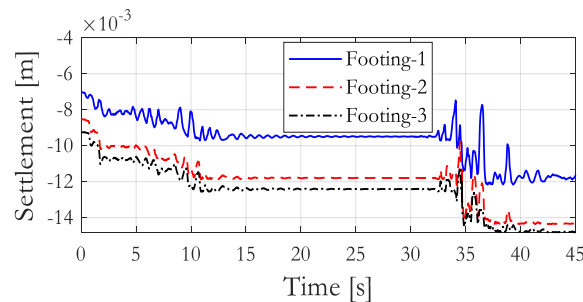


Figure 5-42: Vertical displacement of the bridge foundation

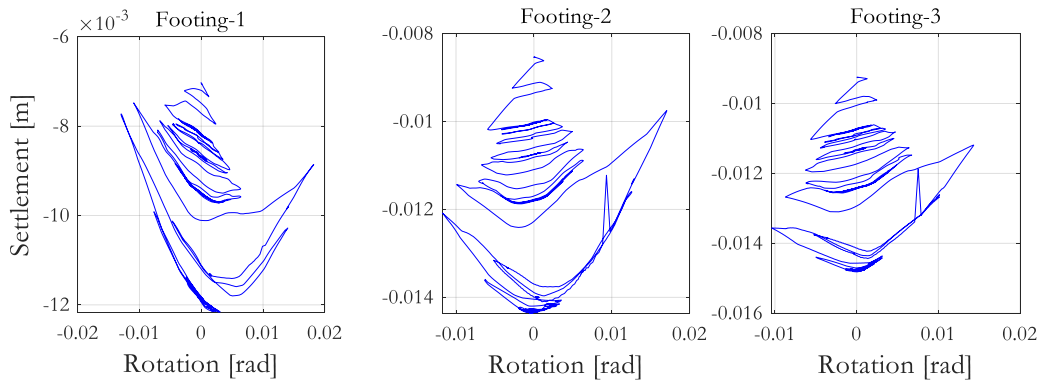


Figure 5-43: Rotation-settlement plot of the bridge foundation

The “Analysis-3” case study of the bridge structure was intentionally added to demonstrate how to explore these rehearsal tests in choosing design parameters for SSI hybrid testing. The parameters of the hybrid test, such as the superstructure properties, soil type, etc., may be altered to achieve prescribed objectives. The effect of using a scaled model of the superstructure, including the structural foundation, as the test specimen during SSI hybrid testing, may also be examined in a rehearsal test. This requires the similitude laws used in the numerical and physical subassemblies to be consistent.

#### 5.4.5 Hybrid testing of soil-structure interaction using LNEC-HS

As briefly discussed in the introduction, laboratory testing of SSI is complex and expensive. Past experimental studies were restricted to only cantilevered mass or tower-like structures and rarely were realistic structural models physically modeled. With the advent of hybrid simulation, full-scale SSI with realistic structural models can be tested. The implementation of SSI test in hybrid simulation using the middleware-free scheme of *LNEC-HS* is an important goal of this research. It will be applied to a structure, accounting for its soil-structure interaction, where the first story of the structure and the soil medium are physically modeled in a laboratory while the remaining part of the structure is represented in a numerical simulation program.

##### 5.4.5.1 Modelling

The first hybrid test is envisaged to be performed on a two-story shear building, shown in Figure 5-44, resting on dry well-graded sand (SP-49), with negligible embedment depth. The columns in the second story are designed to remain elastic throughout the test. However, inelastic deformations are allowed in the first story columns. The structure is analyzed as a 2D problem for simplicity, but the experimental setup is designed to be a 3D steel frame to maintain the frame’s stability and to restrict out-of-plane movements. Rigid diaphragms, supported by beams connecting adjacent columns, model the floor masses of the structure, and the mass of the physical substructure can be easily adjusted by adding blocks of mass on the top of the rigid diaphragm. The properties of the

two-story shear building that was adopted in studying the Smith Predictor compensator, in chapter four, is also considered herein. The first two modal frequencies of the structure are 1.96 Hz and 3.22 Hz, and a 2% viscous damping is included using the Rayleigh damping.

The foundation soil of the structure, which makes part of the physical substructure, is represented using the ESB soil container described above. To achieve the desired properties of the foundation soil, a soil pluviation machine will be used to fill the soil container. The SP-49 sand, with its properties already characterized from past experiments, will represent the foundation soil.

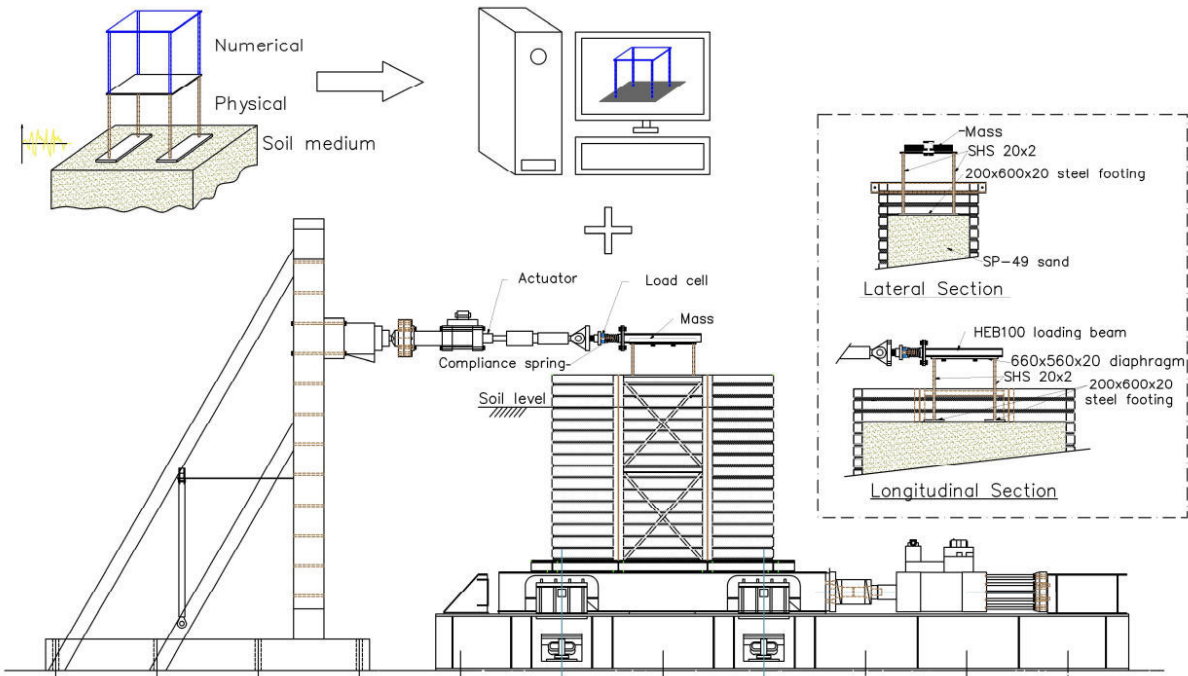


Figure 5-44: Test setup for a soil-structure interaction test in hybrid simulation

In general, a soil container is designed to replicate the characteristics of the soil medium. The design of ESB container assumes that the boundary effects are minimized if the dynamic response of an idealized soil layer, with the internal dimensions of the container, matched the joint response of the soil and the container. To achieve this the base and end walls of the LNEC's soil container will be covered by a thin sheet of aluminum that is glued to the container and covered with a slim layer of glued coarse sand all over its internal face (Zeng & Schofield, 1996). Besides, the soil filling shall be performed by diving the total height of the soil into several layers considering a constant velocity of pluviation. The opening width of the pluviation machine is adjusted according to the height of the soil layer to achieve a relatively homogenous soil deposit.

During the hybrid experiment, a detailed description of the nonlinear response of soil is expected to be captured through an array of transducers. To achieve this, the data acquisition will include displacement transducers at the base of the container and at the level of the foundation. Besides,

acceleration transducers distributed across the height of the container, including at the bottom of the soil container, can help us understand how the base acceleration propagates to the soil surface. The acceleration at the top of the first story need be measured because it serves as an input acceleration to the second floor of the structure which is represented in the numerical simulation program. In addition, a force transducer, such as a load cell, is required for the equivalent force control approach of the auxiliary actuator.

As explained in chapter four, the auxiliary actuator is controlled in displacement feedback but the original command from the numerical substructure is the shear force at the base of the second story. This is accomplished using an additional compliant system as shown in Figure 5-44. According to the conclusion made in chapter four, the adaptive method for added compliance control is more appropriate than the model-based control since the nonlinearity of the test structure is imminent in this case. On the other hand, the feedforward-feedback control ensures the accurate application of the target acceleration at the base of the ESB container. It is noteworthy to recall that the combined properties of the soil medium and the ESB container can be approximated by a SDOF structure, as mentioned above, resulting in the system model presented in Figure 5-26. This system model can be used for the feedforward-feedback control. In the subsequent section, this model is also adopted to analytically represent the current test setup.

#### 5.4.5.2 Problem analysis

The physical substructure of the hybrid experiment can be idealized as a series of linear and nonlinear springs, as shown in Figure 5-45. Herein, the SDOF representation of section 5.4.3 is directly adopted and the first story of the structure is represented by a nonlinear spring to account for the nonlinearity of the soil-structure interaction (Vicencio & Alexander, 2018). The Baber and Noori (Baber & Noori, 1985) extension to the original Bouc-Wen nonlinear hysteretic model is used to model the nonlinear spring. This model accounts for stiffness and strength degradation behavior which is commonly observed in engineering materials.

In this hybrid test, the ST1D is envisioned to drive the ESB, filled with the SP-49 sand, and the first story of the reference structure is erected on the foundation soil. The relationship between command acceleration,  $a_g$ , which is applied to ST1D's servo-controller, and the acceleration measured at ST1D's platen,  $a_1$ , can be evaluated as:

$$G_{a_1 a_g} = \frac{a_1(s)}{a_g(s)} = \frac{G_{a_p u_c}}{s^2} \quad (5.21)$$

where  $G_{a_p u_c}$  is the transfer function from the ST1D's command displacement,  $u_c$ , to the acceleration at the platen,  $a_p$  (see Figure 5-26). In the same manner, the absolute acceleration at the soil surface (FIM),  $a_{2,abs}$ , can be related to  $a_g$  by:

$$G_{a_2 a_g} = \frac{a_{2,abs}(s)}{a_g(s)} = \frac{G_{a_{top} u_c}}{s^2} \quad (5.22)$$

where  $G_{a_{top} u_c}$  is the transfer function from the ST1D's command displacement,  $u_c$ , to the acceleration at the soil surface,  $a_{top}$  (again see Figure 5-26).

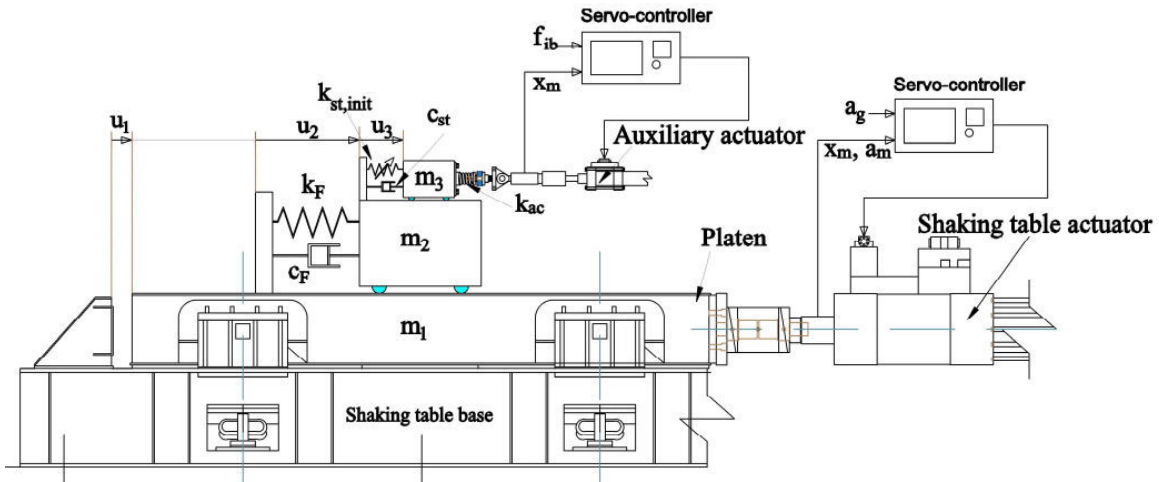


Figure 5-45: Idealization of test setup

In an actual experiment, we only know the target acceleration at the base of the ESB container,  $a_1$ , and it is important to relate it to the foundation input motion,  $FIM$ . This can be achieved by combining the above two equations, which reads:

$$G_{a_2 a_1} = \frac{a_{2,abs}(s)}{a_1(s)} = \frac{G_{a_{top} u_c}}{G_{a_p u_c}} \quad (5.23)$$

As a result of accounting for soil-structure interaction, the ground motion reaching the foundation level, which can be evaluated using  $G_{a_2 a_1}$ , can be smaller or larger than the input ground motion,  $a_1$ . As shown in the frequency response of  $G_{a_2 a_1}$ , the input ground motion can be amplified by a factor of three at the fundamental frequency of the soil system (see Figure 5-46). This amplification factor is dependent of the damping of the soil medium which is equal to 17%.

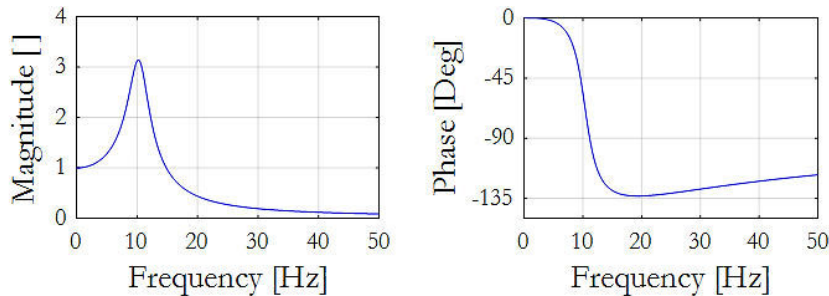


Figure 5-46: Transfer function from target acceleration to foundation input motion

The Simulink program that was used to study the Smith Predictor compensator, in chapter four, was modified to include the SSI representation shown in Figure 5-45, and then adopted in analyzing the hybrid test shown in Figure 5-44 in a simulated environment. To simplify the problem, the Simulink program assumes ideal acceleration tracking of ST1D. Therefore, the acceleration at the base of the ESB container is identical to the command acceleration, i.e.,  $a_1 = ag$ . Besides, the amplitude and time-delay of the transfer function of the auxiliary actuator were assumed to be one and zero, respectively.

The Kobe (1995) earthquake record, scaled to 0.05 g at the  $Sa(T_1)$  of the structure, was used to simulate the response of the hybrid test. The target acceleration, which is the acceleration of the ST1D's platen, is slightly amplified at the foundation level in the frequency interval 1.95-14.5 Hz, as shown in Figure 5-47, and the peak amplification is near 10.5 Hz which is the natural frequency of the soil deposit including the ESB container.

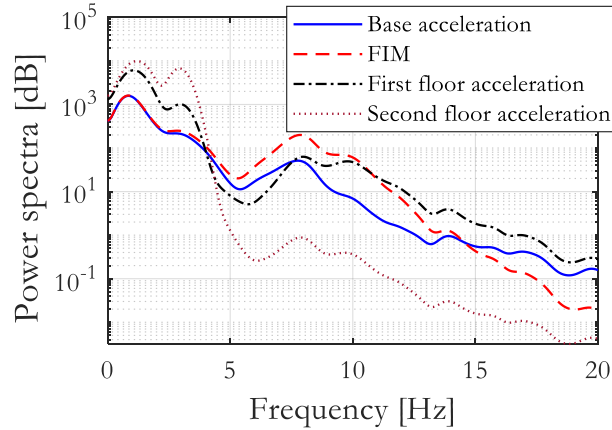


Figure 5-47: Power spectral density of acceleration responses

The lateral displacement response of the structure, shown in Figure 5-48(a), reveals a soft-story mechanism. From the hysteresis plot shown in Figure 5-48(b), it is also evident that the nonlinearity of the structure is concentrated at the first story.

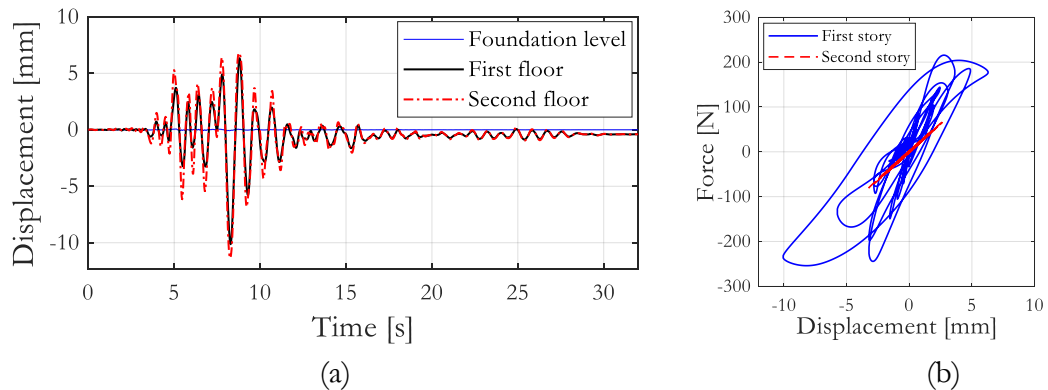


Figure 5-48: (a) Lateral displacement of the two-story shear building subjected to Kobe earthquake, scale to  $Sa(T_1)=0.05$  g; (b) hysteresis plot

It is clear now that the numerical simulation program of the middleware-free scheme of *LNEC-HS* was designed to solve only linear-elastic shear buildings. The response of the structure, presented above, can therefore be favorably reproduced in an actual hybrid test using *LNEC-HS* software framework. Such hybrid testing can be useful to study the influence of SSI in the seismic response of structures with dominant soft-story mechanism.

## 5.5 Summary

In this chapter, soil-structure interaction was explored in the context of substructuring tests. A short and concise description of the development of soil-structure interaction analysis in structural systems was presented first. Then, its implication in the seismic response evaluation of structures was addressed. Later, numerical methods for SSI modeling were discussed, focusing on simplified methods such as the BNWF and macro-element approaches. In the past, the BNWF approach achieved reasonable success in modeling the SSI effects of shallow foundations. Although simplicity and small computational cost are the prime advantages of this approach, it has certain limitations. Therefore, the model parameters need proper tuning so as to ensure a good agreement with experimental tests.

In fast and real-time SSI hybrid testing, where the SSI problem is modeled numerically, the lumped-mass models have been mostly adopted, aiming to work around the high computational cost of the 3D continuum approach. In the implementation described herein, the BNWF approach is also useful due to its small computational cost. Besides, it is readily available in the OpenSees-OpenFresco framework, thus the need for building an interface between the computational and control software is not necessary. Likewise, the macro-element method has less computational cost compared to the 3D finite element model of soil medium, but its inclusion in the framework for hybrid simulation was not explored in the past. This opens an area for future studies that can possibly help to choose the right tool for numerically modeling SSI effects during fast and real-time hybrid testing.

In order to build a link between SSI hybrid testing and the conventional experimental methods, a literature review of the important contributions in the experimental studies for soil-structure interaction was presented. Besides, past experimental studies in SSI hybrid testing were also reviewed. An important question in SSI hybrid testing is the choice for modeling the SSI effects, which can be physical or numerical. Except for one experiment, all the reviewed hybrid tests were performed by numerically modeling the SSI effects. This explains the challenges in conducting hybrid tests whereby the soil-structure interaction effects are represented physically in a laboratory. To this end, this chapter was intended to give directions in addressing this difficulty.

In this chapter, substructuring schemes in shaking table tests, that are applied to SSI testing, were also briefly discussed, using the force splitting approach. Important characteristics of a soil container in 1g shaking table tests were explored and data obtained from identification tests, that were conducted on LNEC's equivalent shear beam container, was utilized in building the complete transfer function of the ST1D. This was developed by representing the soil-filled container, which is rigidly attached to the shaking table, by an equivalent SDOF structure, which allowed to model the control-structure interaction of the ST1D during 1g shaking table tests.

The remaining parts of this chapter were dedicated to a bridge structure case study that was analyzed using the substructuring scheme. The BNWF modeling was adopted to account for the SSI effects

of the bridge structure. This substructuring scheme takes advantage of the finite-element coupling approach to interface the physical and numerical substructures. The primary objectives of this study comprise rehearsing for SSI hybrid testing and as a means for designing hybrid experiments. The bridge was assumed to have shallow foundations and several types of foundation soils were considered. The process of conducting the coupled finite-element simulation, using the OpenSees-OpenFresco framework, was presented. In this substructuring test, a hypothetical test rig for the physical substructure, consisting of three actuators, was also defined.

First, the solution to the substructured model was verified against its monolithic modeling version. The simulated hybrid tests were then conducted by applying ground motion inputs to the bridge. The response of the bridge supported on dense sand, with a relatively high FSv, was dominated by a rocking action and negligible soil plasticity. On the other hand, when considering class C type of clayey foundation soil, the bridge foundation experienced important vertical displacements and soil plastification.

The prime objective of this chapter, which is the implementation of SSI hybrid testing through the middleware-free scheme of *LNEC-HS*, was also explored in this chapter. The test setup for the physical substructure and the substructuring scheme of the reference structure were discussed first, and the laboratory modelling of SSI effects was explained briefly. To analytically explore the hybrid test, the characteristics of the test setup were approximated through a series of linear and nonlinear springs. The relationship between the foundation input motion and the acceleration at the base of the soil medium can therefore be estimated.

Furthermore, a virtual simulation of this hybrid test was conducted in MATLAB/Simulink program. In this response simulation, ideal conditions of the load transfer system were considered to simplify the problem. The plots for the lateral displacements of the structure, as well as the hysteresis curves, proclaim a soft-story mechanism. This characteristics makes the middleware-free scheme of *LNEC-HS* a candidate for the implementation of the SSI hybrid test on the shear building.

To conclude, the simulated substructuring test conducted in this chapter has the potential to guide researchers in designing experiments whereby model parameters can be adjusted before performing experiments. It can also be used to have the sensitivity of test results before conducting actual hybrid tests. More representative results can be obtained by modeling the dynamics of the load transfer system. This chapter introduced a simple approximation for modeling the actuator's time-delay.



## 6 Bayesian Updating of RC Fragilities using Shaking Table Tests

### 6.1 Introduction

In alignment with the research objectives of the thesis work and within the premises of the goals of hybrid simulation, meaning advancing experimental techniques in structural and earthquake engineering and leveraging them, this chapter contributes to the development of Bayesian methods for updating RC fragility curves through shaking table tests.

The enforcement of modern seismic codes started only in the mid-1980s. Thus, many existing buildings are not adequately designed to resist earthquake forces and do not comply with the performance-based earthquake engineering (PBEE) design philosophy. Fortunately, due to the over-strength imposed by the conservatism in design codes, a significant level of lateral forces may be resisted with an acceptable level of damage. However, the presence of such over-strength does not guarantee compliance with the PBEE philosophy whereby seismic safety requirements are enforced. Seismic risk assessment helps governments and interested agencies to draw a decision on whether seismic retrofitting is necessary and economically feasible. It forms the basis for planning of risk mitigation strategies by identifying areas that are subjected to a higher risk.

Seismic risk is obtained by convolving hazard, exposure, and vulnerability functions in a probabilistic framework. In other words, it can be defined as the relationship between loss severity and frequency (Caterino et al., 2018). It requires knowledge of the building stock and its exposure under a given hazard.

Seismic hazard analysis involves the seismic source mechanisms, the distance from the fault to a site, site conditions, etc., typically resulting in a probabilistic description of the ground motions for a given magnitude and site. It quantifies the expected ground intensity measure as a function of the probability of exceedance or return period. Hazard spectra and maps are some of the outcomes of hazard analysis, from which a suite of ground motion records can be extracted for design purposes. For example, a suite of ground motion records with a return period of 475 years (pertains to a 10% probability of exceedance in 50 years) can be generated.

Ground motion records may be classified into near-field and far-field categories. Earthquakes in the range of 10-60 km may be regarded as near-field. However, there is no definite consensus on this range among researchers and guidelines. For illustration, the UBC-97 considers less than 15 kilometers from the earthquake epicenter as a near-field earthquake.

For seismic design, EC8 stipulates the use of a minimum of three different accelerograms for

dynamic analysis. In that case, the most unfavorable response from the three governs the structural design; otherwise, seven (real or artificial) accelerograms can be used for analysis, allowing the average of these responses to be considered in structural design (§4.3.3.4.3, EC8). Similar recommendations are also given by NEHRP (FEMA P750 section 18.3.1.2). On the other hand, for seismic risk analysis, a large number of earthquake records are commonly selected. The records are generally a combination of near-field and far-field motions, with the selection of records being a crucial step in seismic vulnerability analysis. Earthquake records can be grouped by moment magnitude ( $M_w$ ), fault mechanism, source-to-site distance, site, and spectral characteristics, thus making hazard difficult to characterize. Many approaches for seismic hazard analysis have been developed over the past few decades, namely: *Deterministic Seismic Hazard Analysis (DSHA)* and *Probabilistic Seismic Hazard Analysis (PSHA)*. The *DSHA* approach aims at evaluating site-specific seismic hazard governed by the maximum hazard among the controlling sources that affect a site while ignoring the uncertainty in the frequency of exceedance of the earthquake. The source that results in a maximum peak ground acceleration is taken as the controlling source (Kramer, 1996). Contrarily, the *PSHA* treats hazard analysis in a probabilistic manner by considering the uncertainties e.g. in the moment magnitude, fault motion, distance from the epicenter, and attenuation. Hence, the *DSHA* is simply a subset of the *PSHA*. All possible and relevant deterministic earthquake scenarios are considered from all combinations of magnitude and location. These earthquake scenarios are modeled for all possible ground motion probability levels. It results that, for each earthquake scenario, the probabilistic description of the ground motions is obtained, as summarized by the median ground motion properties and their standard deviations (Abrahamson, 2006).

A robust exposure model is also a pre-requisite for seismic risk assessment. The exposure model describes the elements at risk, which can be buildings, population, lifeline systems, or socioeconomic activities. It specifies the location of physical assets and the estimated number of occupants at various times of the day. It may also include the vulnerability information of the assets. Exposure data is quite challenging due to the dynamic nature of the built environment. Data gathered at one time may not be applicable any more after a few years. Exposure models vary depending on the scale of analysis, going from detailed descriptions of characteristics and locations of structural elements to composite models aggregated to larger geographical entities, such as administrative units, cities, or countries. Strictly speaking on residential building stock, data may be gathered from a national housing census, for instance. Thus, this component of the seismic assessment can be highly subjective since a complete exposure model may never be achieved. Besides, the disaggregation of exposure data is important in defining specific vulnerability classes.

Fragility curves, on the other hand, are another component for seismic risk assessment and relate the probability of exceedance of a defined damage state given a hazard level. They can be generated from statistical methods based on post-earthquake data collection (commonly termed empirical methods) or from numerical simulations (Lallemand et al., 2015). The numerical (or analytical) method is widely used for generating fragilities nowadays, while judgmental (expert-opinion)

techniques were typically used in the past.

## 6.2 Fragility modeling

Seismic fragility curves describe the probability of exceeding a given performance or damage state as a function of an intensity measure (IM), e.g. related to the earthquake ground motion intensity, or as a function of a given engineering demand parameter (EDP), e.g. the HAZUS framework. The probability that a damage state ( $DS_i$ ) is reached or exceeded can typically be represented through a lognormal distribution. Damage limit states can be defined in terms of thresholds on EDPs such as maximum inter-story drift, plastic rotation, peak roof displacement, and maximum strain (Choudhury & Kaushik, 2018). Maximum inter-story drift and maximum strain are adopted in this study. A fragility curve can thus be described as the following conditional probability:

$$P[ds \geq DS_i | IM = im] = \Phi \left\{ \frac{\ln \{im / im_m\}}{\beta} \right\} \quad (6.1)$$

where  $im_m$  and  $\beta$  stand for the median intensity measure, such as peak ground acceleration, that corresponds to a particular damage state, and a total logarithmic standard deviation (also termed dispersion), respectively. The median value has the units of the intensity measure chosen, while the dispersion is a dimensionless term. It should be noted that the dispersion parameter is associated with the choice for the IM, i.e., ground motion intensity or EDP. The dispersion parameter is a composite form of the aleatoric and epistemic uncertainties represented by the fragility curves, and can be assumed to be given by:

$$\beta = \sqrt{\beta_R^2 + \beta_U^2} \quad (6.2)$$

where  $\beta_R$  and  $\beta_U$  refer to the aleatoric and epistemic uncertainties, respectively. The inherent randomness of the problem is represented by the aleatoric uncertainty. It is mainly due to record-to-record variability of the ground motions' intensity measure. On the other hand, uncertainties in modeling such as material strength and geometric uncertainties are sources of epistemic uncertainty.

## 6.3 Bayesian framework for updating fragility curves

### 6.3.1 Introduction

Bayesian inference is a method of statistical inference whereby Bayes' theorem is applied to update the probability for a hypothesis as more information becomes available. In the context of this thesis, information is obtained from shaking table tests. Bayesian updating is particularly helpful in analyzing dynamic systems and parameter estimation. Nevertheless, it has a great deal of application in almost all areas of study whereby prior beliefs and parameters are updated once additional

information is available (from observation or from experimental tests). In Bayesian inference, the posterior distribution is obtained using a likelihood function  $p(\text{data}|\theta')$ , i.e. a statistical model that is developed based on additional information, and the prior distribution  $p(\theta')$ :

$$p(\theta|\text{data}) = \frac{p(\text{data}|\theta') \times p(\theta')}{\int p(\text{data}|\theta') \times p(\theta')} \quad (6.3)$$

The posterior point estimate can be calculated from the expectancy of the posterior distribution:

$$\hat{\theta}'' = E[p(\theta|\text{data})] \quad (6.4)$$

Although Bayesian methods are better equipped to model data with small sample sizes, estimates are highly sensitive to the prior distribution. Nevertheless, updating the fragility curve in the context of structural engineering or, more specifically, in earthquake engineering, has been used for a few decades now. Singhal & Kiremidjian (1998) presented a Bayesian update technique for RC buildings using a likelihood that is constructed from building damage data collected during the Northridge earthquake in 1994 (Baker et al., 2015). They constructed confidence bounds around the median values of their fragility curves to represent uncertainties. This updating procedure can be categorized as an update based on observed data. Another approach would be to update fragility curves, derived from less reliable methods, using experimental test results. For example, fragility curves constructed through expert opinion or from an unrepresentative numerical model can be potentially updated using experimental data.

Bayesian updating of fragility curves was also extensively investigated by Porter et al. (2006). Porter presented a simplified method for updating fragility curves that was shortly after adopted by ATC-58. His method for updating fragility curves was based on the principles of unscented transformation (Julier & Uhlmann, 2000), by modeling the fragility function as a joint probability function that is described by a few discrete points. Weights are assigned to these discrete points that are eventually updated using experimental test results.

Koutsourelakis (2010) updated fragility curves using Bayesian inference through the Markov Chain Monte Carlo (MCMC) method. Li et al. (2013) took a similar approach while updating the fragility curves of a bridge overcrossing the Meloland road, in California. In their study, fragility curves that were generated from an incremental dynamic analysis of the bridge model were updated using hybrid test results. The hybrid tests were conducted on eight, 1:25 scale, RC piers, while the rest of the bridge was modeled numerically.

### 6.3.2 Bayesian methods for updating fragilities of RC structures

#### 6.3.2.1 Unscented transformation (UT) approach for Bayesian updating

This approach seeks simplicity and is thus less rigorous than a full-fledged Bayesian inference framework. The unscented transformation takes advantage of the fact that Bayesian updating can be considered as a nonlinear transformation of the prior distribution through a nonlinear likelihood

function. This problem can thus be solved by approximating one of them (the prior or the likelihood). However, the likelihood is commonly complex, which makes approximating it a difficult and non-pragmatic approach. On the other hand, the joint prior distribution can be approximated easily by considering a few discrete points, which form the principle of the unscented transformation (Julier & Uhlmann, 2000). In their formulation, they derived  $2n+1$  sigma points to cover the entire distribution space and showed that these sigma points are enough to approximate at least the first two moments of an  $n$ -dimensional distribution. In this method, median and logarithmic dispersion parameters of a prior distribution,  $\mu'$  and  $\beta'$ , are thus transformed through a nonlinear likelihood function and the posterior parameters,  $\mu''$  and  $\beta''$ , are computed.

The first step in this approach is to define the coordinates of the sigma points,  $s_i$ . The fragility curve is then modeled as a joint distribution of the two random variables,  $\mu'$  and  $\beta'$ , at the sigma points. Thus, five sigma points ( $2n+1$ , for  $n=2$ ) can be conveniently used to approximate the first two moments of the joint distribution, one at the origin and the remaining four points symmetrically spaced in their respective axes. The coordinates of the five sigma points are then defined from the UT formulas, shown in Table 6-1.

Table 6-1: Coordinates of sigma points in Unscented Transformation

General formula	Median	Dispersion
1. For $i=0, s_i = \mu_x$	$s_{0,\mu} = \mu'$	$s_{0,\beta} = \beta'$
2. For $i=1$ to $n, s_i = \mu_x + \gamma \times \sqrt{P_{x,i}}$	$s_{1,\mu} = \mu' + \gamma \sqrt{P_{\mu',1}}$ $s_{2,\mu} = \mu'$	$s_{1,\beta} = \beta'$ $s_{2,\beta} = \beta' + \gamma \sqrt{P_{\beta',2}}$
3. For $i=n+1$ to $2n, s_i = \mu_x - \gamma \times \sqrt{P_{x,i}}$	$s_{3,\mu} = \mu' - \gamma \sqrt{P_{\mu',1}}$ $s_{4,\mu} = \mu'$	$s_{3,\beta} = \beta'$ $s_{4,\beta} = \beta' - \gamma \sqrt{P_{\beta',2}}$

where  $\gamma$  is a scaling parameter and  $P_{x,i}$  are the elements of a covariance matrix. The scaling parameter determines the number of moments that can be matched via this principle. It is calculated as:

$$\gamma = \sqrt{n + \lambda} \quad (6.5)$$

The sum  $n + \lambda=3$  may allow five moments to be matched. The covariance matrix,  $P$ , for the two random variables can be written as:

$$P_{\mu'} = \begin{bmatrix} \sigma_{\mu'}^2 \\ 0 \end{bmatrix}; P_{\beta'} = \begin{bmatrix} 0 \\ \sigma_{\beta'}^2 \end{bmatrix} \quad (6.6)$$

The weight of a sigma point is a function of its position,  $i$ , the scaling parameter,  $\lambda$ , and the dimension of the probability distribution,  $n$ .

$$w'_i = \begin{cases} \frac{\lambda}{\gamma^2}, & \text{if } i = 0 \\ \frac{1}{2\gamma^2}, & \text{if } i \in [1, 2n] \end{cases} \quad (6.7)$$

Now, let us consider an experiment with  $N$  virgin sample structures that are tested in a shaking

table. It is also equivalent to conducting  $N$  stages during a shaking table test on a single virgin sample structure. This staged test is commonly executed by progressively increasing the input intensity in a shaking table without changing the test specimen. Considering a given damage state, a vector of binary numbers,  $\boldsymbol{\epsilon}$ , can be built that represents the exceedance or non-exceedance of the damage state during the shaking table tests. Therefore, the likelihood function for that damage state at each of the five sigma points,  $i$ , can be constructed using the exceedance identifier,  $\boldsymbol{\epsilon}_j$ .

$$L(s_{i,\mu}, s_{i,\beta}) = \prod_{j=1}^N \left\{ 1 - \Phi \left( \frac{\ln(im_j) - s_{i,\mu}}{s_{i,\beta}} \right) \right\}^{1-\boldsymbol{\epsilon}_j} \times \left\{ \Phi \left( \frac{\ln(im_j) - s_{i,\mu}}{s_{i,\beta}} \right) \right\}^{\boldsymbol{\epsilon}_j} \quad (6.8)$$

where  $im_j$  is the magnitude of input motion for the  $j$ th shaking table test or  $j$ th stage of a shaking table test. The size of the vector  $\boldsymbol{\epsilon}$  is  $N$ . Consequently, the prior weights,  $w'_i$ , of the joint distribution can be easily updated via the Bayesian principle after calculating the normalizing constant.

$$p_t(data) = \sum_{i=0}^{2n} w'_i \times L(s_{i,\mu}, s_{i,\beta}) \quad (6.9)$$

$$w''_i = \frac{w'_i \times L(s_{i,\mu}, s_{i,\beta})}{p_t(data)} \quad (6.10)$$

The updated weights,  $w''_i$ , at the five discrete points are then used to calculate the posterior estimates of the median and logarithmic dispersion.

$$\mu'' = \sum_{i=0}^{2n} w''_i \times s_{i,\mu} \quad \beta'' = \sqrt{\sum_{i=0}^{2n} w''_i \times s_{i,\beta}} \quad (6.11)$$

The number of moments that can be matched may be further improved by appropriately selecting the coordinates of sigma points. The ATC-58 approach (Porter et al., 2007) with seven sigma points was also investigated in the current study. Nevertheless, posterior estimates obtained were not more accurate than the results obtained from the approach that uses five sigma points. This fact, added with the extra computational cost for using seven sigma points, resulted in the approach based on five sigma points being considered more efficient.

### 6.3.2.2 Markov Chain Monte Carlo (MCMC) approach for Bayesian updating

#### 6.3.2.2.1 Introduction

The application of Bayesian inference in updating fragility curves leads to a posterior probability distribution that is complex and, in many cases, mathematically intractable. This is mainly due to the normalizing term or the total probability term of the posterior distribution in Bayes' theorem. Markov chain Monte Carlo is a potential technique for tackling this problem. The method literally eliminates the need to calculate this normalizing term and uses Markov chains to approximate a posterior distribution (Gleman et al., 2011).

In the context of earthquake engineering, Bayesian updating is important in studies that involve dynamic systems where new information is continuously added to improve knowledge of a set of parameters. As discussed earlier, the Bayesian update includes:

1. Setting up a full probability model based on prior knowledge
2. Interpretation of new information or experimental test results for calculating a likelihood function
3. Computation of a posterior distribution and evaluation of point estimates

The first two steps are simple to put into practice if some information could be collected on the parameter of interest. The third step, however, can be challenging since most practical problems have large dimensions. The difficulty is essentially in computing the total probability, which is important for the update process. Markov chain simulation, like importance sampling, is a general method for drawing samples of a parameter from an assumed distribution and correcting the sampling for a better approximation of a target distribution (Lynch, 2007). The principle of MCMC is to simulate a random walk in the space of parameters which eventually converges to a stationary distribution. Samples are drawn sequentially, depending on the last drawn samples, forming a Markov chain. The principle behind Markov chain sampling can be expressed as:

$$\pi P = \pi \quad \text{i.e., } \pi_j = \sum_{i \in S} \pi_i p_{i,j} \quad \text{for all } j \quad (6.12)$$

where  $P$  is a state-transition matrix, and  $\pi$  is a stationary distribution on  $S$  whose entries are non-negative, and their summation is one. The random walk algorithm continuously generates samples until the stationarity criterion is met. In practice, convergence is not checked. Instead, simple tests are done to ensure that a stationary distribution is approximately achieved. Such tests include ensuring proper mixing of samples generated and consistent posterior estimates from the first and second halves of the generated data.

#### 6.3.2.2.2 Choice of Prior probability in MCMC

The prior distribution plays an important role in Bayesian statistics, unlike the frequentist approach, thus making Bayesian inference a relatively subjective method. Poorly chosen prior densities can be a source of bias. However, if a representative prior is adopted, accurate results can be obtained with a reasonable computational effort. The issue of the weight given to the prior has been debated for many years now, with users who give more weight to the prior information than the new information or vice-versa. Diffuse priors are commonly used in the latter. This choice may be appropriate if large experimental datasets (reliable and with good coverage) are available and/or if the prior is associated with large uncertainty. In the context of fragility curves that are derived numerically, the prior distribution has a significant weight; consequently, a diffuse prior may not be realistic. This, together with the typically small number of experimental test results, calls for careful construction of the prior information.

For economy of nomenclature, the fragility curve can be written as a function of two parameters,  $\theta_1$  and  $\theta_2$ :

$$P[ds \geq DS_i | IM = im] = \Phi \left\{ \frac{\ln\{im\} - \theta_1}{\theta_2} \right\} \quad (6.13)$$

In the above equation,  $\theta_1$  represents the mean parameter of the lognormal distribution whereas  $\theta_2$  is the logarithmic standard deviation.  $\theta_1$  and  $\theta_2$  are modeled using the lognormal and gamma probability distributions, respectively, with the gamma distribution being selected to keep  $\theta_2$  strictly positive.

$$\begin{aligned} \theta_1 &\sim LN(\mu_{\theta_1}, \sigma_{\theta_1}^2) \\ \theta_2 &\sim Gamma(c, \lambda) \end{aligned} \quad (6.14)$$

The value of  $\sigma_{\theta_1}^2$  can be assigned depending on the knowledge of  $\theta_1$ . If the numerical fragility curves are associated with large uncertainty, due to an unreliable numerical model, large  $\sigma_{\theta_1}^2$  can be considered; otherwise, small values of  $\sigma_{\theta_1}^2$  can be taken. On the other hand,  $\sigma_{\theta_2}^2$  can only be estimated from past experimental tests.

Hazard descriptors used to generate numerical fragility curves and the ground motions used during shaking table tests can correspond to significantly different hazards. In this case, updating the total logarithmic dispersion may not be justified since the experimental tests do not fully model the dispersion on the demand. However, if shaking table tests are conducted using ground motions that represent the important hazard features considered during the analytical derivation of fragilities, the portion of the dispersion parameter,  $\theta_2$ , originated from the uncertainty in the demand may be fully updated. This may imply the need to conduct a large number of experimental tests, which is neither economically justifiable nor the intent of the current objective. Instead, representative ground motion records can be used during the limited number of experimental tests.

Likewise, if uncertainty in the capacity of a structure is considered in analytical fragilities, experimental tests must be conducted in a way to represent the uncertainty in capacity so that the portion of the dispersion originating from uncertainty in the capacity of a structure can be conveniently updated. In this chapter, uncertainty in structural capacity is not considered.

In this study, the compound distribution principle which gives rise to  $\sigma_{\theta_1} = \theta_2/\sqrt{2}$ , recommended by Porter et al. (2006), was adopted and the parameters of the gamma distribution for  $\theta_2$ ,  $c$  and  $\lambda$ , are calculated from  $\mu_{\theta_2}$  and  $\sigma_{\theta_2}$ :

$$\begin{aligned} \mu_{\theta_2} &= \theta_2 \\ \sigma_{\theta_2} &= COV_{\theta_2} \times \theta_2 \end{aligned} \quad (6.15)$$

The coefficient of variation (COV) of  $\theta_2$  can be selected depending on the reliability of its prior value. Porter et al. (2007) reported the range  $[0.5\theta_2, 1.5\theta_2]$  for the 98% confidence interval of  $\theta_2$  based on observed data. This translates to a 98% probability of finding  $\theta_2$  in that range, assuming a normal distribution, and the coefficient of variation becomes 0.21. Then, the prior distribution of a fragility curve can be constructed as a joint probability distribution considering  $\theta_1$  and  $\theta_2$  as

independent random variables.

$$f'(\theta_1, \theta_2) = P(\theta_1 | \mu_{\theta_1}, \sigma_{\theta_1}^2) \times P(\theta_2 | c, \lambda) \quad (6.16)$$

The likelihood function has the same form as the one defined for the five-point approximation method. However, the continuous density function is used as opposed to the discrete approach. The posterior distribution is therefore proportional to the product of the prior and likelihood distributions (with proportionality being used since the normalizing term is not important for the MCMC formulation).

$$f''(\theta_1, \theta_2) \propto L(data | \theta_1, \theta_2) \times f'(\theta_1, \theta_2) \quad (6.17)$$

### 6.3.2.2.3 Metropolis-Hastings algorithm

The Metropolis-Hastings algorithm generates a sequence of correlated random samples whose distributions converge to a target distribution. The algorithm uses a proposal distribution from which samples are drawn and sets an acceptance criterion to accept or reject the samples generated. The parameters of the algorithm are the starting point, the proposal distribution type, and its variance. The steps performed in this algorithm are presented in Table 6-2 in the form of a syntax.

Table 6-2: Metropolis-Hastings algorithm

Initialize: $\boldsymbol{\theta}_t = \begin{bmatrix} \theta_1 \\ \theta_2 \end{bmatrix}_0$ and define: $N_{sim}$
While $i < N_{sim}$
Step 1: Generate a candidate $\boldsymbol{\theta}'_i$ from a proposal distribution $q(\boldsymbol{\theta}_t   \boldsymbol{\theta}_{t-1})$
Step 2: Calculate the acceptance ratio $\alpha = \min \left\{ 1, \frac{L(\varepsilon   \boldsymbol{\theta}'_i) \times f'(\boldsymbol{\theta}'_i)}{L(\varepsilon   \boldsymbol{\theta}_t) \times f'(\boldsymbol{\theta}_t)} \right\}$
Step 3: $u \sim \text{Uniform}(u; 0, 1)$
if $u < \alpha$
$\boldsymbol{\theta}_t = \boldsymbol{\theta}'_i$
else
$\boldsymbol{\theta}_t = \boldsymbol{\theta}_{t-1}$
end
$i = i + 1; t = t + 1$
end

A random walk proposal distribution density defined by a bivariate normal distribution was found sufficient in all applications of the MCMC sampling (Koutsourelakis, 2010), i.e.:

$$q(\boldsymbol{\theta}_t | \boldsymbol{\theta}_{t-1}) \sim N \left( \boldsymbol{\theta}_t, \begin{bmatrix} \sigma_{\theta_1}^2 & 0 \\ 0 & \sigma_{\theta_2}^2 \end{bmatrix} \right) \quad (6.18)$$

The variance of  $q$  is selected after a few exploratory runs whereby proper mixing is carefully investigated. An acceptance ratio of samples in the range 10%–50% is sought in all runs to ensure sufficient mixing of the Markov chains (Koutsourelakis, 2010). At the end of a simulation, samples from the posterior distribution were treated before calculating the point estimates of  $\theta_1$  and  $\theta_2$ . If

the initial value selected is a poor one, i.e. the MCMC algorithm took a long time to attain equilibrium given that the initial value is far from the posterior value, the samples generated before reaching the equilibrium condition, say  $b$ , are discarded. The discarded samples are commonly termed as *burn-in* samples. Burn-in allows one to eliminate the dependency of posterior estimates on the initial condition. In WinBugs, a statistical software for MCMC, a limited choice of prior and likelihood probabilistic functions are available (Thomas et al., 2003). Therefore, the MH algorithm adopted herein was implemented in MATLAB program.

Another important aspect of MCMC sampling is that  $\theta_i$  and  $\theta_{i+1}$  are not independent and they could be highly correlated. Hence, the samples retained after the burn-in process are downsampled with a lag of  $n$  points, termed as thinning. After thinning,  $(N_{sim} - b)/n$  samples are left for estimating the statistics of the posterior distributions. Trace plots shown in Figure 6-1 illustrate the two treatments during an MCMC simulation.

The autocorrelation function (ACF) of the samples obtained after burn-in could be used to estimate the factor,  $n$ , for downsampling the data. The downsampling factor that yields a near-zero autocorrelation among the samples is a good choice. In the example shown in Figure 6-1, the ACF of  $\theta_1$  is initially large. After downsampling the data, by a factor of 40, a 95%-confidence interval, around ACF=0, was obtained, thus ensuring that samples used for estimation are independent. In general, slower decay of the ACF translates into the generation of larger size of data samples, in order to achieve a reliable estimate, since the downsampling factor is also larger.

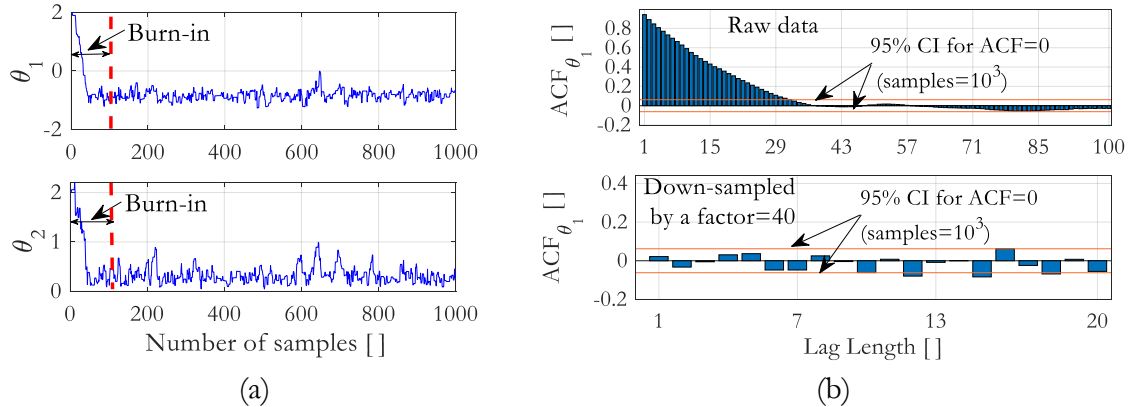


Figure 6-1: (a) Burn-in; (b) autocorrelation function before and after thinning

## 6.4 Updating RC fragilities through sequential shaking table tests

### 6.4.1 Damage based equivalent input intensity

The shaking table test of a structure or structural component is commonly conducted by progressively increasing the intensity of the input motion (Mendes et al., 2013). For instance, a

shaking table test of a portal frame may be conducted in five stages by scaling an earthquake record by 0.1, 0.3, 0.5, 0.7, and 1.0. Shaking table tests have the potential to be used for updating fragility curves, as discussed above. However, the accuracy of the Bayesian updating process is expected to improve with an increase in the size of the experimental dataset. This condition can only be strictly fulfilled by repeating a shaking table test using virgin specimens, which is financially impossible.

The mitigation of this impediment is the motivation behind the attempt of “maximization of information obtained from shaking table tests”. This work tries to find a reasonable representation for an equivalent input intensity whereby each stage, on a stage-wise shaking table test, can be considered as a shaking table test conducted on a virgin specimen. An equivalent energy method was previously explored by some researchers (Coelho et al., 2000), without conclusive results. However, the severity of damage on RC structures is commonly measured by a damage index. The accumulation of damage during the stage-wise tests is therefore accounted for by formulating a damage-based equivalent intensity measure, which is not straightforward.

Several damage indices have been proposed for quantifying damage in the PBEE framework (Rodriguez-Gomez & Cakmak, 1990; Skjaerbaek et al., 1997). The Park-Ang damage index (Park et al., 1987), which is widely used in the assessment of damage of RC structures, was selected for this study. The Park-Ang damage index (DI) is a linear combination of a normalized displacement and normalized hysteresis energy. Thus, the damage index of a sequential shaking table test, at the  $j$ th stage, can be calculated by:

$$DI_{seq}^{stg_j} = \frac{d_{max}^{stg_j}}{d_{ult}} + \beta \times \frac{\sum_{k=1}^j E_h^{stg_k}}{F_y d_{ult}} \quad (6.19)$$

where  $d_{max}$  is the maximum displacement of a structural member;  $\beta$  is a degradation parameter that represents the effect of cyclic response on the damage of a structure, typically taken as 0.05 (Kunnath et al., 1992);  $E_h$  is the hysteresis energy and  $d_{ult}$  is the ultimate displacement capacity. Likewise, the damage index of a non-sequential shaking table test (i.e. executed on a virgin specimen) is computed using equation (6.20). The difference between equations (6.19) and (6.20) is that the hysteretic component of DI in sequential testing is calculated from the cumulative hysteresis energy:

$$DI_{Non-seq}^{stg_j} = \frac{d_{max}^{stg_j}}{d_{ult}} + \beta \times \frac{E_h^{stg_j}}{F_y d_{ult}} \quad (6.20)$$

The ultimate displacement capacity,  $d_{ult}$ , of RC structures may be determined through the expression proposed by Park et al. (1987).

$$d_{ult} = 0.52 l^2 \left( \frac{l}{d} \right)^{0.93} \rho^{-0.27} \rho_w^{0.48} v^{-0.48} f_c^{-0.15} \text{ [in meters]} \quad (6.21)$$

where  $d$  is the effective depth of the cross-section of a structural member (in meters);  $l$  is the shear span length (in meters);  $\rho$  is the normalized steel ratio;  $\rho_w$  is the steel confinement ratio (in

percentage; taken as 0.4% if  $\rho_w < 0.4\%$ );  $\nu$  is the normalized axial stress (taken as 0.05 if  $\nu < 0.05$ ) and  $f_c$  is the concrete strength (in kPa). In this study,  $d_{ult}$  is taken as the post-peak displacement capacity at 20% reduction of the maximum force capacity of a structure. This assumption is consistent with the bilinearization process of capacity curves adopted while defining the yield force,  $F_y$ . For a structure with multiple components resisting lateral forces, in each floor, the global damage index can be calculated by:

$$(\lambda_i)_{component} = \left( \frac{E_{h,i}}{\sum E_{h,i}} \right)_{component} \quad (6.22)$$

$$DI_{global} = \sum (\lambda_i)_{component} \times DI_{i, component} \quad (6.23)$$

Engineering demand parameters (EDP), such as drift, damage index, etc., can be related to an intensity of ground motion input (IM). The natural logarithm of the two parameters was shown to be linearly related (Shome et al., 1998).

$$\ln(EDP) = b \ln(IM) + \ln(a) \quad (6.24)$$

where  $a$  and  $b$  are fitting parameters.  $b$  is the slope of the curve while  $a$  defines the offset term. In equation (6.24), the damage index (DI) can be considered as the EDP and the spectral acceleration at the fundamental frequency ( $S_a(T_1)$ ) as the intensity measure (IM) in formulating the damage-based equivalent intensity measure,  $S_a(T_1)_{eq}$ . The objective of this study is to estimate  $S_a(T_1)_{eq}$  of a non-sequential shaking table test, executed at  $S_a(T_1)$ , that would produce the same damage as that of a sequential shaking table test conducted at the same level of input. To formulate this relationship, equations (6.19) and (6.20) are combined assuming the same fitting coefficients ( $a$  and  $b$ ) for the sequential and non-sequential tests. This assumption is reasonable if complete equivalence is attained between the two cases. Re-arranging the terms,  $S_a(T_1)_{eq}$  can be written as:

$$S_a(T_1)_{eq} = \left\{ \frac{DI_{seq}^{stg_j}}{DI_{Non-seq}^{stg_j}} \right\}^{1/b} \times S_a(T_1) \geq S_a(T_1) \quad (6.25)$$

where  $b$  is the slope of equation (6.24) that is estimated from a non-sequential shaking table test. The proposed  $S_a(T_1)_{eq}$  is investigated numerically through a parametric study in the subsequent sections.

#### 6.4.1.1 Parametric analysis

In this parametric numerical analysis, the input earthquake record intensity during a time-history analysis is increased progressively. The first approach of the test is equivalent to repeating a shaking table test for different input intensities using virgin specimens. For convenience, it will be referred to hereinafter as *non-sequential* analysis. In the second approach, a sequential time-history analysis was conducted by combining all the scaled records to form one long record, as shown in Figure 6-2. To mimic the idle time between stages of a shaking table test, a 10 second free vibration period was

added at the end of each stage of input, excluding the last stage of the input motion. The latter will be referred to as *sequential* analysis in this document. The responses of a RC cantilever column and a RC portal frame, under the *sequential* analysis and *non-sequential* analysis, are therefore studied.

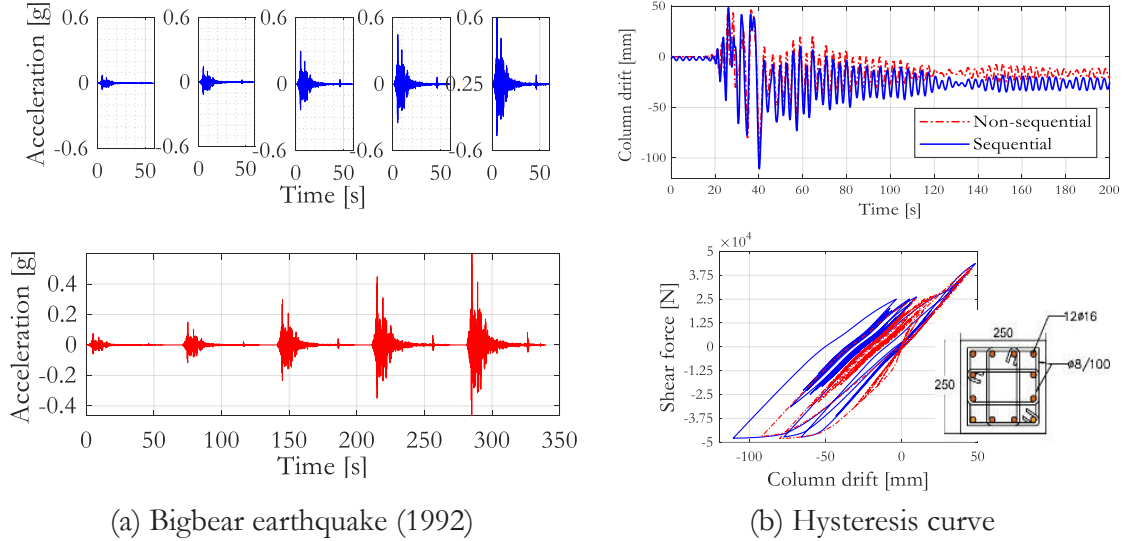


Figure 6-2: (a) 5-stage input acceleration for a sequential analysis (bottom) and non-sequential analysis (top); (b) Hysteretic response of a cantilever column ( $f_1=3$  Hz; 3<sup>rd</sup> stage)

The damage index is calculated at the end of the time-history analyses and the results are compared in a stage-wise manner to depict the cumulative effect of damage in sequential analyses. Besides, the Maximum Inter-Story Drift (MISD) between the two approaches is also compared in order to weigh the effect of the hysteresis energy in both approaches.

The geometric characteristics and reinforcement details of the structures considered are shown in Figure 6-3. The cantilever RC column, 2.5 m high, has a lumped mass at the top and a 250x250 mm<sup>2</sup> cross-section. The parametric modeling of the RC column was carried out by changing its lumped mass and steel reinforcement.

Three modal frequencies, which are 1, 2, and 3 Hz, were chosen to represent common operational frequencies of RC buildings. These frequencies were achieved by changing the lumped mass. The steel reinforcement of the column was also simultaneously varied to model the effect of ductility on this study. Overall, nine RC cantilever columns were explored. The three cross-sections of the column were designed to represent low, middle, and high seismic code designs, respectively.

The two columns of the portal frame have identical characteristics to the cantilever column. Its 4 m-long rigid beam has cross-section's dimensions of 250x400 mm<sup>2</sup>. Likewise, the masses of the portal frame are lumped at the top nodes of the columns and they are varied together with the steel reinforcement of the two columns, thus yielding a total of nine portal frames. The three cross-sections of the column are identified as *Column-A*, *Column-B*, and *Column-C*.

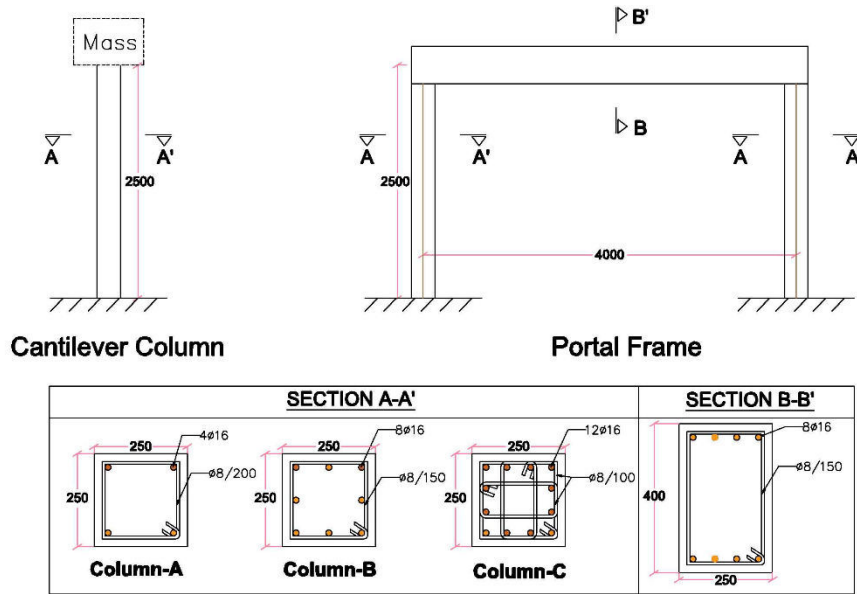


Figure 6-3: Structures considered for damage-based equivalent intensity measure

The cantilever column and the portal frame were modeled in OpenSees to facilitate the parametric analysis. The columns and beam were modeled using the nonlinear BeamColumn element class of OpenSees using the force-based distributed plasticity approach with 5 integration points. To execute this parametric analysis in an automated manner the analysis was conducted through MATLAB. This enabled to vary the analysis parameters automatically and save the data for direct post-processing. The steel rebar has a yield stress of 550 MPa and a strain hardening ratio equal to 0.5%. The steel reinforcement was modeled using the Steel02 uniaxial material (Giuffré-Menegotto-Pinto model) of OpenSees. The steel rebars are modeled without the isotropic hardening property of that model. The compressive strength of concrete for this study was taken as 28.5 MPa. All RC cross-sections have a 25 mm cover to the center of the hoop reinforcement. The Concrete04 uniaxial material of OpenSees (Popovics, 1973) was adopted in modeling the unconfined and confined concrete of the column's cross-sections. During the analysis, a MATLAB function calculates the properties of the confined concrete using Mander et al. (1989) expressions for confined concrete stress and strain which are eventually sourced to the OpenSees input file for the analysis. The ultimate stress of confined concrete was also computed following the Mander et al. (1989) formulation. The ultimate compressive strain of unconfined concrete was set to 0.03, in order to prevent an abrupt drop in the post-peak region which is inherent to the Concrete04 model. The tensile capacity of concrete was modeled considering an ultimate strain of 0.2% and an ultimate stress equal to 14% of the unconfined concrete strength.

Detailed modeling parameters and pushover analysis results, shown in Figure 6-4, for all cantilever columns and portal frames analyzed in this study are presented in Table 6-3. The ultimate displacement of the structure was determined after bilinearizing the capacity curve, based on the initial stiffness, using the equal area method. The post-peak capacity of the cantilever RC column is

significantly different comparing the columns at 1 Hz and 2 Hz fundamental frequency, with a steep post-peak localization in the former. Contrarily, only a slight difference is observed comparing the capacity curves of the columns at 2 Hz and 3 Hz.

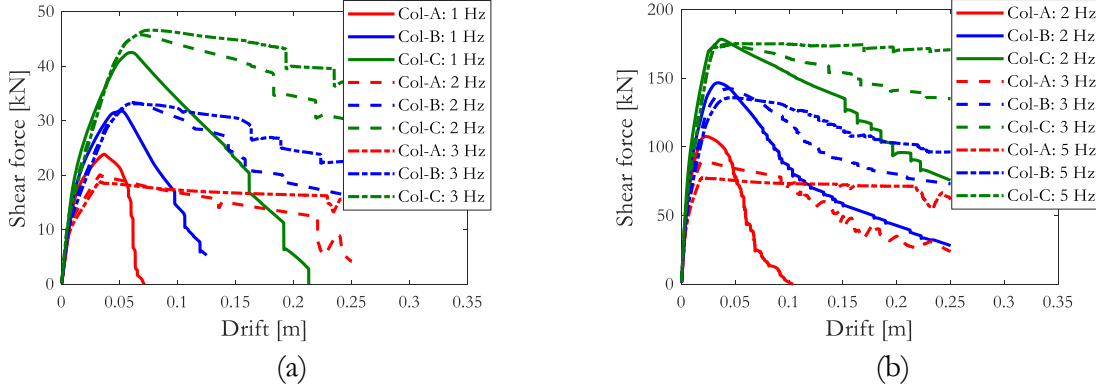


Figure 6-4: Capacity curves: (a) Cantilever RC column and (b) Portal RC frame

On the other hand, the effect of the extra longitudinal and hoop reinforcement added into Columns B and C, and the reduction of hoop spacing, also brought a visible improvement in the capacity and ductility of the cantilever columns. Similar characteristics to the ones depicted for the cantilever columns are displayed in the post-peak response of the portal frames with different column cross-sections and masses.

During the dynamic time-history analyses, sixteen records that are representative of earthquakes in Europe were selected in the range Mw 6-6.5. The earthquake records were selected to have diverse fault-mechanisms, distance from source,  $R_{i,B}$ , and mean period of the record,  $T_m$ . (see Appendix 5 for details). The spectral acceleration at the fundamental frequency,  $S_a(T_1)$ , is a reliable intensity measure in view of the PBEE framework (Hancilar & Çaktı, 2015). Hence,  $S_a(T_1)$  was taken as the intensity measure for the earthquake input motions throughout this chapter.

Table 6-3: Modelling properties and capacity of cantilever RC columns

Cross-section	Frequency [Hz]	Mass [t]	$f_{cc}$ [Mpa]	$e_{cc}$ []	$e_{cu}$ []	$\nu$ []	$d_{ult}$ [m]	$F_y$ [kN]
Column-A	1	39.420	28.520	-0.002	-0.012	0.339	0.055	21.322
	2	10.630				0.091	0.121	17.445
	3	4.790				0.041	0.229	16.841
Column-B	1	43.160	31.390	-0.003	-0.019	0.337	0.077	27.323
	2	11.790				0.092	0.143	28.889
	3	5.320				0.042	0.188	29.259
Column-C	1	50.280	42.290	-0.007	-0.026	0.292	0.099	42.520
	2	14.270				0.083	0.183	40.357
	3	6.470				0.038	0.235	41.840

As mentioned before, the parametric study was carried out to mimic a five-stage shaking table test. For each earthquake record, the *non-sequential* analysis was conducted five times by progressively scaling  $S_a(T_1)$ , while the sequential analysis is executed only once using a combined record. The

scaling of the ground motion is necessarily dependent on the IM selected. In fact, scaling the peak ground acceleration (PGA), for example, controls the structural response better in case of very stiff structures compared to flexible structures. On the other hand, scaling based on  $S_a(T_1)$  controls the structural response better near the dominant frequency of the structure. The ground motion input for the cantilever column was thus scaled at 1, 2 and 3 Hz, while for the portal frame the spectral scaling was done at 2, 3 and 5 Hz.

Table 6-4: Modelling properties and capacity of RC portal frames

Cross-section	Frequency [Hz]	Mass [t]	$f_{cc}$ [Mpa]	$e_{cc}$ []	$e_{cu}$ []	$\nu$ []	$d_{ult}$ [m]	$F_y$ [kN]
Column-A	2	35.500	28.520	-0.002	-0.012	0.174	0.048	98.807
	3	16.100				0.138	0.108	81.258
	5	5.840				0.029	0.250	71.597
Column-B	2	38.790	31.390	-0.003	-0.019	0.173	0.071	130.970
	3	17.740				0.139	0.104	127.282
	5	6.460				0.029	0.157	123.531
Column-C	2	45.460	42.290	-0.007	-0.026	0.151	0.128	158.798
	3	21.440				0.124	0.220	158.268
	5	7.865				0.026	0.250	172.490

The scaling was conducted at  $0.5a_y$ ,  $a_y$ ,  $2a_y$ ,  $3a_y$  and  $4a_y$ , where  $a_y$  is the yield acceleration (or simply  $F_y/m$ ) of the structure. To this end, each combination of frequency and cross-section of the two structures are uniquely scaled because of the difference in spectral ordinate for different frequencies and the difference in yield acceleration among the case studies.

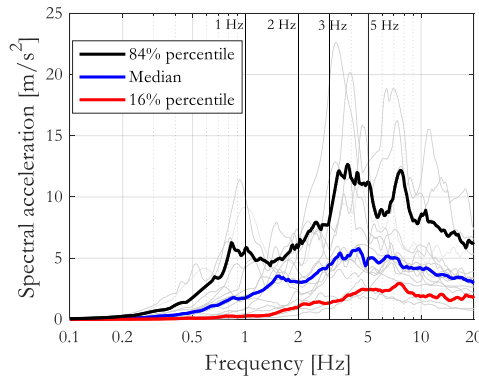


Figure 6-5: Spectral acceleration of unscaled earthquakes

#### 6.4.1.2 Results and discussion

##### 6.4.1.2.1 Effect of cumulative damage

The cantilever column and portal frame structures are subjected to the *non-sequential* analyses and to the *sequential* analysis. The Park-Ang damage index was calculated at the end of each stage of the analysis and the results from both analysis cases are compared. The median value of the damage indices obtained from the sixteen ground motions is used in assessing the effect of cumulative

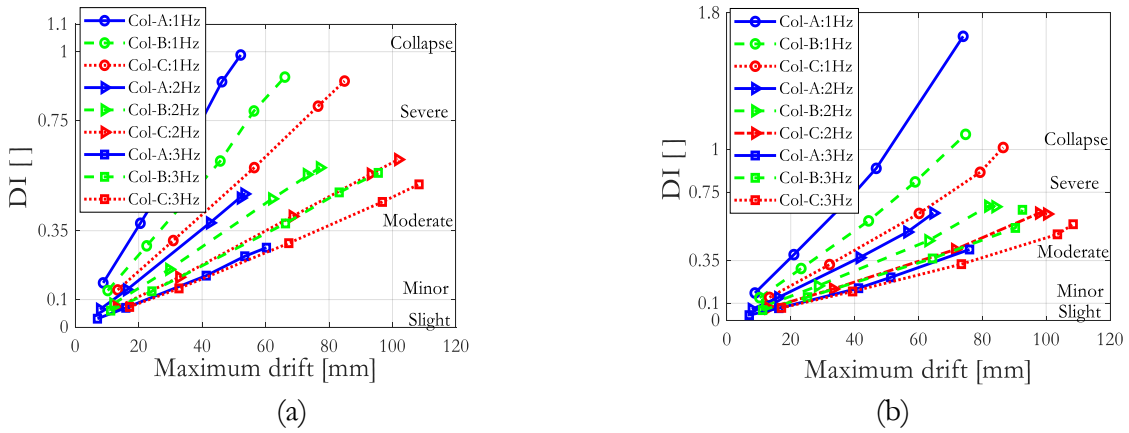


Figure 6-6: DI versus maximum drift plot of the RC cantilever column: (a) *Non-sequential* analysis and (b) *Sequential* analysis

damage during the *sequential* analysis. Hence, the damage index (DI) refers to the median value throughout this discussion. The DI calculated at the end of each stage and the maximum lateral displacement of each stage can be plotted to estimate the effect of hysteresis energy in the damage index. Evidently, a linear plot is achieved in the *non-sequential* analyses due to the small accumulation of hysteresis energy.

The damage recorded at higher stages, typically the 4<sup>th</sup> and 5<sup>th</sup> stages, of the *sequential* analysis, may have a significant contribution from hysteresis energy thus resulting in a curved relationship between the median values of DI and maximum drift. The curve gains more curvature as the nonlinearity of the structures becomes stronger, as shown in Figure 6-6(b). The RC cantilever column at 1 Hz fundamental frequency experienced significant damage at the 5<sup>th</sup> stage, where the DI jumps from 0.9 (near-collapse) to 1.7 (collapse). Contrarily, many of the other cantilever column structures have small jumps in the DI from the 4<sup>th</sup> stage to the 5<sup>th</sup> stage.

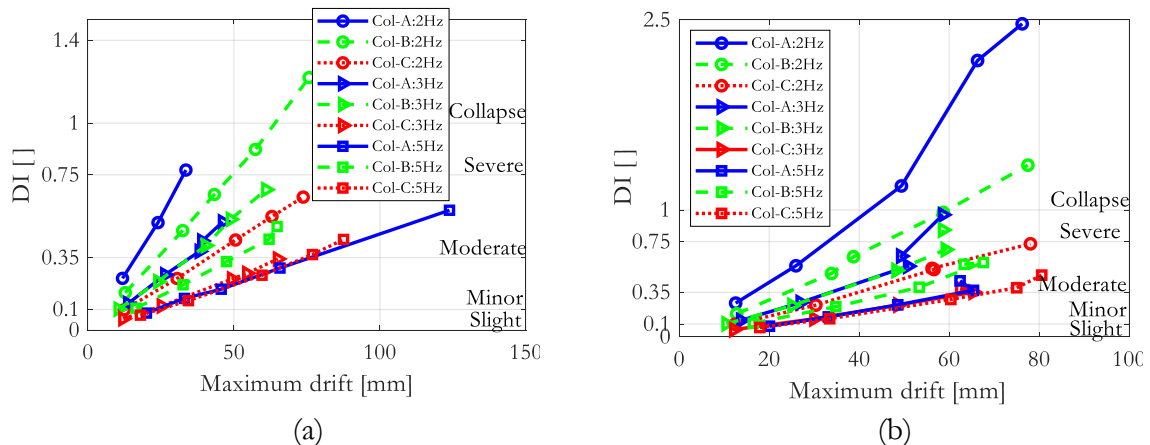


Figure 6-7: DI versus maximum drift plot of the RC portal frame: (a) *Non-sequential* analysis and (b) *Sequential* analysis

Similar arguments are valid for the portal RC frame. Nevertheless, the portal frame damage indices are dominated by the contribution from the maximum drift in both cases (*sequential* and *non-sequential*). However, the portal frame at 2 Hz frequency, with *Column-A* and *Column-B* cross-sections, reached the collapse level mainly since large inertial forces are mobilized. The plots include the physical interpretation of the calculated damage indices based on reports from cyclic uniaxial and biaxial RC column tests reported by Rodrigues et al. (2013).

Figure 6-8 and Figure 6-9 show plots of the damage index with increasing input intensity, comparing the *sequential* and *non-sequential* analysis of the case studies. With increasing frequency, i.e. smaller inertial force, the damage index gets smaller. It is evident that the damage experienced by the structures during the *sequential* and *non-sequential* analysis is nearly identical during the first three or four stages of the test (corresponding to an input acceleration equal to double or triple of their yield acceleration).

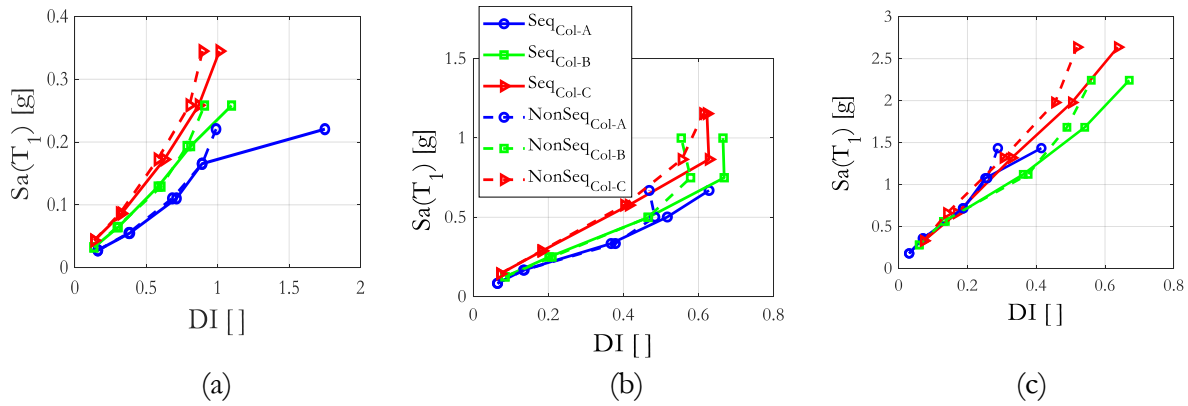


Figure 6-8: DI versus  $Sa(T_1)$  of the RC cantilever column: (a)  $f=1$  Hz, (b)  $f=2$  Hz and (c)  $f=3$  Hz

This infers that the importance of accumulated hysteretic energy in the *sequential* analyses is only significant as the cantilever column undergoes large plastic excursions. *Column-C* registered the smallest damage because it is stiffer than the rest of the columns and has superior ductility.

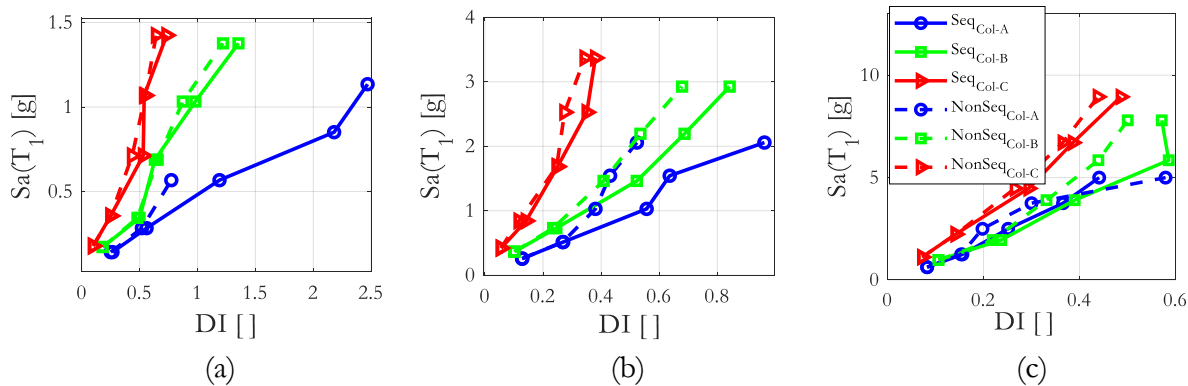


Figure 6-9: DI versus  $Sa(T_1)$  of RC portal frame: (a)  $f=2$  Hz, (b)  $f=3$  Hz and (c)  $f=5$  Hz

Similar comments, on the variation of the DIs with increasing level of ground motion input, are valid for the portal RC frame. At larger inertial input force, the portal frame with *Column-A* cross-section failed to resist the input acceleration (which was scaled to twice of its yield value). Compared with the cantilever column, larger discrepancies in damage indices are recorded between the *sequential* and *non-sequential* analyses.

#### 6.4.1.2.2 Damage-based equivalent first mode spectral acceleration

It was pointed out previously in this chapter that the slope parameter,  $b$ , is necessary for calculating the  $S_a(T_1)_{eq}$ . The slope of the logarithmic fitting of the responses obtained from the *non-sequential* analyses is used in calculating  $S_a(T_1)_{eq}$ . Since  $S_a(T_1)$  is closely related to the frequency of the structure, the fitting was conducted as a function of frequency. This results in three fitting parameters, both for the cantilever and for the portal frame structure. The logarithmic fitting for the portal frame presents a larger dispersion, compared to the cantilever column, since higher modes may have contributed to its response. The dispersion of the median responses is manifested in the  $R^2_{adj}$  of the fitting, as shown in Figure 6-10(b).

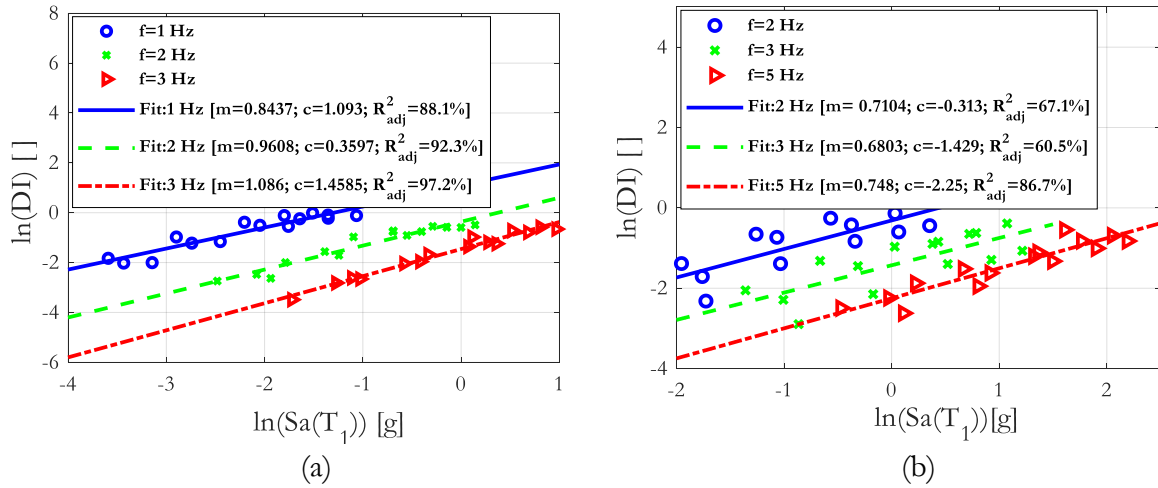


Figure 6-10: Logarithmic fitting: a) cantilever RC column and (b) RC portal frame

The damage index ratio is the ratio of damage index calculated from the *sequential* analysis to damage index derived from the *non-sequential* analysis. Sample-by-sample damage index ratio was calculated at every earthquake input and every stage of the analysis. The median value of the damage index ratio and slope of the fitting parameter,  $b$ , is consequently used in calculating  $S_a(T_1)_{eq}$  using equation (6.25). The damage index ratio data is fitted to a second-order polynomial curve, for calculating  $S_a(T_1)_{eq}$ , for a better representation of the data recorded.

The polynomial is constrained to pass through one at its initial point because of the perfect equality between the *sequential* and *non-sequential* analyses at the first stage of a test. For  $S_a(T_1)$  as large as 1.0 g, the damage index ratio of the RC cantilever column remains below 1.05 while the damage index ratio of the portal frame is very close to one. This might be related to the energy dissipation

mechanism of the portal frame which is more complex than that of the isostatic cantilever column.

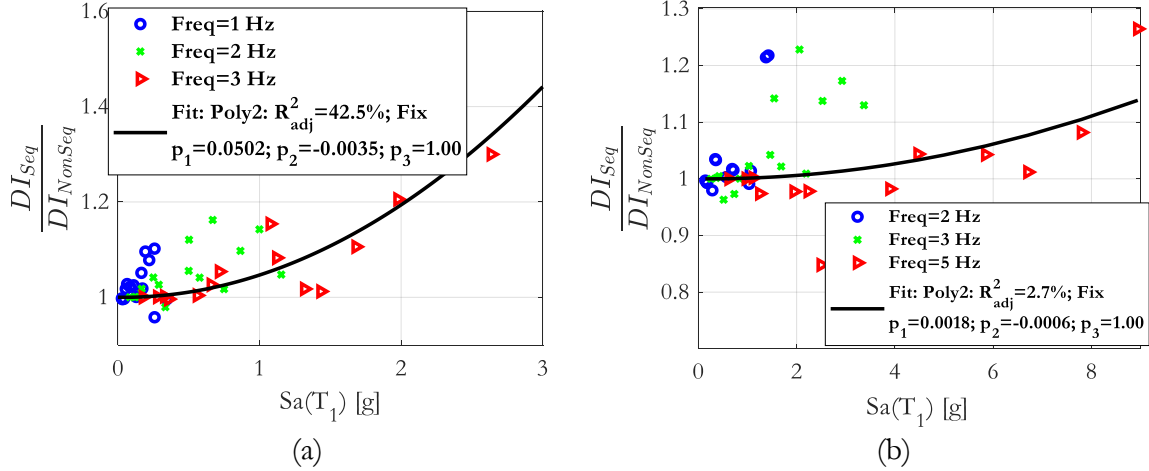


Figure 6-11: Damage index ratio: (a) cantilever RC column and (b) RC portal frame

#### 6.4.1.2.3 Validation of $S_a(T_1)_{eq}$

After computing the  $S_a(T_1)_{eq}$  for every earthquake record and every stage of the analysis, the *non-sequential* analysis was repeated under the modified input,  $S_a(T_1)_{eq}$  (hereinafter referred to as *validation non-sequential* analysis). The responses recorded from the *validation non-sequential* analyses and the response from the *sequential* analysis are compared. The ideal result of a damage index ratio computed from the *sequential* analysis and the *validation non-sequential* analyses should be approximately one. This is expected not to be reached in practice, due to the statistical nature of this approach. Nevertheless, an improvement on the damage index ratio obtained during the *validation* analyses is invaluable.

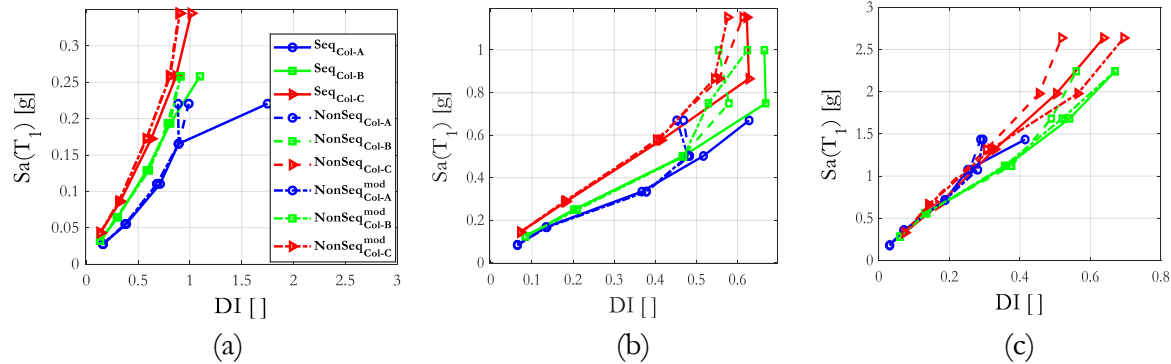


Figure 6-12: Validation of  $S_a(T_1)_{eq}$  for the RC column: (a)  $f=1$  Hz, (b)  $f=2$  Hz and (c)  $f=3$  Hz

Overall, a slight improvement of damage indices is recorded, in both structures, with the introduction of  $S_a(T_1)_{eq}$ . In many of the cases studied herein, the shift in damage indices is favorable with the goal of the validation. However, a few unfavorable cases were recorded, as shown in Figure

6-12(c).

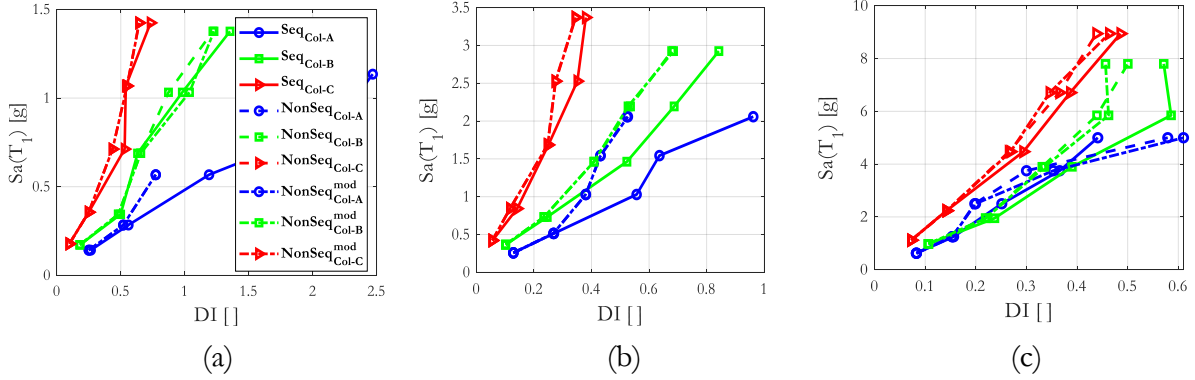


Figure 6-13: Validation of  $S_a(T_1)_{eq}$  for Portal frame: (a)  $f=2$  Hz, (b)  $f=3$  Hz and (c)  $f=5$  Hz

The damage index ratio calculated on the cantilever RC column considering  $S_a(T_1)_{eq}$  has significantly improved from its former magnitude and, somehow, validating the approach proposed in this study. Damage indices from the portal RC frame, however, become unfavorable in the lower range of  $S_a(T_1)$  while slightly improving the response at higher levels of input. During this validation, the initial value of the damage index fitting was not constrained since the *sequential* analysis was carried out at  $S_a(T_1)$  while the *non-sequential* analysis was executed at  $S_a(T_1)_{eq}$ .

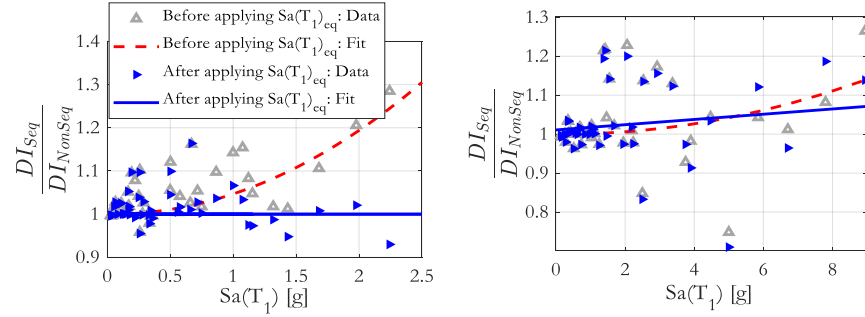


Figure 6-14: Validation of DI ratio: cantilever RC column (left) and RC portal frame (right)

#### 6.4.1.2.4 Conclusion

Considering a modification factor given by  $S_a(T_1)_{eq} / S_a(T_1)$ , an ideal approach for applying it for shaking table tests would consider not only the damage index ratio but the intensity of the ground motion input. Besides,  $S_a(T_1)_{eq}$  cannot be estimated using experimental test results only, because it requires numerical modeling and analysis of the test structure. Furthermore, the proposed approach does not account for the influence of the maximum responses of a test structure corresponding to stages preceding the stage of interest during a stage-wise shaking table test. A closed-form expression for the  $S_a(T_1)_{eq}$  that includes all of its inter-dependencies is challenging and is not the scope of this study. It is apparent that the parametric study conducted in this research does not represent a large portfolio of RC structures, but it allowed us to investigate the reliability of the proposed approach to some extent. Considering its incomplete representativeness and summing up

the results of the parametric study of the two structures, perhaps, it is reasonable to consider the modification factor of  $S_a(T_1)$  of an earthquake record as one when the damage index is below 0.75.

#### 6.4.2 Optimization of Bayesian updating using shaking table tests

It is prudent to ask the question ‘how many virgin shaking table tests or stages during a shaking table test are required to get a reliable update of a fragility curve?’. To partially answer this question, a simulated study on convergence of posterior parameters of a fragility curve was conducted by interpolating and extrapolating shaking table test results. The simulated study was carried out using the unscented transformation approach for updating fragility curves because the MCMC method is computationally demanding. The optimization problem was studied by breaking it down into:

1. The effect of experimental data that does not exceed a DS of interest
2. The optimum size of experiments if all DSs are exceeded

Shaking table test results of an RC frame, which will be introduced later in this chapter, are interpolated using Lagrange polynomials to help us in evaluating the two issues. The shaking table test of the RC frame has 5 stages and the first three HAZUS (FEMA, 2001) damage limit states are exceeded.

##### 6.4.2.1 The effect of experimental data before exceedance of a DS

The first question addresses the effect of updating a fragility curve using experimental test results, such as maximum drift, that does not exceed the fragility curve of a particular DS. The intensity measure of the input acceleration  $S_a(T_1)$  for the shaking table test of the RC frame was uniformly divided into twenty points. A 5-stage simulated experiment was created by interpolating, for the maximum drift, between the first and any of the twenty division points. This way, twenty simulated experiments were generated. The interpolation process, from the true experimental results, uses Lagrange polynomials.

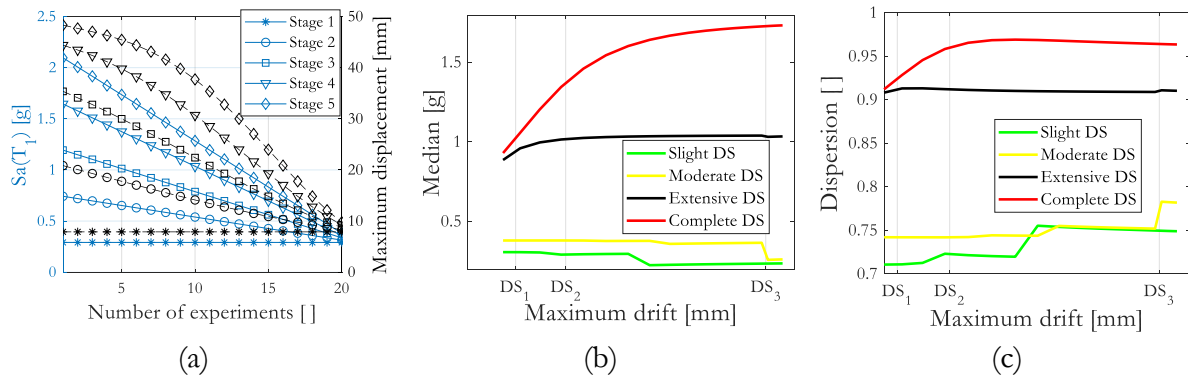


Figure 6-15: Effect of experiments before exceedance of a particular DS: (a) Data for Bayesian update, (b) Posterior value of median and (c) Posterior value of  $\beta$

In Figure 6-15, DS<sub>1</sub>, DS<sub>2</sub>, and DS<sub>3</sub> represent the maximum drift values corresponding to the slight,

moderate, and extensive damage states, respectively. The posterior values of the median parameter for the slight and moderate fragility curves have localized, non-uniform, descents throughout the simulation. The median of the slight DS seems to attain convergence while the complete DS continues to overshoot from its initial value since it is not exceeded during the experimental test. The median of the complete DS increased significantly due to the information obtained from the first two lower damage states, but its rate of increase drops significantly as the experimental tests approach towards the extensive DS. The extensive DS increases approximately 10% of its original value after both the slight and moderate damage states are exceeded but then it drops slightly when it is exceeded.

The posterior value of the dispersion,  $\beta$ , gradually increased in steps in the case of slight DS and moderate DS. The extensive DS posterior  $\beta$  assumed a nearly constant value meaning the numerical estimates were good enough for this damage state. The complete DS, on the other hand, showed a significant rise due to the exceedance of the first two DSs and maintained a nearly constant amplitude during the rest of the simulation. Results suggest an overall sensitivity of posterior estimates to exceedance of a DS in an experiment. Besides, higher DSs may continue to overshoot from data obtained from lower DSs if they are not exceeded.

#### 6.4.2.2 The optimum size of experiments given all DSs are exceeded

The optimum size of experiments is very important in obtaining unbiased posterior estimates while achieving cost-effectiveness during the process of updating fragility curves. The maximum drift recorded during the shaking table test of the RC frame was, again, extrapolated to ensure that all DSs are exceeded. Fifty experiments were considered by extrapolating the response until the frame reaches a maximum drift of 127 mm (with the complete DS threshold being equal to 118 mm). Each experiment has  $n$  stages, [2, 50], distributed across a range of maximum drifts between the first stage and 127 mm, as shown in Figure 6-16.

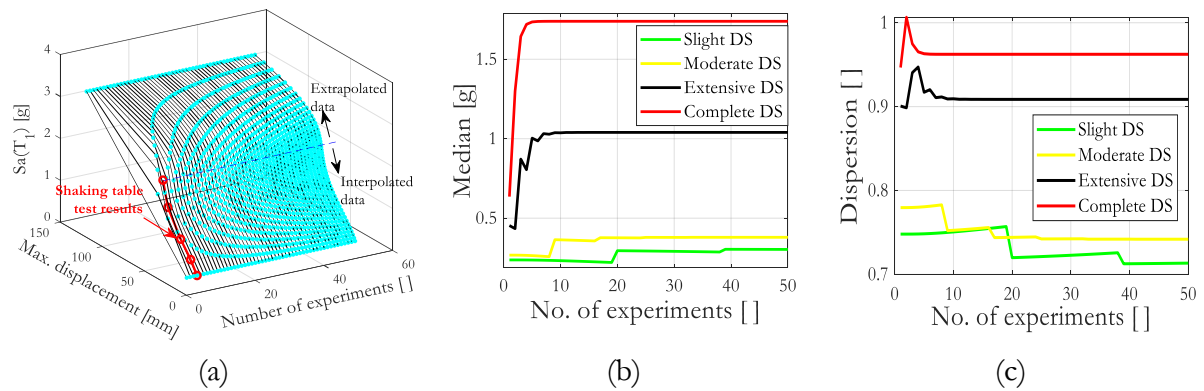


Figure 6-16: Optimum size of experiments for updating fragility curves: (a) Data for Bayesian update, (b) Posterior value of median and (c) Posterior value of  $\beta$

The top two DSs attained convergence for the number of experiments as low as 10. The moderate

DS, on the other hand, attained its converging value at 20 experiments, while the slight DS required 40 experiments to reach its plateau value. The above argument is also valid for dispersion parameters except for the lower two DSs. Slight and moderate DSs assumed constant values at 25 and 40 experiments, respectively. Lower damage states could also be sensitive to experimental data after being exceeded.

To sum up, a reliable update of all damage states may only be ascertained when all damage states are exceeded. Besides, estimating the optimum number of shaking table tests before an experimental campaign can help to improve the fidelity of the fragility updating. The ATC-58 recommends at least six experimental tests on virgin specimens (Porter et al., 2006). Although the current study is not exhaustive and particular to the case study, the optimum number of experimental tests may depend on the level of DS and the experimental test data, among others.

## 6.5 Application case study

### 6.5.1 Two-story RC frame

The MCMC Bayesian inference was applied to a 2D two-bay two-story RC frame which was tested at LNEC's 3D shaking table. The experimental test of the RC frame was carried out during the Teixeira Duarte Award, involving a blind-prediction competition held in 2014, for the response of a non-seismically designed frame. The 1:1.5 reduced scale frame has square outer columns ( $20 \times 20 \text{ cm}^2$ ) and an internal column that has  $20 \times 27 \text{ cm}^2$  dimensions. The beams in the first and second floor-levels have a  $20 \times 33 \text{ cm}^2$  cross-section, while the foundation beam has a larger depth compared to the top-floor beams.

The axial force on the columns was applied by applying a pre-stress force to the Φ26 tendons, which are inserted into the holes and cast to the columns, as shown in Figure 6-17. Tendons were pre-stressed to the desired level and clamped at both ends. The pre-stress forces applied to tendons in the outer and inner columns were approximately 22.8 and 35.4 kN, respectively. Blocks of masses were placed at the mid-span of the floor beams to represent the floor mass. The first floor has two masses on each bay, weighing a total of about 1.18 t per span. Likewise, the second floor has one mass on each bay, weighing about 1.13 t per span. All structural elements are made of concrete grade C10/12 and steel reinforcement of A500 steel grade.

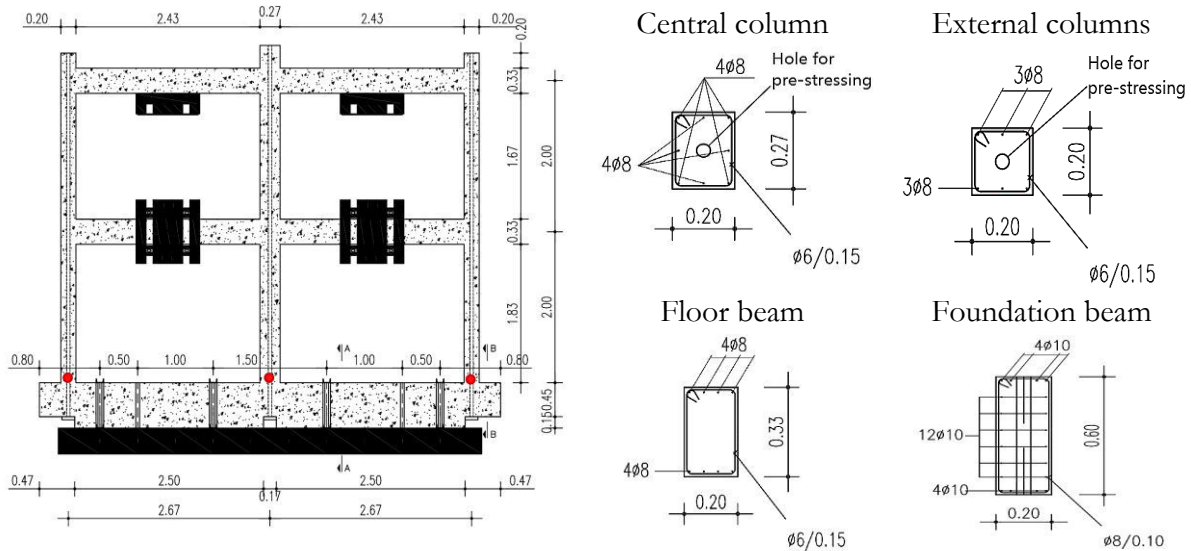


Figure 6-17: 2D RC frame tested under the Teixeira Duarte Award

### 6.5.2 Numerical modeling and generation of fragility curves

The 2D RC frame was modeled in Seismostruct, a nonlinear structural analysis software. All structural elements of the frame were modeled using force-based elements except the foundation beam, where elastic elements were adopted. To simulate the rigid connection of the foundation beam to the shaking table platen, the foundation beam was modeled as rigidly connected to the base. The pre-stressed steel rods, inside the columns, were modeled using an elastic element since it was expected to remain elastic during the test. Constraints were applied at floor levels so that the pre-stress rods deform together with the columns. Permanent axial loads were then applied to the columns, consisting of the pre-stress force transmitted through the steel rods. It should be noted that this approach of modeling allows representing the recentering effect of the rods which prevailed during the experimental test. This work seeks to improve the fragilities derived from this numerical model through the Bayesian updating technique based on the shaking table test results. Steel rebars were modeled using the Menegotto-Pinto steel (Menegotto & Pinto, 1973) model (*stl\_mp*) with 0.5% strain hardening and the concrete was modeled via the Mander et al. (1989) nonlinear concrete model (*con\_ma*).

Incremental dynamic analyses (IDA) (Vamvatsikos & Allin Cornell, 2002) of the RC frame were conducted under a suite of 30 ground motion records with magnitude  $M_w$  between 6 and 6.5. The ground motion suite adopted has been recently selected to serve for the revision of EN 1998–5 and it was originally taken from the PEER NGA West2 ground motion database (detailed information can be found in Appendix 6). The ground motion records have a Joyner -Boore distance to source,  $R_{j,B}$ , less than 30 km and an average shear wave velocity,  $V_{S,30}$ , in the range of 200 – 600 m/s.

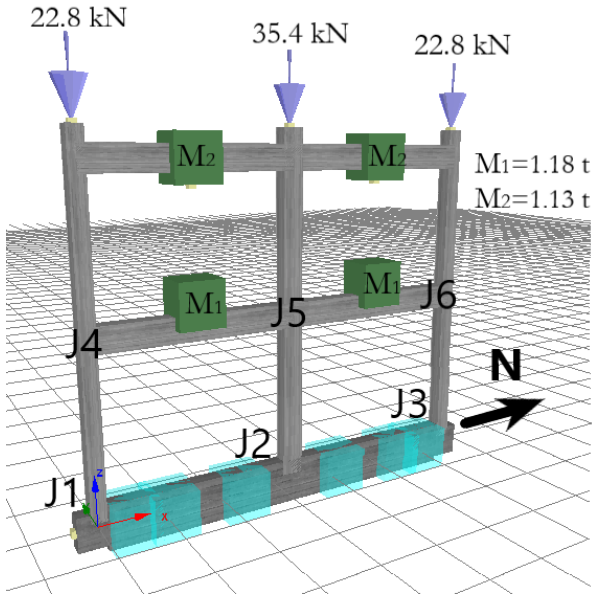


Figure 6-18: Numerical modeling in Seismostruct

No pulse records were included, with the records being selected regardless of their fault mechanism. Besides, European records were given priority in the selection process. All records were initially scaled to 0.1 g at the first modal frequency of the RC frame and the IDA was conducted by progressively increasing the scale factor until collapse or instability is attained.

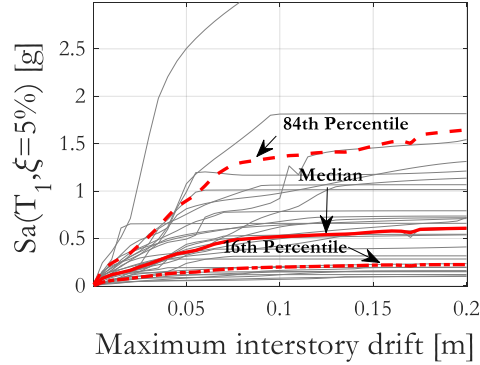


Figure 6-19: First-story IDA capacity curves

The IDA capacity curve under each record was constructed by plotting the maximum inter-story drift of the first floor against the intensity measure of the input motion. The spectral acceleration at the fundamental frequency,  $S_a(T_1)$ , was adopted as the intensity measure of the input motion. Nonetheless, several other intensity measures, such as PGA, PGV, and Average Spectral Acceleration (ASA) were examined as well. The efficiency and sufficiency requirements of numerous intensity measures were also explored while selecting the intensity measure that reduces dispersion in the capacity due to record-to-record variability of input. Figure 6-20 presents capacity curves for different intensity measures. An extensive study on the selection of intensity measures

for probabilistic seismic risk analysis can be found at Biasio (2016).

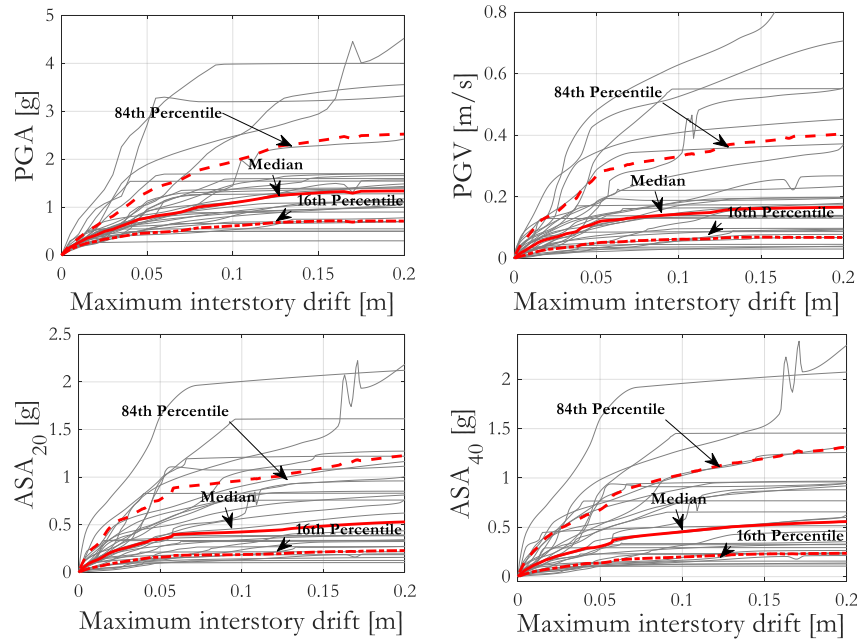


Figure 6-20: First-story IDA capacity curves for PGA, PGV, ASA<sub>20</sub>, and ASA<sub>40</sub>

Both the HAZUS and the Homogenized Reinforced Concrete (HRC) (Rossetto & Elnashai, 2003) damage states, considering the maximum inter-story drift ( $ISD_{max}$ ), were used for constructing the fragility curves. The fragility curves will then be subjected to Bayesian-based updating in subsequent sections of the chapter.

During the IDA, the concrete and steel strains at the base of all columns, shown by red dots in Figure 6-17, were also monitored to help building the fragilities for visually observable damages. The absolute maximum strain in steel rebars was recorded during the IDA and the exceedance of steel yielding and fracture were decided based on threshold strains of 0.275% and 6%, respectively. Two concrete and one steel fibers were monitored in this approach, as shown in Figure 6-21. In the scope of this thesis, the damage states related to yielding and fracturing of steel rebars were not considered for Bayesian updating because it is difficult to inspect such damage states during an experimental test. However, the strain of steel rebars may be monitored during experimental tests which can then be used for updating results that are obtained numerically.

Strain in the concrete cover exceeding +0.01% indicates initiation of cracking while compressive (negative) strains larger than -0.2% translate into spalling of the concrete cover. A concrete strain above 0.6% was set to mark the crushing of the concrete core. For each exceedance criteria, the corresponding maximum inter-story drift ( $ISD_{max}$ ) of the first floor was recorded during the IDA. The dispersion of the recorded  $ISD_{max}$  is characterized by some outliers that might diminish the fidelity of the scheme adopted. Besides, some damage states were not flagged under some of the earthquake records. Eventually, fragilities of the observable damages were constructed from the

IDA analyses.

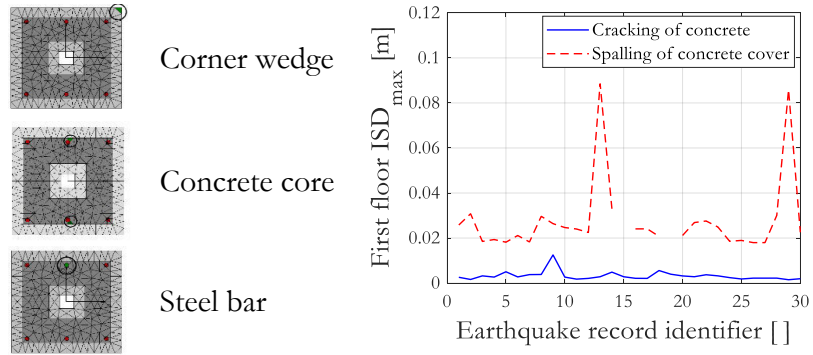


Figure 6-21: Median value of  $ISD_{max}$  for observable damages

### 6.5.3 Experimental test

The shaking table test of the RC frame was carried out using LNEC's 3D shaking table, as mentioned before. The floor masses were modeled through lumped masses that are attached to the RC beams, while the axial force on the columns was applied by pre-stressing the tendons that were inserted in the columns. Afterward, the tendons are clamped at both ends after connecting load cells to record their axial force.

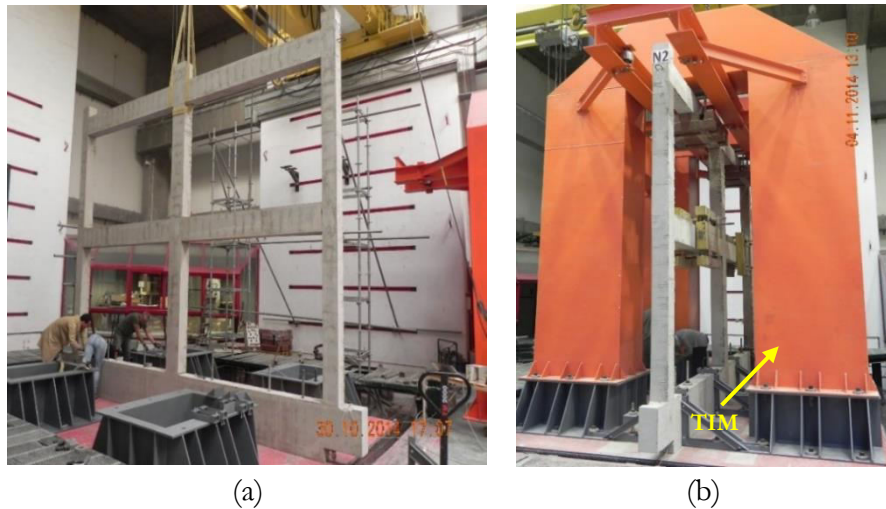


Figure 6-22: Test setup: (a) Mounting RC frame and (b) Mounting the guidance structure

The RC frame was tested inside a 3D steel guidance frame, to effectively guide the frame in-plane and eliminate out-of-plane deformations. The guidance structure has roller bearings at the top, to help guiding the frame's top-most beam, while effectively restricting its lateral movements. It was firmly connected to the shaking table platen, similarly to the RC frame, which was also rigidly attached to the platen of the shaking table using three triangular-shaped steel connectors that clamp the girder beam firmly to the platen.

The tension strength of the A500 steel rebars that were used during the construction of the frame was tested in a laboratory by taking  $\Phi 6$  and  $\Phi 8$  rebars, each three samples. As shown in Figure 6-23, the  $\Phi 6$  rebars have negligible strain-hardening and they are characterized by a short post-yield plateau which is typical of cold-formed steel. On the other hand, the  $\Phi 8$  bars showed a yield plateau around 550 MPa before the strain-hardening trajectory of the strain-stress curve, and they are more ductile compared to the  $\Phi 6$  rebars. Consequently, during the numerical modeling, the yield strength of the longitudinal bars was taken to be 550 MPa.

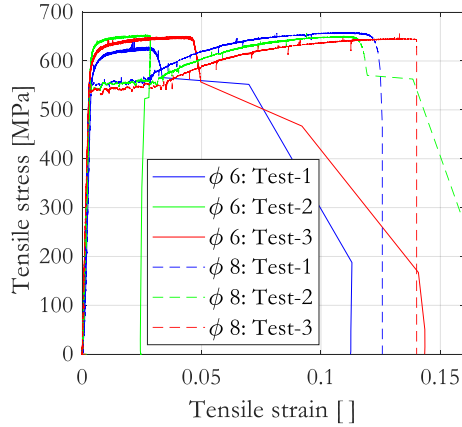


Figure 6-23: Tensile tests of steel reinforcement

The seismic action was defined by a reference spectrum built from the limit values estimated for the acceleration, velocity, and displacement of the shaking table and considering the 84% percentile of the amplification factors proposed by Newmark & Hall (1982).

The target acceleration to the shaking table input corresponds to an artificial accelerogram generated from the reference spectrum and it was scaled to a peak horizontal acceleration of 0.1 g, 0.2 g, 0.32 g, 0.52 g, and 0.72 g, resulting in five test stages with proportional acceleration inputs.

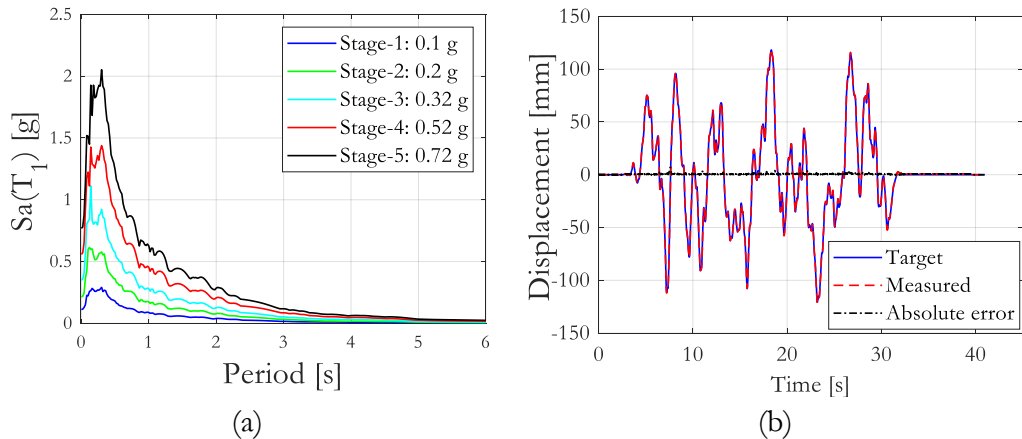


Figure 6-24: (a) Input spectra; (b) Performance of shaking table controller at stage-5

The experimental test was thus conducted in five stages with progressively increasing intensity of target input. The shaking table control was done in displacement using a PID controller in the real-time inner loop, while the displacement command to the shaking table was prepared by an offline adaptation process that uses an iterative correction procedure for achieving the target motion. Consequently, a good matching between the target and measured displacements was achieved, over the frequency range of interest, with minimal error in tracking as shown in Figure 6-24(b). At the end of the test, the structure's first natural frequency dropped to approximately 50% of its initial value, as shown in Figure 6-25.

The structural responses, such as the maximum inter-story drift and maximum acceleration at the floor levels, were calculated from the recordings of the instrumentation. Besides, the experimental test was recorded by a video camera to facilitate in identifying the initiation of some of the most important physical (or observable) damage states of the RC frame.

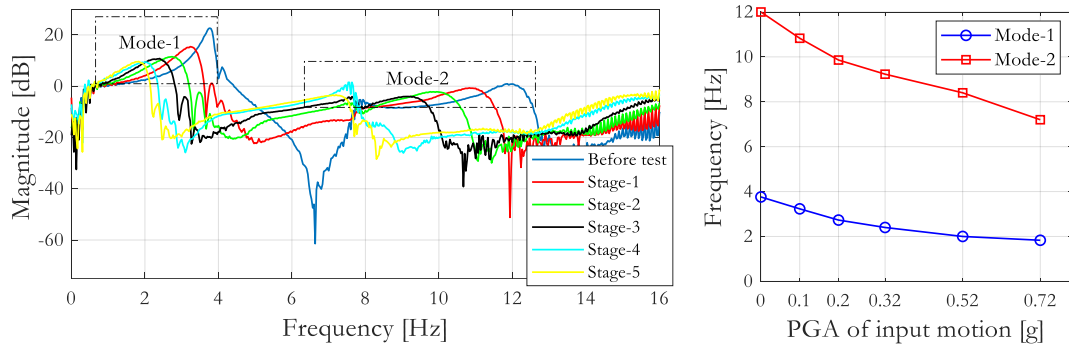


Figure 6-25: Evolution of frequencies during the stages of the shaking table test

#### 6.5.4 Bayesian updating of analytical fragilities

To explore the Bayesian inference of RC fragilities, the MCMC approach in the Bayesian update was applied considering two types of damage states: one based on the maximum inter-story drift and another strain-based damage state. The latter was updated through visually observed data, using the degree of structural damage observed during the shaking table test. The fragilities of physical damage were initially built based on the strain-monitored locations of the frame. Regarding the damage states based on the maximum inter-story drift, the HAZUS damage states, and the Homogenized Reinforced Concrete (HRC) damage states were used in constructing the fragility curves. The maximum inter-story drift at the first-floor level of the frame, recorded during the shaking table test, was used in determining the exceedance parameter,  $\epsilon$  (see equation (6.8)).

The strain-based fragilities were built by monitoring strain levels on a limited number of locations of the frame. Hence prior distribution may be biased; nevertheless, the locations with the highest probability of damage were chosen to yield a conservative estimate of the strain levels responsible for the observable damages considered. The ideal evaluation for relating strain levels to observable

damage would consider the median value of strain from fibers of all representative cross-sections in the entire frame. However, such evaluation is onerous especially considering large structures.

#### 6.5.4.1 HAZUS damage states

The HAZUS guidelines provide an average inter-story drift ratio of RC frames (FEMA, 2001: table 6.3) considering four damage states: slight, moderate, extensive, and complete. The case study frame correspond to the Low-Rise and Low-Code category of the HAZUS damage classification. Four fragility curves are therefore calculated from the IDA results of the numerical model. In this work, the complete damage state is modified to represent the damage state at a 20% reduction of the maximum strength of the frame (referred hereinafter as "Complete\*"). The fragilities constructed from the numerical modeling were then updated via the two Bayesian approaches discussed in this chapter. The update was carried out using the results of the five stages of the shaking table test conducted on the RC frame. The maximum input intensity, in terms of peak horizontal acceleration, during the shaking table test was only 0.72 g and the final damage level of the structure was between the extensive and complete damage states. Consequently, the intensity of the input to the shaking table ( $S_a(T_1=3 \text{ Hz})$ ) was not corrected, consistently with the conclusions of the damage-based equivalent intensity measure study. During the update process, the likelihood function was constructed from the exceedance criteria, presented in Table 6-5, built by comparing the maximum inter-story drift, recorded at each stage of the test, with the HAZUS' damage state drift values.

Table 6-5: Exceedance parameter,  $\epsilon$ , for the HAZUS damage states

Stages	$S_a(T_1)$ [g]	$S_a(T_1)_{eq}$ [g]	ISD <sub>max</sub> [mm]	Inter-story drift for HAZUS Damage states			
				Slight	Moderate	Extensive	Complete*
I	0.2911	0.2911	7.886	0	0	0	0
2	0.5822	0.5822	15.475	1	0	0	0
3	0.9316	0.9316	27.321	1	1	0	0
4	1.5138	1.5138	42.453	1	1	0	0
5	2.0960	2.0960	48.323	1	1	1	0

As pointed out earlier, the prior value of the median,  $\theta_1$ , is modeled as a lognormal distribution while the prior value of the logarithmic dispersion,  $\theta_2$ , is modeled via a Gamma distribution. The dispersion of the prior value of  $\theta_1$  is modeled as  $\sqrt{2}/2$  of  $\theta_2$  and the Gamma distribution parameters for  $\theta_2$  were calculated by taking the coefficient of variation of the prior  $\theta_2$  to be 0.21.

Bayesian inference, based on the MCMC approach and the ATC-58 approach (also referred to as the unscented transformation (UT) approach in this chapter), is applied to the numerical fragilities and the results of the two updating procedures are compared. During the MCMC update, one million samples are generated using the Metropolis-Hastings algorithm; the first 2000 samples are discarded to eliminate the effect of the initial value, as discussed previously. The remaining samples

were also thinned by a factor of 20, selected from the autocorrelation relationship of the samples.

Point estimates of the posterior fragility curves, shown in Table 6-6, were then obtained by fitting the final retained data to their respective distribution types. To make the comparison between the ATC-58 method and the MCMC approach consistent, the parameters of their prior fragilities were taken to be identical.

Table 6-6: Posterior point estimates of HAZUS damage states: MCMC vs ATC-58

	Prior		Posterior estimates						
			MCMC				UT/ATC-58		
DS	$\theta'_1$ [g]	$\theta'_2$	AR [%]	$\theta''_1$ [g]	$\sigma_{\theta''_1}$	$\theta''_2$	$\sigma_{\theta''_2}$	$\theta''_1$ [g]	$\theta''_2$
Slight	0.1283	0.7106	34.84	0.1546	0.0847	0.7577	0.1535	0.2174	0.7516
Moderate	0.1530	0.7419	32.79	0.2564	0.1360	0.8124	0.1654	0.3577	0.7549
Extensive	0.3417	0.9086	29.91	0.7882	0.4733	0.9585	0.2021	1.0251	0.9118
Complete*	0.5351	0.9624	30.08	1.4212	0.9260	0.9884	0.2118	1.5881	0.9742

The Acceptance Ratio (AR) that was recorded during the MCMC update, in the range 30-35%, justifies the adequacy of the variance matrix considered for the proposal distribution, as shown in Figure 6-26. The point estimates of  $\theta_2$  from the MCMC are in the order of the ATC-58 estimates because of a relatively narrow prior distribution of  $\theta_2$ .

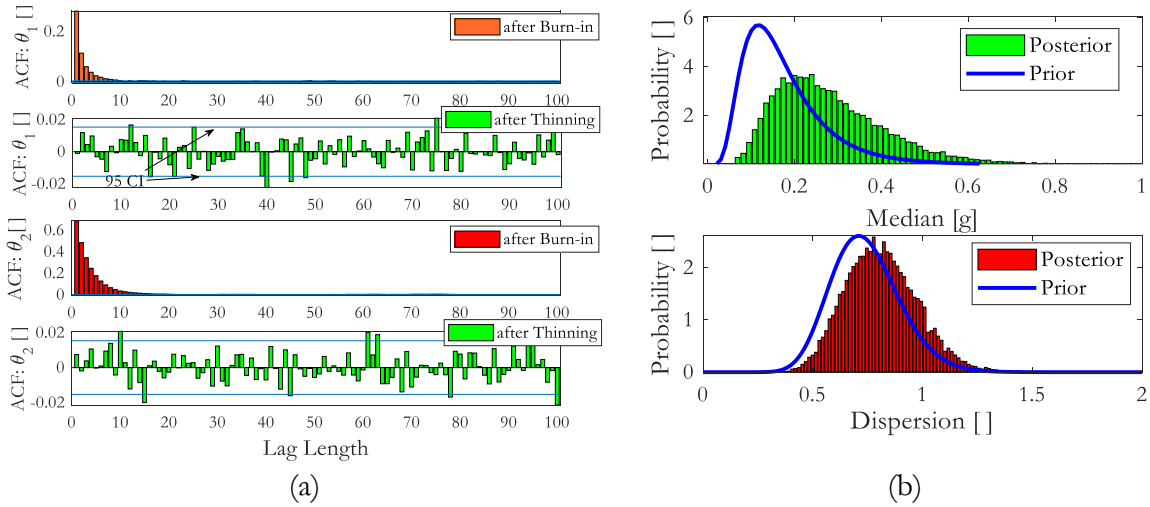


Figure 6-26: MCMC results: (a) Auto-correlation function (ACF) and (b) Prior vs. posterior distributions

Both Bayesian updating approaches reduce the fragility associated with the prior distributions derived numerically, which is reflected in the increase of the median IM required to reach a given damage state. In all four damage states, the median estimates from the ATC-58 method resulted in a less fragile structure, i.e., overestimating the capacity of the structure when compared to the estimates of the MCMC method. This could be the result of the approximations made in the ATC-

58 method.

With the increase in the level of damage, the dispersion of the posterior estimate of  $\theta_1$  from MCMC was observed to rise while the estimate of the posterior logarithmic dispersion,  $\sigma_{\theta_2''}$ , remained nearly constant. The latter can be interpreted as experimental results being consistent with the prior belief of  $\theta_2$  because the prior and posterior estimates of  $\theta_2$  are marked by approximately equal COV value.

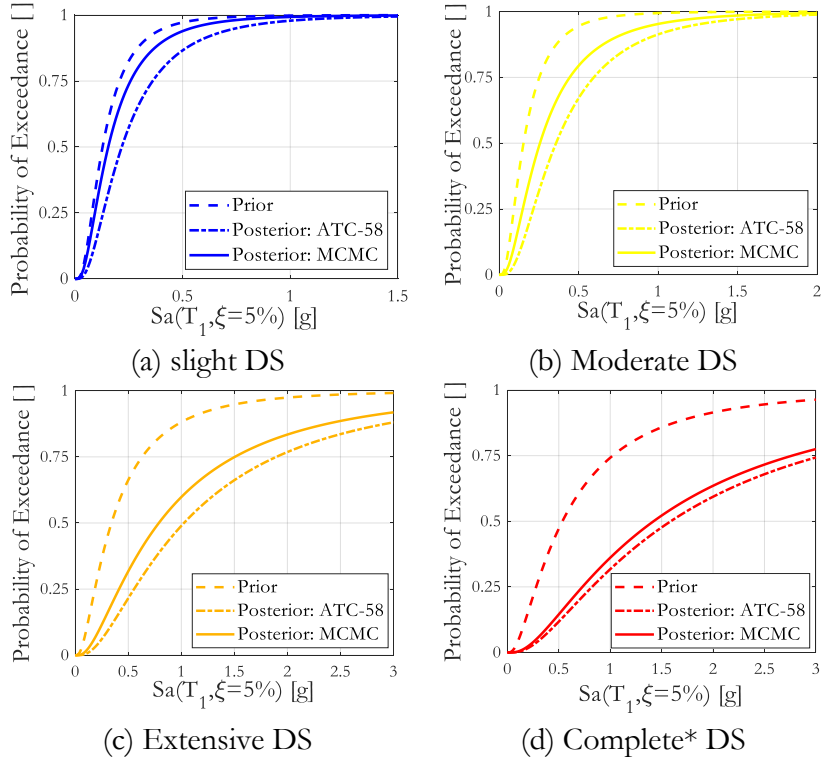


Figure 6-27: Bayesian updating of case study fragilities for HAZUS damage states

Contrarily, the variance of the posterior distribution of the median parameter has significantly changed from the prior belief. This characteristic can be depicted in Figure 6-27(b). In the MCMC updating, the auto-correlation function (ACF) was used to reduce the inherent correlation of the samples generated by the Metropolis algorithm. On average, the 95% confidence interval of the zero correlation was used as the target for the thinning process. Here, the results of the Bayesian updating conducted on the HAZUS damage states are only presented (the results of the HRC damage states can be found in Appendix 7).

#### 6.5.4.2 Strain-based damage states

Updating the analytical fragility curves for observable damage states such as cracking, spalling, etc., is also one of the goals of this study. As such, a detailed damage assessment at the end of each stage of the shaking table test was conducted. To reduce the subjectivity during the assessment of damage, the degree and nature of the damage observed during the test were identified based on damage data

of RC structures from experimental tests conducted in the past.

The exceedance criterion was eventually determined via visual inspection of damage during the experimental test. Photo and video recordings were mainly used during the construction of the exceedance matrix. Figure 6-28 shows photos taken during the test, indicating the initiation of important structural damages in the frame structure.

It should be noted that the principle for the damage-based equivalent intensity of input ground motion does not apply here because the fragilities are functions of the maximum inter-story drift of the first floor. Instead, the effect of cumulative damage, if any, is manifested in the strain levels attained at the monitored locations of the structure.

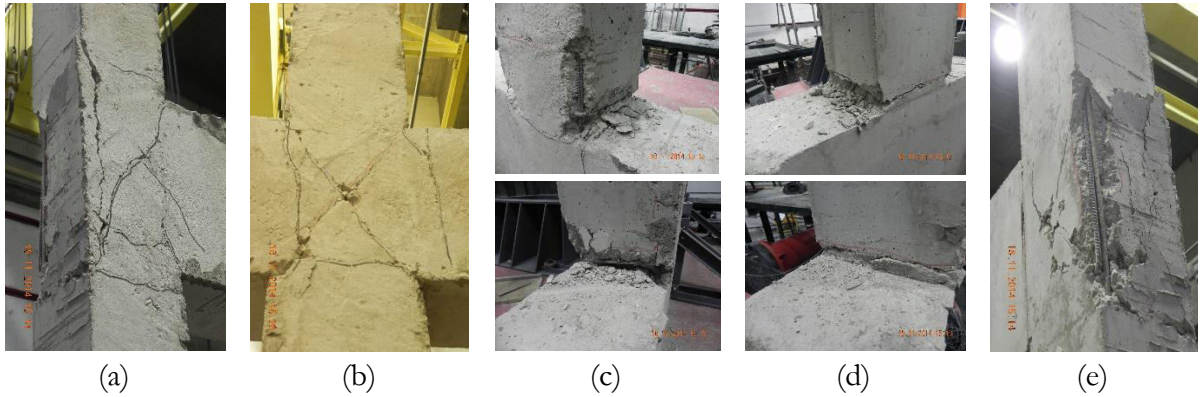


Figure 6-28: (a) Damage of the J6 beam-column joint; (b) damage of the J5 beam-column joint; (c) flexural damage at the base of the middle column (J2); (d) crushing of concrete core at the J1 joint; (e) damage of the J4 beam-column joint (see Figure 6-18 to locate joints)

Table 6-7: Exceedance parameter,  $\epsilon$ , for the observable damage states

Test stages	ISD <sub>max</sub> [mm]	Visual inspection		
		Cracking	Spalling	Crushing
1	7.886	0	0	0
2	15.475	1	0	0
3	27.321	1	0	0
4	42.453	1	1	0
5	48.323	1	1	1

The posterior estimate of the median value of the maximum inter-story drift for the initiation of cracking is larger than that of the analytical fragility curve. Contrarily, the maximum inter-story drift estimate for the initiation of spalling of the cover concrete is reduced. Similarly, the MCMC updating has reduced the inter-story drift for the crushing damage state, as opposed to the ATC-58 approach, which increased the drift value. The characteristics displayed by the MCMC estimates are therefore not consistent with the observations made on the HAZUS damage states. On the other hand, the ATC-58 estimates ( $\theta_1''$ ), both in the HAZUS and strain-based damage states, are larger

than their analytical counterparts.

Table 6-8: Posterior point estimates of observable damage states: MCMC vs ATC-58

	Prior		Posterior						
			MCMC				UT/ATC-58		
Damage	$\theta'_1$ [mm]	$\theta'_2$	AR [%]	$\theta''_1$ [mm]	$\sigma_{\theta''_1}$	$\theta''_2$ [ ]	$\sigma_{\theta''_2}$	$\theta''_1$ [mm]	$\theta''_2$
Cracking	2.7	0.4392	36.27	3.6398	1.199	0.5083	0.0971	4.3	0.4578
Spalling	24.04	0.3829	33.44	21.34	5.171	0.3768	0.0804	27.52	0.3885
Crushing	44.40	0.2738	39.94	42.81	9.225	0.2760	0.0584	44.77	0.2658
Crushing*	44.40	0.2738	40.40	41.32	13.015	0.2823	0.1195	44.57	0.2260

\*: Bayesian updating considering a diffuse prior

During the IDAs, the estimation for crushing of the concrete core was not as reliable as the cracking and spalling damage states. Its analytical fragility curve did not include ground-motion instances that reached the plateau region of the capacity curve before exceeding the crushing-strain limit of the monitored fibers. Therefore, a diffuse prior was also considered taking  $\sigma_{\theta'_1}=\theta'_2$  and doubling the COV of  $\theta'_2$ , i.e.,  $\sigma_{\theta'_2}=0.42$ .

As shown in Figure 6-29, the MCMC estimates shifted according to the weight assigned to the prior distribution. On the other hand, the estimate from the ATC-58 approach has different responses to the POEs above and below the median value. To this end, analytical fragility curves that are derived from a calibrated model, thus a non-diffuse prior, may be suitable with small experimental data.

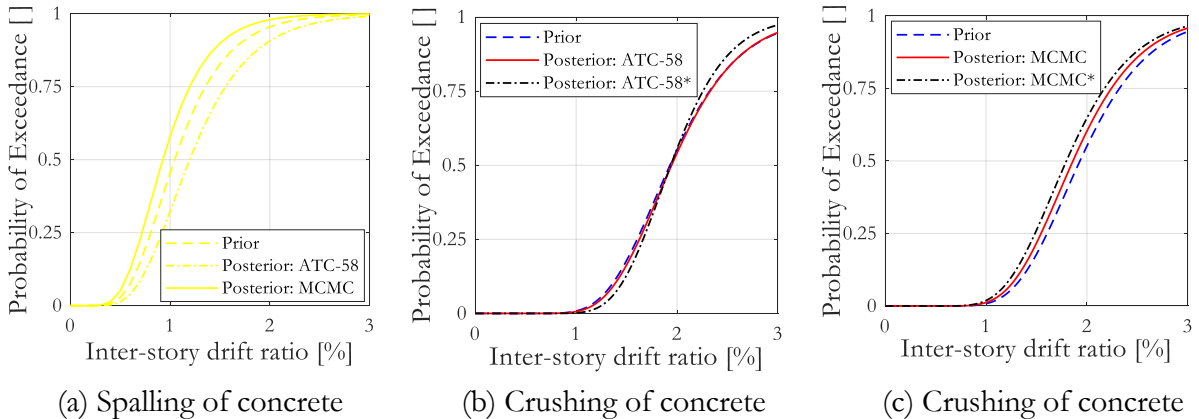


Figure 6-29: Bayesian updating of strain-based damage states

## 6.6 Summary

In this chapter, Bayesian updating of RC fragilities through shaking table tests was discussed in depth. The subject under discussion was presented methodically starting from an introduction to

seismic risk analysis in PBEE and the role of fragility curves in the framework for seismic risk. The simplified ATC-58 approach and the Markov chain Monte Carlo method were explained elaborately. A significant portion of the chapter is dedicated to a parametric analysis aiming at the maximal utilization of a shaking table test output for Bayesian updating.

Incremental dynamic analyses were conducted on a virgin specimen in a stage-wise manner by progressively increasing the intensity of input. The objective of this maximization is to have damage equivalence between an  $n$ -stage *sequential* shaking table test and shaking table tests that are conducted on  $n$  virgin test structures. Damage-based equivalent input intensity for the *sequential* testing is therefore proposed and validated through a parametric analysis. Two RC structures, a cantilever column and a 2D portal frame, were used in this parametric analysis. Through this analysis, the proposed damage-based correction of the intensity measure appears to be more suitable only for RC structures with significant damage levels, i.e., damage index greater than 0.75.

Another important issue in the Bayesian updating process studied in this chapter was the optimum number of shaking table tests that are needed for a minimal bias in estimating the parameters of the posterior distribution. The simulated study conducted on this subject was not able to yield generalized information. Nevertheless, the simulation showed that experimental test outputs should exceed a damage limit state of interest for a realistic updating of its fragility curve. Besides, it was found that the optimum number of experimental tests required may be estimated before experimental testing.

The Bayesian updating proposed was then applied using results from a shaking table test conducted at LNEC on a 2D RC frame. Incremental dynamic analyses were conducted by numerically modeling the test structure to compute its analytical fragility curves. These fragility curves represented the prior distribution. Three damage limit states' descriptions were considered in this study: HAZUS, HRC, and a strain-based damage state. The prior fragilities were then updated through the shaking table test output using both the ATC-58 and MCMC approaches. The MCMC approach, although it comes with a larger computational cost, was found to be a more robust approach that lends pragmatism and flexibility. Its advantage over using the ATC-58 method is perhaps more pronounced in the presence of less reliable, or complex, prior fragilities.

# 7 Conclusions and Future Works

## 7.1 Conclusions

In a nutshell, the research work presented in the last six chapters explored the potential of hybrid simulation and shaking table tests in structural and earthquake engineering. In the literature review of hybrid simulation, a thorough investigation of the current frameworks, time-stepping algorithms, experimental errors, delay compensation methods, control algorithms, and prediction-correction methods for command generation of actuators was conducted. More importantly, a three-loop architecture for hybrid simulation was developed and validated in the scope of this thesis.

Firstly, in support of the parametric studies presented in chapter three, system identification of the uniaxial shaking table, ST1D, was performed. The elastic, hysteretic, and inertial forces of the ST1D were estimated by taking advantage of the periodicity of input signals. The output-input frequency response function of the ST1D was determined using a noise input signal. Finally, a constrained nonlinear least-square optimization algorithm was adopted in estimating the parameters of the ST1D by combining the output-input FRF, the closed-form equation of the uniaxial shaking table and the estimated forces. The identification was conducted systematically whereby the dynamics of the ST1D was first identified for bare shaking table conditions and then extended in determining the system dynamics of the shaking table when it is rigidly attached to a SDOF structure. Therefore, the characteristics of the ST1D can be easily obtained for any payload without performing additional characterization tests.

Secondly, the virtual (also known as simulated) hybrid testing approach was taken to explore some of the important aspects of hybrid simulation, because this approach is flexible and economically viable for conducting parametric studies. After introducing the principles and software frameworks for virtual hybrid simulation, three different applications were proposed. In the first application, it was used in choosing time-stepping algorithms and their parameters, considering a moment resisting steel frame, by introducing the Energy Error Indicator (EEI) criteria. From these studies, it was concluded that the  $\alpha$ -OS scheme, explicit and unconditionally stable for softening systems, has superior performance for fast and real-time hybrid simulations. Nevertheless, error accumulation, particularly during collapse simulation, may require iterative methods, such as the NMHS. In the latter, 5-10 iterations have proven computational efficiency.

In the second application, a simplified approach for conducting stability analysis of hybrid simulation, in the frequency domain, was proposed using Routh's stability criterion. It explored the influence of the properties of the physical substructure in the stability of a hybrid test. This work was carried out on a hypothetical test setup using the ST1D model; hence, the ST1D's transfer function (including a SDOF experimental substructure) was adopted. Taking a SDOF reference

structure and by changing the partitioning of its structural properties, a stability contour was developed. This partitioning refers to the percentages of mass, damping, and stiffness of the SDOF reference structure assigned to the physical and numerical substructures. The stability contours obtained in the frequency-domain were then validated in the time-domain. In this validation work, the time-domain results were found to be in good agreement with the frequency-domain estimates.

The initial work, which was performed on linear-elastic structures, was extended to include inelastic SDOF systems through the nonlinear Bouc-Wen hysteretic model in MATLAB/Simulink program. Its validation was again successful. Besides, the inelastic structure has shown improved stability margins compared to the elastic counterparts. The increased energy dissipation of nonlinear systems explains this observation.

In the past, reliability and sensitivity studies in hybrid tests were carried out using the PCE surrogate modeling technique. These studies were envisioned to assist in designing reliable and representative hybrid experiments. They can also be adopted for estimating failure probabilities of structures and components which can be useful for developing reliability guidelines in design codes. In this work, the M-DRM approach, in combination with the maximum entropy principle, was proposed and implemented using the OpenSees-OpenFresco framework for virtual hybrid testing. First, numerical studies were carried out and the potential of the proposed technique was examined thoroughly. Then, it was validated using actual hybrid tests.

The proposed technique employs the Gauss-quadrature integration rule to effectively reduce the number of hybrid tests needed while evaluating global sensitivity indices. Before applying it to case studies, the optimum number of integration points (or Gauss order), which is directly proportional to the number of hybrid simulation tests needed, was investigated numerically using a steel MRF structure. In this study, 5-7 integration points were found to be adequate. The number of model evaluations can therefore be significantly reduced compared to other expensive methods, such as the Monte Carlo method, thus fulfilling the prime goal of this work — reducing the number of hybrid tests required for a sensitivity evaluation. The reliability studies that were performed in conjunction with the M-DRM method combine the principles of fractional moments and maximum entropy. Here, a MATLAB program was developed to execute a two-step process in minimizing an objective function necessary for estimating the full probabilistic distribution of a structural response from a handful of experiments (hybrid tests). Overall, promising results were obtained by comparing the outcomes of the proposed method with the results obtained from the Monte Carlo simulation.

The outcomes of hybrid experiments, previously performed, were finally adopted to validate the proposed approach. During this validation, a slight modification was made to the conventional method of calculating the cut-off functions in the M-DRM technique, meaning they were estimated by interpolating responses from a surrogate PCE model of the problem. The global sensitivity indices obtained from the proposed method agree well with the estimates of the PCE method. The same is true for the reliability output of the two approaches. Therefore, the proposed technique can

be regarded as an effective approach for reducing the computational cost of including experimental methods for sensitivity and reliability analysis.

In chapter four, a three-loop architecture software framework for hybrid simulation, termed *LNEC-HS*, was conceived and developed to incorporate two different schemes. The first scheme uses the OpenFresco framework as a middleware, hence corresponds to a middleware-based scheme. It was implemented as a state-machine software using LabVIEW programming. The software was designed to be flexible and modular so that the future extension of the framework becomes easy. This scheme was programmed to effectively communicate with the numerical substructure through TCP/IP socket using the *LNTCP* program. The functionalities of the simulation coordinator enable the software to synchronously handle network communication, command generation, and error compensation. Displacement commands to actuators are continuously generated through extrapolation-interpolation methods using Lagrange polynomials. Since the extrapolation-interpolation methods that use only past displacements may aggravate the stability conditions of hybrid tests, interpolation algorithms including the last-predicted displacement as well as extrapolation-interpolation algorithms which use velocities were implemented. The adaptive time-series (ATS) technique for delay compensation, implemented in the control block of the simulation coordinator, is responsible for compensating errors in the control process. The simulation coordinator communicates, seamlessly, with the PID controller of the framework that is deployed at the FPGA module of the control hardware.

On the other hand, the second scheme was implemented, without a middleware, by inheriting all the working principles of the first scheme. It uses a simple numerical solver inside LabVIEW, thus obliterating the need for a TCP/IP network. This scheme was developed in light of improving the speed limitation of the first scheme but, most importantly, to build a framework for hybrid simulation suitable for conducting soil-structure interaction tests.

Finally, *LNEC-HS* software was validated by conducting hybrid tests of a one-story two-bay steel moment-resisting frame whereby one of its outer columns was physically modeled in a test rig that uses the ST1D as an actuator. Before conducting the hybrid test, the initial stiffness of the test specimen was estimated from dynamic identification tests, and the initial coefficients of the ATS compensator were determined from a second-order estimator using the response of the ST1D to noise input. During the *open-loop* hybrid tests, small gaps at connections of the test rig were identified and effectively reduced. In the actual hybrid test, an important overshooting error of the controller was observed, and higher-mode excitation was identified, but the overall performance of the hybrid test was reasonable compared to its numerical counterpart. Thus, the capability of *LNEC-HS* software in performing a hybrid test was demonstrated.

Furthermore, the middleware-free scheme of *LNEC-HS* requires advanced control strategies, namely acceleration tracking of a shaking table and force-based control of actuators. Hence, model-based feedforward-feedback control and an added compliance scheme for model-based equivalent force control were investigated in chapter four. The LQG feedback-control, together with a

modified feedforward control, was implemented for tracking the shaking table acceleration. Afterwards, the control algorithm was examined using LabVIEW as a simulation program, considering a two-story shear building that is rigidly attached to a uniaxial shaking table. The robustness of the implemented algorithm and the tuning parameters were explored in this numerical study. Besides, model deviations due to the nonlinearities of a test specimen were also addressed. Overall, the feedforward-feedback controller has shown good performance, but the difficulties in tuning its parameters were highlighted in this study.

Likewise, the adequacy of the added compliance approach for the equivalent force control, which uses the Smith predictor compensation, was studied. First, the frequency response of the controller was examined in a parametric study. Following the implementation of the controller in MATLAB/Simulink, the dynamic analysis of a two-story shear building was conducted for a suite of ground motions. The importance of using the Smith predictor compensation as well as its sensitivity to errors in modeling the test structure and to experimental errors, such as the time-delay of an actuator, were explored. These studies disclosed that this control approach could lead to potential errors when applied to lightly damped structures. Besides, the stiffness of the compliance spring must be chosen accounting for the stroke capacity of the actuator. Hence, there exists a tradeoff between the accuracy of the force control and the stroke capacity. In the end, the implementation of an adaptive method for force control, that takes advantage of the ATS compensator, was addressed because it can adaptively track the nonlinearities of a loading system and a test specimen. These qualities cannot be achieved using the Smith Predictor compensation.

In chapter five, a brief literature review of soil-structure interaction, including its numerical modeling, was presented. This study was focused on simplified numerical methods for modeling SSI such as the BNWF method and the macro-element methods since they are suitable for performing rapid hybrid testing. In the past, an extensive calibration of the BNWF model was performed, which is discussed here, and somewhat linked to this study. Besides, a literature review of some important soil-structure interaction experimental studies was conducted so as hybrid tests can benefit from techniques applied in 1g shaking table and centrifuge tests. These techniques include the preparation of soil fill as well as ESB container during an experiment.

The principle of splitting a dynamic load in substructuring tests, where the experimental setup includes a shaking table and an additional actuator, was discussed and the influence of a soil container in modeling the boundary of a soil medium was briefly addressed. The transfer function of a system comprising a soil-filled equivalent shear beam container, rigidly attached to the ST1D, was derived by combining the transfer function of the bare ST1D and an equivalent SDOF that represents the characteristics of the soil-filled ESB. This transfer function can be readily used in the model-based controllers that were developed in the scope of the thesis.

Later in this chapter, rehearsal tests for SSI in hybrid simulation were conducted. These simulated tests were envisioned for rehearsing actual hybrid experiments as well as for designing experiments. The rehearsal test was conducted on a bridge case study that was damaged during the Northridge

earthquake, 1940. It was implemented by taking advantage of the finite element coupling approach integrated into the OpenSees-OpenFresco framework. Hence, the numerical and physical substructures were implemented and analyzed in the OpenSees software by modeling the SSI effects using the BNWF model. In this work, the response of the bridge was explored considering different classes of soil foundation to demonstrate the capability of such rehearsal testing in designing experiments. In summary, this study showed that rehearsal tests during SSI hybrid testing can be valuable to gain control over the test parameters before an actual experiment. Furthermore, they can serve as a guide in designing such experiments to achieve outcomes of interest.

Towards the end of chapter five, the implementation of SSI hybrid testing through the middleware-free scheme of *LNEC-HS* was investigated. The substructuring scheme a two-shear building and the test setup envisaged for the SSI hybrid test were explained. The test setup includes LNEC's ESB container, dry sand and the first story of the shear building. The physical substructure was idealized as a series of linear and nonlinear springs, and the system model was derived. First, using this system model, the amplification of input ground motion, that was applied at the base of the ESB container, when reaching the foundation level was estimated. Second, the whole hybrid test was modeled using MATLAB/Simulink and the response of the structure was simulated under the Kobe (1995) earthquake. The outcome of this simulated hybrid test reveals a soft-story mechanism of the structure thus making the middleware-free scheme of *LNEC-HS* adequate for conducting such a hybrid test because it was developed assuming the numerical substructure remains elastic throughout the response simulation.

As mentioned earlier, the main objective of this research work is to build a reliable and economical framework for the dynamic testing of structures using hybrid simulation. Nevertheless, and without loss of generality, the optimal utilization of all types of experimental tests fall in the same context of the maximization of the output and value of information resulting from those tests. Therefore, in chapter six, Bayesian updating of RC fragility curves through shaking table tests was explored through the ATC-58 and Markov-Chain Monte Carlo (MCMC) approaches. After discussing the implications of updating fragility curves in the global framework of seismic risk assessment, the principles of Bayesian updating using the Unscented Transformation, which is the basis for the ATC-58 approach, and the MCMC were presented. Some precautions that are necessary for a successful MCMC updating process, as well as the data post-processing required after performing the Metropolis-Hastings algorithm, were elaborated with examples.

Firstly, the concept of maximal utilization of the output from shaking table tests was investigated. Its main goal is to convert shaking table tests of a single test specimen, conducted in  $n$  sequential stages, to  $n$  equivalent shaking table tests that are conducted using  $n$  similar and undamaged (virgin) test specimens. In this work, this equivalence was carried out by relating the damage index (DI) and the ground motion intensity ( $Sa(T_i)$ ) and, consequently, a correction to the intensity measure,  $Sa(T_i)$ , was proposed to account for the damage accumulation in sequential shaking table tests. This correction factor was studied numerically by conducting dynamic analyses of cantilever column and

portal frame RC structures subjected to a suite of ground motions. The parametric study, which was intended to validate the proposed scheme, revealed that the approach is suitable in the presence of significant damage of a structure, typically for DI above 0.75. Besides, the dispersion of the proposed scheme increases as structures gets more complex.

Secondly, two important questions which are important for a pragmatic updating of fragility curves were investigated. The influence, in the outcome of the Bayesian updating, due to the exceedance of an  $i$ th damage state ( $DS_i$ ) during experimental tests was the first addressed in a small parametric study. Even though this study is not exhaustive, it showed that the exceedance of a particular damage state is important for the convergence of its posterior estimates. The second question is related to the optimal number (or stages) of shaking table tests for a reliable Bayesian updating, which was again investigated in a small parametric simulation. The outcome of this study has minor inconsistencies in the lower DSs; nonetheless, provided that all damage states are exceeded, it showed that a minimum number of 10 experimental tests may be adequate. This finding is more conservative compared to the ATC-58 recommendation (at least 6 experimental tests).

Finally, the proposed approach was implemented in a 2D RC frame case study. Incremental dynamic analysis of the structure was conducted to generate its fragility curves. These analytical fragility curves serve as priors to the Bayesian updating framework. Subsequently, these fragility curves were updated through real shaking table test results of the case study structure. The Bayesian updating work, both using the ATC-58 and MCMC, was carried out using the maximum lateral displacement (drift) recorded by sensors during the shaking table test. Furthermore, three damage models, namely the HAZUS, HRC, and strain-based (physical) damage states, were considered to examine the updating process across a range of guidelines. In most cases, the ATC-58 approach resulted in a less fragile estimate compared to the MCMC approach. Besides, in the presence of a less reliable prior distribution (diffuse prior) or complex prior distribution, the MCMC technique may be more robust compared to the ATC-58 method.

## 7.2 Future works

In the current research, a software framework, the middleware-based scheme of *LNEC-HS*, was developed and validated using hybrid tests on a moment-resisting steel frame. Besides, a faster middleware-free scheme was developed, integral to *LNEC-HS*, to support soil-structure interaction tests in hybrid simulation. The latter was somehow validated in a simulated hybrid simulation and its application to actual hybrid testing is ongoing in a new research project. Furthermore, several topics were explored and discussed in the context of dynamic testing of structures; and some of the explored areas can be developed further in the future. Thus, some of the envisioned future works are discussed below:

- ❖ When examining the choice of time-stepping algorithms and their parameters for hybrid simulation tests, a limited parametric study was conducted. However, a more exhaustive

numerical study must be done to fully understand the robustness of time-stepping algorithms to errors during hybrid testing. This parametric study would include the variability in structure type, level of structural damage, damping characteristics, ground motion input, and the nature of experimental errors. A selected outcome of the numerical study may then be validated using hybrid experiments.

- ☒ Combining the principles of maximum entropy and fractional moments, derived from the M-DRM technique, the full probabilistic description of a response function can be accurately reproduced by solving an optimization problem. However, the objective function is non-convex and noncontinuous, thus making the efficient solution to the optimization problem difficult. Hence, more efficient algorithms may need to be considered in the future. Besides, a robust algorithm needs to optimize the number of fractional moments, that are used in the estimation process. The Genetic algorithm, in combination with the Akaike Information Criterion (AIC), is perhaps a candidate scheme.
- ☒ The software framework, *LNEC-HS*, developed in the scope of this thesis promotes ease for its future extension. Currently, the middleware-based scheme of this software has a two-point control, i.e., one control parameter and two response parameters are transmitted to-and-fro between the control software and the OpenFresco framework. However, future applications may require hybrid tests with more than one control parameter, for example in multi-axial testing. Therefore, the extension of this two-point control to a four-point control, and even to user-defined control points, is a future task.
- ☒ The LQG feedback controller, implemented herein, was examined in a numerical study, but the validation of this controller in actual shaking table experiments (or in a hybrid test involving the acceleration tracking of a shaking table) could be valuable. These experimental tests can be used to examine the adequacy of the tuning parameters adopted during the numerical study.
- ☒ In this work, the performance of the equivalent force control approach, with and without the presence of the Smith predictor compensator, was examined analytically; hence, results obtained from this numerical study need to be verified in experimental tests. These experimental tests may be used in estimating the loss in force at the connection between an actuator and a compliance spring. The same experimental tests could also be used to examine the ATS-based equivalent force controller and to perform a comparison between the adaptive and non-adaptive compensators which is valuable for future experiments.
- ☒ The coupling between a shaking table and an auxiliary actuator in SSI hybrid testing can be investigated in the future through low-excitation experimental tests. The merits of synchronizing their controllers can also be explored at the same time.
- ☒ In general, the speed of a hybrid test that is conducted using the OpenFresco middleware

is limited due to the TCP/IP latency. The middleware-free scheme, where two degrees of freedom are controlled in the physical substructure, was therefore implemented in *LNEC-HS* software to improve the speed of execution of hybrid tests and as it is suitable to problems such as soil-structure interaction. Nevertheless, it has certain limitations because LabVIEW programming does not offer computational resources that are geared towards finite-element modeling. Consequently, the numerical solver is limited to linear-elastic numerical substructures. Hence, a numerical program capable of simulating the nonlinear response of the numerical substructure needs to be integrated into the software framework, without imposing significant speed limitations. A candidate method may be developed using MATLAB programming which interacts with the LabVIEW-based control and coordination software through dynamic link libraries (dlls). For example, the Model Interface Toolkit (MIT) provides a method for creating a LabVIEW-based user interface for a Simulink model. It converts the Simulink model into a dynamic link library allowing the model to run in a real-time target. The Simulink model could be then designed to execute MATLAB functions that are responsible for solving the nonlinear response of the numerical substructure.

- ☒ In the MCMC approach for Bayesian updating, the coefficient of variation of the prior distribution was taken to be 0.21. This value was adopted from the ATC-58 recommendation, due to the lack of any other experimental data. Validation of this information from experimental data needs to be addressed in the future. This validation is particularly important to the fidelity of the ATC-58 estimates as opposed to the MCMC technique since the latter can be more robust to the complexity and variance of the prior distribution provided that adequate experimental data is available.
- ☒ The Bayesian updating of the strain-based fragility curves of the 2D RC frame case study had challenges since the analytical fragilities were derived from a few locations, i.e., only strains at critical locations of the frame were monitored; hence, a more rigorous approach may be necessary to avoid any bias. Furthermore, rectifying the subjectivity of defining the exceedance criteria from observed damage is also part of future works.
- ☒ In direct continuation to the work done on the Bayesian updating of RC fragility curves, its application to the global seismic risk assessment is the next step. In future works, the impact of Bayesian updating in the framework for seismic risk assessment needs to be evaluated. Before doing so, however, the representativeness of the test specimens, during shaking table tests, to the building set used for deriving the analytical fragilities needs to be investigated. The same applies to the representativeness of the ground motion set used in the experimental tests.

---

References

---

- Abbiati, G., Marelli, S., Bursi, O. S., Sudret, B., & Stojadinovic, B. (2015). Uncertainty Propagation and Global Sensitivity Analysis in Hybrid Simulation using Polynomial Chaos Expansion. *Fourth International Conference on Soft Computing Technology in Civil, Structural and Environmental Engineering*, Stirlingshire, Scotland.
- Abbiati, G., Marelli, S., Tsokanas, N., Sudret, B., & Stojadinović, B. (2021). A global sensitivity analysis framework for hybrid simulation. *Mechanical Systems and Signal Processing*, 146, 106997. <https://doi.org/10.1016/j.ymssp.2020.106997>
- Abrahamson, N. (2006). Seismic hazard assessment: problems with current practice and future developments. *First European Conference on Earthquake Engineering and Seismology*, Geneva, Switzerland.
- Abramowitz, M., & Stegun, I. A. (1972). *Handbook of Mathematical Functions with Formulas, Graphs, and Mathematical Tables*. Dover publications, Washington, D.C, USA.
- Ahmadianeh, M., & Mosqueda, G. (2008). Hybrid simulation with improved operator-splitting integration using experimental tangent stiffness matrix estimation. *Journal of Structural Engineering*, 134(12), 1829–1838.
- Ahmadianeh, M., & Mosqueda, G. (2009). Online energy-based error indicator for the assessment of numerical and experimental errors in a hybrid simulation. *Engineering Structures*, 31(9), 1987–1996.
- Anagnost, J. J., & Desoer, C. A. (1991). An elementary proof of the Routh-Hurwitz stability criterion. *Circuits Systems and Signal Processing*, 10(1), 101–114.
- Applied Technology Council [ATC-40]. (1996). *Seismic Evaluation and Retrofit of Concrete Buildings*. Volume 1, Report No. SSC 96-01, California, USA.
- Astrom, K. J., & Bjorn, W. (1986). *Computer Controlled Systems: Theory and Design*. 3rd Edition, Prentice Hall, China.
- Baber, T. T., & Noori, M. N. (1985). Random vibration of degrading, pinching systems. *Journal of Engineering Mechanics*, 111(8), 1010–1026.
- Bairrao, R., & Severn., R. (2007). *Experiences under ECOLEADER — European Consortium of Laboratories for Earthquake and Dynamic Experimental Research*. ISBN 972-49-1972-2, 2007, CASCADE report, n.8.
- Baker, J. W., Gokkaya, B. U., & Deierlein, G. G. (2015). Illustrating a Bayesian approach to seismic collapse risk assessment. *12th International Conference on Applications of Statistics and Probability in Civil Engineering, ICASP 2015*, Vancouver, Canada.
- Balomenos, G. P., & Pandey, M. D. (2016). Finite element reliability and sensitivity analysis of structures using the multiplicative dimensional reduction method. *Structure and Infrastructure Engineering*, 12(12), 1553–1565.

- Behrouz Forouzan A. (2010). *TCP/IP Protocol Suite, 4th ed.* McGraw-Hill, Lisbon, Portugal.
- Berveiller, M., Sudret, B., & Lemaire, M. (2006). Stochastic finite element: A non intrusive approach by regression. *European Journal of Computational Mechanics*, 15(1–3), 81–92.
- Biasio, M. De. (2016). *Ground motion intensity measures for seismic probabilistic risk analysis.* Ph.D. thesis, Université de Grenoble, France.
- Bonelli, A., & Bursi, O. S. (2004). Generalized- $\alpha$  methods for seismic structural testing. *Earthquake Engineering and Structural Dynamics*, 33(10), 1067–1102.
- Boore, D. M. (2002). Effect of baseline corrections on displacements and response spectra for several recordings of the 1999 Chi-Chi, Taiwan, earthquake. *Bulletin of the Seismological Society of America*, 91(5), 1199–1211.
- Boore, D. M., Stephens, C. D., & Joyner, W. B. (2002). Comments on baseline correction of digital strong-motion data: Examples from the 1999 Hector Mine, California, earthquake. *Bulletin of the Seismological Society of America*, 92(4), 1543–1560.
- Boulanger, B. R. W., Curras, C. J., Member, S., Kutter, B. L., Wilson, D. W., Member, A., & Abghari, A. (1999). Seismic soil-pile-structure interaction experiments and analyses. *Journal of Geotechnical and Geoenvironmental Engineering*, 125(9), 750–759.
- Bousias, S. N. (2014). Seismic Hybrid Simulation of Stiff Structures : Overview and Current Advances. *Journal of Structures*, 2014, 1–8.
- Broderick, B. M., & Elnashai, A. S. (1995). Analysis of the failure of interstate 10 freeway ramp during the Northridge earthquake of 17 January 1994. *Earthquake Engineering & Structural Dynamics*, 24(2), 189–208.
- Bursi, O. S., & Wagg, D. (2008). *Modern Testing Techniques for Structural Systems Dynamics and Control.* CISM Courses and Lectures, Vol. 502, Springer, New York, USA.
- Carrion, J. E., & Spencer, B. F. (2007). *Model-based Strategies for Real-time Hybrid Testing, NSEL Report Series, Report No. NSEL-006, Department of Civil and Environmental Engineering, University of Illinois at Urbana-Champaign, USA.*
- Carrion, J. E., Spencer , B. F., & Phillips, B. M. (2009). Real-time hybrid simulation for structural control performance assessment. *Earthquake Engineering & Engineering Vibration*, 8(4), 481–492.
- Carvalho, A. T., Bilé Serra, J., Oliveira, F., Morais, P., Ribeiro, A. R., & Santos Pereira, C. (2010). Dynamic soil container and sand pluviator for 1g seismic load tests on anchored retaining wall. *7th International Conference on Physical Modelling in Geotechnics (ICPMG 2010)*, Zurich, Switzerland.
- Caterino, N., Azmoodeh, B. M., & Manfredi, G. (2018). Seismic Risk Mitigation for a Portfolio of Reinforced Concrete Frame Buildings through Optimal Allocation of a Limited Budget. *Advances in Civil Engineering*, <https://doi.org/10.1155/2018/8184756>.
- CEA. (2000). *Icons European Program: Seismic tests on R/C walls with uplift, CAMUS-4 Specimen.* ISEMT/EMSI/RT/00-027, Commissariat à l'Energie Atomique, Saclay, France.
- Chae, Y., Karim, K., & Ricles, J. M. (2013). Adaptive time series compensator for delay

- compensation of servo-hydraulic actuator systems for real-time hybrid simulation. *Earthquake Engineering & Structural Dynamics*, 42(11), 1697–1715.
- Chae, Y., Rabiee, R., Dursun, A., & Kim, C. Y. (2018). Real-time force control for servo-hydraulic actuator systems using adaptive time series compensator and compliance springs. *Earthquake Engineering and Structural Dynamics*, 47(4), 854–871.
- Chang, B., Raychowdhury, P., Hutchinson, T., Thomas, J., Gajan, S., & Kutter, B. (2007). Frame-Wall-Foundation Structural Systems Through Centrifuge Testing. *4th International Conference on Earthquake Geotechnical Engineering*, Thessaloniki, Greece.
- Chang, M., & Kim, J. K. (2019). Pseudo-dynamic Test for Soil-Structure Interaction Analysis using Shake Tables. *KSCE Journal of Civil Engineering*, 23, 2313–2323. <https://doi.org/10.1007/s12205-019-1631-8>
- Chang, S. Y. (1997). Improved numerical dissipation for explicit methods in pseudo-dynamic tests. *Earthquake Engineering and Structural Dynamics*, 26(9), 917–929.
- Chatzigogos, C. (2007). *Comportement sismique des fondations superficielles : vers la prise en compte d'un critère de performance dans la conception*. Ph.D. thesis, L'école Polytechnique, France.
- Chatzigogos, C. T., Figini, R., Pecker, A., & Salençon, J. (2010). A macroelement formulation for shallow foundations on cohesive and frictional soils. *International Journal for Numerical and Analytical Methods in Geomechanics*, 35(8), 902–931.
- Chatzigogos, C. T., Pecker, A., & Salençon, J. (2009). Macroelement modeling of shallow foundations. *Soil Dynamics and Earthquake Engineering*, 29(5), 765–781.
- Chatzigogos, Charisis T., Alain, P., Yilmaz, M. T., & Dietz, M. (2011). Pseudo-dynamic test techniques with SSI. *Seismic Engineering Research Infrastructures for European Synergies (SERIES)*, Workpackage WP14 – JRA3, Deliverable D14.1.
- Chen, C., & Ricles, J. M. (2010). Tracking Error-Based Servohydraulic Actuator Adaptive Compensation for Real-Time Hybrid Simulation. *Journal of Structural Engineering*, 136(4), 432–440.
- Chen, C., & Ricles, J. M. (2012). Analysis of implicit HHT- $\alpha$  integration algorithm for real-time hybrid simulation. *Earthquake Engineering & Structural Dynamics*, 41(11), 1021–1041.
- Chen, C., & Ricles, J. M. (2009). Servo-Hydraulic Actuator Control for Real-Time Hybrid Simulation. *American Control Conference*, St. Louis, Missouri, USA.
- Chen, C., Ricles, J. M., Hodgson, I. C., & Sause, R. (2008). Real-Time Multi-Directional Hybrid Simulation of Building Piping Systems. *14th World Conference on Earthquake Engineering*, Beijing, China.
- Chen, C., Ricles, J. M., Marullo, T. M., & Mercan, O. (2009). Real-time hybrid testing using the unconditionally stable explicit CR integration algorithm. *Earthquake Engineering & Structural Dynamics*, 38(2009), 23–44.
- Chopra, A. K. (2012). *Dynamics of Structures: Theory and Applications to Earthquake Engineering*. 4th

- Edition, Prentice Hall, New York.
- Choudhury, T., & Kaushik, H. B. (2018). Component Level Fragility Estimation for Vertically Irregular Reinforced Concrete Frames. *Journal of Earthquake Engineering*, 24(6), 1–25.
- Chowdhury, R., Rao, B. N., & Prasad, M. A. (2009). High-dimensional model representation for structural reliability analysis. *Communications in Numerical Methods in Engineering*, 25(4), 301–337.
- Chung, J., & Hulbert, G. M. (1993). A time integration algorithm for structural dynamics with improved numerical dissipation: The generalized- $\alpha$  method. *Journal of Applied Mechanics, Transactions ASME*, 60(2), 371–375.
- Coelho, E., Campos-Costa, A., & Carvalho, E. (2000). Assessment of experimental seismic response through damage evaluation. *Proceedings of 12th World Earthquake Conference*, Auckland, New Zealand.
- Combescure, D., & Chaudat, T. (2000). *Icons European program seismic tests on R/C walls with uplift; CAMUS IV specimen*. ICONS Project, CEA/DRN/DMT Report, SEMT/EMSI/RT/00-27/4.
- Combescure, D., & Pegon, P. (1997).  $\alpha$ -Operator Splitting time integration technique for pseudodynamic testing. Error propagation analysis. *Soil Dynamics and Earthquake Engineering*, 16(7–8), 427–443.
- Conte, J., & Trombetti, T. (2000). Linear dynamic modeling of a uni-axial servo-hydraulic shaking. *Earthquake Engineering & Structural Dynamics*, 29(9), 1375–1404.
- Correia, A.A., & Paolucci, R. (2021). A 3D coupled nonlinear shallow foundation macro-element for seismic soil-structure interaction analysis. *Earthquake Engineering and Structural Dynamics (Submitted)*.
- Correia, António Araújo. (2011). *a Pile-Head Macro-Element Approach To Seismic Design of Extended Pile-Shaft-Supported Bridges*. Ph.D. thesis, Civil Engineering, Università degli Studi di Pavia, Italy.
- Correia, António Araújo, Costa, A. C., & Candeias, P. (2015). Towards real-time hybrid testing of RC frames with masonry infills. *EU-US-Asia Workshop on Hybrid Testing*, JRC, Ispra, Italy.
- Cremer, C., Pecker, A., & Davenne, L. (2002). Modelling of nonlinear dynamic behaviour of a shallow strip foundation with macro-element. *Journal of Earthquake Engineering*, 6(2), 175–211.
- Cremer, C. (2001). *Modélisation du comportement non linéaire des fondations superficielles sous séisme*. Ph.D. thesis, Laboratoire de Mécanique et de Technologie, France.
- Cremer, Cécile, Pecker, A., & Davenne, L. (2001). Cyclic macro-element for soil-structure interaction: Material and geometrical non-linearities. *International Journal for Numerical and Analytical Methods in Geomechanics*, 25(13), 1257–1284.
- Darby, A. P., Blakeborough, A., & Williams, M. S. (2001). Improved control algorithm for real-time substructure testing. *Earthquake Engineering & Structural Dynamics*, 30(3), 431–448.
- Darby, A. P., Williams, M. S., & Blakeborough, A. (2002). Stability and delay compensation for real-time substructure testing. *Journal of Engineering Mechanics*, 128(12), 1276–1284.

- Dermitzakis, S. N., & Mahin, S. A. (1985). Development of substructuring techniques for on-line computer controlled seismic performance testing. *UCB/EERC-85/04 Report to NSF*, University of California, Berkeley, USA.
- Dietz, M., Tang, Z., Taylor, C. A., & Li, Z. (2015). Substructuring for Soil Structure Interaction using a Shaking Table. *Geotechnical, Geological and Earthquake Engineering*, 35, 141–158.
- Dimitrios, L. (2012). *Sidesway collapse of deteriorating structural systems under seismic excitations*. Ph.D. thesis, Stanford University, USA.
- Dong, B. (2015). *Large-scale experimental, numerical, and design studies of steel MRF structures with nonlinear viscous dampers under seismic loading*. Ph.D. thesis, Lehigh University, USA.
- Duque, J., & Bairrao, R. (2000). LNEC Experiences and Strategies in Earthquake Simulation. Recent Developments. *12th World Conference on Earthquake Engineering*, Auckland, New Zealand.
- Dyke, S. J., Spencer, B. F., Quast, P., & Sain, M. K. (1995). Role of control-structure interaction in protective system design. *Journal of Engineering Mechanics*, 121(2), 322–338.
- Ebenbauer, C., & Allgöwer, F. (2006). Stability Analysis for Time-Delay Systems using Rekasius's Substitution and Sum of Squares. *IEEE Conference on Decision and Control*, New Orleans, LA, USA.
- EC8 – Part 1. (2004). *Eurocode 8: Design of structures for earthquake resistance – Part 1: General rules, seismic actions and rules for buildings*. prEN 1998-1:2004, European Committee for Standardization (CEN), Belgium.
- EC8 – Part 5. (2004). *Eurocode 8: Design of structures for earthquake resistance – Part 5: Foundations, retaining structures and geotechnical aspects*. prEN 1998-1:2004, European Committee for Standardization (CEN), Belgium.
- Efron, B., & Stein, C. (1981). The Jackknife estimate of variance. *The Annals of Statistics*, 9(3), 586–596.
- Elkhorabi, T., & Mosalam, K. M. (2007). Towards error-free hybrid simulation using mixed variables. *Earthquake Engineering & Structural Dynamics*, 36(11), 1497–1522.
- Faccioli, E., Vanini, M., & Paolucci, R. (1998). *TRISEE: 3D site effects and soil-foundation interaction in earthquake and vibration risk evaluation*. Technical report. <http://www.crs4.it/trisee>
- FEMA. (2001). Earthquake Loss Estimation Methodology, technical manual, Hazus-MH 2.1. *Prepared by the American Society of Civil Engineers for the Federal Emergency Management Agency*, Washington, USA.
- Fenves, G. L., Mckenna, F., Scott, M. H., & Takahashi, Y. (2004). An Object-Oriented Software Environment for Collaborative Network Simulation. *13th World Conference on Earthquake Engineering*, Vancouver, British Columbia, Canada.
- Fernandois, G. A., & Spencer, B. F. (2017). Model-based framework for multi-axial real-time hybrid simulation testing. *Earthquake Engineering and Engineering Vibration*, 16(4), 671–691.
- Figini, R., Paolucci, R., & Chatzigogos, C. T. (2012). Measuring bias in structural response caused

- by ground motion scaling. *Earthquake Engineering and Structural Dynamics*, 41(3), 475–493.
- Filiatrault, A., Leger, P., & R., T. (1994). On the computation of seismic energy in inelastic structures. *Engineering Structures*, 16(6), 425–436.
- Forouzan, B., Shaloudegi, K., & Nakata, N. (2017). Force-Based Hybrid Simulation : Concept, Numerical Algorithm and Experimental Verification. *The 13th International Workshop on Advanced Smart Materials and Smart Structures Technology*, Tokyo, Japan.
- Friedman, A., Dyke, S. J., Phillips, B., Ahn, R., Dong, B., Chae, Y., Castaneda, N., Jiang, Z., Zhang, J., Cha, Y., Ozdagli, A. I., Spencer, B. F., Ricles, J., Christenson, R., Agrawal, A., & Sause, R. (2015). Large-Scale Real-Time Hybrid Simulation for Evaluation of Advanced Damping System Performance. *Journal of Structural Engineering*, 141(6), 04014150.
- Gajan, S., & Kutter, B. L. (2007). A contact interface model for nonlinear cyclic moment-rotation behavior of shallow foundations. *4th International Conference on Earthquake Geotechnical Engineering*, Thessaloniki, Greece.
- Gajan, S., Phalen, J., & Kutter, B. (2003a). Soil–foundation–structure interaction: shallow foundations. Centrifuge Data Report for SSG03. *Report Number: UCD/CGMDR-03/02*, University of California, Davis, CA, USA.
- Gajan, S., Phalen, J., & Kutter, B. (2003b). Soil–foundation structure interaction: shallow foundations. Centrifuge Data Report for SSG02. *Report Number: UCD/CGMDR-03/01*, University of California, Davis, CA, USA.
- Gajan, Sivapalan, Kutter, B. L., Phalen, J. D., Hutchinson, T. C., & Martin, G. R. (2005). Centrifuge modeling of load-deformation behavior of rocking shallow foundations. *Soil Dynamics and Earthquake Engineering*, 25(7–10), 773–783.
- Gao, X., Castaneda, N., & Dyke, S. J. (2013). Real time hybrid simulation: from dynamic system, motion control to experimental error. *Earthquake Engineering & Structural Dynamics*, 42(6), 815–832.
- Gazetas, B. G. (1991). Formulas and charts for impedances of surface and embedded foundations. *Journal of Geotechnical Engineering*, 117(9).
- Gazetas, G. (1991). Foundations Vibrations. In *Foundation Engineering Handbook* (pp. 553–591). Springer, Boston, MA.
- Genz, A. (1987). Numerical Integration: Recent Developments, Software and Applications. *Proceedings of the NATO Advanced Research Workshop on Numerical Integration*, Halifax, Canada.
- Gleman, A., Brooks, S., Jones L, G., & Meng, X.-L. (2011). *Handbook of Markov chain Monte Carlo*. Chapman and Hall/CRC, New York.
- Gunay S., M. M. . (2014). Enhancement of real-time hybrid simulation on a shaking table configuration with implementation of an advanced control method. *Earthquake Engineering & Structural Dynamics*, 44(5), 657–675.
- Guo, T., Chen, C., Xu, W., & Sanchez, F. (2014). A frequency response analysis approach for

- quantitative assessment of actuator tracking for real-time hybrid simulation. *Smart Materials and Structures*, 23(4).
- Hakuno, M., Shidawara, M., & Hara, T. (1969). Dynamic destructive test of a cantilever beam controlled by an analog-computer. *Proceedings of the Japan Society of Civil Engineers*, 171, 1–9 (in Japanese).
- Hancilar, U., & Çaktı, E. (2015). Fragility functions for code complying RC frames via best correlated IM–EDP pairs. *Bulletin of Earthquake Engineering*, 13(11), 3381–3400.
- Hanley, J., Stojadinovic, B., Sivaselvan, M., Reinhorn, A., & Mosqueda, G. (2003). Continuous Hybrid Simulation with Geographically Distributed Substructures. *1st International Conference in Advances in Experimental Structural Engineering*, 449–456, Nagoya, Japan.
- Harden, C., Hutchinson, T., Martin, G. R., & Bruce L. Kutter. (2005). Numerical Modeling of the Nonlinear Cyclic Response of Shallow Foundations. *Technical Report 2005/04*, PEER, University of California, Berkeley, CA, USA.
- Harden, C. W., & Hutchinson, T. C. (2009). Beam-on-nonlinear-winkler-foundation modeling of shallow, rocking-dominated footings. *Earthquake Spectra*, 25(2), 277–300.
- Hashemi, M. J., R, M. D. C., & Mosqueda, G. (2017). Evaluation of integration methods for hybrid simulation of complex structural systems through collapse Abstract : *Earthquake Engineering & Engineering Vibration*, 16(4), 745–746.
- Haukaas, T., & Der Kiureghian, A. (2005). Parameter Sensitivity and Importance Measures in Nonlinear Finite Element Reliability Analysis. *Journal of Engineering Mechanics*, 131(10), 1013–1026.
- Hessabi, R. M., & Mercan, O. (2011). Phase and amplitude error indices for error quantification in pseudo-dynamic testing. *Earthquake Engineering & Structural Dynamics*, 41(10), 1347–1364.
- Hessabi, R. M., & Mercan, O. (2015). *Assessment Measures for Hybrid Simulation : A Discussion of Recent Developments*, <https://nees.org/resources/13483>.
- Hilber, H. M., Hughes, T. J. R., & Taylor, R. L. (1977). Improved numerical dissipation for time integration algorithms in structural dynamics. *Earthquake Engineering and Structural Dynamics*, 5(3), 283–292.
- Horiuchi, T., Inoue, M., & Konno, T. (2000). Development of a real-time hybrid experimental system using a shaking table. *12th World Conference on Earthquake Engineering*, 1–8.
- Horiuchi, T., Inoue, M., Konno, T., & Namita, Y. (1999). Real-time hybrid experimental system with actuator delay compensation and its application to a piping system with energy absorber. *Earthquake Engineering and Structural Dynamics*, 28(10), 1121–1141.
- Hughes, T. J. R., Pister, K. S., & Taylor, R. L. (1979). Implicit-explicit finite elements in nonlinear transient analysis. *Computer Methods in Applied Mechanics and Engineering*, 17–18, 159–182.
- Igarashi, A., Iemura, H., Suwa, T., Horiuchi, T., Inoue, M., & Konno, T. (2000). Development of substructured shaking table test method. *12th World Conference on Earthquake Engineering*,

- Auckland, New Zealand.
- Iniewski, K., McCrosky, C., & Minoli, D. (2008). TCP/IP Protocol Suite. In *Network Infrastructure and Architecture* (pp. 137–181). John Wiley & Sons, Inc.
- Inverardi, P. L. N., & Tagliani, A. (2003). Maximum Entropy Density Estimation from Fractional Moments. *Communications in Statistics- Theory and Methods*, 32(2), 327–345.
- Jeffrey, L. C., James, R. A., Margaret, W. H., & Wright, P. E. (1998). Convergence properties of the Nelder–Mead simplex method in low dimensions. *SIAM Journal on Optimization*, 9(1), 112–147.
- Julier, S., & Uhlmann, J. (2000). A New Method for the Nonlinear Transformation of Means and Covariances in Filters and Estimators. *IEEE Transactions on Automatic Control*, 45(3), 477.
- Jung, R. Y., & Shing, P. B. (2006). Performance evaluation of a real-time pseudo-dynamic test system. *Earthquake Engineering and Structural Dynamics*, 35(7), 789–810.
- Jung, R. Y., Shing, P. B., Stauffer, E., & Thoen, B. (2007). Performance of a real-time pseudo-dynamic test system considering nonlinear structural response. *Earthquake Engineering and Structural Dynamics*, 36(12), 1785–1809.
- Karsan, I. D., & Jirsa, J. O. (1969). Behavior of Concrete Under Compressive Loadings. *Journal of the Structural Division*, 95(12), 2543–2564.
- Kausel, E., Whitman, R. V., Morray, J. P., & Elsabee, F. (1978). The spring method for embedded foundations. *Nuclear Engineering and Design*, 48(2–3), 377–392.
- Kim, Hong K. (2009). *Extending Hybrid Simulation Methods in OpenFresco Software Framework*. Ph.D. thesis, University of California, Berkeley.
- Kim, Hong Ki. (2011). *Development and implementation of advanced control methods for hybrid simulation*. Ph.D. thesis, University of California, Berkeley, USA.
- Kim, S. J., Christenson, R., Phillips, B., & B.F. Spencer. (2012). Geographically Distributed Real-Time Hybrid Simulation of MR Dampers for Seismic Hazard Mitigation. *20th Analysis & Computation Specialty Conference*, pp.382-393, Chicago, Illinois, USA.
- Kim, S. J., Holub, C. J., & Elnashai, A. S. (2011). Experimental investigation of the behavior of RC bridge piers subjected to horizontal and vertical earthquake motion. *Engineering Structures*, 33(7), 2221–2235.
- Kim, Y., Kabeyasawa, T., Matsumori, T., & Kabeyasawa, T. (2012). Numerical study of a full-scale six-story reinforced concrete wall-frame structure tested at E-Defense. *Earthquake Engineering & Structural Dynamics*, 41(8), 1217–1239.
- Koduru, S. D., & Haukaas, T. (2010). Feasibility of FORM in finite element reliability analysis. *Structural Safety*, 32(2), 145–153.
- Kolay, C. (2016). *Parametrically Dissipative Explicit Direct Integration Algorithms for Computational and Experimental Structural Dynamics*. Ph.D. thesis, Lehigh University, USA.
- Kolay, C., & Ricles, J. M. (2014). Development of a family of unconditionally stable explicit direct

- integration algorithms with controllable numerical energy dissipation. *Earthquake Engineering & Structural Dynamics*, 43(9), 1361–1380.
- Kolay, C., & Ricles, J. M. (2019). Improved Explicit Integration Algorithms for Structural Dynamic Analysis with Unconditional Stability and Controllable Numerical Dissipation. *Journal of Earthquake Engineering*, 23(5), 771–792.
- Koutsourelakis, P. S. (2010). Assessing structural vulnerability against earthquakes using multi-dimensional fragility surfaces: A Bayesian framework. *Probabilistic Engineering Mechanics*, 25(1), 49–60.
- Kramer, S. L. (1996). *Geotechnical Earthquake Engineering*. Prentice Hall Upper Saddle River, NJ, USA.
- Kunnath, S. K., Reinhorn, a. M., & Lobo, R. F. (1992). IDARC Version 3.0: A Program for the Inelastic Damage Analysis of Reinforced Concrete Structures. *Technical Report NCEER-92-0022*, University at Buffalo, New York, USA.
- Kwon, O.-S., Nakata, N., Elnashai, A., & Spencer, B. (2005). A framework for multi-site distributed simulation. *Journal of Earthquake Engineering*, 9(5), 741–753.
- Kwon, O.-S., Nakata, N., Park, K., Elnashai, A., & Spencer, B. (2007). *User Manual and Examples for UI-SIMCOR v2.6 (Multi-Site Substructure Pseudo-Dynamic Simulation Coordinator) and NEES-SAM v2.0 (Static Analysis Module for NEESgrid)*. University of Illinois, Illinois, USA.
- Kwon, O.-S., Spencer, B. F., Elnashai, A. S., & Nakata, N. (2007). The UI-SimCor Hybrid Simulation Framework. *2nd World Forum on Collaborative Research in Earthquake Engineering*, Ispra, Italy.
- Lallemand, D., Kiremidjian, A., & Burton, H. (2015). Statistical procedures for developing earthquake damage fragility curves. *Earthquake Engineering & Structural Dynamics*, 44(9), 1373–1389.
- Lallich, S., & Pastor, D. (2007). Communications in Statistics - Theory and Methods: Preface. *Communications in Statistics - Theory and Methods*, 36(14), 2475–2476.
- Lanese, I. (2012). *Development and Implementation of an Integrated Architecture for Real-Time Dynamic Hybrid Testing in the Simulation of Seismic Isolated Structures*. Ph.D. thesis, Pavia, Italy.
- Lee, S. K., Park, E. C., Min, K. W., & Park, J. H. (2007). Real-time substructuring technique for the shaking table test of upper substructures. *Engineering Structures*, 29(9), 2219–2232.
- Li, J., Spencer, B. F., & Elnashai, A. S. (2013). Bayesian updating of fragility functions using hybrid simulation. *Journal of Structural Engineering*, 139(7), 1160–1171.
- Lin, Y. Z. (2009). *Real-time hybrid testing of an MR damper for response reduction*. Ph.D. thesis, the University of Connecticut, USA.
- Lindsay, G. B., Pilla, S. R., & Basak, P. (2000). Moment-based approximations of distributions using mixtures: theory and applications. *Annals of the Institute of Statistical Mathematics*, 52(2), 215–230.
- Liu, W., Hutchinson, T. C., Kutter, B. L., Hakhamaneshi, M., Aschheim, M. A., & Kunnath, S. K. (2013). Demonstration of compatible yielding between soil-foundation and superstructure

- components. *Journal of Structural Engineering (United States)*, 139(8), 1408–1420.
- Liu, W. K., & Belytschko, T. (1982). Mixed-time implicit-explicit finite elements for transient analysis. *Computers and Structures*, 15(4), 445–450.
- Loh, W. L. (1996). On Latin Hypercube sampling. *Annals of Statistics*, 24(5), 2058–2080.
- Luco, J. E., Ozcelik, O., & Conte, J. P. (2010). Acceleration tracking performance of the UCSD-NEES shake table. *Journal of Structural Engineering*, 136(5), 481–490.
- Lynch, S. M. (2007). *Introduction to Applied Bayesian Statistics and Estimation for Social Scientists*. Springer.
- Ma, F., Zhang, H., Paevere, P., Bockstedte, A., & Foliente, G. C. (2004). Parameter analysis of the differential model of hysteresis. *Applied Mechanics*, 71(3), 342–349.
- Magonette, G. (2001). Development and application of large-scale continuous pseudo-dynamic testing techniques. *Philosophical Transactions of the Royal Society A: Mathematical, Physical and Engineering Sciences*, 359(1786), 1771–1799.
- Magonette, G. E., & Negro, P. (1998). Verification of the pseudodynamic testmethod. *European Earthquake Eng.*, XII(1), 40–50.
- Mahin, S. A., & Williams, M. E. (1980). Computer controlled seismic performance testing. *Dynamic Response of Structures: Experimentation, Observation, Prediction and Control*. American Society of Civil Engineers, New York, USA.
- Mander, J. B., Priestley, J. N., & Park, R. (1989). Theoretical stress-strain model for confined concrete. *Journal of Structural Engineering*, 114(8), 1804–1826.
- Maugeri, M., Musumeci, G., Novità, D., & Taylor, C. A. (2000). Shaking table test of failure of shallow foundation subjected to an eccentric load. *Soil Dynamics and Earthquake Engineering*, 20(5–8), 435–444.
- McKenna, F. (2011). OpenSees: A framework for earthquake engineering simulation. *Computing in Science and Engineering*, 13(4), 58–66.
- Mekki, M., Elachachi, S. M., Breysse, D., Nedjar, D., & Zoutat, M. (2014). Soil-structure interaction effects on RC structures within a performance-based earthquake engineering framework. *European Journal of Environmental and Civil Engineering*, 18(8), 945–962.
- Memari, M., Wang, X., Mahmoud, H., & Kwon, O. S. (2020). Hybrid Simulation of Small-Scale Steel Braced Frame Subjected to Fire and Fire following Earthquake. *Journal of Structural Engineering (United States)*, 146(1), 1–15.
- Mendes, L. A., Campos, A. C., Candeias, P., Costa, A., & Guerreiro, L. (2013). seismic tests on two geometrically identical RC structures designed for different ductility levels: Part I-Experimental analysis. *Earthquake Engineering & Structural Dynamics*, 99, 119.
- Menegotto, M., & Pinto, P. (1973). Method of analysis of cyclically loaded RC plane frames including changes in geometry and nonelastic behavior of elements under normal force and bending. *Symposium on the Resistance and Ultimate Deformability of Structures Acted on by Well Defined Repeated Loads, International Association for Bridge and Structural Engineering*, Zurich, Switzerland.

- Mercan, O., & M. Ricles, J. (2007). Stability and accuracy analysis of outer loop dynamics in real-time pseudodynamic testing of SDOF systems. *Earthquake Engineering & Structural Dynamics*, 36(11), 1523–1543.
- Mercan, O., & Ricles, J. M. (2009). Experimental studies on real-time testing of structures with elastomeric dampers. *Journal of Structural Engineering*, 135(9), 1124–1133.
- Merrit, H. E. (1967). *Hydraulic control systems*. John Wiley & Sons, Inc., New York . London . Sydney.
- Meyerhof, G. G. (1963). Some Recent Research on the Bearing Capacity of Foundations. *Canadian Geotechnical Journal*, 1(1), 16–26.
- Milev, M., Inverardi, P. N., & Tagliani, A. (2012). Moment information and entropy evaluation for probability densities. *Applied Mathematics and Computation*, 218(9), 5782–5795.
- Mirza Hessabi, R., Ashasi-Sorkhabi, A., & Mercan, O. (2014). A new tracking error-based adaptive controller for servo-hydraulic actuator control. *Journal of Vibration and Control*, 22(12), 2824–2840.
- MOOG. (2002). *Electrohydraulic Valves, A Technical Look*, Moog Inc., USA.
- Mosqueda, G., & Ahmadizadeh, M. (2008). Integration Methods for Improved Stability and Accuracy of Hybrid Simulations. *14th World Conference on Earthquake Engineering*, Beijing, China.
- Mosqueda, G, Ahmadizadeh, M., & Department. (2007). Combined implicit or explicit integration steps for hybrid simulation. *Earthquake Engineering and Structural Dynamics*, 36(15), 2325–2343.
- Mosqueda, Gilberto, Stojadinovic, B., & Mahin, S. A. (2007a). Real-time error monitoring for hybrid simulation. Part I: Methodology and experimental verification. *Journal of Structural Engineering*, 133(8), 1109–1117.
- Mosqueda, Gilberto, Stojadinovic, B., & Mahin, S. A. (2007b). Real-time error monitoring for hybrid simulation. Part II: Structural response modification due to errors. *Journal of Structural Engineering*, 133(8), 1109–1117.
- Muğan, A. (2003). Discrete equivalent time integration methods for transient analysis. *International Journal for Numerical Methods in Engineering*, 57(14), 2043–2075.
- Mylonakis, G., & Gazetas, G. (2000). Seismic soil-structure interaction: Beneficial or detrimental? *Journal of Earthquake Engineering*, 4(3), 277–301.
- Mylonakis, G., Syngros, C., Gazetas, G., & Tazoh, T. (2006). The role of soil in the collapse of 18 piers of Hanshin expressway in the Kobe earthquake. *Earthquake Engineering and Structural Dynamics*, 35(5), 547–575.
- Nakashima, M., Akazawa, T., & Sakaguchi, O. (1993). Integration method capable to controlling experimental error growth in substructure pseudo dynamic test (in Japanese). *Journal of Structure and Construction Engineering, AJJ*, 454, 61–71.
- Nakashima, M., Kaminosomo, T., & Ishida, M. (1990). Integration techniques for substructure pseudodynamic test. *Proceedings of 4th U.S. National Conference on Earthquake Engineering*, 2, 515–524, California, USA.

- Nakashima, M., & Masaoka, N. (1999). Real-time on-line test for MDOF systems. *Earthquake Engineering and Structural Dynamics*, 28(4), 393–420.
- Nakashima, Masayoshi, Kato, H., & Takaoka, E. (1992). Development of real-time pseudo-dynamic testing. *Earthquake Engineering & Structural Dynamics*, 21(1), 79–92.
- Nakata, N. (2010). Acceleration trajectory tracking control for earthquake simulators. *Engineering Structures*, 32(8), 2229–2236.
- Nakata, N., & Stehman, M. (2012). Substructure shake table test method using a controlled mass: formulation and numerical simulation. *Earthquake Engineering and Structural Dynamics*, 41(14), 1977–1988.
- Nakata, N., & Stehman, M. (2014). Compensation techniques for experimental errors in real-time hybrid simulation using shake tables. *Smart Structures and Systems*, 14(6), 1055–1079.
- National Institute of Standards and Technology [NIST]. (2012). Soil-Structure Interaction for Building Structures. *NIST GCR*, 12(917–21), Maryland, United States.
- National Instruments. (2016). *Implementing the PID Algorithm with the PID VIs*. NI.Com. [http://zone.ni.com/reference/en-XX/help/371361N-01/lvpidmain/pid\\_vi\\_algs/](http://zone.ni.com/reference/en-XX/help/371361N-01/lvpidmain/pid_vi_algs/)
- Negro, P., Paolucci, R., Pedretti, S., & Faccioli, E. (2000). Large scale soil-structure interaction experiments on sand under cyclic loading. *12th World Conference on Earthquake Engineering*, Auckland, New Zealand.
- Neild, S. A., Stoten, D. P., Drury, D., & Wagg, D. J. (2005). Control issues relating to real-time substructuring experiments using a shaking table. *Earthquake Engineering and Structural Dynamics*, 34(9), 1171–1192.
- Newmark, N., & Hall, W. (1982). Earthquake Spectra and Design. *Engineering Monographs on Earthquake Criteria, Structural Design, and Strong Motion Records*, EERI, Berkeley, CA, USA.
- Newmark, N. M. (1959). A Method of Computation for Structural Dynamics. *Journal of Engineering Mechanics, ASCE*, 85(3), 67–94.
- Nova, R., & Montrasio, L. (1991). Settlements of shallow foundations on cohesionless soils. *Géotechnique*, 41(2), 243–256.
- Ogata, K. (2009). *Modern Control Engineering*. 5th Edition, Prentice Hall, New York.
- Ohtomo, K., Suehiro, T., Kawai, T., & Kanaya, K. (2003). Substantial cross-section plastic deformation of underground reinforced concrete structures during strong earthquakes (in Japanese). *Journal of Japan Society of Civil Engineers*, 724(I–62), 157–175.
- Ozcelik, O., Luco, J. E., Conte, J. P., Trombetti, T. L., & Restrepo, J. I. (2008). Experimental characterization, modeling and identification of the NEES-UCSD shake table mechanical system. *Earthquake Engineering & Structural Dynamics*, 37(2), 243–264.
- Pais, A., & Kausel, E. (1988). Approximate formulas for dynamic stiffnesses of rigid foundations. *Soil Dynamics and Earthquake Engineering*, 7(4), 213–227.

- Pan, P., Nakashima, M., & Tomofuji, H. (2005). Online test using displacement-force mixed control. *Earthquake Engineering and Structural Dynamics*, 34(8), 869–888.
- Paolucci, R., Shirato, M., & Yilmaz, M. T. (2008). Seismic behaviour of shallow foundations: Shaking table experiments vs numerical modelling. *Earthquake Engineering and Structural Dynamics*, 37(4), 577–595.
- Park, Y. J., Ang, A. H. S., & Wen, Y. K. (1987). Damage-Limiting Aseismic Design of Buildings. *Earthquake Spectra*, 3(1), 1–26.
- Pecker, A., Paolucci, R., Chatzigogos, C., Correia, A. A., & Figini, R. (2012). The role of non-linear dynamic soil-foundation interaction on the seismic response of structures. *Second International Conference on Performance-Based Design in Earthquake Geotechnical Engineering*, Taormina, Italy.
- Pegon, P. (2008). Continous PsD testing with substructuring. In *Modern Testing Techniques for Structural Systems Dynamics and Control* (pp. 197–262). CISM Courses and Lectures, Vol. 502, Springer, New York, USA.
- Phillips, B. M. (2012). Model-Based Framework for Real-Time Dynamic Structural Performance Evaluation. *NSEL Report Series, Report No. NSEL-031*, University of Illinois, Illinois, USA.
- Phillips, B. M., & Spencer, B. F. (2012). Model-based feedforward-feedback actuator control for real-time hybrid simulation. *Journal of Structural Engineering*, 139(7), 1205–1214.
- Phillips, B. M., Takada, S., Spencer, B. F., & Fujino, Y. (2014). Feedforward actuator controller development using the backward-difference method for real-time hybrid simulation. *Smart Structures and Systems*, 14(6), 1081–1103.
- Phillips, B. M., Wierschem, N. E., & Spencer Jr, B. F. (2014). Model-based multi-metric control of uniaxial shake tables. *Earthquake Engineering & Structural Dynamics*, 43(5), 681–699.
- Pierluigi, N., Alberto, P., Giorgio, P., & Aldo, T. (2010). Stieltjes moment problem via fractional moments. *Applied Mathematics and Computation*, 216(11), 3307–3318.
- Popovics, S. (1973). A numerical approach to the complete stress-strain curve of concrete. *Cement and Concrete Research*, 3(5), 583–599.
- Porter, K., Kennedy, R., & Bachman, R. (2006). Developing Fragility Functions for Building Components for ATC-58. *Applied Technology Council, Redwood City, CA, USA*.
- Porter, K., Kennedy, R., & Bachman, R. (2007). Creating fragility functions for performance-based earthquake engineering. *Earthquake Spectra*, 23(2), 471–489.
- Pratt, J., Krupp, B., & Morse, C. (2002). Series elastic actuators for high fidelity force control. *Industrial Robot*, 29(3), 234–241.
- R.Zhang, P.V.Lauenstein, & B.M.Phillips. (2015). Substructure Real-time Hybrid Simulation With a Small-scale Uni-axial Shake Table. *6th International Conference on Advances in Experimental Structural Engineering & 11th International Workshop on Advanced Smart Materials and Smart Structures Technology*, University of Illinois, Urbana-Champaign, USA.
- Rackwitz, R. (2001). Reliability analysis - A review and some perspectives. *Structural Safety*, 23(4),

- 365–395.
- Raychowdhury, P. (2008). *Nonlinear Winkler-based Shallow Foundation Model for Performance Assessment of Seismically Loaded Structures*. Ph.D. thesis, University of California, San Diego, USA.
- Raychowdhury, P., & Hutchinson, T. C. (2009). Performance evaluation of a nonlinear Winkler-based shallow foundation model using centrifuge test results. *Earthquake Engineering and Structural Dynamics*, 38(5), 679–698.
- Reinhorn, A. M., Sivaselvan, M. V., Weinreber, S., & Shao, X. (2004). A Novel Approach To Dynamic Force Control. *Third European Conference on Structural Control*, Vienna, Austria.
- Ricles, J. M., & Chen, C. (2008). Development of direct integration algorithms for structural dynamics using discrete control theory. *Journal of Engineering Mechanics*, 134(8), 676–683.
- Rodrigues, H., Arêde, A., Varum, H., & Costa, A. (2013). Damage evolution in reinforced concrete columns subjected to biaxial loading. *Bulletin of Earthquake Engineering*, 11(5), 1517–1540.
- Rodriguez-Gomez, S., & Cakmak, A. S. (1990). Evaluation of seismic damage indices for reinforced concrete structures. *Technical Report NCEER-90-0022*, Princeton University, New Jersey, USA.
- Rosebrok, K., & Kutter, B. (2001a). Soil–foundation structure interaction: shallow foundations. Centrifuge Data for the KRR02 Test Series. *Data Report UCD/CGMDR-01/10*, University of California, Davis, CA, USA.
- Rosebrok, K., & Kutter, B. (2001b). Soil–foundation structure interaction: shallow foundations. Centrifuge Data Report for the KRR01 Test Series. *Data Report UCD/CGMDR-01/09*, University of California, Davis, CA, USA.
- Rosebrok, K., & Kutter, B. (2001c). Soil–foundation structure interaction: shallow foundations. Centrifuge Data Report for the KRR03 Test Series. *Data Report UCD/CGMDR-01/11*, University of California, Davis, CA, USA.
- Rossetto, T., & Elnashai, A. (2003). Derivation of vulnerability functions for European-type RC structures based on observational data. *Engineering Structures*, 25(10), 1241–1263.
- Sabnis, G. M., Harris, H. G., & White, R. N. (1983). Structure Modeling and Experimental Techniques. *Journal of Dynamic Systems, Measurement, and Control*, 105(4), 307–307.
- Saouma, V., & Sivaselvan, M. (2008). *Hybrid simulation: Theory, Implementation and Applications*. Taylor & Francis, New York, USA.
- Sarma, S. K., & Iossifelis, I. S. (1990). Seismic bearing capacity of shallow strip footings. *Géotechnique*, 40(2), 265–273.
- Schellenberg, A. H., Becker, T. C., & Mahin, S. A. (2016). Hybrid shake table testing method: Theory, implementation and application to midlevel isolation. *Structural Control and Health Monitoring*, 24(5), e1915.
- Schellenberg, A. H., Huang, Y., & Mahin, S. A. (2019). Structural finite element software coupling using adapter elements. *CMES - Computer Modeling in Engineering and Sciences*, 120(3), 719–737.

- Schellenberg, A. H., Mahin, S. A., & Fenves, G. L. (2009). Advanced Implementation of Hybrid Simulation. *PEER Report 2009/104*, University of California, Berkeley, USA.
- Schellenberg, A. H., Yang, T., Mahin, S. A., & Stojadinovic, B. (2008). Hybrid simulation of structural collapse. *14th World Conference on Earthquake Engineering*, Beijing, China.
- Schellenberg, A., Kim, H., Mahin, S. A., & Fenves, G. L. (2008). Environment independent implementation of a software framework for fast local and geographically distributed hybrid simulations. *14th World Conference on Earthquake Engineering*, Beijing, China.
- Schellenberg, A., Shao, B., & Mahin, S. (2017). Developemnt of a Large-Scale 6Dof Hybrid Shake Table and Application To Testing Response Modification Devices for Tall Buildings. *16th World Conference on Earthquake Engineering*, Santiago, Chile.
- Schellenberg, Andreas., & Mahin, S. (2006). Integration of hybrid simulation within the general-purpose computational framework OpenSees. *8th National Conference on Earthquake Engineering*, San Francisco, CA, USA.
- Schellenberg, Andreas, Kim, H. K., Takahashi, Y., Fenves, G. L., & Mahin, S. A. (2007). *OpenFresco Command Language Manual*, University of California, Berkeley, USA.
- Schneider, S. P., & Roeder, C. W. (1994). An inelastic substructure technique for the pseudo-dynamic test method. *Earthquake Engineering & Structural Dynamics*, 23(7), 761–775.
- Shao, X., & Reinhorn, A. M. (2012). Development of a controller platform for force-based real-time hybrid simulation. *Journal of Earthquake Engineering*, 16(2), 274–295.
- Shao, Xiaoyun, Reinhorn, A. M., & Sivaselvan, M. V. (2011). Real-Time Hybrid Simulation Using Shake Tables and Dynamic Actuators. *Journal of Structural Engineering*, 137(7), 748–760.
- Shield, C. K., French, C. W., & Timm, J. (2001). Development and implementation of the effective force testing method for seismic simulation of large-scale structures. *Philosophical Transactions of the Royal Society A: Mathematical, Physical and Engineering Sciences*, 359(1786), 1911–1929.
- Shing, P. B., & Mahin, S. A. (1987). Elimination of spurious higher-mode response in pseudo-dynamic tests. *Earthquake Engineering & Structural Dynamics*, 15(4), 425–445.
- Shirato, M., Kouno, T., Asai, R., Nakatani, S., Fukui, J., & Paolucci, R. (2008). Large-scale experiments on nonlinear behavior of shallow foundations subjected to strong earthquakes. *Soils and Foundations*, 48(5), 673–692.
- Shome, N., Cornel, C. A., Bazzurro, P., & Carballo, J. E. (1998). Earthquakes, Records and Nonlinear Responses. *Earthquake Espectra*, 14(3), 469–500.
- Singhal, A., & Kiremidjian, A. (1998). Bayesian updating of fragilities with application to RC frames. *Journal of Structural Engineering*, 124(8), 922–929.
- Sivaselvan, M. V. (2006). A Unified View of Hybrid Seismic Simulation Algorithms. *8th US National Conference on Earthquake Engineering*, San Francisco, California, USA.
- Sivaselvan, Mettupalayam V., Reinhorn, A. M., Shao, X., & Weinreber, S. (2008). Dynamic force control with hydraulic actuators using added compliance and displacement compensation.

- Earthquake Engineering and Structural Dynamics*, 37(15), 1785–1800.
- Sivaselvan, Mettupalayam V, Reinhorn, A. M., Shao, X., & Weinreber, S. (2007). Dynamic Force Control with Hydraulic Actuators Using Added Compliance and Displacement Compensation. *Earthquake Engineering & Structural Dynamics*, 37(15), 1785–1800.
- Skjaerbaek, P. S., Nielsen, Søren, R. K., Kirkegaard, H. P., & Cakmak, A. S. (1997). Experimental Study of Damage Indicators for a 2-Bay, 6-Storey RC-Frame. *Fracture and Dynamics*, R9725(87).
- Spencer, B. F., Elnashai, A., Kuchma, D., Ricles, J., Abdoun, T., Kim, S. J., Holub, C., Roy, S., Radwan, H., Nakata, N., & Marullo, T. M. (2006). *Multi-Site Soil-Structure-Foundation Interaction Test (MISST)*. Lehigh University, USA.
- Spencer, B., Finholt, T., Foster, I., Kesselman, C., Beldica, C., Futrelle, J., Gullapalli, S., Hubbard, P., Liming, L., Marcusiu, D., Pearlman, L., Severance, C., & Yang, G. (2004). NEESgrid: A Distributed Collaboratory for Advanced Earthquake Engineering Experiment and Simulation. *13th World Conference on Earthquake Engineering*, Vancouver, British Columbia, Canada.
- Stefanaki, A., Sivaselvan, M. V., Tessari, A., & Whittaker, A. (2015b). Soil-foundation-structure interaction investigations using hybrid simulation. *23rd Conference on Structural Mechanics in Reactor Technology*, Division V, Paper ID 730, Manchester, UK.
- Stefano Marelli, B. S. (1996). a Framework for Uncertainty Quantification in MATLAB. *Vulnerability, Uncertainty, and Risk ©ASCE 2014, Hang 1989*, 2554–2563.
- Stefanou, G. (2009). The stochastic finite element method: Past, present and future. *Computer Methods in Applied Mechanics and Engineering*, 198(9–12), 1031–1051.
- Stehman, M. (2014). *Advances in shake table control and substructure shake table testing*. Ph.D. Thesis, Civil Engineering Department, Johns Hopkins University, USA.
- Stehman, M., & Nakata, N. (2016). IIR Compensation in Real-Time Hybrid Simulation using Shake Tables with Complex Control-Structure-Interaction. *Journal of Earthquake Engineering*, 20(4), 633–653.
- Stoten, D. P., & Gómez, E. G. (2001). Adaptive control of shaking tables using the minimal control synthesis algorithm. *Philosophical Transactions of the Royal Society A: Mathematical, Physical and Engineering Sciences*, 359(1786), 1697–1723.
- Strepelias, E., Stathas, N., Palios, X., & Bousias, S. (2020). Hybrid Simulation Framework for Multi-hazard Testing. *American Journal of Civil Engineering*, 8(1), 10–19.
- Sudret, B. (2008). Global sensitivity analysis using polynomial chaos expansions. *Reliability Engineering and System Safety*, 93(7), 964–979.
- Sudret, B., & Der Kiureghian, A. (2002). Comparison of finite element reliability methods. *Probabilistic Engineering Mechanics*, 17(4), 337–348.
- Tagliani, A. (1999). Hausdorff moment problem and maximum entropy: A unified approach. *Applied Mathematics and Computation*, 105(2–3), 291–305.
- Takahashi, Y., & Fenves, G. L. (2006). Software framework for distributed experimental–

- computational simulation of structural systems. *Earthquake Engineering & Structural Dynamics*, 35(3), 267–291.
- Takanashi, K., & Nakashima, M. (1987). Japanese activities on on-line testing. *Journal of Engineering Mechanics*, 113(7), 1014–1031.
- Tekeste, G. G., Correia, A. A., & Costa, A. G. (2019). Reliability and Global Sensitivity Analysis in Hybrid Simulations using Surrogate Probabilistic Modelling. *11º Congresso Nacional de Sismologia e Engenharia Sísmica*, Lisbon, Portugal.
- Tekeste, G. G., Correia, A. A., & Costa, A. G. (2017a). Stability analysis of a real-time shake table hybrid simulation for linear and non-linear SDOF systems. *7th International Conference on Advances in Experimental Structural Engineering*, 641–659, Pavia, Italy.
- Tekeste, G. G., Correia, A. A., & Costa, A. G. (2017b). Virtual hybrid simulation tests accounting for experimental errors. *First European Conference on OpenSees*, 14–17, Porto, Portugal.
- Terzaghi, K. (1943). Theoretical Soil Mechanics. In *Theoretical Soil Mechanics*. John Wiley and Sons, Inc.
- Thewalt, C. R., & Mahin, S. A. (1987). Hybrid solution techniques for generalized pseudodynamic testing. In *UCB/EERC - 87/09 Report to NSF, University of California, Berkeley, USA*.
- Thewalt, C., & Roman, M. (1994). Pseudo-dynamic tests. *Journal of Structural Engineering*, 120(9), 2768–2781.
- Thomas, A., Best, N., & Way, R. (2003). *WinBugs User Manual* (Version 1.4). <https://doi.org/http://www.mrc-bsu.cam.ac.uk/wp-content/uploads/manual14.pdf>
- Toki, K., Sato, T., Kiyono, J., Garmroudi, N. K., Oshima, K., & Yoshikawa, M. (1990). Hybrid experiments on nonlinear earthquake-induced soil-structure interaction. *Earthquake Engineering and Structural Dynamics*, 19(5), 709–723.
- Trifunac, M. D., & Todorovska, M. I. (1999). Reduction of structural damage by nonlinear soil response. *Journal of Structural Engineering*, 125(1), 89–97.
- Ugalde, J. A., Kutter, B. L., Jeremic, B., & Gajan, S. (2007). Centrifuge modeling of rocking behavior of bridges on shallow foundations. Fourth International Conference on Earthquake Engineering. *Fourth International Conference on Earthquake Engineering*, Thessaloniki, Greece.
- Vamvatsikos, D., & Allin Cornell, C. (2002). Incremental dynamic analysis. *Earthquake Engineering and Structural Dynamics*, 31(3), 491–514.
- Van Coile, R., Balomenos, G. P., Pandey, M. D., & Caspee, R. (2017). An Unbiased Method for Probabilistic Fire Safety Engineering, Requiring a Limited Number of Model Evaluations. *Fire Technology*, 53(5), 1705–1744.
- Veletsos, A.S., & Nair, V. V. (1975). Seismic interaction of structures on hysteretic foundations. *Journal of Structural Engineering*, 101(1), 109–129.
- Veletsos, Anestis S., & Meek, J. W. (1974). Dynamic behaviour of building-foundation systems. *Earthquake Engineering & Structural Dynamics*, 3(2), 121–138.

- Verma, M., & Sivaselvan, M. V. (2019). Impedance matching control design for the benchmark problem in real-time hybrid simulation. *Mechanical Systems and Signal Processing*, 134. <https://doi.org/10.1016/j.ymssp.2019.106343>
- Vicencio, F., & Alexander, N. A. (2018). Dynamic interaction between adjacent buildings through nonlinear soil during earthquakes. *Soil Dynamics and Earthquake Engineering*, 108, 130–141.
- Wang, Q., Wang, J. T., Jin, F., Chi, F. D., & Zhang, C. H. (2011). Real-time dynamic hybrid testing for soil-structure interaction analysis. *Soil Dynamics and Earthquake Engineering*, 31(12), 1690–1702.
- Whyte, C. A., & Stojadinovic, B. (2014). High-Precision Displacement Control for Hybrid Simulation of the Seismic Response of Stiff Reinforced Concrete Shear Walls. *10th U.S. National Conference on Earthquake Engineering*, Anchorage, Alaska, USA.
- Wolf, J. P. (1985). Dynamic soil-structure interaction. In William J. Hall (Ed.), *Dynamic soil-structure interaction*. Prentice-Hall, Inc., Englewood, New Jersey, USA.
- Wolf, John P. (1989). Soil-structure-interaction analysis in time domain. *Nuclear Engineering and Design*, 111(3), 381–393.
- Wolf, John P., & Deeks, A. J. (2004). Foundation Vibration Analysis: A strength-of-Materials Approach. In *Elsevier*, Oxford, UK.
- Wu, B., Xu, G., Li, Y., Wang, Z., Jiang, H., Shing, P. B., & Ou, J. (2007). Development of equivalent force control method for pseudo-dynamic and real-time substructure tests. *Earthquake Engineering & Structural Dynamics*, 36(9), 1127–1149.
- Xu, H., & Rahman, S. (2004). A generalized dimension-reduction method for multidimensional integration in stochastic mechanics. *International Journal for Numerical Methods in Engineering*, 61(12), 1992–2019.
- Yang, C. Y., Dong, G. J., Ren, X. S., You, S., & Schellenberg, A. (2015). Real-time hybrid testing on a girder bridge model by using shaking-table and actuator. *6th International Conference on Advances in Experimental Structural Engineering & 11th International Workshop on Advanced Smart Materials and Smart Structures Technology*, University of Illinois, Urbana-Champaign, USA.
- Yang, Y.-S., Tsai, K.-C., Elnashai, A. S., & Hsieh, T.-J. (2012). An online optimization method for bridge dynamic hybrid simulations. *Simulation Modelling Practice and Theory*, 28, 42–54. <https://doi.org/10.1016/j.simpat.2012.06.002>
- You, S., & Schellenberg, A. (2017). Test Rehearsal Methods for Quasi Static and Real-Time Hybrid Simulations. *16th World Conference on Earthquake Engineering*, Santiago, Chile.
- Yun, X., & Gardner, L. (2017). Stress-strain curves for hot-rolled steels. *Journal of Constructional Steel Research*, 133(June 2017), 36–46.
- Zeng, X., & Schofield, A. N. (1996). Design and performance of an equivalent-shear-beam container for earthquake centrifuge modelling. *International Journal of Rock Mechanics and Mining Sciences & Geomechanics Abstracts*, 46(1), 83–102.

- Zhang, C., & Jiang, N. (2017). A shaking table real-time substructure experiment of an equipment–structure–soil interaction system. *Advances in Mechanical Engineering*, 9(10), 1–12.
- Zhang, J., & Du, X. (2010). A Second-Order Reliability Method With First-Order Efficiency. *Journal of Mechanical Design*, 132(10), 101006.
- Zhang, R., Phillips, B. M., Taniguchi, S., Ikenaga, M., & Ikago, K. (2017). Shake table real-time hybrid simulation techniques for the performance evaluation of buildings with inter-story isolation. *Structural Control and Health Monitoring*, 24(10), 1–19.
- Zhang, X. (2013). *Efficient Computational Methods for Structural Reliability and Global Sensitivity Analyses*. Ph.D. thesis, University of Waterloo, USA.
- Zhang, X., & Pandey, M. D. (2013). Structural reliability analysis based on the concepts of entropy, fractional moment and dimensional reduction method. *Structural Safety*, 43(July 2013), 28–40.
- Zhang, X., & Pandey, M. D. (2014). An effective approximation for variance-based global sensitivity analysis. *Reliability Engineering and System Safety*, 121, 164–174.
- Zhao, J., French, C., Shield, C., & Posbergh, T. (2003). Considerations for the development of real-time dynamic testing using servo-hydraulic actuation. *Earthquake Engineering and Structural Dynamics*, 32(11), 1773–1794.
- Zhao, Jian, French, C., Shield, C., & Posbergh, T. (2006). Comparison of tests of a nonlinear structure using a shake table and the EFT method. *Journal of Structural Engineering*, 132(9), 1473–1481.
- Zhao, Jian, Shield, C., French, C., & Posbergh, T. (2005). Nonlinear system modeling and velocity feedback compensation for effective force testing. *Journal of Engineering Mechanics*, 131(3), 244–253.
- Zhou, M. X., Wang, J. T., Jin, F., Gui, Y., & Zhu, F. (2014). Real-time dynamic hybrid testing coupling finite element and shaking table. *Journal of Earthquake Engineering*, 18(4), 637–653.



---

## Appendix-1

---

### Hybrid test setup adopted for the experimental validation of M-DRM technique

The rack-pinion systems (No.10) convert motion along the vertical actuator axes  $y_1$  and  $y_2$  to rotations  $u_1$  and  $u_2$ , respectively, which are imposed on the plate specimen (No.6) through aluminum clamps (No.3). Horizontal actuators along  $x_1$  and  $x_2$  control the position of the moving frame (No.4) which is mounted on two profiled rail guides using ball bearings (No. 5). In this manner, the axial deformation of the plate specimen,  $u_3$ , matches the position of the frame.

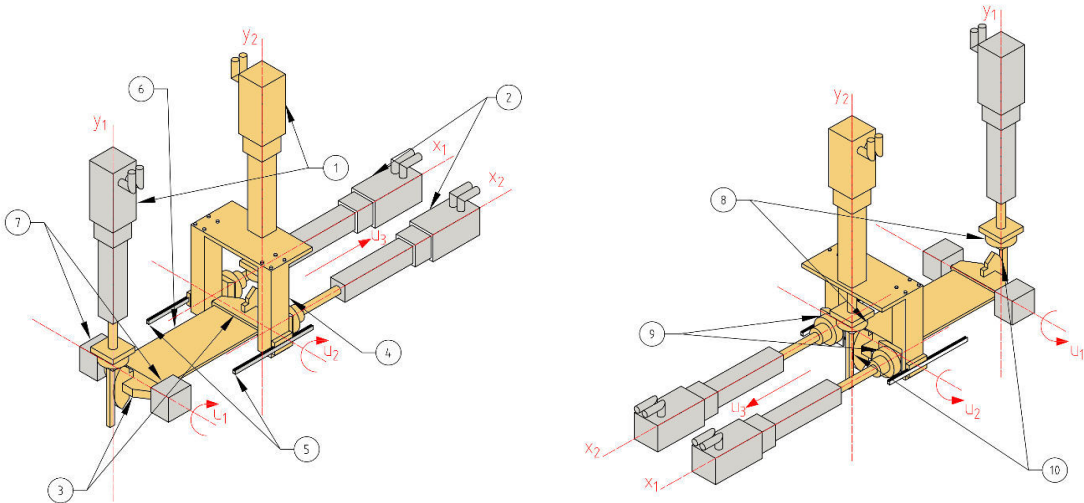


Figure A-1: Axonometric view of a test rig for hybrid simulation of a simply supported beam<sup>6</sup> (with permission from Abbiati et al. (2020))

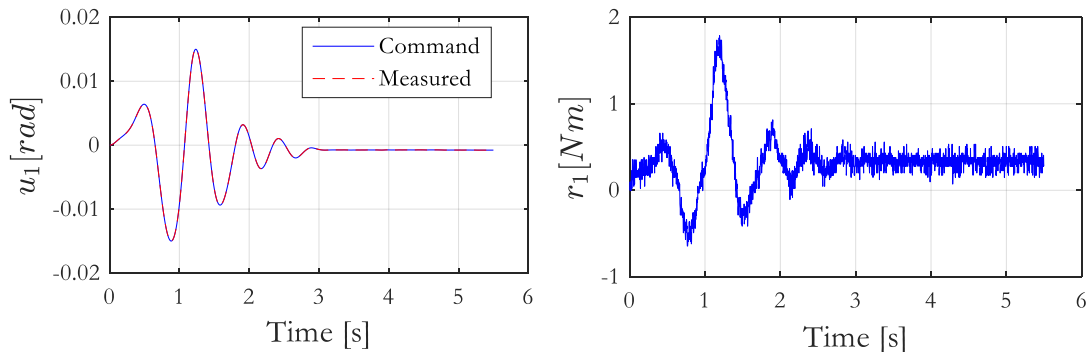


Figure A-2: Hybrid test outputs at the mean values of the random variables

---

<sup>6</sup>Figure A-1: (1) Vertical actuators; (2) Horizontal actuators; (3) Installation clamps; (4) Moving frame; (5) Profiled rail guides; (6) Plate specimen; (7) Hinges; (8) Vertical actuator load cells; (9) Horizontal actuator load cells; (10) Rack-pinion system. Note: The moving parts are colored in yellow while the grey parts are fixed to the reaction frame. The latter is omitted for clarity.

---

## Appendix-2

---

### **Equations of the Bivariate formulation of M-DRM technique (Zhang, 2013)**

The general formulation for the bivariate approximation of the M-DRM method is given by:

$$r = g(Z) \approx \sum_{1 \leq i < j \leq n} g_{i,j}(z_{i,j}) - (n-2) \sum_{i=1}^n g_i(z_i) + \frac{(n-1)(n-2)}{2} g_0 \quad (\text{A.1})$$

where  $n$  is the number of random input variables of the response function  $r$  and the bivariate cut-off function,  $g_{i,j}(z_{i,j})$ , can be expressed as:

$$g_{i,j}(z_{i,j}) = g(c_1, c_2, \dots, c_{i-1}, z_i, c_{i+1}, \dots, c_{j-1}, z_j, c_{j+1}, \dots, c_{n-1}, c_n) \quad (\text{A.2})$$

where  $c$  is the mean value of a random variable. The response function  $r$  is therefore approximated as:

$$r \approx \frac{[g_0]^{\frac{(n-1)(n-2)}{2}} \prod_{i=1}^{n-1} \prod_{j=i+1}^n E[g_{i,j}(z_{i,j})]}{\left[ \prod_{i=1}^n E[g_i(z_i)] \right]^{n-2}} \quad (\text{A.3})$$

The  $\alpha$ th-order fractional moment can be shown to be:

$$M_r^\alpha = \frac{[g_0]^{\frac{\alpha(n-1)(n-2)}{2}} \prod_{i=1}^{n-1} \prod_{j=i+1}^n E[g_{i,j}(z_{i,j})]^\alpha}{\prod_{i=1}^n E[g_i(z_i)]^{\alpha(n-2)}} \quad (\text{A.4})$$

The expectation parameter,  $E$ , in the above equation can be evaluated as:

$$\begin{aligned} E[\{g_{i,j}(z_{i,j})\}^\alpha] &= \int_{\bar{z}_i} \int_{\bar{z}_j} (g(z_{i,j}))^\alpha f_i(z_i) dz_i f_j(z_j) dz_j \approx \sum_{m=1}^L \sum_{q=1}^L w_m w_q \{g_{i,j}(z_{m,q})\}^\alpha \\ E[\{g_i(z_i)\}^\alpha] &= \int_{\bar{z}_i} (g(z_i))^\alpha f_i(z_i) dz_i \approx \sum_{m=1}^L w_m \{g_i(z_m)\}^\alpha \end{aligned} \quad (\text{A.5})$$

where  $g_{i,j}(z_{m,q})$  is the model response evaluated at the  $m$ th point of variable  $i$  and the  $q$ th point of variable  $j$  while the remaining input variables are at their mean values;  $w_m$  is the  $m$ th weight of the variable  $i$ ;  $w_q$  is the  $q$ th weight of the variable  $j$ ; and  $L$  is the order of the Gauss quadrature.

---

## Appendix-3

---



Figure A-3: Photo taken during the hybrid simulation test of a one-story two-bay steel MRF (one of its outer columns is represented physically in the laboratory)

**OpenSees-OpenFresco Tcl file for conducting hybrid test of the steel MRF shown in Figure 4-20 (developed to validate *LNEC-HS* software)**

```

# File: 2bayFrame_ST1DhybridTest.tcl
# Units: [N, mm]
# Written by: Gidewon Goitom (Gidewon.tekeste@ua.pt; gtekeste@l nec.pt)
# Affiliation: University of Aveiro and LNEC
# Created: 27-11-2017
# Modified: 22-1-2018
# Revision: 1

# Properties of the test structure

# Height=1.805 m
# Width of each bay=3.60 m
# Columns: Fixed at the base and hinged at the top
# Beams: Truss elements

# Properties of the S355 HEB 100 hot-rolled steel

# A=26.0 cm2; Iy=449.5 cm4; E=210 GPa; fy=355 MPa; fu=510 MPa
# Section modulus: We,y=89.91 cm3; Wp,y=104.2 cm3
# Material model: Steel02 (Giuffré-Menegotto-Pinto steel)
# Elastic strain=0.17%; Ultimate strain=18.24%
# Kinematic hardening=0.0114; Isotropic hardening=0 (both in compression & tension)
# Yielding displacement~36.71 mm
# -----

```

```

# Start of model generation
#
# Make sure all dlls are in the same folder as the OpenSees.exe
model BasicBuilder      -ndm 2          -ndf 3
# Load OpenFresco
loadPackage OpenFresco
# Create data directory
Set DataDir OutPutffile
file mkdir $DataDir

# Define geometry of the model

set massEdgeCol           5.00
set massCentralCol        10.00
# node $tag $xCrd $yCrd -mass $massX $massY $massZ
Node    1     0.00          0.00
Node    2     3600.00 0.00
Node    3     7200.00 0.00
Node    4     0.00          1805.00      -mass
          $massEdgeCol           $massEdgeCol      1e-6
Node    5     3600.00 1805.00      -mass      $massCentralCol
          $massCentralCol       1e-6
Node    6     7200.00 1805.00      -mass      $massEdgeCol
          $massEdgeCol           1e-6

# Node Fixity

# fix $nodeTag $DX $DY $RZ
Fix    1     1     1     1
Fix    2     1     1     1
Fix    3     1     1     1
Fix    4     0     1     0
Fix    5     0     1     0
Fix    6     0     1     0

# Define materials

#uniaxialMaterial Steel02 $matTag $Fy $E $b $R0 $cR1 $cR2 $a1 $a2 $a3 $a4
UniaxialMaterial Steel02 1 355 2.1e5 0.0114 18.5 0.925 0.15 0.0 1.0 0.0 1.0
#
# Define OpenFresco objects
#
# Define control points

# expControlPoint $cpTag <-node $nodeTag> $dof $rspType <-fact $f> <-lim $l $u> <-isRel>...
ExpControlPoint 1 -node 4 ux disp -fact 1.0
ExpControlPoint 2 -node 4 ux disp      -fact 1.0 ux force -fact 1.0

```

### # Define experimental control

```
# expControl LabVIEW tag      ipAddr <ipPort> -trialCP cpTags -outCP cpTags
ExpControl LabVIEW 1 "192.168.2.50" 3416 -trialCP 1 -outCP 2
```

### # Define experimental setup

```
#expSetup OneActuator $tag <-control $ctrlITag> $dir -sizeTrialOut $t $o <-trialDispFact $f>...
expSetup OneActuator 1 -control 1 2 -sizeTrialOut 3 3 -trialDisplFact 1 1 1 -outDisplFact 1 1 1 -
outForceFact 1 1 1
```

### # Define experimental site

```
# expSite LocalSite $tag $setupTag
```

```
expSite LocalSite 1 1
```

```
#geomTransf type $tag
```

```
geomTransf PDelta 1
```

```
#-----
```

### # Numerical elements

```
#-----
```

### # Beam elements

```
# element truss $eleTag $iNode $jNode $A $matTag
```

```
element truss 4 4 5 3912 1; # IPE 240
```

```
element truss 5 5 6 3912 1; # IPE 240
```

### # Column elements

```
# Column sections: HEB 100
```

```
set d 100; # depth
```

```
set bf 100; # flange width
```

```
set tf 10; # flange thickness
```

```
set tw 6; # web thickness
```

```
set nfdw 10; # number of fibers along dw
```

```
set nftw 2; # number of fibers along tw
```

```
set nfbf 10; # number of fibers along bf
```

```
set nftf 4; # number of fibers along tf
```

```
set secID 1
```

```
set matID 1
```

```
set dw [expr $d - 2*$tf]
```

```
set y1 [expr -$d/2]
```

```
set y2 [expr -$dw/2]
```

```
set y3 [expr $dw/2]
```

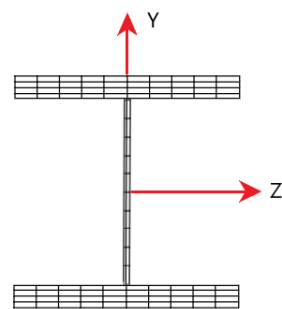
```
set y4 [expr $d/2]
```

```
set z1 [expr -$bf/2]
```

```
set z2 [expr -$tw/2]
```

```
set z3 [expr $tw/2]
```

```
set z4 [expr $bf/2]
```



```

section fiberSec $secID {
    # nfIJ nfJK yI zI yJ zJ yK zK yL zL
    patch quadr $matID $nfbf $nftf $y1 $z4 $y1 $z1 $y2 $z1 $y2 $z4; #
    Flange
    patch quadr $matID $nftw $nfdw $y2 $z3 $y2 $z2 $y3 $z2 $y3 $z3; # web
    patch quadr $matID $nfbf $nftf $y3 $z4 $y3 $z1 $y4 $z1 $y4 $z4; #
    Flange
}

set ip 5; # number of integration points
#element nonlinearBeamColumn $eleTag $iNode $jNode $np $IDsec $IDTransf
element nonlinearBeamColumn 2 2 5 $ip 1 1
element nonlinearBeamColumn 3 3 6 $ip 1 1
#
#-----#
# Define experimental element
#-----
# Stiffness matrix of the experimental substructure (Outer column). It was obtained from a Hammer
test.
set      k11          288090.0
set      k12          0.00
set      k13          0.00
set      k21          0.00
set      k22         1128.3
set      k23        -1234.7e3
set      k31          0.00
set      k32        -1234.7e3
set      k33         1.322e9
# expElement beamColumn $eleTag $iNode $jNode $transTag -site $siteTag -initStif $Kij <-iMod>
<-rho $rho>
expElement beamColumn 1 1 4 1 -site 1 -initStif $k11 $k12 $k13 $k21 $k22 $k23 $k31 $k32 $k33
#
#-----#
# Define gravity loads
#-----
# Create a Plain load pattern
pattern Plain 1 "Linear" {
    # Create nodal loads at nodes 4 5 6
    # nd          FY           FX           MZ
    load        4            0.0          [expr -$massEdgeCol *9810]
    0.0
    load        5            0.0          [expr -$massCentralCol
    *9810]  0.0
    load        6            0.0          [expr -$massEdgeCol *9810]
    0.0
}

```

```

# -----
# Gravity analysis setting
# -----
# Create the system of equation
system BandGeneral
# Create the DOF numberer
numberer Plain
# Create the constraint handler
constraints Plain
# Create the convergence test
test NormDispIncr 1.0e-6 10
# Create the integration scheme
integrator LoadControl 0.1
# Create the solution algorithm
algorithm Newton
# Create the analysis object
analysis Static
# End of analysis generation

# Recorder for gravity analysis

recorder Node -file Gravity_Dsp.out -time -node 4 5 6 -dof 1 2 3 disp
recorder Element -file Gravity_Frc.out -time -ele 1 2 3 force
# -----
# Gravity analysis
# -----
if {[analyze 10] == 0} {
    puts "\nGravity load analysis completed"
} else {
    puts "\nGravity load analysis failed"
    exit -1
}

# Generating the model for a dynamic time-history analysis
# -----
# Set the gravity loads to be constant & reset the time in the domain
loadConst -time 0.0
remove recorders
#-----
# Define dynamic loads
# -----
# Set time series to be passed to the uniform excitation; here, time series must have [mm, s] units
set dt 0.02
# Set scale factor for the time series
set scale 0.1
timeSeries Path 1 -filePath Elcentro.txt -dt $dt -factor [expr 9810*$scale]

```

```

# create UniformExcitation load pattern
# pattern UniformExcitation $tag $dir -accel $tsTag <-vel0 $vel0>
pattern UniformExcitation 2 1 -accel 1
#
# Eigenvalue analysis
#
set nEigenI 3; # 3 Eigen values
set lambdaN [eigen [expr $nEigenI]]; # perform eigenvalue analysis
set lambdaI [lindex $lambdaN [expr 0]]; # first eigenvalue
set w [expr pow($lambdaI,0.5)]; # first mode circular frequency
# calculate damping parameters
set zeta 0.02; #  $\xi=2\%$ 
set a0 [expr $zeta*2.0*$w]; # apply mass proportional damping
set alphaM $a0; # D = alphaM*M
set betaK 0.0; # D = betaK*Kcurrent
set betaKinit 0.0; # D = beatKinit*Kinit
set betaKcomm 0.0; # D = betaKcomm*KlastCommit
# Rayleigh Damping
# D = $alphaM * M + $betaK * Kcurrent +$betaKinit * Kinit + $betaKcomm * KlastCommit
rayleigh $alphaM $betaK $betaKinit $betaKcomm
#
# Dynamic time-history analysis setting
#
# Create the system of equations
system BandGeneral
# Create the DOF numberer
numberer Plain
# Create the constraint handler
constraints Plain
# Create the convergence test
test NormDispIncr 1.0e-6
# Create the integration scheme
integrator AlphaOS 0.9
# Create the solution algorithm
algorithm Linear -tangent
# Set time step of analysis (if different from the time step of the time series, OpenSees interpolates it)
set ts 0.004
# Create the analysis object
analysis Transient
# End of analysis generation

# Recorder for time-history analysis

# Node recorders
recorder Node -file $DataDir/Node_Dsp.out -time -node 4 5 6 -dof 1 disp
recorder Node -file $DataDir/Node_rot.out -time -node 1 -dof 3 disp
recorder Node -file $DataDir/Node_Vel.out -time -node 4 5 6 -dof 1 vel
recorder Node -file $DataDir/Node_Acc.out -time -node 4 5 6 -dof 1 accel

```

```

recorder Node -file $DataDir/Node_Rxn.out -time -node 1 2 3 -dof 1 reaction
recorder Node -file $DataDir/Node_RxnWithIner.out -time -node 1 2 3 -dof 1
reactionIncludingInertia
# Element recorders
recorder Element -file $DataDir/Elmt_Frc.out -time -ele 1 2 3 localForces
recorder Element -file $DataDir/Elmt_Frc_basic.out -time -ele 1 2 3 basicForces
recorder Element -file $DataDir/Elmt_Def.out -time -ele 1 2 3 basicDeformations
# Control and Daq experimental recorders
expRecorder Control -file $DataDir/Control_ctrlDsp.out -time -control 1 ctrlDisp
expRecorder Control -file $DataDir/Control_daqDsp.out -time -control 1 daqDisp
expRecorder Control -file $DataDir/Control_daqFrc.out -time -control 1 daqForce
# End of recorder generation
#
#-----#
# Display Eigenvalue analysis and perform time-history analysis
#-----#
# Write eigenvalues to a txt file and display them in the command prompt
set EigenFileID [open $DataDir/Eigen.txt w]
set pi [expr acos(-1.0)]
set lambda [eigen -fullGenLapack 3]
puts "\nEigenvalues at start of transient:"
puts "| lambda | omega | period | frequency |"
puts $EigenFileID "\nEigenvalues at start of transient:"
puts $EigenFileID "| lambda | omega | period | frequency |"
foreach lambda $lambda {
    set omega [expr pow($lambda,0.5)]
    set period [expr 2.0*$pi/$omega]
    set frequ [expr 1.0/$period]
    puts [format "| %5.3e | %8.4f | %7.4f | %9.4f |" $lambda $omega $period $frequ]
    puts $EigenFileID [format "| %5.3e | %8.4f | %7.4f | %9.4f |" $lambda $omega $period
    $frequ]
}
#
#-----#
# Graphical display
#-----#
set h 2500
# recorder display $windowTitle $xLoc $yLoc $xPixels $yPixels <-file $fileName>
recorder display "Deformed shape" 10 10 500 500 -wipe
prp $h $h 1
vup 0 1 0
vpn 0 0 1
viewWindow -5000 5000 -4000 4000
# display $arg1 $arg2 $amplification
display 1 2 20
# Open output file for writing
set outFileID [open elapsedTime.txt w]

```

```
# -----
# Perform transient analysis
# -----
set nDataPts 2400; # number of data points in the time-series
set tTot [time {
for {set i 1} {$i < [expr $dt/$ts*$nDataPts]} {incr i} {
    set t [time {analyze 1 $ts}]
    puts $outFileID $t
    puts "step $i"
}
}]
puts "Transient Analysis completed"
puts "\nElapsed Time = $tTot \n"
close $outFileID
wipe
exit
# End of analysis
```

---

## Appendix-4

---

**OpenSees-OpenFresco TCL code for conducting a rehearsal hybrid test of a bridge case study using the finite-element coupling approach in combination with the BNWF model for soil-structure interaction.**

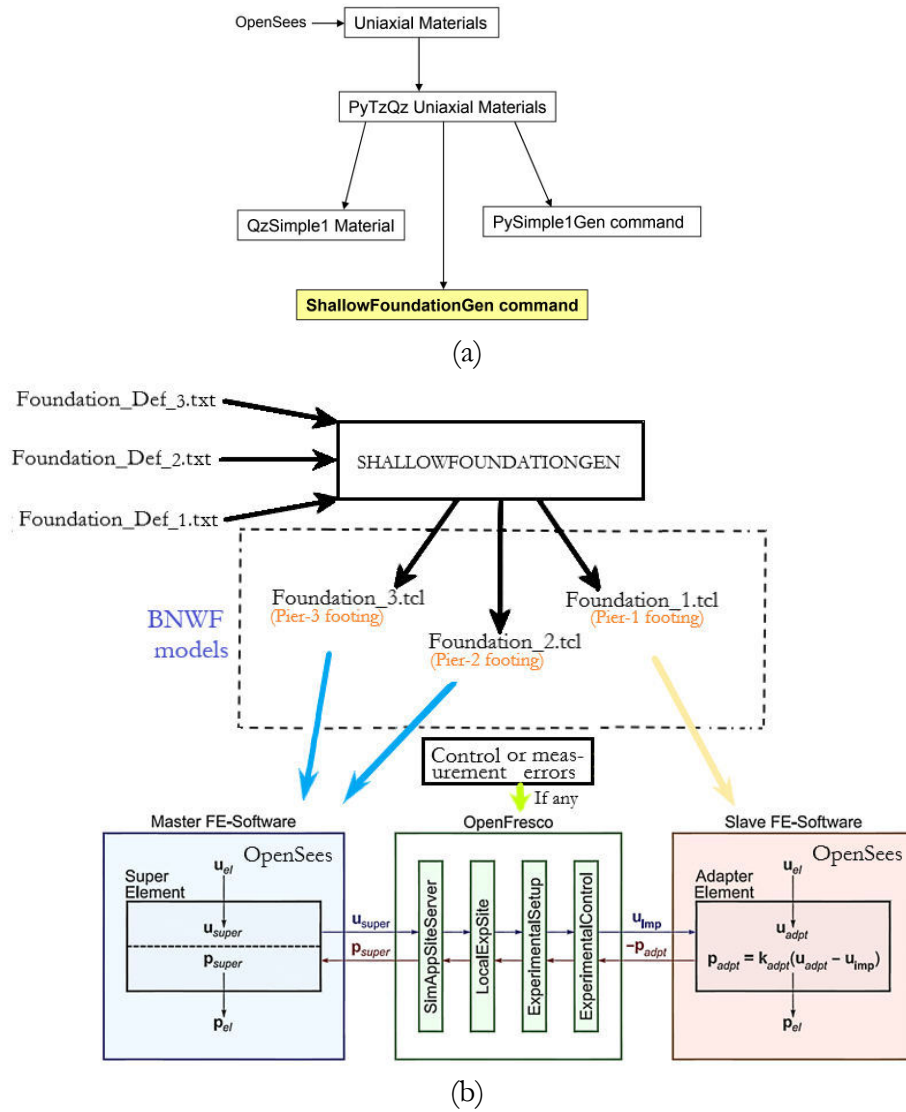


Figure A-4: (a) Hierarchy of ShallowFoundationGen in the uniaxial materials class of the OpenSees software framework; (b) Schematic diagram for conducting a rehearsal hybrid test of the bridge case study (refer to Figure 5-27) using the finite-element coupling approach and the BNWF model for soil-structure interaction

## # INPUT FILE FOR SHALLOWFOUNDATIONGEN

```

# Filename: Foundation_Def_1/2/3.txt
# Written by: Gidewon Goitom Tekeste
# Affiliation: University of Aveiro and LNEC (Gidewon.tekeste@ua.pt and gtekeste@lnec.pt)
# Aim: To pass the geometry of the structural foundation and the soil properties to the
# ShallowFoundationGen class of the OpenSees software. This class generates TCL files of the
# BNWF model which can be sourced in the master and slave programs.
# Units: [kg, m, s]
# Definition of the foundation soil: Soil classes B and C are defined following the EC-8
# stipulated values
# SoilProp $SoilType $c $Phi $Gamma $G $Nu $Crad $Tp

```

### # INFO:

```

# SoilType: SoilType=1 and SoilType=2 represent clayey and sandy soils, respectively
# c: cohesion resistance of soil
# Phi: angle of friction of soil (in degrees)
# Gamma: unit weight of soil
# G: shear modulus
# Crad: viscous damping representing the radiation damping effect
# Nu: Poisson's ratio of soil
# Tp: tension capacity of soil (in fraction)

```

```

SoilProp 2 0.0 45.0 20000 132.1e6 0.4 0.05 0.1; # soil class B: sand
# SoilProp 2 0.0 30.0 18000 36.7e6 0.4 0.05 0.1; # soil class C: sand
# SoilProp 1 150000 0.0 18000 36.7e6 0.4 0.05 0.1; # soil class C: clay

```

```
# FootProp $Lf $Bf $Hf $Df $Ef $Wg $beta
```

### # INFO:

```

# Lf: footing length
# Bf: footing width
# Hf: footing height
# Df: embedment depth
# Ef: Young's modulus of the structural foundation
# Wg: total weight applied to the footing
# Beta: inclination of the load on the foundation with respect to the vertical axis (in
# degrees)

```

```
FootProp 2.84 0.69 0.7 0.7 68.9e9 283.31e6 0.0
```

```
# MeshProp $Rk $Re $le/Lf
```

# Define the above parameters using values reported on 'Numerical Models for Analysis and Performance-Based Design of Shallow Foundations Subjected to Seismic Loading' (Harden et al., 2005).

**# INFO:**

```
#      Rk: stiffness intensity ratio (kend/kmid)
#      Re: end length ratio (Lend/Lf)
#      le/Lf: spacing of vertical springs as a fraction of the total footing length
```

```
MeshProp 2.0 0.1 0.1
```

```
# End of input data
```

**# INPUT FILE FOR MASTER PROGRAM**

```
# Aim: To build a master program for conducting a coupled analysis
```

```
# Units: [kg, m, s]
```

```
wipe
```

```
# Create data directory
```

```
set DataDir OutPut
```

```
file mkdir $DataDir
```

```
# Create ModelBuilder
```

```
model BasicBuilder -ndm 2 -ndf 3
```

```
# Load OpenFresco package
```

```
# Make sure all dlls are in the same folder as openSees.exe
```

```
loadPackage OpenFresco
```

**# Define bridge span length**

```
set spanLen1 27.203
```

```
set spanLen2 23.698
```

```
set spanLen3 32.258
```

```
set spanLen4 30.798
```

**# Define geometry of bridge piers**

```
set PierHeight1 -6.096
```

```
set PierHeight2 -6.576
```

```
set PierHeight3 -6.096
```

```
set PierDia 1.219
```

**# Define geometry of the structural foundation**

```
set FoundWidth 2.743
```

```
set FoundLen 4.572
```

```
set FoundDepth 0.991
```

```
set gammaConcrete 24.0e3
```

```
set Foundmass [expr $FoundWidth*$FoundLen*$FoundDepth*$gammaConcrete/9.81]
```

```
set mleft 124.790e3
```

```
set m1 233.600e3
```

```

set m2      256.700e3
set m3      289.200e3
set mright   141.292e3
# Define axial forces on the piers
set    p1    2288.60e3
set    p2    2515.47e3
set    p3    2834.40e3
# Define structural nodes
node  1     0.0                      0.0
node  2     $spanLen1                0.0
node  3     [expr $spanLen1 + $spanLen2] 0.0
node  4     [expr $spanLen1 + $spanLen2 + $spanLen3] 0.0
node  5     [expr $spanLen1 + $spanLen2 + $spanLen3 + $spanLen4] 0.0
node  6     $spanLen1                [expr
$PierHeight1]
node  7     [expr $spanLen1 + $spanLen2]  [expr
$PierHeight2]
node  8     [expr $spanLen1 + $spanLen2 + $spanLen3]  [expr
$PierHeight3]
node  66   $spanLen1                [expr
$PierHeight1]
# Mass assignment
mass  1     $mleft      1.e-6  1.e-6
mass  2     $m1         1.e-6  1.e-6
mass  3     $m2         1.e-6  1.e-6
mass  4     $m3         1.e-6  1.e-6
mass  5     $mright     1.e-6  1.e-6
mass  6     $Foundmass  1.e-6  1.e-6
mass  7     $Foundmass  1.e-6  1.e-6
mass  8     $Foundmass  1.e-6  1.e-6
# Nodal fixity
fix   1     0     1     0
fix   5     0     1     0
fix   66   0     1     0
#
# Define elements & section properties
#
set    piersectag  1
set    PI       3.1415926
set    ecu      -0.02

```

**# Define section geometry**

```

set    coverPier          50.8e-3; # cover to reinforcing steel in piers
set    numBarsPier_1stLayer 4; # number of longitudinal rebars of the pier (1st layer)
set    numBarsPier_2ndLayer 8; # number of longitudinal bars of the pier (2nd layer)
set    barDia              35.81e-3; # equivalent to #11 US bar
set    barAreaPier         [expr $PI*pow($barDia,2)/4]; # Area of rebar

```

**# Material IDs**

```

set    IDconcU      1; # material ID tag of confined cover concrete
set    IDconcConf    2; # material ID tag of unconfined cover concrete
set    IDreinf       3; # material ID tag of the steel reinforcement
#-----

```

**# Strength of concrete**

```

#-----
set    fc_unconf     [expr -35.00e6]; unconfined concrete strength
set    ft            [expr 1.937e6]
set    conffact      1.420; # pre-calculated confinement ratio
set    fc_conf       [expr $conffact*$fc_unconf]; # confined concrete strength
set    ec            -0.0025
set    ecu           -0.02

```

**# Unconfined concrete**

```

set    fc1U    $fc_unconf; # compressive strength
set    eps1U   $ec; # strain at maximum strength
set    fc2U    [expr 0.2*$fc1U]; # ultimate stress
set    eps2U   $ecu; # strain at ultimate stress
set    Ec      [expr 4700.0*sqrt(-$fc1U/1.e6)*1.e6]; # elastic Modulus

```

**# Confined concrete**

```

set    fc1Conf     $fc_conf; # compressive strength
set    eps1Conf    [expr $eps1U*(1+5*($fc1Conf/$fc1U-1))]; # strain at maximum
strength ecc=eco(1+5*(fc1Conf/fc1U-1))
set    fc2Conf     [expr 0.20*$fc1Conf]; # ultimate stress
set    eps2Conf    $ecu; # strain at ultimate stress

```

**# Tensile strength of concrete**

```

set    ft      [expr $ft]; # tensile strength
set    Ets    [expr $ft/0.0025]; # tension softening stiffness
set    et     0.0025

```

**# Define the properties of steel rebars**

```

set    Fy      413.68e6; # yielding stress
set    Es      210e9; # Young's modulus of steel
set    Bs      0.01; # strain-hardening ratio
set    R0      18
set    cR1     0.925

```

```

set      cR2    0.15

# Define properties of the bridge deck
set      MassDeck   [expr $mleft+$mright+$m1+$m2+$m3]
set      LenDeck    [expr $spanLen1 + $spanLen2 + $spanLen3 + $spanLen4]
set      Adeck      [expr $MassDeck/($gammaConcrete/9.81)/$LenDeck]
set      Edeck      [expr 4700.0*sqrt(-$fc1U/1.e6)*1.e6]
set      Ideck      [expr (1/12*(8*pow(0.2,3)+7*pow(0.14,3)+3*0.2*pow(1.6,3))
                           +8*0.2*pow(0.9,2)+7*0.14*pow(0.87,2))]

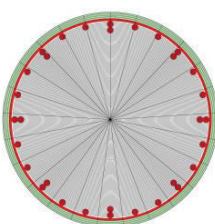
#-----
# Definition of materials and section properties
#-----

# Unconfined concrete
uniaxialMaterial Concrete04 $IDconcU $fc1U $eps1U $eps2U $Ec $ft $et

# Confined concrete
uniaxialMaterial Concrete04 $IDconcConf $fc1Conf $eps1Conf $eps2Conf $Ec $ft $et

# Rebars
uniaxialMaterial Steel02 $IDreinf $Fy $Es $Bs $R0 $cR1 $cR2

# Section properties
section fiberSec $PierSecTag  {


    set numSubdivCirc1 4; # No. of circular divisions on the cover
                          concrete
    set numSubdivRad 25; # No. of radial divisions
    set numSubdivCirc2 50; # No. of circular divisions of the core
                          concrete

# patch circ $matTag $numSubdivCirc $numSubdivRad $yCenter $zCenter $intRad $extRad
<$startAng $endAng>
patch circ $IDconcU $numSubdivCirc1 $numSubdivRad 0.0 0.0 [expr $PierDia/2.0-
$coverPier] [expr $PierDia/2.0] 0. 360.; # cover concrete
patch circ $IDconcConf $numSubdivCirc2 $numSubdivRad 0.0 0.0 0.0 [expr $PierDia/2.0-
$coverPier] 0. 360.; # core concrete

# layer circ $matTag $numBar $areaBar $yCenter $zCenter $radius <$startAng $endAng>
set theta1 [expr 360.0/$numBarsPier_1stLayer]; # increment angle between bars in the 1st layer
layer circ $IDreinf $numBarsPier_1stLayer $barAreaPier 0.0 0.0 [expr $PierDia/2.0-$coverPier-
$barDia/2.] $theta1 360.

```

```

set theta2 [expr 360.0/$numBarsPier_2ndLayer]; # increment angle between bars in the 2nd layer
layer circ $IDreinf $numBarsPier_2ndLayer $barAreaPier 0.0 0.0 [expr $PierDia/2.0-
$coverPier-$barDia*3. / 2.] $theta2 360.

}

# Define geometric transformation

set PierTransfTag 1
geomTransf Corotational $PierTransfTag
set DeckTransfTag 2
geomTransf Linear $DeckTransfTag

# Pier connectivity

set numIntgrPts 5 # number of integration points for force-based element
element nonlinearBeamColumn 1 6 2 $numIntgrPts $PierSecTag $PierTransfTag
element nonlinearBeamColumn 2 7 3 $numIntgrPts $PierSecTag $PierTransfTag
element nonlinearBeamColumn 3 8 4 $numIntgrPts $PierSecTag $PierTransfTag

# Deck connectivity

# element elasticBeamColumn $eleTag $iNode $jNode $A $E $Iz $transfTag <-mass
$massDens> <-cMass>

element elasticBeamColumn 4 1 2 $Adeck $Edeck $Ideck 2
element elasticBeamColumn 5 2 3 $Adeck $Edeck $Ideck 2
element elasticBeamColumn 6 3 4 $Adeck $Edeck $Ideck 2
element elasticBeamColumn 7 4 5 $Adeck $Edeck $Ideck 2

# Foundation connectivity; source TCL files generated by the ShallowFoundationGen
command

set FoundationTag_pier2 2
set FoundationTag_pier3 3
# ShallowFoundationGen $FoundationTag $ConectNode $InputFileName $FootCondition
set Type 5; # Foundation boundary condition for “nonlinear base with nonlinear sliding
allowed”

ShallowFoundationGen $FoundationTag_pier2 7 "Foundation_Defn_2.txt" $Type
ShallowFoundationGen $FoundationTag_pier3 8 "Foundation_Defn_3.txt" $Type
source Foundation_$FoundationTag_pier2.tcl
source Foundation_$FoundationTag_pier3.tcl

```

---

```

#-----
# Define OpenFresco objects
#-----

# Definition of experimental error

# expSignalFilter ErrorSimUndershoot $tag $error; if Sig_i+1> Sig_i, sig=Sig_i+1=Sig_i+1-
error and vice-versa

set error1 0.00; # control and measurement error
expSignalFilter ErrorSimUndershoot 1 $error1

# Control points

# expControlPoint $cpTag <-node $nodeTag> $dof $rspType <-fact $f> <-lim $l $u> <-
isRel>

expControlPoint 1 -node 6 1 disp 2 disp 3 disp
expControlPoint 2 -node 6 1 disp 2 disp 3 disp 1 force 2 force 3 force

# Define experimental control

# expControl SimFEAdapter $tag ipAddr $ipPort <-ctrlFilters (5 $filterTag)> <-daqFilters (5
$filterTag)>
expControl SimFEAdapter 1 "127.0.0.1" 44000 -trialCP 1 -outCP 2 -ctrlFilters 1 0 0 0 0 -
daqFilters 1 0 0 0 0

# Define experimental setup

# expSetup OneActuator $tag <-control $ctrlTag> $dir -sizeTrialOut $t $o <-trialDispFact $f>
expSetup NoTransformation 1 -control 1 -dir 2 1 3 -sizeTrialOut 3 3 -trialDispFact 1 1 1 -
outDispFact 1 1 1 -outForceFact 1 1 1

# Define experimental site

# expSite LocalSite $tag $setupTag
expSite LocalSite 1 1

# Define experimental element

# Stiffness matrix derived for the dry sandy soil, SP-49

set k11 0.308e9
set k12 0.0
set k13 0.0
set k21 0.0
set k22 0.8135E9
set k23 0.0
set k31 0.0
set k32 0.0
set k33 0.1133e9

```

```

# expElement twoNodeLink $eleTag $iNode $jNode -dir $dirs -site $siteTag -initStif $Kij <
orient <$x1 $x2 $x3> $y1 $y2 $y3> <-pDelta Mratios> <-iMod> <-mass $m>
expElement twoNodeLink 10 66 6 -dir 1 2 3 -site 1 -initStif $k11 $k12 $k13 $k21 $k22 $k23
$k31 $k32 $k33 -orient 0 1 0 -1 0 0
#-----
# Gravity analysis
#-----

# Define recorder for gravity analysis

recorder Node -time -file $DataDir/NodeDisp_g.out -node 1 2 6 7 8 -dof 2 disp
recorder Element -file $DataDir/Elementforce_g.out -time -ele 1 2 3 localForce

# Define gravity loads

pattern Plain 1 "Linear" {
    load 2 0.0 [expr -$p1] 0.00
    load 3 0.0 [expr -$p2] 0.00
    load 4 0.0 [expr -$p3] 0.00
}

# Define analysis parameters

system UmfPack
constraints Plain
test NormDispIncr 1.0e-6 1000 0
algorithm Newton
numberer RCM
integrator LoadControl 0.001
analysis Static
analyze 1000
puts "Gravity Analysis completed"

# Eigen Value Analysis: To compute damping and display modal frequencies

set lambda [eigen -fullGenLapack 5]
set omega1 [lindex $lambda 0]
set w1 [expr pow($omega1,0.5)]; # w1 (1st mode circular frequency)
set omega2 [lindex $lambda 1]
set w2 [expr pow($omega2,0.5)]; # w2 (2nd mode circular frequency)
puts "\nEigenvalues at start of transient:"
puts "| lambda | omega | period | frequency |"

```

```

foreach lambda $lambda {
    set omega [expr pow($lambda,0.5)]
    set period [expr 2.0*$PI/$omega]
    set frequ [expr 1.0/$period]
    puts [format "| %5.3e | %8.4f | %7.4f | %9.4f |" $lambda
        $omega $period $frequ]
}
loadConst -time 0.0
remove recorders
#-----
# Graphical display
#-----
set h 100
recorder display "Deformed shape" 20 20 500 500 -wipe
prp $h $h 1
vup 0 1 0
vpn 0 0 1
viewWindow -75 75 -75 75
display 1 5 20
# Define recorder for dynamic time-history analysis
recorder Node -time -file $DataDir/NodeDisp.out -node 1 2 3 4 5 6 7 8 -dof 1 2 3 disp
recorder Node -time -file $DataDir/NodeVel.out -node 1 2 3 4 5 6 7 8 -dof 1 2 3 vel
recorder Node -time -file $DataDir/NodeAccel.out -node 1 2 3 4 5 6 7 8 -dof 1 2 3 accel
recorder Element -file $DataDir/Elementforce.out -time -ele 1 2 3 localForce
# Recorder for footing springs (Left, right or middle)
recorder Node -time -file $DataDir/midSprLdisp.out -node $endFootNodeL_1 -dof 1 2 3 disp
recorder Element -file $DataDir/midSpringLforce.out -time -ele $endSprEleL_1 force
source DynamicAnalysis.tcl; # adds Rayleigh damping and then performs time-history analysis
wipe
exit
# End of analysis

```

**# INPUT FILE FOR SLAVE PROGRAM**

```

# Aim: To build a slave program for conducting a coupled analysis
wipeAnalysis

# Create data directory
set DataDir OutPut
file mkdir $DataDir

# Create ModelBuilder
model BasicBuilder -ndm 2 -ndf 3

# Load OpenFresco package
loadPackage OpenFresco

# Define bridge pier geometry
set PierHeight1 -6.096
set PierDia 1.219

# Define foundation geometry
set FoundWidth 2.743
set FoundLen 4.572
set FoundDepth 0.991
set Foundmass [expr $FoundWidth*$FoundLen*$FoundDepth*24.e3/9.81]

# Define structural nodes
Node 1 0.0 0.0
Node 2 0.0 [expr $PierHeight1]
#-----

# Define elements & sections
#-----
set PierSecTag 1; # assign a tag number to the column section
set PI 3.1415926
set ecu -0.02

# Define section properties
set coverPier 50.8e-3; # column cover to reinforcing steel
set numBarsPier_1stLayer 24; # number of longitudinal bars in the 1st layer
set numBarsPier_2ndLayer 8; # number of longitudinal bars in the 2nd layer
set barDia 35.81e-3; # US bar No.11
set barAreaPier [expr $PI*pow($barDia,2)/4]; # area of rebar

```

**# Material IDs**

```
set IDconcU      1
set IDconcConf   2
set IDreinf       3
```

**# Concrete compressive strength**

```
set fc_unconf    [expr -35.00e6]
set ft           [expr 1.937e6]
set conffact     1.420
set fc_conf      [expr $conffact*$fc_unconf]
set ec           -0.0025
set ecu          -0.02
```

**# unconfined concrete**

```
set fc1U    $fc_unconf
set eps1U   $ec
set fc2U    [expr 0.2*$fc1U]
set eps2U   $ecu
set Ec      [expr 4700.0*sqrt(-$fc1U/1.e6)*1.e6]
```

**# confined concrete**

```
set fc1Conf    $fc_conf
set eps1Conf   [expr $eps1U*(1+5*($fc1Conf/$fc1U-1))]
set fc2Conf    [expr 0.20*$fc1Conf]
set eps2Conf   $ecu
```

**# Concrete tensile strength**

```
set ft        [expr $ft]
set Ets      [expr $ft/0.0025]
set et        0.0025
```

**# Rebar**

```
set Fy        413.68e6
set Es        210e9
set Bs        0.01
set R0        18
set cR1       0.925
set cR2       0.15
```

---

**# Define materials and sections**


---

**# Unconfined concrete**

```
uniaxialMaterial Concrete04 $IDconcU $fc1U $eps1U $eps2U $Ec $ft $e
```

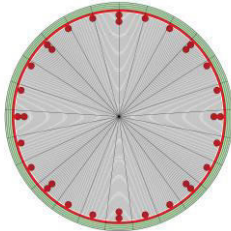
**# Confined concrete**

```
uniaxialMaterial Concrete04 $IDconcConf $fc1Conf $eps1Conf $eps2Conf $Ec $ft $et
```

**#Rebars**

```
uniaxialMaterial Steel02 $IDreinf $Fy $Es $Bs $R0 $cR1 $cR2
```

```
section fiberSec $PierSecTag {
```



```
    set numSubdivCirc1 4; # No. of circular divisions on the cover  
    concrete
```

```
    set numSubdivRad 25; # No. of radial divisions
```

```
    set numSubdivCirc2 50; # No. of circular divisions of the core  
    concrete
```

```
#patch circ $matTag $numSubdivCirc $numSubdivRad $yCenter $zCenter $intRad $extRad  
<$startAng $endAng>
```

```
patch circ $IDconcU $numSubdivCirc1 $numSubdivRad 0.0 0.0 [expr $PierDia/2.0-$coverPier]  
[expr $PierDia/2.0] 0. 360.; # cover concrete
```

```
patch circ $IDconcConf $numSubdivCirc2 $numSubdivRad 0.0 0.0 0.0 [expr $PierDia/2.0-$coverPier]  
0. 360.; # core concrete
```

```
#layer circ $matTag $numBar $areaBar $yCenter $zCenter $radius <$startAng $endAng>
```

```
set theta1 [expr 360.0/$numBarsPier_1stLayer]; # increment angle between bars in the 1st layer
```

```
layer circ $IDreinf $numBarsPier_1stLayer $barAreaPier 0.0 0.0 [expr $PierDia/2.0-$coverPier-$barDia/2.] $theta1 360.
```

```
Set theta2 [expr 360.0/$numBarsPier_2ndLayer]; # increment angle between bars in the 2nd layer
```

```
layer circ $IDreinf $numBarsPier_2ndLayer $barAreaPier 0.0 0.0 [expr $PierDia/2.0-$coverPier-$barDia*3./2.] $theta2 360.
```

```
}
```

```
set PierTransfTag 1
```

```
geomTransf Corotational $PierTransfTag
```

**# Pier connectivity**

```
set numIntgrPts 5
```

```
element nonlinearBeamColumn 1 2 1 $numIntgrPts $PierSecTag $PierTransfTag
```

**# Foundation connectivity**

```
set FoundationTag_pier1 1
```

```
# ShallowFoundationGen $FoundationTag $ConnectNode $InputFileName $FootCondition
```

```
set Type 5; # foundation boundary condition for “nonlinear base with nonlinear sliding allowed”
```

```

ShallowFoundationGen $FoundationTag_pier1 2 "Foundation_Defn_1.txt" $Type
source Foundation_$FoundationTag_pier1.tcl
# element adapter eleTag -node Ndj ... -dof dofNdi -dof dofNdj ... -stif Kij ipPort <-mass
Mij>
element adapter 100 -node 1 -dof 1 2 3 -stif 1e12 0 0 0 1e12 0 0 0 1e12 44000

# Define analysis parameters

system UmfPack
# create the DOF numberer
numberer Plain
# create the constraint handler
constraints Plain
# create the convergence test
test NormDispIncr 1.0e-6 1000
# create the integration scheme
integrator LoadControl 1.0
algorithm Newton
# create the analysis object
analysis Static

# Define recorders

recorder Node -time -file $DataDir/NodeDisp_pier1.out -node 1 2 -dof 1 2 3 disp
recorder Element -file $DataDir/Elementforce_pier1.out -time -ele 1 localForce
recorder Element -file $DataDir/Control_ctrlDsp.out -time -ele 100 ctrlDisp
record
analyze 320000; # Number of model evaluations in the slave can be larger than that of the
master-#program since the master program works with an iterative integrator
wipe
exit
# End of analysis

```

---

## Appendix-5

---

**Ground motion suite for the parametric study on  $S_a(T_1)_{eq}$** 

 Table A-1: Ground motion suite for the  $S_a(T_1)_{eq}$  parametric study

Record	Earthquake	Year	Fault mechanism	$M_w$	$R_{i, B}$	$V_{S,30}$	PGA	PGV	$T_m$	$T_p$
					[km]	[m/s]	[m/s <sup>2</sup> ]	[m/s]	[s]	[s]
1	Big Bear-01	1992	strike slip	6.46	7.31	430.36	5.344	0.345	0.286	2.246
2	Chalfant Valley-02	1986	strike slip	6.19	28.2	359.23	0.786	0.02	0.164	1.705
3	Chi-Chi Taiwan	1999	Reverse	6.20	25.17	305.85	2.804	0.265	0.877	1.723
4	Christchurch	2011	Reverse Oblique	6.20	14.41	280.26	3.928	0.475	0.821	1.723
5	Coalinga-01	1983	Reverse	6.36	28.11	246.07	2.571	0.349	0.917	2.028
6	Dinar	1995	Normal	6.40	0.00	219.75	3.2	0.453	0.892	2.113
7	Friuli Italy-01	1976	Reverse	6.50	14.97	505.23	3.503	0.229	0.4	2.340
8	Irpinia Italy-02	1980	Normal	6.20	20.38	382	0.683	0.036	0.358	1.723
9	Joshua Tree	1992	strike slip	6.10	28.97	425.02	2.105	0.117	0.33	1.556
10	L'Aquila	2009	Normal	6.30	6.35	488.00	1.470	0.097	0.247	1.908
11	Mammoth Lake	1980	Normal Oblique	6.06	1.10	382.12	4.115	0.238	0.326	1.494
12	Morgan Hill	1984	strike slip	6.19	26.42	215.54	0.771	0.095	0.751	1.705
13	Northridge	1994	Reverse	6.05	18.49	316.46	1.548	0.035	0.195	1.478
14	Palm Springs	1986	Reverse Oblique	6.06	29.56	407.61	2.252	0.082	0.246	1.494
15	Parkfield	2004	strike slip	6.00	3.83	378.99	6.082	0.254	0.25	1.405
16	Umbria Marche	1997	Normal	6.00	0.8	317	1.947	0.179	0.606	1.405

## Appendix-6

**Ground motion suite for IDAs of the RC frame tested under the Teixeira Duarte Award (referred to as SPARCS frame)**

Table A-2: Suite of ground motions for the IDAs of the SPARCS frame

Record	Earthquake	Year	NGA west n <sup>0</sup>	Component	Fault mechanism	$M_w$	$R_{j, B}$	$V_{S,30}$	PGA	$T_m$
							(km)	(m/s)	(m/s <sup>2</sup> )	(s)
1	Christchurch	2011	RSN8067	10E	Reverse Oblique	6.2	14.41	280	3.928	0.821
2	Christchurch	2011	RSN8124	86W	Reverse Oblique	6.2	9.43	293	2.832	0.563
3	L'Aquila	2009	RSN4477	1XTE	Normal	6.3	6.35	488	1.470	0.247
4	Parkfield	2004	RSN4067	090	strike slip	6.0	2.35	558	1.674	0.186
5	Parkfield	2004	RSN4070	021	strike slip	6.0	3.83	379	6.082	0.25
6	Parkfield	2004	RSN4074	090	strike slip	6.0	4.36	340	1.844	0.571
7	Parkfield	2004	RSN4081	090	strike slip	6.0	6.27	237	2.462	0.427
8	Chi-Chi_ Taiwan	1999	RSN2457	024N	Reverse	6.2	18.47	428	0.876	0.776
9	Chi-Chi_ Taiwan	1999	RSN2618	065N	Reverse	6.2	25.17	306	2.804	0.877
10	Umbria Marche	1997	RSN4346	000	Normal	6.0	18.86	401	0.770	0.611
11	Umbria Marche	1997	RSN4349	000	Normal	6.0	0.8	317	1.947	0.606
12	Dinar	1995	RSN1141	090	Normal	6.4	0	220	3.200	0.892
13	Northridge	1994	RSN1658	090	Reverse	6.1	18.34	278	1.090	0.323
14	Northridge	1994	RSN1660	090	Reverse	6.1	18.49	316	1.548	0.195
15	Big Bear-01	1992	RSN901	091	strike slip	6.5	7.31	430	5.344	0.286
16	Joshua Tree	1992	RSN6877	180	strike slip	6.1	25.04	292	2.058	0.466
17	Joshua Tree	1992	RSN6876	180	strike slip	6.1	28.97	425	2.105	0.33
18	Griva Greece	1990	RSN815	NS	Normal	6.1	26.75	455	0.495	0.472
19	Palm Springs	1986	RSN521	045	Reverse Oblique	6.1	29.56	408	2.252	0.246
20	Palm Springs	1986	RSN530	000	Reverse Oblique	6.1	10.08	312	1.575	0.497
21	Chalfant Valley-02	1986	RSN551	000	strike slip	6.2	29.35	382	0.589	0.505
22	Chalfant Valley-02	1986	RSN556	270	strike slip	6.2	28.2	359	0.786	0.164
23	Kalamata	1986	RSN564	NS	Normal	6.2	6.45	382	2.340	0.59

24	Morgan Hill	1984	RSN464	255	strike slip	6.2	26.42	216	0.771	0.751
25	Coalinga-01	1983	RSN338	000	Reverse	6.4	28.11	246	2.571	0.917
26	Coalinga-01	1983	RSN346	000	Reverse	6.4	28.58	309	1.310	0.781
27	Mammoth Lake	1980	RSN230	090	Normal Oblique	6.1	1.1	382	4.115	0.326
28	Irpinea Italy-02	1980	RSN297	000	Normal	6.2	14.73	496	0.612	1.05
29	Irpinea Italy-02	1980	RSN303	000	Normal	6.2	20.38	382	0.683	0.358
30	Friuli Italy-01	1976	RSN125	000	Reverse	6.5	14.97	505	3.503	0.4

The spectral accelerations of the ground motion suite, presented in Table A-2, are shown in Figure A-5 together with the comparison between the spectral accelerations of the ground motion suite and that of the input ground motion adopted during the shaking table test of the SPARCS frame.

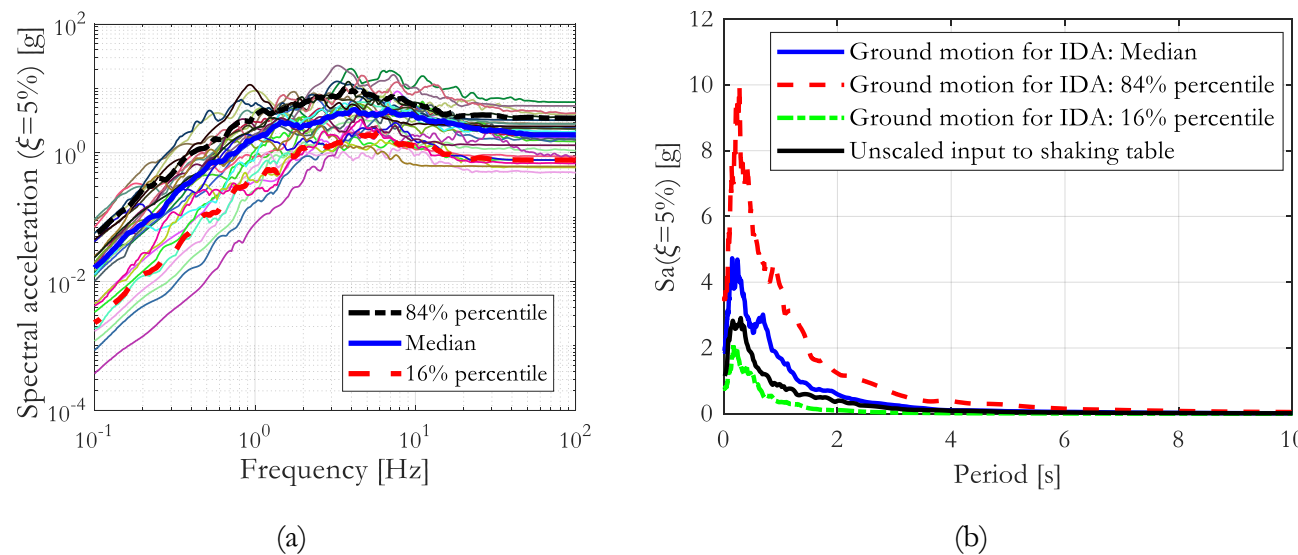


Figure A-5: (a)  $Sa(\xi=5\%)$  of ground motion suite adopted for IDA of the SPARCS frame; (b) spectral acceleration of the ground motion input to the shaking table test and its comparison to earthquake records adopted during the IDAs of the SPARCS frame

---

## Appendix-7

---

### **Bayesian updating of the analytical fragility curves of the SPARCS frame considering the Homogenized Reinforced Concrete (HRC) damage states**

The HRC guidelines for damages states include six levels of damage, namely: slight, light, moderate, extensive, partial collapse, and collapse. These damages states are partially exceeded during the shaking table test of the SPARCS frame, as reflected in Table A-3.

Table A-3: Exceedance parameter,  $\epsilon$ , for the HRC damage states

Stages	$S_a(T_1)$ [g]	$S_a(T_1)_{eq}$ [g]	ISD <sub>max</sub> [mm]	Exceedance, $\epsilon$ , for HRC Damage states (DS)					
				Slight [mm]	Light [mm]	Moderate [mm]	Extensive [mm]	Partial collapse [mm]	Collapse [mm]
1	0.2911	0.2911	7.886	1	0	0	0	0	0
2	0.5822	0.5822	15.475	1	1	0	0	0	0
3	0.9316	0.9316	27.321	1	1	1	0	0	0
4	1.5138	1.5138	42.453	1	1	1	0	0	0
5	2.0960	2.0960	48.323	1	1	1	0	0	0

The results of Bayesian updating of the HRC fragilities, using the MCMC and ATC-58 approaches, are presented in Table A-4. Contrary to the observations reported from the HAZUS damage states, the MCMC gave less conservative estimates compared to the ATC-58 approach, from the standpoint of the capacity of structures to resist earthquake motion, i.e., the MCMC estimates were less fragile, in all damage states except in the slight DS, compared to that of the ATC-58 method (see Figure A-6 for details).

Table A-4: Posterior point estimates of HRC damage states: MCMC vs ATC-58

DS	Prior		Posterior						
			MCMC				UT/ATC-58		
	$\theta'_1$ [g]	$\theta'_2$	AR [%]	$\theta''_1$ [g]	$\sigma_{\theta''_1}$	$\theta''_2$ [g]	$\sigma_{\theta''_2}$	$\theta''_1$ [g]	$\theta''_2$
Slight	0.2040	0.2968	38.32	0.1834	0.0406	0.2944	0.0629	0.1969	0.2947
Light	0.2461	0.2943	35.82	0.3100	0.0648	0.3078	0.0656	0.2947	0.3055
Moderate	0.4650	0.3824	33.56	0.6004	0.1523	0.3966	0.0840	0.5799	0.3963
Extensive	0.8184	0.5443	32.52	2.017	0.7248	0.5577	0.1179	1.5807	0.5463
Partial collapse	1.0826	0.5781	32.79	2.2349	0.8697	0.5881	0.1247	2.0994	0.5853
Collapse	1.2577	0.6010	33.82	2.8045	1.1965	0.6064	0.1290	2.3595	0.6121

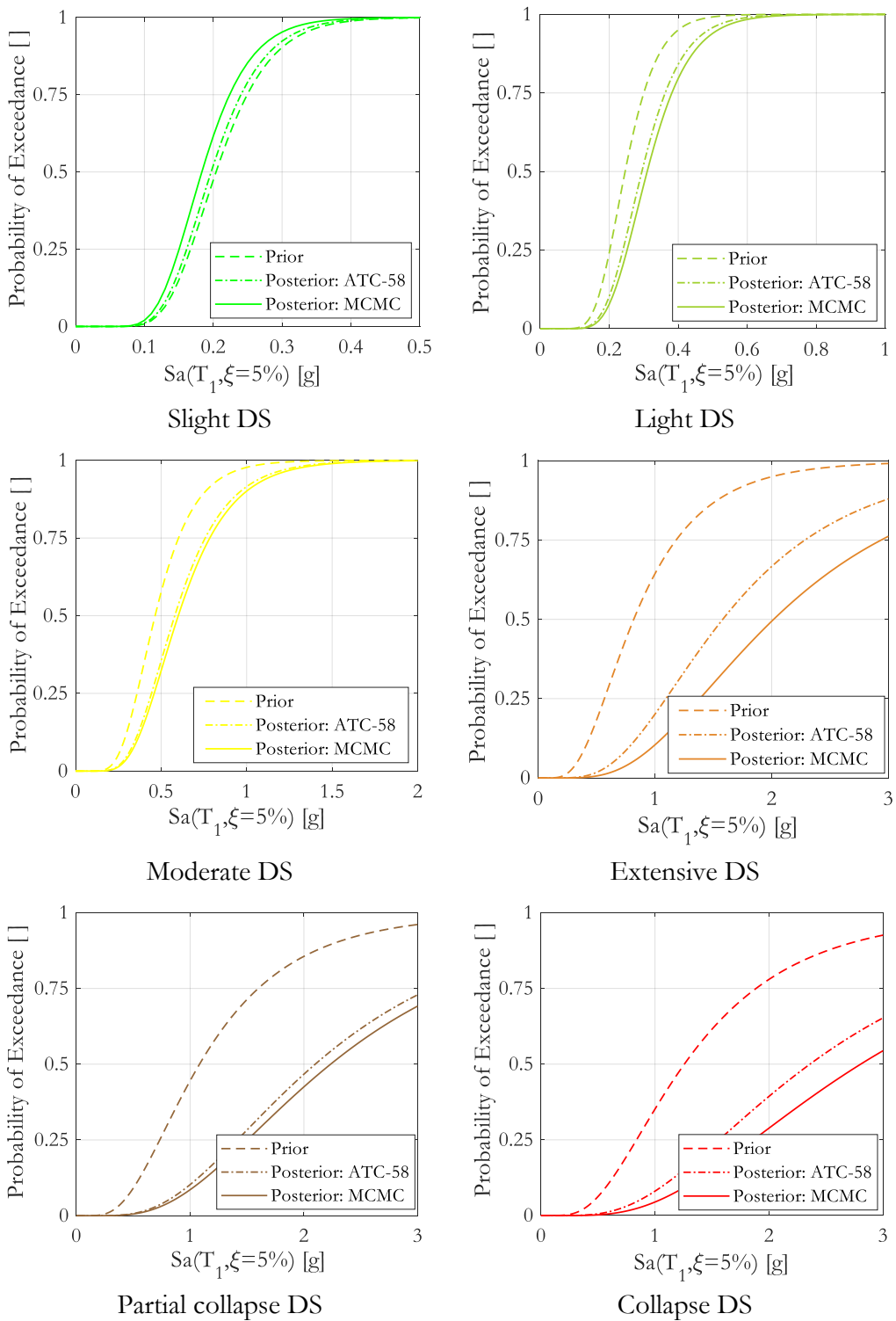


Figure A-6: Bayesian update of SPARCS frame considering HRC damage states